Ultrahigh Charge Density Ion-Exchange Membranes

by

David Kitto

A dissertation submitted in partial fulfillment
of the requirements for the degree of
Doctor of Philosophy
(Chemical Engineering)
in the University of Michigan
2024

Doctoral Committee:

Assistant Professor Jovan Kamcev, Chair
Professor Ronald Larson
Professor Anne McNeil
Associate Professor Nirala Singh

David Kitto

dkitto@umich.edu

ORCID iD: 0000-0001-6863-2731

© David Kitto 2024

Acknowledgements

I cannot fail to acknowledge the host of important individuals who helped me reach this milestone. My doctorate degree has been halfway between a job and a labor of love, making it quite a capstone to my formal education. Starting at the beginning, I absolutely have to thank my parents, Brant and Kristin, for enabling me and encouraging me as far back as I can remember (and, I'm told, even before then). I've had a lot of opportunities to be an experimental child, and they have always been open to learning how to handle what life throws my way. Without your valuing learning and education; or without your valuing curiosity and investigation; or without the life advice you continue to provide, I would have run out of steam long ago. And I can hardly continue this list without mentioning Elizabeth. We bonded over science, and we've learned how to survive grad school alongside one another. I can't even begin to imagine where I'd be without you, so I'm not sure I can list out how important you are. All I know is that your support means the world to me.

I am proud to have helped establish the Kamcev lab at Michigan. Jovan, thank you for taking a chance on me as one of your first students, and thank you for letting me work with you to establish a top-tier membrane research lab. Learning to be a scientist from your vision and precision was such a unique grad school experience, and I appreciate the opportunity to learn this field from the ground up. Carolina and José, you who I spent most of my time with during my degree, and you two made my lab time enjoyable even when the experiments got tedious. You

were my friends and collaborators when the lab peaked at nearly 20 members, but I feel unshakably bound to you from the time when there were just the four of us.

I only got to Michigan by learning the ropes of polymer science at Minnesota. I learned the most basic tenets of research from Chris and Kailong, and I still fondly look back on running projects alongside William in the Ellison lab. This is where I decided on my career path; the details of the past five years started with the undergraduate research experiences I had with you all. Along the way, I also picked up practical engineering experience from my colleagues and mentors at United Technologies. Cody, Josh, both Marks, and Sara, you shared so much of your valuable experience. My time in industry helped shape me into a research engineer, rather than a research scientist.

I also must acknowledge those who have joined Jovan, José Carolina, and I as these five years went on. Mentoring younger students in our lab was the most rewarding part of completing this degree: Jacquelyn, I appreciate you entrusting me to guide your research for three years. I'm so proud of the growth I got to witness as you came into your own as a scientist, and I'm grateful to have bonded with you over the years, from shared shows to photographed birds. As a co-worker, I'm happy to have developed membrane science alongside Greg, Riley, Harsh, Lisby, Debashis, and EJ. And I can't help but be especially proud of bringing chemistry to this engineering lab with Min Gyu, Cass, Leah, Nathan, Wen-Wei, and Anish. I immensely value learning from you all and helping each other cope with grad school, thank you for all the memories. And I can't wait to see what you all accomplish!

Taking a step back, I owe much of my mental health and even-keeled coping to the friends who have helped balance my life and my time. Roscoe friends, including Matthew, Thomas, Tyler, Jacob, and Andrew, have kept me focused on the future and excited about life. I connected with

Ravi, Kolt, Eli, and Grant to celebrate Train Thursday many times, and this kept me grounded in my hobbies and interests. Newer Ann Arbor friends, especially Logan and Kristi, have kept me social in a time when it was easy to get used to staying isolated. And of course, my siblings, Alex, Maura, and Greta, have kept me engaged in the family goings-on despite being so far away from Roscoe.

I have many others I could thank, including professors, mentors, and colleagues. We maybe didn't interact with me weekly, monthly, or even yearly. But I have so many fond memories of enjoying time spent with influential people in my life, which all cumulated into me being here, completing this dissertation. In the interest of time and space, I will end with an acknowledgement for the amazing research community which I found myself in. I had no idea what obscure group of global researchers I'd be joining when I began working on membranes; what a community I found myself in. To membrane scientists, especially Benny and the countless contemporaries I met in the extended Freeman family, thank you for the warm welcome.

Table of Contents

Acknowledgements ii

List of Tables x

List of Figures xii

List of Appendices xvi

Abstract xviii

Chapter 1 Introduction 1

1.1 Water and Energy Management via Electrochemical Technologies 1

1.2 Electrochemical Technologies Need Better Ion-Exchange Membranes 3

1.3 Goals of this Dissertation 7

Chapter 2 Materials and Methods 11

2.1 Monomer and Membrane Preparation 11

2.1.1 Reagents 11

2.1.2 Monomer Syntheses 13

2.1.3 Imidazolium Membrane Syntheses 21

2.1.4 Conventional Membrane Syntheses 23

2.1.5 Commercial Ion-Exchange Membranes 24

2.1.6 Counter-Ion Exchange and Equilibration 31

2.2 Characterization of Membrane Structural Properties 32

2.2.1 Room Temperature Water Content 32

2.2.2 Temperature-Controlled Water Content 33

2.2.3 Polymer and Membrane Densities 34

2.2.4 Charge Content 34
2.3 Characterization of Ion Transport Properties 37
2.3.1 Counter-Ion Sorption 37
2.3.2 Co-Ion Sorption 38
2.3.3 Salt Permeability 39
2.3.4 Salt-Equilibrated Ionic Conductivity 40
2.3.5 Water-Equilibrated Ionic Conductivity 41
2.3.6 Single-Ion Diffusion Coefficients 42
2.3.7 Arrhenius Activation Energy of Ion Diffusion 44
2.4 Supplemental Membrane Characterizations 47
2.4.1 Polymer Gel Fraction 47
2.4.2 Thermogravimetric Analysis (TGA) 48
2.4.3 Differential Scanning Calorimetry (DSC) 48
2.4.4 Dynamic Mechanical Analysis (DMA) 49
2.4.5 Small- and Wide- Angle X-Ray Scattering (SAXS and WAXS) 50
2.4.6 Fourier-Transform Infrared Spectroscopy (FTIR) 52
2.4.7 Raman Spectroscopy 52
2.5 Molecular Dynamics (MD) Methodology 53
2.5.1 Simulation Parameterization 53
2.5.2 IEM Simulation Design 54
2.5.3 Infinite Dilution Simulation Design 57
2.5.4 Simulation Analyses 57
2.6 Literature Reference Data and Statistical Processing 58
2.6.1 Structural Properties of IEMs Reported in the Literature 59
2.6.2 Ionic Diffusivities of Ions in Aqueous Solution at Infinite Dilution 60

2.6.3 Intrinsic Properties of Ions 63
2.6.4 Statistical Correlation Analysis 66
2.6.5 Vibrational Spectroscopy Peak Analysis 67
Chapter 3 Fundamental Models of Ion Transport Phenomena in Charged Membranes 70
3.1 Conductivity and Selectivity Metrics 71
3.2 Donnan Equilibrium and Ion Partitioning in Charged Membranes 73
3.3 The Mackie-Meares Tortuosity Model 76
3.4 Manning's Counter-Ion Condensation Theory 77
3.5 Percolation of Polymer Blends by De Gennes 82
3.6 Backing Effects in Reinforced Ion-Exchange Membranes 84
Chapter 4 The Current State of Ion-Exchange Membranes 86
4.1 Introduction 86
4.2 The Conductivity / Selectivity Trade-Off in IEMs 89
4.3 Structure-Property Relationships in Commercial IEMs 93
4.4 Developments in the Structure of IEMs 96
4.5 The Charge Density of Dry Polymers 101
4.6 Strategies and Potential Challenges for Highly Charged IEMs 103
4.7 Conclusions 107
Chapter 5 Predicting the Conductivity-Selectivity Trade-Off and Upper Bound 109
5.1 Introduction 109
5.2 Model Development 111
5.3 Model Validation 114
5.4 Implications for Designing New IEMs 117
5.5 Conclusions 120
Chapter 6 Fast and Selective Ion Transport in Ultrahigh Charge Density Ion-Exchange Membranes 121

6.1 Introduction 121
6.2 Membrane Structures 123
6.3 Salt-equilibrated Transport Properties 125
6.4 DI Water Equilibrated Transport Properties 128
6.5 Conclusions 130
Chapter 7 Electrostatic Limits to Pursuing High Charge Densities 133
7.1 Introduction 133
7.2 Membrane Structures 135
7.3 Performance and Partition Selectivities of C_nVI_2 IEMs 140
7.4 Counter-Ion Condensation in UHCD IEMs 142
7.4.1 Rationalizing Manning Condensation in Varied-Cross-Linking C_4VI_2 IEMs 145
7.4.2 Rationalizing Manning Condensation in C_nVI_2 IEMs 146
7.5 Critical Onset Phenomena in C_nVI_2 IEMs 149
7.6 Conclusions 152
Chapter 8 Morphological Constraints in Highly Swollen Ion-Exchange Membranes 154
8.1 Introduction 154
8.2 Membrane Structures 157
8.3 Water-Equilibrated Conductivity in Phase Separated Membranes 161
8.3.1 Model Development 163
8.3.2 Comparison Between Model and Experiment 167
8.4 NaCl Partitioning in Phase Separated Membranes 171
8.4.1 Model Development 174
8.4.2 Comparison Between Model and Experiment 176
8.5 Conclusions 178
Chapter 9 Ion-Specific Differences in Diffusion Behavior across Charged Polymer Membranes 181

9.1 Introduction 181
9.2 Modes of Investigation 186
9.3 Activation Energy of Diffusion in the Membranes 187
9.4 Correlating SIEs in IEMs 192
9.5 The Nature of SIE Interactions in IEMs 196
9.5.1 Hydration of Ions in IEMs 197
9.5.2 Ion Pairing in IEMs 203
9.6 The Source of Diffusion Energy Barriers in IEMs 210
9.7 Conclusions 213
Chapter 10 Conclusions and Recommendations 215
10.1 Summary of Conclusions 215
10.2 Recommendations for Future Work 218
10.2.1 Test Additional UHCD IEM Structures 218
10.2.2 Validate the In-Device Performance of UHCD IEMs 219
10.2.3 Determine the Mechanism of Donnan Exclusion in UHCD IEMs 220
10.2.4 Test Predictions of Pearson's HSAB 221
10.2.5 Intensify the use of Data Science IEM Research 221
Appendices 223
Bibliography 317

List of Tables

Table 2.1: Monomer synthesis conditions. 14

Table 2.2: Details of the purchased commercial IEMs. 26

Table 2.3: Structure of commercial IEMs. 29

Table 2.4: Cubic fits of limiting equivalent conductances of ions in aqueous solution. 62

Table 2.5: Tabulated ion parameters. 64

Table 7.1: C_nVI_2 membrane recipes. 136

Table 7.2: C_nVI_2 equilibrium membrane properties. 137

Table 8.1: C_4VI_2 thermal membrane recipes. 159

Table 8.2: C_4VI_2 thermal membrane equilibrium properties. 160

Table 8.3: Saturated network swelling of UHCD IEMs. 178

Table 9.1: Water coordination and hydration numbers. 198

Appendix Table A.1: Symbols and variables used throughout the manuscript. 224

Appendix Table B.1: Condensation in commercial IEMs. 231

Appendix Table D.1: Membrane Synthesis Recipes: 258

Appendix Table D.2: Gravimetric Membrane Properties: 260

Appendix Table D.3: Volumetric Membrane Properties. 260

Appendix Table D.4: Melting enthalpy of water in UHDC IEMs. 264

Appendix Table E.1: Additional C_nVI_2 membrane properties 277

Appendix Table F.1: Additional C_4VI_2 thermal membrane properties 282

Appendix Table G.1: Membrane Recipes. 306

Appendix Table G.2: Gravimetric membrane structural properties. 307

Appendix Table G.3: Volumetric membrane structural properties. 308
Appendix Table G.4: Validation of equivalent circuits at high temperatures. 309
Appendix Table G.5: Accepted ionic conductivities. 310
Appendix Table G.6: Polymerization simulation conditions. 311
Appendix Table G.7: Network incorporation properties. 312
Appendix Table G.8: AEM conversion and hydration properties. 313
Appendix Table G.9: CEM conversion and hydration properties. 314
Appendix Table G.10: Water coordination of ions in dilute aqueous solution. 315
Appendix Table G.11: States of water in the IEM. 316

List of Figures

Figure 1.1: Electrochemical technologies in the Water-Energy Nexus. 3

Figure 1.2: Ion selective transport in ion-exchange membranes (IEMs). 4

Figure 1.3: Anion-exchange membrane water electrolyzer (AEMWE) schematic. 5

Figure 1.4: Electrodialysis (ED) schematic. 6

Figure 2.1: Representative ^{1}H NMR spectrum of C_4VI_2 (400 MHz, DMSO). 15

Figure 2.2: Representative ^{1}H NMR spectrum of C_2VI_2 (400 MHz, DMSO). 16

Figure 2.3: Representative ^{1}H NMR spectrum of C_3VI_2 (400 MHz, DMSO). 17

Figure 2.4: Representative ^{1}H NMR spectrum of C_5VI_2 (400 MHz, DMSO). 18

Figure 2.5: Representative ^{1}H NMR spectrum of C_6VI_2 (400 MHz, DMSO). 19

Figure 2.6: Representative ^{1}H NMR spectrum of C_7VI_2 (400 MHz, DMSO). 20

Figure 2.7: Representative ^{1}H NMR spectrum of C_2VI (400 MHz, DMSO)..... 21

Figure 2.8: Monomer structures used for conventional ion-exchange membrane synthesis. 24

Figure 2.9: Photographs of the commercial IEMs purchased for characterization..... 28

Figure 2.10: A modified Randles equivalent circuit. 46

Figure 2.11: Preparation of IEMs *in silico*..... 55

Figure 3.1: Polymer fixed charge spacing. 79

Figure 4.1: The conductivity / selectivity trade-off for 1 m NaCl. 91

Figure 4.2: Selectivity contributions for commercial IEMs contacting 1 m NaCl. 92

Figure 4.3: Selectivity correlations for commercial IEMs contacting 1 m NaCl. 94

Figure 4.4 Structure of literature IEMs. 98

Figure 4.5 Sorted contour plots. 100

Figure 4.6: Maximum charge densities. 103
Figure 5.1: Model for the conductivity/selectivity upper bound. 114
Figure 5.2: Accuracy in the linearization of the upper bound model. 116
Figure 5.3: Model predictions for future IEMs. 119
Figure 6.1: The IEM performance trade-off. 122
Figure 6.2: Preparation of UHCD IEMs. 124
Figure 6.3: UHCD IEM performance contacting 1 m NaCl. 126
Figure 6.4: UHCD IEM performance contacting DI water. 129
Figure 7.1: C_nVI_2 monomers and membranes. 136
Figure 7.2: C_nVI_2 contour plot. 138
Figure 7.3: States of water in C_nVI_2 IEMs. 139
Figure 7.4: Transport properties of C_nVI_2 IEMs equilibrated with 1 m NaCl. 141
Figure 7.5: Reduced linear charge densities in UHCD IEMs. 144
Figure 7.6: Tacticity in vinylimidazolium IEMs. 147
Figure 7.7: Cross-linker effects on inter-charge spacing. 149
Figure 7.8: Mechanical and scattering properties of C_nVI_2 IEMs. 151
Figure 8.1: Conductivity of highly swollen UHCD IEMs. 156
Figure 8.2: Phase separated membrane appearances. 157
Figure 8.3 Ionic conductivity of IEMs with varied morphology. 162
Figure 8.4: Modeled ionic conductivities in phase separated IEMs. 169
Figure 8.5: Counter-ion transport in phase separated IEMs equilibrated with 1 m NaCl. 172
Figure 8.6: Co-ion transport in phase separated IEMs equilibrated with 1 m NaCl. 173
Figure 8.7: Modeling of co-ion sorption in phase separated IEMs. 177
Figure 9.1: Activation energies of ion diffusion. 189
Figure 9.2: Linear free energy relationships. 191

Figure 9.3: Correlation analysis for membrane activation energies. 194
Figure 9.4: States of water in the IEMs. 201
Figure 9.5: Fixed charge group/counter-ion radial distribution functions. 204
Figure 9.6: Ion pairing detected via vibrational spectroscopy. 206
Figure 9.7: Energy of ion/ion interactions from MD simulations. 209
Figure 9.8: Correlation analysis for mobile ions in the IEM. 212
Appendix Figure B.1: Ion transport properties of commercial IEMs contacting 5 m NaCl. 228
Appendix Figure B.2: Comparison of 1 m and 5 m NaCl ion transport. 229
Appendix Figure B.3: Qualitative structure effects on ion transport. 230
Appendix Figure C.1: The derivation of the Donnan-Meares-Manning model. 233
Appendix Figure C.2: Single-point model predictions. 234
Appendix Figure C.3: Upper bound model inputs. 235
Appendix Figure C.4: Additional model predictions future IEMs. 236
Appendix Figure C.5: Upper Bound Modeling for membranes contacted by 5 m NaCl. 237
Appendix Figure D.1: Membrane FTIR. 266
Appendix Figure D.2: TGA for UHCD IEMs. 267
Appendix Figure D.3: SAXS for UHCD IEMs. 268
Appendix Figure D.4: DMA results for UHCD IEMs. 269
Appendix Figure D.5: Dry membrane DSC for UHCD IEMs. 270
Appendix Figure D.6: Water melting thermograms of UHCD IEMs. 271
Appendix Figure D.7: Freezable and non-freezable hydration numbers of UHCD IEMs. 272
Appendix Figure D.8: Diffusion selectivity of UHCD IEMs. 273
Appendix Figure D.9: Performance improvements of UHCD IEMs. 274
Appendix Figure D.10: Chloride conductivity comparison. 275
Appendix Figure D.11: Unmarked UHCD IEM photo. 276

Appendix Figure E.1: Vibrational spectroscopy of C_nVI_2 IEMs. 278
Appendix Figure E.2: Polymer chain mobility in C_nVI_2 IEMs. 279
Appendix Figure E.3: Thermal degradation of C_nVI_2 IEMs. 280
Appendix Figure F.1: Empirical partitioning equation for homogeneous C_4VI_2 IEMs. 281
Appendix Figure G.1: Water volume fractions. 288
Appendix Figure G.2: Water uptake at various temperatures. 289
Appendix Figure G.3: Arrhenius plots of membrane ion diffusivities. 290
Appendix Figure G.4: Arrhenius plots of aqueous solution ion diffusivities. 291
Appendix Figure G.5: Arrhenius pre-factors for ion diffusion. 292
Appendix Figure G.6: Linear free energy relationships. 293
Appendix Figure G.7: Arrhenius plots of corrected ion diffusivities. 294
Appendix Figure G.8: Arrhenius activation energies of ion diffusion. 295
Appendix Figure G.9: Arrhenius pre-factors for ion diffusion. 296
Appendix Figure G.10: Linear free energy residuals. 297
Appendix Figure G.11: Diffusivity parity lines. 298
Appendix Figure G.12: Pre-polymer simulation equilibration. 299
Appendix Figure G.13: System-level variables during polymerization. 300
Appendix Figure G.14: Chain growth progression. 301
Appendix Figure G.15: Counter-ion/water interactions at infinite dilution. 302
Appendix Figure G.16: Counter-ion /water interactions in IEMs. 303
Appendix Figure G.17: Fixed charge group/water interactions in the IEMs. 304
Appendix Figure G.18: Differential scanning calorimetry thermograms. 305

List of Appendices

Appendix A Mathematical Symbols 224

Appendix B Supplemental Content for Chapter 4 228

Appendix C Supplemental Content for Chapter 5 233

C.1 Supplemental Figures 233

C.2 The Donnan-Meares-Manning Model for the Upper Bound 238

C.3 The Upper Bound Model for Composite Membranes 242

C.4 Alternate Forms of the Upper Bound Model 245

C.4.1 Removing Point-Line Electrostatics (Ideal Donnan Model) 245

C.4.2 Estimating the Reduced Linear Charge Density ξ 248

C.4.3 Condensed Counter-Ion Diffusion Model 248

C.4.4 Upper Bound Model for Multivalent Ions 250

Appendix D Supplemental Content for Chapter 6 256

D.1 Modifications to the Upper Bound Model 256

D.2 Membrane Preparation 258

D.3 Polymer Properties of UHCD IEMs 261

D.4 Transport Properties of UHCD IEMs 264

D.5 Supplementary Figures 266

Appendix E Supplemental Content for Chapter 7 277

Appendix F Supplemental Content for Chapter 8 281

Appendix G Supplemental Content for Chapter 9 283

G.1 Correcting Diffusivities for Obstruction Effects 283

G.2 Validation of Simulated Membrane Structures 285
G.2.1 Pre-Polymer Solutions 285
G.2.2 Polymerization 286
G.2.3 Equilibration 286
G.3 Supplementary Figures 288
G.4 Supplementary Tables 306

Abstract

Electrochemical technologies play a crucial role in industries such as water treatment, resource recovery, energy storage, and power generation. With the growing demand for desalination, hydrogen fuel, and storage of renewable energy, the significance of these technologies will only continue to increase. Central to each of these applications are ion-exchange membranes (IEMs), which are polymers that enable essential ion transport. Given their widespread use in electrochemical devices, advancements in IEM design can significantly enhance the performance of technologies across various industrial sectors.

To improve IEMs, it is crucial to understand the current state of their development and design. This was accomplished by analyzing extensive data sets comprising 40 commercially available IEMs and >1000 membranes reported in the literature. By integrating this diverse data set with state-of-the-art thermodynamic and transport models, we produced the Donnan-Meares-Manning model for the upper bound of selective ion transport in IEMs. This model revealed that tortuosity and charge dilution scale equally and oppositely with the water content of membranes, leading to the observed trade-off between charge selectivity and counter-ion conductivity. Additionally, analysis of this model was able to pinpoint the most promising strategies for enhancing IEM performance: increasing charge contents and increasing diffusion selectivities.

The most direct route to achieving superior ion transport properties was increasing the polymer charge content. Following this direction, we produced ultrahigh charge density (UHCD) IEMs. These unprecedented materials achieved combinations of fast and selective ion transport

previously unreached by commercial and reported IEMs. Case studies on the most selective and most conductive UHCD IEMs refined this design strategy. Specifically, increases in charge contents beyond 8 mol / L[polymer] incurred strong electrostatic penalties which mitigate many of the expected improvements in ion transport properties. Similarly, across multiple morphological membrane structures, increases in water contents beyond 0.66 L[water] / L[membrane] led to a reduction in ion diffusivities due to the generation of non-conductive water domains. Both of these findings provide practical guidance for the continued study of UHCD IEMs and help understand the forces governing ion transport in these materials.

The Donnan-Manning-Meares model also indicated that improved diffusion selectivities would improve membrane performance; however, it is not clear how to prepare membranes meeting this criterion. To develop a better fundamental understanding of how to control the diffusivity of target ions within membranes, we examined the energetics of ion diffusion for 15 ions in representative IEMs. We observed strong ion-specific effects, finding a 0.5 – 13 kJ/mol increase in the energy barrier for ion diffusion in IEMs containing various counter-ions. Supplemental experiments and molecular dynamics simulations helped to isolate the ion softness as a causal predictor of the energy barrier for crossing these membranes. According to Pearson's Hard/Soft Acid/Base theory, the ion softness reflects electrostatic interactions through the malleability of ion hydration shells, suggesting that varying structure of polymeric fixed charge groups will be essential for regulating diffusional selectivity between similar ions. These results could be the first step towards achieving finely tunable control over ion diffusivities in IEMs.

Chapter 1 Introduction

1.1 Water and Energy Management via Electrochemical Technologies

Managing resources to meet rising water and energy demands is increasingly challenging. In our fragile and rapidly changing climate, fresh water reserves in traditionally water-rich locations are strained, and water-poor areas experience longer periods of water shortages[1,2]. As rates of desalination increase to meet water needs, the lack of sustainable brine waste management becomes more problematic. Zero-liquid-discharge (ZLD), which aims to reuse all components of the brine waste, is recognized as the best solution to avoid the environmental impacts of desalination waste; Unfortunately, ZLD technology is not yet mature enough for commercial water treatment plants[3,4]. Ideally, the energy for water production and brine treatment facilities would come from renewable sources[5]. However, establishing this energy infrastructure consumes large amounts of minerals and water[6,7], and operations in the energy sector are some of the greatest consumers of water in the United States[8]. Thus, increasing desalination rates can also significantly increase water consumption. These interdependent challenges require improved resource management strategies.

The ubiquity of integrated and cyclic challenges related to water and energy management has been recognized and addressed by government authorities, who coined the name "Water-Energy Nexus"[7,9]. Solutions to energy problems must avoid an increased dependence on water in the energy sector, especially if water treatment is sourced from energy-intensive technologies. Similarly, solutions to water scarcity must not excessively rely on energy intensive processes, or water demands will rise in turn. More nuanced approaches to the availability and sustainability of

both water and energy are essential in order to reverse the current downward trajectory of the Water-Energy Nexus[8].

Improving existing technologies and developing new technologies in both the water and energy sectors could help address these shortages. Recently, industrial processes across various disciplines have been shifting towards membrane-based technologies. Membranes are valued for their reduced energy footprint because they avoid phase changes, unlike many comparable separation methods[10]. This shift includes the water and energy sectors, which rely on membrane-based electrochemical technologies. Electrochemical devices are utilized in nearly every aspect of the Water-Energy Nexus, including water treatment, resource recovery, waste stream treatment, energy generation, and energy storage (Figure 1.1)[1,5]. Central to each one of these applications are ion-exchange membranes, or IEMs[11–13]. The ability of IEMs to selectively transport charged species, unlike the non-selective diaphragm separators they typically replace, has supercharged the electrochemical industry by enabling the direct production of various chemicals[14,15]. The widespread use of membrane separations means that improved membranes can significantly impact future technological development. This dissertation seeks to address problems within the Water-Energy Nexus by advancing IEMs.

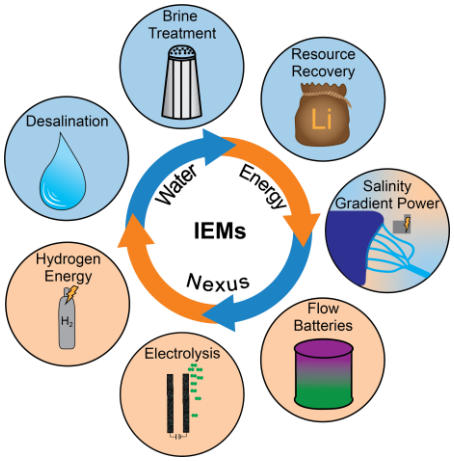


Figure 1.1: Electrochemical technologies in the Water-Energy Nexus.

1.2 Electrochemical Technologies Need Better Ion-Exchange Membranes

IEMs are solvent-swollen charged polymers (Figure 1.2) used to promote and regulate ion transport in electrochemical systems[16–18]. Most often, the use case of IEMs is for an aqueous system, and water is the de-facto solvent for IEMs characterization. Electroneutrality must be maintained in the membrane, so the fixed ions imply the presence of oppositely charged mobile ions. Thus, the immobile ions attached to the polymer create an imbalance in cation and anion transport. The oppositely charged ions are referred to as counter-ions, while the similarly charged ions are referred to as co-ions. With this nomenclature, counter-ion transport is always preferred over co-ion transport. Positively charged membranes create an excess of negatively charged mobile ions and are referred to as anion-exchange membranes (AEMs). Accordingly, negatively charged membranes create an excess of positively charged mobile ions and are referred to as cation-exchange membranes (CEMs). AEMs and CEMs can be used individually or in combination to regulate transport of species in electrochemical devices due to their unique ability to differentiate ions of opposite charge.

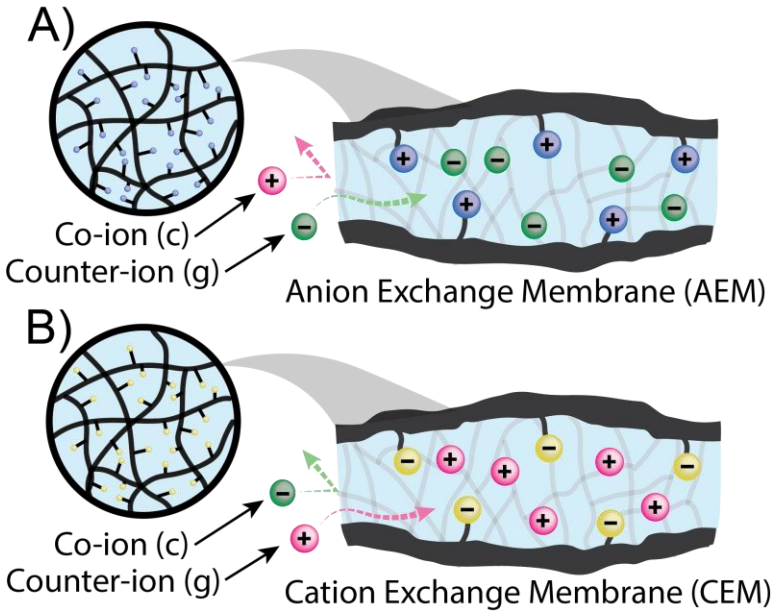


Figure 1.2: Ion selective transport in ion-exchange membranes (IEMs). A) Typical anion-exchange membrane (AEM) structure with cations affixed to the polymer backbone. B) Typical cation-exchange membrane (CEM) structure with anions affixed to the polymer backbone.

Electrochemical devices are often designed around the reaction of specific ions at one or both electrodes. To facilitate device performance, IEMs ensure the correct species reaches the appropriate electrode while limiting the access of undesirable contaminants. One example of this design is an anion-exchange membrane water electrolyzer (AEMWE, Figure 1.3)[15,19]. Water electrolyzers produce sustainable hydrogen fuel for combustion or conversion back into electricity. Modern zero-gap AEMWEs operate with dry cathodes to create higher-value hydrogen and avoid costly drying operations, making it vital for the AEM to allow rapid water transport. Simultaneously, hydroxide ions produced during water reduction must reach the anode by back-diffusing across the AEM. The supporting electrolyte, typically KOH, can leach current if allowed to enter the membrane; the AEM must therefore have high anion conductivity but poor cation conductivity. During operation, the membrane must also prevent mixing of the gases on either side of the membrane-electrode assembly. For successful production of green hydrogen, it is crucial for the AEM to reliably and efficiently perform each of these functions.

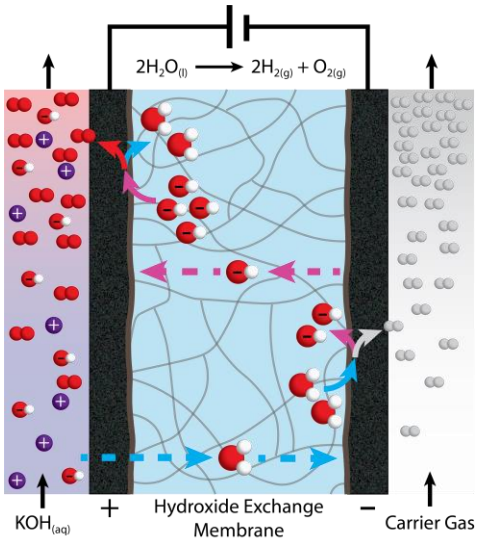


Figure 1.3: Anion-exchange membrane water electrolyzer (AEMWE) schematic.

Other technologies focus solely on ion separations across the membranes instead of reactions at the electrodes. Electrodialysis (ED) is the most common technology of this type, employing alternating pairs of AEMs and CEMs in a membrane stack to desalinate water (Figure 1.4)[20,21]. Within the stack, anions are driven towards the positively charged electrode, while cations are driven in the opposite direction towards the negatively charged electrode. The alternating AEM/CEM pairs facilitate ion transport out of half the chambers in a stack but minimize ion transport out of the other half, provided the IEMs maintain sufficient cation/anion selectivity. The dilute stream of water is the product in ED, so water transport across desalination IEMs must be suppressed; otherwise, osmosis promotes diluate water leakage into the concentrate stream. Although diluate streams contribute significant ohmic losses in a desalination stack, membrane conductivities should be low enough to avoid wasteful energy expenditure spent on membrane conduction. Modifications to traditional ED place additional demands on IEMs, such as facilitating like-charge separations or enabling water splitting, further increasing the reliance on IEM performance[20].

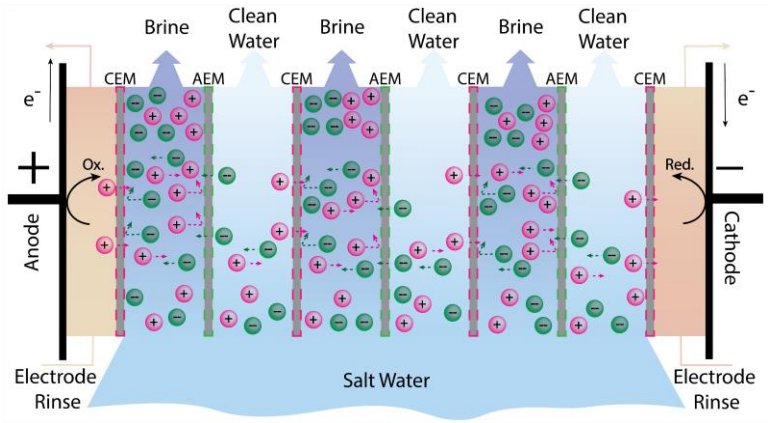


Figure 1.4: Electrodialysis (ED) schematic.

Beyond just enabling transport, the IEM must also survive the operational conditions of electrochemical devices. Historically, the caustic and oxidative stability of IEMs had limited their applications until the commercial availability of Nafion membranes revolutionized the chemical stability of CEMs[22]. Beyond just caustic chemicals, viable membranes must survive pressure gradients, elevated salinities, and poor hydration environments without sacrificing performance[23–25].

In AEMWE, ED, and many other technologies ingrained in the Water-Energy Nexus, membranes have not been optimized to the necessary performance levels. Improvements to IEM can significantly enhance the energy efficiency and energy intensity of commercialized technologies and can even elevate developing technologies into practical viability. For instance, improved IEMs could reduce the levelized cost of water for brackish water desalination via ED, making ED more cost-effective than the current dominant desalination technology in this space, reverse osmosis[26]. Additionally, ED circumvents key issues in brine treatment which have limited other treatment options, but the economics need to be improved via IEM development[27,28]. Selective electrodialysis also has the potential to replace current methods of recovering lithium from brines, so long as IEMs can maintain selectivities while exposed to high salinity solutions[29].

In the energy sector, brine and seawater inputs could facilitate economically competitive electricity production via reverse ED, but this analysis is again contingent on the development of membranes with improved conductivity and selectivity[30,31]. Enhancing IEM hydroxide conductivity is essential for producing green hydrogen using non-platinum-grade catalysis[25]. Increasing water diffusion within the AEM has been shown to improve the operational lifetimes of AEM fuel cells, which presents a significant economic barrier to their adoption[32]. Recently, effective management of cation transport has been identified as a crucial but poorly understood factor for carbon capture/valorization via CO_2 electrolysis, prompting researchers to seek more selective membranes[33–38]. Although there are many means to improve electrochemical device performance, IEMs are a viable route to enhance a myriad of technologies.

1.3 Goals of this Dissertation

In this dissertation, I aim to improve the fundamental understanding of ion transport in IEMs and unlock design strategies to produce IEMs with exceptional ion transport properties. Among all the demands for IEM performance, fast and selective ion transport is a relatively universal requirement that has recently become more thoroughly understood at a fundamental level. These trends highlight the ion transport properties of IEMs as a promising area of investigation. I used thermodynamic and transport models to elucidate membrane structural features with the most potential to improve the speed and selectivity of ion transport in high-performance IEMs. I validated one model prediction by synthesizing custom monomers which enabled the preparation of IEMs with unprecedented combinations of conductivity and selectivity. I followed another model prediction by seeking a clearer understanding of diffusion energy barriers within IEMs, revealing a solvent-mediated interaction which governs ion conduction speeds.

Successfully incorporating these radical IEM design strategies into commercial production will improve the performance of nearly every technology discussed in this section.

The next two chapters detail the experimental techniques, thermodynamic models, and transport models that constitute the foundation of this dissertation. Precise transport characteristics of membranes, supplemented with structural properties and a molecular-level understanding of transport phenomena, enable targeted improvements to the properties of new IEMs which macroscopic device testing simply cannot facilitate.

In Chapter 4, I aim to establish benchmarks for the performance and structure of IEMs. I partnered with my lab mate to survey 40 state-of-the-art membranes available for purchase; by selecting membranes marketed for a wide variety of applications, this extensive survey represents the possibilities currently available for manufacturing IEMs at scale. We characterized the charge content, water content, ion concentrations, and ion diffusivities of these materials to understand the current standard for IEMs. To determine the extent of development past these commercial materials, I also analyzed the structural properties of ~1000 IEMs from ~200 recent publications. Unsurprisingly, IEMs reported in the literature have advanced past commercialized membrane design strategies. Through this extensive collection, I described the advances in IEM design made over recent decades and identified the underexplored avenues for continued improvement.

Leveraging recent advances in modeling ion transport in IEMs, Chapter 5 synthesizes the discrete Donnan-Manning and Meares-Manning models into a single unified equation that predicts the upper bound of ion transport performance in IEMs. This equation was rigorously validated using the commercial membrane data set produced in Chapter 4. My modeling revealed the quantitative origin of the trade-off observed between the ionic conductivity and charge selectivity

of IEMs. I also analyzed the properties which influence the location of the upper bound and assessed their potential to improve ion transport properties of IEMs.

Chapter 5 reveals that the charge density of the dry polymer membrane holds the greatest promise for drastically improving the ion transport properties of IEMs. Following this direction, in Chapter 6 I developed IEMs with exceptionally high charge contents that led to order-of-magnitude improvements in the joint conductivity/selectivity performance compared to commercial IEMs. I designed and synthesized a controlled system of monomers to prepare these "ultrahigh charge density" (UHCD) IEMs, producing a range of different membranes. Combining high charge contents with different water contents resulted in UHCD IEMs designed for both high-selectivity and high-conductivity applications. Furthermore, by using structural descriptions of these new UHCD IEMs in the model from Chapter 5, I accurately predicted the salt-equilibrated and DI water-equilibrated transport properties of these materials. The modeling success demonstrates the method by which UHCD IEMs achieve their outstanding transport properties and provides a fundamental understanding of ion transport in these unique materials.

A simple UHCD framework advanced the conductivity/selectivity trade-off in Chapter 6 but left the high-selectivity and high-conductivity regions unoptimized. In Chapter 7 and Chapter 8, I refine the design strategy of UHCD IEMs to specifically understand the potential for extreme ion transport properties in these materials. Chapter 7 reveals a soft cap on the benefits to be derived from increasing the polymer charge density. These results indicate that electrostatic repulsion degrades IEM selectivities once inter-chain electrostatic effects are comparable to those of intra-chain electrostatic effects. In Chapter 8, I examine the ion transport properties of highly swollen UHCD IEMs. Using two methods to regulate network swelling, I probed the impact of water arrangement within IEMs and vetted two models for ion transport in phase separated membranes.

These results further refine the design strategy for UHCD IEMs by identifying an optimal cross-link density that yields the maximum ionic conductivity for a given polymer chemical structure.

Parallel to the pursuit of UHCD IEMs, Chapter 9 explores another promising route for improved conductivity/selectivity performance: diffusion selectivities. Chapter 5 demonstrated the importance of diffusion selectivities but emphasized that the precise prediction of diffusional speed-ups and slow-downs in IEMs is beyond the capabilities of current models. To understand the nature of counter-ion diffusion in IEMs, I examined the energetics of diffusion within IEMs through the lens of specific ion effects (SIEs). I characterized the energy barrier of transport across representative IEMs, observing strong ion-specific trends. To explain these results, I collaborated with my lab mates to employ data science analyses and molecular dynamics simulations. These techniques helped us develop a molecular-level understanding of counter-ion diffusion in IEMs, supported by supplemental spectroscopic and calorimetric characterizations. We found that the interplay of mobile ion and fixed charge hydration dictates the SIEs in these representative membranes.

Finally, Chapter 10 summarizes these results and reflects on their implications for the future design of improved IEMs. Next steps are identified to continue exploring and understanding transport phenomena in novel IEMs.

Chapter 2 Materials and Methods

The contents of Chapter 2 include the preparation and characterization techniques employed throughout the remainder of this dissertation. This includes laboratory techniques for the synthesis of small molecules and polymers for the purpose of producing membranes and the experimental characterization of membrane properties. Further, for molecular dynamics work in Chapter 9, the preparation and characterization of simulated membranes are included in Section 2.5. Additionally, data repositories representing established commercial membrane properties or reported ion properties are provided, as they will be drawn upon to contextualize and interpret collected data throughout this dissertation.

2.1 Monomer and Membrane Preparation

This section details the preparation of each ion-exchange membrane (IEM) prior to experimental characterization. While some IEMs were purchased, others were polymerized from monomers. Some monomers were commercially available, while other monomers were synthesized prior to polymerization. Each IEM was stored in DI water or aqueous salt solutions prior to characterization to ensure that the IEM contained the ions desired for an experiment.

2.1.1 Reagents

Salts and salt solutions were purchased as follows: Sodium chloride (NaCl, ≥99%), and cesium chloride (CsCl, ≥99.5%) were purchased from Fisher Bioreagents (Fair Lawn, NJ). Cesium Chloride (CsCl, ≥99.999% purity) was purchased from Thermo Scientific (Ward Hill, MA).

Sodium bromide (NaBr, ≥99%), sodium iodide (NaI, ≥99.5%), sodium nitrate ($NaNO_3$, ≥99.0%), ammonium nitrate (NH_4NO_3, ≥98%), and potassium chloride (KCl, 99.0-100.5%) were purchased from Sigma-Aldrich (St. Louis, MO). Sodium fluoride (NaF, 99%) was purchased from Alfa Aesar (Heysham, United Kingdom). Sodium nitrite ($NaNO_2$, ≥97%), sodium sulfate (Na_2SO_4, ≥99%), lithium chloride (LiCl, ≥98.5%), trace metal sulfuric acid (H_2SO_4, 93-98% with <1 ppb metals), trace metal nitric acid (HNO_3, 67-70% with<1 ppb metals), sodium hydroxide (NaOH, ≥97.0%) potassium hydroxide (KOH, ≥85.0%), and hydrogen peroxide (H_2O_2, aqueous, 29.0-32.0%) were purchased from Fisher Chemical (Fair Lawn, NJ). Tetramethylammonium chloride (NMe_4Cl, >99.0%) was purchased from Supelco (Bellafonte, PA). Magnesium chloride solution ($MgCl_2$, aqueous, 1 M) and calcium chloride solution ($CaCl_2$, aqueous, 1 M) were purchased from Honeywell-Fluka (Charlotte, NC).

Solvents were purchased as follows: 1-propanol (certified) was purchased from Fisher Bioreagents (Fair Lawn, NJ). n-heptane (99%) was purchased from Fisher Chemical (Fair Lawn, NJ). Acetonitrile (reagent) and diethyl ether (reagent) were purchased from Fisher Chemical (Fair Lawn, NJ).

Synthesis reagents were purchased as follows: 3-Sulfopropyl methacrylate potassium salt (SPM, 98%), [2-(Methacryloyloxy)ethyl] trimethylammonium chloride solution (MOETMA, aqueous, 75%), and 1-hydroxycyclohexyl phenyl ketone (HCPK) were purchased from Sigma-Aldrich (St. Louis, MO). Gylcerol dimethacrylate (GDMA, mixed isomers, >90.0%), 1-vinylimidazole (VI, ≥98%), and 1,7-dibromoheptane (≥98%) were purchased from TCI Chemicals (Portland, OR). 2,2'-Azobis(2-methylpropionamidine) dihydrochloride (V-50, 98%), bromoethane (98%), 1,2-dibromoethane (99%), and 4-methoxyphenol (99%) were purchased from Thermo Scientific (Ward Hill, MA). 1,3-dibromopropane (98%) and 1,4-dibromobutane (≥98%)

were purchased from Alfa Aesar (Heysham, United Kingdom). 1,5-dibromopentane (98%) and 1,6-dibromohexane (98%) were purchased from Acros Organics (Fair Lawn, NJ).

Throughout the work in this dissertation, Type I Deionized (DI) water was generated using a Mili-Q IQ 7000 Water Purification System (Burlington, MA) which produced 18.2 MΩ•cm and less than 10 ppb TOC.

2.1.2 Monomer Syntheses

The following section describes specific procedure for the synthesis of polymerizable imidazolium monomers. For convenience, the reaction conditions are summarized in Table 2.1. To confirm the successful synthesis of the products, both Nuclear Magnetic Resonance (NMR) spectroscopy and Fourier-Transform Infrared Spectroscopy (FTIR) spectra were collected on each product. ^{1}H NMR was performed using a Varian MR400 400 MHz 9.4 T spectrometer (Palo Alto, CA) at ambient temperature. Attenuated Total Reflectance (ATR)-FTIR was performed using a Thermo Fisher Nicolet Smart iTX iS20 (Billerica, MA). FTIR results were interpreted in the context of previous imidazolium analyses[39]. Diagnostic imidazolium vibrations that indicate quaternization of the imidazole nitrogen atoms are listed for each monomer. For each product, the yield was calculated as the recovered impure product compared against the expected yield of the reaction. The purity and conversion of the product were calculated based on NMR integrations of water and α-protons of the remaining alkyl bromide.

Table 2.1: Monomer synthesis conditions. The concentration of VI, reaction scale, and molar ratios used to prepare the imidazolium monomers in this dissertation.

Monomer	VI Concentration (M)	Reaction Scale (mL)	VI Equivalents (% of R-Br)
C_2VI_2	2	125	250
C_3VI_2	1	250	170
C_4VI_2	1	250	130
C_5VI_2	1	250	170
C_6VI_2	1	250	170
C_7VI_2	1	125	170
C_2VI	1	250	60

3,3'-(butane-1,4-diyl)bis(1-vinyl-3-imidazolium) dibromide (C_4VI_2):

The cross-linker C_4VI_2 as synthesized similarly to previously reported methods[40–42]. A 500 mL round bottom flask was charged with 220 mL of acetonitrile and 1.5 g of polymerization inhibitor 4-methoxyphenol under atmospheric conditions. Then, 11.5 mL (96.3 mmol) of 1,4-dibromobutane and 22.6 mL (250 mmol) of VI were added to the reaction vessel. The light-yellow solution was magnetically stirred for 3 days at 60 ºC. During this time, white solids precipitated onto the walls of the flask. After reacting for 3 days, the solution was cooled, and the acetonitrile was removed via rotary evaporation at 30 ºC. The remaining off-white solid was triturated in ~200 mL diethyl ether to remove unreacted reagents, then collected and washed with additional diethyl ether (~400 mL). The product was then dried under high vacuum at room temperature, yielding a fluffy white solid. This procedure achieved nominally 95 wt% yield with 4 wt% entrained water and 1 mol% unreacted bromide. ^{1}H NMR (400 MHz, $(CD_3)_2SO$) δ: 9.81 (s, H_A), 8.29 (s, H_B), 8.04 (s, H_C), 7.36 (dd, H_D), 6.04 (dd, H_E), 5.41 (dd, H_F), 4.32 (t, H_G), 1.88 (t, H_H) ppm (Figure 2.1). ATR-FTIR: 3059 (w, N-(CH)-N C-H stretch), 1550 (s, ring asymmetric C-N stretch), 1162 (s, ring symmetric C-N stretch), 737 (m, ring C=C asymmetric bend) cm^{-1}.

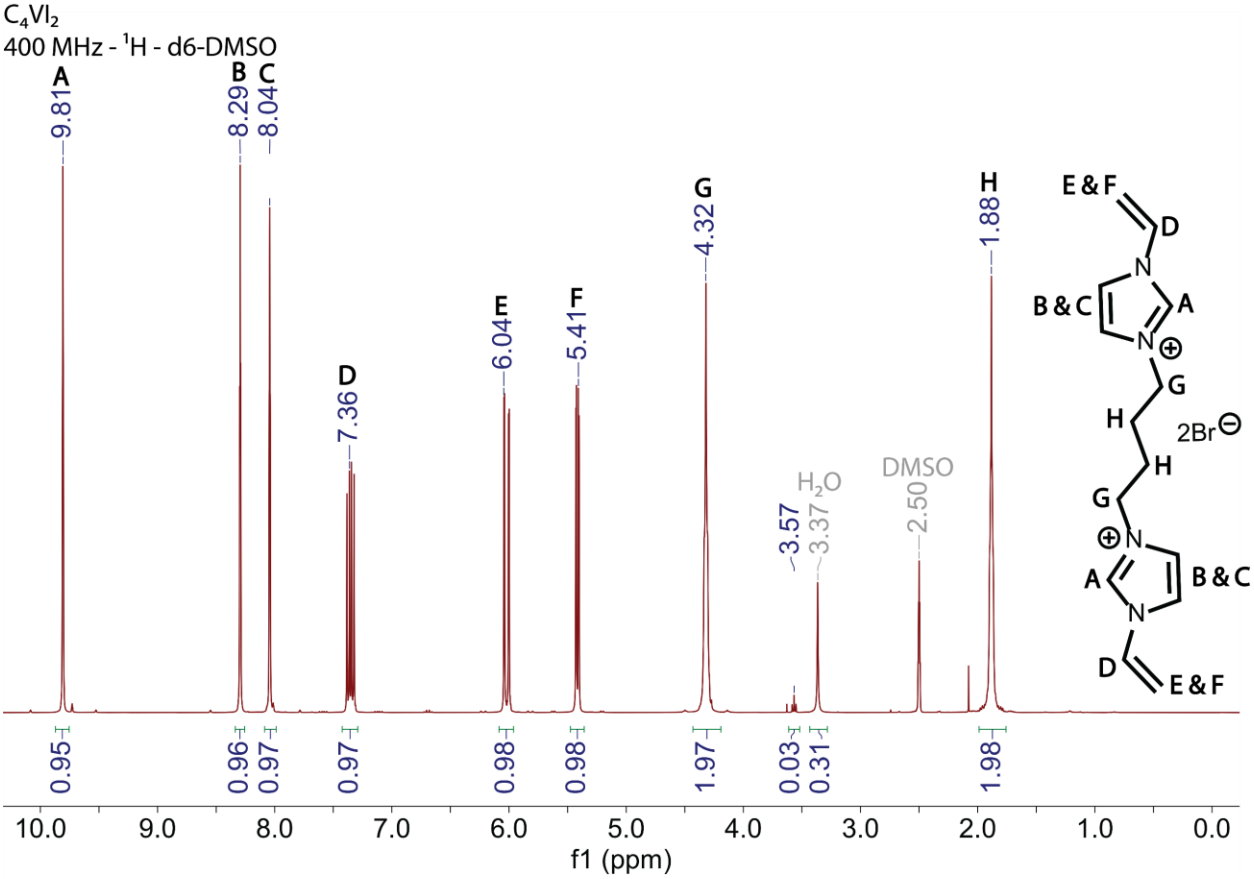


Figure 2.1: Representative ^{1}H NMR spectrum of C_4VI_2 (400 MHz, DMSO).

3,3'-(ethane-1,2-diyl)bis(1-vinyl-3-imidazolium) dibromide (C_2VI_2):

This reaction was carried out similarly to C_4VI_2, but on a smaller scale and using the appropriate bromoalkane. A 250 mL round bottom flask was charged with 110 mL acetonitrile, 1.5 g 4-methoxyphenol, 4.3 mL (49.7 mmol) 1,2-dibromoethane, and 22.6 mL (250 mmol) VI. The dried product was a fluffy white solid. This procedure achieved nominally 100 wt% yield with 20 wt% entrained water and 3 mol% unreacted bromide. ^{1}H NMR (400 MHz, $(CD_3)_2SO$) δ: 9.57 (s, H_A), 8.24 (s, H_B), 7.87 (s, H_C), 7.35 (dd, H_D), 5.89 (dd, H_E), 5.46 (dd, H_F), 4.80 (s, H_G) ppm (Figure 2.2). ATR-FTIR: 3049 (w, N-(CH)-N C-H stretch), 1551 (s, ring asymmetric C-N stretch), 1173 (s, ring symmetric C-N stretch), 768 (m, ring C=C asymmetric bend) cm^{-1}.

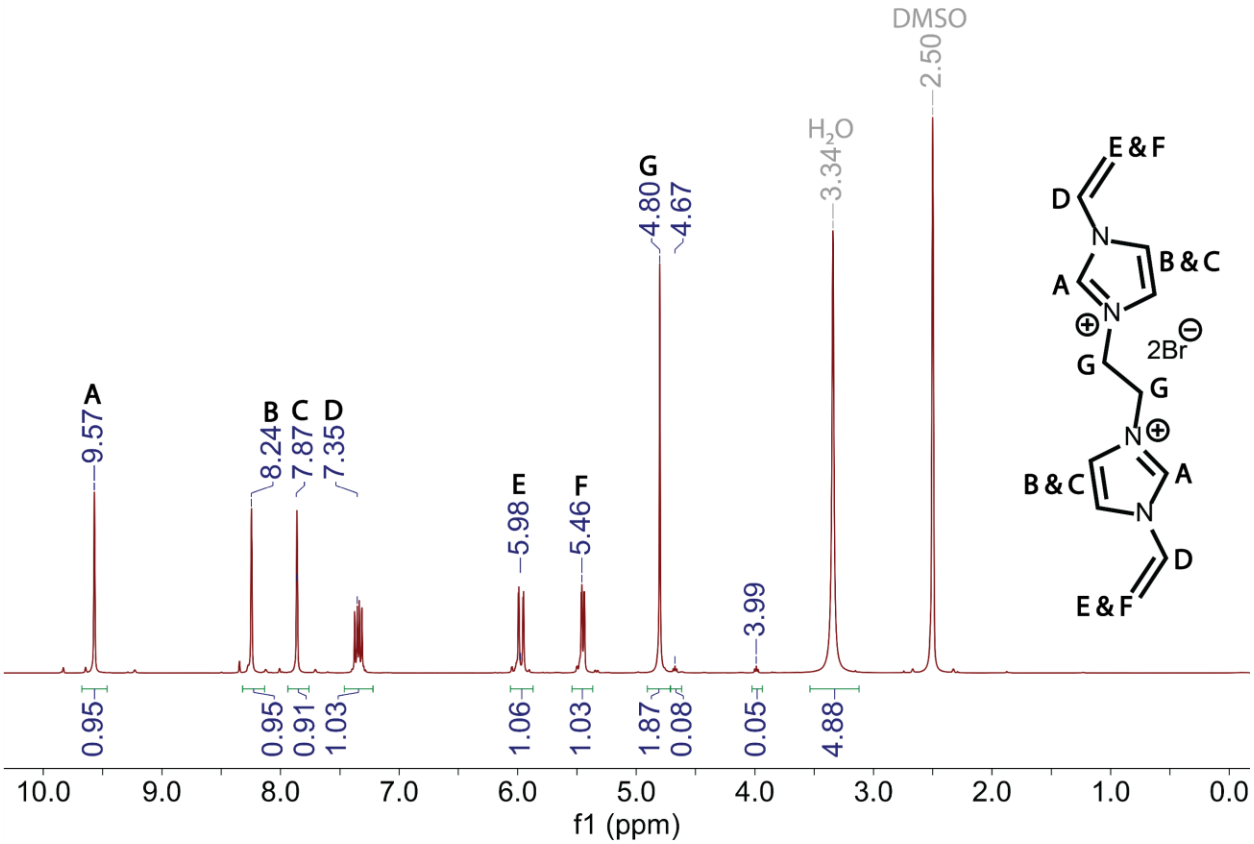


Figure 2.2: Representative ^{1}H NMR spectrum of C_2VI_2 (400 MHz, DMSO).

3,3'-(propane-1,3-diyl)bis(1-vinyl-3-imidazolium) dibromide (C_3VI_2):

This reaction was carried out similarly to C_4VI_2, except the bromoalkane was 7.5 mL (73.6 mmol) of 1,3-dibromopropane. The dried product was a fluffy white solid. This procedure achieved nominally 85 wt% yield with 2 wt% entrained water and 2 mol% unreacted bromide. ^{1}H NMR (400 MHz, $(CD_3)_2SO$) δ: 9.79 (s, H_A), 8.29 (s, H_B), 8.05 (s, H_C), 7.35 (dd, H_D), 6.05 (dd, H_E), 5.44 (dd, H_F), 4.35 (t, H_G), 2.53 (m, H_H) ppm (Figure 2.3). ATR-FTIR: 3032 (w, N-(CH)-N C-H stretch), 1551 (s, ring asymmetric C-N stretch), 1178 (s, ring symmetric C-N stretch), 739 (m, ring C=C asymmetric bend) cm^{-1}.

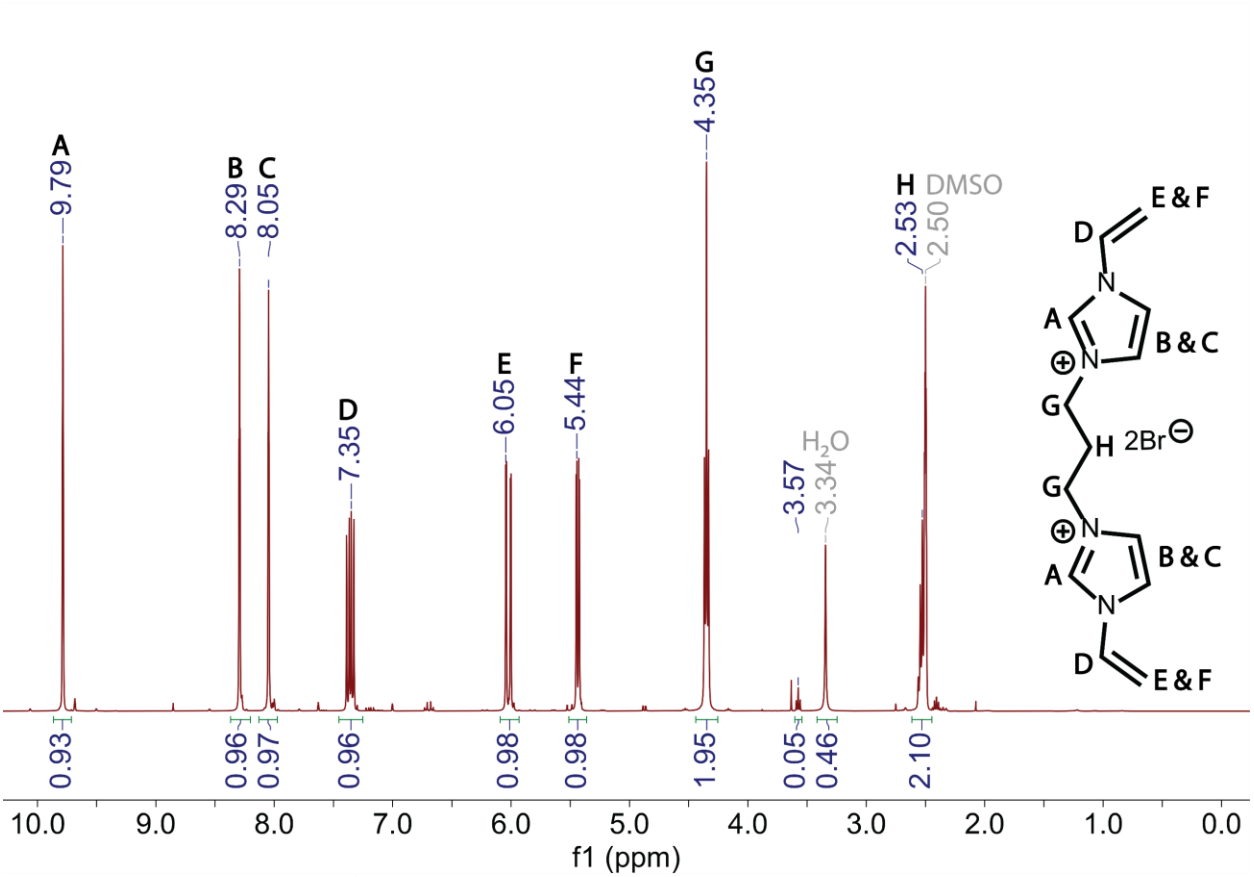


Figure 2.3: Representative ^{1}H NMR spectrum of C_3VI_2 (400 MHz, DMSO).

3,3'-(pentane-1,5-diyl)bis(1-vinyl-3-imidazolium) dibromide (C_5VI_2):

This reaction was carried out similarly to C_4VI_2, except the bromoalkane was 10 mL (73.5 mmol) of 1,5-dibromopentane. The dried product was a fluffy white solid. This procedure achieved nominally 92 wt% yield with 1 wt% entrained water and 1 mol% unreacted bromide. ^{1}H NMR (400 MHz, $(CD_3)_2SO$) δ: 9.81 (s, H_A), 8.29 (s, H_B), 8.05 (s, H_C), 7.36 (dd, H_D), 6.04 (dd, H_E), 5.43 (dd, H_F), 4.26 (t, H_G), 1.90 (m, H_H), 1.27 (m, H_I) ppm (Figure 2.4). ATR-FTIR: 3035 (w, N-(CH)-N C-H stretch), 1550 (s, ring asymmetric C-N stretch), 1172 (s, ring symmetric C-N stretch), 742 (m, ring C=C asymmetric bend) cm^{-1}.

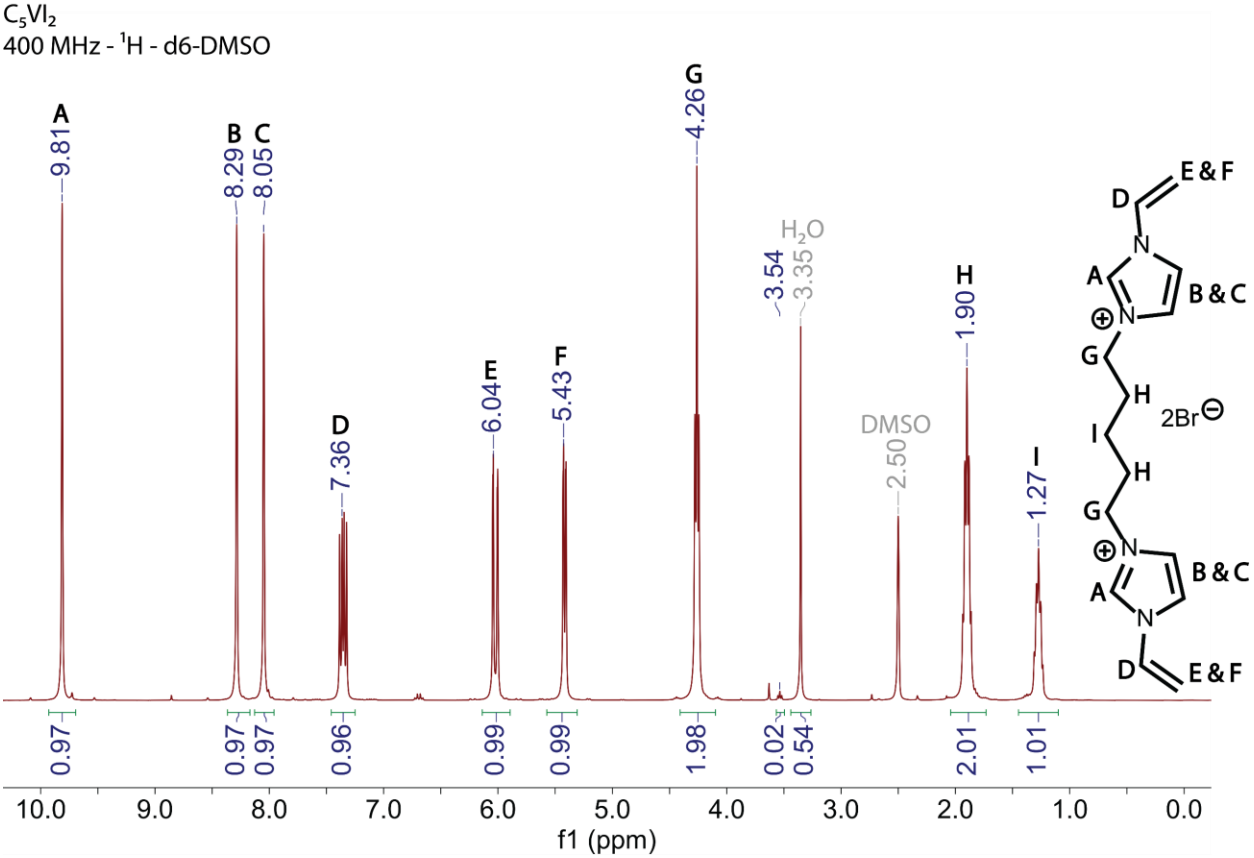


Figure 2.4: Representative ^{1}H NMR spectrum of C_5VI_2 (400 MHz, DMSO).

3,3'-(hexane-1,6-diyl)bis(1-vinyl-3-imidazolium) dibromide (C_6VI_2):

This reaction was carried out similarly to C_4VI_2, except the bromoalkane was 11.3 mL (73.6 mmol) of 1,6-dibromohexane. The dried product was a fluffy white solid. This procedure achieved nominally 93 wt% yield with 2 wt% entrained water and 2 mol% unreacted bromide. ^{1}H NMR (400 MHz, $(CD_3)_2SO$) δ: 9.79 (s, H_A), 8.28 (s, H_B), 8.03 (s, H_C), 7.34 (dd, H_D), 6.04 (dd, H_E), 5.42 (dd, H_F), 4.24 (t, H_G), 1.84 (br t, H_H), 1.30 (br s, H_I) ppm (Figure 2.5). ATR-FTIR: 3071 (w, N-(CH)-N C-H stretch), 1551 (s, ring asymmetric C-N stretch), 1176 (s, ring symmetric C-N stretch), 733 (m, ring C=C asymmetric bend) cm^{-1}.

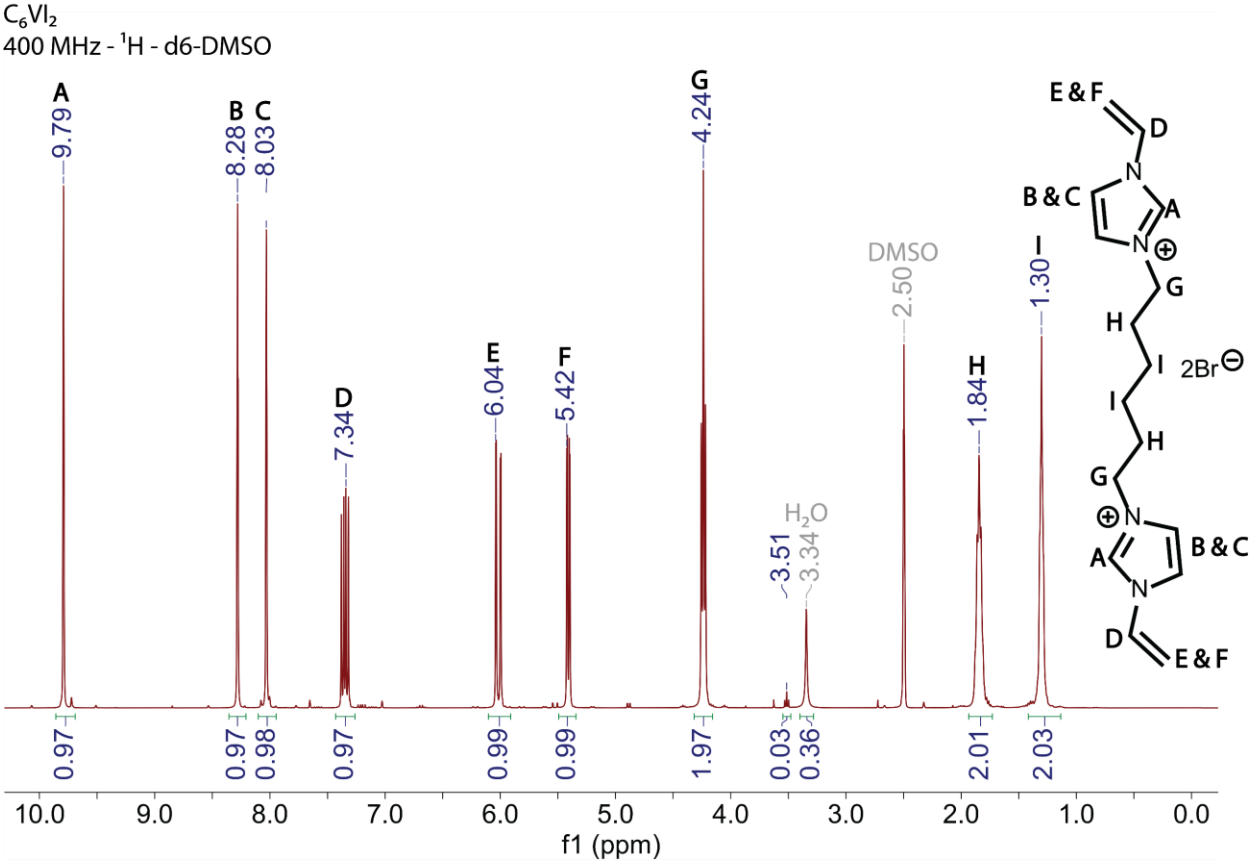


Figure 2.5: Representative ^{1}H NMR spectrum of C_6VI_2 (400 MHz, DMSO).

3,3'-(heptane-1,7-diyl)bis(1-vinyl-3-imidazolium) dibromide (C_7VI_2):

This reaction was carried out similarly to C_4VI_2, but on a smaller scale and using the appropriate bromoalkane. A 250 mL round bottom flask was charged with 110 mL of acetonitrile, 0.75 g 4-methoxyphenol, 6.3 mL (36.9 mmol) 1,7-dibromoheptane, and 11.3 mL (125 mmol) VI. The dried product was a fluffy white solid. This procedure achieved nominally 95 wt% yield with 4 wt% entrained water and 1 mol% unreacted bromide. ^{1}H NMR (400 MHz, $(CD_3)_2SO$) δ: 9.74 (s, H_A), 8.27 (s, H_B), 8.01 (s, H_C), 7.33 (dd, H_D), 6.02 (dd, H_E), 5.42 (dd, H_F), 4.22 (t, H_G), 1.83 (m, H_H), 1.32 (m, H_I), 1.27 (m, H_J) ppm (Figure 2.6). ATR-FTIR: 3039 (w, N-(CH)-N C-H stretch), 1546 (s, ring asymmetric C-N stretch), 1179 (s, ring symmetric C-N stretch), 729 (m, ring C=C asymmetric bend) cm^{-1}.

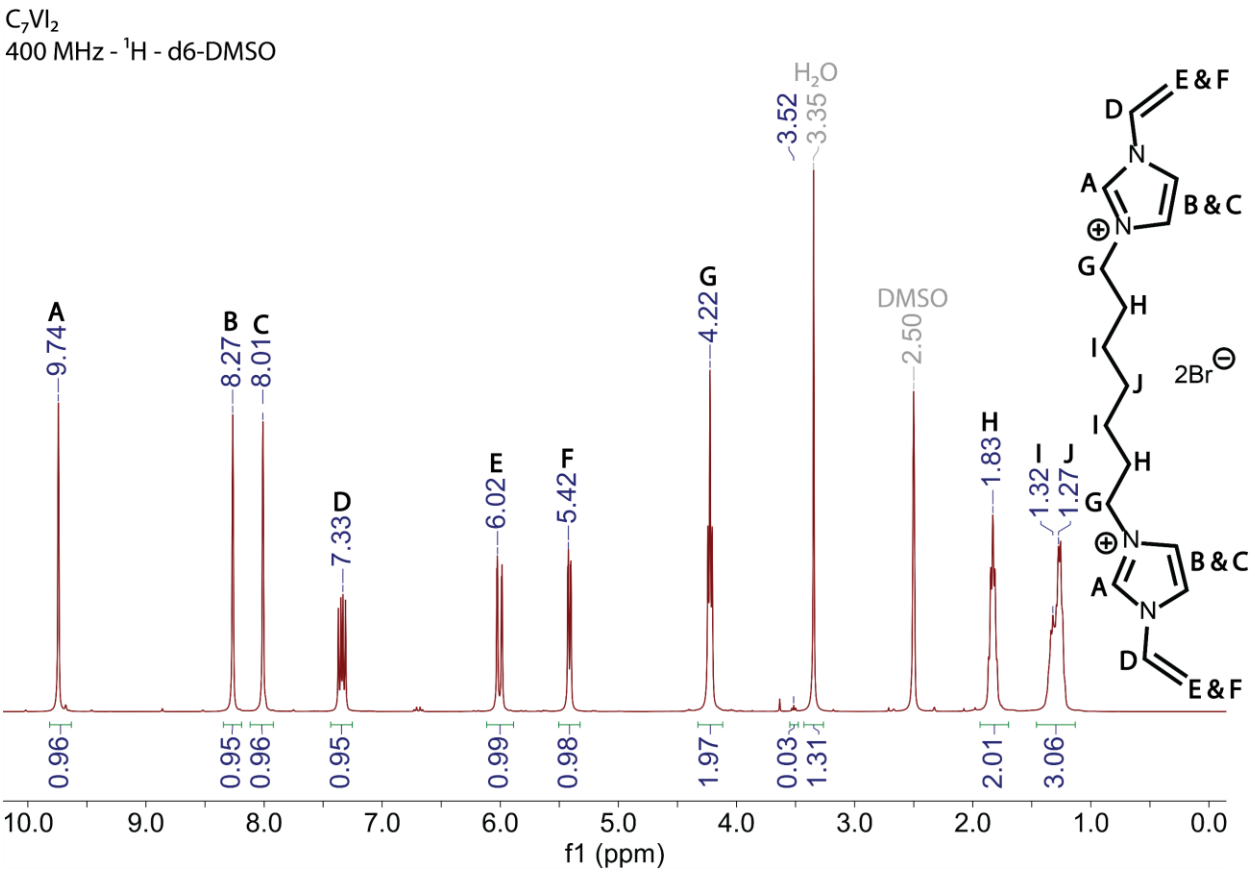


Figure 2.6: Representative ^{1}H NMR spectrum of C_7VI_2 (400 MHz, DMSO).

1-vinyl-3-ethylimidazolium bromide (C2VI):

C_2VI was synthesized similarly to previously reported procedures[43–45]. A 500 mL round bottom flask was charged with 150 mL acetonitrile and 1.5 g of polymerization inhibitor 4-methoxyphenol under atmospheric conditions. Then, 31 mL (418 mmol) of bromoethane and 22.6 mL (250 mmol) of VI were added to the reaction vessel. The light-yellow solution was magnetically stirred for 2 days at 40 ºC. During this time, the reaction media retained a homogeneous appearance. After reacting for 2 days, the solution was cooled, and the acetonitrile was removed via rotary evaporation at 30 ºC, precipitating an off-white slush. The solids were triturated in ~200 mL diethyl ether to remove unreacted reagents, then collected and washed with additional diethyl ether (~400 mL). The product was then dried under high vacuum at room

temperature, yielding a fluffy white solid. This procedure achieved nominally 70 wt% yield with 3 wt% entrained water and no reagent impurities. ^{1}H NMR (400 MHz, $(CD_3)_2SO$) δ: 9.75 (s, H_A), 8.28 (s, H_B), 8.02 (s, H_C), 7.35 (dd, H_D), 6.04 (dd, H_E), 5.41 (dd, H_F), 4.25 (q, H_G), 1.45 (t, H_H) ppm (Figure 2.7). ATR-FTIR: 3056 (w, N-(CH)-N C-H stretch), 1544 (s, ring asymmetric C-N stretch), 1168 (s, ring symmetric C-N stretch), 716 (m, ring C=C asymmetric bend) cm^{-1}.

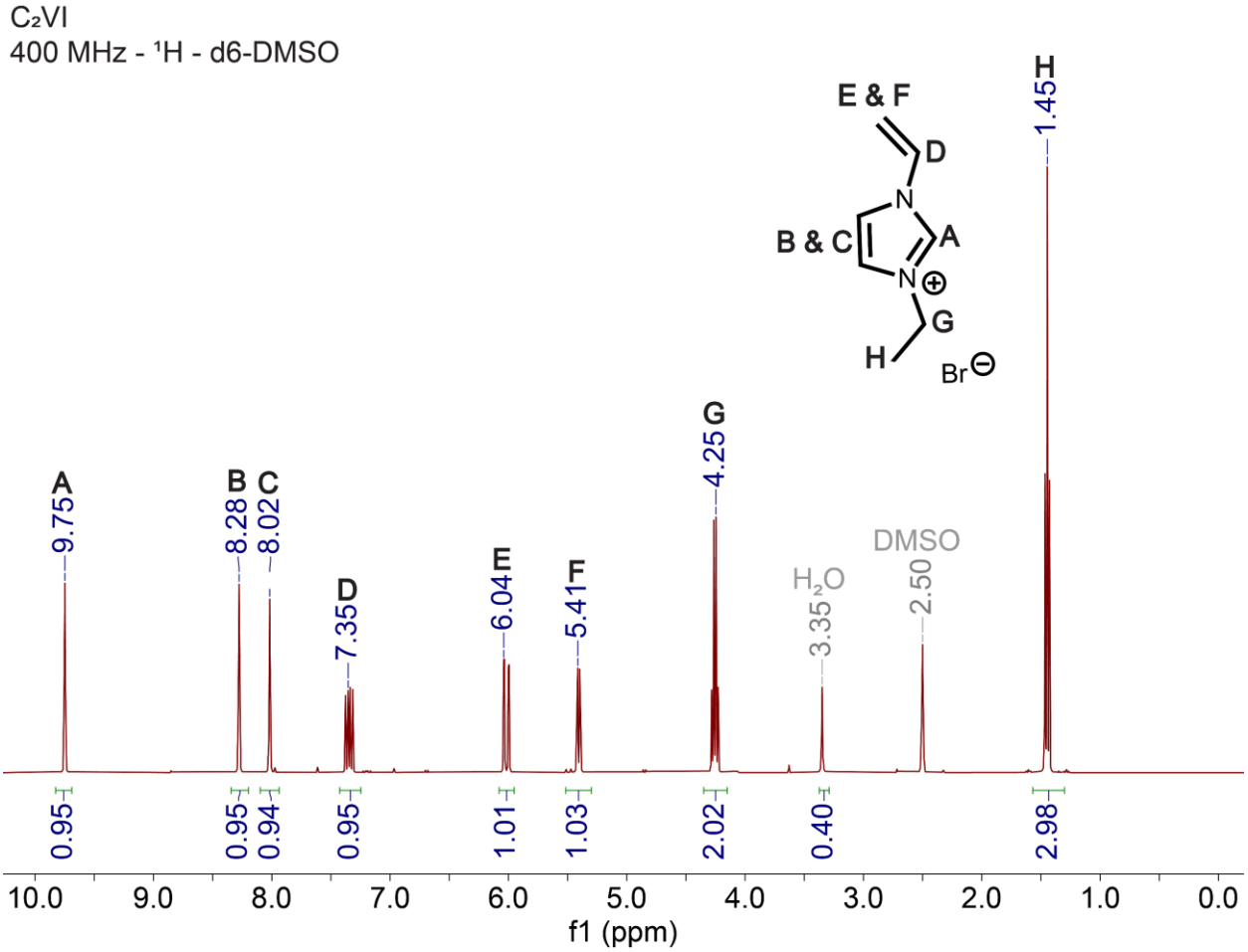


Figure 2.7: Representative ^{1}H NMR spectrum of C_2VI (400 MHz, DMSO).

2.1.3 Imidazolium Membrane Syntheses

Ultrahigh charge density (UHCD) imidazolium membranes were prepared using both thermally-initiated and UV-initiated free radical polymerization techniques. The thermal pre-

polymer solutions were prepared using V-50 as an initiator, while the UV pre-polymer solutions were prepared using HCPK as an initiator. These IEMs utilized the imidazolium monomers synthesized in Section 2.1.2. To prepare either pre-polymer solutions, the prescribed monomer(s) and water were mixed in a 20 mL glass scintillation vial using a magnetic stir bar. The solutions were mixed at 45 ºC, becoming clear and homogeneous after approximately 10 minutes. The appropriate initiator was added and given 10 minutes to dissolve at 45 ºC, affording a clear homogeneous solution again. Pre-polymer solutions for UV-initiated polymerization were ready for use, once the initiator dissolved, but solutions for thermally-initiated polymerization were degassed prior to polymerization. To degas these solutions, the solution was placed under high vacuum until the rate of dissolved gas removal fell below one bubble escape per second.

The densities of the pre-polymer solutions (ρ_{pp}) were measured using five aliquots of solution sampled at room temperature (21 ± 1 °C). 0.5 mL of solution ($V_{aliquot}$) was withdrawn from a well-mixed pre-polymer solution using a 1 mL Eppendorf Xplorer micropipette (Enfield, CT). The liquid was then dispensed onto a Sartorius MCA-125P-2S00 semi-microanalytical mass balance (Gottingen, Germany) where its mass ($m_{aliquot}$) was recorded. ρ_{pp} was calculated as:

$$\rho_{pp} = \frac{m_{aliquot}}{V_{aliquot}} \tag{2.1}$$

Solutions for UV-initiated polymerization were cast between two quartz plates separated by ~300 μm metal spacers. These plates were placed in a Spectronics Spectrolinker XL-1000 UV cross-linking oven (Melville, NY) with 365 nm light bulbs. The solution was approximately 14 cm below the UV bulbs and was exposed to a nominal intensity of 2900 μW/cm^2. The plates were irradiated by UV light for 40 minutes on one side, after which they were separated to recover the membrane. The membrane was immediately placed in DI water. Membranes were allowed to sit

in DI water for at least 24 hours with greater than three solution changes to remove any unreacted monomer.

Solutions for thermally-initiated polymerization were cast between two silanized glass plates separated by ~300 μm metal spacers. The plates were then placed in a Thermo Fisher Scientific (Waltham, MA) HERAtherm 60 L forced convection oven for 40 min at 85 ºC. Afterwards, without separating the glass plates, the membrane and plates were placed in a bath of DI water at 45 ºC. While submerged, the glass plates were slowly separated to allow water to wet the membrane surface. Membrane films were removed and placed in a storage container of DI water. Membranes were allowed to sit in DI water for at least 24 hours with greater than three solution changes to remove any unreacted monomer.

2.1.4 Conventional Membrane Syntheses

In this dissertation, I utilized MOETMA and SPM as the charged monomers to prepare conventional AEMs and CEMs, respectively. GDMA served as a neutral cross-linker and V-50 as a thermal initiator for both the AEMs and the CEMs. The structure of these monomers is shown in Figure 2.8. To prepare a recipe, the prescribed charged monomer, cross-linker, and solvent were mixed with magnetic stirring in a 20 mL glass scintillation vial. The solution became homogeneous after approximately 30 minutes of stirring at room temperature, at which point thermal initiator V-50 was added. The V-50 was allowed to dissolve over another 30 minutes, producing a clear, homogeneous pre-polymer solution. Densities of pre-polymer solutions were measured using the same method described in Section 2.1.3.

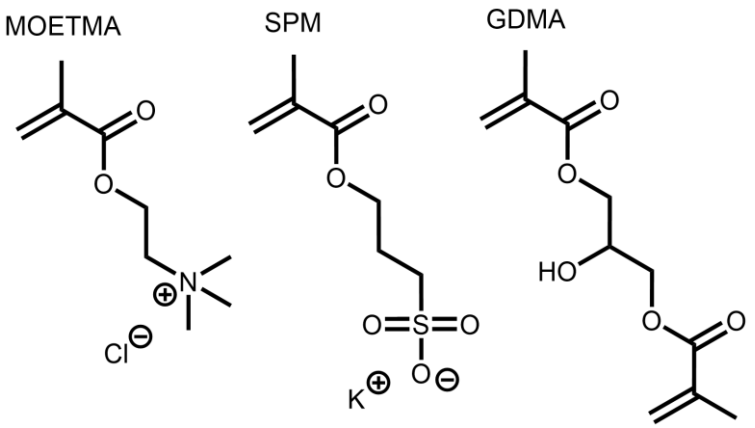


Figure 2.8: Monomer structures used for conventional ion-exchange membrane synthesis.

To run the polymerization, the pre-polymer solution was cast between two glass plates that had been pretreated using a KOH / IPA base bath for 3 hours. Metal spacers were placed between the plates to enforce a membrane thickness of ~300 μm. The plates were then placed in a Thermo Fisher Scientific (Waltham, MA) HERAtherm 60 L forced convection oven for 40 min at 85 ºC. Afterwards, the glass plates were separated and the membrane film was placed in DI water. Membranes were allowed to sit in DI water for at least 24 hours with greater than three solution changes to remove any unreacted monomer.

2.1.5 Commercial Ion-Exchange Membranes

Commercial IEMs designed for various applications were purchased for characterization. We classify membranes into two broad categories based on the advertised application, “Desalination” (electrodialysis, membrane capacitive deionization, etc.) and “Energy” (fuel cell, electrolysis, flow batteries, etc.). The IEMs classified as “Desalination” membranes are: Selemion AMVN and CMVN; Neosepta ASE and CSE; Fujifilm Type 2, 10, and 12 AEMs and CEMs; Fumasep FAB-PK, FAM-PP, FAS, FKB-PK, FKM-PP and FKS; Ralex AMH-PES, AMH-PP, CMH-PES and CMH-PP; Membranes International AMI-7001 and CMI-7000; PCCell PCSA and PCSK; Veolia AR103P, AR213T, CR61P, and CR62T. The membranes classified as “Energy”

are: Nafion 117 and Nafion 212; Sustainion X37-50 Grade RT and B22-50 Grade T; Xergy AEM-Pention-72-15, PEM-Aquivion-830, PEM-Dyneon-800, and PEM-Nafion-1100; Orion AMX and CMX; Solvay Aquivion; and Versogen PiperION.

The commercial IEMs were purchased from various membrane vendors, which are listed alongside the dates of purchase in Table 2.2. Based on manufacturer recommendations, various pre-treatments were necessary upon receipt of the membranes. Chemour and Solvay membranes were boiled in 3 % H_2O_2, then 0.5 M H_2SO_4, and then DI water for one hour each before soaking in DI water for one week. Dioxide Materials membranes were placed backing-up in 1 M KOH at room temperature for 8 hours, followed by backing removal and immersion in 1 M KOH for 16 hours. Orion membranes were placed in 1 M NaOH for 24 hours. Mega-Ralex membranes were placed in DI water for 48 hours. PiperION membranes were placed in 0.5 M NaOH for 2 hours. All IEMs were stored in 0.5 M NaCl after the pre-treatment steps. All IEMs without manufacturer-specified pre-treatments were stored in 0.5 M NaCl immediately after receipt.

This wide array of IEMs possessed various fixed charge groups, polymer backbones, composite structures, and network structures. To document these various structures, we photographed a representative circle of each commercial IEM, presented in Figure 2.9. We also assembled manufacturer technical data sheets and, if available, detailed investigations into the structures of these IEMs. These results are summarized in Table 2.3.

Table 2.2: Details of the purchased commercial IEMs. The membrane name, manufacturer, vendor, and date of receipt for each commercial IEM studied.

Membrane	Manufacturer	Supplier	Date Received
AMVN	AGC-Selemion	AGC Chemicals Americas, Inc.	4/10/2023
CMVN	AGC-Selemion	AGC Chemicals Americas, Inc.	4/10/2023
ASE	ASTOM-Neosepta	Ameridia	3/10/2022
CSE	ASTOM-Neosepta	Ameridia	3/10/2022
Nafion 117	Chemour	Fuel Cell Store	4/13/2022
Nafion 212	Chemour	Fuel Cell Store	3/11/2022
X37-50 Grade RT	Dioxide Materials-Sustainion	Dioxide Materials	8/10/2022
B22-50 Grade T	Dioxide Materials-Sustainion	Dioxide Materials	8/10/2022
Type 12 AEM	Fujifilm	Fujifilm North America Corp.	5/31/2022
Type 12 CEM	Fujifilm	Fujifilm North America Corp.	5/31/2022
Type 10 AEM	Fujifilm	Fujifilm North America Corp.	5/31/2022
Type 10 CEM	Fujifilm	Fujifilm North America Corp.	5/31/2022
Type 2 AEM	Fujifilm	Fujifilm North America Corp.	5/31/2022
Type 2 CEM	Fujifilm	Fujifilm North America Corp.	5/31/2022
FAB-PK	Fumatech BWT GmbH – Fumasep	Fuel Cell Store	9/21/2022
FAM-PP	Fumatech BWT GmbH – Fumasep	Fuel Cell Store	3/11/2022
FAS	Fumatech BWT GmbH – Fumasep	Fuel Cell Store	3/11/2022
FKB-PK	Fumatech BWT GmbH – Fumasep	Fuel Cell Store	3/11/2022
FKM-PP	Fumatech BWT GmbH – Fumasep	Fuel Cell Store	3/11/2022
FKS	Fumatech BWT GmbH – Fumasep	Fuel Cell Store	9/21/2022

Membrane	Manufacturer	Supplier	Date Received
AEM-Pention-72-15	Xergy-XION	FFI Ionix Inc.	4/21/2022
PEM-Aquivion-830	Xergy-XION	FFI Ionix Inc.	4/21/2022
PEM-Dyneon-800	Xergy-XION	FFI Ionix Inc.	4/21/2022
PEM-Nafion-1100	Xergy-XION	FFI Ionix Inc.	4/21/2022
AMX	Orion	Orion	5/25/2022
CMX	Orion	Orion	8/10/2022
AMH-PES	Mega-Ralex	MemBrain	9/16/2022
AMH-PP	Mega-Ralex	MemBrain	9/16/2022
CMH-PES	Mega-Ralex	MemBrain	9/16/2022
CMH-PP	Mega-Ralex	MemBrain	9/16/2022
AMI-7001	Membranes International	Membranes International, Inc.	4/1/2022
CMI-7000	Membranes International	Membranes International, Inc.	4/1/2022
PCSA	PCCell	Pccell GmbH	10/17/2022
PCSK	PCCell	Pccell GmbH	10/17/2022
Aquivion	Solvay	Fuel Cell Store	4/28/2022
AR103P	Veolia-Ionics	Veolia-Ionics	2021
AR213T	Veolia-Ionics	Veolia-Ionics	2021
CR61P	Veolia-Ionics	Veolia-Ionics	2021
CR62T	Veolia-Ionics	Veolia-Ionics	2021
PiperION	Versogen	Fuel Cell Store	3/11/2022

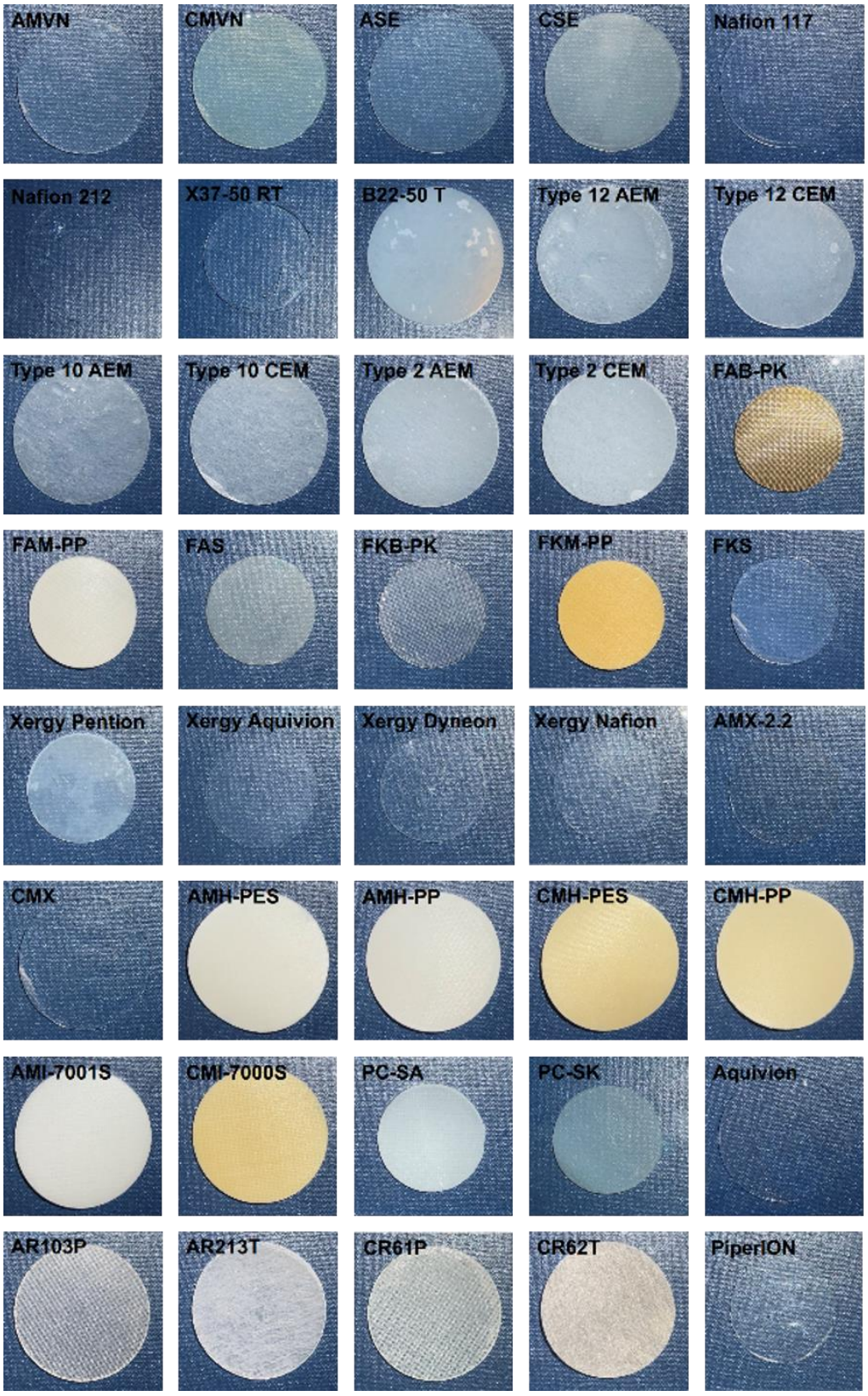


Figure 2.9: Photographs of the commercial IEMs purchased for characterization.

Table 2.3: Structure of commercial IEMs. Known structural information available for commercial IEMs through manufacturer and literature sources.

Membrane Name	Charge	Fixed Charge Group	Backbone	Composite Structure	Cross-linked	Ref.
AMVN	AEM	Trimethyl Ammonium	Styrene	PVC Backing with PVC Binder	Yes	[18,46–49]
CMVN	CEM	Sulfonate	Styrene	PVC Backing with PVC Binder	Yes	[18,46–49]
ASE/AMX-FG	AEM	Trimethyl Ammonium	Styrene	PVC Backing with PVC Binder	Yes	[18,47,50–52]
CSE/CMX-FG	CEM	Sulfonate	Styrene	PVC Backing with PVC Binder	Yes	[18,47,50–52]
Nafion 117	CEM	Sulfonate	Perfluorinated, long-chain	N/A	N/A	[53,54]
Nafion 212	CEM	Sulfonate	Perfluorinated, long-chain	N/A	N/A	[53,54]
X37-50 Grade RT	AEM	Tetramethyl Imidazolium	Styrene	N/A	Yes	[55–58]
B22-50 Grade T	AEM	Tetramethyl Imidazolium	Styrene	ePTFE Pore Filled	Yes	[55,57,59]
Type 12 AEM	AEM	Unknown	Unknown	Polyolefin Backing	Unknown	[60]
Type 12 CEM	CEM	Unknown	Unknown	Polyolefin Backing	Unknown	[60]
Type 10 AEM	AEM	Trimethyl Ammonium	Amide	Polyolefin Backing	Unknown	[51,60]
Type 10 CEM	CEM	Sulfonate	Amide	Polyolefin Backing	Unknown	[51,60]
Type 2 AEM	AEM	Trimethyl Ammonium	Amide	Polyolefin Backing	Unknown	[51,60]
Type 2 CEM	CEM	Sulfonate	Amide	Polyolefin Backing	Unknown	[51,60]

Membrane Name	Charge	Fixed Charge Group	Backbone	Composite Structure	Cross-linked	Ref.
FAB-PK	AEM	Unknown	Unknown	PEEK Backing	Unknown	[18]
FAM-PP	AEM	Unknown	Unknown	PP Backing	Unknown	[18]
FAS	AEM	Unknown	Unknown	N/A	Unknown	[18]
FKB-PK	CEM	Unknown	Unknown	PEEK Backing	Unknown	[18]
FKM-PP	CEM	Unknown	Unknown	PP Backing	Unknown	[18]
FKS	CEM	Unknown	Unknown	N/A	Unknown	[18]
Xergy-Pention 72-15% 30um	AEM	Trimethyl Ammonium	Norbornene	ePTFE Pore Filled	15%	[61–63]
Xergy-Aquivion 830 30um	CEM	Sulfonate	Perfluorinated, long-chain	ePTFE Pore Filled	N/A	[62,64]
Xergy-Dyneon 800 30um	CEM	Unknown	Perfluorinated	ePTFE Pore Filled	N/A	[62,65]
Xergy-Nafion 1100 30um	CEM	Sulfonate	Perfluorinated, long-chain	ePTFE Pore Filled	N/A	[62,66]
AMX-2.2	AEM	Trimethyl Ammonium	Phenylene	Unknown	Unknown	[67–71]
CMX	AEM	Trimethyl Ammonium	Phenylene	Unknown	Unknown	[67–71]
AMH-PES	AEM	Trimethyl Ammonium	Unknown	PES Fabric Backing with PE Binder	Unknown	[72]
AMH-PP	AEM	Trimethyl Ammonium	Unknown	PP Fabric Backing with PE Binder	Unknown	[73]
CMH-PES	CEM	Sulfonate	Unknown	PES Fabric Backing with PE Binder	Unknown	[74,75]
CMH-PP	CEM	Sulfonate	Unknown	PP Fabric Backing with PE Binder	Unknown	[76]

Membrane Name	Charge	Fixed Charge Group	Backbone	Composite Structure	Cross-linked	Ref.
AXM-100S / AMI-7001S	AEM	Trimethyl Ammonium	Styrene	Fabric Backing	Yes	[77]
CXM-200S / CMI-7000S	CEM	Sulfonate	Styrene	Fabric Backing	Yes	[78]
PC-SA	AEM	Trimethyl Ammonium	Unknown	Unknown	Unknown	[79,80]
PC-SK	CEM	Sulfonate	Unknown	Unknown	Unknown	[79,80]
Aquivion E98-15S	CEM	Sulfonate	Perfluorinated, short-chain	N/A	N/A	[81]
AR103P	AEM	Trimethyl Ammonium	Styrene	PP Fabric Backing	Yes	[82,83]
AR213T	AEM	Unknown	Unknown	Polyester Fabric Backing	Yes	[82,83]
CR61P	CEM	Sulfonate	Styrene	PP Fabric Backing	Yes	[82,83]
CR62T	CEM	Unknown	Unknown	Polyester Fabric Backing	Yes	[82,83]
PiperION	AEM	Piperidinium	Phenylene	N/A	N/A	[57,84,85]

2.1.6 Counter-Ion Exchange and Equilibration

It is crucial to ensure that IEMs are equilibrated with a contacted salt solution for equilibrium characterization. Even in DI water, the counter-ion form of the IEM depends on the history of salt exposure, so the salt solution exposure history is of the utmost importance. When contacting DI water, most AEMs were characterized in the chloride (Cl^-)form and most CEMs were characterized in the sodium (Na^+) form. Additionally, all salt-equilibrated membrane experiments in this dissertation were performed on IEMs contacting aqueous NaCl solutions. To convert conventional IEMs to these ion forms, membranes were exposed to 1 M NaCl over the course of three days with at least six solution changes. The developed UHCD IEMs required

additional exposure, so UHCD IEMs were subject to at least 30 solution changes over the course of one week. For DI water characterization, counter-ion converted IEMs were placed in DI water for at least one day with at least three solution changes. Both UHCD and conventional IEMs were equilibrated with salt solutions over three days with at least six solution changes.

To prepare IEMs for DI water characterization in counter-ion forms other than Cl^- and Na^+, a similar procedure was followed. IEMs were exposed to a 1 M salt solution containing the desired counter-ion over three days with at least six solution changes followed by exposure to DI water for at least one day with at least three solution changes. AEMs were converted to the fluoride (F^-) form using NaF, the bromide (Br^-) form using NaBr, the iodide (I^-) form using NaI, the nitrite (NO_2^-) form using $NaNO_2$, the nitrate (NO_3^-) form using $NaNO_3$, and the sulfate (SO_4^{2-}) using Na_2SO_4. CEMs were converted to the lithium (Li^+) form using LiCl, the sodium (Na^+) form using NaCl, the cesium (Cs^+) form using CsCl, the ammonium (NH_4^+) form using NH_4NO_3, the tetramethylammonium (NMe_4^+) form using NMe_4Cl, the magnesium (Mg^{2+}) form using $MgCl_2$, and the calcium (Ca^{2+}) form using $CaCl_2$.

2.2 Characterization of Membrane Structural Properties

To understand how each IEM derives its performance properties, it is essential to characterize the structure of the membrane. This section details the methods to determine the thermodynamic variables which enter into structure-property relationship analyses and modeling.

2.2.1 Room Temperature Water Content

The water content of membranes held at room temperature (21 ± 1 ºC) were determined similarly to previously reported techniques[86]. For each experiment, five membrane samples equilibrated with DI water were randomly selected from a jar containing samples from several

different polymerizations of the same recipe. The hydrated mass (m_{wet}), hydrated surface area (A), and hydrated thickness (ℓ) were collected for membrane samples using a Sartorius MCA-125P-2S00 semi-microanalytical mass balance (Goetingen, Germany), Image-J photo processing, and a Mitutoyo IP65 micrometer (Kawasaki, Japan), respectively. To ensure no extraneous water remained on the surface of the membrane, we quickly blotted both sides of each sample dry using a Kimwipe, moving fast enough to ensure no internal water evaporated from the sample. These samples were then dried under vacuum in a Lab-Line vacuum oven (Thermo Fisher Scientific, Waltham, MA). The samples were periodically removed and weighed until the mass had stabilized, and this stable value was considered the dry mass of the sample, m_{dry}. The water uptake, WU, and water volume fraction, ϕ_w, of the membranes were calculated via:

$$WU = \frac{m_{wet} - m_{dry}}{m_{dry}} \tag{2.2}$$

$$\phi_w = \frac{(m_{wet} - m_{dry})/\rho_w}{A * \ell} \tag{2.3}$$

where ρ_w represents the density of water, assumed to be 1 g/mL.

To accelerate drying, heat typically applied as samples dried in the vacuum oven. However, some counter-ion forms degraded upon exposure to heat. When heated, UHCD IEMs were dried at 110 ºC, while conventional IEMs were dried at 85 ºC. AEMs in the F^-, NO_2^-, and SO_4^{2-} forms were dried under vacuum without heating.

2.2.2 Temperature-Controlled Water Content

The WU of membranes were also measured for IEMs at controlled temperatures. Prior to measurements, hydrated membrane coupons were equilibrated at the measurement temperature for 24 hours. The procedure of measuring m_{wet}, then A, then ℓ was similar to that of the room temperature experiment, except that between each step, the IEM was immersed in a temperature-

controlled solution of DI water. For each step, membranes were out of the water for approximately 20 seconds, then held at temperature in the water for a full minute. Samples were then dried as normal.

2.2.3 Polymer and Membrane Densities

Dried water content samples were also used to determine hydrated membrane and dry polymer densities (ρ_m and ρ_p, respectively). After samples reached their dry mass, they were removed from the vacuum oven a final time and immersed in n-heptane. The measured weight of the immersed sample was recorded as m_{hept}. Samples were then removed and allowed to dry completely. By knowing the density of this auxiliary non-solvent (ρ_{hept}), Archimedes' principle could be used to determine the volume of the dried sample, which often did not retain the simple flat geometry of its hydrated state. With this information, the hydrated membrane and dry polymer densities were calculated according to:

$$\rho_m = \frac{m_{wet}}{A * \ell} \tag{2.4}$$

$$\rho_p = \frac{m_{dry}}{\left(m_{dry} - m_{hept}\right)/\rho_{hept}} \tag{2.5}$$

2.2.4 Charge Content

To determine the charge content of the IEMs, dried samples from water content experiments were treated to remove the counter-ions initially present in the sample (n_g). The removal process varied across different IEMs and counter-ion forms, as outlined below. Once a solution containing counter-ions was obtained, the concentration of ions was determined. Metal cation concentrations were determined using an Agilent 4210 Microwave Plasma Atomic Emission Spectrometer (MP-AES, Agilent, Santa Clara, CA) using an aqueous nitric acid matrix.

Organic cation concentrations were determined using a Dionex IonPac cation-exchange chromatograph (Thermo Fisher Scientific, Waltham, MA) with aqueous methanesulfonic acid as the mobile phase. All anion concentrations were determined using a Dionex Integrion anion-exchange chromatograph (Thermo Fisher Scientific, Waltham, MA) with aqueous potassium hydroxide as the mobile phase. Knowing the concentration and volume of the solution allowed calculation of n_g for the sample.

Commercial and UHCD IEMs were always subject to a staged desorption technique to remove counter-ions. AEMs were placed in an initial volume of 0.03 m NaI, while CEMs were placed in 0.03 m trace metal grade CsCl. After 24 hours, the initial volume of solution was removed and replaced with additional desorption solution. This process was repeated 4-5 times. After complete desorption, the solution from each stage was combined and the total desorption volume was fixed to 250 mL. These solutions were then characterized via elemental analysis as described above.

The conventional lab-made AEMs in various counter-ion forms were desorbed slightly differently. SO_4^{2-} form membranes were subject to the same procedure as the commercial AEMs, but F^-, Cl^-, Br^-, NO_2^-, and NO_3^- form membranes were treated to a single-stage 100 mL desorption solution. To characterize I^- form samples, a staged desorption was performed using 1 M Na_2SO_4.

Conventional lab-made CEMs in organic counter-ion forms were subject to a staged desorption similarly to the commercial CEMs, except the desorption solution was 0.01 m $MgCl_2$. Conventional lab-made CEMs in metal counter-ion forms were not desorbed, but were instead digested using piranha solution. Dry membranes in the Li^+, K^+, Cs^+, Mg^{2+}, and Ca^{2+} form were placed in a 20 mL scintillation vial alongside 4 mL piranha solution (a 3:1 mixture of H_2SO_4 and

H_2O_2) that was prepared *in-situ*. Piranha solutions were heated to 50 ºC and stirred for 3 days. After 24 hours, membranes were reduced to small pieces, and after 48 hours, the solutions appeared homogeneous and possessed no signs of insoluble membrane pieces. These piranha solutions were diluted using the nitric acid matrix for analysis. To mitigate Na^+ leaching from borosilicate scintillation vials, 8 mL screw-cap pyrex test tubes were used for dry membranes containing Na^+. Na^+ samples were otherwise treated identically to the other digestion samples.

Once samples were processed to obtain n_g, by electroneutrality, the number of fixed charge groups in the membrane could also be calculated. For divalent ions, this required accounting for the counter-ion valence in the electroneutrality charge balance (z_g). Charge contents, including the ion-exchange capacity (IEC), the fixed charge density ($C_A^{m,t}$), the fixed charge concentration ($C_A^{m,w}$), the membrane hydration number (λ), and the maximum charge density (C_A^{max}) were calculated according to:

$$IEC = \frac{|z_g| n_g}{m_{dry}} \tag{2.6}$$

$$C_A^{m,t} = \frac{|z_g| n_g}{A * \ell} \tag{2.7}$$

$$C_A^{m,w} = \frac{|z_g| n_g}{(m_{wet} - m_{dry})/\rho_w} = \frac{1}{\lambda \bar{V}_w} \tag{2.8}$$

$$C_A^{max} = \frac{|z_g| n_g}{(m_{dry} - m_{hept})/\rho_{hept}} \tag{2.9}$$

Here, $\bar{V}_w$ represents the molar volume of water in the membrane, which is assumed to be the bulk value of 18 mL/mol.

When working with divalent ions, it is necessary to assess whether stray cations or anions disrupted the charge balance between fixed charge groups and divalent counter-ions. Based on the

counter-ion conversion procedure described in Section 2.1.6, extra Na^+ or Cl^- ions could have been present. In the randomized structure of an IEM, an isolated charge group may create a situation where a divalent counter-ion electroneutralizes one fixed charge and one mobile ion, even when equilibrated with DI water. To verify that this did not occur in the IEMs studied here, we digested SO_4^{2-} form AEM coupons to confirm that no Na^+ was detected. Similarly, we digested then neutralized Mg^{2+} and Ca^{2+} form CEM coupons to confirm that no Cl^- was detected. For every IEM tested in divalent counter-ion forms, no stray ions were detected.

2.3 Characterization of Ion Transport Properties

The transport of ions across IEMs can be measured using both concentration gradient-driven and electric potential-driven transport. Both forms of ion motion can give insight into the nature of diffusion within the IEMs when coupled with the concentrations of diffusing species. This section details the characterization techniques for ion transport properties in IEMs contacting both salt solutions and DI water.

2.3.1 Counter-Ion Sorption

The counter-ion concentration in membranes equilibrated with aqueous NaCl solutions was measured using the drying and NaI and CsCl multi-stage desorption techniques employed for membrane water charge content determination (see Sections 2.2.1 and 2.2.4). Briefly, samples which had been equilibrated with an external NaCl solution characterized to determine m_{wet}, A, and ℓ. Then, after carefully blotting sample surfaces dry with a KimWipe, membrane coupons were fully dried in a heated vacuum oven until a stable mass was achieved. For membranes with a high amount of salt partitioning, salt crystals were observed to form within the membranes upon drying. These samples were handled carefully to ensure that the entire amount of salt remained

within the sample. The dried samples were then subject to the multi-stage desorption procedure, and the desorption solution was analyzed via elemental analysis. The counter-ion concentration in the membrane at each external salt concentration was calculated via:

$$C_g^{m,t} = \frac{n_g}{SA * \ell} \tag{2.10}$$

$$C_g^{m,w} = \frac{n_g}{(m_{wet} - m_{dry})/\rho_w} \tag{2.11}$$

Here, $C_g^{m,t}$ is the counter-ion concentration per volume of hydrated membrane, and $C_g^{m,w}$ is the counter-ion concentration per volume of water in the membrane. This experiment also permitted calculation of the salt-equilibrated water contents via Equations 2.2 and 2.3.

2.3.2 Co-Ion Sorption

Co-ion concentrations in membranes equilibrated with NaCl salt solutions were determined via a DI water desorption technique. Membranes coupons were characterized to determine m_{wet}, A, and ℓ similarly to the counter-ion concentration experiments. Then, after carefully blotting sample surfaces dry with a KimWipe, membrane coupons were immersed in DI water for at least two days to allow the mobile salts to desorb from the membrane. To ensure this process resulted in a quantifiable concentration of co-ions in the desorption solution, the solution volume was adjusted based on the membrane size. For example, 100 mL of DI water was used for membranes thicker than 100 μm, while 50 or 25 mL of DI water was used for membranes thinner than 100 μm. The moles of co-ions (n_c) in the desorption solution (Cl^- for CEMs and Na^+ for AEMs) were measured using elemental analysis. The co-ion concentration in the membrane was calculated via:

$$C_c^{m,t} = \frac{n_c}{SA * \ell} \tag{2.12}$$

$$C_c^{m,w} = C_c^{m,t}/\phi_w \tag{2.13}$$

Here, $C_c^{m,t}$ is the co-ion concentration per volume of hydrated membrane, and $C_c^{m,w}$ is the co-ion concentration per volume of water in the membrane. ϕ_w is the water volume fraction of membrane equilibrated with the external salt solution, which was determined during the counter-ion concentration experiment.

2.3.3 Salt Permeability

The salt permeability coefficients of the membranes contacting aqueous NaCl solutions were measured using custom PermeGear side-by-side jacketed glass diffusion cells (Hellertown, PA) according to a previously reported procedure[87]. A single membrane equilibrated with DI water was placed between two butyl rubber gaskets, and the rubber-membrane-rubber stack was clamped between the diffusion cells. The rubber gaskets prevented the leakage of solution during the experiments. The openings in the cells and gaskets were aligned to ensure a clearly defined area of 1.77 cm^2 for salt transport across the membrane. The downstream side was filled with 34 mL DI water, and the upstream side was filled with 34 mL of aqueous salt solution. Each chamber was magnetically stirred and sealed with Teflon stoppers and Parafilm. The temperature of the solutions was regulated by flowing 22 ºC water through the jacketed chambers using a Fisher Isotemp 4100 R20 bath circulator (Pittsburgh, PA). A WTW LR 325/01 conductivity probe (Weilheim, Germany) was placed in the downstream chamber to track the change in solution conductivity as a function of time. The probes were calibrated with NaCl standards to allow conversion of the measured conductivity to the salt concentration. Salt permeability experiments lasted between 10 minutes and 48 hours, where lower permeabilities required a longer measurement duration. Once the experiment was completed, the cells were emptied of solution and disassembled, and the thickness of the exposed membrane area was quickly measured. The salt permeability coefficient (P_s) was calculated via:

$$P_s = \left(\frac{V\ell}{2A}\right)\frac{d}{dt}\left(\ln\left(1 - \frac{2C_s^{s,r}[t]}{C_s^{s,d}[0]}\right)\right) \quad 2.14$$

In this equation, V is the volume of solution in each chamber, A is the area of membrane exposed for transport, ℓ is the membrane thickness, t is the time, $C_s^{s,d}[0]$ is the concentration of the upstream chamber at time $t = 0$, and $C_s^{s,r}[t]$ is the concentration of the downstream chamber at time t. The slope was evaluated in the pseudo-steady state regime, after transient effects were observed to have completely dissipated.

2.3.4 Salt-Equilibrated Ionic Conductivity

The ionic conductivity of membranes equilibrated with external NaCl solutions was measured via electrochemical impedance spectroscopy (EIS) employing the direct-contact method in the through-plane configuration. We utilized our recently-developed stacking technique we develop and thoroughly detail in our methods papers[88,89]. The main points are summarized below.

Through-plane conductivity experiments were performed at room temperature (21 ± 1 ºC). The stacking technique we utilized required at least eight individual coupons of a given IEM. The membrane coupons were assembled into stacks of either 1, 2, 3, or 4 membranes, and the stacks were then treated as single samples for the duration of the measurement. The thickness of the stacked samples was recorded using a Mitutoyo IP65 micrometer (Kawasaki, Japan) and the stack was compressed between two 1.27 cm diameter gold-plated copper electrodes in a BioLogic sample holder (Knoxville, TN). The compressed electrodes were in turn sealed in a BioLogic controlled environment sample holder (CESH). A BioLogic SP-300 potentiostat was used for the collection of EIS scans at 100 mV oscillating voltage over a frequency range of 3 MHz to 100 Hz. The single x-intercept of the resultant Nyquist plot was taken as the total resistance of the cell containing the loaded sample. After a membrane stack was characterized, the membranes were

separated, re-mixed, and new stacks were randomly assembled. This process was repeated until at least two replicates of each stack size were measured. The membrane ionic conductivity (κ) was calculated via:

$$\kappa = \frac{d\ell}{d(R_c A_x)} \tag{2.15}$$

Here, R_c is the cell resistance, A_x is the cross-sectional area available for conduction, and ℓ is the path length between the electrodes. In the through-plane configuration, ℓ is the thickness of the membrane stack, and A_x is the area of the electrodes.

2.3.5 Water-Equilibrated Ionic Conductivity

The ionic conductivity of membranes equilibrated with DI water was measured using EIS employing the direct-contact method in the in-plane configuration. To isolate the membrane impedance response, we utilized the varying length technique from our recent conductivity methods paper[88]. This experiment is similar to that for the stacking method through-plane ionic conductivity measurements described in Section 2.3.4, but with slight modifications. To measure the in-plane ionic conductivity, we utilized rectangular samples 20 – 30 mm long and 2 – 8 mm wide. In addition to the thickness, the exact width of membrane coupons was determined as the average of three measurements using Fowler Ultra-Cal V 6" calipers (Valencia, CA). Samples were placed across four perpendicular 1 cm long gold-plated copper electrodes. Samples were again compressed against these electrodes and placed in a sealed BioLogic CESH. Two-probe EIS spectra were collected using various combinations of two electrodes at a time, which allowed the distance between electrodes to vary between 1.0, 1.3, and 1.6 cm. For each path length, the total cell resistance was taken to be the extrapolated right-most x-intercept of the Nyquist plot. With this data, Equation 2.15 was again employed to isolate the membrane ionic conductivity. In the in-

plane configuration, the path length (ℓ) is the distance between the electrodes, and the cross-sectional area (A_x) is the rectangle formed by the membrane thickness and width.

2.3.6 Single-Ion Diffusion Coefficients

Coupling ionic conductivity and salt permeability measurements with equilibrium ion partitioning measurements, described over the past four subsections, enables the extraction of single ion diffusion coefficients in the membrane[90,91]. Within the Nernst-Einstein framework, κ of a membrane contacting a single electrolyte solution is given by [16–18]:

$$\kappa = \frac{F^2}{RT}\left(z_g^2 C_g^{m,t} D_g^m + z_c^2 C_c^{m,t} D_c^m\right) \tag{2.16}$$

where F is Faraday's constant, R is the ideal gas constant, T is absolute temperature, z_g and z_c are the counter-ion and co-ion valence, respectively, $C_g^{m,t}$ and $C_c^{m,t}$ are the counter-ion and co-ion concentrations in the membrane, respectively, and D_g^m and D_c^m are the counter-ion and co-ion diffusivities in the membrane, respectively. The superscript "t" in the concentration term denotes that the concentration is based on the total volume of the swollen membrane. P_s for membranes contacting a single electrolyte solution is given by[18,92]:

$$P_s = K_s D_s^m = \left(\frac{C_s^{m,t}}{C_s^s}\right)\left(\frac{D_g^m D_c^m\left(z_g^2 C_g^{m,t} + z_c^2 C_c^{m,t}\right)}{z_g^2 C_g^{m,t} D_g^m + z_c^2 C_c^{m,t} D_c^m}\right) \tag{2.17}$$

where K_s is the salt partition coefficient, D_s^m is the salt diffusion coefficient, $C_s^{m,t}$ is the concentration of mobile salt in the membrane, C_s^s is the concentration of salt in the external solution, and all the other terms have been previously defined. Like κ, P_s is directly related to the concentrations and diffusivities of ions in the membrane; however, the κ and P_s equations are linearly independent of each other. With experimental results for κ, P_s, $C_g^{m,t}$, and $C_c^{m,t}$ (all obtained

for samples contacting the same external salt solution), Equations 2.16 and 2.17 can be solved simultaneously to obtain D_g^m and D_c^m.

This straightforward methodology for extracting single ion diffusion coefficients relies on several important assumptions. The first assumption relates to the validity of the Nernst-Einstein equation, which connects the ion mobility to the ion diffusivity[93]. The Nernst-Einstein equation assumes uncorrelated motions of ions in the presence of an electric field. Recent simulation studies have provided evidence supporting this assumption for membranes that do not allow partitioning for a significant amount of salt (e.g., below 1 mol/L[sorbed water])[93]. Second, frame of reference and thermodynamic non-ideal effects that may be present in the concentration gradient-driven experiments have been neglected in Equation 2.17. However, such effects appear to be negligible at low salt concentrations and offset one another at higher concentrations[92]. Third, this treatment neglects the presence of contact ion pairs between mobile ions or between counter-ions and fixed charge groups. Such electroneutral ion pairs would contribute to the measurements of $C_g^{m,t}$ and $C_c^{m,t}$. However, mobile contact ion pairs would contribute only to concentration gradient-driven transport experiments (P_s) and not to electric potential-driven transport (κ), assuming contact ion pairs are unresponsive to an electric field. Thus, the presence of contact ion pairs would pose challenges in determining single-ion diffusion coefficients using this methodology. This final point is once again negligible for low salt concentrations but may become troublesome at higher concentrations.

Determining D_g^m for ions in IEMs equilibrated with DI water is a much easier process than that for ions in salt solution-equilibrated IEMs. The three assumptions outlined above are most valid in IEMs with minimal salt partitioning, and salt partitioning does not occur for IEMs

equilibrated with DI water. Further, without co-ions present, D_g^m can be isolated without permeability or partitioning experiments. Setting $C_c^{m,t} = 0$ in Equation 2.16 yields:

$$\kappa = \frac{F^2}{RT} z_g^2 C_g^{m,t} D_g^m = \kappa_g \tag{2.18}$$

Here, κ has been given the subscript "g" because the conductivity due to a single species has been isolated; κ_g is the counter-ion conductivity of the IEM. By invoking electroneutrality, we can replace $C_g^{m,t}$ with the charge density of the IEM, $C_A^{m,t} = \left|z_g/z_A\right| C_g^{m,t}$, where z_A is the valence of the fixed charge groups (for essentially every IEM, $|z_A| = 1$). Therefore, if the charge content of an IEM is known, measuring the DI water equilibrated conductivity is the only experiment required to determine D_g^m and κ_g for counter-ions in the water-equilibrated IEM.

2.3.7 Arrhenius Activation Energy of Ion Diffusion

The energetics of ion diffusion in IEMs can be extracted from temperature-varied transport data using the Arrhenius equation[94,95]:

$$D_i^m = D_0^m \exp\left(-\frac{E_a^m}{RT}\right) \tag{2.19}$$

Here, D_i^m is the diffusivity of an ion i at absolute temperature T, E_a^m is the Arrhenius activation energy of ion diffusion in the membrane, D_0^m is the Arrhenius pre-factor for unhindered ion diffusion in the membrane, and R is the ideal gas constant. Describing diffusion using these two parameters is a helpful way to understand the limitations and interactions which affect transport in the IEM.

To collect sufficient data to extract the Arrhenius parameters from Equation 2.19, we measured the ionic conductivity, κ, for IEMs equilibrated with DI water at 10, 20, 30, 40, 50, and 60 °C. Samples were prepared identically to the room temperature experiments described in

Section 2.3.5 with two key differences. Inside the sealed CESH, we included moist filter paper and standing water to establish a humid environment which would limit membrane dehydration. Then, the entire CESH was placed inside a Binder KB53 Refrigerated Incubator (Tuttlingen, Germany) held at the experimental temperature for approximately 2.5 hours. Frequency sweeps probed the impedance response to an oscillating 100 mV potential from 3 MHz to 100 Hz every five minutes during the experiment.

The conductivity was extracted from impedance scans using a modified Randles circuit (Figure 2.10) to isolate the resistance of the membrane film[88]. The membrane resistance was normalized to the sample geometry as:

$$\kappa = \frac{\ell}{R_m A_x} \tag{2.20}$$

Here, ℓ is the path length, R_m is the membrane resistance extracted from the equivalent circuit, and A_x is the cross-sectional area of the membrane coupon. To automate the temperature variation, we sought to validate the results of the equivalent circuit fit at the temperature most difficult to fit. We compared the membrane conductivity extracted from the equivalent circuit fit with the membrane conductivity extracted from the varying length method described in Section 2.3.5. If the two methods produced conductivity measurements in agreement with each other, we proceeded to use the equivalent circuit at lower temperatures. The reduced conductivity at lower temperatures ensured the accessible frequencies of our potentiostat measured more the membrane impedance response than at higher temperatures, producing a more reliable equivalent circuit fitting. If the two methods did not agree, we attributed the discrepancy to inadequate data for the equivalent circuit and repeated the comparison at lower temperatures. Once the methods agreed, the equivalent circuit was used for all lower temperatures. From the conductivity measured at each temperature, ion diffusion coefficients were extracted using Equation 2.18.

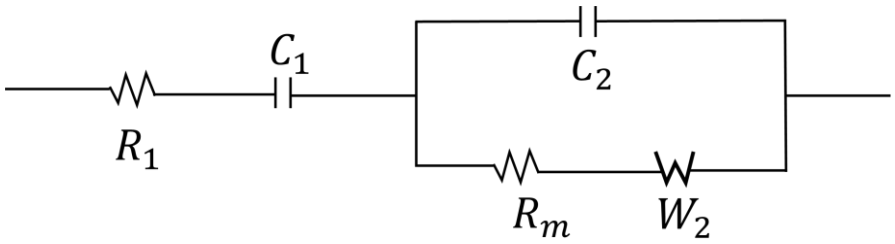


Figure 2.10: A modified Randles equivalent circuit. This modified version of the Randles circuit which was used to extract the membrane resistance (R_m) from measured electrochemical impedance spectroscopy (EIS) data.

The Arrhenius parameters can be fit directly from Equation 2.19; however, it is typical to linearize the equation into Arrhenius coordinates[96]:

$$\ln(D_i) = \ln(D_0) - \frac{E_a}{R}\left(\frac{1}{T}\right) \qquad 2.21$$

This version of the Arrhenius equation illustrates that plotting $\ln(D_i)$ against T^{-1} produces a linear fit where the intercept can give D_0 and the slope can give E_a. Although empirical at first, this formulation of diffusion has been given a fundamental interpretation through Eyring's transition state theory (TST)[95,97]. For simplicity, discussion in this dissertation is limited to the empirical Arrhenius definitions, though further work might extract greater insight from the TST disambiguation.

To produce a statistically appropriate estimate of the Arrhenius parameters from our experimental data, we avoided performing an ordinary least-squares linear regression. After transforming our data to Arrhenius coordinates and assuming that the uncertainty in temperature was relatively small, we performed a general least-squares linear regression as described by York[98]. This regression technique weights the residuals by the inverse variance of the data point and re-centers the analysis on the first moment in both x and y coordinates.

2.4 Supplemental Membrane Characterizations

Beyond the simple interpretation of ion transport derived from macroscopic charge contents and water contents of IEMs, additional characterization techniques are useful in understanding the nature of solute transport in membranes. These following experiments are more throughout amongst polymer science and can grant deeper insight into local interactions and structures within IEMs.

2.4.1 Polymer Gel Fraction

The gel fractions (GFs) of membranes were determined through an integrated membrane synthesis and water uptake procedure[99] (c.f. Sections 2.1.3, 2.1.4, and 2.2.1). Pre-polymer solutions was precisely weighed on the casting plates prior to polymerization. By accounting for the solvent in the pre-polymer solution, this step allows for calculation of the monomer mass which might be incorporated into this batch of membrane, $m_{initial}$. This solution was polymerized as normal, and the resultant membranes were still placed in DI water to remove unreacted reagents. These membranes were left in the as-synthesized counter-ion form and were never exposed to salt solutions. Only membrane syntheses producing whole, unbroken membrane coupons were accepted for GF experiments. These membranes were dried using the same procedure as the water uptake experiments. In this context, the constant dry mass represents the mass of monomer incorporated into the membrane, m_{gel}. The gel fraction was then calculated via:

$$GF = \frac{m_{gel}}{m_{initial}} \tag{2.22}$$

2.4.2 Thermogravimetric Analysis (TGA)

TGA was performed using a TA Instruments TGA Q550 (New Castle, DE) with a dry nitrogen purge and a temperature ramp rate of 7 ºC/min. Before the test, nominally 4 mg of membrane sample (equilibrated with ambient humidity) was loaded and then heated to 100 ºC. Samples were held at 100 ºC for 30 minutes to acquire a dry mass, and test results were then normalized to this mass. Samples were heated to a final temperature of 450 ºC. To confirm reproducibility, three samples replicates per membrane were tested.

2.4.3 Differential Scanning Calorimetry (DSC)

Differential scanning calorimetry (DSC) was performed on both hydrated and dried membrane samples using a TA Instruments DSC250 (New Castle, DE). Dry samples were nominally 3 mg, hydrated samples were nominally 5 mg, and all tests employed a nitrogen gas purge. Characterization of dried membranes utilized a non-hermetic TZero aluminum pan, while that of hydrated membranes utilized a hermetically sealed TZero aluminum pan.

Dry polymer samples were equilibrated with the ambient humidity overnight before loading into the analysis pan. The partially-dried samples were annealed in the DSC at 120 ºC for 30 minutes at the start of the test to completely dry the membrane. The samples were then cooled to -80 ºC at a rate of 20 ºC/min before heating to 250 ºC at a rate of 5 ºC/min. The cooling and heating cycles were then repeated a second time. To analyze samples with a uniform thermal history, all reported thermograms represent the second heating cycle. Dry membranes were tested in triplicate to confirm reproducible results.

Hydrated membrane samples were blotted dry to remove surface water similarly to the water uptake experiments (Section 2.2.1) before quickly sealing the samples in the hermetic pans. These samples were not annealed, but were immediately quenched from 40 ºC to -80 ºC at

20 ºC/min, where they were held for 10 min before heating to 40 ºC at a ramp rate of 10 ºC/min. The enthalpy of melting for water in the membrane was obtained by integrating the melting peak of the heating curve. The integration limits of the melting peak were identified by examining the derivative of the heat flow vs. temperature curve. The calculated enthalpy, initially normalized by the mass of the hydrated membrane sample, was re-normalized to the amount of water in the membrane (ΔH_m^m) using the measured water uptake of the membrane. To calculate the fraction of freezable water in the membrane, f_f,we assume that entrained water would yield the same enthalpy of freezing as the bulk value, ΔH_m^s = 333 J/g, which is the standard assumption to make in this analysis[100–102].

$$f_f = \frac{\Delta H_m^m}{\Delta H_m^s} \tag{2.23}$$

2.4.4 Dynamic Mechanical Analysis (DMA)

Dynamic mechanical analysis (DMA) testing employed a TA Instruments DMA850 (New Castle, DE) with a submersion film clamp, dry air heated purge gas, and 18 N load cell. Rectangular membrane samples were used for mechanical testing, and the specific dimensions of each sample were quantified using Fowler Precision UltraCal V 6” calipers (Valencia, CA). Samples were secured in the testing clamp using a torque wrench and applying less than 2 in.-lbs of torque. Tests were performed on samples completely submerged in DI water, and a 20 minute equilibration period ensured that samples reached the bath temperature prior to the start of the test. An initial pre-test force of 5 mN was applied to each sample to acquire the equilibrium length. Each membrane was first subject to a strain sweep at 0.333 Hz and 30 ºC to establish the linear response region. Then, frequency sweeps were collected at 30 ºC and 0.03 % strain. Finally, temperature ramps were collected at 1 Hz and 0.03 % strain with a 2 ºC/min ramp rate. Two

replicate frequency scans were collected for additional samples to confirm reproducibility. Storage moduli (E') were extracted from these scans at 0.03 % strain, 30 ºC, and 1 Hz for further analysis.

The swelling-reduced storage modulus (E'_{SR}) can be calculated from measurements on swollen polymer networks to isolate the mechanical properties of the dry polymer[103,104]. Most IEMs synthesized in this dissertation deform or break when dried, so we used this method to assess dry polymer networks. The correction is necessary because swelling beyond the relaxed state of the polymer network after polymerization adds strain to the network before the onset of the mechanical testing[105]. Per the Bray-Merrill framework, we accounted for this strain by considering the relaxed and swollen polymer volume fractions ($\phi_{p,r}$ and $\phi_{p,s}$, respectively). This transformation is performed via the following equations[105]:

$$\phi_{p,s} = 1 - \phi_w \tag{2.24}$$

$$\phi_{p,r} = \frac{w_{pp}\rho_{pp}}{\rho_p} \tag{2.25}$$

$$E'_{SR} = E'\left(\phi_{p,s}\right)^{1/3}\left(\phi_{p,r}\right)^{-2/3} \tag{2.26}$$

Here, w_{pp} is the monomer mass fraction in the pre-polymer solution and ρ_{pp} is the overall density of the pre-polymer solution.

2.4.5 Small- and Wide- Angle X-Ray Scattering (SAXS and WAXS)

X-ray scattering experiments for hydrated and dried membrane samples were performed in the Dual-Source and Environmental X-ray Scattering facility operated by the Laboratory for the Research on the Structure of Matter at the University of Pennsylvania. We would like to thank Dr. Iryna Golovina for her assistance with this experiment, and acknowledge the funding sources for this facility: the National Science Foundation through grants MRSEC 17-20530 and MRI 17-25969, the ARO DURIP through grant W911NF-17-1-0282, and the University of Pennsylvania.

Small-angle X-ray scattering (SAXS) and wide-angle X-ray scattering (WAXS) experiments were performed using a Xeuss 2.0 (Xenocs) equipped with a GeniX3D to generate a Cu Kα source beam of 8 keV (wavelength ~ 1.54 Å). A PILATUS detector with 1M pixels and 100k pixels was used for SAXS and WAXS experiments, respectively. For dry samples, the experiments were performed by mounting the dry polymer films on a general sample holder. The SAXS experiments were performed using a 1 tube configuration to cover a q-range of 0.021-1.02 $Å^{-1}$ with a sample-to-detector distance (SD) of 566.66 mm and an exposure time of 900 sec. The WAXS measurements collected simultaneously covered a q-range of 1.1-3.1 $Å^{-1}$ with a SD of 155.22 mm. For hydrated samples, SAXS and WAXS measurements were performed by employing a gel cell (or button cell) and adding a drop of water to keep the samples hydrated throughout the duration of the experiments. The gel cells were 0.5 mm in thickness and equipped with an 11 mm diameter top window and a 7 mm diameter bottom window made from a 50 μm Kapton film to suppress water evaporation. For SAXS measurements, 0 tube (SD = 361.48 mm) and 3 tube (SD = 2508.26 mm) configurations were used to cover the q-range of 0.33-1.5 $Å^{-1}$ and 0.0049-0.23 $Å^{-1}$, respectively, with 900 sec of exposure time in both configurations. The WAXS measurements collected simultaneously covered a q-range of 1.1-3.1 $Å^{-1}$ with a SD of 156.39 mm.

The 2D scattering spectra for both dry and hydrated samples were collected at room temperature. The SAXS and WAXS scattering profiles were azimuthally integrated into I(q) 1D plots. The data using different tube configurations for SAXS were concatenated into one plot using BioXTAS RAW[106]. The scattering from the Kapton windows employed for the hydrated samples was subtracted from the total scattering spectra using the transmission factors measured for each configuration and sample.

2.4.6 Fourier-Transform Infrared Spectroscopy (FTIR)

Fourier-Transform Infrared Spectroscopy (FTIR) spectra were collected for dried and hydrated membranes with an attenuated total reflectance (ATR) probe using a Thermo Fisher Nicolet Smart iTX iS20 (Billerica, MA). Hydrated membranes were equilibrated with DI water, blotted dry on one side, and then clamped down with the blotted side facing the ATR diamond. For spectra of the dried membranes, samples were dried under vacuum as reported for water content experiments (Section 2.2.1) and samples were clamped onto the ATR diamond immediately after removal from the drying oven. For both dried and hydrated samples, the spectra were recorded over 64 scans at a spectral 0.48 cm^{-1} resolution, lasting approximately 1 minute. Within this minute, water peaks did not significantly change in the sample spectrum, suggesting that water gain/loss was minimal.

2.4.7 Raman Spectroscopy

Raman spectra were collected for dried and hydrated membranes using a 532 nm, 100 mW laser and a RenCam CCD detector within a Renishaw InVia Raman microscope (West Dundee, IL). Spectra were collected in static scan mode from 260 to 2000 cm^{-1} with 1800 lines/mm grating and a 65 μm slit. The spectral resolution was 1.53 cm^{-1} and 32 replicate scans were performed per sample. Samples were held in sealed borosilicate glass vials during collection. Hydrates samples were immersed in DI water within the glass vial. Dry samples were dried in a vacuum oven as reported for water content experiments (Section 2.2.1) and then sealed in the glass vial with an argon headspace. Due to the varied path lengths inherent to this method of confocal spectroscopy, quantitative comparisons of spectral intensities were not performed between different samples.

2.5 Molecular Dynamics (MD) Methodology

When experimental methods are insufficient to fully explain transport phenomena, atomistic molecular dynamics (MD) simulations can help develop a deeper understanding of IEM structure-property relationships. For this work, MD simulations were performed using the Expanse resource at the San Diego Supercomputing Center through allocation CHM230048 from the Advanced Cyberinfrastructure Coordination Ecosystem: Services & Support (ACCESS) program[107], which is supported by National Science Foundation grants #2138259, #2138286, #2138307, #2137603, and #2138296. To couple experimental analyses with MD simulations in Chapter 9, the following techniques were employed.

2.5.1 Simulation Parameterization

MD simulations were performed using the Large-scale Atomic/Molecular Massively Parallel Simulator (LAMMPS)[108]. Water was modeled using the transferable intermolecular potential with four points (TIP4P/2005)[109]. This water model was for its accurate representation of the density, coordination number, surface tension, dielectric constant, and self-diffusion coefficient of bulk water[110]. The parameterization of alkali and halide ions for the TIP4P/Ew water model was used as it accurately replicates solution properties (e.g., solvation energy, coordination number, hydrated radius, and solute diffusivity) in simulations containing TIP4P/2005[111,112]. Non-bonded interactions and bonds in multiatomic molecules were parameterized using the optimized potentials for liquid simulation (OPLS) force field[113,114]. Non-bonded interactions were modeled via Lennard Jones and Coulombic parameters. Bonded interactions include interatomic bonds, angles, dihedrals, and impropers. Pairwise interactions were computed for both Lennard Jones and Coulombic potentials up to a cutoff of 10 Å. Beyond this cutoff, Coulombic pairwise interactions were evaluated using the particle-particle particle-mesh algorithm.

Simulated multiatomic molecules included the monomers shown in Figure 2.8: [2-(Methacryloyloxy)ethyl] trimethylammonium (MOETMA), 3-Sulfopropyl methacrylate (SPM), glycerol dimethacrylate (GDMA). Additional multiatomic molecules included: tetramethylammonium (NMe_4^+), ammonium (NH_4^+), nitrate (NO_3^-), and water. Alkali metal ions included: lithium (Li^+), sodium (Na^+), potassium (K^+), and cesium (Cs^+). Halide ions included: fluoride (F^-), chloride (Cl^-), bromide (Br^-), and iodide (I^-).

The isothermal-isobaric (NPT) ensemble was utilized to hold the number of atoms (*N*), domain pressure (*P*), and domain temperature (*T*) constant[115]. A Nosé-Hoover style thermostat and barostat were used to control temperature and pressure, respectively. The time step during simulation was 1 fs.

2.5.2 IEM Simulation Design

To generate ion-exchange membrane (IEM) simulation domains suitable for equilibrium sampling, subsequent steps of pre-polymer solution equilibration, polymerization, ion exchange, swelling, and equilibration were performed. Figure 2.11 depicts this workflow visually.

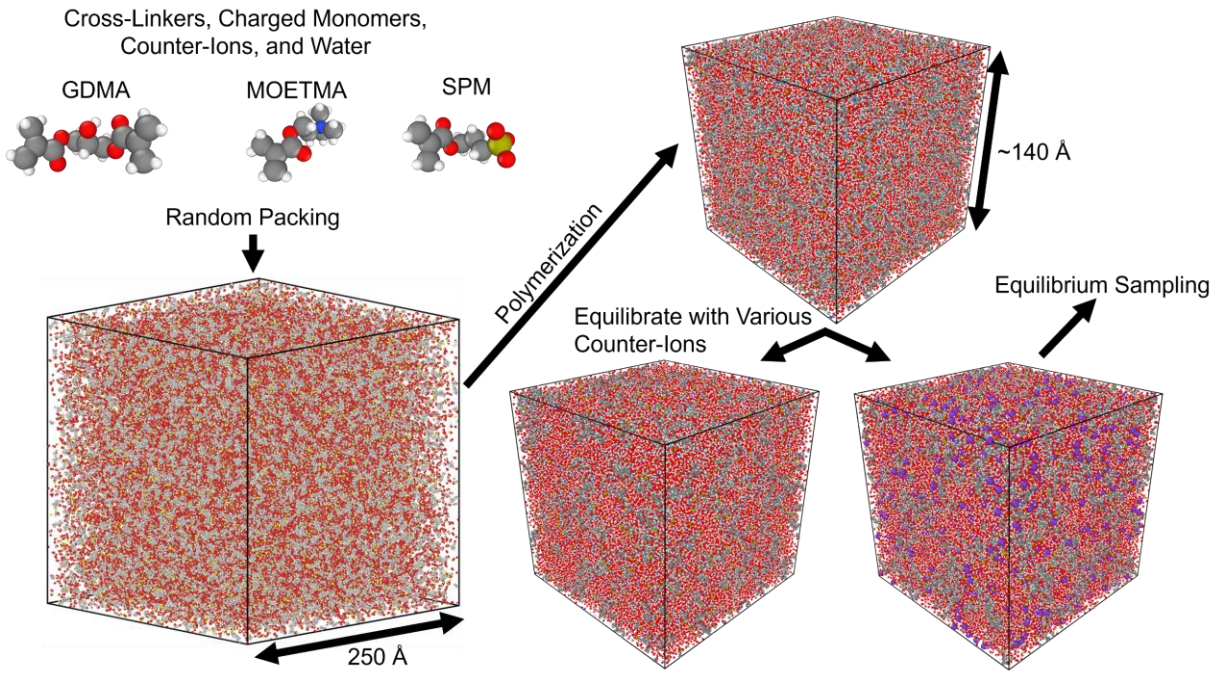


Figure 2.11: Preparation of IEMs *in silico*. The steps taken to prepare IEM domains from pre-polymer solutions in LAMMPS for MD analysis.

IEMs were prepared *in silico* via polymerization of a charged monomer and cross-linker in water. The simulations were designed to match the experimental conditions described in Section 2.1.4 as closely as possible. First, an oversized domain (250^3 $Å^3$) was randomly packed with GDMA cross-linkers, charged monomers, counter-ions, and water. For the anion-exchange membranes (AEMs), the charged monomer was MOETMA, and the counter-ion was Cl^-. For the cation-exchange membranes (CEMs), the charged group monomer was SPM, and the counter-ion was K^+.

After packing, the domain was equilibrated using an NPT ensemble for 3 ns. During equilibration, the domain was held at 1 atm and 300 K. Within this ensemble, domain volume is allowed to change to maintain the applied pressure. Equilibration was continued until the pre-polymer solution density reached a constant value.

During in-lab synthesis of the IEMs, the methacrylate chain growth reaction was initiated using a free radical initiator, V-50, and reactions were promoted via elevated temperature. To accurately replicate in-lab polymerization conditions, an NPT ensemble was used to increase the domain temperature to 358.15 K while maintaining the pressure at 1 atm. The number of initiated methacrylate groups was determined by assuming that all initiator added to the experimental pre-polymer solution was consumed. The ratio of initiated methacrylate groups on GDMA molecules to those on the charged monomers was set proportional to their concentrations in the simulation. No GDMA molecules had both methacrylate groups initiated. All initiations were performed at the beginning of the simulation and no new initiations occurred during polymerization.

Polymerization of the IEM via chain initiation and radical propagation was performed using REACTER[116,117]. REACTER enables the use of reactive MD for select reactions, including growth of networked methacrylate polymers[116,117]. To recreate the chain initiation behavior, only initiated methacrylate groups were candidates for propagation reactions. To enable chain growth, after a single successful propagation reaction, the newly added methacrylate group was designated as initiated and therefore a possible candidate for a new propagation reaction.

Polymerization was carried out until fewer than 10 new polymerization reactions occurred per simulated ns. This threshold was deemed a sufficient trade-off between the crosslinking of the final polymer and the investment of computational effort, selected to produce gel fractions similar to those typically reported for cross-linked methacrylate IEMs[86].

Once polymerization was completed, all remaining unreacted monomers were deleted. Then, the ion form of the membrane was converted by replacing the counter-ion (Cl^- or K^+), if necessary, and inserting/deleting water molecules to match the corresponding experimental water

uptake. After these changes, IEMs were equilibrated in an NPT ensemble at 300 K and 1 atm for 1 ns.

2.5.3 Infinite Dilution Simulation Design

To compare results of IEM simulations against simulated aqueous solution conditions, domains of ions at infinite dilution (ID) were prepared using the same parameters as the IEM simulations. Infinite dilution simulations were performed using 100 mobile ions and 52,300 water molecules. Simulations were initialized and equilibrated via a similar process as the IEM pre-polymer solutions.

2.5.4 Simulation Analyses

Equilibrium sampling of the equilibrated IEM and ID domains was performed using an NPT ensemble 300 K and 1 atm for 5 ns. During equilibrium sampling, trajectory data of the water molecules, counter-ions, and (for IEM simulations) polymer networks were saved every 1000 fs.

Within LAMMPS, the command *compute rdf* was utilized to determine radial distribution functions (RDFs, $g(r)$). For a central atom / candidate atom pair, $g(r)$ is the probability of finding a candidate atom a within a shell of radius r around the central atom ($\rho(r)$) normalized against the probability of finding a candidate atom in that shell if the density of the candidate atom within that shell was equivalent to the bulk density of the candidate atom in the simulation (ρ_0). With this definition, $g(\infty) = 1$. These functions were evaluated at all simulated timesteps with a radial step size of 0.01 Å up to the pairwise cutoff of 10 Å.

RDFs involving water were calculated using the position of oxygen within the water molecules. RDFs involving multiatomic ions were calculated using the position of the central atom of the ion: nitrogen for NH_4^+, NMe_4^+, NO_3^-, and $RNMe_3^+$ in MOETMA; sulfur for RSO_3^- in SPM.

RDFs for counter-ion / water pairs were determined for both IEM and ID simulations. Additionally, RDFs for fixed charge / water and fixed charge / counter-ion pairs were determined for IEM simulations. The sizes of primary coordination shells were determined by the location of minima in the RDFs. The density of species was integrated from the center atom to the radius of the coordination shell to extract the coordination number.

The radial distance profile for the free energy of interaction between a central atom and a candidate atom, $G(r)$ can be determined as[118,119]:

$$G(r) = -k_B T \ln P(r) \tag{2.27}$$

Here, k_B is the Boltzmann constant and $P(r)$ is the probability of a candidate atom being located a distance r from the central atom. The probability function can be determined from $g(r)$ using the following equation:

$$P(r) = \frac{g(r)}{\sum g(r)} \tag{2.28}$$

From the energy of interaction profiles, three key metrics were calculated. First, the energy of interaction between a central and candidate molecule located in a coordination shell, per candidate molecule, could be extracted from the local minima associated with that coordination shell. Second, the same value normalized per central molecule could be calculated by integrating the product of coordination number and interaction energy. Finally, the energy required for a candidate molecule to leave the vicinity of a central molecule can be taken as the difference between the corresponding local energy minimum and the next-closest local energy maximum.

2.6 Literature Reference Data and Statistical Processing

Various data sets were harvested from published sources to supplement the experiments performed in these chapters. Additionally, in Chapter 9, statistical correlation tools were utilized

to connect experimental data with values collected from the literature. This section details data management and statistical tools employed within this dissertation.

2.6.1 Structural Properties of IEMs Reported in the Literature

The structural properties of IEMs developed in the literature within the past two decades were compiled to contextualize IEM data throughout this dissertation. These properties included, at a minimum, the ion-exchange capacity, IEC, and water uptake, WU. If values were reported, results were also collected for the dry polymer density, ρ_p, fixed charge density, $C_A^{m,t}$, fixed charge concentration, $C_A^{m,w}$, and membrane hydration number, λ. Additionally, when available, the room temperature ionic conductivity (κ) of these membranes were recorded alongside the structural parameters.

To find these membranes, Google Scholar and Web of Science searches were conducted using search terms "ion-exchange membrane," "anion-exchange membrane," "cation-exchange membrane," "hydroxide-exchange membrane," "proton-exchange membrane," "charged membrane," "ion-conducting membrane," "ion-selective membrane," "cation-conducting membrane," "cation-selective membrane," "anion-conducting membrane," and "anion-selective membrane." Additionally, the same terms were utilized with spaces instead of hyphens. Further, qualifiers such as "highly charged," "dimensionally stable," and similar common claims were added to sample different sections of the literature. This survey of literature IEMs comprises >200 literature sources and >1000 unique IEMs[99,120–320]. The results of this survey are primarily presented and discussed in Chapter 4.

2.6.2 Ionic Diffusivities of Ions in Aqueous Solution at Infinite Dilution

The transport behavior of ions at infinite dilution in aqueous solution were collected to contextualize IEM data throughout this dissertation. Beyond room temperature transport, ion diffusion at various temperatures are required to calculate the solution activation energies of diffusion, E_a^s. To develop an comprehensive suite of ion diffusion data, we sourced conductance data of salts from literature papers over the past century[321–355]. Often, the data were expressed as limiting equivalent conductances at infinite dilution (Λ^0); however, some sources reported enough data to determine Λ^0 without performing the calculation. For these sources, we calculated Λ^0using the Lattey form[356] of Kohlrausch's Law:

$$\Lambda = \Lambda^0 - \frac{A\sqrt{c}}{1 + B\sqrt{c}} \qquad 2.29$$

In this equation, Λ is the equivalent conductance at a finite concentration and c is the concentration expressed in molality. A is a slope grounded in the Debye-Hückel-Onsager framework, while B is a size parameter[344], similar to Bjerrum's extension of Debye-Hückel's theory[357]. More adjustable parameters, such as those used in the Jones-Dole form of Kohlrausch's Law, extend the concentration range of experimentation[344,357,358]. We selected the Lattey form as a trade-off between requiring low of concentrations and including too many fitting parameters. To extract Λ^0 from experimental data, B was adjusted to maximize the linearity of Λ with the function $\sqrt{c}/\left(1 + B\sqrt{c}\right)$.

Most sources reporting on identical salts and temperatures were in reasonable agreement with each other. When one source disagreed on a salt, it was always for a salt where a clear majority consensus could be determined, and the anomalous reference was excluded from analysis. All the assembled conductance data monotonically increased with temperature, as should be expected.

Following Harned and Owen[359], salt conductance data was fit using a cubic polynomial using data from 0 to 100 ºC. The salt limiting equivalent conductances were then parsed into single-ion limiting equivalent conductances. It is typical to perform this step by relying on KCl conductances because the transference number of KCl remains relatively constant across temperatures below 50 ºC[351,354,360]. By considering discrepant sources, we elected to use a nominal cation transference of 0.495 for KCl at all temperatures, which agrees with all reported values within 1 %. Once both K^+ and Cl^- single-ion limiting equivalent conductances were calculated, other KX and MCl salts could have the KCl contribution subtracted off, yielding additional single-ion conductances (λ_i^0):

$$\Lambda_{MX}^0 = \lambda_{M^+}^0 + \lambda_{X^-}^0 \qquad 2.30$$

NMe_4Cl data was not readily available, so we added an intermediate calculation using the picrate ion, Pic^-. Using NH_4Cl, NH_4Pic, and NMe_4Pic, $\lambda_{NMe_4^+}^0$ could be calculated via this same procedure. To the best of our knowledge, NO_2^- conductance data has only been reported by Klemenc and Hayek[347], ranging from 0 to 30 ºC. All other ions spanned the full range of temperatures studied in this manuscript, exceeding the range 10 – 60 ºC. The range of validity and cubic fits for each λ_i^0 are given in Table 2.4.

Table 2.4: Cubic fits of limiting equivalent conductances of ions in aqueous solution. The limiting equivalent conductance of ions as a function of the temperature in Celsius (t).

Ion	Range (ºC)	$\lambda_i^0\ (S \cdot cm^2/eq)$
F^-	5 – 90	$0.32\text{x}10^{-5}t^3 + 2.85\text{x}10^{-3}t^2 + 1.06t + 26.67$
Cl^-	0 – 100	$0.58\text{x}10^{-5}t^3 + 3.43\text{x}10^{-3}t^2 + 1.30t + 40.50$
Br^-	0 – 90	$4.25\text{x}10^{-5}t^3 + -1.68\text{x}10^{-3}t^2 + 1.42t + 41.58$
I^-	0 – 65	$-0.42\text{x}10^{-5}t^3 + 4.34\text{x}10^{-3}t^2 + 1.26t + 42.26$
NO_2^-	0 – 30	$-0.57\text{x}10^{-5}t^3 + -8.13\text{x}10^{-3}t^2 + 1.34t + 44.00$
NO_3^-	0 – 100	$-5.97\text{x}10^{-5}t^3 + 10.18\text{x}10^{-3}t^2 + 0.99t + 40.65$
SO_4^{2-}	0 – 100	$-5.97\text{x}10^{-5}t^3 + 13.12\text{x}10^{-3}t^2 + 1.36t + 41.18$
Li^+	0 – 90	$7.65\text{x}10^{-5}t^3 + -3.51\text{x}10^{-3}t^2 + 0.84t + 18.34$
Na^+	0 – 100	$-2.79\text{x}10^{-5}t^3 + 8.45\text{x}10^{-3}t^2 + 0.72t + 26.60$
K^+	0 – 100	$0.57\text{x}10^{-5}t^3 + 3.36\text{x}10^{-3}t^2 + 1.28t + 39.70$
Cs^+	0 – 90	$0.98\text{x}10^{-5}t^3 + 4.45\text{x}10^{-3}t^2 + 1.25t + 43.44$
NH_4^+	0 – 100	$2.34\text{x}10^{-5}t^3 + 1.00\text{x}10^{-3}t^2 + 1.33t + 38.01$
NMe_4^+	0 – 90	$2.34\text{x}10^{-5}t^3 + 0.22\text{x}10^{-3}t^2 + 0.88t + 21.03$
Mg^{2+}	0 – 90	$5.66\text{x}10^{-5}t^3 + 1.29\text{x}10^{-3}t^2 + 0.88t + 27.29$
Ca^{2+}	0 – 90	$13.39\text{x}10^{-5}t^3 + -8.36\text{x}10^{-3}t^2 + 1.29t + 28.71$
Pic^-	0 – 100	$4.25\text{x}10^{-5}t^3 + -1.68\text{x}10^{-3}t^2 + 1.42t + 41.58$

Using the profiles for λ_i^0, single-ion diffusion coefficients at infinite dilution (D_i^s) could be calculated using the Nernst-Einstein framework for a single conducting ion (Equation 2.18). To express the Nernst-Einstein equation using equivalent conductances, we substitute for the conductivity, $\kappa_i = \Lambda_i * (|z_i|C_i^s)$. Therefore, for aqueous salt solutions at infinite dilution we can write:

$$\lambda_i^0 = \frac{F^2}{RT}|z_i|D_i^s \qquad 2.31$$

Here, κ_i is the conductivity due to species i, C_i^s is the concentration of species i in aqueous solution, z_i is the valence of species i, D_i^s is the diffusivity of species i in aqueous solution at absolute temperature T and infinite dilution, F is Faraday's constant, and R is the ideal gas constant.

Two recent studies[322,361] reported good agreement between calculated Nernst-Einstein diffusion coefficients and measured experimental diffusion coefficients for ions in dilute aqueous solution, giving us some confidence in the reliability of this transformation. The Nernst-Einstein values of D_i^s can then be used to calculate E_a^s.

2.6.3 Intrinsic Properties of Ions

Ion properties proposed to explain trends amongst ions were sourced from the literature for each counter-ion form studied in this dissertation (F^-, Cl^-, Br^-, I^-, NO_2^-, NO_3^-, SO_4^{2-}, Li^+, Na^+, K^+, Cs^+, NH_4^+, NMe_4^+, Mg^{2+}, and Ca^{2+}). Marcus compiled many of his experimental results in his textbooks in 1997 and 2015, titled *Ion Properties* and *Ions in Solution and their Solvation*, respectively[362,363]. These texts provided invaluable and convenient sources for ion information. However, some of the values considered in our study were not available in Marcus's books. Gregory reports the radial charge density, þ, which we source from their recent study[364]. Marcus in 1994 reports a geometric hydrogen bonding character of ions which was not fully incorporated into his textbooks[365]. Finally, Nightingale assembled various ionic radii in 1959, which we utilize to describe the size of ions in this solution[366]. These literature properties are listed below in Table 2.5. Values are generally not available for NO_2^-, but NO_2^- values have been included as available.

Table 2.5: Tabulated ion parameters. The enthalpy of hydration[363] (ΔH_H), entropy of hydration[363] (ΔS_H), free energy of hydration[363] (ΔG_H), magnetic susceptibility[363] (χ), polarizability[363] (α), softness[363] (σ), Jones-Dole viscosity parameter[363] (B), surface tension increments[363] ($d\sigma/dn$), and hydrogen bond disruption factor[365] (ΔG_{HB}) of each ion under study. Values are tabulated from the given sources.

Ion	ΔH_H $\left(\frac{kJ}{mol}\right)$	ΔS_H $\left(\frac{J}{mol \cdot K}\right)$	ΔG_H $\left(\frac{kJ}{mol}\right)$	$-\chi$ $\left(\frac{mm^3}{kmol}\right)$	α (Å^3)	σ $(-)$	B $\left(\frac{L}{mol}\right)$	$d\sigma/dn$ $\left(\frac{mN \cdot L}{m \cdot mol}\right)$	ΔG_{HB} $(-)$
F^-	-510	-137.2	-469	13.0	0.88	-0.36	0.127	1.10	0.08
Cl^-	-367	-75.7	-344	28.0	3.42	0.21	-0.005	1.20	-0.61
Br^-	-336	-58.8	-318	39.0	4.85	0.47	-0.033	0.95	-0.80
I^-	-291	-35.9	-280	56.7	7.51	0.80	-0.073	0.35	-1.09
NO_2^-	-412	-93.7	-384	15.0	3.45	0.45	-0.024	---	-0.52
NO_3^-	-312	-83.4	-286	23.0	4.13	0.33	-0.045	0.45	-0.68
SO_4^{2-}	-1035	-200.4	-975	40.0	5.47	-0.08	0.206	1.15	-0.21
Li^+	-531	-141.8	-489	3.0	0.03	-1.32	0.146	0.65	0.28
Na^+	-416	-111.2	-383	2.3	0.26	-0.90	0.085	0.90	-0.03
K^+	-334	-74.3	-312	11.2	1.07	-0.88	-0.009	0.80	-0.52
Cs^+	-283	-58.6	-266	34.0	2.73	-0.84	-0.047	0.50	-0.69
NH_4^+	-329	-111.6	-301	65.0	1.86	-0.90	-0.008	0.40	-0.18
NMe_4^+	-209	-144.1	-166	65.0	9.08	0.51[†]	0.123	-0.40	-0.47
Mg^{2+}	-1949	-331.2	-1837	5.0	-0.28	-0.71	0.385	1.65	0.78
Ca^{2+}	-1602	-252.4	-1527	8.0	0.63	-0.96	0.298	1.50	0.34

[†]The value of 0.51 is corrected from a reported value of 0.11 in Marcus,[363] following from values in the original source[362,367].

Table 2.5 continued: The bare radius[363] (r_b), hydrated radius[366] (r_H), Stokes radius[366] (r_S), the corresponding ion charge densities (CD_b, CD_H, and CD_S, respectively), and the radial charge density[368] (þ) of each ion under study. Values are tabulated from the given sources.

Ion	r_b (Å)	r_H (Å)	r_S (Å)	CD_b $\left(\frac{nC}{m^3}\right)$	CD_H $\left(\frac{nC}{m^3}\right)$	CD_S $\left(\frac{nC}{m^3}\right)$	þ $\left(\frac{nC}{m \cdot mol}\right)$
F^-	1.33	1.66	3.52	-16.26	-8.36	-0.88	-0.864
Cl^-	1.81	1.21	3.32	-6.45	-21.60	-1.05	-0.625
Br^-	1.96	1.18	3.30	-5.08	-23.29	-1.06	-0.563
I^-	2.20	1.19	3.31	-3.59	-22.71	-1.06	-0.490
NO_2^-	1.92	---	---	-5.41	---	---	-0.648
NO_3^-	2.00	1.29	3.35	-4.78	-17.82	-1.02	-0.626
SO_4^{2-}	2.30	2.30	3.79	-6.29	-6.29	-1.41	-1.025
Li^+	0.69	2.38	3.82	116.47	2.84	0.69	3.161
Na^+	1.02	1.84	3.58	36.06	6.14	0.83	1.524
K^+	1.38	1.25	3.31	14.56	19.59	1.06	0.924
Cs^+	1.70	1.19	3.29	7.79	22.71	1.07	0.608
NH_4^+	1.48	1.25	3.31	11.80	19.59	1.06	0.960
NMe_4^+	2.80	2.05	3.67	1.74	4.44	0.77	0.540
Mg^{2+}	0.72	3.47	4.28	205.03	1.83	0.98	3.579
Ca^{2+}	1.00	3.10	4.12	76.53	2.57	1.09	2.094

2.6.4 Statistical Correlation Analysis

To identify correlations between experimental data and ion properties in the literature which could potentially explain these trends, we used a correlation plot method to select for correlated ion properties. The set of ion parameters discussed in the literature is very diverse and outnumbers the ions characterized in experimental dataset within this dissertation, so this rudimentary screening method was necessary to reach a text matrix suitable for more sophisticated statistical analyses. The correlation plot screening was facilitated by the function *corrplot* in MATLAB (R2024a).

A linear least-squares regression test between observed membrane properties and tabulated ion properties was performed for every pair of independent and dependent variables. The correlations were described using Pearson correlation coefficients (r) and then subject to a two-tailed Student's t-Test to identify statistically correlations ($r \neq 0$) beyond a significance threshold of $\alpha = 0.05$. To ensure that sorting between anions and cations did not arbitrarily influence the results, only the magnitudes of charge density values were used (rather than making all anions negative and all cations positive). Signed values were still utilized for measures of interaction, such as the softness, σ, and hydrogen bond distruption, ΔG_{HB}. This screening reduced the number of independent ion properties, allowing all hits to be analyzed via principal component analysis (PCA)

PCA allowed us to directly compare the correlated ion factors. This second-level analysis helped simplify the physical interpretation of phenomena contributing to the observed experimental trends in our IEMs. PCA methods in chemical sciences have been covered extensively in Malinowski's seminal textbook[369]. PCA reduces the dimensionality of complex data sets by grouping modes of variance into principal components (PCs). Although all components are

required to exhaustively account for all modes of variance in the data set, often PCs are more efficient than measurable variables at explaining data variance. Typically, two or three PCs can account for nearly all the variance in an interconnected data set, even though there may be significantly more than three variables. To identify the number of PCs required to explain variance in a data set, it is standard to perform a *Skree Plot* analysis to assess PC significance[369]. In all of our PCA analyses, only the first two PCs were required to explain >90% of the variance in the data set. To show the relationship between variables in these PCs, a biplot is used to map ion properties onto the first two principal components (PC1 and PC2). Factors grouped close to each other on the biplot are considered highly correlated within the context of the analyzed variables, while orthogonality indicates less similar modes of variance.

2.6.5 Vibrational Spectroscopy Peak Analysis

Peak locations in vibrational spectroscopy results were calculated via gaussian peak fitting of the spectra using the *fit* function in MATLAB (R2024a). Location bounds were used to ensure peak areas remained positive. We report 95% confidence intervals of peak locations, and fit spectra were accepted when confidence intervals did not exceed 2 cm^{-1} in either direction of the central peak location. To prevent biasing the data via baseline adjustments, spectral pre-processing (i.e., baseline correction or spectra normalization) was not performed. When plotting, individual spectra were normalized to the intensity of their respective charge group's peak location.

Contact ion-pairs of certain ions have been evidenced in Raman spectroscopy by peak-shifting of Raman scattering modes associated with the ionic species[370–373]. We utilize this technique by analyzing vibrational modes of the IEM fixed charge groups in wet and dry states. For dry IEMs, counter-ions and fixed charge groups have no hydrating waters to separate them, so the dry peak should correspond to fixed charge groups participating in a contact ion pair.

Meanwhile, in hydrated IEMs, one peak may correspond to fixed chare groups only contacting water, while other peaks may represent other coordination states. Crucially, in hydrated membranes, contact ion pairs would have the same peak location as detected in the dry state. Multivalent ions cannot stoichiometrically form contact ion pairs with every fixed charge group without a perfect distribution of two fixed charge groups local enough to both contact each ion. This complicates the assumption of full contact ion pairing in the dry state, so multivalent ions are not included in the quantitative spectroscopy analysis.

This analysis is contingent on identifying a signal corresponding to the fixed charge groups and sensitive to contact ion pairing. Vibrational spectroscopy is often utilized to assess interactions within CEMs containing RSO_3^- or other fixed charge groups[374–376], so we confidently analyze the symmetric S–O vibrations in the proximity of 1045 cm^{-1}. Unfortunately, comparable analyses are lacking in the AEM literature. Some of this is systematic: RSO_3^- exposes the charge-carrying oxygens, while the charge-carrying nitrogen of $RNMe_3^+$ is sheltered by the pendant methyl groups. However, we believe some of the reason is derived from the mystery of the C–N stretching mode. While amines are thoroughly documented in reference materials, there is less data available for ammoniums[377]. Primary and secondary ammonium data have some reported assignments, but tertiary and quaternary ammoniums are unrepresented. Many membrane researchers have assigned an FTIR signal to C–N stretching of $RNMe_3^+$ groups to verify functionalization of polymer materials; however, we believe that the assignments are not always well-supported. Instead of referencing a specific claim, we reason through the assignment of the C–N stretch from comparable spectra.

We primarily based our assignment for the quaternary ammonium C–N vibration peak based on the NIST standard spectrum for NMe_4Cl[378]. Only three prominent peaks are present in

this spectrum: ν = 930-960, 1400-1415, and 1480-1510 cm^{-1}. By analogue to tertiary amines, both peaks at higher wavenumbers likely correspond to C–H vibrational modes among the methyl groups[377]. Meanwhile, tertiary amines and primary ammoniums both are reported to exhibit C–N stretches from 900 – 1000 cm^{-1}, suggesting that this final peak of NMe_4Cl corresponds to a C–N stretch and not a peak corresponding to O–H or C–H vibration[377].

Chapter 3 Fundamental Models of Ion Transport Phenomena in Charged Membranes

Water-swollen polymeric ion-exchange membranes (IEMs) are dense membranes where water is intimately mixed with the polymer chains. This structure creates a unique environment that significantly affects ion transport. Unlike membranes with well-defined pores, the polymer/solvent mixture prevents well-developed viscous flow[379]. Instead, transport in IEMs is described using the Solution Diffusion (SD) model[380]. This framework identifies two steps involved in crossing a membrane: the partitioning step at the membrane-solution interface, where a species must enter or exit the membrane, and the diffusion step within the membrane, where a species must diffuse from one side of the membrane to the other. To fundamentally understand ion transport in IEMs, it is essential to investigate the concentrations and diffusivities of species within the IEM.

The models introduced in this section provide a framework for understanding (and sometimes predicting) the transport properties of IEMs. Section 3.1 connects the macroscopic transport properties of IEMs to the concentrations and diffusivities of the SD model. Then, Sections 3.2 and 3.3 present two widely utilized models that establish basic structure-property relationships for transport in IEMs. The remainder of Chapter 3 includes more advanced treatments of membrane transport phenomena, which will be utilized to improve the accuracy of the initial approximations derived from the core models. These theories often relate ion transport properties, measurable via the processes described in Section 2.3, to the structural properties of IEMs, measurable via the processes described in Section 2.2. The understanding derived from these

models underscores the importance of supplementing measurements of membrane performance with ion partitioning and single-ion diffusion coefficient experiments.

3.1 Conductivity and Selectivity Metrics

To understand how ion transport models predict the performance of IEMs, it is crucial to define the key performance metrics[91,381]: the counter-ion conductivity (κ_g) and charge selectivity ($\alpha_{g/c}$). The subscripts g and c represent the charges of the mobile ions. IEMs have ionizable functional groups attached to the polymer backbone that enable their selective transport properties. the electrostatics of cationic membranes encourage the transport mobile anions (anion-exchange membranes, AEMs), while those of anionic membranes encourage the transport of transport mobile cations (cation-exchange membranes, CEMs). Designating species g and c allows us to define ions relative to the membrane charge: counter-ions (g) have opposite charge to the fixed charge groups (A), while co-ions (c) have similar charge to the fixed charge groups. Thus, for both AEMs and CEMs, counter-ions are the ions with enhanced transport, while co-ions are the ions with suppressed transport.

We define κ_g and $\alpha_{g/c}$ in line with other membrane transport fields[91]. κ_g is the permeation coefficient of the desirable counter-ion species. $\alpha_{g/c}$ is the ratio of counter-ion conductivity to co-ion conductivity, or the number of desirable species passing the membrane per leakage of undesirable species. We calculate the counter-ion conductivity using the Nernst-Einstein relationship[16–18]:

$$\kappa_g = \frac{F^2}{RT} z_g^2 C_g^{m,t} D_g^m \tag{3.1}$$

Here, z_i is the signed valence of ion i, $C_i^{m,t}$ is the concentration of species i in the membrane (per total volume of membrane), and D_i^j is the diffusivity of species i in phase j. Additionally, T is the

absolute temperature, R is the molar gas constant, and F is Faraday's constant. The Nernst-Einstein relationship connects conductivities and diffusivities by asserting that the response to an applied electrochemical potential gradient must be identical, whether it be a gradient in activity or in electric potential. The Nernst-Einstein relationship is thought to be reasonably accurate for most IEMs[93] and will be used throughout this dissertation. The charge selectivity is defined then as:

$$\alpha_{g/c} = \frac{\kappa_g}{\kappa_c} = \frac{z_g^2 C_g^{m,t} D_g^m}{z_c^2 C_c^{m,t} D_c^m} \tag{3.2}$$

There are other metrics used to define IEM performance in the relevant literature[91]. Most commonly, the total ionic conductivity (κ) and the permselectivity (Π) are used. κ is directly measured, but Π is defined using transport numbers of ions (t_i^j). t_i^j represents the fraction of current carried by species i in phase j. Both of these performance metrics relate less directly to the passage of counter- and co-ions[91] than those we define in Equations 3.1 and 3.2 , so we focus exclusively on the simpler terms defined previously. However, for interconversion, we can also define κ_g and $\alpha_{g/c}$ in terms of electrochemical parameters. The results are:

$$\kappa_g = t_g^m \kappa \tag{3.3}$$

$$\alpha_{g/c} = \frac{t_g^m}{t_c^m} \tag{3.4}$$

It is often helpful to discuss normalized values of performance metrics, denoted by an overbar: $\bar{\kappa}_g$ and $\bar{\alpha}_{g/c}$. This normalization corrects for speed differences between ions[91]. In aqueous solution, ions diffuse at different rates[358], meaning that even without IEM intervention, diffusivities would not be equal. A practical example is NaCl, where chloride ions diffuse approximately 50% faster than sodium ions at room temperature[358]. Thus, AEMs contacting NaCl will perform better than CEMs contacting NaCl, even if all membrane interactions are identical.

The normalized performance metrics remove this bias by normalizing D_i^m with the corresponding solution diffusivity, D_i^s:

$$\bar{\kappa}_g = \frac{F^2}{RT} z_g^2 C_g^{m,t} \frac{D_g^m}{D_g^s} \tag{3.5}$$

$$\bar{\alpha}_{g/c} = \frac{z_g^2 C_g^{m,t} D_g^m}{z_c^2 C_c^{m,t} D_c^m} \frac{D_c^s}{D_g^s} \tag{3.6}$$

Although the actual performance of a membrane depends on non-normalized values, the science of membrane design is more easily discussed using the normalized values. This approach ensures a fair comparison of IEM performance across different ion species.

3.2 Donnan Equilibrium and Ion Partitioning in Charged Membranes

Because IEM polymers contain fixed charge groups, the concentration of mobile anions and mobile cations in the membrane will not be stoichiometrically equivalent. Instead, they will be offset to maintain electroneutrality with the fixed charge groups[16,17]. For an IEM contacting a single salt electrolyte solution, the electroneutrality condition is expressed as:

$$z_A C_A^{m,w} + z_c C_c^{m,w} + z_g C_g^{m,w} = 0 \tag{3.7}$$

Here, $C_i^{m,w}$ represents the concentration of species i per volume of water in the membrane. The normality of counter-ions ($z_g C_g^{m,w}$) must always exceed the normality of co-ions and must always be greater than or equal to the normality of the fixed charge groups. This is because the concentration of co-ions may be zero, but an IEM always contains fixed charge groups. When contacting DI water, there are no co-ions in the membrane, but when contacting a salt solution, co-ions enter the membrane. This phenomenon is referred to as ion sorption, or more formally, ion partitioning.

Ion partitioning in homogeneous IEMs is governed by Donnan equilibrium[16,17]. This model enforces equilibrium at the interface between the membrane and the surrounding solution. The basis of Donnan Theory is the equal electrochemical potential of each species at the membrane-solution interface:

$$\Delta\mu_i^{m-s} = RT\ln\left(\frac{a_i^{m,w}}{a_i^s}\right) + z_i F\Delta\Psi^{m-s} + \Delta(\bar{V}_i P)^{m-s} \tag{3.8}$$

Here, μ_i^j is the electrochemical potential of species i in phase j, a_i^j is the activity of species i in phase j, Ψ^j is the electric potential in phase j, $\bar{V}_i^j$ is the partial molar volume of species i in phase j, and P^j is the pressure in phase j. Additionally, ΔX^{m-s} represents the difference in property X from the membrane phase to the solution phase. When discussing the thermodynamics of ion partitioning, it is crucial to express concentrations and activities in the membrane per volume of sorbed water, $j = m, w$, as this aligns the reference states of infinite dilution[382].

To derive the main expression for Donnan equilibrium, the PV term is neglected. Due to the relatively low molar volumes of salts and an assumption of relatively low viscoelastic network pressures from the polymer, the PV term is typically not large compared to the other terms[16]. The Donnan potential is defined as $\Psi_{Don} = \Delta\Psi^{m-s}$, such that at equilibrium when $\Delta\mu_i^{m-s} = 0$:

$$\Psi_{Don} = \frac{RT}{z_i F}\ln\left(\frac{a_i^s}{a_i^{m,w}}\right) \tag{3.9}$$

Because counter-ions and co-ions equilibrate across the same interface, the Donnan potential experienced by each ion must be the same. By equating Equation 3.9 for counter-ions and co-ions in a single salt system, the equilibrium condition becomes:

$$\left(a_g^{m,w}\right)^{\nu_g}(a_c^{m,w})^{\nu_c} = \left(a_g^s\right)^{\nu_g}(a_c^s)^{\nu_C} \tag{3.10}$$

Here, we use ν_i to represent the number of molecules of ion i present in one salt molecule. Electroneutrality of the salt gives the relation between ν_i and the ion valence: $z_g\nu_g + z_c\nu_c = 0$.

For IEMs, due to the presence of immobile fixed charge groups, Equation 3.10 can be re-written using Equation 3.7 to make the counter-ion concentration in the membrane implicit.

$$\left(\left|\frac{z_A}{z_g}\right| C_A^{m,w} + \left|\frac{z_c}{z_g}\right| C_c^{m,w}\right)^{\nu_g} (C_c^{m,w})^{\nu_c} = \Gamma \nu_g^{\nu_g} \nu_c^{\nu_c} (C_s^s)^{(\nu_g+\nu_c)} \quad 3.11$$

The above equation introduces C_s^s to represent the concentration of salt in the external solution, replacing the concentrations of the individual ions. Furthermore, activities have been replaced with concentrations by introducing Γ, the Donnan ideality ratio, which collects the individual ion activity coefficients into a single term. These substitutions are made according to:

$$a_i^j = \gamma_i^j C_i^j \quad 3.12$$

$$\Gamma = \left(\gamma_\pm^s\right)^{(\nu_g+\nu_c)} / \left(\gamma_g^m\right)^{\nu_g} (\gamma_c^m)^{\nu_c} \quad 3.13$$

Here, the activity coefficients of species i in phase j are γ_i^j, and the mean ion activity coefficient $\gamma_\pm^j$ is used to simplify salt activities, where $\left(\gamma_\pm^j\right)^{(\nu_g+\nu_c)} = \left(\gamma_g^j\right)^{\nu_g} \left(\gamma_c^j\right)^{\nu_c}$. It is typical to use the semi-empirical Pitzer model[383,384] to describe $\gamma_\pm^s$ when studying IEMs, but then to resolve γ_g^m and γ_c^m separately using membrane-specific activity models[385]. Equation 3.11 is a useful expression of Donnan equilibrium because it is explicit in all the factors which affect co-ion partitioning into the IEM.

To reduce the complexity of Equation 3.11, a simplifying assumption is typically made. Many salts being studied are 1-1 salts, meaning that both the cation and anion are monovalent species. Further, essentially all IEMs contain monovalent fixed charge groups. Thus, $|z_A| = |z_g| = |z_c| = \nu_g = \nu_c = 1$. It is then possible to isolate $C_c^{m,w}$ in the above expression for a relatively straightforward equation[385,386]:

$$C_c^{m,w} = \sqrt{\left(\frac{C_A^{m,w}}{2}\right)^2 + \Gamma(C_s^s)^2} - \frac{C_A^{m,w}}{2} \quad 3.14$$

Setting $\Gamma = 1$ yields a special case referred to as the Ideal Donnan (ID) model. The ID model does not necessarily assume that ions behave ideally, but merely that ions within the membrane behave exactly as ideally as the ions in the contacting salt solution, $\gamma_i^m = \gamma_i^s$. The ID model is easy to use, because activity models are unnecessary; however, the ID model generally under-predicts co-ion concentrations in IEMs. Suppression of co-ion partitioning into the membrane is a key component required to confer charge selectivity in IEMs (Equation 3.2), so the performance of IEMs is generally over-predicted using ID theory. Nevertheless, the ID model is used throughout the literature and its predictions can serve as a helpful benchmark when studying IEMs.

3.3 The Mackie-Meares Tortuosity Model

Ion diffusion coefficients in IEMs are typically lower than in aqueous solutions due to physical effects (e.g., tortuosity) and specific interactions between the ions and polymer[16,387]. Various physical models for predicting the diffusion coefficients in water-swollen polymers have been proposed[388]. In conventional IEMs, the greatest barriers to ion diffusion are physical effects, typically handled by either Yasuda's theory for free volume effects or the Mackie-Meares model for polymer tortuosity. The Yasuda model requires 1-2 adjustable parameters to implement, whereas the Mackie-Meares model contains 0 adjustable parameters and is fully predictive. Despite the simplicity of the Mackie-Meares model, it has shown remarkable success at describing ion diffusion in IEMs[90,389,390]. Throughout this dissertation, we use this model to capture obstruction effects in IEMs. Mackie and Meares assumed that ion diffusion coefficients in IEMs are lower than in aqueous solutions due to tortuosity effects imposed by the impassable polymer

chains, which are molecularly mixed with the interstitial solution[389]. The main result of the Mackie-Meares model is:

$$\frac{D_i^m}{D_i^s} = \tau^{-2} = \left(\frac{\phi_w}{2-\phi_w}\right)^2 \quad 3.15$$

Here, D_i^j represents the diffusivity of species i in phase j, τ represents the tortuosity of the swollen IEM, and ϕ_w represents the water volume fraction.

Equation 3.15 predicts an order of magnitude reduction in effective diffusivity when $\phi_w = 0.48$, demonstrating how quickly obstruction effects can limit diffusion in polymer membranes. According to this model, the diffusion mechanism of the species within the membrane water is identical to that in aqueous solution—the path taken around the polymer chains is simply elongated. There are many other proposed effects that describe speeding-up or slowing-down of the actual diffusion jumps performed by species in IEMs; however, the full >10x decrease in effective diffusivities from obstruction effects typically represent the dominant effect even in relatively highly swollen IEMs[90,389,390].

3.4 Manning's Counter-Ion Condensation Theory

Non-ideal effects on ion partitioning and diffusion in IEMs have recently been modeled via a quantitative and predictive model called Manning's Counter-Ion Condensation Theory, or Manning Condensation[385]. Manning developed this framework to describe the point-line electrostatics of polyelectrolyte solutions in the 1960s[391], but more recently, Kamcev, Freeman, Paul, and Manning applied this mathematical framework to IEMs[386,392]. Because IEMs are essentially polyelectrolytes in the solid state, the modeled electrostatic effects were accurately predicted in various membrane systems. Since its introduction, Manning Condensation has become one of the most widely used predictive models describing IEM performance[385]. Manning's theories

were applied to IEMs through the Donnan-Manning model for ion partitioning and the Meares-Manning model for ion diffusion, improving the models introduced in the previous sections.

Manning's counter-ion condensation theory is centered around the reduced linear charge density, ξ (Figure 3.1) ξ compares the distance between fixed charge groups (b) to the characteristic distance of electrostatic forces (known as the Bjerrum length, λ_B):

$$\xi = \frac{\lambda_B}{b} = \frac{e^2}{4\pi\varepsilon_0\varepsilon^m k_B T b} \tag{3.16}$$

Here, e is the elementary charge, ε_0 is the permittivity of free space, ε^m represents the average dielectric constant of the membrane, and k_B is the Boltzmann constant. b can be calculated from the molecular structure of the polymer. For ethylene-based polymer backbones, the calculation is[385,392]:

$$\frac{b}{2.5\ \text{Å}} = 1 + \frac{n_n}{n_{ch}} \tag{3.17}$$

Here, n_{ch} and n_n represent the mole fraction of charged and neutral repeat units, respectively, and 2.5 Å is the projection length of the backbone in the repeat units[103]. ε^m may also be approximated using the structure of the IEM via[386,393]:

$$\varepsilon^m = \varepsilon^w \phi_w + \varepsilon^p (1 - \phi_w) \tag{3.18}$$

Here, ε^w is the dielectric constant of water, typically set to 78, and ε^p is the dielectric constant of the dry polymer, typically approximated as 6. To avoid the approximation in Equation 3.18, or when there is insufficient information to employ Equation 3.17, ξ has been used as a single adjustable parameter in the model. However, when ξ is estimated from the membrane structure, the model is capable of predicting experimental ion partitioning results in homogeneous membranes[385].

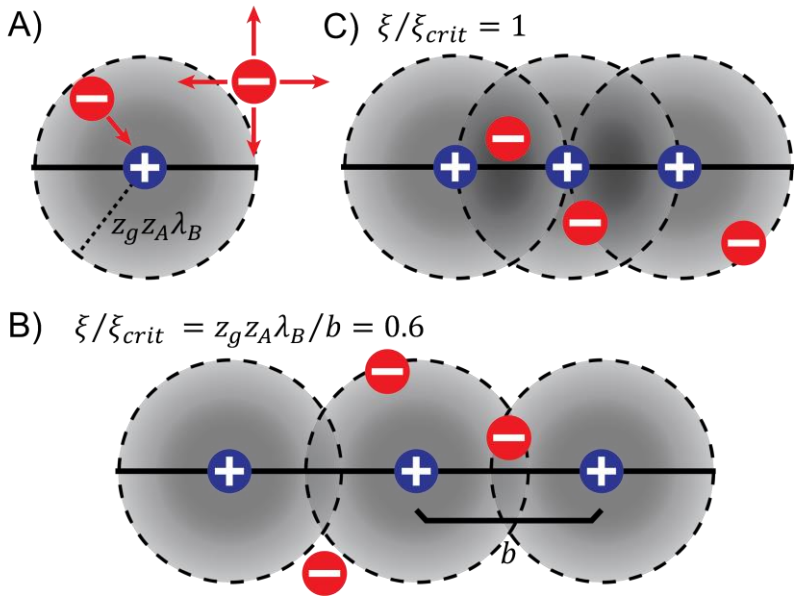


Figure 3.1: Polymer fixed charge spacing. a) Within a distance of $z_A z_g \lambda_B$, counter-ions must overcome the attractive force of a fixed ion to diffuse away. In an isolated two-ion system, this energy barrier is not insurmountable, but does increase as the counter-ion approaches the fixed charge group. b) When considering adjacent fixed charge groups along a polyelectrolyte, separated by a distance b, the system may exhibit regions of overlapping electrostatic influence. Beyond $\xi/\xi_{crit} = 0.5$, these overlapped regions create local minima of energy away from the fixed charge groups. c) Beyond $\xi/\xi_{crit} = 1$, the region of adjacent electrostatic influence no longer overlaps away from the fixed charge groups, but at the location of the fixed charges. This means that the local energy minima created by the overlap have intersected the absolute energy minima, deepening the energy well for counter-ions and resulting in condensation.

Counter-ion condensation occurs when ξ exceeds a critical value, ξ_{crit}, defined using the ion valences as $\xi_{crit} = 1/|z_A z_g|$. For $\xi/\xi_{crit} > 1$, the fixed charge groups along the polymer backbone are spaced so closely that electrostatic repulsive forces necessitate some form of relief[391,394] (Figure 3.1c). The polymer chain restricts the fixed charge groups near one another, so oppositely charged counter-ions must localize themselves along the polymer backbone, reducing the effective net charge of the polymer. These counter-ions are considered condensed and have no freedom to diffuse away from the polymer backbone. Condensed counter-ions are thought to retain their hydration shell, some mobility along the polymer backbone, and the freedom to exchange with nearby counter-ions. Counter-ions condense in sufficient number such that the effective

charge density of un-neutralized fixed charge groups becomes ξ_{crit}. Thus, the fraction of uncondensed counter-ions ($f_{g,u}$), which are osmotically active and remain available to contribute to Donnan equilibrium, is[385]:

$$f_{g,u} = \begin{cases} 1 & for\ \xi \leq \xi_{crit} \\ \dfrac{C_A^{m,w}\xi_{crit}}{\xi} + \nu_g \left|\dfrac{z_g}{z_A}\right| C_s^{m,w} & for\ \xi \geq \xi_{crit} \\ \hline C_A^{m,w} + \nu_g \left|\dfrac{z_g}{z_A}\right| C_s^{m,w} & \end{cases} \quad 3.19$$

The fraction of condensed counter-ions is quantified via: $f_{g,c} = 1 - f_{g,u}$. As implied by the mechanism discussed above, counter-ions will only condense to neutralize the fixed charge groups, so the counter-ions that formally maintain electroneutrality with the co-ions will not condense. Co-ions always remain uncondensed, so $f_{c,u} = 1$.

Manning's theory describes the nonidealities affecting uncondensed counter-ions using a point-line adaptation of the Debye-Hückel theory[391]. Ion activity coefficients are expressed as[385]:

$$\ln(\gamma_i^m) = \ln(f_{i,u}) - \frac{1}{2}\begin{cases} \dfrac{C_A^{m,w}\left(\dfrac{\xi}{\xi_{crit}}\right)\left(\dfrac{z_i}{z_g}\right)^2}{C_A^{m,w} + \left|\dfrac{z_c}{z_A}\right|(\nu_g + \nu_c)C_s^{m,w}} & for\ \xi \leq \xi_{crit} \\ \dfrac{C_A^{m,w}\left(\dfrac{z_i}{z_g}\right)^2}{C_A^{m,w} + \left(\dfrac{\xi}{\xi_{crit}}\right)\left|\dfrac{z_c}{z_A}\right|(\nu_g + \nu_c)C_s^{m,w}} & for\ \xi \geq \xi_{crit} \end{cases} \quad 3.20$$

This expression for γ_i^m may be solved for both counter-ions (g) and co-ions (c) and inserted into Γ, allowing Equation 3.11 or 3.14 to relax the assumptions of the ID model. This is referred to as the Donnan-Manning (DM) model.

Manning also described the effect of condensation and point-line electrostatics on ion diffusion in the presence of charged polymers[395,396]. This framework was also applied to IEM systems by Kamcev *et al.* to accurately describe ion transport in IEMs[90,385]. Diffusion coefficients

of uncondensed counter-ions are subject to an electrostatic friction effect described by the function A[385]:

$$A = \frac{1}{z_g^2}\begin{cases} \sum_{m_1=-\infty}^{+\infty}\sum_{m_2=-\infty}^{+\infty}\left(\frac{\pi\xi_{crit}}{\xi}(m_1^2+m_2^2)+1+\frac{\left|\frac{z_c}{z_A}\right|(\nu_g+\nu_c)C_s^{m,w}}{C_A^{m,w}}\right)^{-2} & for\ \xi \le \xi_{crit} \\ \sum_{m_1=-\infty}^{+\infty}\sum_{m_2=-\infty}^{+\infty}\left(\pi(m_1^2+m_2^2)+1+\frac{\xi\left|\frac{z_c}{z_A}\right|(\nu_g+\nu_c)C_s^{m,w}}{\xi_{crit}C_A^{m,w}}\right)^{-2} & for\ \xi \ge \xi_{crit} \end{cases} \quad 3.21$$

where $(m_1, m_2) \neq (0,0)$

Here, m_1 and m_2 are arbitrary summation indices. These ions are still affected by tortuosity from Equation 3.15, so the diffusivity of uncondensed ions ($D_{i,u}^m$) is given by:

$$\frac{D_{i,u}^m}{D_i^s} = \left(\frac{\phi_w}{2-\phi_w}\right)^2\left(1-\frac{z_i^2}{3}A\right) \quad 3.22$$

For typical inputs to Equation 3.22, the obstruction effects are dominant and the electrostatic effects only contribute a small correction[397].

The treatment above is generally sufficient to describe co-ion transport; however, the diffusivity of counter-ions must account for the fraction of condensed and uncondensed ions (Equation 3.19). The average diffusivity of the counter-ions is the weighted sum of the condensed and uncondensed ion diffusivities:

$$D_g^m = f_{g,u}D_{g,u}^m + f_{g,c}D_{g,c}^m \quad 3.23$$

The diffusivity of condensed counter-ions is difficult to predict[90]. It is common to approximate condensed counter-ions as immobile, i.e., $D_{g,c}^m \cong 0$. However, experimental evidence suggests that some mobility is still present for these ions[395,398–400]. Therefore, an adjustable parameter is used to account for condensed counter-ion transport[90]:

$$\frac{D_{g,c}^{m}}{D_{g}^{s}} = \frac{\alpha}{3} \tag{3.24}$$

Here, the factor of 3 was introduced to account for directionality. So far, all evidence suggests that α is large enough that $D_{g,c} > D_{g,u}$, although the amount of data available to make this comparison is quite limited[385].

3.5 Percolation of Polymer Blends by De Gennes

The models presented in the previous sections are designed for homogeneous, single-phase IEMs. This singular phase is the intimately mixed water-swollen polymer, called the ion-exchange polymer phase ($j = ixp$). When another phase is present, the ion-exchange polymer does not comprise the entire membrane ($ixp \neq m, t$), and further modeling considerations are necessary to develop an accurate description of the transport phenomena.

One way in which a second phase can be introduced into the IEM is through a polymer blend[401]. When the two polymer phases enable ion transport at different rates, the total membrane transport properties will be derived from the constituent polymer phases. When the polymer miscibility and mixing ratios are tuned to form isolated domains of a minority phase, the Maxwell model is generally utilized to describe the obstructed transport. However, when the polymer mixture forms a co-continuous blend, the Equivalent Box Model (EBM) by Kolařík[402,403] is more appropriate[401]. This model builds upon a percolation model developed by De Gennes[404], and in the limit of very different transport properties (e.g., the conductivity of one phase is much greater than that of the other phase, $\kappa_i^1 \gg \kappa_i^2$) the EBM prediction is equivalent to the model of De Gennes.

The De Gennes percolation model was developed to describe the total conductivity of a conductive phase interspersed with random non-conductive features[404,405]. Based on the locations and clustering of the non-conductive domains, efficiencies of the various pathways through the

conductive phase will change, giving a non-linear relationship between the observed conductivity and the volume fraction of non-conductive material. This relationship takes the form:

$$\frac{\kappa_i^{tot}}{\kappa_i^{ixp}} = \left(\frac{\phi_{ixp}^{tot} - \phi_{ixp,p}^{tot}}{1 - \phi_{ixp,p}^{tot}}\right)^{\tau_p} = \left(1 - \frac{1 - \phi_{ixp}^{tot}}{1 - \phi_{ixp,p}^{tot}}\right)^{\tau_p} \quad for\ \phi_{ixp}^{tot} > \phi_{ixp,p}^{tot} \qquad 3.25$$

Here, κ_i^j is the conductivity of species i in phase j, ϕ_j^{tot} is the volume fraction of phase j in the total membrane, $\phi_{j,p}^{tot}$ represents the critical percolation threshold for phase j in the membrane, and τ_p is an ordering factor which describes the arrangement of material for conduction. A value of $\tau_p > 1$ indicates the presence of dead-ends, or conductive material that is not useful for transport. Meanwhile, a value of $\tau_p < 1$ indicates resilient conduction pathways that preserve the conductive character of the membrane. The range requirement for ϕ_{ixp}^{tot} necessitates that the conductive phase percolates the membrane; if no conductive pathways exist, the conductivity of the membrane must approach 0. The first definition of Equation 3.25 is the way in which the De Gennes model has been used in the literature, but the second definition of Equation 3.25 makes the limiting behavior more obvious. As $\phi_{ixp}^{tot} \to 1$, the second term disappears and $\kappa_i^{tot} \to \kappa_i^{ixp}$.

To use the De Gennes model or the EBM for multi-phase IEMs, values for $\phi_{j,p}^{tot}$ and τ_p are needed. Often, these parameters are fit to describe experimental results [401]. However, theoretical values have been proposed[402]: Utracki identified $\phi_{j,p}$ to be 0.156 for anisotropic spherical domains[406,407] and De Gennes derived $\tau_p = 11/6 \cong 1.83$ for their percolation solution in three dimensions[404]. Experimental values often differ from these theoretical values based on the specific nature of the polymer system, but many systems are best described by values of $\phi_{j,p}^{tot}$ and τ_p near these theoretical figures[401,402].

3.6 Backing Effects in Reinforced Ion-Exchange Membranes

Like the discussion in Section 3.5, this section aims to describe the effects of embedding a non-conductive polymer in a two-phase IEM. Whereas the models discussed previously detail macromolecular mixtures of polymers, IEMs are often reinforced with a non-conductive polymer that is not subject to processing alongside the IEM. Commercial IEMs typically consist of an ion-exchange polymer phase polymerized either within a porous polymer mat or around a woven/non-woven polymer fiber mat[18,408,409]. These two motifs can be referred to as "pore-filled" and "fiber-reinforced," respectively. Although these composite structures are sometimes employed to regulate IEM performance, these structures are typically used with the primary goal of reinforcing a glassy, brittle ion-exchange polymer into a mechanically robust IEM ready for shipping and installation.

With a specific backing on-hand, it is possible to isolate the effects of that backing on ion-transport[392,408]. Polymer backings are treated as inert supports which only obstruct transport, consuming dead volume within the IEM and contributing to a more tortuous path for ion diffusion. Thus, experimentally determining the porosity (ε_b) and tortuosity (τ_b) of a backing allows predictions of an ion-exchange polymer to be adjusted to properties of a total IEM. Alternatively, ε_b and τ_b allow the experimental properties of a composite IEM to be transformed into the properties of the constituent ion-exchange polymer. Unfortunately, commercial IEM suppliers typically keep their backing structures proprietary, precluding experimental determination of ε_b and τ_b. However, it is important to be keenly aware of backing effects, which cannot be ignored while discussing fundamental transport phenomena in composite IEMs.

The total concentration of ions in the composite membrane ($C_i^{m,t}$), which is readily measured, is lower than the concentration of ions in the ion-exchange polymer (C_i^{ixp}) because of the dead volume effect[387]. The correction factor is ε_b:

$$C_i^{m,ixp} = \frac{C_i^{m,t}}{\varepsilon_b} \tag{3.26}$$

The water content of the membrane is affected similarly:

$$\phi_w^{ixp} = \frac{\phi_w^{tot}}{\varepsilon_b} \tag{3.27}$$

Here, ϕ_w^{ixp} refers to the water volume fraction normalized against the total volume of water and polymer comprising the ion-exchange polymer phase, while ϕ_w^{tot} is the experimentally accessible property normalized against the total volume of the composite IEM. C_A^{max} values are transformed identically to $C_i^{m,t}$ values. Notably, ion concentrations expressed per water in the membrane, $C_i^{m,w}$, do not require transformation. If water is sorbed entirely within the ion-exchange polymer, as should be the case when using hydrophobic polymer supports, there is no water in the backing phase to correct for.

Apparent ion diffusivities are impacted by the tortuosity of the support via[387]:

$$D_i^{m,ixp} = D_i^{m,t}\tau_b^2 \tag{3.28}$$

Here, we use ixp and t to denote the phase in which the effective diffusivity has been completely accounted for. The local diffusivity of species in the ion-exchange polymer is not expected to be affected by the presence of the backing; only the distance traveled to cross the IEM is expected to change.

Chapter 4 The Current State of Ion-Exchange Membranes[1]

4.1 Introduction

Ion-exchange membranes (IEMs) are used in a wide range of technologies, each of which weighs the importance of various transport properties differently[410]. Thus, the value an IEM provides to one technology does not always translate to another. Examples of the disparate roles filled by IEMs in electrochemical technologies are given in Section 1.2. These differences have led to numerous communities of researchers investigating IEMs, and because of this separation, it can be difficult to develop a broad picture of the current state of IEM development.

What is considered common knowledge for one set of IEM researchers remains obscure for others, meaning that some outstanding challenges in IEM design might already be answered, but for a different application. Recent attempts to utilize membrane for applications unintended by their manufactures have been surprisingly successful[411], demonstrating the advantage of testing a wide range of applications for polymer membranes. However, it is not obvious where to look for opportunities to utilize membranes across applications, in part because characterizations reported in different IEM sub-fields don't always overlap. Essentially the only aspects preserved between each research community is the ion-exchange capacity (IEC) and the water uptake (WU), which

[1]This chapter is based on a pair of completed manuscripts which have been published in peer reviewed journals. The first reference is: David Kitto and Jovan Kamcev. "The Need for Ion-Exchange Membranes with High Charge Density," J. Membr. Sci., 677, 121608 (2023). DOI: 10.1016/j.memsci.2023.121608. The second reference is: Carolina Espinoza* and David Kitto* (*co-first authors) and Jovan Kamcev. "Counter-Ion Conductivity and Selectivity Tradeoff for Commercial Ion-Exchange Membranes at High Salinities," ACS Appl. Polym. Mater., 5, 10324 (2023). DOI: 10.1021/acsapm.3c02102. C.E. collected water content, charge content, and ion partitioning data. J.K. assisted in collecting conductivity and permeability data. C.E. and J.K. assisted in the analysis of commercial membrane data. J.K. supervised both of these works.

are the two baseline structural properties that are reported for every IEM developed. However, as highlighted in Section 1.2, it is becoming clearer that most electrochemical technologies benefit from both a high ionic conductivity, κ (which affects the energy intensity of each process), and high charge selectivity, $\alpha_{g/c}$ (which affects the efficiency of many processes). The ubiquity of κ_g and $\alpha_{g/c}$ make them appealing targets for a generalized comparison of IEMs between fields.

It is widely acknowledged that $\alpha_{g/c}$ and κ_g are anti-correlated[412–416], so they must be considered in tandem. In separation applications, the performance of membranes is commonly evaluated using "upper bound" plots, which plot the ratio of permeabilities between two species against the permeability of the more permeable species[417]. This is because trade-off between selectivity and permeability is observed for nearly all synthetic membranes[418]. Standard trade-off plots quickly allow identification of highly selective membranes, highly permeable membranes, or membranes with the best combinations of the two. However, for IEM research areas, these analyses typically plot the permselectivity against the total ionic conductivity[412–416]. Both of these performance metrics are common and useful, but neither have the simple and intuitive interpretation of typical upper bound plots. To address this inconsistency and added complexity, our lab has recently proposed a reformulated upper bound plot for IEMs (Section 3.1)[419]. However, this new upper bound needs reliable data to populate the trade-off. Ideally, a relatively high concentration would be utilized, which challenges the IEMs and will allow for the highly selective membranes to be distinguished from the less selective membranes.

Studies that investigate the transport properties of a wide range of membranes at high salinities are scarce. Notably, Coronell and coworkers characterized the water and salt permeability of 20 commercially available IEMs contacted by 4.0 M NaCl solutions, as well as the equilibrium counter-ion and co-ion concentrations of the same membranes contacted by 0.5 M

NaCl solutions[420]. The use of 4.0 M NaCl solutions makes this study one of the most significant contributions to date for understanding the transport properties of commercial IEMs contacted by brines. However, the study did not include measurements of the ionic conductivity of the membranes, which is critical for understanding electric field-driven transport of IEMs and generating conductivity/selectivity trade-off plots. Additionally, equilibrium ion concentrations in the IEMs contacting the brine (i.e., 4 M NaCl) were not determined experimentally. Finally, with the exception of Nafion N115, all of the membranes used in this study are primarily marketed towards desalination applications. As discussed previously, a wide variety of IEM structures have been developed for other applications which may hold promise for applications such as desalination. A new data set of membranes would be necessary to fill the reformulated upper bound plot.

In this chapter, combining the results of two published manuscripts[421,422], I aim to present a picture of current IEMs. I first detail the efforts in our lab to characterize an array of 40 commercial IEMs which are marketed for an array of applications. We construct a trade-off plot for commercial IEMs from this data and assess the structure-property relationships which can be derived from these membranes. Then, to assess the extent to which IEM research has advanced past these commercialized processes, I utilize 1000 membrane structures sourced from recent publications to develop a perspective of new IEM designs. Again, we attempt to sample a broad range of IEM applications and literature spaces to develop a comprehensive picture of the advances in IEM design. The combined results of these investigations help to set goals for the continued development of IEMs with superior transport properties.

4.2 The Conductivity / Selectivity Trade-Off in IEMs

In the reformulated trade-off, we developed definitions for IEM performance which aligned with the definitions used in other membrane separation fields: on the y-axis, the selectivity is simply the ratio of conductivities attributed to two species, and on the x-axis is the conductivity due to the more permeable species. The details of these changes are given in Section 3.1, but the key results are the definitions for the normalized counter-ion conductivity ($\bar{\kappa}_g$) and normalized charge selectivity ($\bar{\alpha}_{g/c}$). These performance metrics are defined for IEMs contacting single 1-1 electrolytes as:

$$\bar{\kappa}_g = \frac{F^2}{RT} C_g^{m,t} \frac{D_g^m}{D_g^s} \tag{4.1}$$

$$\bar{\alpha}_{g/c} = \frac{\bar{\kappa}_g}{\bar{\kappa}_c} = \frac{C_g^{m,t}}{C_c^{m,t}} \frac{D_g^m D_c^s}{D_c^m D_c^s} \tag{4.2}$$

Here, $C_i^{m,t}$ represents the concentration of ion i per total volume of membrane, D_i^m represents the diffusivity of ion i in the membrane, and D_i^s represents the diffusivity of species i in aqueous solution at infinite dilution. Additionally, F is Faraday's constant, R is the ideal gas constant, and T is the absolute temperature. The ions considered include $i = g$, the counter-ions, and $i = c$, the co-ions.

To populate the trade-off, we purchased 20 commercial anion-exchange membranes (AEMs) and 20 commercial cation-exchange membranes (CEMs) which are advertised to be designed for various energy and water-based electrochemical applications. The details of purchasing commercial IEMs are given in Section 2.1.5. These membranes possess a wide array of fixed charge groups, composite backings, and polymer backbones. By selecting a wide range of targeted applications and structures, and by considering such a large number of IEMs, we aimed

to truly represent the full range of IEM designs. We track the membranes based on their intended sector of use (desalination vs. energy) and their charge (AEMs vs. CEMs) to identify trends in the results. To the best of our abilities, this survey of commercial IEMs was constructed to develop an upper bound constraining all commercialized IEM production capabilities.

We characterized ion transport these IEMs while contacting both 1 m and 5 m NaCl, which are representative of the high-salinity brine applications. Brine treatment is the developing IEM application perhaps most in need of simultaneously improved κ_g and $\alpha_{g/c}$, making it a natural target application for this data set. The results for IEMs contacting 1 m NaCl are presented in the main text, with the results for 5 m NaCl included in Appendix C.

A clear tradeoff is observed between $\bar{\alpha}_{g/c}$ and κ_g, shown in Figure 4.1, where no membranes fall in the highly-conductive, highly-selective region of the plot. Instead, membranes with high selectivity tend to have low counter-ion conductivity, while membranes with high counter-ion conductivity exhibit low selectivity. Most membranes for energy applications fall within the lower right region of the plot (i.e., low selectivity and high counter-ion conductivity), while most desalination membranes fall within the upper left region of the plot (i.e., high selectivity and low counter-ion conductivity). All energy CEMs exhibit high counter-ion conductivity and low selectivity, which is reasonable because they are all intended for use in fuel cells and electrolyzers. In contrast, the energy AEMs span a much wider range of counter-ion conductivity and selectivity combinations because some of these membranes (e.g., Sustainion B22-50 Grade T and Xergy Pention) are also marketed towards applications such as flow batteries, which demand high selectivity.

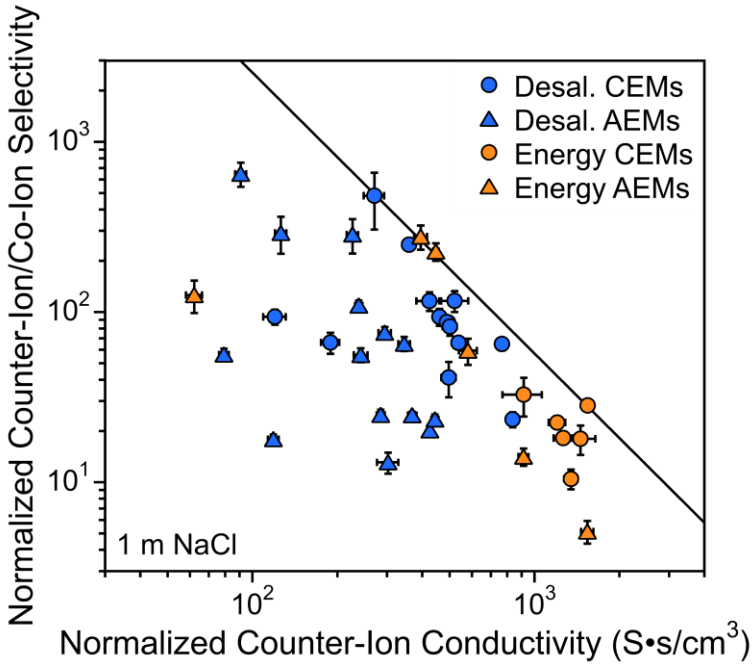


Figure 4.1: The conductivity / selectivity trade-off for 1 m NaCl. The normalized charge selectivity ($\bar{\alpha}_{g/c}$) vs. normalized counter-ion conductivity ($\bar{\kappa}_g$) for commercial membranes contacting 1 m NaCl solutions. The solid black line represents an empirically drawn "upper bound," which is of the form $\bar{\alpha}_{g/c} = \beta \bar{\kappa}_g{}^{-\lambda}$. For 1 m NaCl, $\beta = 5.08 \times 10^6$ and $\lambda = 1.65$.

High performance membranes should ideally exhibit both high counter-ion conductivity and high selectivity. At 1 m NaCl, there are four membranes that fall along the empirically drawn upper bound line, which represents the best combinations of counter-ion conductivity and selectivity amongst these commercial IEMs. These include one desalination CEM (Fumasep FKB-PK), two energy AEMs (Xergy Pention 72-15 and Orion AMX), and one energy CEM (Solvay Aquivion). Notably, there are no desalination AEMs that fall on the upper bound, and there are significantly more desalination CEMs than AEMs that are near the upper bound. This observation suggests that there is room for further improvement in the intrinsic performance of AEMs used for desalination applications. However, from a practical viewpoint, this is not a serious issue because the chloride counter-ions in AEMs are inherently faster than the sodium counter-ions in CEMs at

comparable membrane properties. That is, the absolute selectivities and counter-ion conductivities of the best performing AEMs and CEMs are more comparable than the normalized parameters.

$\bar{\alpha}_{g/c}$ can be decoupled into the partitioning selectivity ($\left(\alpha_{g/c}\right)_K = C_g^m/C_c^m$) and the normalized diffusion selectivity ($\left(\bar{\alpha}_{g/c}\right)_D = \left(D_g^m/D_g^s\right)/(D_c^m/D_c^s)$) to evaluate their individual contributions to $\bar{\alpha}_{g/c}$. Figure 4.2 presents $\left(\alpha_{g/c}\right)_K$ and $\left(\bar{\alpha}_{g/c}\right)_D$ as decoupled trade-off plots. In general, most IEMs exhibit $\left(\alpha_{g/c}\right)_K > 10$ and $\left(\bar{\alpha}_{g/c}\right)_D < 10$, demonstrating that partitioning contributes more to the total selectivity than differences in cation and anion diffusivities. However, three membranes (FAB-PK, FKB-PK, and PCSA) exhibit $\left(\bar{\alpha}_{g/c}\right)_D > 10$, with their partition selectivities at a similar order of magnitude. These membranes have significantly lower water content than the rest of the membranes, suggesting a potential correlation between membrane swelling and $\left(\bar{\alpha}_{g/c}\right)_D$ (further discussed below).

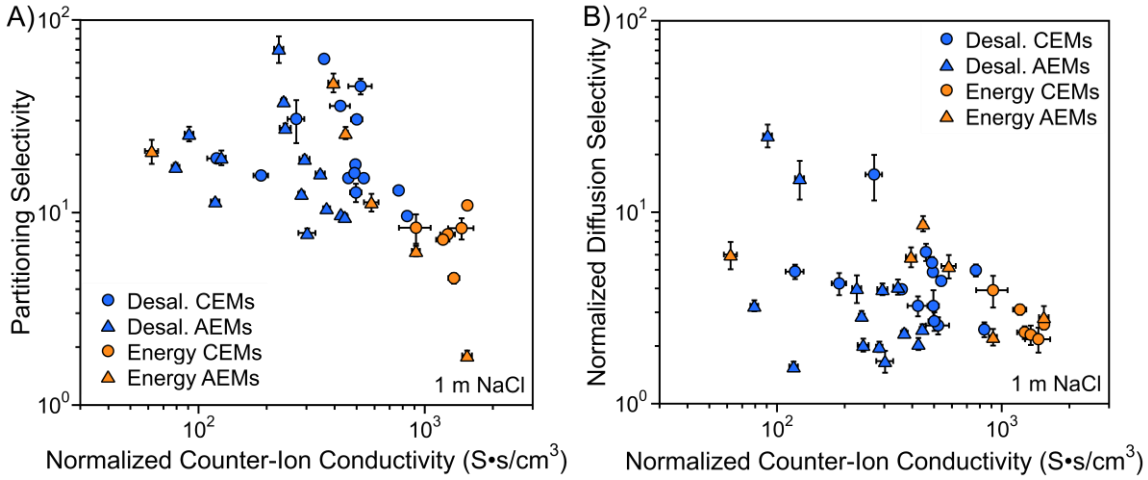


Figure 4.2: Selectivity contributions for commercial IEMs contacting 1 m NaCl. A) The partitioning selectivity ($\left(\alpha_{g/c}\right)_K$) plotted against the normalized counter-ion conductivity ($\bar{\kappa}_g$). B) The normalized diffusion selectivity ($\left(\bar{\alpha}_{g/c}\right)_D$) plotted against $\bar{\kappa}_g$. Standard propagation of

uncertainty methods were used to calculate uncertainties from measurements on at least 4 independent samples.

The trade-off at 5 m NaCl (Appendix Figure B.1) displays similar trends as at 1 m NaCl, but with nominally lower selectivities. The partition selectivities of all IEMs decrease to a significantly greater extent than the diffusion selectivities when contacted by 5 m NaCl, mainly due to weakened Donnan exclusion (c.f. Figure 4.2A and Appendix Figure B.1B). The diffusion and partition selectivities of IEMs contacted by 5 m NaCl are of similar magnitudes, suggesting that strategies aimed at enhancing diffusion selectivities of IEMs could be particularly effective at high salinities. For $\bar{\kappa}_g$, Appendix Figure B.2 demonstrates that some membranes exhibit enhanced conductivity, while others exhibit worsened conductivity as the IEM is brought from 1 m to 5 m NaCl. Interestingly, we observe a strong correlation: IEMs with worsened $\bar{\kappa}_g$ suffer the greatest reduction in $\bar{\alpha}_{g/c}$, while IEMs with enhanced $\bar{\kappa}_g$ experience less severe reductions in $\bar{\alpha}_{g/c}$. This correlation could relate to osmotic deswelling, correlated ion motion, or contact ion pairs, each of which are expected to become more extreme at brine concentrations. A controlled study on IEMs of known structure would likely be necessary to determine the nature of this trend.

4.3 Structure-Property Relationships in Commercial IEMs

According to Donnan theory, the co-ion concentration in IEMs is significantly influenced by the fixed charge group concentration ($C_A^{m,w}$) of the membrane (see Section 3.2). Figure 4.3A plots $\left(\alpha_{g/c}\right)_K$ against $C_A^{m,w}$ for the membranes considered in this study. In general, $\left(\alpha_{g/c}\right)_K$ increases with increasing $C_A^{m,w}$. At comparable $C_A^{m,w}$ values, the desalination IEMs demonstrate higher partition selectivities compared to the energy IEMs. This difference could be due to phase separation in the energy IEMs. Notably, many energy IEMs are made from linear polymers that can phase separate into hydrophilic and hydrophobic domains during the fabrication process[423].

Inhomogeneous distributions of fixed charges resulting from phase separation could increase co-ion partitioning in IEMs and thereby lower the partitioning selectivity[424,425]. Unfortunately, detailed information on the morphology of these membranes and the distribution of fixed charge groups within the membranes would be required to test this hypothesis.

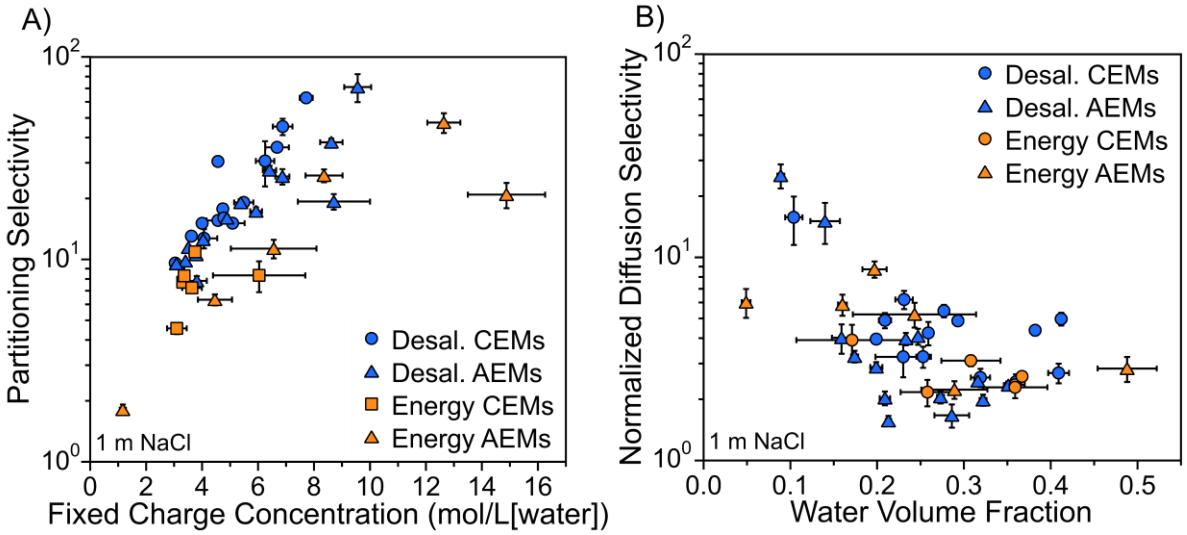


Figure 4.3: Selectivity correlations for commercial IEMs contacting 1 m NaCl. A) The partitioning selectivity ($\left(\alpha_{g/c}\right)_K$) plotted against the fixed charge concentration ($C_A^{m,w}$). B) The normalized diffusion selectivity ($\left(\bar{\alpha}_{g/c}\right)_D$) plotted against the water volume fraction (ϕ_w). Standard propagation of uncertainty methods were used to calculate uncertainties for the selectivities from measurements on at least 4 independent samples.

The observed differences in $\left(\alpha_{g/c}\right)_K$ at comparable $C_A^{m,w}$ values could also be due to variations in membrane non-ideal effects, such as counter-ion condensation,[426] introduced in detail in Section 3.4. Counter-ion condensation leads to an effective decrease in $C_A^{m,w}$ and would move a data point leftwards on Figure 4.3A. Due to a lack of information about the composition of these commercial membranes, we were unable to predict the extents of counter-ion condensation. Instead, we fitted the experimental ion partitioning results to the Donnan-Manning model to estimate the extent of counter-ion condensation. The results are presented in Appendix Table B.1.

For desalination IEMs contacted by 1 m NaCl, between 0 and 70% of counter-ions appear to be condensed, which falls within the expected range of previous reports[426].

The water content of IEMs significantly impacts ion diffusion coefficients in the membrane[427]. Figure 4.3B plots $\left(\bar{\alpha}_{g/c}\right)_D$ against ϕ_w (the water volume fraction) for membranes contacted by 1 m NaCl. Although there is significant scatter in the results, high values of $\left(\bar{\alpha}_{g/c}\right)_D$ were achieved exclusively by membranes having low ϕ_w. The underlying reasons for this behavior are not clear, since the fundamental understanding of ion diffusion in IEMs is not as advanced as that of ion partitioning[426]. The significant scatter in the results suggests that factors beyond ϕ_w likely influence $\left(\bar{\alpha}_{g/c}\right)_D$. For all membranes, $\left(\bar{\alpha}_{g/c}\right)_D > 1$, indicating faster diffusion of the desirable counter-ion species than the undesirable co-ion species. This result may be due to the ability of condensed counter-ions to migrate along the polymer backbone, which has recently been proposed as a mechanism for counter-ion diffusion in IEMs that exhibit counter-ion condensation[428,429]. This result may also be due to electroosmotic water transport that potentially speeds up the transport of counter-ions in electric field-driven experiments[430]. Fundamental studies on IEMs with well-defined structures are needed to better understand counter-ion diffusion in IEMs, specifically the high values of $\left(\bar{\alpha}_{g/c}\right)_D$ in membranes with low ϕ_w.

We also examined the effects of non-quantitative membrane structural properties, such as the fixed charge group chemistry, the polymer backbone chemistry, and the nature of the mechanical reinforcement. These properties have been tabulated from the literature in Table 2.3, and the tradeoff plots are presented in Appendix Figure B.3. The proprietary nature of the structures of commercial IEMs limited the extent of this analysis, but some interesting trends were nevertheless present. All membranes with polyphenylene backbones were located near the upper bound, especially for the data set collected with 5 m NaCl. Additionally, pore-filled composite

structures were utilized for IEMs near the 1 m NaCl upper bound. To learn more about these structural effects, controlled studies with known membrane structures are likely necessary.

4.4 Developments in the Structure of IEMs

To probe how the properties of IEMs might have improved in the literature beyond those of commercially available IEMs, we sought to assemble experimental values of the water volume fraction and fixed charge concentration (ϕ_w and $C_A^{m,w}$) for a wide range of recently developed membranes. These parameters helped rationalize both $\left(\alpha_{g/c}\right)_K$ and $\left(\bar{\alpha}_{g/c}\right)_D$ for the commercial membranes surveyed in the previous section. Additionally, both parameters widely utilized as explanations for observed values of κ, where additional water (high ϕ_w or low $C_A^{m,w}$) increases ion conduction speeds. However, these parameters are linked by the fixed charge density, $C_A^{m,t}$:

$$C_A^{m,t} = \phi_w C_A^{m,w} \tag{4.3}$$

Therefore, $C_A^{m,t}$ represents the ability of an IEM to simultaneously possess high ϕ_w and high $C_A^{m,w}$.

Unfortunately, across the surveyed literature space reporting new developments in IEMs, ϕ_w, $C_A^{m,t}$, and $C_A^{m,w}$ were seldom reported together. We therefore needed to make a few reasonable assumptions to obtain these parameters. The IEC and WU, which are universally reported, can be used to estimate $C_A^{m,w}$ via:

$$C_A^{m,w} = \frac{IEC \cdot \rho_w}{WU} \tag{4.4}$$

where ρ_w is the density of water in the membrane, which is generally assumed to be equal to that of bulk water. By assuming volume additivity, the water volume fraction can be estimated from WU, ρ_w, and density of the dry polymer, ρ_p, via:

$$\phi_w = \frac{WU}{WU + \rho_w/\rho_p} \tag{4.5}$$

Finally, $C_A^{m,t}$ can be estimated from Equation 4.3, 4.4, and 4.5 combined. Thus, the IEC, WU, and ρ_p are the only parameters required to calculate ϕ_w, $C_A^{m,t}$, and $C_A^{m,w}$. However, ρ_p is seldom reported when new IEMs are introduced. Making use of Equations 4.3, 4.4, and 4.5, approximately 12% of the surveyed studies explicitly reported or implicitly implied values for ρ_p. Values for IEMs made from hydrocarbon polymers typically ranged between 1.1-1.4 g/mL, with an average of 1.25 and a standard deviation of 0.20 g/mL. To complete this survey, we approximated a dry polymer density of 1.25 g/mL in cases where the actual dry polymer density was not reported.

Assuming volume additivity to estimate the total volume of membranes is convenient when experiments and data are constrained, such as in this perspective; however, this assumption may not always be reasonable. A more accurate methodology would involve measuring the actual hydrated volume of the membrane. While measuring the volume of hydrated membranes is not uncommon, many of the surveyed manuscripts report linear, areal, and volumetric swelling values that are not connected to volumetric water and charge contents. Notably, one study examines whether volume additivity holds for microporous IEMs, finding good agreement between swelling measurements and water content measurements[431]. Other manuscripts report data that allows for a similar comparison, but do not discuss the subject in their own analysis[99,432,433]. We find that error introduced by assuming volume additivity reaches up to 10 % for these membranes, but is often less. Based on these limited data, we believe that the assumption of volume additivity is a reasonable first approximation for IEM swelling and suitable for our purposes in this perspective.

Key results of our extensive literature survey are presented in Figure 4.4. In Figure 4.4A, $C_A^{m,w}$ is plotted against ϕ_w, and $C_A^{m,t}$ is represented by the contour lines calculated using Equation 4.3. This contour plot illustrates the interplay between these three parameters for IEMs reported in the past several decades. To better visualize the distribution of fixed charge density, Figure 4.4B

presents a histogram of $C_A^{m,t}$. The same values are reported in dark symbols for the commercial membranes surveyed in this chapter, and it is immediately apparent that membrane development has produced a wider range of properties than are commercially available. However, one striking observation from Figure 4.4 is the rather narrow range of $C_A^{m,t}$. Nearly all membranes have $C_A^{m,t}$ between 0-3 mol / L[membrane]. The average and median $C_A^{m,t}$ values are 1.42 and 1.35 mol/L[membrane], respectively, and the standard deviation is 0.65. Out of the ~1,000 membranes that we surveyed, only 25 membranes have $C_A^{m,t}$ greater than 3 mol / L[membrane] and only 3 membranes have $C_A^{m,t}$ greater than 4 mol / L[membrane]. Meanwhile, $C_A^{m,t}$ varied over a significantly broader range (0 – 65 mol / L[water]), and ϕ_w accessed nearly the entire spectrum of possible values (0.0 – 0.9 L[water] / L[membrane]).

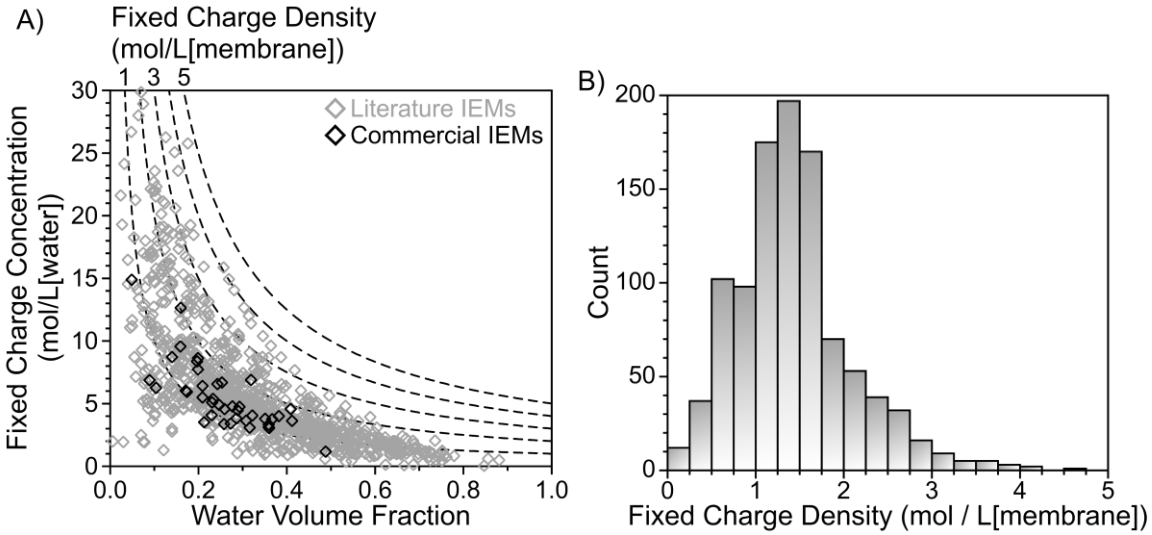


Figure 4.4 Structure of literature IEMs. A) The fixed charge concentration, $C_A^{m,w}$, plotted against the water volume fraction, ϕ_w, with te fixed charge density, $C_A^{m,t}$, shown using contour lines. The ~1000 membranes sourced from the published literature are shown in gray and the commercial IEMs surveyed in this chapter are shown in black. B) A histogram of the $C_A^{m,t}$ values reported in the literature.

Due to the relatively small variation in $C_A^{m,t}$, there is an apparent coupling between $C_A^{m,w}$ and ϕ_w. Membranes with high ϕ_w generally have low $C_A^{m,w}$. Such membranes typically exhibit

high κ but rather poor $\alpha_{g/c}$ due to relatively weak Donnan exclusion. IEC values are bounded within a relatively narrow range (approximately 0-5 meq / g[polymer]), so high $C_A^{m,w}$ are attained primarily by driving down WU of the IEMs (see Equation 4.4). Such membranes tend to exhibit high $\alpha_{g/c}$ but rather low κ, due to slow ion diffusion in the polymer rich membranes (see the Mackie-Meares model in Section 3.3). Thus, this coupling between $C_A^{m,w}$ and ϕ_w manifests in a performance tradeoff between $\alpha_{g/c}$ and κ[416,419,434]. These results suggest that a structural trade-off lies behind the performance trade-off in Figure 4.1. Breaking the structural trade-off requires membranes with higher $C_A^{m,t}$ (i.e., moving towards the upper right region of the plot in Figure 4.4A).

To gain deeper insight into the state of developing IEMs for certain applications, we separated the data set into the same broad categories as the commercial membranes: the membrane charge and the intended use case. Figure 4.5A presents a contour plot in which CEMs and AEMs are distinguished by color and symbol. The absolute ranges for $C_A^{m,t}$, $C_A^{m,w}$, and ϕ_w of CEMs and AEMs are similar. However, there are significantly more AEMs with $C_A^{m,t}$ > 2 mol / L[membrane] and $C_A^{m,w}$ > 17 mol / L[water]. Furthermore, there are very few CEMs simultaneously exhibiting $C_A^{m,t}$ > 2 mol / L[membrane] and ϕ_w > 0.35 (i.e., highly charged and moderately to highly swollen).

The lack of CEMs having high $C_A^{m,w}$ could be due to the relatively hydrophilic nature of the sulfonate functional group, which is used almost exclusively as the fixed charge group in CEMs. In the reported IEMs, high $C_A^{m,w}$ values are primarily achieved by having reasonably high IEC values and very low WU values. The hydrophilic nature of the sulfonate groups could preclude attaining low water content in CEMs while maintaining reasonably high IEC values. This is a lesser issue for AEMs since the functional groups used in AEMs[435] (e.g., quaternary ammoniums,

imidazoliums, pyridiniums, etc.) are more hydrophobic than sulfonates. That is, a given high IEC would generally lead to more swelling in a CEM than in an AEM, essentially diluting $C_A^{m,t}$ to a greater extent. Thus, it may be fruitful to explore alternative, less hydrophilic charged groups in CEMs to access a broader range of fixed charge concentrations and densities. These results suggest that the performance of systems that require both CEMs and AEMs (e.g., electrodialysis, membrane capacitive deionization) may be limited by the performance of the CEMs.

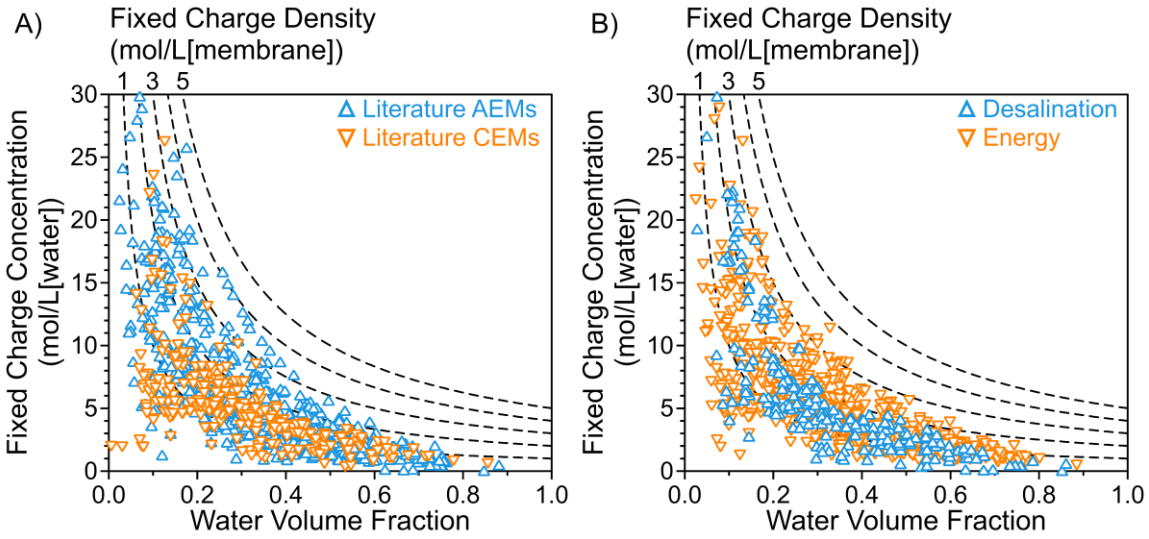


Figure 4.5 Sorted contour plots. Contour plots of literature membranes comparing A) AEMs and CEMs and B) desalination and energy IEMs. AEMs and desalination IEMs are shown as blue triangles pointing upwards on their respective plots. CEMs and energy IEMs are shown as orange triangles pointing downwards on their respective plots.

The second distinction was made between IEMs developed for desalination applications and those developed for energy applications. Figure 4.5B presents a contour plot in which IEMs for desalination and energy applications are distinguished by color and symbol. In both the desalination and energy research areas, the absolute ranges for $C_A^{m,t}$, $C_A^{m,w}$, and ϕ_w are quite similar. However, virtually no IEMs proposed for desalination simultaneously exhibit $C_A^{m,t}$ > 2 mol / L[membrane] and ϕ_w > 0.3, while there is a substantial number of IEMs proposed for energy applications that surpass these values. In other words, the performance bounds for

energy IEMs have advanced further than those for desalination IEMs. A relatively low barrier strategy for improving the performance of desalination technologies such as electrodialysis or membrane capacitive deionization could be to adopt these high-performance IEMs that have been developed for energy applications.

4.5 The Charge Density of Dry Polymers

When targeting IEMs with high $C_A^{m,t}$, it is instructive to define an upper limit for this parameter. For a given membrane, the maximum fixed charge density, C_A^{max}, is attained when the membrane is in the dry state and the entire volume is occupied by the polymer chains and free volume elements between the chains. As water molecules partition into a membrane, the volume of the membrane expands, and $C_A^{m,t}$ decreases from this maximum value. In some cases, it may be possible for the initial water sorption to occur without significantly changing the membrane volume as water molecules fill free volume elements in the membrane.[105,436] However, the fraction of this type of water should be quite small, as most of the water molecules that partition into IEMs appear to contribute to an increase in the total membrane volume (as discussed in the previous section). The maximum charge density, which depends on the chemical structure of the polymer and the packing of the polymer chains when a membrane is formed, is readily calculated from the IEC and dry polymer density via:

$$C_A^{max} = IEC \cdot \rho_p \tag{4.6}$$

Defined in this way, the maximum charge density is dependent only on the polymer backbone and functionalization and is completely independent of the water content achieved while hydrated. Further, other volumetric charge contents can be calculated from C_A^{max} using ϕ_w:

$$C_A^{m,t} = C_A^{max}(1 - \phi_w) \tag{4.7}$$

$$C_A^{m,w} = C_A^{max}(1 - \phi_w)/\phi_w \quad 4.8$$

Figure 4.6 presents C_A^{max} as a function of ϕ_w for the ~1000 literature membranes and 40 commercial membranes considered in this chapter. Most IEMs have maximum charge densities between 0 and 5 mol / L[polymer], and only 15 membranes have maximum charge densities between 5 and 6 mol / L[polymer]. Although the data points are quite scattered, there appears to be a weak correlation between the maximum charge density and water volume fraction. That is, most membranes that have high maximum charge density tend to swell more, so a smaller fraction of the maximum charge density is realized. This correlation is centered around the commercial membrane data points, suggesting these very well-represented structures in the literature are related to those which have been commercialized. The correlated behavior observed in this plot ultimately helps to explain the narrow range of $C_A^{m,t}$ observed in Figure 4.4A. To realize higher $C_A^{m,t}$, IEMs with high C_A^{max} values and restricted swelling should be targeted (Equation 4.7). The IEC of membranes varies over a significantly broader range than ρ_p and is easier to synthetically control; thus, membranes with high IEC values should be targeted to increase the upper limit of the maximum charge density[437].

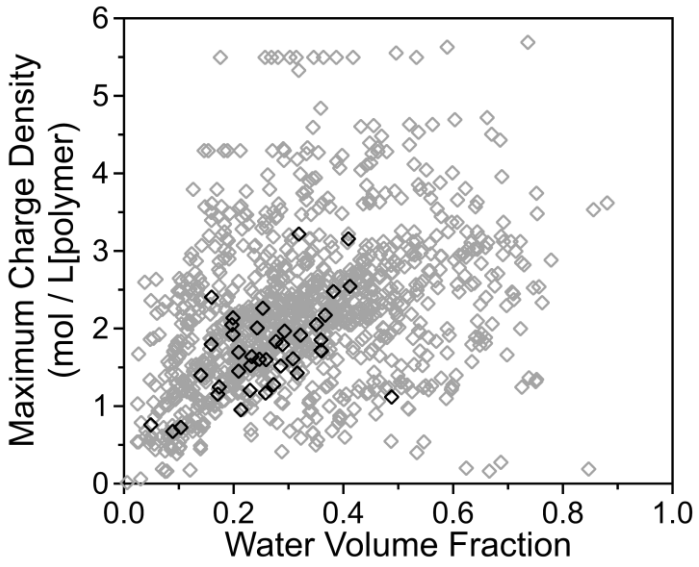


Figure 4.6: Maximum charge densities. The maximum charge density (C_A^{max}) plotted against the water volume fraction for ~1000 IEMs literature IEMs and 40 commercial IEMs. The literature IEMs are shown in gray, while the commercial IEMs are shown in black.

4.6 Strategies and Potential Challenges for Highly Charged IEMs

Figure 4.4 illustrates how difficult it is to synthesize IEMs with $C_A^{m,t}$ greater than 3 mol / L[membrane]. Of the ~1000 membranes reported in over 200 publications, only 6 sources report data suggesting $C_A^{m,t}$ greater than this threshold. The discussion below highlights the key strategies used in these studies that enabled this marked level of charge density.

The highest charge density IEMs in Figure 4.4 were synthesized by employing techniques that simultaneously introduce both cross-links and charged groups. This strategy can be implemented by either polymerizing charged cross-linkers or by cross-linking polymers via reactions that form charged groups (e.g., a polymer backbone containing a chloromethyl group can be cross-linked with a molecule containing at least two tertiary amines, yielding quaternary ammonium cations). Carter et al. implemented the former strategy by synthesizing bis-imidazolium cross-linkers which enabled the synthesis of high C_A^{max} membranes[438]. By polymerizing charged cross-linkers in highly concentrated solutions, Carter et al. maximized the

effective cross-link density and produced low water content membranes; coupled with high IECs, this strategy afforded high $C_A^{m,t}$ (~4.5 mol / L[membrane] for the most densely charged membrane). Ge et al. enacted the second strategy by synthesizing "hyperbranched" materials, wherein charged cross-linking structures were formed in situ between polymer side chains in a complex branched structure[439]. Ge et al. report that localizing such a high cross-linking density to the hydrophilic region of the membranes produced favorable microstructure, and this is reflected in the high $C_A^{m,t}$ of the membrane (~3.3 mol / L[membrane]). Both of these studies highlight cross-link formation as an effective strategy for reducing membrane swelling.

Another successful method for achieving high $C_A^{m,t}$ involves the preparation of membranes from phase-separated block copolymers. This strategy introduces distinct hydrophilic and hydrophobic domains into the membrane structure, where the uncharged domain restricts the swelling of the highly charged domain. Zhu et al. magnified the difference between the hydrophilic and hydrophobic blocks in a block copolymer made from styrene functionalized with a quaternary ammonium (charged segment) and fluorinated styrene (uncharged segment)[440]. The stark chemical difference between the highly charged and the heavily fluorinated blocks enabled the authors to synthesize IEMs with efficient phase separated morphology and high $C_A^{m,t}$ (~3.7 mol / L[membrane]). Comparatively, Jin et al. prepared IEMs from poly(para-phenylene) block copolymers with targeted cross-linking in the hydrophilic domain[441]. By heavily cross-linking the hydrophilic domain in the block copolymers while in a non-swollen state, the authors achieved a six-fold reduction in the water content relative to an un-cross-linked block copolymer membrane, nearly tripling the charge density of the material (~3.4 mol / L[membrane]). As both mentioned block copolymer examples demonstrate, the swelling reduction provided by nano-structuring is rarely sufficient to produce very densely charged IEMs without judicious selection

of the structures comprising each domain. Lastly, we note that the use of block copolymers as IEMs can result in both positive and negative effects. While they may provide mechanical reinforcement, swelling constraints, and conductive pathways, they may also reduce the conductive volume, increase the complexity of preparation, and lead to membrane anisotropy[442,443].

Phase separation has also been implemented on a smaller length scale than that of block copolymers, which is deemed "micro-phase separation". Although the polymer structure is not intentionally segregated into distinct phases, the process of membrane preparation naturally creates different domains, which may significantly affect the location of water in the hydrated membrane.[444] Ghorai et al. synthesized micro-phase separated CEMs using sulfonated polytriazoles, where the angled polymer backbone and abundant hydrogen bond receivers reportedly create a densely packed membrane when prepared with proton counter-ions[445]. These CEMs attained $C_A^{m,t}$ of ~3mol / L[membrane]. Du et al. prepared AEMs from a linear polymer with specific bulky sidechains, which were brominated and then cross-linked using poly(vinylimidazole)[446]. These AEMs attained charge densities of ~3 mol / L[membrane]. Both of these strategies involve the creation of a unique polymer architecture which then gets locked in via added interactions, yielding an advantageous micro-phase structure.

Alongside strategies for achieving high $C_A^{m,t}$, it is also worth considering the potential downsides of high $C_A^{m,t}$. We have emphasized the importance of preparing and studying membranes with higher charge densities based on the empirical trends and equations that govern ion transport in IEMs, which recommend increasing $C_A^{m,t}$ without hesitation. However, practical concerns and non-ideal behavior may present challenges in using and developing high charge density membranes. We have already discussed the need to break the tendency of highly charged

polymers to dilute their charge density with excessive swelling (the anti-correlation between $C_A^{m,w}$ and ϕ_w). Developing novel and improved ways of constraining hydrophilic polymer swelling will be the first difficult step, but researchers will almost certainly face additional challenges after the membranes have been synthesized.

First, it can be seen from the collected data that linear polymers with unconstrained swelling rarely achieve high $C_A^{m,t}$. By losing access to linear polymers, lab-scale study of high $C_A^{m,t}$ membranes could be slowed down, simply fewer labs will be equipped to prepare such membranes. Second, the balance of osmotic and chain-coiling forces governing membrane swelling is likely to become more delicate as the magnitude of each force in equilibrium increases. That is, mechanical and dimensional stability may limit the range of achievable $C_A^{m,t}$ even more than synthetic limitations. It is likely that practical concerns such as these depend on the synthetic strategy. Perhaps we shall see that, between charged cross-linking, block copolymers, microheterogeneity, and other unknown methods of achieving high charge density, these physical constraints may be more distinguishing than the transport properties.

Increasing the charge density of membranes can lead to counter-ion condensation (Section 3.4), which reduces the effective charge density of a membrane[392,426,447,448]. The extent of counter-ion condensation is predicted to increase as fixed charge groups are placed closer to each other[99]. Experimental partitioning studies investigating counter-ion condensation in materials with charge densities greater than 2 mol / L[membrane] have not been performed yet[426]; however, from the limited data available, commercial membranes do not seem to exhibit increased counter-ion condensation at higher charge densities within this limit[420]. The results presented earlier in this chapter for commercial IEMs agree with these published results, somewhat suppressing this concern. We must also consider that, while counter-ion condensation is detrimental for partitioning

selectivities, its effects on counter-ion conduction are less clear. There are some studies that report condensation improves the membrane conductivity[428,449], while others report the opposite effect[429,447,450]. Ultimately, the impact of counter-ion condensation and other deviations from ideal behavior will need to be studied experimentally in high $C_A^{m,t}$ materials once they are synthesized.

4.7 Conclusions

Current commercial IEMs are subject to a trade-off between counter-ion conductivity and counter-ion/co-ion selectivity when contacting reasonably concentrated salt solutions. IEMs used for energy applications (e.g., electrolysis) generally exhibit high counter-ion conductivity but low selectivity. Conversely, IEMs used for desalination applications (e.g., electrodialysis) generally exhibit high counter-ion/co-ion selectivity but low counter-ion conductivity. When contacted with 1 m NaCl solutions, the partition selectivities of the IEMs are significantly higher than the diffusion selectivities, whereas both selectivities are comparable in magnitude when the membranes are contacted by 5 m NaCl. The partition selectivities correlate well with the fixed charge group concentration, while high diffusion selectivities are achieved exclusively by membranes that have exceptionally low water content.

Although membranes have been which promise greater performance than current commercial IEMs, they are limited by the same constraints. IEMs developed in recent decades are bounded within a rather narrow range of fixed charge densities, which significantly impacts IEM performance. We highlighted notable exceptions where investigators cleverly tuned the strength and density of swelling-reduction effects to achieve notable charge densities. However, such examples represent less than 1% of the membranes surveyed. Moreover, high charge density membranes (>4 mol / L[membrane]) have only been accessed at relatively low water contents. Membranes with high charge density (>4 mol / L[membrane]) and moderate to high water content

have not been reported to the best of our knowledge. Developing such materials would represent a significant advancement in IEM design, breaking the structural trade-off and potentially breaking the ion transport performance trade-off discussed in this chapter.

By comparing IEMs produced in somewhat separated portions of the literature, our results encourage more interdisciplinary cross-referencing in future IEM research. Surveying a diverse set of 40 commercial IEMs demonstrated different design of membranes depending on the application. Further, the expansive collection of ~1000 literature IEMs identified progress in material design has not been equal between the fields of IEM study. We believe that future intermixing desalination and energy research practices will lead to improved understandings of ion transport phenomena and accelerated IEM design advances.

Chapter 5 Predicting the Conductivity-Selectivity Trade-Off and Upper Bound[2]

5.1 Introduction

Virtually all synthetic membranes for separation applications exhibit a trade-off between permeability and selectivity[451]. For binary separations, this trade-off is typically demonstrated by plotting the permeability of the more permeable species on the x-axis and the ratio of the permeabilities of the two species on the y-axis. This format, pioneered by Robeson in the 1990s for gas separation membranes[417,451], almost always reveals an unpopulated upper-right quadrant, indicating the scarcity of membranes that achieve both high selectivity and high permeability. This empty quadrant is sectioned off from the data-populated region by an upper bound line, which Robeson initially drew empirically. A theoretical foundation for this permeability/selectivity trade-off in gas separation membranes was later provided by Freeman[452]. Notably, both the slope and intercept of the upper bound line for a gas pair could be described using the inherent structural properties of the gases and membranes. This significant development sharpened the focus of membrane researchers, directing design efforts in the quarter century since its introduction. In this study, we present a model that explains the trade-off between ionic conductivity and selectivity observed in ion-exchange membranes (IEMs)[416,419,453–460].

Across the diverse applications of IEMs (Section 1.2), different operating conditions give rise to different prioritizations of membrane conductivities and selectivities, mandating a case-by-

[2]This chapter is based on a completed manuscript which has been published in a peer reviewed journal. This reference is: David Kitto and Jovan Kamcev. "Predicting the conductivity/selectivity trade-off and upper bound in ion-exchange membranes," ACS Energy Lett., 9, 4, 1346-1352 (2024). DOI: 10.1021/acsenergylett.4c00301. J.K. assisted in the mathematical derivation and supervised this work.

case membrane design approach. Understanding the trade-off between ionic conductivity and counter-ion/co-ion selectivity is essential for designing novel membranes with optimized transport properties, ultimately improving the performance of these electrochemical technologies. It is empirically known that IEMs swollen excessively with water exhibit high ionic conductivities at the expense of diminished selectivities, while low water content IEMs often exhibit the reverse set of properties[416,455,457,460,461]. Previous modeling efforts to rationalize this observation, notably by Yip and coworkers, have produced complex systems of equations underpinning the trade-off relationship[455,458]. However, these modeling efforts have not achieved an analytical expression for the upper bound relationship in the same instructive manner as in Freeman's seminal study for gas separation membranes. The insights offered by a definitive upper bound equation remain particularly elusive because model evaluations often involve comparison with a small number of IEMs, rather than the hundreds of data points that firmly established the upper bounds in Robeson's original study. Consequently, a simple equation for the conductivity/selectivity upper bound in IEMs has neither been proposed nor properly vetted against a wide range of materials.

The set of commercial IEMs characterized in Chapter 4 present a unique opportunity. Because we studied membranes with different polymer backbones (e.g., polystyrene, polyamide, polynorbornene, polyphenylene, polytetrafluoroethylene) and structures (homogeneous composites, heterogeneous composites, or non-composites), the resultant trade-off plot (Figure 4.1) defines the performance limits of current state-of-the-art IEMs. In the present study, enabled by this expansive data set, we derive an explicit linear relationship describing the conductivity/selectivity upper bound of current IEMs by combining robust models that relate ion partitioning and diffusion in the membrane to structural properties of IEMs. The final model employs a single adjustable parameter, which has a clearly understood definition and can be readily

measured for new materials. This model advances our current understanding of the conductivity/selectivity trade-off and paves the way for the frontier of IEM design.

5.2 Model Development

The ion transport properties in the upper bound model are the counter-ion / co-ion charge selectivity, $\bar{\alpha}_{g/c}$, and the counter-ion conductivity, $\bar{\kappa}_g$, which were introduced in Section 3.1. These equations are reproduced here for IEMs contacting aqueous 1-1 single-salt solutions:

$$\bar{\kappa}_g = \frac{F^2}{RT} C_g^{m,t} \frac{D_g^m}{D_g^s} \tag{5.1}$$

$$\bar{\alpha}_{g/c} = \left(\alpha_{g/c}\right)_K \left(\bar{\alpha}_{g/c}\right)_D = \left(\frac{C_g^{m,t}}{C_c^{m,t}}\right)\left(\frac{D_g^m D_c^s}{D_c^m D_g^s}\right) \tag{5.2}$$

Here, $C_i^{m,t}$ represents the concentration of ion i in the membrane (per volume of total membrane), D_i^m represents the diffusivity of ion i in the membrane, and D_i^s represents the diffusivity of ion i in aqueous solution at infinite dilution. $i = g$ refers to counter-ions, which are anions in anion-exchange membranes (AEMs) or cations in cation-exchange membranes (CEMs), while $i = c$ refers to co-ions, which are defined opposite of counter-ions. Additionally, F is Faraday's constant, R is the ideal gas constant, and T is the absolute temperature. The total charge selectivity is distributed between two components: the partitioning selectivity ($\left(\alpha_{g/c}\right)_K$) and the diffusion selectivity ($\left(\bar{\alpha}_{g/c}\right)_D$). These definitions make use of the Nernst-Einstein equation, which is discussed in detail alongside the performance metrics in Section 3.1.

From Equations 5.1 and 5.2, deriving an explicit equation for the conductivity/selectivity upper bound requires models that predict $C_g^{m,t}$, $C_c^{m,t}$, D_g^m, and D_c^m. To accomplish this, we use the Donnan-Manning and Meares-Manning models for ion transport in homogeneous IEMs, introduced in Section 3.4. These models have successfully described ion transport in a range of

IEMs and are able to relate ion concentrations and diffusivities in the membrane to just three structural properties; we are able to incorporate them with one another using the maximum charge density (C_A^{max}, mol [fixed charge] / L [dry polymer]) as defined by Equations 4.7 and 4.8. C_A^{max} joins the water volume fraction (ϕ_w, L [water] / L [hydrated membrane]) and the reduced linear charge density (ξ) as inputs to the fundamental models predicting ion transport properties of IEMs. Quantitative predictions of counter-ion diffusion in IEMs remains elusive, so for simplicity, $\left(\bar{\alpha}_{g/c}\right)_D$ in Equation 5.2 is treated as a single adjustable parameter in the upper bound model.

The combination of constituent models into the Donnan-Meares-Manning model for the conductivity/selectivity upper bound is detailed in Section C.2. The steps of this derivation are illustrated in Appendix Figure C.1. Because many commercially available IEMs are mechanically-reinforced composites, the predictions for commercial membranes must also account for composite effects on the effective ion concentrations and diffusivities in the membrane[408]. In Section C.3, we utilize relationships for the porosity (ε_b) and tortuosity (τ_b) of the support (introduced in Section 3.6), which allows the model to capture the performance of commercial composite IEMs. Finally, various modifications to the model are provided in Section C.4, including: a simplified model without counter-ion condensation which may be especially useful for highly concentrated salt solutions (Section C.4.1), an advanced condensation model for when the membrane structure is understood at a molecular level (Section C.4.2), a variant where counter-ion diffusivity is modeled via counter-ion condensation theory (Section C.4.3), and a generalized model for multivalent ions (Section C.4.4). For simplicity, the discussion below is limited to 1-1 electrolytes such as NaCl.

The resulting predictions of $\bar{\kappa}_g$ and $\bar{\alpha}_{g/c}$ for homogeneous IEMs are given by:

$$\bar{\kappa}_g = \frac{F^2\left(\bar{\alpha}_{g/c}\right)_D}{1.16RT} C_A^{max} \frac{\phi_w^2(1-\phi_w)}{(2-\phi_w)^2} \tag{5.3}$$

$$\bar{\alpha}_{g/c} = \frac{\left(\bar{\alpha}_{g/c}\right)_D}{\xi \exp(1)} \left(\frac{C_A^{max}}{a_s^s}\right)^2 \frac{(1-\phi_w)^2}{\phi_w^2} \tag{5.4}$$

where a_s^s is the activity of salt in the external solution, and all other terms have been defined previously. To reach the final equation for the upper bound, we combine Equations 5.3 and 5.4 via the ϕ_w^2 term and assume that secondary scaling effects from ϕ_w are relatively minimal, allowing us to conditionally approximate $\phi_w \to 0$. The final linearized equation for the conductivity/selectivity upper bound is:

$$\log\left(\bar{\alpha}_{g/c}\right) = \log\left(\frac{F^2 (C_A^{max})^3 \left(\bar{\alpha}_{g/c}\right)_D^2}{12.56RT\xi (a_s^s)^2}\right) - \log\left(\bar{\kappa}_g\right) \tag{5.5}$$

Equation 5.5 is of the same form as the empirically drawn line, $\bar{\alpha}_{g/c} = \beta \bar{\kappa}_g{}^{-\lambda}$. The slope, $-\lambda$, is a function of the salt symmetry (Equation C.48), where $\lambda = 1$ for symmetric salts like NaCl. That is, the slope is not influenced by experimental conditions or membrane properties. The negative sign of the slope arises from the opposing scaling of the ion selectivity and counter-ion conductivity with $\phi_w^{\pm 2}$. The intercept β reveals the parameters that affect the trade-off between counter-ion conductivity and selectivity. The membrane properties that affect the intercept β include C_A^{max} (and therefore the ion-exchange capacity, IEC, and dry polymer density, ρ_p, since $C_A^{max} = IEC \cdot \rho_p$), $\left(\bar{\alpha}_{g/c}\right)_D$, and ξ. The weighting of $(C_A^{max})^3$ underscores the significant importance of the polymer charge content in membrane design, as Chapter 4 introduced qualitatively.

5.3 Model Validation

To validate the model for the conductivity/selectivity trade-off in IEMs, we compare the model predictions to data from 40 commercial IEMs characterized with aqueous 1 m NaCl solutions in Chapter 4. Figure 5.1A presents the membrane parameters that appear in the intercept of Equation 5.5, $(C_A^{max})^3\left(\bar{\alpha}_{g/c}\right)_D^2/\xi$, plotted against the implicit membrane parameter, ϕ_w. Figure 5.1B presents a comparison between the measured $\bar{\alpha}_{g/c}$ and $\bar{\kappa}_g$ values and those predicted by the model for the upper bound line of composite IEMs, which is of the same form as Equation 5.5 (see Section C.4.4). Membranes predicted to perform well in Figure 5.1A are clustered near the upper bound in Figure 5.1B. Simultaneously, membranes near the upper bound typically have large intercept functions. These coupled trends suggest that Equation 5.5 successfully describes the upper bound by achieving a good prediction for the performance of each membrane. Appendix Figure C.2 presents a parity plot of the modeled and measured selectivity when model inputs are specific to each membrane, demonstrating that the selectivity of each membrane can be predicted reasonably well using this model.

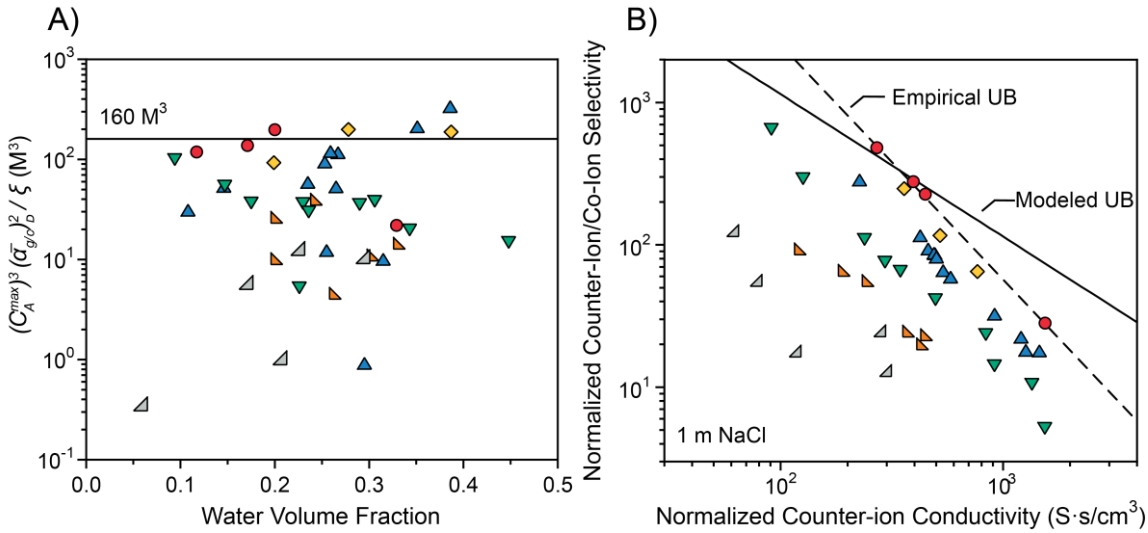


Figure 5.1: Model for the conductivity/selectivity upper bound. A) The intercept function, $(C_A^{max})^3\left(\bar{\alpha}_{g/c}\right)_D^2/\xi$, plotted against ϕ_w for 40 commercial membranes characterized with 1 m

NaCl solutions. The line indicates the representative intercept function for membranes that are near the upper bound, 160 M^3. Membranes for which ξ could not be resolved were assigned a value of $\xi = 0.754$ as discussed in Section C.4.1. B) The normalized counter-ion/co-ion selectivity, $\bar{\alpha}_{g/c}$, plotted against the normalized counter-ion conductivity, $\bar{\kappa}_g$, for 40 commercial membranes characterized with 1 m NaCl solutions. The solid line indicates the predictions of Equation 5.5 using an intercept function of 160 M^3. The dashed line represents an empirically drawn upper bound with $\lambda = 1.65$ and $\beta = 5.08 \times 10^6$. Data colors and shapes correspond to the distance from the empirical upper bound; each membrane has the same color and shape on both graphs.

The model can identify high-performing membranes even at high water contents, as demonstrated in Figure 5.1A, despite assuming $\phi_w \to 0$ in the derivation of Equation 5.5. This result is reasonable because the primary scaling with ϕ_w is implicitly accounted for, as discussed in Section C.2. The broad agreement between the model and data is remarkable given the assumptions and generality underpinning its derivation. The largest deviation between predictions and data occurs with highly conductive membranes, where the upper bound prediction suggests that currently available highly conductive membranes do not reach their potential for selectivity. Highly conductive membranes often have high ϕ_w, worsening some of the assumptions contained in Equation 5.5 and partially explaining this discrepancy.

Comparing the full model (which does not assume $\phi_w \to 0$) predictions to the experimental data for the commercial IEMs is impossible because of the composite backing effects, as discussed in Section C.3. However, the linearized model can be compared with the full model for the case of homogeneous IEMs. This comparison is presented in Figure 5.2, demonstrating that the linearized model in Equation 5.5 does not deviate significantly from any of the more rigorous predictions for current IEMs.

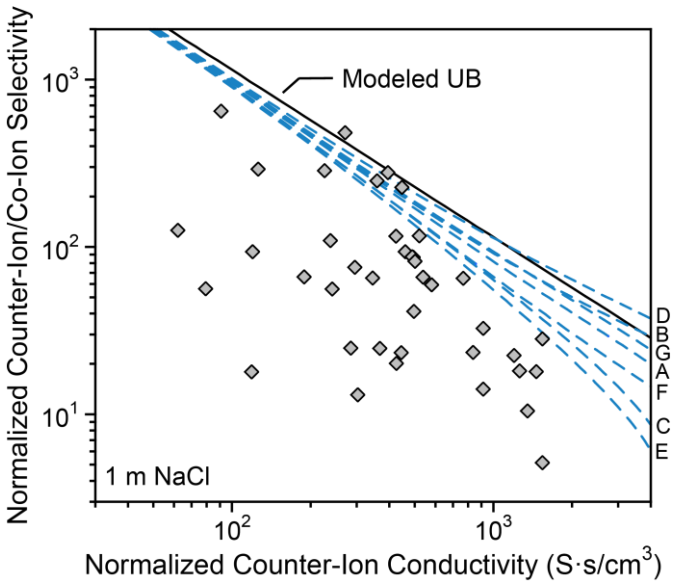


Figure 5.2: Accuracy in the linearization of the upper bound model. A comparison of the fully parameterized upper bound predictions with the linearized prediction of Equation 5.5 for IEMs characterized with 1 molal NaCl. The full model represents the nonlinear system of equations defined in Section C.2, with no assumptions beyond those present in the Donnan-Manning and Meares-Manning models. Equation 5.5 is shown for an intercept function of 160 M^3. The fully parameterized models also each have the same intercept function, but the individual components are different, as outlined below. The full model predictions are only applicable for non-composite, homogeneous IEMs, but the commercial membrane data are shown for reference. Line A: $C_A^{max} = 2.34\ M$, $\left(\bar{\alpha}_{g/c}\right)_D = 5$, $\xi = 2$. Line B: $C_A^{max} = 1.17\ M$, $\left(\bar{\alpha}_{g/c}\right)_D = 10$, $\xi = 1$. Line C: $C_A^{max} = 4.93\ M$, $\left(\bar{\alpha}_{g/c}\right)_D = 2$, $\xi = 3$. Line D: $C_A^{max} = 1.47\ M$, $\left(\bar{\alpha}_{g/c}\right)_D = 10$, $\xi = 2$. Line E: $C_A^{max} = 4.31\ M$, $\left(\bar{\alpha}_{g/c}\right)_D = 1$, $\xi = 2$. Line F: $C_A^{max} = 1.86\ M$, $\left(\bar{\alpha}_{g/c}\right)_D = 5$, $\xi = 1$. Line G: $C_A^{max} = 2.68\ M$, $\left(\bar{\alpha}_{g/c}\right)_D = 5$, $\xi = 3$.

Equation 5.5 predicts that differences in membrane properties only shift the intercept of the upper bound. As a result, the model implies that each parameter that enters the intercept function can compensate for the others. That is, there are multiple routes to make membranes that reach the upper bound: a low C_A^{max} can be compensated by a large $\left(\bar{\alpha}_{g/c}\right)_D$ and a small ξ; a low $\left(\bar{\alpha}_{g/c}\right)_D$ compensated by a large C_A^{max} and small ξ; or a high ξ compensated by a large C_A^{max} and $\left(\bar{\alpha}_{g/c}\right)_D$. This multiplicity is highlighted in Appendix Figure C.3, which isolates each component of the intercept function. Comparing Appendix Figure C.3 with Figure 5.1B reveals that some

membranes achieve a high intercept function via outstanding C_A^{max} or outstanding $\left(\bar{\alpha}_{g/c}\right)_D$ values, whereas other membranes are just slightly above average in every respect. Although C_A^{max}, $\left(\bar{\alpha}_{g/c}\right)_D$, and ξ are currently considered independent and uncorrelated, this analysis suggests they may become correlated when one parameter is optimized. Developing a deeper understanding of counter-ion diffusion is key to understanding the nature of this compensation effect.

5.4 Implications for Designing New IEMs

We can use the predictions of Equation 5.5 to guide membrane design. C_A^{max} has the most significant impact on the intercept function due to its cubic exponent. However, $\left(\bar{\alpha}_{g/c}\right)_D$ varies over the greatest range for the membranes we have already analyzed (Appendix Figure C.3B). ξ has the lowest exponential effect and varies over a relatively small range (Appendix Figure C.3C), suggesting that it has the least power to drastically change the upper bound. Although there is no direct correlation known between C_A^{max} and ξ, both are measures of charge density, so we might expect that $C_A^{max} \sim \xi^3$; this assumption would reduce the intercept function scaling of C_A^{max} to 8/3. This scaling analysis suggests that the detrimental effects of counter-ion condensation, modeled by Manning's theory, do not outweigh the benefits of an increased volumetric charge density. Because $\left(\bar{\alpha}_{g/c}\right)_D$ is an adjustable parameter, we currently cannot specify precisely which membrane structures achieve high or low diffusion selectivities. We note that high diffusion selectivities in this data set were achieved exclusively by membranes with low water content, suggesting that the term might contribute to a steeper upper bound slope if it were to be fully resolved. With this reservation in mind, increasing C_A^{max} is currently the most practical route towards advancing the upper bound.

We can predict improvements in IEM performance based on reasonable inputs for C_A^{max}, $\left(\bar{\alpha}_{g/c}\right)_D$, and ξ. C_A^{max} is the parameter most readily controlled via the synthetic conditions, so we consider various cases for a given input of C_A^{max}. Based on the data used to validate the model, $\left(\bar{\alpha}_{g/c}\right)_D^2/\xi$ assumes values ranging from 1 to 100. This window of 2 orders of magnitude is expected to contain all membranes of the given C_A^{max} until design breakthroughs reach unprecedented values of $\left(\bar{\alpha}_{g/c}\right)_D$. Without a deeper understanding of counter-ion diffusion in IEMs, we do not speculate on advances past this limit.

Three values for C_A^{max} are helpful to consider in this analysis, as illustrated in Figure 5.3A, which presents the maximum charge density vs. water volume fraction for the 40 commercial membranes alongside approximately 1000 recently reported IEMs (comparable to Figure 4.6 in Chapter 4). First, $C_A^{max} = 3\ M$ constrains current commercial membranes as well as most new IEMs reported over the past two decades. Second, $C_A^{max} = 6\ M$ limits the most densely charged "laboratory-made" membranes reported in the literature. Finally, we theorize the upper limit of IEM charge density to be $C_A^{max} \sim 10\ M$. Strong acid/base polyelectrolytes currently do not reach these charge densities without fully dissolving in water; however, 10 M can serve as an aspirational target. This final value represents the model prediction for the maximum conductivity/selectivity performance that is attainable for IEMs separating counter-ions from co-ions. Each of these cases is illustrated in Figure 5.3B, and additional cases are provided in Appendix Figure C.4.

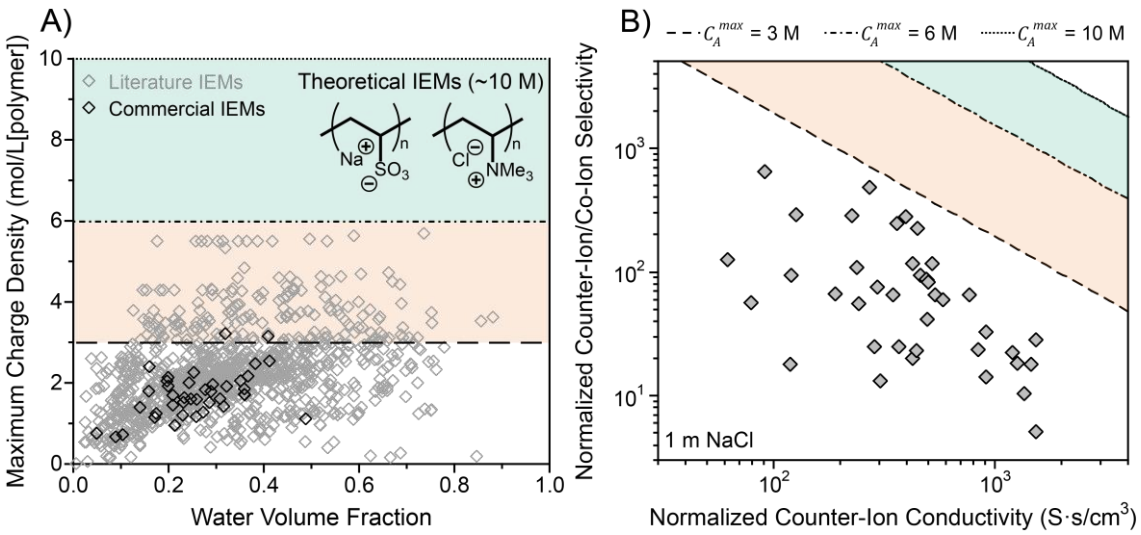


Figure 5.3: Model predictions for future IEMs. A) The maximum charge density, C_A^{max}, plotted against the water volume fraction, ϕ_w. The empty black symbols represent the commercial membranes discussed Chapter 4, the empty grey symbols represent "laboratory-made" membranes discussed in Chapter 4, and the upper limit of the graph represents our estimate of C_A^{max} for the highly charged polyelectrolytes depicted in the plot. B) Model predictions of the upper bound for various input parameters. Each line represents a scenario marked in A) with dashed lines. Long dashes: $C_A^{max} = 3\ M$; mixed dashes: $C_A^{max} = 6\ M$; short dashes: $C_A^{max} = 10\ M$. Each line was calculated using the nominal case of $\left(\bar{\alpha}_{g/c}\right)_D^2/\xi = 10$.

In our analysis of the dataset presented in Figure 5.1, the intercept function for the upper bound line is 160 M^3. Using an optimistic estimate of $\left(\bar{\alpha}_{g/c}\right)_D^2/\xi = 100$, this corresponds to $C_A^{max} = 1.17\ M$. The model predicts that increasing C_A^{max} to 10 M without altering $\left(\bar{\alpha}_{g/c}\right)_D$ or ξ would result in a 624-fold increase in the intercept function. That is, Equation 5.5 suggests that enhancements in C_A^{max} could lead to improvements in counter-ion/co-ion separations by up to 2.8 orders of magnitude. However, achieving such densely charged membranes poses significant design challenges due to the coupling between membrane charge and water content (Section 4.6). Despite previous calls in the literature to focus on increasing the membrane charge content[462,463], there has not been a substantial improvement in this aspect of IEMs over the past two decades. To address the issue of dissolution or breakage in highly charged materials, current research has shifted towards developing finely controlled microstructures and heavily cross-linked polymers.

Nevertheless, more precise control of the polymer structure is necessary to create stable membranes with C_A^{max} greater than 6 mol / L[polymer].

5.5 Conclusions

The conductivity/selectivity upper bound model presented in this chapter highlights the substantial potential for advancement in the field of IEMs. Future research on IEMs should prioritize the development of membranes with higher C_A^{max} values, as this factor has the strongest influence on the position of the upper bound line. Furthermore, control of the membrane water volume fraction will yield membranes with carefully balanced combinations of counter-ion conductivity and selectivity. Membranes with enhanced conductivities and selectivities have the potential to significantly improve technologies such as reverse electrodialysis and redox flow batteries by increasing their charge efficiency while lowering their energy consumption. In water electrolysis applications, more conductive and selective membranes are crucial for minimizing co-ion crossover and electrode fouling, thereby enhancing efficiency and stability. The role of co-ion crossover in CO_2 electrolysis is a developing area of research, with initial studies indicating its impact on various factors such as membrane hydration and stability, salt precipitation at electrodes, and product selectivity. Membranes designed with precise transport properties are essential to manage these effects and optimize overall system performance. This improved understanding of the trade-off between conductivity and selectivity in IEMs paves the way for the precise design of next-generation membranes.

Chapter 6 Fast and Selective Ion Transport in Ultrahigh Charge Density Ion-Exchange Membranes[3]

6.1 Introduction

Chapter 4 identified that currently ion-exchange membranes (IEMs) are plagued by a pernicious trade-off between counter-ion conductivity and selectivity (Figure 4.1), which limits their effectiveness in these applications. However, Chapter 5 elucidated the fundamental basis for the trade-off relationship and developed a predictive model for the upper bound line (Figure 6.1A), which characterizes the best available combinations of conductivity and selectivity. This theoretical analysis revealed that the charge content of membranes (C_A^{max}, mol/L[dry polymer]) most strongly influences the position of the upper bound line, while the water content (ϕ_w, water volume fraction) controls the specific location of a membrane on this line (Figure 6.1B-D). Higher charge contents in membranes are broadly beneficial, as this shifts the upper bound line towards the upper right quadrant. Meanwhile, the optimal membrane water content depends on the prioritization of conductivity versus selectivity for the intended application.

[3]This chapter is based on a completed manuscript which is currently under peer review. This publication will be: David Kitto, José C. Díaz, Carolina Espinoza, Jacquelyn Zamora, and Jovan Kamcev, "Fast and Selective Ion Transport in Ultrahigh Charge Density Membranes." J.C.D., C.E., and J.Z. assisted with membrane synthesis and water content characterizations. C.E. collected calorimetry data. J.K. supervised this work.

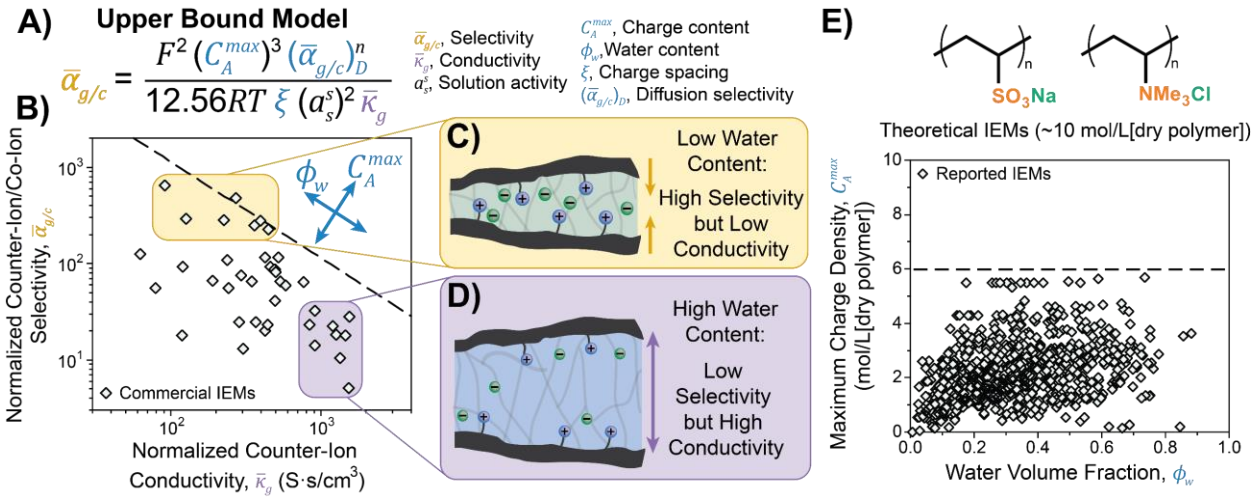


Figure 6.1: The IEM performance trade-off. A) A predictive equation for the upper bound of IEM performance, derived in detail in Chapter 5 and modified slightly in Section D.1. Membrane structural properties are shown in blue, the selectivity (y-axis) is shown in yellow, and the conductivity (x-axis) is shown in purple. B) The normalized counter-ion/co-ion selectivity, $\bar{\alpha}_{g/c}$, plotted against the normalized counter-ion conductivity, $\bar{\kappa}_g$, for 40 commercial IEMs discussed in Chapter 4. The dashed line was calculated per the equation in part A. C) A schematic of low water content IEMs, which populate the upper left of the trade-off plot. D) A schematic of high water content IEMs, which populate the lower right of the trade-off plot. E) The maximum charge density, C_A^{max}, plotted against the water volume fraction, ϕ_w, for 40 commercial membranes and approximately 1000 membranes discussed in Chapter 4. The dashed line represents an empirical limit beyond which no IEMs have been reported.

Synthesizing dimensionally stable membranes with exceptionally high charge content presents an enormous challenge. In the case of membranes made from linear polymers, a certain fraction of the polymer must be hydrophobic to maintain mechanical integrity, which inherently constrains the space available for ions. Elevating the charge content in such linear polymer membranes often leads to excessive swelling and, ultimately, dissolution. Membranes made from cross-linked polymers typically incorporate uncharged cross-linkers, which anti-correlates the membrane swelling resistance with the charge content. These limitations have resulted in a substantial gap between the highest charge contents of reported membranes (<6 mol/L[dry polymer]) and the theoretical potential of highly charged polyelectrolytes (~10 mol/L[dry polymer]), as depicted in Figure 6.1E.

This study presents a general framework for designing IEMs that achieve substantially higher charge contents than those reported previously while spanning a wide range of water contents, effectively populating this gap in the IEM materials space. In line with predictions from the upper bound model, the membranes with ultrahigh charge densities (UHCD) exhibit marked improvements in both counter-ion conductivity and selectivity compared to existing materials, advancing the frontier of IEM performance.

6.2 Membrane Structures

We synthesized UHCD membranes with tunable water content via the co-polymerization of a strategically selected monomer and cross-linker (Figure 6.2A-B, with detailed methods in Sections 2.1.2 and 2.1.3). The monofunctional monomer, C_2VI, is notable due to its compact charged structure, minimizing extraneous atoms and consequently resulting in a highly charged polymer backbone. The cross-linker, C_4VI_2, is essentially double the structure of C_2VI; this permits the introduction of cross-links without modifying the polymer backbone or reducing the charge content (Section D.2). These monomers are inexpensive and easy to prepare in large quantities, are highly soluble in water, and can be readily co-polymerized into free-standing polymer films (Figure 6.2C). Critically, this synthetic strategy is compatible with roll-to-roll processing techniques commonly employed in the production of commercial IEMs[464,465]. Therefore, these membranes have a viable pathway towards scalable manufacturing.

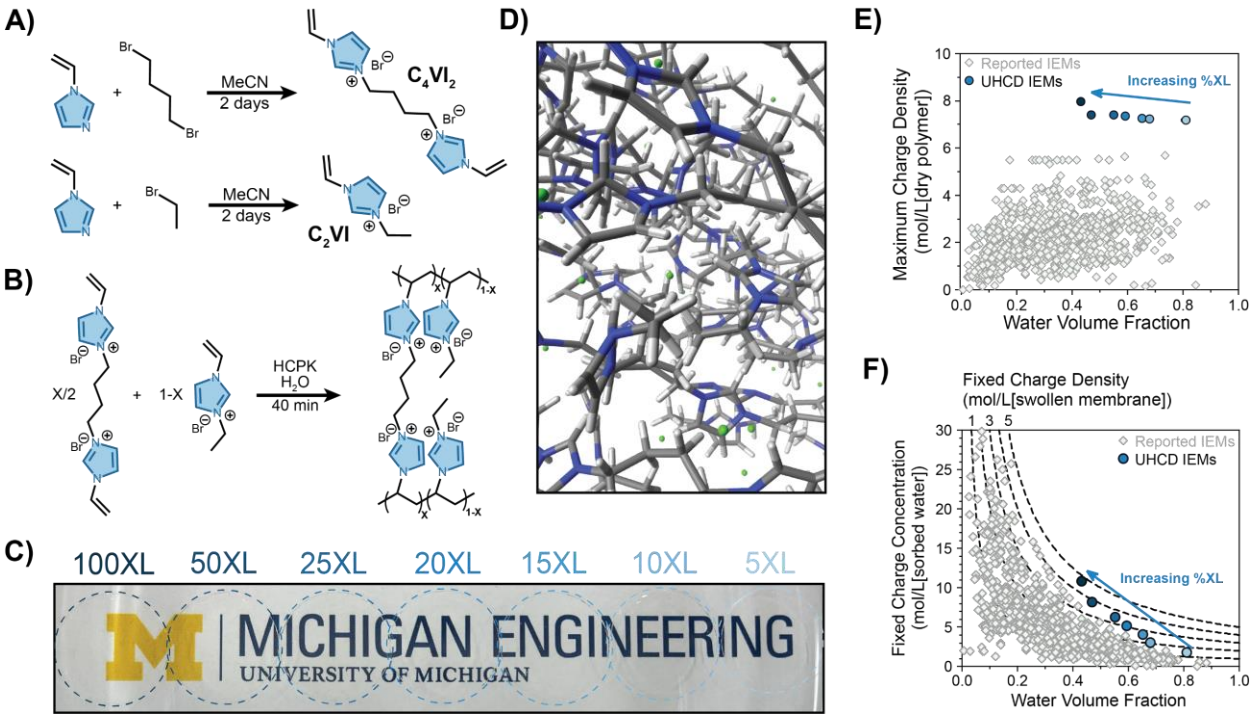


Figure 6.2: Preparation of UHCD IEMs. A) Synthetic scheme for preparing the monomers C_4VI_2 and C_2VI. B) Synthetic scheme for the co-polymerization of C_4VI_2 and C_2VI monomers to yield UHCD membranes. "X" represents both the mass fraction of C_4VI_2 and the fraction of imidazolium groups participating in a cross-linking structure. The membranes are labeled as %XL, where % is "X". C) Photograph of free-standing films of each membrane immersed in water. Dashed lines were added to identify the membranes. The unmarked photograph is shown in Appendix Figure D.11. D) A 3D rendering of the 100XL membrane generated using Avogadro[466]. E) The maximum charge density, C_A^{max}, plotted against the water volume fraction, ϕ_w, for the reference data (Chapter 4) and the UHCD membranes. F) The fixed charge concentration, $C_A^{m,w}$, plotted against the water volume fraction, ϕ_w (with the fixed charge density, $C_A^{m,t}$, denoted by the contour lines), for the reference data (Chapter 4) and the UHCD membranes.

The UHCD membranes attain unprecedented combinations of charge and water contents (Figure 6.2E), achieving the highest volumetric charge densities (mol/L[swollen membrane]) reported to date across the entire water content range (Figure 6.2F). Notably, some UHCD membranes are the first to approach volumetric charge densities of 5 mol/L[swollen membrane] and join only three other reported IEMs with charge densities greater than 4 mol/L[swollen membrane]. Comprehensive ion and polymer structural characterizations indicate that these UHCD membranes are nearing the limit of charge contents feasible in homogeneous IEMs. The

challenges faced in further increasing the charge content are primarily due to limitations in polymerization kinetics and the increasing demand for hydrating water, as discussed in Section D.3.

6.3 Salt-equilibrated Transport Properties

We characterized the transport properties of the UHCD membranes with 1 m NaCl solutions to evaluate their performance under high salinity conditions. Figure 6.3A presents the counter-ion conductivities and selectivities of these membranes alongside those of the commercial state-of-the-art membranes characterized in Chapter 4. The theoretical upper bound for the UHCD membranes, based on the updated parameters for the upper bound model, is also illustrated (detailed model usage is provided in Section D.1). The model describes the UHCD results reasonably well, highlighting that ion transport across the membranes follows well understood mechanisms. Notably, the UHCD membranes demonstrate substantial improvements in both counter-ion conductivity and selectivity relative to the commercial membranes, essentially redefining the upper bound. For example, the UHCD membrane with comparable selectivity to the most selective commercial membranes exhibits 4.5 to 13 times higher conductivity (Appendix Figure D.9). Similarly, the UHCD membrane with comparable conductivity to the most conductive commercial membranes exhibits 8 to 44 times higher selectivity (Appendix Figure D.9). Given that these UHCD membranes span a wide range of conductivity/selectivity combinations, all surpassing those of commercial membranes, they allow for the selection of the optimal membrane configuration tailored to specific application needs.

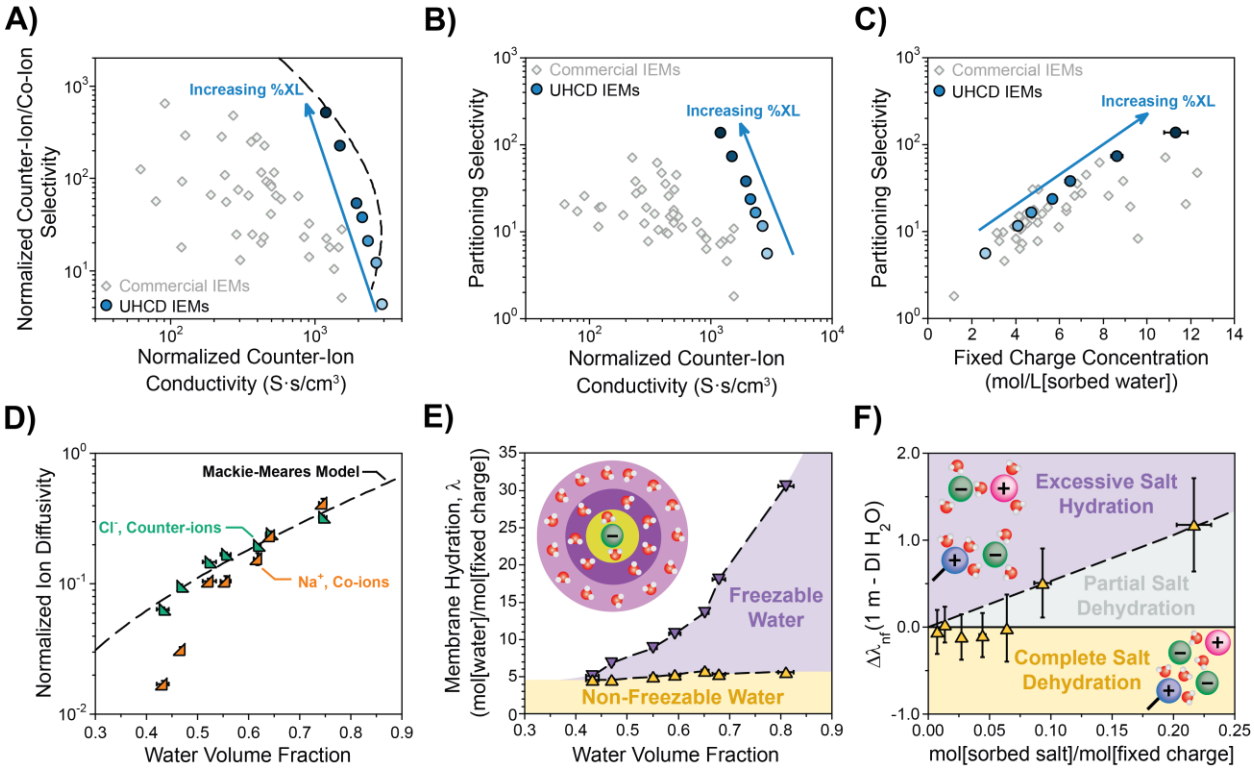


Figure 6.3: UHCD IEM performance contacting 1 m NaCl. A) The normalized counter-ion/co-ion selectivity plotted against the normalized counter-ion conductivity for the reference data (Chapter 4) and the UHCD membranes. The dashed line represents the modeled upper bound of the UHCD membranes (Section D.1). B) The partitioning selectivity (ratio of counter-ion to co-ion concentration) plotted against the normalized counter-ion conductivity for the reference data (Chapter 4) and the UHCD membranes. C) The partitioning selectivity plotted against the fixed charge concentration for the reference data (Chapter 4) and the UHCD membranes. D) Counter-ion and co-ion diffusion coefficients in the membrane normalized by the infinite dilution diffusivity plotted against the membrane water volume fraction. E) The freezable and non-freezable hydration numbers plotted against the water volume fraction for the UHCD membranes equilibrated with DI water. F) The change in non-freezable hydration number from DI water to 1 m NaCl plotted against the ratio of sorbed salts to imidazolium fixed charges for the UHCD membranes. The solid line is placed at 0, while the dashed line has a slope of 5.35, which is the hydration number of NaCl in dilute solutions[467].

Independently considering the partitioning and diffusion contributions to the overall ion transport process in the UHCD membranes offers a clearer understanding of their exceptional performance. At comparable partitioning selectivities, the UHCD membranes demonstrate markedly higher conductivities than the commercial IEMs (Figure 6.3B). The partitioning selectivities increase with increasing fixed charge group concentration (mol/L[sorbed water]),

following a similar trend as the commercial membranes (Figure 6.3C). The improved performance in Figure 6.3B is therefore primarily due to enhanced counter-ion conduction at a given fixed charge concentration. The Mackie-Meares tortuosity model (Section 3.3) explains the faster Cl^- diffusion due to the increase in the membrane water volume fraction (Figure 6.3D). Therefore, the outstanding performance of the membranes is linked to the synergy of high fixed charge concentrations and water volume fractions (Figure 6.3F) enabled by the extremely high membrane charge content (Figure 6.3E).

Although the diffusion coefficients of the Cl^- counter-ions in the UHCD membranes can be modeled accurately, the diffusion coefficients of the Na^+ co-ions are suppressed in the more selective membranes (Figure 6.3D). This difference leads to diffusion selectivities greater than unity (Appendix Figure D.8), which further improve the membrane selectivities. We rationalize the co-ion diffusivity suppression by examining the role of water within the membranes (Figure 6.3E). In the membranes with lower water content, the 5 waters strongly bound by each chloride/imidazolium pair constitute most of the water in the membrane. This water-starved environment creates a deficit of water for salt molecules that partition into the membrane, where only the two highest water content membranes contain sufficient water to independently hydrate the Na^+ co-ions crossing the membrane (Figure 6.3F). In the lower water content membranes, the total amount of hydrating waters remains constant with the partitioning of NaCl (Figure 6.3F), suggesting that these ions are sharing waters of hydration with the fixed charge groups, counter-ions, or other partitioned salts. Such bulky or immobilized paired species would impede the diffusion of Na^+ across the membrane, manifesting in the observed diffusion selectivities.

These analyses reveal the exceptional performance of the UHCD membranes is primarily attributable to their high charge and water content functioning in tandem. Specifically, the high

charge content of these membranes results in high partition selectivities, while the high water content facilitates fast ion diffusion, thereby yielding high ion conductivities. The high charge contents also enable the binding of a substantial number of water molecules in the lower water content membranes and contribute to reasonably high diffusion selectivities, further enhancing the performance. In contrast, existing membranes with high fixed charge group concentrations typically have low water content (Figure 6.1F), which hinders ion diffusion. Conversely, existing membranes with high water content typically have low fixed charge group concentrations (Figure 6.1F), resulting in low selectivities. The UHCD membranes successfully combine these desirable attributes—high charge and high water content—to redefine the counter-ion conductivity/selectivity upper bound.

6.4 DI Water Equilibrated Transport Properties

In IEM applications such as fuel cells and water electrolyzers, high counter-ion conductivity is prioritized over selectivity because such systems are generally operated with pure water[468,469]. Higher counter-ion conductivities typically result in reduced area resistances, thereby decreasing the energy consumption of the device. The exceptional ionic conductivities of these UHCD membranes make them highly desirable for these electrochemical applications operating with DI water. The ionic conductivity of the UHCD membranes in DI water increases with rising water content, reaches a peak, and then declines upon further increases in water content (Figure 6.4A). This behavior is a result of two competing factors. First, the counter-ion diffusion coefficients increase with increasing water content over the entire water content range, aligning with predictions of the Mackie-Meares model (Figure 6.4B). Conversely, an increase in water content leads to a decrease in the volumetric density of counter-ions (Figure 6.2F), reducing the number of conducting species. A simple ionic conductivity model combining these two effects

captures this trend without adjustable parameters (Figure 6.4A, with model details in Section D.1). Notably, the maximum ionic conductivity attained by the UHCD membranes (44.8 mS/cm) is unprecedented, representing the highest room temperature ionic conductivity recorded for AEMs in the Cl^- counter-ion form (Appendix Figure D.10).

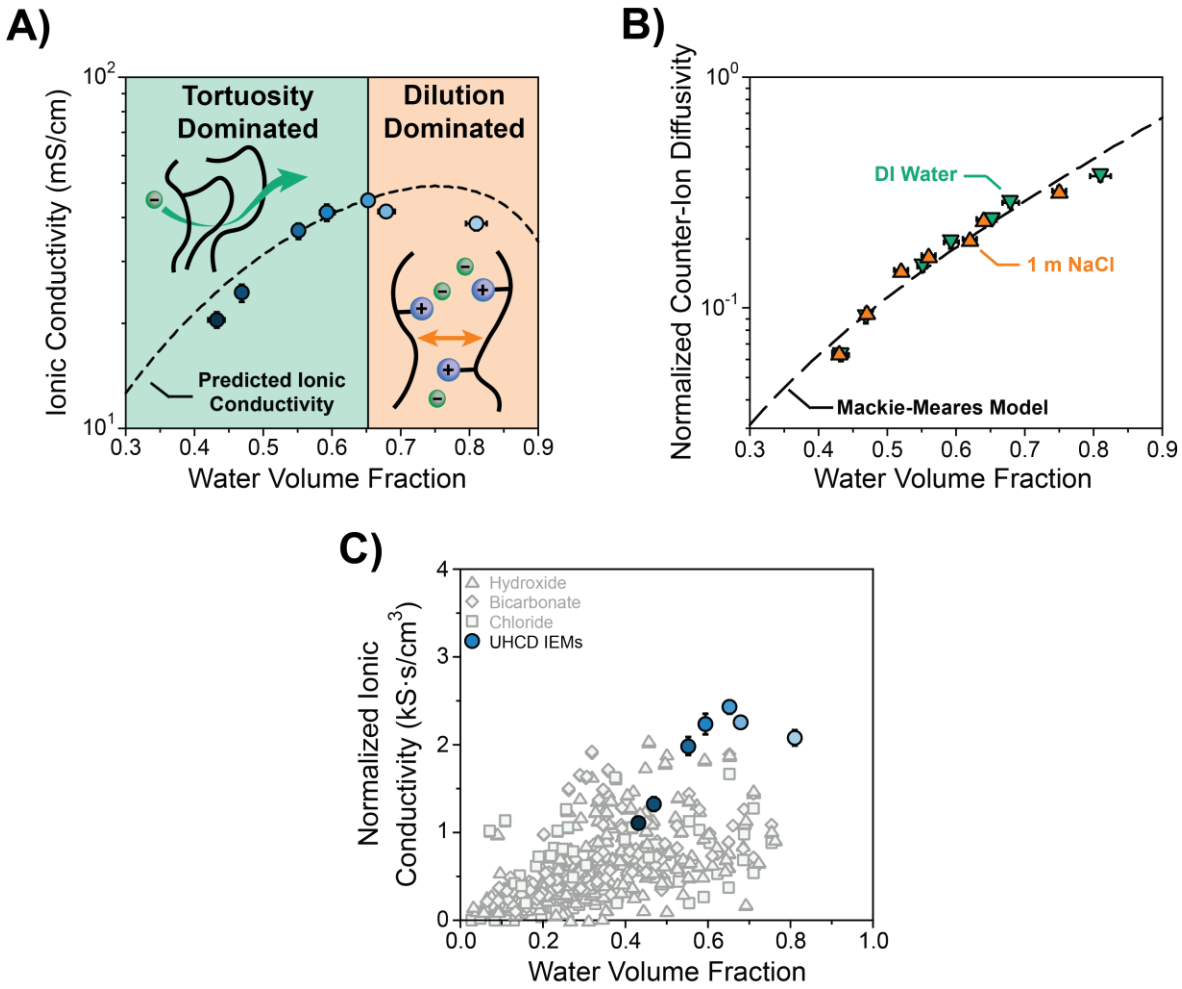


Figure 6.4: UHCD IEM performance contacting DI water. A) The ionic conductivity, κ, plotted against the water volume fraction , ϕ_w, for the UHCD membranes equilibrated with DI water. The dashed line represents the model prediction (Section D.2). B) The counter-ion diffusivity in the membrane normalized by the infinite dilution diffusivity (D_g^m/D_g^s) plotted against ϕ_w for the UHCD membranes contacting DI water and 1 m NaCl. C) The ionic conductivity normalized by the infinite dilution diffusivity (κ/D_g^s) plotted against ϕ_w of reported membranes (Chapter 4) and

the UHCD membranes contacting DI water. The UHCD membranes were characterized with chloride counter-ions.

To further contextualize the exceptional ionic conductivity of the UHCD membranes, we also compiled room temperature (21 ± 1 °C) ionic conductivity data for recently reported AEMs in the hydroxide and bicarbonate counter-ions forms, which are relevant for fuel cells and electrolyzers. To enable a fair comparison, the ionic conductivity values of all membranes were normalized to the infinite dilution diffusivity of the respective ions, accounting for the inherent mobility differences among ions (Section 3.1). This normalized conductivity is theoretically an intrinsic property of the membrane and is therefore expected to remain consistent across different counter-ions. Four of the UHCD membranes exhibit normalized ionic conductivity values surpassing all previously reported AEMs, with the rest of the UHCD membranes outperforming most existing AEMs. The highest normalized conductivity observed, 2.43 $kS \cdot s/cm^3$ (corresponding to the Cl^- conductivity of 44.8 mS/cm) translates into anticipated room temperature ionic conductivities of 116 mS/cm for hydroxide and 24.4 mS/cm for bicarbonate.

6.5 Conclusions

The enhanced performance of IEMs has the potential to influence the market dynamics of various electrochemical technologies, either by expanding their market share or by elevating them to practical viability[26–30,32]. Recent process and technoeconomic analyses specifically underscore the importance of advancements in membrane conductivity and selectivity. For example, improved IEMs could reduce the levelized cost of water for brackish water desalination via electrodialysis (ED), making it more cost-effective than reverse osmosis, the current dominant desalination technology in this space[26]. Additionally, ED shows promise for managing brine waste from reverse osmosis processes, which is a notable challenge in water desalination[27,28]. In this context, higher

selectivities and conductivities are required to substantially reduce the cost of operating ED with brines. In the energy sector, the use of brine and seawater as inputs could lead to economically competitive electricity production via reverse ED, contingent on the development of membranes with improved conductivity and selectivity[30]. Furthermore, membranes with high ionic conductivities and solvent diffusivities could improve the operational lifetimes of AEM fuel cells, which currently presents a noteworthy barrier in their application[32]. Lastly, the development of IEMs with fixed charge densities of 5.0 mol/L[swollen membrane] could enable efficient lithium recovery from salt lake brines[29]. Due to their outstanding properties, the UHCD membranes meet many of these criteria to a greater extent than other IEMs, potentially leading to meaningful improvements in each of these technologies.

In this work, we have outlined a universal design strategy for polymer membranes characterized by exceptionally high charge content and adjustable water content. These UHCD membranes demonstrate unparalleled combinations of counter-ion conductivity and selectivity at high salinities. Additionally, the UHCD membranes achieve the highest DI water room temperature ionic conductivities reported to date. The ease of tunability inherent in these materials enables their adaptation to various devices, focusing either on selectivity, conductivity, or a combination of both. The affordability of the raw materials used in synthesizing the UHCD membranes as well as their ease of fabrication ensures that the adoption of these membranes will not be economically prohibitive. While the current study focused on imidazolium-based structures to demonstrate the proof of concept, the underlying design principles are broadly applicable and can be implemented with a range of different chemical structures. The future development of UHCD membranes incorporating diverse chemical motifs per this design strategy is expected to extend to cation transport (i.e., negatively charged membranes). New structures may also integrate

secondary properties such as water transport, caustic stability, or dimensional stability, alongside the remarkable ion transport properties showcased in this study. Considering the diverse requirements of different electrochemical technologies, a broad spectrum of membranes is needed. We anticipate that the adoption of UHCD design methodologies will catalyze the emergence of a new era of high-performance IEMs, effectively meeting the varied needs of these technologies and substantially decreasing their energy consumption.

Chapter 7 Electrostatic Limits to Pursuing High Charge Densities[4]

7.1 Introduction

Ultrahigh charge density (UHCD) ion-exchange membranes (IEMs) having moderate and high water volume fractions (ϕ_w) offer an excellent balance of charge selectivity ($\alpha_{g/c}$) and counter-ion conductivity (κ_g). However, our initial investigation of UHCD IEMs in Chapter 6 did not yield membranes that surpassed the selectivities of the most selective commercial IEMs. The upper bound model (Figure 6.3) indicates that these materials, at $C_A^{max} \sim 7.4\ M$, could achieve higher selectivities, contingent upon the synthesis of IEMs with lower ϕ_w. As discussed in Section 1.2, applications like brine treatment via electrodialysis (ED) require membranes with high $\alpha_{g/c}$[470]. High-concentration brines degrade the Donnan selectivity that is essential for the selectivity of IEMs (Section 3.2), while extreme concentration gradients between concentrate and diluate streams increase undesirable ion transport. Thus, brine treatment applications are only viable with membranes that maintain high $\alpha_{g/c}$ under these challenging conditions. Therefore, IEMs with higher $\alpha_{g/c}$ than the current commercial benchmark would be particularly beneficial for brine treatment applications.

The traditional approach to enhance $\alpha_{g/c}$ in IEMs focuses on improving the partitioning selectivity ($\left(\alpha_{g/c}\right)_K$) by increasing the fixed charge concentration ($C_A^{m,w}$)[385,410]. This approach is

[4]This chapter has not yet been published. Contributions to this chapter were also made by: José C. Díaz, Carolina Espinoza, Jacquelyn Zamora, and Jovan Kamcev. I would also like to acknowledge Gregory Reimonn and Nathan Bryant for helpful discussions regarding this analysis. J.C.D, J.Z., and J.K. assisted with membrane synthesis. C.E. collected calorimetry data. J.K. supervised this work.

based on Donnan Theory (Equation 3.14), which predicts low co-ion partitioning ($C_c^{m,w}$) in IEMs with high $C_A^{m,w}$, driving larger selectivities through $\left(\alpha_{g/c}\right)_K \propto C_A^{m,w}/C_c^{m,w}$ (Equation C.4). Our survey of commercial IEMs in Chapter 4 showed a strong correlation between $\left(\alpha_{g/c}\right)_K$ and $C_A^{m,w}$ (Figure 4.3A), supporting this strategy. Many IEMs do achieve high $C_A^{m,w}$: commercial IEMs reach up to 15 molal (m), while literature membranes often nearly double this value, reaching ~25 m (Figure 4.4A). A select few reported IEMs claim exceptionally high $C_A^{m,w}$, reaching as high as 65 m. However, achieving high values of $C_A^{m,w}$ almost exclusively coincides with low ϕ_w, which reduces κ_g. Although these highly charged membranes could technically treat brines, the process would not be economical. Low-conductivity membranes become the primary source of Ohmic losses in a brine treatment ED stack due to the high conductivity of brine solutions[470], leading to increased voltage requirements and, in turn, increased costs for treating brine. Therefore, at a given selectivity, κ_g will determine the commercial feasibility of an IEM for brine treatment applications. As analyzed in Chapter 5, $\alpha_{g/c}$ and κ_g are united in a trade-off relationship, so these factors cannot be controlled independently. Brine treatment applications need membranes that occupy the high-selectivity region of the trade-off plot; however, the high-selectivity portion of the new UHCD upper bound (Figure 6.3A) is currently vacant.

The most reliable way to increase $\alpha_{g/c}$ without sacrificing κ_g is to increase the maximum charge density, C_A^{max} (Chapter 5). Furthermore, to achieve greater selectivities than those obtained with the UHCD IEMs in Chapter 6, it is desirable to prepare membranes with $\phi_w < 0.4$. A potential solution to these design constraints is to shorten the cross-linker carbon chain length, thereby increasing C_A^{max} through the removal of neutral atoms. These shorter cross-linking monomers would also increase the cross-link density of the IEMs, potentially leading to a reduction in ϕ_w. This modification simultaneously targets an increased $\alpha_{g/c}$ through both

identified mechanisms (increasing C_A^{max} and lowering ϕ_w), making it a promising strategy to explore. Various dibromo alkane reagents are commercially available, so it is a relatively straightforward task to analyze analogous cross-linking structures to the C_4VI_2 monomer used in Chapter 6.

To test the potential for improved selectivities using UHCD imidazolium IEMs, we prepared various membranes targeting low ϕ_w. The membranes were synthesized using vinyl imidazolium cross-linkers (C_nVI_2) with carbon chain lengths n = 2, 3, 4, 5, 6, and 7. We observed nominal improvements in $\alpha_{g/c}$ without sacrificing the exceptional κ_g of the C_4VI_2 membranes in Chapter 6; however, the selectivity did not improve as much as anticipated. We employed Manning's counter-ion condensation theory to rationalize the trend in $\alpha_{g/c}$, and supplemented this analysis with discussion of other critical onset phenomena observed in these UHCD IEMs. The insights gained from this analysis refine the UHCD design strategies of Chapter 6, introducing a constraint on the charge content of IEM polymers. We reveal that the charge content of IEMs has a soft cap, beyond which further increases to C_A^{max} do not yield drastically better IEMs.

7.2 Membrane Structures

To develop a more complete understanding of how cross-linker chain lengths affect transport properties of UHCD IEMs, we prepared both larger and smaller cross-linkers than C_4VI_2 (Figure 7.1). Monomers with $n = 1$ were not prepared because the synthesis of the $n = 2$ monomer already required more aggressive reaction conditions than the other monomers, presumably due to the electrostatic repulsion derived from placing imidazolium cations so close together. Preparing monomers with $n = 2$ through $n = 7$ provided 6 data points surrounding the previously studied $n = 4$ materials. Monomer synthesis procedures and characterization results are described in Section 2.1.2.



Figure 7.1: C_nVI_2 monomers and membranes. A) The chemical structure of monomers used in this chapter. B) Photograph of the membranes prepared from corresponding monomers.

Free-standing homopolymer IEMs were prepared via free radical photopolymerization as described in Section 2.1.3 and using the recipes listed below in Table 7.1. Each membrane had a translucent, yellow/clear appearance (Figure 7.1B), indicating reasonably homogeneous structures at the length scale of visible light. The water solubility of each monomer varied with n, so the pre-polymer solution concentration was adjusted to prepare each membrane at the saturation point of the corresponding monomer. The volumetric membrane properties (water volume fraction, ϕ_w, fixed charge density, $C_A^{m,t}$, fixed charge concentration, $C_A^{m,w}$, maximum charge density, C_A^{max}, and membrane hydration number, λ) of each membrane are given in Table 7.2. Gravimetric membrane properties (water uptake, WU, ion-exchange capacity, IEC, and dry polymer density, ρ_p) are also included in Appendix Table E.1.

Table 7.1: C_nVI_2 membrane recipes. The pre-polymer co-monomer ratios, total water contents, and initiator contents expressed as fractions of the pre-polymer solution.

Membrane	C_nVI_2 Monomer (wt% monomer)	Water Content (wt% solution)	HCPK Initiator (wt% monomer)
C_2VI_2 ($n = 2$)	100	46.5	0.2
C_3VI_2 ($n = 3$)	100	18.7	0.3
C_4VI_2 ($n = 4$)	100	26.0	0.2
C_5VI_2 ($n = 5$)	100	15.1	0.3
C_6VI_2 ($n = 6$)	100	20.7	0.2
C_7VI_2 ($n = 7$)	100	15.8	0.2

Table 7.2: C_nVI_2 equilibrium membrane properties. Water contents and charge contents expressed as water volume fractions, fixed charge densities, fixed charge concentrations, maximum charge densities, and membrane hydration numbers. Reported uncertainties represent the standard deviation of at least five independent measurements.

Membrane	ϕ_w (L [water] / L [membrane])	$C_A^{m,t}$ (mol / L [membrane])	$C_A^{m,w}$ (mol / L [water])	C_A^{max} (mol / L [dry polymer])	λ (mol [water] / mol [charge])
C_2VI_2	0.567 ± 0.007	4.10 ± 0.25	7.25 ± 0.37	9.13 ± 0.04	7.66 ± 0.40
C_3VI_2	0.433 ± 0.008	5.30 ± 0.24	12.26 ± 0.54	8.60 ± 0.03	4.53 ± 0.20
C_4VI_2	0.432 ± 0.012	4.67 ± 0.14	10.82 ± 0.25	7.96 ± 0.02	5.14 ± 0.12
C_5VI_2	0.420 ± 0.013	4.32 ± 0.18	10.32 ± 0.18	7.07 ± 0.01	5.38 ± 0.09
C_6VI_2	0.442 ± 0.015	4.30 ± 0.15	9.75 ± 0.21	7.02 ± 0.02	5.70 ± 0.12
C_7VI_2	0.425 ± 0.029	4.02 ± 0.13	9.50 ± 0.49	6.63 ± 0.03	5.85 ± 0.30

The charge and water contents of new UHCD IEMs are compared to those of other reported IEMs in Figure 7.2. The water contents achieved by the $n = 3, 5, 6$, and 7 IEMs were similar to those achieved by the lowest ϕ_w C_4VI_2 IEM. Despite having different network formation conditions and cross-linker lengths, $\phi_w \sim 0.4$ appears to be the minimum water content for these UHCD IEMs. The $n = 2$ IEM is a notable outlier, only achieving ϕ_w as low as 0.567. The C_2VI_2 recipe required more water than the other C_nVI_2 IEMs, so the higher ϕ_w is reasonable—low pre-polymer solution concentrations generally increase swelling in the equilibrated membrane[105]. The $n = 2$ monomer synthesis appears to be inhibited by charge repulsion, so it is reasonable to expect that this highly charged monomer requires more water than the less charge-dense monomers to dissolve in aqueous solution. The resulting $C_A^{m,w}$ and $C_A^{m,t}$ values of the C_nVI_2 IEMs follow the trend expected from their C_A^{max} and ϕ_w values. As larger cross-linking structures reduce C_A^{max}, the other measures of charge content are also reduced. C_2VI_2 is hampered by its high ϕ_w, achieving $C_A^{m,t}$ that is comparable with C_7VI_2 despite having a greater C_A^{max}. Consequently, C_3VI_2 exhibits the greatest charge contents in its swollen state; additionally, C_3VI_2 is the only membrane we are

aware of which exceeds $C_A^{m,t} = 5\ mol/L[total\ membrane]$. Compared to the commercial IEMs, C_3VI_2 has more than twice the ϕ_w of any IEM with comparable $C_A^{m,w}$ and more than twice the $C_A^{m,w}$ of any IEM with comparable ϕ_w. Compared to IEMs reported in the literature, all five new C_nVI_2 IEMs demonstrate $C_A^{m,t} > 4\ M$, alongside C_4VI_2 and only 3 other reported membranes.

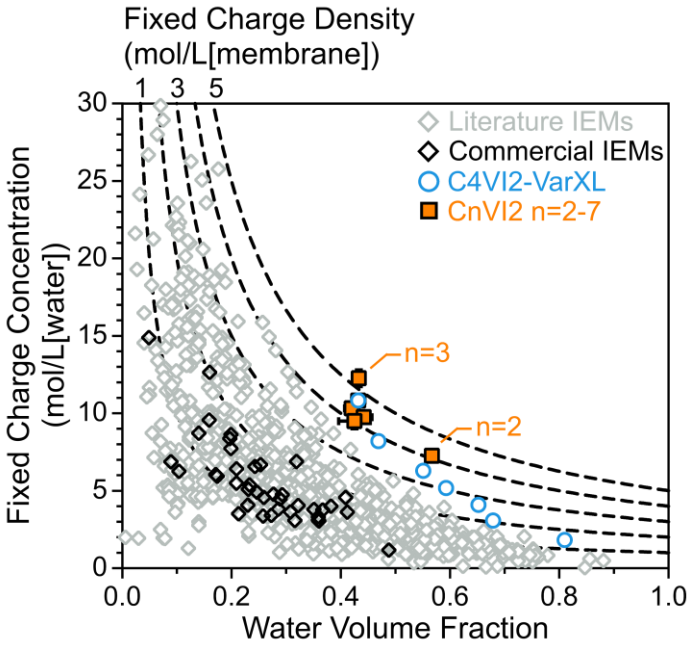


Figure 7.2: C_nVI_2 contour plot. The fixed charge concentration plotted against the water volume fraction for C_nVI_2 IEMs and previously reported IEMs. Fixed charge densities indicated as contour lines. Gray diamonds represent membranes reported in the open literature and black diamonds represent commercially available IEMs, both of which are discussed in Chapter 4. Blue circles represent the varied-cross-linking C_4VI_2 IEMs discussed in Chapter 6. Uncertainties on these data points have been omitted for clarity. Orange squares represent the C_nVI_2 UHCD IEMs discussed in this chapter. Select data points have been labeled with n for clarity. For these materials, uncertainties represent the standard deviation of measurements made on at least five independent samples.

Convergence of the ϕ_w values of C_nVI_2 membranes can be further analyzed by considering the states of water in these IEMs using the differential scanning calorimetry (DSC) techniques described in Section 2.4.3. In aqueous media, ions possess a shell of strongly oriented hydrating waters that are not freezable, so the melting of water in IEMs provides a probe of the *in-situ* ion hydration. When analyzing states of water, water molecules in the membrane can be categorized

as freezable or non-freezable. It is helpful to analyze the states of water using λ, the number of water molecules per fixed charge group. We report λ_f and λ_{nf}, the freezable and non-freezable hydration number of the membrane, for C_nVI_2 membranes in Figure 7.3. Although hydrophilic, non-ionic species in IEMs can affect the states of water in IEMs, the imidazolium chlorides (ImCl) are the only hydrophilic species in the C_nVI_2 IEMs. This simple structure allows for an easier states of water analysis, as was the case for the states of water analysis in Figure 6.3E.

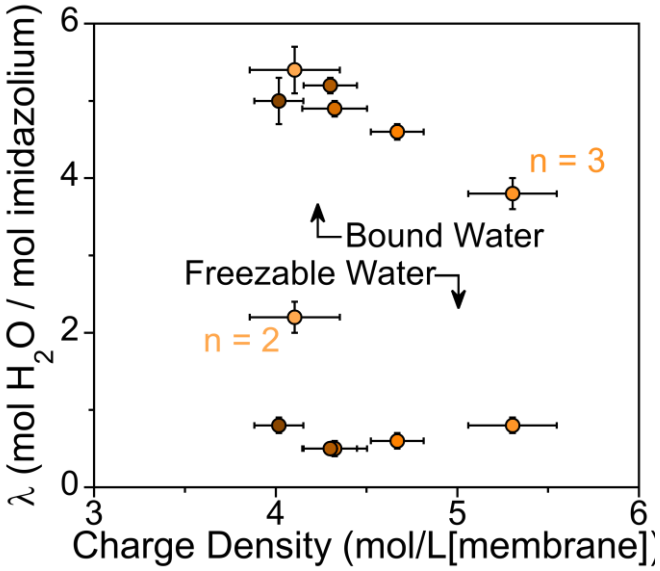


Figure 7.3: States of water in C_nVI_2 IEMs. The freezable and non-freezable hydration number of C_nVI_2 membranes equilibrated with DI water plotted against the fixed charge density. Standard propagation of uncertainty methods were used to calculate uncertainties from measurements on at least five independent samples. Lighter shading indicates smaller values of n, while darker shading indicates larger values of n. Select data have been labeled with n for clarity.

In the $n = 2 - 7$ IEMs, λ_f remained very small, indicating that most water in these IEMs is strongly oriented by a hydrophilic moiety. C_2VI_2 stands out by having additional freezable water, even though λ_{nf} is similar to the other C_nVI_2 membranes. In Chapter 6, we observed that λ_{nf} for C_4VI_2 IEMs remains constant regardless of how much excess water (λ_f) was present in the IEM, indicating that the hydration number of the ImCl salt is ~5. Most of the λ_{nf} values in Figure 7.3

cluster at 5 as well, supporting that 5 is a good estimate of the ImCl hydration number. The only appreciably different membrane is C_3VI_2, which was measured to have $\lambda_{nf} = 3.77 \pm 0.18$. These results suggest that some ion dehydration might be present in C_3VI_2, and that further reductions in IEM swelling for these highly charged polymers would continue to dehydrate these ions. Clearly, it is possible to produce imidazolium IEMs with $\lambda < 5$, but there is undoubtedly a significant energy barrier to overcome. For now, we suspect $\lambda = 4$ is an approximate minimum for this system.

7.3 Performance and Partition Selectivities of C_nVI_2 IEMs

C_2VI_2 and C_3VI_2 each represent the most densely charged IEM (high $C_A^{m,w}$ and $C_A^{m,t}$) available at a given ϕ_w due to their exceptional C_A^{max} values. From the upper bound modeling in Chapter 5, these IEMs are predicted to advance the conductivity/selectivity upper bound beyond the C_4VI_2 membranes. The 1 m NaCl transport properties of C_nVI_2 membranes are compared against commercial IEMs and the varied-cross-linking C_4VI_2 IEMs in Figure 7.4A. As expected, some new UHCD IEMs achieve higher normalized selectivities ($\bar{\alpha}_{g/c}$) than the varied-cross-linking C_4VI_2 IEMs; however, some details of these performance metrics are unexpected. C_5VI_2 is the most selective IEM studied, despite having a lower charge density than C_3VI_2. C_3VI_2 is more conductive than C_4VI_2, but the improvement is only marginal. In the high normalized conductivity ($\bar{\kappa}_g$) region of the plot, the high C_A^{max} of C_2VI_2 suggests it should possess higher $\bar{\kappa}_g$ and $\bar{\alpha}_{g/c}$ than C_4VI_2 IEMs with comparable ϕ_w; instead, C_2VI_2 falls below the line of C_4VI_2 IEMs. In summary, the conductivity follows the expected order for the IEMs with comparable ϕ_w, with $n = 3 > 4 > 5 > 6 > 7$, but not for $n = 2$. The selectivity trends can only be rationalized by C_A^{max} differences for $n = 5 > 6 > 7$.

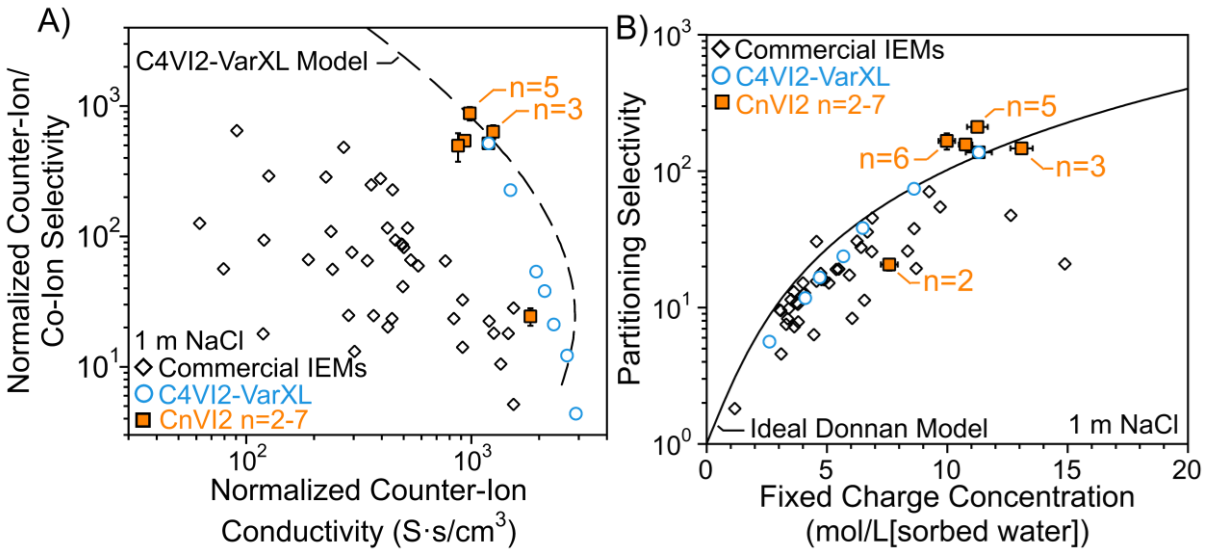


Figure 7.4: Transport properties of C_nVI_2 IEMs equilibrated with 1 m NaCl. A) The normalized counter-ion/co-ion selectivity plotted against the normalized counter-ion conductivity. B) The partitioning selectivity plotted against the fixed charge concentration. In both figures, black diamonds represent the commercial IEMs discussed in Chapter 4, blue circles represent the varied-cross-linking C_4VI_2 IEMs discussed in Chapter 6, and the orange squares represent the C_nVI_2 membranes discussed in the present chapter. Select data points have been labeled using n for clarity. The dashed lines represent model predictions of the data. The model in panel A is the upper bound model used to predict C_4VI_2 performance, which is derived in Chapter 5. The model in panel B is the Ideal Donnan (ID) model derived in Section 3.2. Standard propagation of uncertainty methods were used to calculate uncertainties from measurements on at least four independent samples.

To understand the unexpected selectivity results, we isolated the partitioning selectivity, $(\alpha_{g/c})_K$, from the data in Figure 7.4A. $(\alpha_{g/c})_K$ typically provides most of the charge selectivity for IEMs. Partitioning selectivities are generally a function of $C_A^{m,w}$, so Figure 7.4B presents $(\alpha_{g/c})_K$ as a function of $C_A^{m,w}$ for the commercial and UHCD IEMs. This figure also shows the predictions of the Ideal Donnan (ID) model, which is derived in Section 3.2. The ID model is the simplest model for ion partitioning in IEMs, assuming that nonidealities in the membrane are identical to those in the external salt solution. Typically, IEMs are experimentally observed to be less ideal than salt solutions, and selectivities are overpredicted by the ID model[385]. This trend is

evident in Figure 7.4B, where only one commercial IEM achieves higher selectivity than predicted by the ID model.

Surprisingly, partitioning selectivities of UHCD IEMs are predicted reasonably well by the ID model. The varied-cross-linking C_4VI_2 IEMs follow the model closely at high $C_A^{m,w}$, but exhibit negative deviations from the modeled selectivities at low $C_A^{m,w}$. Among the UHCD IEMs, C_2VI_2 exhibits the greatest deviation from the ID model, displaying a selectivity that is half an order of magnitude lower than the predictions. Meanwhile, for $n > 4$, the C_nVI_2 IEMs exhibit partitioning selectivities higher than those predicted by the ID model. Although the ID model helps to benchmark the performance of IEMs, it does not offer any explanation for observed deviations. To explore a likely source of membrane nonidealities, we employ Manning's theory for counter-ion condensation in the following section.

7.4 Counter-Ion Condensation in UHCD IEMs

The leading model used to connect IEM partitioning results to fundamental structure-property relationships is Manning's theory for counter-ion condensation[385]. We provide a detailed introduction to this model in Section 3.4, then incorporate Manning condensation into the upper bound model discussed in Chapter 5. The equations are straightforward to apply to the UHCD IEM partitioning results; however, a conceptual examination of the counter-ion condensation phenomenon is necessary to interpret the results. To briefly introduce the most important concepts[385,391,392]: Manning condensation centers around electrostatic repulsion along a polymer backbone. Fixed charge groups are separated by a linear distance b along the polymer backbone (3.17), and the dielectric environment accommodates electrostatic repulsion based on the Bjerrum length, λ_B. The ratio of these distances, $\xi = \lambda_B/b$ (Equation 3.16), is called the reduced linear charge density. A certain amount of electrostatic repulsion (ξ_{crit}, which is unity for IEMs

contacting 1-1 salts like NaCl) can be accommodated by the membrane system. However, if the polymer exceeds this critical value ($\xi > \xi_{crit}$), counter-ion condensation must occur. When $\xi > \xi_{crit}$, the energetic relief of localizing a counter-ion alongside the fixed charge groups and polymer backbone exceeds the entropic benefits of allowing the counter-ion to diffuse freely. Thus, counter-ions condense until the marginal energy benefit of continued condensation becomes zero ($\xi_{effective} = \xi_{crit}$).

Ion partitioning is affected by counter-ion condensation because condensed counter-ions are not osmotically active and cannot participate in the interfacial equilibrium at the surface of the membrane, thereby reducing the Donnan potential of the IEM (Equation 3.9). Increased counter-ion condensation (i.e., increased ξ) leads to a reduction in $\left(\alpha_{g/c}\right)_K$. Manning condensation is predicted to be more prevalent in: 1) IEMs with relatively low water contents, because the lack of freezable water lowers the total dielectric constant of the membrane and thus increases λ_B (Equation 3.18); and 2) IEMs with a high fraction of polymeric repeat units containing a fixed charge group, because b decreases as the fixed charge groups are forced closer together (Equation 3.17). Each UHCD IEM in Figure 7.4 contains a fixed charge group at every backbone repeat unit, which should minimize b and cause counter-ion condensation to be extremely prevalent in UHCD IEMs. If b is identical for each UHCD IEM, λ_B should provide the only differences to ξ, and membranes with greater ϕ_w should exhibit lower ξ. Meanwhile, UHCD IEMs with similar ϕ_w should have similar ξ.

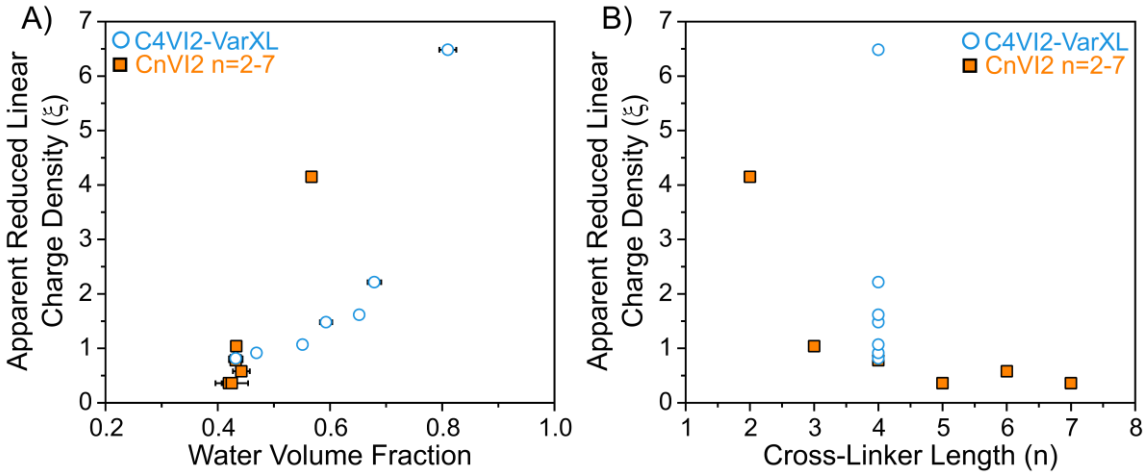


Figure 7.5: Reduced linear charge densities in UHCD IEMs. A) The apparent reduced linear charge density plotted against the water volume fraction. B) The apparent reduced linear charge density plotted against the cross-linker length. Uncertainties represent the standard deviation of at least five independent samples. Reduced linear charge densities were extracted by fitting co-ion partitioning results for membranes equilibrated with 1 m NaCl using the Donnan-Manning (DM) model (Section 3.4).

To test these expected trends, we used the Donnan-Manning (DM) model to extract apparent values of ξ from the co-ion partitioning results of UHCD IEMs equilibrated with 1 m NaCl (Figure 7.5). These one-point error minimizations produce ξ values that perfectly describe the partitioning results. Unexpectedly, the extracted ξ values cannot be explained via the conventional definitions of Manning condensation described previously. In Figure 7.5A, the fitted ξ values increase with increasing ϕ_w, completely contradicting the dielectric dependence of ξ. In Figure 7.5B, ξ is constant as predicted for $n = 5$, 6, and 7; however, ξ increases for $n = 4$ and 3, despite essentially no change in ϕ_w or the fraction of charged repeat units. C_2VI_2 is not directly comparable to the other C_nVI_2 membranes due to its increased ϕ_w, but it can be compared to the series of varied-cross-linking C_4VI_2 IEMs. ξ for C_2VI_2 exceeds that of the C_4VI_2 IEM with comparable ϕ_w, showing that $n = 2$ follows the same pattern as $n = 3$ and 4.

It should be reasonable for these unique UHCD IEMs to deviate from a model built to describe more conventional IEM materials. To amend this, we explore possible explanations for

the observed trends. While preserving the core concepts of Manning condensation, we reevaluate how common assumptions made in the application of the DM model could change when considering UHCD IEMs.

7.4.1 Rationalizing Manning Condensation in Varied-Cross-Linking C_4VI_2 IEMs

The trend of increasing ξ with increasing ϕ_w in the varied-cross-linking C_4VI_2 IEMs could be due to dielectric exclusion, which is a phenomenon not included in the DM model. Treated quantitatively via the Born model[471,472], dielectric exclusion describes the reluctance of ions to enter phases that are poor solvation environments, i.e., low dielectric constant phases. Dielectric exclusion can act in conjunction with Manning condensation and has recently been modeled via the Donnan-Manning-Born framework[472]. While Manning's theory predicts that low ϕ_w membranes will inefficiently exclude co-ions due to increased condensation, the Born model predicts that these low ϕ_w membranes will exclude co-ions extremely well due to an increase in dielectric exclusion.

By not capturing dielectric exclusion in the DM model, the trend in apparent ξ values may be misleading. Without incorporating dielectric exclusion into this model, the apparent value of ξ must change to accommodate any dielectric exclusion effects actually present in the data set. This highlights the danger of ascribing physical meaning to fitting parameters without a clever experimental design to ensure the phenomenon in question is unambiguously isolated. Unfortunately, we are unable to apply the Donnan-Manning-Born model to these UHCD IEMs. Using the Born model requires advanced and prohibitive characterization, including dielectric relaxation spectroscopy and small-angle neutron scattering[472]. Without these characterizations, the three-adjustable-parameter model would not yield any reliable insights. Modeling C_4VI_2 IEMs

with the Donnan-Manning-Born framework is beyond the scope of this study but is likely a promising next step toward understanding ion activities within UHCD IEMs.

7.4.2 Rationalizing Manning Condensation in C_nVI_2 IEMs

Without fully understanding the total magnitude of ξ for C_nVI_2 IEMs (see Section 7.4.1), this section attempts to explain the relative trend in apparent counter-ion condensation. Using the traditional equations for Manning condensation in IEMs, it is difficult to rationalize how ξ does not vary significantly for n = 5, 6, and 7, but increases significantly as n reaches 4, 3, and 2. As discussed in Figure 7.5, differences in ϕ_w cannot explain the dependence of ξ on n, so the dielectric exclusion argument presented in Section 7.4.1 does not apply. Instead, the dependence of ξ on n can be rationalized via geometric effects of cross-linked IEMs. Although many traditional IEMs are described using a strictly linear interpretation of the charge group spacing parameter (defining b using Equation 3.17) this is not always the case[385]. Ji *et al.* analyzed a poly(ethylene glycol diacrylate) cross-linked IEM using the DM model and found that the traditional method of calculating b was insufficient[473]. Instead, these authors incorporated the geometric size of their cross-linker into their modeling efforts. Because Ji *et al.* worked with a large poly(ethylene glycol diacrylate) cross-linker, fixed charge groups were farther away from each other than could be captured by treating the entire cross-link as one repeat unit in a linear polymer backbone. The geometric analysis performed by Ji *et al.* dramatically improved the predictions of the DM model for their IEM system[385,473]. We believe that the incorporation of fixed charge groups directly into the cross-linking network of UHCD IEMs necessitates similar geometric considerations.

For cross-linked imidazolium IEMs, incorporating cross-linker geometries could lower b. Manning condensation considers electrostatic repulsion between fixed charge groups forced into close proximity by covalent bonds, which describes not just the polymer backbone connections,

but also the intramolecular bis(imidazolium) cross-linking structure (Figure 7.1A). To perform this analysis, we compare the size of an extended cross-linking monomer structure with the spacing of imidazoliums along the vinyl-derived polymer backbone. However, to assess these distances accurately, we need to consider the polymer tacticity. Tacticity is typically not a major factor for calculating b because typical side-chain IEMs permit some fixed charge group mobility after polymerization. However, because bis(imidazolium) membranes incorporate fixed charges directly into the network structure, polymerization fixes the charge groups in place. Further, the imidazoliums are immediately adjacent to the polymerizable site, so the tacticity of the polymer network should heavily impact the separation of adjacent imidazoliums (Figure 7.6).

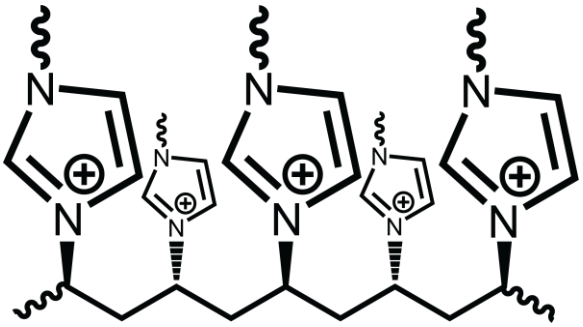


Figure 7.6: Tacticity in vinylimidazolium IEMs. A syndiotactic backbone has separation along the chain as well as out-of-plane spacing. For clarity, the connecting cross-links are not shown.

Due to steric bulk and charge repulsion, we expect a strong preference for syndiotactic polymerization in these IEMs. If the projected length of a (-CH_2-CHR-) repeat unit is 2.5 Å[103,392], syndiotactic polymerization places the nearest in-plane neighbor along the vinyl backbone at 5 Å. The out-of-plane neighbor separation can be crudely approximated by considering the bond geometry, which would cause syndiotactic imidazoliums to project away from each other (Figure 7.6). A first approximation of this geometry is given by $\sqrt{(2.5\ \text{Å})^2 + \left(2\ell \sin\left(\frac{109.5}{2}\right)\right)^2}$, where the first term represents the backbone spacing and the second term represents the out-of-plane spacing.

Here, ℓ is the distance from the polymer backbone to the center of the imidazolium ring, and 109.5 º is used as the bond angle of tetrahedral carbon structures. An interesting case to consider is when the in-plane and out-of-plane distances are equal; this occurs at $\ell = 2.65$ Å. Because the center of the imidazolium ring should be slightly greater than the projection length of the ring's C-N–C bonding structure, $\ell = 2.65$ Å is a fair approximation for this system. For the simplicity of discussion, we will use $\ell = 2.65$ Å and approximate that each imidazolium is equidistant from the four nearest-neighbor imidazoliums.

The approximate backbone spacing of 5 Å becomes the threshold where cross-linking imidazoliums become more relevant. Once the size of the cross-linking monomer is small enough to place the connected imidazoliums within 5 Å of each other, the cross-link connection enters the first ring of nearest neighbors for each imidazolium. Not only will this single fixed charge group contribute to electrostatic repulsion, but the inter-chain separation of unconnected imidazoliums will also enter the first, second, or third tier of adjacent fixed charge groups. This cascading increase in dimensionality of the IEM condensation profile should lead to a strong non-linear increase in the extent of condensation. Starting with a long bis(imidazolium) cross-linker, decreasing n should initially change very little because the vinyl backbone dominates the nearest neighbor condensation phenomena. Once inter-chain nearest neighbors begin to contribute toward electrostatic repulsion and condensation, decreasing n should dramatically increase ξ. By analyzing the relative trends, we should be able to observe this intra-chain/inter-chain transition without completely predicting ξ.

Using the same projection length as the polymer backbone[103], we estimate the spacing between imidazoliums participating in a cross-link as $1.25n$ (Å). Setting the critical threshold to 5 Å, intra-chain repulsion should dominate for $n > 4$, and counter-ion activity coefficients should

remain relatively constant. When $n \leq 4$, inter-chain repulsion is predicted to become relevant, and counter-ion activity coefficient should begin to rapidly decrease. This trend is perfectly represented by the experimental partitioning results (Figure 7.7). For $n = 5$, 6, and 7, no net change is observed in the activity of counter-ions. For $n = 4$, a slight decrease is observed, approaching the predictions of the ID model. Then, for $n = 3$ and 2, the activity decreases at an accelerating rate.

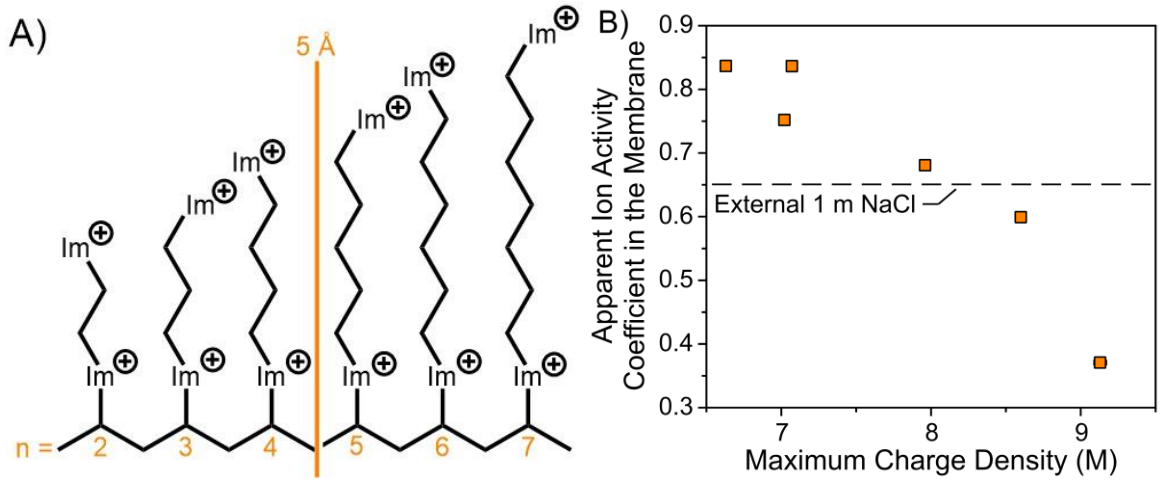


Figure 7.7: Cross-linker effects on inter-charge spacing. A) The cross-linker size passes a threshold where inter-chain effects compete with intra-chain condensation effects. B) The measured counter-ion activity coefficients in C_nVI_2 IEMs as a function of n. The dashed line indicates the counter-ion activity coefficient of the external 1 m NaCl salt solution, which corresponds to the predictions of the ID model for the counter-ion activity coefficient in the IEMs.

7.5 Critical Onset Phenomena in C_nVI_2 IEMs

The explanation in Section 7.4.2 for the sudden reduction of counter-ion activity in C_nVI_2 IEMs relies on relative trends in apparent values of the fitted parameter, ξ. As discussed in Section 7.4.1, it is easy to misinterpret results extracted from a fitted parameter, even if the data follows the expected trend extremely well. Because we cannot develop a complete understanding of ion non-idealities in these IEMs, we examined other properties of the C_nVI_2 IEMs. Charge repulsion should affect the polymer in more aspects than just counter-ion activities, so we examined the polymer network formation, dynamics, and arrangement for critical onset phenomena as a function

of n. We relied on a suite of common polymer characterization techniques (thermogravimetric analysis, TGA, differential scanning calorimetry, DSC, dynamic mechanical analysis, DMA, Fourier-transform infrared spectroscopy, FTIR, and small-angle x-ray scattering, SAXS) to understand the C_nVI_2 IEMs.

Some of the results from this comprehensive characterization suggest there are minimal differences between membranes. FTIR results (Appendix Figure E.1) demonstrate that the extent of partial cross-linker incorporation into the network does not change appreciably with different n. The signal corresponding to unreacted vinyl moieties is constant for each IEM. The DSC results (Appendix Figure E.2) for the dry polymers potentially show a glass transition for C_2VI_2, but no such transition for the other membranes. It is difficult to rationalize this sudden onset of polymer mobility. In the dry state, C_2VI_2 membranes are the most relaxed network due to the added water required to polymerize these materials, and this is likely contributing to the increased polymer mobility in the dry membranes. The thermal stability measured via TGA (Appendix Figure E.3) shows more incremental changes in the chloride-mediated thermal degradation of the imidazoliums across the C_nVI_2 IEMs. Smaller n cross-linkers retained additional weight after imidazolium loss, suggesting the presence of less volatile degradation byproducts. These TGA results could indicate a change in the location of the chloride/imidazolium reaction. However, the TGA results do not conclusively indicate what changes are detected in the thermal degradation mechanism.

The DMA investigation provided more conclusive findings. The swelling-reduced storage modulus (E'_{SR}) is a direct measure of the deformation resistance of the polymer network, with differences due to solvent swelling removed[105,474]. Extensive polymer physics modeling has connected E'_{SR} to the cross-linking extent of the polymer[103,104,475], and this method can be utilized

to identify the presence of ineffective cross-links. Dead-ends, primary loops, and to a lesser degree, secondary loops are the primary features that contribute to ineffective cross-linking[476], so analyzing E'_{SR} against the expected density of cross-links can detect dead ends and loops. The monomer structure in the C_nVI_2 membranes creates a tri-functional cross-linking node immediately adjacent to each imidazolium, so the theoretical cross-linking density of the dry polymer is equivalent to C_A^{max} in this system. Figure 7.8A demonstrates that for $n = 7 - 4$, E'_{SR} increases somewhat linearly with increasing theoretical cross-linking density (proxied by C_A^{max}). However, at $n = 4$, E'_{SR} reaches a maximum. For $n = 3$ and 2, E'_{SR} decreases as the theoretical cross-linking density increases. These DMA results reveal that the cross-linking network formation is altered for membranes beginning at $n = 4$, coinciding with the results of the condensation analysis.

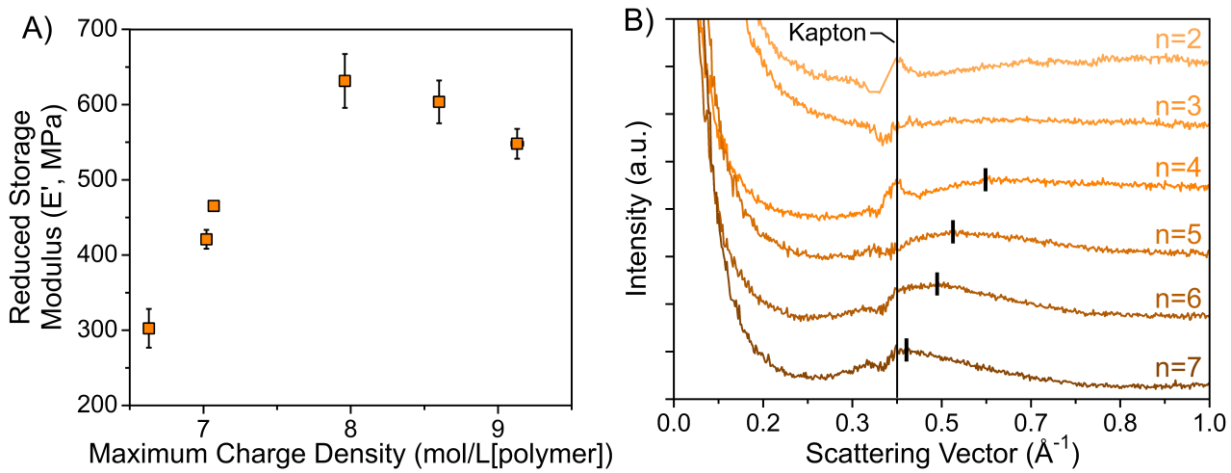


Figure 7.8: Mechanical and scattering properties of C_nVI_2 IEMs. A) The swelling-reduced storage modulus of the hydrated membranes is plotted against the maximum charge density. Uncertainties represent the standard deviation of measurements made on at least 3 independent samples. B) Small-angle x-ray scattering (SAXS) results for hydrated IEMs. Peaks attributable to the polymers are identified via tick marks. Kapton, which was used to secure the samples during measurement, was sometimes picked up by the instrument and is marked at $q = 0.4$ Å^{-1}.

The SAXS results also displayed critical onset phenomena. From the varied-cross-linking C_4VI_2 IEMs (Appendix Figure D.3), a signal corresponding to the backbone spacing between fully

extended cross-links[477,478] was identified in the vicinity of $q \sim 0.6\ \text{Å}^{-1}$. This interpretation is supported by the SAXS results of C_nVI_2 IEMs (Figure 7.8B) for $n = 4 – 7$, where, as n increases, the scattering vector (q) decreases. Smaller values of q correspond to longer length scale features, tracking the increase in cross-linker length. However, for $n = 3$ and 2, the signal corresponding to backbone spacing disappears. Starting at $n = 5$, the signal begins to blend into larger scattering vectors (smaller distances); after $n = 4$, no minimum signal is observed at $q \sim 0.2\ \text{Å}^{-1}$, denoting the disappearance of order at small length scales. The arrangement (or lack thereof) between polymer backbones directly measures the assembly of the polymer network structure. The results presented in Figure 7.8B demonstrate that the polymerization of C_2VI_2 and C_3VI_2 constrains the network in ways not experienced by the larger cross-linking monomers. Thus, the SAXS results are consistent with the condensation analysis and the DMA analysis.

7.6 Conclusions

In this chapter, I sought to increase the charge selectivity of UHCD membranes by preparing more densely charged and swelling-constrained polymer materials than the initial set of UHCD IEMs. I successfully synthesized membranes with maximum charge densities, C_A^{max}, as high as 9 mol / L[dry polymer] and fixed charge densities, $C_A^{m,t}$, as high as 5.3 mol / L[hydrated membrane]. These values are the highest reported C_A^{max} and $C_A^{m,t}$, respectively, that I am aware of. However, these membranes were limited to $\phi_w > 0.4$. A state of water analysis revealed that $\phi_w \sim 0.4$ corresponds to the primary hydration shells of the imidazolium and chloride ions in these materials, which would be difficult to exude from the IEMs. Additionally, I uncovered the rapid onset of non-ideal ion behavior in these highly charged membranes, which precluded significant improvements to charge selectivities.

Instead of achieving higher selectivities, I leveraged these results to advance the fundamental understanding of ion transport in UHCD IEMs and refine the design principles recommended for preparing future UHCD IEMs. My previous analysis suggested that the benefits of increasing C_A^{max} would always outpace the detrimental effects of counter-ion condensation. However, by cross-analyzing ion-activity coefficients, mechanical responses, and backbone arrangements in new C_nVI_2 membranes, I identified the onset of electrostatic repulsive effects which severely limit the performance of densely charged IEMs. When the polymer begins to incur inter-chain electrostatic forces which rival those of intra-chain forces, electrostatic network strains begin to dramatically alter the polymer and ion transport properties of the IEM. Without a clear way to mitigate the observed decrease in selectivity, this critical threshold of inter-chain repulsion could be a soft cap for polymer charge densities. Even though C_A^{max} can reach values >8 M, IEMs with $C_A^{max} \sim 8\ M$ have already gained most of the benefits to be derived from increases to charge densities. I advise that it may be more beneficial for the literature to focus on the design of IEMs with $C_A^{max} \sim 8\ M$.

Chapter 8 Morphological Constraints in Highly Swollen Ion-Exchange Membranes[5]

8.1 Introduction

Electrochemical applications that are operated with pure water (e.g., fuel cells or electrolyzers, see Section 1.2) require membranes that have high ionic conductivity (κ_g). Due to their exceptionally high charge content, UHCD IEMs could meet this need. When equilibrated with DI water, the UHCD IEM with a water volume fraction (ϕ_w) of 0.66 exhibited the highest κ_g ever reported for chloride, to the best of our knowledge (see Chapter 6). κ_g of membranes with higher ϕ_w were lower, somewhat defying the trend predicted by the Mackie-Meares model (Figure 6.4A). According to this model, the highest κ_g for a given maximum charge density (C_A^{max}) should occur at $\phi_w = 0.76$, a full 10 percentile points higher than the experimentally observed 0.66. The disagreement between experimental and predicted κ_g at high ϕ_w demonstrates that ion transport in highly swollen IEMs is not understood as well as that in IEMs having more moderate ϕ_w. In this chapter, we advance the fundamental understanding of ion transport in highly swollen cross-linked IEMs, particularly focusing on the role of membrane morphology.

The water swelling of polymers is controlled via either hydrophobicity or cross-linking; because IEMs are charged, IEM swelling is typically controlled via introduction of cross-linking structures. Most commercial IEMs of known structure are cross-linked (Table 2.3). Varying the

[5]This chapter has not yet been published. Contributions to this chapter were also made by: Jacquelyn Zamora and Jovan Kamcev. I would also like to acknowledge Min Gyu Shin for helpful discussions regarding this analysis. J.Z. prepared membranes for this analysis and assisted with water content and ion partitioning characterizations. J.K supervised this work.

cross-linking density of the imidazolium network was how water contents were varied in Chapter 6; however, there is another way to change the water content of a material. When cross-linked polymers are synthesized in the presence of a solvent, the network must form around the solvent molecules. Bray and Merrill formalized this concept and defined a relaxed state of swelling, which is the swelling of the polymer immediately after network formation[105]. When immersed in a favorable solvent, the network elasticity only acts to suppress swelling beyond this initial relaxed state. Thus, for a constant cross-linking monomer fraction, synthesizing the polymer in the presence of additional solvent forces the network cross-links to form less densely. Diluting pre-polymer solutions is therefore a straightforward approach to increase the equilibrium ϕ_w.

We synthesized a series of membranes with varying water content using this approach by diluting the pre-polymer solution. Figure 8.1 compares κ_g for two series of C_4VI_2 membranes: one consists of cross-linked homopolymers where IEMs were prepared with various pre-polymer concentrations (referred to as "varied-concentration IEMs"); the other consists of co-polymers prepared with various cross-linker contents but always at saturated concentrations (discussed thoroughly in Chapter 6 and referred to as "varied-cross-linking IEMs"). Except for the cross-linking extent and relaxed network swelling, these materials are essentially identical (i.e., they have equivalent C_A^{max}, and thus also similar values of other metrics for charge contents, namely $C_A^{m,t}$ and $C_A^{m,w}$, at a given ϕ_w). As demonstrated in Figure 8.1A, κ_g of the IEMs with high ϕ_w differed by approximately a factor of 2 when equilibrated with DI water. In contrast, the IEM series behaved essentially identically when equilibrated with 1 m NaCl solutions (Figure 8.1B).

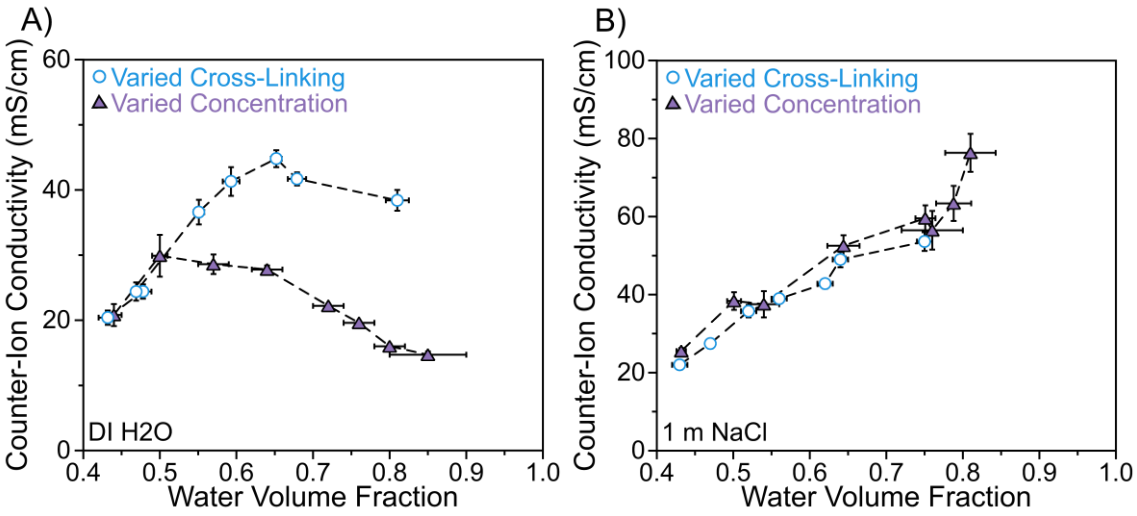


Figure 8.1: Conductivity of highly swollen UHCD IEMs. Membranes prepared with varied cross-linking densities are shown as blue circles and are discussed thoroughly in Chapter 6. Membranes prepared with varied polymerization concentrations are shown as purple triangles and are discussed in the remainder of Chapter 8. A) Counter-ion conductivities plotted against water volume fraction for membranes in the chloride form equilibrated with DI water. B) Counter-ion conductivities plotted against water volume fraction for the membranes in the chloride form equilibrated with 1 m NaCl. The error bars represent the standard deviation of at least five independent measurements.

A likely source of the difference in conductivity between the two series of membranes is the variations in their morphologies. Although the average charge and water contents of the two series are identical, the varied-concentration IEMs with high ϕ_w turned opaque, indicating possible phase separated (Figure 8.2). In contrast, the varied-cross-linking IEMs translucent, suggesting a more uniform structure. Thus, the water and polymer arrangement in these two series may differ significantly, and these differences likely affect their transport properties. We investigated how these two methods of increasing ϕ_w influence the membrane structure and the resultant ion transport properties. Specifically, we aimed to determine how these methods might additively increase ϕ_w, and whether exploring these synthesis routes could impact the κ_g dependence on ϕ_w.

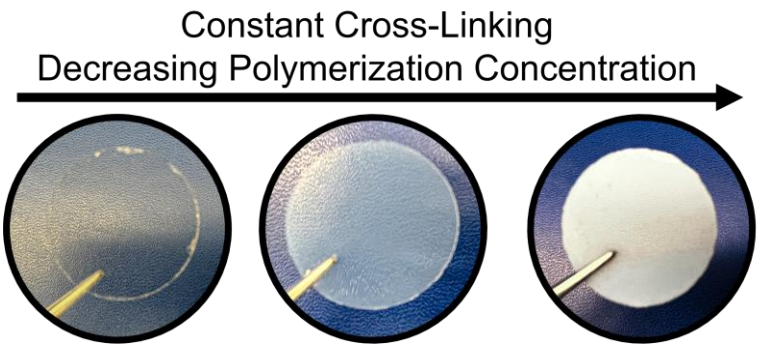


Figure 8.2: Phase separated membrane appearances. Membranes prepared from the same polymer backbone but at different concentrations.

In this chapter, we synthesized an array of membranes with varying cross-linking densities and polymerization concentrations, allowing us to isolate controlled sub-series of membranes for more detailed analysis. We leveraged the extensively established polymerization-induced phase separation (PIPS) literature to guide our morphological investigation of these materials[479]. Notably, a solvent-rich phase could be detected in the phase separated varied-concentration IEMs. These bulk-like domains of water affect both the partitioning and diffusion of ions in these IEMs. We rationalized the partitioning data with a simple additive model, which separately considers partitioning in the solvent-rich and polymer-rich phases. We used a percolation model developed by De Gennes[404] (see Section 3.5) to interpret the ion diffusion results. Although this framework is not yet predictive, we tested multiple conditions to validate its application to our data. Ultimately, we identified preparation methods that yield nearly a 10% increase in κ_g compared to the most conductive membrane from Chapter 6, demonstrating the utility of this design principle for developing IEMs with exceptionally high ionic conductivity.

8.2 Membrane Structures

The membranes discussed in the remainder of Chapter 8 are thermally polymerized UHCD imidazolium IEMs. While phase separated membranes could also be prepared via

photopolymerization, membranes prepared via thermal polymerization exhibited superior mechanical integrity. Thus, we prepared all the reported membranes using the thermal polymerization methods described in Section 2.1.3. The monomers (C_4VI_2 and C_2VI) used in the membrane synthesis were prepared according to methods described in Section 2.1.2. The membranes are named according to the cross-linking fraction and water content of the pre-polymer solution. The recipes for the membranes are given in Table 8.1.

The macroscopic membrane structural properties (water volume fraction, ϕ_w, fixed charge density, $C_A^{m,t}$, fixed charge concentration, $C_A^{m,w}$, maximum charge density, C_A^{max}, and membrane hydration number, λ) for IEMs equilibrated with DI water are reported in Table 8.2. Additional membrane properties (including the water uptake, WU, ion-exchange capacity, IEC, dry polymer density, ρ_p, and visual appearance) are included in Appendix Table F.1.

Various groups of membranes are utilized as a controlled subsection of this extensive list of materials. Some groups depend on the preparation conditions in Table 8.1. First, a series of membranes prepared with constant pre-polymer water content but varied cross-linking (analogous to the photopolymerized membranes studied in Chapter 6) can be selected by examining: 100X-26W, 75X-26W, 50X-26W, 25X-26W, 20X-26W, 15X-26W, 10X-26W, 5X-26W. A complementary series of membranes prepared with constant cross-linking but varied pre-polymer water content can be selected by examining: 100X-26W, 100X-33W, 100X-40W, 100X-50W, 100X-62W, 100X-65W, 100X-70W, 100X-75W. Three smaller subsets also fall into the second category: 1) 75X-26W, 75X-40W, 75X-65W, and 75X-73W; 2) 50X-26W, 50X-40W, 50X-61W, and 50X-69W; and 3) 25X-26W, 25X-40W, 25X-58W, and 25X-69W.

Table 8.1: C_4VI_2 thermal membrane recipes. The pre-polymer co-monomer ratios, total water contents, and initiator contents expressed as fractions of the pre-polymer solution.

Membrane	C_4VI_2 Monomer (wt% monomer)	Water Content (wt% solution)	V-50 Initiator (wt% monomer)
100X-26W	100	26	1.0
100X-33W	100	33	1.0
100X-40W	100	40	1.0
100X-50W	100	50	1.0
100X-63W	100	63	1.0
100X-65W	100	65	1.0
100X-70W	100	70	1.0
100X-75W	100	75	1.0
75X-26W	75	26	1.0
75X-40W	75	40	1.0
75X-65W	75	65	1.0
75X-73W	75	73	1.0
50X-26W	50	26	1.0
50X-40W	50	40	1.0
50X-61W	50	61	1.0
50X-69W	50	69	1.0
25X-26W	25	26	1.0
25X-40W	25	40	1.0
25X-58W	25	58	1.0
25X-69W	25	69	1.0
20X-26W	20	26	1.0
15X-26W	15	26	1.0
10X-26W	10	26	1.0
5X-26W	5	26	1.0

Table 8.2: C_4VI_2 thermal membrane equilibrium properties. Water contents and charge contents expressed as water volume fractions, fixed charge densities, fixed charge concentrations, maximum charge densities, and membrane hydration numbers. Reported uncertainties represent the standard deviation of at least five independent measurements.

Membrane	ϕ_w (L [water] / L [membrane])	$C_A^{m,t}$ (mol / L [membrane])	$C_A^{m,w}$ (mol / L [water])	C_A^{max} (mol / L [dry polymer])	λ (mol [water] / mol [charge])
100X-26W	0.440 ± 0.007	4.86 ± 0.06	11.06 ± 0.21	8.13 ± 0.14	5.02 ± 0.09
100X-33W	0.503 ± 0.012	3.97 ± 0.08	7.91 ± 0.14	7.60 ± 0.17	7.03 ± 0.12
100X-40W	0.574 ± 0.015	3.79 ± 0.11	6.61 ± 0.06	7.95 ± 0.12	8.40 ± 0.07
100X-50W	0.637 ± 0.017	2.92 ± 0.09	4.59 ± 0.02	7.76 ± 0.17	12.11 ± 0.04
100X-63W	0.721 ± 0.020	2.09 ± 0.09	2.90 ± 0.06	7.92 ± 0.13	19.17 ± 0.43
100X-65W	0.761 ± 0.016	1.97 ± 0.07	2.59 ± 0.06	8.01 ± 0.18	21.44 ± 0.51
100X-70W	0.803 ± 0.015	1.77 ± 0.18	2.21 ± 0.18	8.42 ± 0.43	25.16 ± 2.10
100X-75W	0.872 ± 0.051	1.40 ± 0.08	1.61 ± 0.02	8.39 ± 0.56	34.52 ± 0.42
75X-26W	0.447 ± 0.017	4.79 ± 0.13	10.76 ± 0.47	8.44 ± 0.38	5.16 ± 0.22
75X-40W	0.564 ± 0.021	3.64 ± 0.14	6.47 ± 0.06	8.01 ± 0.06	8.58 ± 0.09
75X-65W	0.756 ± 0.014	1.81 ± 0.03	2.40 ± 0.05	7.57 ± 0.15	23.13 ± 0.48
75X-73W	0.871 ± 0.035	1.31 ± 0.06	1.51 ± 0.03	7.58 ± 0.19	36.84 ± 0.64
50X-26W	0.479 ± 0.026	4.34 ± 0.23	9.11 ± 0.75	7.82 ± 0.24	6.10 ± 0.50
50X-40W	0.594 ± 0.019	3.60 ± 0.06	6.08 ± 0.09	8.03 ± 0.09	9.14 ± 0.14
50X-61W	0.755 ± 0.014	2.04 ± 0.09	2.71 ± 0.10	7.71 ± 0.28	20.52 ± 0.76
50X-69W	0.833 ± 0.034	1.49 ± 0.11	1.79 ± 0.08	7.57 ± 0.27	31.05 ± 1.32
25X-26W	0.583 ± 0.025	3.66 ± 0.16	6.29 ± 0.26	7.99 ± 0.35	8.83 ± 0.37
25X-40W	0.663 ± 0.034	2.80 ± 0.14	4.23 ± 0.11	7.70 ± 0.10	13.15 ± 0.35
25X-58W	0.737 ± 0.022	1.85 ± 0.06	2.51 ± 0.08	7.54 ± 0.28	22.11 ± 0.74
25X-69W	0.883 ± 0.037	1.12 ± 0.09	1.27 ± 0.10	7.32 ± 0.14	43.76 ± 3.61
20X-26W	0.611 ± 0.014	3.07 ± 0.07	5.03 ± 0.03	7.34 ± 0.05	11.04 ± 0.07
15X-26W	0.659 ± 0.021	2.58 ± 0.08	3.92 ± 0.12	7.34 ± 0.27	14.16 ± 0.44
10X-26W	0.728 ± 0.018	2.10 ± 0.05	2.89 ± 0.04	7.15 ± 0.09	19.22 ± 0.29
5X-26W	0.860 ± 0.017	1.44 ± 0.04	1.67 ± 0.04	7.26 ± 0.15	33.18 ± 0.73

Two additional groups of membranes are identified based on the equilibrium material properties listed in Table 8.2. These membranes have essentially identical macroscopic properties to one another but exhibit different extents of phase separation. The first group is identified as those membranes having $\phi_w \cong 0.58$: 100X-40W, 50X-40W, and 25X-26 (precise values are, respectively, 0.574 ± 0.015, 0.594 ± 0.019, and 0.582 ± 0.025). The second group is identified as those membranes having $\phi_w \cong 0.75$: 100X-65W, 50X-61W, 25X-58W, and 10X-26W (precise values are, respectively, 0.761 ± 0.016, 0.755 ± 0.014, 0.737 ± 0.022, and 0.732 ± 0.010). These membranes are listed in order of increasing homogeneity, as characterized by their qualitative level of opacity (Appendix Table F.1)

In all the membranes reported here, C_A^{max} is essentially constant due to the structural similarity between the cross-linking monomer (C_4VI_2) and the monofunctional monomer (C_2VI), (see Chapter 6). The macroscopic membrane properties in Table 8.2 can be reduced to just two degrees of freedom (C_A^{max} and ϕ_w, as discussed in Chapter 4 and Chapter 5), so any value of ϕ_w implies a corresponding value for $C_A^{m,t}$, $C_A^{m,w}$, and λ. For the series of membranes with constant preparation conditions (either constant cross-linking extent or constant pre-polymer water content), differences in transport properties could be explained entirely via differences in ϕ_w and the membrane morphology. For the series of membranes with constant ϕ_w, differences in transport properties could be explained entirely via differences the membrane morphology.

8.3 Water-Equilibrated Conductivity in Phase Separated Membranes

The results in Figure 8.1 demonstrate that morphological effects on κ_g are strongest in DI water. To benchmark each of the IEMs in this investigation, we measured the room temperature chloride conductivity of DI water-equilibrated membranes using the technique described in Section 2.3.5. Since each membrane has the same C_A^{max}, the Mackie-Meares conductivity model

used in Figure 6.4A predicts that all the data should fall along a single curve. This model, originally developed for homogeneous membranes, does not account for potential membrane phase separation[389], so it should not accurately describe the phase separated membrane conductivities. This expectation is confirmed by the data presented in Figure 8.3. Although the model reasonably predicts the results for low-swelling membranes prepared with saturated pre-polymer solutions (the lowest ϕ_w reported for each cross-linking extent), the results for IEMs prepared with additional water deviate from the model predictions. In the high ϕ_w region, where even the homogeneous IEMs show a negative deviation from the model predictions, the phase separated membranes exhibit a significantly greater negative deviation. The extent of conductivity suppression increases with increasing cross-linking. At every ϕ_w, membranes with greater cross-linking extents appear more phase separated than membranes with lesser cross-linking extents. Thus, the negative deviation in conductivity also increases with increasing phase separation.

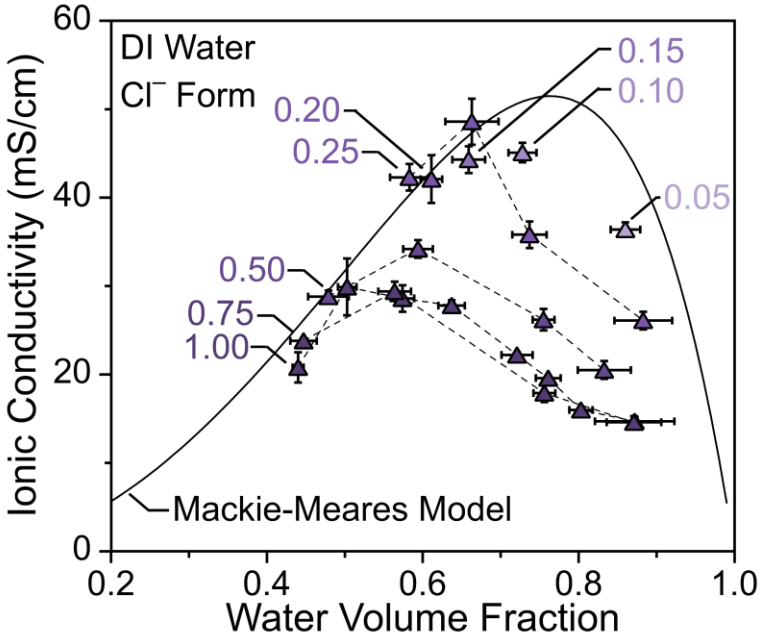


Figure 8.3 Ionic conductivity of IEMs with varied morphology. The room temperature DI water-equilibrated ionic conductivity of membranes in the Cl^- form plotted against ϕ_w. The lowest ϕ_w IEM of each cross-linking content is labeled with x. The solid black line indicates the Mackie-Meares model predicted ionic conductivity trend. The dashed lines connect IEMs prepared with

identical cross-linker contents. The error bars represent the standard deviation of at least five independent measurements.

Diluting the pre-polymer solution (traveling from left to right along the cross-linking tie-lines) initially leads to an increase in κ_g, followed by a decrease. Although this shape is vaguely represented by the Mackie-Meares model, the shape and height of the experimental data do not match the modeled values. Notably, the most conductive IEM surveyed (25X-40W, 48.2 mS/cm) was not prepared with a saturated pre-polymer solution. The 25X-40W membrane also appears homogeneous, suggesting that some dilution of the pre-polymer solution does not significantly alter the membrane morphology. This maximum observed conductivity occurs at essentially the same ϕ_w as the maximum observed conductivity in Chapter 6 (0.663 vs. 0.652, respectively), despite having different recipes. Understanding the evolution of membrane morphology with increasing ϕ_w could explain the exceptionally high κ_g of 25X-40W and provide guidelines for future membrane design.

8.3.1 Model Development

We modified the Mackie-Meares conductivity model from Chapter 6 to account for the phase separated morphology of these IEMs. Because the phase separation occurs during polymerization (all pre-polymer solutions were clear and appeared homogeneous), we expect the morphology of these IEMs to be similar to that of other network polymers that exhibit polymerization induced phase separation (PIPS)[479]. Many of the membranes in this study are homopolymers (100X series), so this rules out other potential sources for structural heterogeneities, such as non-ideal co-polymerization between multiple co-monomers. As the kinetic polymer chain grows during polymerization, favorable interactions between monomer and solvent are diminished, causing the partially polymerized system to become a metastable mixture

of polymer, monomer, and solvent. Eventually, spinodal decomposition occurs, and excess solvent is ejected from the newly formed polymer-rich phase into a solvent-rich phase. Per this reported mechanism for PIPS, the amount of solvent that the polymer-rich phase can accommodate should depend on the polymer solubility parameters and cross-linking density. So, for a given polymer chemistry and cross-linking extent, regardless of how much solvent was initially mixed with the monomer, all excess solvent beyond a critical value is ejected into the solvent-rich phase of the resulting membrane. Through the spinodal decomposition intrinsic to PIPS, we expect the solvent-rich phase to be co-continuous with the polymer-rich phase[479].

Co-continuous morphologies in the phase separated membranes align with the assumptions of the De Gennes percolation model for transport in polymer blends, described in Section 3.5. However, other assumptions in this model must be assessed. We must evaluate whether a PIPS system be morphologically equivalent to a blend of two immiscible polymers and whether the conductivity of one phase is much greater than the other, as is assumed in the De Gennes model. The first point is rather simple: in both the polymer-rich and solvent-rich phases, polymer is present. For a polymer blend, if one phase swells more than the other phase while maintaining the co-continuous morphology, the system would remain a polymer blend. Taken to a very large difference in swelling, this is essentially the description of a PIPS membrane. Thus, we believe the morphological structure created by the spinodal decomposition of our PIPS IEMs is similar to that of a polymer blend. The second assumption requires a deeper analysis.

The conductivity comparison is counter-intuitive, because chloride diffusion is faster in bulk water than in the constrained environment of a swollen ion-exchange polymer. However, per the solution-diffusion model[380], we must consider the concentration of diffusing species as well. When equilibrated with DI water, there are no mobile cations in the AEMs, so any chloride ions

in the bulk water domains would get there by leaving behind all cations helping to maintain electroneutrality. Electroneutrality only needs to be obeyed macroscopically, so this argument does not necessarily preclude an anion entering a large water domain. However, as the domain grows, the energy barrier associated with leaving the imidazolium cations behind grows larger. Therefore, we conclude that the concentration of mobile ions should be essentially zero for any appreciably sized solvent domains contained in membranes equilibrated with DI water. As the ion concentration in the water domain approaches zero, so does the conductivity, satisfying the condition that the ion-exchange polymer is much more conductive than the bulk water phase.

To integrate these ideas into a conductivity model, we define a new parameter, $\phi_{w,sat}^{ixp}$, which quantifies the maximum water accommodated within a homogeneous polymer network. This parameter functions as a saturation point for the membrane: if $\phi_w^{tot} \leq \phi_{w,sat}^{ixp}$, all the water can incorporate into the ion-exchange polymer phase (scripted mathematically as ixp), and no phase separation occurs. For $\phi_w^{tot} \geq \phi_{w,sat}^{ixp}$, phase separation must occur, dividing the water between phases of ion-exchange polymer and bulk water. The two phases of the total IEM can be described using Equation 8.1:

$$\phi_{ixp}^{tot} + \phi_{bulk}^{tot} = 1 \tag{8.1}$$

Here, ϕ_j^{tot} represents the volume fraction of phase j ($j = ixp$ or $bulk$) in the total membrane. The water distributes into the two phases, producing:

$$\phi_{ixp}^{tot}\phi_w^{ixp} + \phi_{bulk}^{tot}\phi_w^{bulk} = \phi_w^{tot} \tag{8.2}$$

where ϕ_w^j represents the volume fraction of water normalized against the volume of phase j. According to the mechanism of PIPS described above, for all $\phi_w^{tot} \geq \phi_{w,sat}^{ixp}$, we can set $\phi_w^{ixp} =$

$\phi_{w,sat}^{ixp}$ and $\phi_{w}^{bulk} = 1$. Using these definitions and Equation 8.1, the water mass balance simplifies to an expression for the ion-exchange polymer and bulk water volume fractions:

$$\phi_{bulk}^{tot} = \frac{\phi_{w}^{tot} - \phi_{w,sat}^{ixp}}{1 - \phi_{w,sat}^{ixp}} \; for \; \phi_{w}^{tot} \geq \phi_{w,sat}^{ixp} \tag{8.3}$$

$$\phi_{ixp}^{tot} = 1 - \phi_{bulk}^{tot} = \frac{1 - \phi_{w}^{tot}}{1 - \phi_{w,sat}^{ixp}} \; for \; \phi_{w}^{tot} \geq \phi_{w,sat}^{ixp} \tag{8.4}$$

Here, the extent of phase separation (ϕ_{bulk}^{tot}), has been isolated as the function of just two variables: the water volume fraction of the entire phase separated membrane, ϕ_{w}^{tot}, which is experimentally measurable, and the water volume fraction of the ion-exchange polymer at the onset of phase separation, $\phi_{w,sat}^{ixp}$, which is a function of the polymer structure and cross-linking extent. As ϕ_{w}^{tot} increases beyond $\phi_{w,sat}^{ixp}$, the added water contributes to increased phase separation; as $\phi_{w}^{tot} \to 1$, we have the intuitive asymptote that $\phi_{bulk}^{tot} \to 1$ as well, with the interpretation that the "membrane" is entirely bulk water.

Using Equation 8.1, ϕ_{bulk}^{tot} can be directly inserted into the De Gennes model, which is provided as a function of $(1 - \phi_{ixp}^{tot})$ in Equation 3.25. The result is:

$$\frac{\kappa_{g}^{tot}}{\kappa_{g}^{ixp}} = \left(1 - \frac{\phi_{bulk}^{tot}}{1 - \phi_{ixp,p}^{tot}}\right)^{\tau_p} \; for \left(1 - \phi_{ixp,p}^{tot}(1 - \phi_{w,sat}^{ixp})\right) \geq \phi_{w}^{tot} \geq \phi_{w,sat}^{ixp} \tag{8.5}$$

Here, κ_{g}^{j} is the counter-ion conductivity in phase j, $\phi_{ixp,p}^{tot}$ represents the critical percolation threshold for phase j in the membrane, and τ_p is an ordering factor which describes the arrangement of material for conduction. In this equation, the percolation requirement $\phi_{ixp}^{tot} > \phi_{ixp,p}^{tot}$ has been transformed to limit ϕ_{w}^{tot}. Thus, the range of validity is for ϕ_{w}^{tot} values which produce phase separation, but phase separation large enough to prevent the ion-exchange phase from percolating through the membrane. Using Equation 8.5, we can obtain an expression for the

De Gennes percolation theory applied to IEMs subject to PIPS and equilibrated with DI water, defined for a full range of ϕ_w^{tot} values.

$$\frac{\kappa_g^{tot}}{\kappa_g^{ixp}} = \begin{cases} 1 & for\ \phi_w^{tot} \le \phi_{w,sat}^{ixp} \\ \left(1 - \dfrac{\phi_w^{tot} - \phi_{w,sat}^{ixp}}{\left(1-\phi_{ixp,p}^{tot}\right)\left(1-\phi_{w,sat}^{ixp}\right)}\right)^{\tau_p} & for\ \phi_w^{tot} \le \left(1-\phi_{ixp,p}^{tot}(1-\phi_{w,sat}^{ixp})\right) \\ 0 & for\ \phi_w^{tot} \ge \left(1-\phi_{ixp,p}^{tot}(1-\phi_{w,sat}^{ixp})\right) \end{cases} \quad 8.6$$

To fully predict κ_g^{tot}, the Mackie-Meares model for homogeneous IEM conductivities can be inserted as an expression for κ_g^{ixp}. Incorporating PIPS phenomena, this model becomes:

$$\frac{\kappa_g^{ixp}}{\lambda_g^0} = \begin{cases} C_A^{max}(1-\phi_w^{tot})\left(\dfrac{\phi_w^{tot}}{2-\phi_w^{tot}}\right)^2 & for\ \phi_w^{tot} \le \phi_{w,sat}^{ixp} \\ C_A^{max}\left(1-\phi_{w,sat}^{ixp}\right)\left(\dfrac{\phi_{w,sat}^{ixp}}{2-\phi_{w,sat}^{ixp}}\right)^2 & for\ \phi_w^{tot} \ge \phi_{w,sat}^{ixp} \end{cases} \quad 8.7$$

Here, λ_g^0 is the limiting equivalent conductance of the counter-ion at infinite dilution. After phase separation occurs, the ionic conductivity of the ion-exchange polymer phase is constant, based on the fixed ϕ_w^{ixp}. Except for this restricted change at $\phi_w^{tot} \ge \phi_{w,sat}^{ixp}$, the model is identical to that discussed in Chapter 6.

8.3.2 Comparison Between Model and Experiment

The ionic conductivity model for membranes that exhibit PIPS developed in the previous section incorporates three known quantities (λ_g^0, C_A^{max}, and ϕ_w^{tot}) and three unknown quantities ($\phi_{w,sat}^{ixp}$, $\phi_{ixp,p}^{tot}$, and τ_p). Because $\phi_{ixp,p}^{tot}$ and τ_p relate to the nature of the PIPS spinodal decomposition, we should expect these parameters to be somewhat universal but depend on the nature of the chemical system, such as the cross-linker functionality, cross-linker size, solvent surface tension, solvent self-interaction, or ion diffusional jump length. In our data set, all of these

properties are constant. Meanwhile, $\phi_{w,sat}^{ixp}$ quantifies the ability of the ion-exchange polymer to accommodate water, so this parameter should scale with the cross-linking density of the IEM. Heavily cross-linked polymers should accommodate less water than loosely cross-linked membranes, so $\phi_{w,sat}^{ixp}$ should decrease with increasing cross-linking. We can test this assumption at four different extents of cross-linking within our data set. Taken together, our well-controlled synthesis scheme provides an ideal testing ground for modeling the effect PIPS structures have on transport. With four series of constant cross-linking, varied-concentration IEMs, we can fit six parameters across 20 data points. $\phi_{ixp,p}^{tot}$ and $\phi_{w,sat}^{ixp}$ relate ϕ_w^{tot} to the phase separation, while τ_p relates the morphology to the rate of conductivity loss, so the individual facets of the model can be isolated and discussed.

The results of the model fittings are shown in Figure 8.4. For each series of constant-cross-linking IEMs, the model does an excellent job of describing the conductivity data. The optimization of universal parameters $\phi_{ixp,p}^{tot}$ and τ_p resulted in $\phi_{ixp,p}^{tot} = 0$ and $\tau_p = 0.592$. These parameters do not agree with the theoretical values of 0.156 and 1.83, respectively; however, both values correspond to features that can be seen clearly in the data. $\phi_{ixp,p}^{tot}$ determines the ϕ_w^{tot} at which the IEM essentially becomes non-conductive. This was not observed in any of the data sets up to $\phi_w^{tot} \sim 0.90$, demonstrating that $\phi_{ixp,p}^{tot}$ is not large enough to constrain these IEMs. Additionally, the downward slope at high ϕ_w^{tot} is concave-down, clearly indicating that $\tau_p < 1$. The single value of 0.592 describes the rate of conductivity loss quite well for each series, which is consistent with a singular mechanism of forming the co-continuous phases. Because $\tau_p < 1$, the IEMs do not appear to contain conductive regions that are ineffective (i.e., dead end conduction pathways); rather, IEMs appear to contain efficient organization of conduction pathways to preserve conductivity in the presence of phase separation. The saturation points of each network

followed the expected trend of 100XL ~ 75XL < 50XL < 25XL. These series are described by $\phi_{w,sat}^{ixp} = 0.487, 0.485, 0.540,$ and 0.643, respectively.

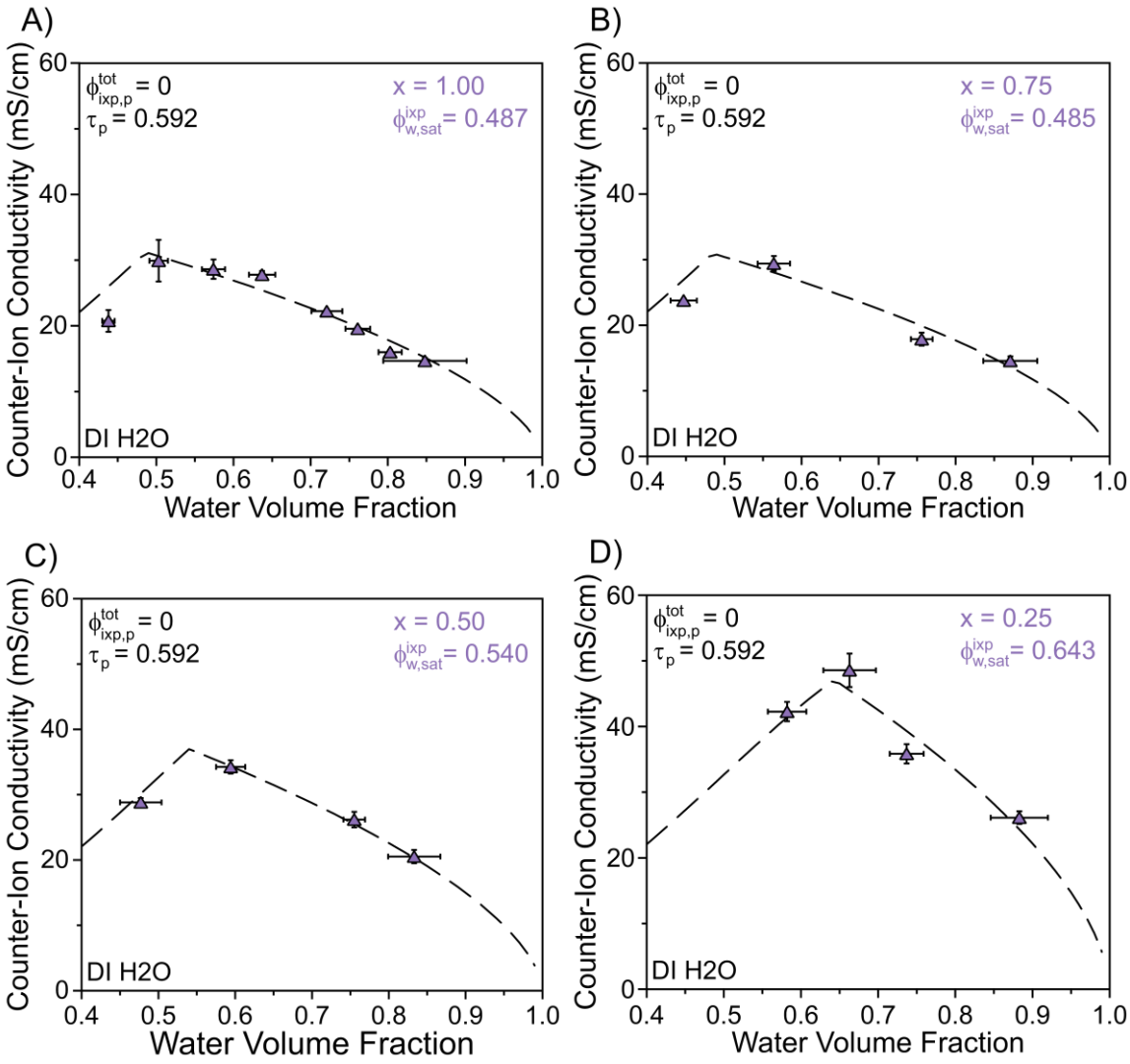


Figure 8.4: Modeled ionic conductivities in phase separated IEMs. The room temperature DI water-equilibrated chloride-form ionic conductivity of IEM series having constant cross-linker content plotted against the water volume fraction. A) 100XL, B) 75XL, C) 50XL, D) 25XL. The dashed lines are the predictions of proposed conductivity model using the parameters listed in the figures The error bars represent the standard deviation of at least five independent measurements.

The values for the universal parameters can be rationalized based on the differences between our PIPS membranes and the polymer blends that produced the accepted theoretical values of $\phi_{ixp,p}^{tot}$ and τ_p. Polymer blends typically exhibit conductivity decay which is concave-up,

having $\tau_p > 1$ and losing conductivity faster when the non-conductive phase is introduced[402,404,405]. However, unlike an insulating secondary polymer in a polymer blend, the water in membranes exhibiting PIPS is only non-conductive when feature sizes are large enough. For small water domains, the polymeric fixed charge groups bordering either side of bulk water could be close enough for a counter-ion to cross the water domain. Thus, not all phase separation should be obstructive, and the loss of ionic conductivity should lag the introduction of bulk water domains. This mechanism of efficient conductive pathways would result in $\tau_p < 1$, as was observed in the experimental data.

Having pure-water domains as the second phase in membranes exhibiting PIPS also helps to understand the fitted value of $\phi_{ixp,p}^{tot}$. Because the minority phase is just water, any small domains of ion-exchange polymer which do not percolate with the rest of the polymer network would be freely suspended in solution. If these domains are on the surface of the membrane, they could simply dissolve away into the solution. If these domains are on the surface of the membrane, they could simply dissolve away into the solution. Or, if these domains are in the interior of the membrane, they should be either entangled with the surrounding network or able to contact a portion of the network. These mechanisms eliminate the possibility of non-percolated polymer domains, so $\phi_{ixp,p}^{tot} \sim 0$ seems extremely reasonable.

Our description of DI water ionic conductivities was quite successful using the model developed in the previous section. We suspect that our fitted parameters might be universally applicable to other PIPS IEMs, providing a deeper understanding of phase separation effects on ion transport. Although we did not predict $\phi_{w,sat}^{ixp}$ for our various cross-linking extents, the fitted values essentially coincide with the ϕ_w^{tot} at the onset of opacity.

The modeling results also provide a potential explanation regarding the optimization of DI water conductivities. If ion passage across narrow, bulk-like water domains is indeed the explanation for $\tau_p < 1$, the same explanation can rationalize why 25X-40W might possess an ionic conductivity greater than a less cross-linked IEM prepared from a saturated polymerization solution having the same ϕ_w^{tot}. Passable bulk water domains contribute no added tortuosity to the membrane, so small amounts of phase separation (which forms only narrow water features through the IEM) would be beneficial to counter-ion transport.

8.4 NaCl Partitioning in Phase Separated Membranes

Section 8.3 provides a quantitative description of the decrease in conductivity in water-equilibrated IEMs exhibiting PIPS. However, we also aim to understand how phase separation affects the transport properties of these IEMs when equilibrated with salt. Notably, the counter-ion conductivities of phase separated and homogeneous IEMs are nearly identical when equilibrated with 1 m NaCl (Figure 8.1B). The presence of mobile co-ions in bulk water regions of the membranes should enable counter-ion diffusion across these domains, but this description fails to rationalize the convergence of counter-ion conductivities in such drastically different IEMs. To develop a deeper understanding of the transport properties of our salt-equilibrated IEMs, we use the solution-diffusion model to decouple the partitioning and diffusion contributions to counter-ion transport. For this investigation, we consider the two series of IEMs with charge and water contents, but different morphological arrangements of the polymer and water (Figure 8.5). These results are shown alongside the specific values of ϕ_w^{tot} for the three $\phi_w^{tot} \cong 0.58$ IEMs and the four $\phi_w^{tot} \cong 0.75$.

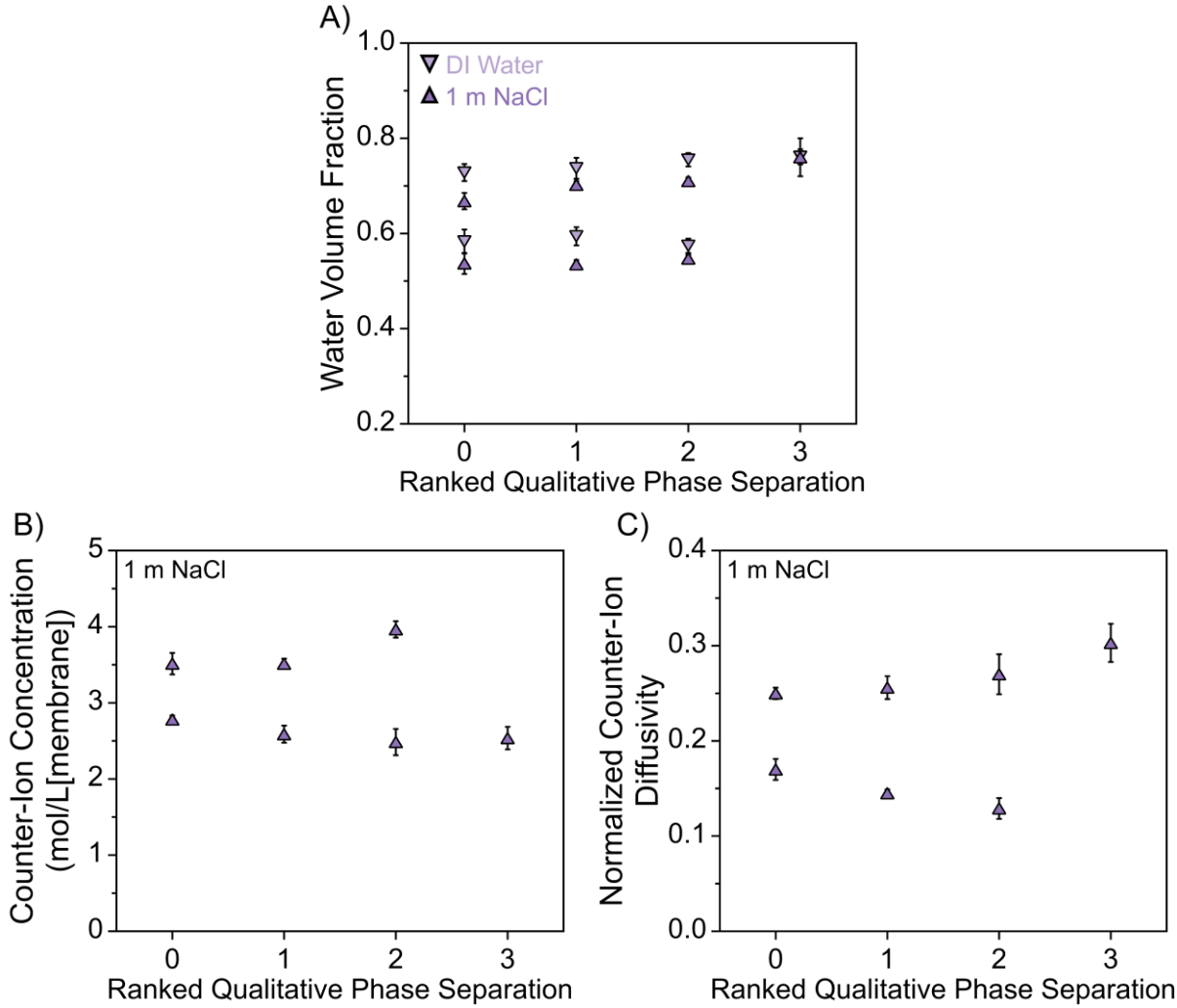


Figure 8.5: Counter-ion transport in phase separated IEMs equilibrated with 1 m NaCl. A) The water volume fraction for IEMs equilibrated with DI water and 1 m NaCl. B) The counter-ion concentration for IEMs equilibrated with 1 m NaCl. C) The counter-ion diffusivity for IEMs equilibrated with 1 m NaCl. Each figure is shown as a function of increasing pre-polymer water content, corresponding to increased apparent phase separation. 0 represents a homogeneous membrane, while 3 represents the most phase separated membrane. The error bars represent the standard deviation of at least five independent measurements.

These membranes were selected based on their similar ϕ_w^{tot} measured when equilibrated with DI water. However, as the external salt concentration increases to 1 m NaCl, ϕ_w^{tot} of the membranes decrease due to osmotic deswelling, which describes the membrane response to a decrease in the external solution water activity caused by increased salt concentration. Except for 100X-65W, which exhibits the greatest phase separation, IEMs of the same series experienced

similar extent of osmotic deswelling, maintaining a comparable (but lower) ϕ_w^{tot} across the series. As shown in Figure 8.5B and C, PIPS does not significantly affect the transport of counter-ions in salt-equilibrated IEMs. Both the concentrations and diffusivities of counter-ions in the IEMs equilibrated with 1 m NaCl do not strongly depend on the membrane morphology. This result is rather surprising, considering the extent of differences observed in the ionic conductivities of DI water-equilibrated IEMs (see Figure 8.1). Counter-ion concentrations are generally less sensitive to the external solution salt concentration, so any transport differences between homogeneous and phase separated IEMs might be more prevalent in the co-ion transport results, which we examine in Figure 8.6.

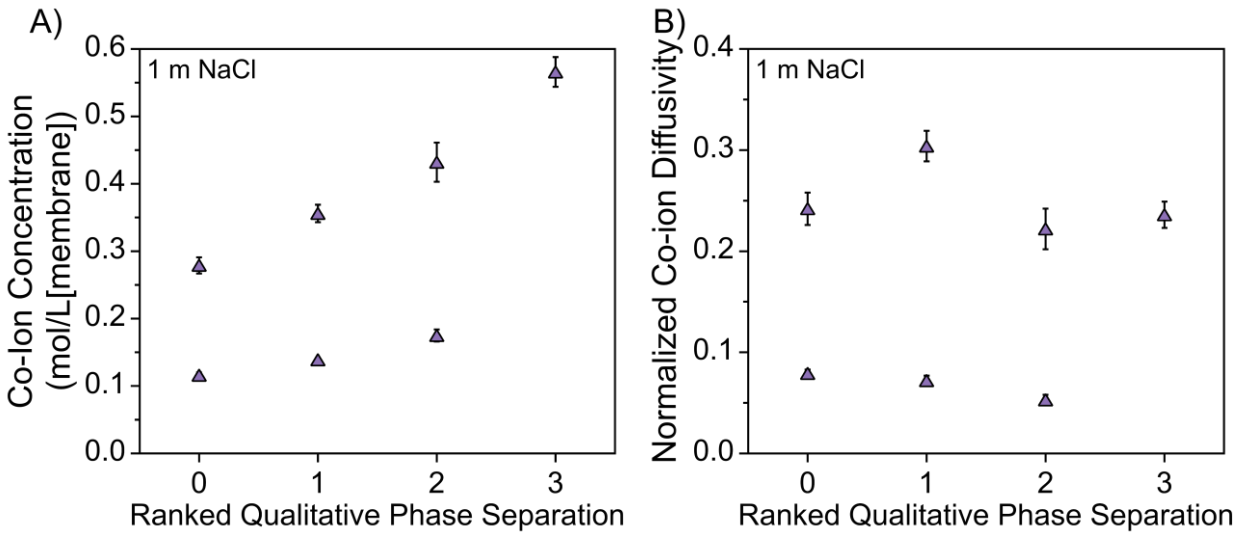


Figure 8.6: Co-ion transport in phase separated IEMs equilibrated with 1 m NaCl. A) The co-ion concentration for IEMs equilibrated with 1 m NaCl. B) The co-ion diffusivity for IEMs equilibrated with 1 m NaCl. Each figure is shown as a function of increasing pre-polymer water content, corresponding to increased apparent phase separation. 0 represents a homogeneous membrane, while 3 represents the most phase separated membrane. The error bars represent the standard deviation of at least five independent measurements.

Figure 8.6 reveals that the co-ion concentrations in both series of IEMs increase as the extent of PIPS increases. In contrast, there is no clear trend in the co-ion diffusivities. Like the results for the counter-ion diffusivities, it is surprising to observe that the co-ion diffusivity does not change

significantly as the morphology of the IEMs is dramatically altered. In contrast, the change in co-ion concentration with the extent of phase separation follows an intuitive trend. As the extent of PIPS increases, there is more bulk water in the IEM, which should confer minimal resistance to the equilibrium partitioning of salt into the membrane. In light of these findings, we explore the co-ion partitioning differences due to PIPS in the following section.

8.4.1 Model Development

Co-ion partitioning is evidently the transport property most sensitive to PIPS in salt-equilibrated IEMs. In this section, we develop a model to quantitatively describe changes in equilibrium co-ion concentrations with changes in the extent of PIPS in the IEMs. The model is physically consistent with the ionic conductivity model developed in Section 8.3.1. The membrane is modeled as consisting of two co-continuous phases: an ion-exchange polymer phase (ixp) and a bulk water phase ($bulk$). The total co-ion concentration in the membrane, $C_c^{m,t}$, is equal to the sum of co-ions in the ion-exchange phase ($C_{c,ixp}^{tot}$) and co-ions in the bulk water phase ($C_{c,bulk}^{tot}$):

$$C_c^{m,t} = C_{c,ixp}^{tot} + C_{c,bulk}^{tot} \tag{8.8}$$

If the bulk water domains have negligible resistance to salt partitioning, the concentration of salt in this phase should be simply equal to that of the external salt solution.

$$C_{c,bulk}^{tot} = \phi_{bulk}^{tot} C_c^{bulk} = \phi_{bulk}^{tot} C_c^s \tag{8.9}$$

Here, C_c^{bulk} is the concentration of co-ions in the bulk water phase normalized to the volume of the bulk water phase, rather than the total membrane volume, and C_c^s is the concentration of co-ions in the external salt solution. Connecting the above equations to experimentally measurable values, we substitute Equation 8.3 in for ϕ_{bulk}^{tot}, giving:

$$C_{c,bulk}^{tot} = \frac{\phi_w^{tot} - \phi_{w,sat}^{ixp}}{1 - \phi_{w,sat}^{ixp}} C_c^s \; for \; \phi_w^{tot} \geq \phi_{w,sat}^{ixp} \tag{8.10}$$

To accurately resolve $C_{c,ixp}^{tot}$, we need to accurately model C_c^{ixp}. As discussed in Chapter 7, we currently lack the understanding necessary to predict co-ion concentrations in these unprecedented UHCD IEMs from first principles. To accurately model the effects of PIPS, we will instead use an empirical correlation to solve for C_c^{ixp}. We can effectively interpolate reasonable estimates for C_c^{ixp} using the co-ion concentrations of the homogeneous UHCD IEMs. With constant C_A^{max}, ϕ_w^{tot} is the only difference between homogeneous UHCD IEMs, enabling the use of an empirical log-log function for co-ion partitioning results at each external concentration of NaCl (see Appendix Figure F.1). The interpolation of co-ion partitioning results is therefore described using these two inputs, giving a function: $C_c^{ixp}\{C_c^s, \phi_w^{ixp}\}$. The contributions of the ion-exchange polymer phase to the total membrane co-ion partitioning are then weighted using ϕ_{ixp}^{tot} (as defined per Equation 8.4):

$$C_{c,ixp}^{tot} = \phi_{ixp}^{tot} C_c^{ixp}\{C_c^s, \phi_w^{ixp}\} \tag{8.11}$$

$$C_{c,ixp}^{tot} = \frac{1 - \phi_w^{tot}}{1 - \phi_{w,sat}^{ixp}} C_c^{ixp}\{C_c^s, \phi_w^{ixp}\} \; for \; \phi_w^{tot} \geq \phi_{w,sat}^{ixp} \tag{8.12}$$

The empirical function $C_c^{ixp}\{C_c^s, \phi_w^{ixp}\}$ could theoretically be replaced with a thermodynamic prediction of ion sorption for PIPS systems where ion sorption in homogeneous IEMs is better understood. Because ion partitioning in UHCD IEMs is not fully understood, a fully integrated model for co-ion partitioning into PIPS UHCD IEMs is beyond the scope of this study.

Combining the above relationships yields the final result of the partitioning model:

$$C_c^{m,t} = \begin{cases} C_c^{ixp}\{C_c^s, \phi_w^{tot}\} & for\ \phi_w^{tot} \le \phi_{w,sat}^{ixp} \\ \dfrac{(1-\phi_w^{tot})C_c^{ixp}\{C_c^s, \phi_{w,sat}^{ixp}\} + (\phi_w^{tot} - \phi_{w,sat}^{ixp})C_c^s}{1-\phi_{w,sat}^{ixp}} & for\ \phi_w^{tot} \ge \phi_{w,sat}^{ixp} \end{cases} \quad 8.13$$

In this equation, $C_c^{m,t}$ and ϕ_w^{tot} are experimentally measurable and C_c^s is defined by the experimental conditions. Therefore, the only unknown in this equation is $\phi_{w,sat}^{ixp}$, representing the extent of phase separation implicit in ϕ_w^{tot}. $\phi_{w,sat}^{ixp}$ can be extracted by fitting the model to a set of co-ion partitioning data. Again, because of the design of membranes in this study, we expect that $\phi_{w,sat}^{ixp}$ should only be a function of the cross-linking content of the pre-polymer mixture. Because of the mechanism that produces PIPS, $\phi_{w,sat}^{ixp}$ is expected to decrease with increasing cross-linker content.

8.4.2 Comparison Between Model and Experiment

To rigorously investigate the utility of Equation 8.13, we supplemented the 1 m NaCl data with intermediate partitioning data at concentrations of 0.1, 0.2, and 0.5 m NaCl. Varying the external salt concentration for each IEM allowed us to examine the data as a log-log sorption curve, which is the typical way to plot data of this type[426]. The experimental co-ion partitioning results and model fits are shown in Figure 8.7. For each membrane, the co-ion concentration in the membrane increased linearly in log-log coordinates, as expected. For higher concentrations, the model described each membrane well. At lower external concentrations, the model overpredicted the concentration of NaCl in the membrane. The ability of the partitioning model to describe the effects of phase separation on ion partitioning in multiple membranes over this entire concentration range is remarkable, given the simple nature of the model.

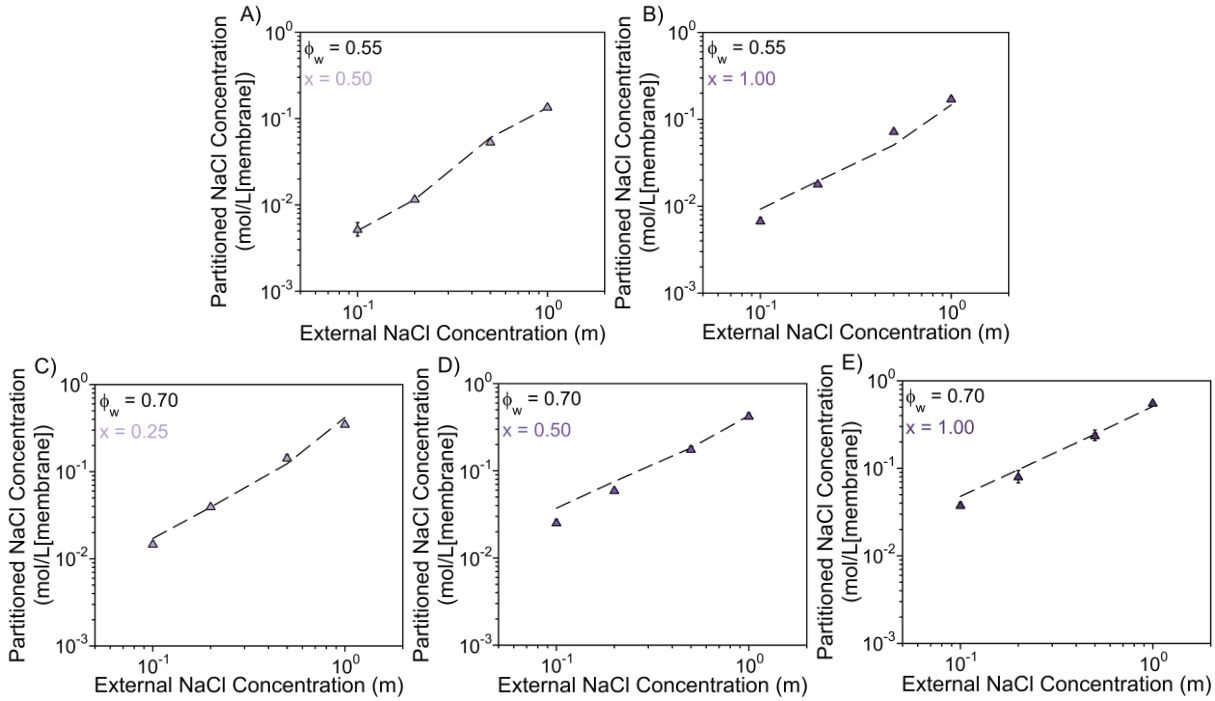


Figure 8.7: Modeling of co-ion sorption in phase separated IEMs. The co-ion concentration plotted against the external NaCl concentration for PIPS IEMs. Visual phase separation increases from left to right for the two series of PIPS IEMs: A) 50X-40W; B) 100X-40W; C) 25X-58W; D) 50X-61W; E) 100X-65W. The values for ϕ_w^{tot} are listed on each plot. The dashed lines represent the partitioning model. The values of $\phi_{w,sat}^{ixp}$ fit from the model were: 100X, 0.507; 50X, 0.551; 25X, 0.708.

Having two independent models for extracting $\phi_{w,sat}^{ixp}$, the ionic conductivity model and the co-ion partitioning model allow for a comparative analysis of their results. Model fitting to extract physically meaningful parameters always carries some uncertainty, as the indirectly obtained fitting parameters might not accurately represent the phenomena they are intended to describe. By comparing the apparent threshold for PIPS as measured via ion conduction, salt partitioning, and visual inspection, we can improve our confidence in the mechanisms described in each model. The values of $\phi_{w,sat}^{ixp}$ for 100XL, 50XL, and 25XL IEMs are reported in Table 8.3. The 75XL membranes were not included in the partitioning study, so no estimate is available for this entry. The agreement between the $\phi_{w,sat}^{ixp}$ values independently obtained from the conductivity

and partitioning results is immediately apparent. Moreover, the values correlate well with the visual appearance phase separation in the membranes. The values obtained from the partitioning model are systematically greater than those obtained from the conductivity model. The difference increases for lower cross-linker contents, but these membranes exhibit less phase separation overall, so the signal fit by the models are weaker. All three series of apparent $\phi_{w,sat}^{ixp}$ values trend monotonically upwards with decreasing cross-linking extent, as expected from the discussed mechanism of PIPS. Table 8.3 demonstrates that modeling bulk-like water domains in UHCD IEMs experiencing PIPS can consistently explain DI water ionic conductivity and salt-equilibrated co-ion partitioning data.

Table 8.3: Saturated network swelling of UHCD IEMs. The maximum water present in a homogeneous ion-exchange polymer phase extracted from the conductivity modeling in Section 8.3 and from the partitioning model in Section 8.4. Visual inspection results are estimated from the membrane appearances listed in Appendix Table F.1.

Cross-Linking	Apparent $\phi_{w,sat}^{ixp}$		
	Visual Inspection	Conductivity Model	Partitioning Model
100XL	0.503 – 0.574	0.487	0.507
75XL	0.447 – 0.564	0.485	---
50XL	0.479 – 0.594	0.540	0.551
25XL	0.663 – 0.737	0.643	0.708

8.5 Conclusions

In this chapter, we stratified a large set of controlled transport data describing UHCD IEMs with essentially constant C_A^{max} to elucidate some complexities of ion transport in membranes exhibiting PIPS. Following the traditional mechanism of PIPS, we described the phase separated IEMs as a two-phase blend consisting of a saturated, swollen polymer network penetrated by pure

solvent domains. We modeled counter-ion transport in DI water-equilibrated IEMs using a combination of the Mackie-Meares model for polymer tortuosity and the De Gennes model for percolation of polymer blends. Independently, we described NaCl partitioning in the phase separated IEMs using a simple phase additivity model. Both the diffusion and partitioning models relied on the same parameter: the volume fraction of water in the ion-exchange phase at the onset of PIPS: $\phi_{w,sat}^{ixp}$. The extracted values of this parameter from these two models were in reasonable agreement with each other and with the visual onset of phase separation, suggesting that the PIPS structures described in each model accurately reflect the IEMs.

These results will help navigate design parameters of IEMs for applications which require high membrane conductivities at low external concentrations, such as fuel cells or electrolyzers. Our analysis reveals that IEM conductivities will be enhanced when IEMs swell near $\phi_{w,sat}^{ixp}$. Evidently, very small bulk-like water domains (i.e., small extents of PIPS) can enhance counter-ion transport. Because the tortuosity/charge trade-off produces a maximum conductivity at $\phi_w^{tot} \sim 0.66$, cross-linking should be adjusted to produce $\phi_{w,sat}^{ixp} \sim 0.66$. The 25% cross-linked IEMs possess a saturated swelling of $\phi_{w,sat}^{ixp} \cong 0.65$, helping them achieve a chloride conductivity of 48.6 ± 2.6 mS/cm, which is the highest reported chloride conductivity, to the best of our knowledge.

Increased water domain sizes (i.e., increased extents of PIPS) limit the conductivity of water equilibrated IEMs, but the conductivity of IEMs contacting concentrated external solutions is not significantly affected. It is easier to process phase separated IEMs than homogeneous IEMs at increased water contents because phase separated materials can be prepared as homopolymers, completely eliminating the supply chain required to add the co-monomer. In this manner, our

understanding of PIPS phenomena may also encourage process simplifications for IEM production targeting higher salinity applications.

Chapter 9 Ion-Specific Differences in Diffusion Behavior across Charged Polymer Membranes[6]

9.1 Introduction

Separating ions of similar charge is becoming an increasingly desirable tool in chemical processing[6,480–482]. A notable example of such a separation is the recovery of lithium from salt-lake brines, where efficient extraction of lithium requires the removal of magnesium, sodium, and potassium ions[483]. In light of the growing demand for lithium batteries, driven by the electrification of economic sectors such as transportation, no satisfactory solution for this separation exists[6,484–486]. Beyond lithium, there is a rising demand for numerous other like-charge separations. These include extracting nitrate for recycling fertilizer and reducing environmental levels[487], removing fluoride from drinking water[488], recovering and reusing radioactive isotopes like cesium from nuclear waste and environmental water[489,490], recovering rare earth metals for magnets[482], and extracting uranyl ions from seawater[491]. These examples highlight the broad impact and importance of improving like-charge separations, which can significantly enhance the management of critical resources.

Membranes offer an energy-efficient solution for like-charge separations, but their effectiveness varies depending on the type of separation. Typically, separations involving ions of

[6]This chapter has not yet been published. Contributions to this chapter were also made by: Gregory Reimonn, Riley Vickers, Carolina Espinoza, José C. Díaz, Bryan R. Goldsmith, and Jovan Kamcev. I also acknowledge Harsh Patel for fruitful discussions regarding this analysis. G.R. collected Raman spectra, performed vibrational spectroscopy interpretations, and assisted with the statistical correlation analyses. R.V. performed molecular dynamics simulations and assisted with the statistical correlation analyses. C.E. collected calorimetry data. J.C.D. assisted in conductivity characterization methodology and Arrhenius data processing. B.R.G. and J.K. supervised this work.

different valence are more easily achieved by membranes than those involving ions with the same valence. For example, monovalent-selective ion-exchange membranes (IEMs) leverage electrostatic forces to exclude divalent ions more effectively than monovalent ions, thereby achieving like-charge separation[481,492,493]. Furthermore, ions with higher valence exhibit significantly greater hydrated sizes than ions of lower valence, enabling nanofiltration membranes to achieve charge and size-based separation of like-charged ions[480,482]. Multivalent ions possess larger electron shells capable of forming coordination complexes, facilitating targeted adsorptive removal[480,482,492]. In contrast, successful separation of monovalent ions by membranes has mostly been achieved with protons or hydroxides due to their unique hopping transport mechanism, i.e., Grotthus transport. This mechanism significantly outpaces vehicular ion diffusion, enabling selective proton or hydroxide transport across membranes over other monovalent ions[492,493].

The difficulty in achieving monovalent ion separations underscores the success of biological potassium ion channels, which use precise oxygen coordination to transport potassium over sodium across cell membranes with exceptional selectivity[492,494]. Efforts to replicate this effect in synthetic systems for monovalent cation separations are ongoing, but have met with limited success. To deploy biological ion channels on a large scale for separation applications, significant advancements in biomimetic membrane processing are required[492,495]. Scaling challenges also hinder the widespread use of materials such as MXenes, graphene, covalent organic frameworks, and metal organic frameworks. While some of these materials have demonstrated high like-charge selectivities on small scales[496,497], their potential for widespread application remains limited[495]. Given these challenges, new approaches are required to advance like-charge ion separations.

When assessing the utility of IEMs for like-charge separations, a major barrier is the lack of well-understood counter-ion diffusion mechanisms. The diffusivity of counter-ions in IEMs is not well understood, although many IEMs exhibit counter-ion diffusivities greater than would be expected based on obstruction models (Chapter 5). Like-charge diffusion selectivities are even less understood than opposite-charge diffusion selectivities, so the prospects of using IEMs in like-charge separations would be greatly enhanced by a fundamental understanding of why counter-ion diffusion is sometimes accelerated in IEMs. To facilitate a deeper understanding of diffusion selectivities for like-charge separations, specific ion effects (SIEs) are a promising phenomenon to investigate. SIEs are defined as differences in electrostatic behavior between ions that are not captured in their simplified treatment as point charges[363,364,498,499], and as such, they may relate to counter-ion/fixed charge interactions in IEMs.

Charged polymers have notably exhibited SIEs in numerous settings, with these trends famously described in the Hofmeister series[500]. Hofmeister and other researchers have created hierarchical series of ions because various measurable properties of polyelectrolyte/salt solutions change when one of the two ions that comprise an electrolyte is replaced with another[368,501]. Since IEMs are essentially networks of polyelectrolytes, the extensive history of polyelectrolyte SIEs suggests that IEMs may hold potential for like-charge monovalent ion separations. However, SIEs in IEMs are not well understood on a fundamental level, hindering the design of IEMs for specific like-charge separations.

Although SIEs in polyelectrolytes are better understood than in IEMs, both systems remain unpredictable. The ordering of the Hofmeister or Hofmeister-inspired series varies with the observable property being studied[364]. Moreover, the qualitative order of the series does not predict the relative strength of SIEs. This uncertainty persists because the quantitative ion property that

determines any chosen order of a Hofmeister series is still unclear[363,364,498]. Most explanations, including the one originally proposed by Hofmeister, focus on the extent of ion interaction with surrounding water molecules[364,500]. These explanations have collectively developed into Collin's Law of Matching Water Affinities (LMWA)[364,498]. A popular iteration of the LMWA equates the Hofmeister series to the Lyotropic series, which is unambiguously ordered by the ion enthalpies of hydration[364,498,499]. However, other metrics of water affinity are also evoked in the LMWA, including the Jones-Dole *B* viscosity coefficient[363,364,498,502], surface tension dependence[363,499], dynamic hydration number of the ion[503], and hydration entropies or free energies[502]. Aside from the LMWA, ion-centric sources of SIEs have also been proposed, including the volumetric charge density[364,499,503], linearized charge density[502], bare or hydrated radius[363,498,499,502], polarizability[363,499], softness[364,504], and Lewis acidity/basicity[364] of the ion. With this plethora of potential explanations, selecting the independent source of any given SIE is challenging. Therefore, to exploit SIEs for like-charge membrane-based separations, it is crucial to understand the role of SIEs in ion transport across IEMs.

Membrane-specific SIEs lack the extensive research history of polyelectrolyte SIEs; however, several investigations have addressed the topic[505–507]. For example, it has been demonstrated that the size of N-alkyl ammonium fixed charge groups in anion-exchange membranes (AEMs) influences the selective transport of monovalent anions[508]. Trimethylammonium-containing membranes displayed minimal selectivity between different anions, whereas membranes with longer alkyl chains on the ammonium fixed charge group preferentially transported less-hydrated anions (i.e., nitrate or bromide) over more-hydrated anions (i.e., chloride or fluoride). We have recently demonstrated that highly hydrated cations (i.e., sodium and lithium) encounter additional energy penalties in weakly swollen cation-exchange

membranes (CEMs) compared to less-hydrated cations (i.e., potassium and cesium)[509]. While general ion trends could be explained by Coulombic interactions, the electrostatic model could not account for the additional energy penalty for smaller, more hydrated cations, implicating a non-Coulombic, ion-specific effect. Epsztein *et al*. have studied both monovalent cations and anions in commercial AEMs and CEMs, finding that the free energy of hydration correlates with the general trend of the ion activation energies of diffusion[510]. These authors speculate that dehydration and orientation of the ions at the membrane interface give rise to this trend, with less hydrated ions being transported more readily, even in highly swollen brackish water desalination IEMs. These studies exemplify like-charge monovalent ion selectivities under different conditions; however, the mechanism of the observed SIEs was not fully elucidated.

Beyond the studies of SIEs in IEMs, an exemplary investigation by Ritt *et al*. recently examined the selective transport of numerous anions in cellulose acetate reverse osmosis membranes[511]. These authors employed machine learning approaches to correlate experimental transport properties with membrane structural features and ion properties, performing cross-analyses similar to those performed with polyelectrolytes[368]. Their findings revealed that no single property could account for the variations in ion diffusion activation energies. Rather, a network of interrelated ion and membrane properties was necessary to accurately describe ion transport behavior in the membrane. The depth of analysis required by Ritt *et al*. to capture the underlying phenomena underscores the complexity of SIEs in dense polymer membranes. To the best of our knowledge, comprehensive studies with a comparable level of analysis have not been performed in IEMs, despite their structural similarities to polyelectrolytes.

To develop a more fundamental understanding of SIEs in IEMs, we performed a comprehensive experimental and modeling investigation into the diffusive transport of eight

cations and seven anions in homogeneous IEMs with well-defined chemical structures. We measured the energy barrier for diffusion experienced by each ion in the membranes, quantified the portion of energy attributable to interactions with the membrane, and used data science techniques to identify the ion properties most related to the observed SIEs. All-atom molecular dynamics (MD) simulations on these model membrane systems validate the experimental observations and support the proposed mechanism of IEM-derived SIEs. Our findings indicate that ion softness, which quantifies the malleability of water solvating an ion, correlates strongly with the energy required to diffuse across these IEMs. The diffusion behavior of ions changes dramatically upon entering the membrane when waters can simultaneously hydrate the fixed charges and the mobile ion simultaneously. These findings are a major breakthrough in understanding what drives ion diffusion speeds in IEMs.

9.2 Modes of Investigation

This chapter relies on data sets to facilitate a thorough investigation of SIEs in IEMs. To collect experimental results, membranes were synthesized in the lab via the techniques in Section 2.1.4 and using the recipes listed in Appendix Table G.1. Additionally, membranes were prepared *in silico* via the molecular dynamics simulations techniques described in Section 2.5.2. To facilitate analysis of the experimental results, literature reference data for ion transport and thermodynamic properties were utilized as described in Sections 2.6.2 and 2.6.3, respectively.

The IEMs used in this work are derived from [2-(Methacryloyloxy) ethyl] trimethylammonium (MOETMA), 3-sulfopropyl methacrylate (SPM), and glycerol dimethacrylate (GDMA), shown in Figure 2.8. MOETMA and GDMA were copolymerized to form AEMs in the chloride form, while SPM and GMDA were copolymerized to form CEMs in the potassium form. In the text, we refer to ions using elemental symbols. For the cations studied,

Li^+ is lithium, Na^+ is sodium, K^+ is potassium, Cs^+ is cesium, NH_4^+ is ammonium, NMe_4^+ is tetramethylammonium, Mg^{2+} is magnesium, and Ca^{2+} is calcium. For the anions studied, F^- is fluoride, Cl^- is chloride, Br^- is bromide, I^- is iodide, NO_2^- is nitrite, NO_3^- is nitrate, and SO_4^{2-} is sulfate. Additionally, for the fixed charge groups: $RNMe_3^+$ is the trimethylammonium fixed charged groups of MOETMA in the AEMs and RSO_3^- is the sulfonate fixed charge groups of SPM in the CEMs.

Some statistical analyses and the MD simulations excluded select ions: NO_2^-, SO_4^{2-}, Mg^{2+}, and Ca^{2+}. The divalent ions appear to follow different trends than the monovalent ions (as discussed in the main text), and with only three divalent ions under study, the mechanism of these differences would confound other analyses. Very limited availability of literature data for aqueous NO_2^- prevented analysis akin to the other monovalent ions. These ions are included as raw data points where appropriate.

9.3 Activation Energy of Diffusion in the Membranes

We synthesized cross-linked AEMs and CEMs with similar chemical structures, differing only in the chemical identity of the fixed charge group. These IEMs were designed to exhibit nearly identical water and charge contents in their Cl^- and Na^+ forms, respectively. Aligning the membrane properties with these common ions, considered relatively average in the Hofmeister and LMWA series, ensures a proper comparison of the anion and cation data. By considering both cation and anion data in a single test matrix, we aim to describe universal SIEs that are present in both AEMs and CEMs. After membrane synthesis and counter-ion exchange, we measured the charge and water contents of the IEMs in each counter-ion form to investigate any counter-ion dependent swelling differences and quantify the extent of counter-ion conversion. The counter-ion

conversions were successful (Appendix Table G.2), with gravimetric charge contents measured to be within 18% of the theoretical ion-exchange capacities (IECs). The water volume fractions, ϕ_w, varied minimally across most membrane counter-ion forms (Appendix Table G.3 and Appendix Figure G.1), with all 15 ions averaging to $\phi_w \cong 0.54 \pm 0.05$.

We measured the ionic conductivities of the IEMs in each counter-ion form as a function of temperature from 10 – 60 ºC (Appendix Table G.4 and Appendix Table G.5) by extracting the membrane resistance from EIS measurements via the direct contact method (Section 2.3.7). For each ion, the membrane water content at 10 ºC and 60 ºC did not deviate from the values measured at room temperature (Appendix Figure G.2), indicating that any temperature dependence of the ionic conductivity is due to ion diffusion rather than to changes in ion concentration. The ionic conductivities and diffusivities (calculated from the Nernst-Einstein equation) increase monotonically with temperature as shown in the Arrhenius plots (Appendix Figure G.3). Comparing the membrane diffusivities to those in aqueous solution (Appendix Figure G.4) reveals a key difference: while the CEM preserves the relative order of cation diffusion coefficients of aqueous solution, the relative order of anion diffusion coefficients in the AEM is essentially reversed. Specifically, ion diffusion coefficients in the CEM and in aqueous solution generally increase with decreasing size of the hydrated ion, whereas the opposite trend is observed for the AEMs. These trends are also reflected in the measured activation energies of diffusion in the membrane (E_a^m), shown in Figure 9.1. Although E_a^m values are unilaterally greater than those in an aqueous solution (E_a^s), the magnitude of the discrepancy is generally larger for the anions than for the cations. For large hydrated ions, both F^- and Li^+ show a similar increase in E_a^m relative to E_a^s. However, the difference between E_a^m and E_a^s becomes larger down the halide series towards I^-, while this difference decreases down the alkali series towards Cs^+. The multiatomic and

multivalent ions do not stand out except for NMe_4^+, which experiences the highest E_a^m in the CEMs. These significant differences between like-charged ions indicate the presence of specific ion effects (SIEs) in these IEMs.

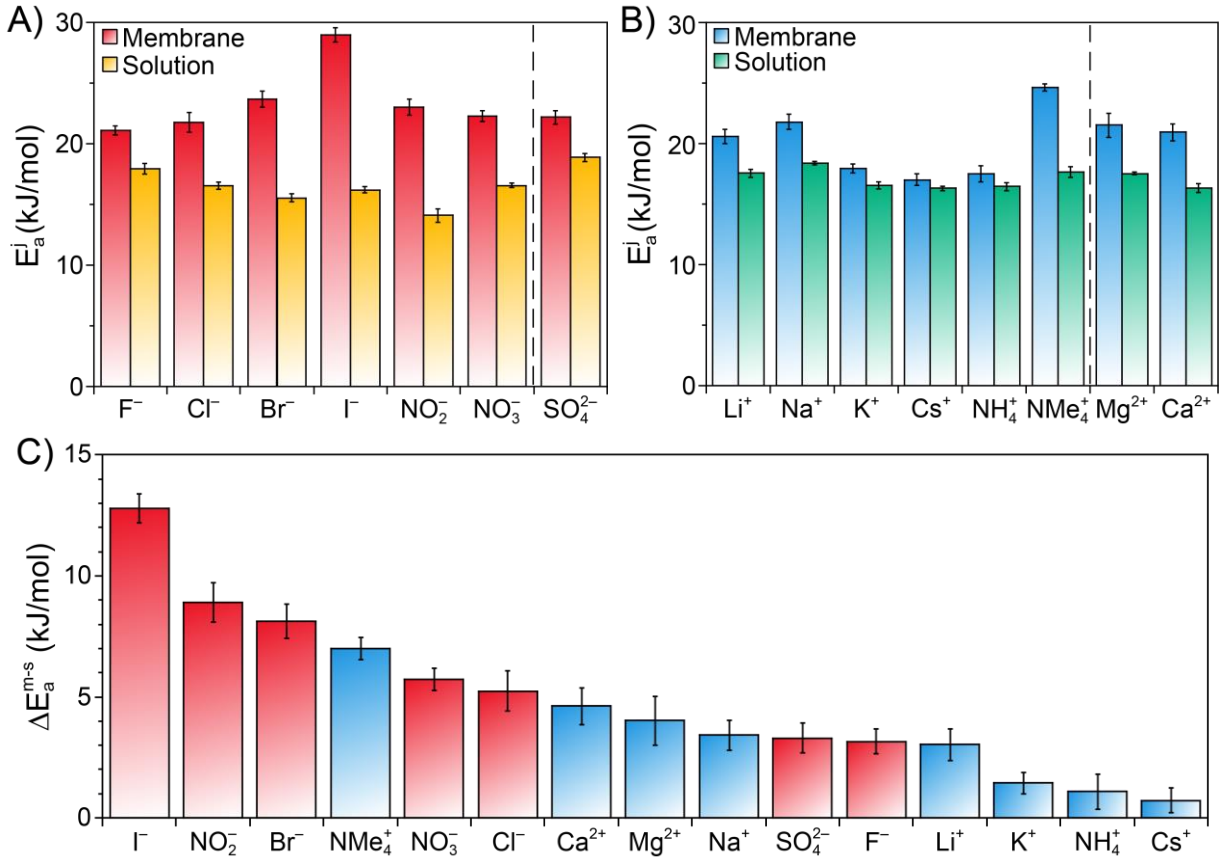


Figure 9.1: Activation energies of ion diffusion. Activation energies in IEMs (E_a^m) and in aqueous solution at infinite dilution (E_a^s) for a) anions in AEMs and b) cations in CEMs. Uncertainties for E_a^m represent the standard error of the mean Arrhenius fit performed on four independently measured ionic conductivity data sets. Uncertainties for E_a^s represent the standard error of the mean Arrhenius fit on the sampled data from the cubic fit of literature data (cubic fits are listed in Table 2.4). The solution activation energy for NO_2^- is calculated over a narrower temperature range than the other ions, as discussed in Section S2.6.2. c) Activation energy differences (ΔE_a^{m-s}) for ions in this study. Uncertainties were calculated from the standard errors of the activation energies using standard error propagation methods.

To elucidate the nature of SIEs in the IEMs, it is crucial to normalize the diffusion behavior in the membrane for the inherent differences between ions. Consequently, we focus the subsequent discussion on the additional energy barrier experienced by the ion to diffuse in the membrane

relative to an aqueous solution, $\Delta E_a^{m-s} = E_a^m - E_a^s$. Additionally, we consider the pre-factor component of the Arrhenius equation (D_0, Appendix Figure G.5) to fully interpret the data. D_0 represents the diffusivity of the ion in the limit of having no enthalpic barrier to ion transport (infinite temperature), so D_0 can be thought of as an enthalpically unhindered ion diffusivity. Interestingly, ion diffusion in both the membrane and aqueous solution exhibits a "compensation effect" through a linear free energy relationship (Appendix Figure G.6). This phenomenon describes how Arrhenius pre-factors correlate with Arrhenius activation energies, especially in polymer chain-limited solute transport[512,513], but recently in hydrated ion transport as well[511,514,515]. Beyond the isolated membrane and solution diffusivity data, Figure 9.2A demonstrates that the energy barriers imposed by the IEMs (ΔE_a^{m-s}) are almost perfectly compensated among monovalent ion pre-factors (D_0^m/D_0^s). The positive slope of the trend indicates that ions experiencing greater energy barriers in the membrane also have the potential for faster unhindered diffusion. A positively correlated linear free energy effect essentially dampens the practical impact of membrane interactions because D_o^m and E_a^m affect the measured diffusivities in opposing directions. Thus, the two factors compensate for one another.

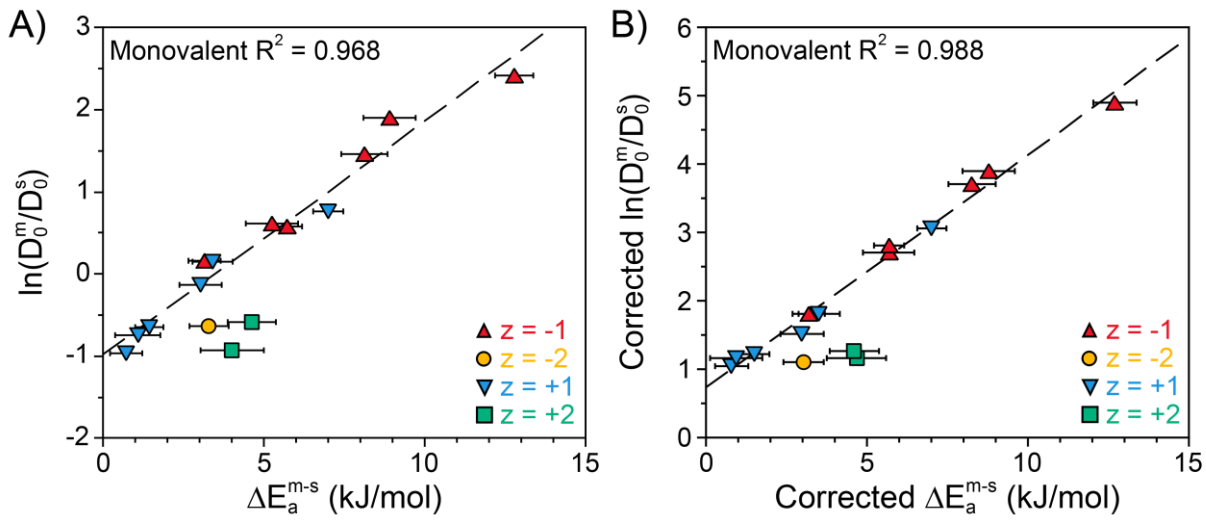


Figure 9.2: Linear free energy relationships. Linear free energy relationships for a) diffusivities referenced to the total membrane system and b) corrected diffusivities referenced to the un-obstructed membrane volume available for diffusion. The corrected diffusion coefficients were calculated by accounting for polymer tortuosity effects using the Mackie-Meares model. The dashed lines represent linear fits of the monovalent ions. Divalent ion data are shown but not included in the linear regression. Uncertainties were calculated from standard errors of the activation energies and pre-factors using standard error propagation methods.

The compensation effect presented in Figure 9.2A is atypical because the y-intercept is negative, implying that for low ΔE_a^{m-s}, despite the added energy barrier to transport, unhindered ion diffusion would be slower in the membrane than in an aqueous solution. We rationalize this apparent contradiction of the compensation effect by considering the tortuosity of the membrane, which obstructs ion diffusion even in the absence of ion-polymer interactions. The results in Figure 9.2B are corrected for obstruction effects by reconstructing the Arrhenius linear free energy data using diffusion coefficients that have been normalized for tortuosity effects via the Mackie-Meares model (Section G.1). This corrected plot is improved in two important ways. First, the y-intercept of the linear fit is positive, indicating that any increase in the membrane energy barrier produces a compensating increase in unhindered diffusivity through the linear free energy effect. Unlike the shift in D_0^m, the values of E_a^m remain essentially unchanged by this correction (c.f. Appendix Figure G.8 and Appendix Figure G.9). Second, the corrected analysis also increases the statistical

confidence in the presence of the compensation effect in these systems. Specifically, there is a nominal increase in the R^2 of the linear regression, accompanied by a transition from a relatively heteroskedastic/parabolic residual distribution to a more homoskedastic/random residual distribution (Appendix Figure G.10).

In both iterations of the linear free energy plot, the results for the monovalent ions closely follow the linear free energy relationship, suggesting that a unified theory should be able to explain the SIEs observed for both the anions and the cations in the IEMs. Additionally, the strong correlation between D_0^m/D_0^s and ΔE_a^{m-s} indicates that the theory only needs to explain one of these variables. In contrast, the results for the multivalent ions do not align with the same general linear free energy relationship as the monovalent ions, suggesting that diffusion of these species in the membranes may be influenced by different factors than those affecting the diffusion of monovalent ions. Additional data on multivalent ions will be required to better understand diffusion of divalent ions in these IEMs. The corrected linear free energy plot also demonstrates a surprising feature: As much as the Mackie-Meares model can be relied upon, many ions are diffusing faster in the IEMs than in aqueous solution (Appendix Figure G.11). That is to say, the increased D_0^m overpowers the increased E_a^m at temperatures as low as 21 ºC for many ions.

9.4 Correlating SIEs in IEMs

In this section, we focus our analysis on explaining the observed variation in ΔE_a^{m-s} values for the monovalent ions. We considered a comprehensive suite of plausible ion parameters that have been helpful in explaining SIEs in other systems (Section 2.6.3). Due to the large number of ion properties (Table 2.5) and limited number of ions under study, correlations were analyzed in two stages (Section 2.6.4). First, we performed an array of pair-wise Pearson correlation tests with a threshold of $\alpha = 0.05$ to identify each ion property that correlates with ΔE_a^{m-s}. Then, more

nuanced correlations within this reduced property set were identified by reducing the dimensionality of the system using principal component analysis (PCA). PCA is a powerful method of isolating the primary modes of variation within complex data sets by grouping covaried variables into principal components (PCs) which efficiently capture trends present in the data[369]. Thus, PCA is an excellent tool to identify the most appropriate method of quantifying a phenomenon when many similar descriptors are available, as is the case for SIE ion parameters.

PCA helps to visualize complex information in a variety of ways, but for this analysis, the biplot is the most helpful. Variable contributions to the most important PCs are plotted as vectors, normalized in magnitude by the total variance captured by those PCs[369]. Long vectors with near-0º or near-180º angles of separation indicate variables sharing essentially all modes of variation within the data set (i.e., the parameters are strongly correlated or anti-correlated). Orthogonal vectors separated by approximately 90º represent variables which share minimal variance (i.e., the parameters are weakly correlated), and abnormally short vectors correspond to variables which do not fit clearly into either of the plotted PCs. The results of this statistical analysis are presented in Figure 9.3.

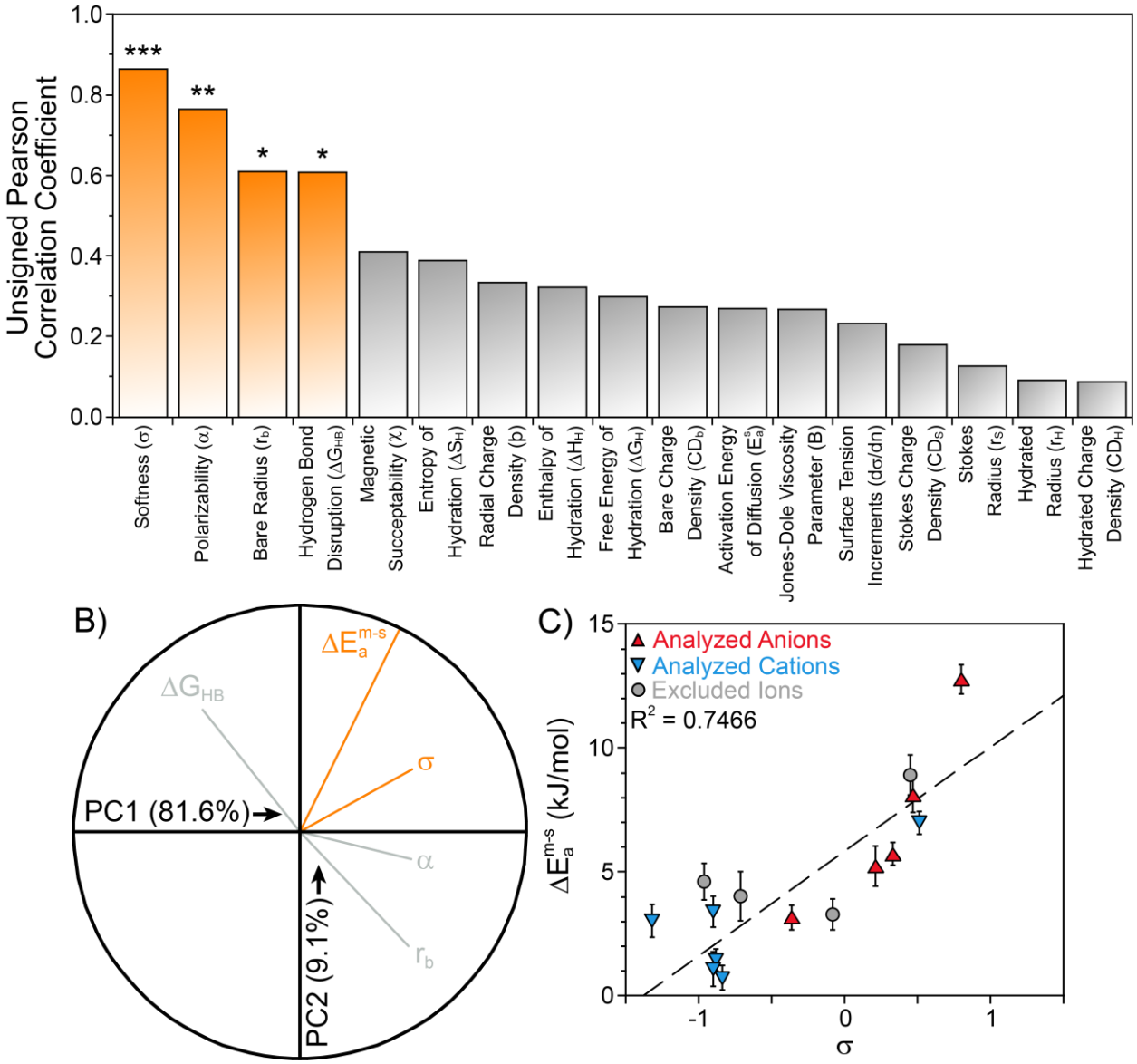


Figure 9.3: Correlation analysis for membrane activation energies. a) Unsigned Pearson correlation coefficients for a pairwise analysis of ΔE_a^{m-s} with each ion property considered in this study. Asterisks indicate significance at $p < 0.05$, 0.01, and 0.001. b) Biplot of significant ion properties correlated with ΔE_a^{m-s}. Each principal component (PC) is labeled with the fraction of captured variance from the data set; together, PCs 1 and 2 describe > 90 % of the variance in the data. c) ΔE_a^{m-s} plotted against the softness (σ) for the ions considered in this study. Uncertainties were calculated from standard errors of the activation energies using standard error propagation methods.

The Pearson correlation test was able to remove most ion parameters from consideration (Figure 9.3A). Only four ion properties were significantly correlated with ΔE_a^{m-s}. Notably, E_a^s itself was not a significant hit, indicating a shift in the nature of ion diffusion within the IEMs. The

PCA results highlight how some correlations are more useful to consider than others. The two principal components on the axes explain over 90 % of the variance in the data set (Figure 9.3B), and ΔE_a^{m-s} has the longest vector, which together indicate that the Pearson correlation screening successfully selected ion properties connected to ΔE_a^{m-s}. These selected properties include: the bare radius of the ion, r_b, the free energy of hydrogen bond disruption of the ion, ΔG_{HB}, the polarizability of the ion, α, and the softness of the ion σ. It is evident that α, r_b and ΔG_{HB}, which exhibit vectors nearly perpendicular to that of ΔE_a^{m-s}, account for different modes of variability within the data set than ΔE_a^{m-s}. Conversely, σ correlates the most strongly with ΔE_a^{m-s} (Figure 9.3C).

σ is referred to as softness because it quantifies the extent to which ionization of a species is compensated by ion-solvent interactions[362,516,517]. Practically, σ can be viewed as the malleability of the ion hydration shell, analogous to the malleability of the ion electron shell, α. Ions with excess stability due to solvation are considered "soft" and they do not bind waters very strongly[517]—soft ions typically have large bare radii like I^- or NMe_4^+. Conversely, when solvating an ion does not compensate the energy of formation, the energy deficit causes an ion to bind its hydrating waters strongly and become "hard"[517]—hard ions typically have small bare radii like F^- or Li^+. Pearson's Hard/Soft Acid/Base Theory (HSAB), which was primarily developed by Ahrland and Pearson in the 1960s[504,518], utilizes ion softness as a predictor for the extent of interactions between different ions. Although it is utilized sparingly in recent polyelectrolyte literature[364], HSAB stands out from other SIE theories because it provides a quantitative prediction of interaction extents[519] which are enabled by the extensive characterizations carried out by Marcus[520,521]. Essentially, HSAB operates on the principle of like-like interactions, and serves as a thermodynamically-grounded precursor for the more popular LMWA[364].

9.5 The Nature of SIE Interactions in IEMs

Although HSAB proposes a mechanism for ion/ion interaction, the correlation between ΔE_a^{m-s} and σ does not verify this mechanism. Before assessing the utility of HSAB for understanding SIEs in IEMs, we sought a molecular understanding of the interactions driving ΔE_a^{m-s} via atomistic molecular dynamics (MD) simulations. Starting from simulated pre-polymer solutions analogous to those used experimentally, we polymerized an AEM and CEM using the Large-Scale Atomic/Molecular Massively Parallel Simulator (LAMMPS)[108]. Subsequent exchange and equilibration steps resulted in IEMs with 11 varied counter-ion forms (Figure 2.11). MD simulations employed TIP4P/2005[109] and TIP4P/Ew[111,112] parametrization for the water and mobile ions, respectively, and used the optimized potential for liquid simulation (OPLS) force field[113,114] for other close-range interactions. Equilibrium interactions were assessed in IEM domains with side lengths of approximately 140 Å, which contained over 2,500 mobile counter-ions.

To anchor the insights gained from MD simulations to the physical IEMs, simulation results were compared with experimental data whenever possible. First, the comparability of simulated IEMs and those synthesized in the lab was assessed in Section G.2. To summarize the key points briefly: The water contents of both the pre-polymer solution and polymerized membranes were fixed according to the experimentally measured water contents. Simulated IEMs achieve similar hydrated densities to the experimental IEMs, indicating that water interactions and molecular packing were captured reasonably well by the MD parameterization. Further, the IECs of simulated IEMs are only slightly higher than experimentally determined IECs, indicating that the total incorporation of monomer into the membranes was comparable. We performed equilibrium characterization of the *in-silico* IEMs by extracting radial distribution functions

(RDFs) and corresponding interaction energy profiles between fixed charges, mobile ions, and waters. To reference our results against literature values and normalize counter-ion/water interactions, we also simulated ion hydration at infinite dilution with no polymer present. The infinite dilution ion/water coordination results obtained via the simulations agreed reasonably well with accepted values collected by Marcus[363] (Appendix Table G.10), giving confidence that ion/water interactions are captured reasonably well via our parameterization.

9.5.1 Hydration of Ions in IEMs

A critical component of HSAB theory is ion hydration. Ion/water interactions are also predominantly used to explain SIEs through Collin's LMWA. The ubiquity of ion hydration made ion/water interactions an essential interaction to probe using the MD simulations. An ion is stabilized via its hydration shell so disruption of this hydration environment (as IEMs might do, containing only ~50 % water in our case) would cause an ion to behave quite differently than it would in a highly hydrating environment. Some waters are strongly oriented to the ion and are referred to as the dynamic hydration shell or primary hydration shell[357,363,522]. Other waters in the vicinity of ions help solvate the ion to a lesser extent and are considered part of the ion coordination shell only. Ions with strong electrostatic fields are small and have lower surface areas, so the number of hydrating waters (HN) and number of coordinating waters (CN) are typically anti-correlated[357,363,522]. Akin to the narrative of HSAB, densely charged ions exert a strong enough electric field to strongly orient a large fraction of the adjacent water dipoles, while larger ions weakly orient an even greater number of coordinated waters.

MD simulations provide easy access to CN values via RDF analyses. While HN values are not immediately accessible by MD simulations, trends in CN can give insight into the hydration state of ions inside the IEMs. Full RDFs and interaction energies are provided in Appendix Figure

G.15 – Appendix Figure G.17, but differences in simulated IEM and infinite dilution water contents preclude direct comparisons for some facets of these RDFs. Instead, the CN values presented in Table 9.1 demonstrate the key results. In the first two columns, comparing the infinite dilution hydration numbers, HN_{g-w}^{ID}, reported in the literature to the simulated infinite dilution coordination numbers, CN_{g-w}^{ID}, yields the expected result: more waters coordinate each simulated ion than are experimentally measured to hydrate the ion ($CN_{g-w}^{ID} > HN_{g-w}^{ID}$). Further, as the surface area of the bare ion increases, HN_{g-w}^{ID} decreases, while CN_{g-w}^{ID} increases, in accordance with the discussion above.

The results change for counter-ions in the simulated IEMs, as demonstrated by examining the coordination numbers of the alkali halides in the simulated IEMs, CN_{g-w}^{IEM}. The polymer should displace waters from the surroundings of ions, so it is expected that $CN_{g-w}^{IEM} < CN_{g-w}^{ID}$. After this broad reduction in coordination, the CEM maintains the infinite dilution trend of $Cs^+ > K^+ > Na^+ > Li^+$. In contrast, anions subvert the infinite dilution results, where CN_{g-w}^{AEM} values decrease in the order of $F^- > Cl^- > Br^- > I^-$. This reversal in coordination numbers mirrors the reversal in experimental diffusivity and activation energy trends for the AEM. There are also two noteworthy comparisons: F^- maintains a very similar coordination shell in the AEM as at ID (6.2 and 6.1, respectively), while Li^+ loses coordinating waters to the extent that $CN_{g-w}^{IEM} < HN_{g-w}^{ID}$ (2.6 < 4.2). From these CN results, F^- would be expected to maintain the most solution-like behavior, while Li^+ would be expected to display the strongest signs of dehydration.

Table 9.1: Water coordination and hydration numbers. The average dynamic hydration number of ions in aqueous solution (HN_{g-w}^{ID}) reported by Marcus[363] is listed alongside the simulated results. These include the primary coordination number of water for each counter-ion (CN_{g-w}^{j}), where $j = ID$ for infinite dilution and $j = IEM$ for the simulated IEMs, the primary coordination number of water for the fixed charge groups (CN_{A-w}^{IEM}) in IEMs of each counter-ion form, and the total

membrane hydration number of the simulation (λ) The corresponding RDFs are given in Appendix Figure G.15 – Appendix Figure G.17.

Ion	HN_{g-w}^{ID} [363]	CN_{g-w}^{ID}	CN_{g-w}^{IEM}	CN_{A-w}^{IEM}	λ
F^-	4.2	6.2	6.1	23.7	24.0
Cl^-	2.0	6.7	6.0	22.2	19.0
Br^-	1.3	7.1	5.9	21.0	17.3
I^-	0.9	7.4	5.4	19.2	13.9
NO_3^-	1.6	10.1	6.7	20.0	16.7
Li^+	4.2	4.1	2.6	9.7	20.5
Na^+	3.3	5.9	4.7	8.9	19.9
K^+	2.3	7.0	5.6	7.4	18.9
Cs^+	1.7	8.3	6.7	6.7	18.3
NH_4^+	1.9	7.0	5.5	6.6	19.0
NMe_4^+	2.1	31.5	21.4	6.0	17.7

The total availability of water in the simulated IEMs is also affected by the fixed charge groups. The final two columns of Table 9.1 compare the number of coordinated waters and the total number of waters per fixed charge group in each IEM (CN_{A-w}^{IEM} and λ). For $RNMe_3^+$ in the AEMs, $CN_{A-w}^{IEM} > \lambda$ (this is also characteristic of the NMe_4^+ form CEMs, where $CN_{g-w}^{IEM} > \lambda$). To rectify this apparent contradiction in the mass balance of water, we conclude that coordinating waters must be shared between bulky methylammonium groups. With such a constrained distribution of waters, this conclusion implies that anion coordinating waters are likely shared with the $RNMe_3^+$ fixed charge groups as well. The $RNMe_3^+$ RDF shows two constituent peaks within the primary coordination shell (Appendix Figure G.17A), which might correspond to some of these different populations of water with shared coordination. For CEMs, water sharing is likely not the case, since RSO_3^- fixed charge groups coordinate only 6 – 10 waters. Interestingly, the largest CN_{A-w}^{IEM} is observed in the Li^+ form, suggesting that Li^+ is not dehydrated due to a lack of available

space or water. Instead, the results imply that Li^+ ions release hydration waters because they assemble some other more favorable coordination shell. The RDF of RSO_3^- water coordination (Appendix Figure G.17B) demonstrates a shoulder unique to the Li^+ form, raising the possibility that RSO_3^- waters are rearranged to accommodate a different structure, adding credence to an explanation rooted in the formation of Li^+ and RSO_3^- ion pairs, as discussed in the next section.

It is difficult to experimentally assess the hydration shells of ions in IEMs. However, one technique that gives an *in situ* state of water analysis is differential scanning calorimetry[509,523–525] (DSC, Appendix Figure G.18). The results from this technique help to corroborate the MD hydration results and connect the coordination-based analysis to a hydration-based analysis. DSC gives access to the *in situ* hydration environment of ions because the strongly-oriented hydration shell is considered non-freezable water, while the weakly-coordinated or non-coordinated waters are considered to be freezable[526,527]. Non-freezing water is evident in the melting peak of water inside the membrane, which is less than predicted based on the water content of the IEMs and the known melting enthalpy of bulk water. Using the DSC results, the membrane hydration number can be decoupled into its freezable and non-freezable components: $\lambda = \lambda_f + \lambda_{nf}$ (Appendix Table G.11). States of water analyses can be limited by the binding of waters to non-ionic hydrophilic moieties in polymer membranes such as alcohols or esters, which complicate the analysis of these methacrylate IEMs. However, by examining the trend of λ_{nf} for the same membrane in different counter-ion forms, we can attempt to isolate the contribution of mobile ions. Specifically, by plotting λ_{nf} against the expected contribution from the counter-ion (the equivalent hydration number, $HN_{g-w}^{ID}/|z_g|$), we can decouple counter-ion effects into the slope, while leaving polymer backbone/fixed charge group effects in the extrapolated y-intercept. We present DSC results decoupled in this manner in Figure 9.4.

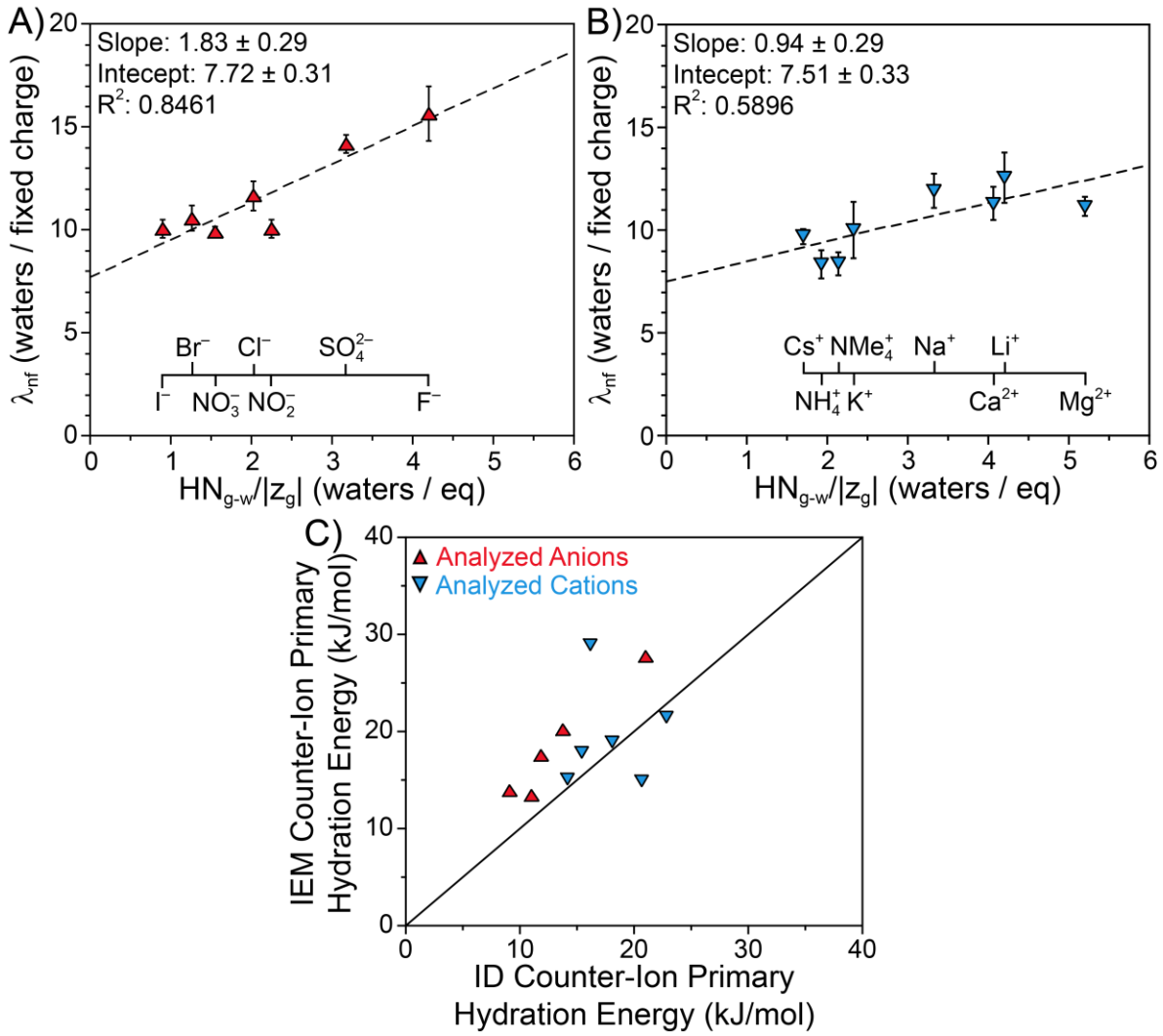


Figure 9.4: States of water in the IEMs. The non-freezable hydration number of the membrane (λ_{nf}) plotted against the equivalent hydration number of the counter-ion ($HN_{g-w}^{ID}/|z_g|$) for a) anions in the AEM and b) cations in the CEM. The location of individual ions is given on a second x-axis. Uncertainties represent the standard deviation of the data, calculated using standard error propagation methods. c) Parity plot of the total free energy of counter-ion/water interaction per counter ion in the IEM and infinite dilution simulations.

Both the AEM and CEM state of water analyses produced reasonably linear trends between λ_{nf} and $HN_{g-w}^{ID}/|z_g|$, suggesting that the extent of counter-ion hydration in the membranes is continuous across the range of ions studied. The slope for the cation results is near unity, indicating that ions essentially maintain their infinite dilution hydration in the IEM. The slope of the anion plot exceeds unity, revealing that increasing $HN_{g-w}^{ID}/|z_g|$ causes nearly double that increase in

λ_{nf}. The difference in AEM and CEM trends are similar to the coordination results from the simulations, where CEMs maintain infinite dilution behavior but AEMs exhibit differences. The analysis of Table 9.1 revealed that AEMs likely create shared coordination shells between counter-ions and fixed charge groups, which would be consistent with a slope above one in Figure 9.4A. Oppositely charged ions can cooperate to orient waters in the same direction (water dipoles pointing toward the cation and away from the anion), so shared waters would be oriented more strongly and potentially become non-freezable. To test this theory, the energy of hydration of the primary coordination shells for each counter-ion is presented in Figure 9.4C (see Section 2.5.4) as a parity plot between IEM and infinite dilution conditions. NO_3^- and most cations fall near the parity line, indicating that these ions maintain similar hydration as in solution. Other anions and NMe_4^+ fall above the parity line, indicating that the free energy derived from hydration interactions in the IEM exceed those of infinite dilution. As expected, Li^+ is the only ion with appreciably lower hydration energy in the IEM. The results of this IEM/infinite dilution parity plot agree with the slopes extracted from the states of water analysis, both capturing key differences between the hydration of anions and cations in these IEMs.

The fixed charge group hydration makes up a portion of the y-intercept of each plot, which represents λ_{nf} in the limit of having no counter-ion hydration. The AEM and the CEM each have the same backbone chemistry, so the contribution of non-ionic hydrophilic moieties should be the same for each membrane. This similarity allows us to examine the difference in hydration number between $RNMe_3^+$ and RSO_3^-, because these head groups are the only structural difference between the AEM and CEM polymers. We might reasonably expect that $RNMe_3^+$ and NMe_4^+ have similar hydration numbers due to their comparable structure ($HN_{A-w}^{AEM} \sim 2$). In contrast, the nearest common ionic analogue for RSO_3^- is SO_4^{2-}, which has two formal charges and four pendant

oxygens instead of one formal charge and three pendant oxygens. This imprecise comparison has led to competing schools of thought, where it can be reasoned that RSO_3^- and SO_4^{2-} have identical hydration numbers ($HN_{A-w}^{CEM} = 6$)[509], or it can be claimed that the more delocalized sulfonate should have a lesser equivalent hydration number than sulfate ($HN_{A-w}^{CEM} < 3$). Experimentally, we observe that the y-intercept is very similar for the AEM and CEM (7.72 ± 0.31 and 7.51 ± 0.33, respectively). This suggests that the hydration number of RSO_3^- is not appreciably different from that of $RNMe_3^+$; therefore, our experimental results suggest that $HN_{A-w}^{CEM} \sim 2$. With both values of $HN_{A-w}^{IEM} \sim 2$, we can conclude that both fixed charge groups coordinate a full hydration shell in each simulated IEM counter-ion form.

9.5.2 Ion Pairing in IEMs

The second component of HSAB theory involves ion binding interactions. In SIE analyses, ion properties are employed as proxies for the tendency of ions to form ion pairs. The hydration analysis above indirectly implicated Li^+/RSO_3^- pairing and the potential for solvent-shared ion pairs in the AEMs. In this section, we examine ion pairing in the IEMs by considering fixed charge group/counter-ion RDFs from the MD simulations. Figure 9.5 shows the RDFs and nearest-neighbor coordination numbers of counter-ions relative to the fixed charge groups (CN_{A-g}^{IEM}) in AEMs and CEMs. The distribution functions in these plots are directly comparable because the ratio of fixed charge group to counter-ion is identical in each simulation. In the AEMs, NO_3^- achieves the closest distance of approach, while F^- maintains greater separation than other anions. Additionally, for each anion, $CN_{A-g}^{IEM} > 1$, reaching as high as 2.44 for I^-. A coordination number of 1 suggests a singular cation/anion interaction, while a value of 2 indicates that two counter-ions are nominally equidistant from each fixed charge group. To complete the mass

balance, $CN_{A-g}^{IEM} \sim 2$ also implies that many anions reside partway between two $RNMe_3^+$ groups. F^- uniquely adopts a more pair-wise interaction with $RNMe_3^+$ at a comparatively large distance, which is consistent with the solution-like hydration environment surrounding F^-.

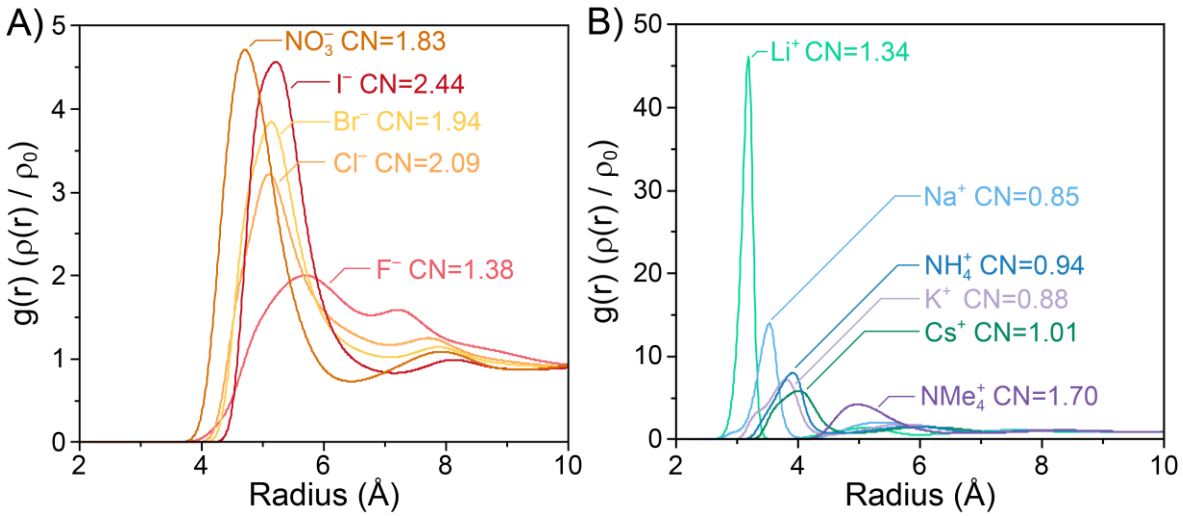


Figure 9.5: Fixed charge group/counter-ion radial distribution functions. The radial distribution function ($g(r)$) for the pair formed by fixed charge group central atoms ($RNMe_3^+$ in panel a and RSO_3^- in panel b) and the centers of the mobile ions. The number of ions present before the first minimum in density, i.e., the primary coordination number, is listed for each ion.

The cations display a very different trend than the anions. NMe_4^+ and Cs^+ RDFs peak at 2 – 5x their mean-field density like the anions, but NH_4^+, K^+, Na^+, and especially Li^+ clustered at greater densities. Notably, Li^+ reached 45x greater density than the mean-field value. Additionally, most cations have $CN_{A-g}^{IEM} \sim 1$, indicating fewer shared interactions between multiple RSO_3^- and the same counter-ion. However, NMe_4^+ and Li^+ had $CN_{A-g}^{IEM} > 1$. Whereas the NMe_4^+/RSO_3^- interactions appear similar to $RNMe_3^+$ coordination with mobile anions, the nature of Li^+ coordination is different. When the RDF maximum is close to the mean-field density, the coordination is essentially caused by spatial constraints, but with the greater magnitude, coordination is increasingly a result of favorable energetics. The Li^+ RDF therefore indicates a

highly stabilized structure, sometimes incorporating multiple RSO_3^- and Li^+. This explanation is consistent with the displacement of both RSO_3^- and Li^+ water coordination shells (Appendix Figure G.17B and Table 9.1, respectively). This intimate paired structure completely dominates the Li^+ RDF, but the RDF for Na^+ shows a small shoulder at this same location, suggesting that some Na^+ counter-ions might adopt a similar configuration. Larger bare cations also display a low-distance shoulder, which could indicate a small population of strongly interacting fixed charge group/counter-ion pairs.

To experimentally test the possibility of ion pairing in these IEMs, we turned to *in-situ* vibrational spectroscopy. Raman spectroscopy has demonstrated sensitivity to ion pairing structures of two ions without hydrating waters between them, called contact ion pairs[370–373]. Gaussian deconvolution of ionic peaks allows for identification of unique coordination structures through the peak locations as discussed in Section 2.6.5. Although it is challenging to assign deconvoluted peaks to specific physical phenomena in the membranes, we generated confidence in our interpretation by comparing dry spectra in various counter-ion forms. In the absence of water, contact ion pairing is guaranteed, and the extent of interaction should definitively scale with the bare radius of the counter-ion.

The dry membrane spectra in Figure 9.6A and B qualitatively demonstrate that the location of the $RNMe_3^+$ peak in AEMs and RSO_3^- peak in CEMs trends with the radius of the ion. The trend is more pronounced in the CEMs than the AEMs, but small ions like Li^+ and F^- cause high-energy shifts, while large ions like Cs^+ and I^- cause low-energy shifts. These results are quantified in Figure 9.6C and D, where one deconvoluted peak for the AEMs and two deconvoluted peaks for the CEMs increase in vibration energy as the bare radius of the ion decreases. The spectra of dry membranes align with the expected trends, providing confidence that our experiments are

sensitive to ion pairing in these membranes. Potentially, the Raman results even detect two modes of contact ion pairing the CEMs. If the coordination results of the MD simulations are representative of that in the experimental membranes, the two CEM species could correspond to a counter-ion pairing with either one or two RSO_3^- groups. Alternatively, the two species might be single-oxygen pairing and multiple-oxygen pairing within a single RSO_3^- headgroup. A detailed molecular interpretation of the two modes of contact ion pairing detected in these CEMs would be difficult to ascertain and is beyond the scope of this study.

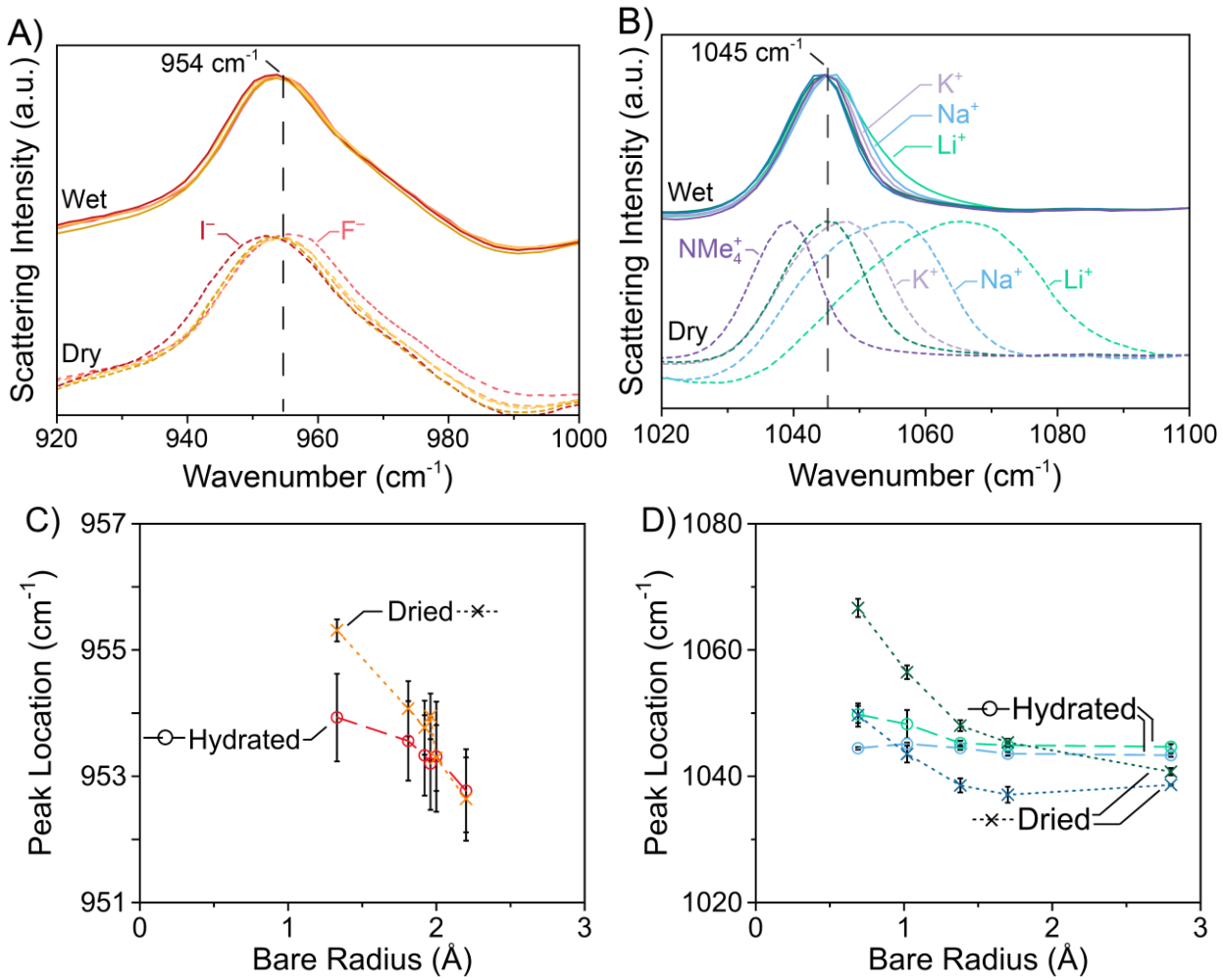


Figure 9.6: Ion pairing detected via vibrational spectroscopy. Raman results for hydrated and dried membranes in monovalent counter-ion forms. a) Spectra of the $RNMe_3^+$ C-N stretch of AEMs. b) Spectra of the RSO_3^- S-O symmetric stretch of CEMs. Notable counter-ion spectra were labeled, while overlapping results were left unlabeled for clarity. Spectra have been baseline-

corrected and normalized for qualitative comparisons, but the Gaussian deconvolution analysis was performed on raw spectra per Section S2.1. c) and d) Deconvoluted peak locations of the fixed charge groups in the hydrated and dried membranes for AEMs and CEMs, respectively. Circle points with long dashes represent hydrated conditions, while X points with small dashes represent dry conditions. Uncertainties are 95% confidence intervals for peak locations in the Gaussian deconvolution. In panels b and d, the NH_4^+ results have been omitted due to atypical spectra.

Only a single C-N peak was detected in the spectra of the hydrated membranes; as shown in Figure 9.6C, this C-N peak does not shift beyond the uncertainty of the Gaussian fit as counter-ions are varied. With such small variation in the peak location in hydrated membranes, this peak location is assigned to water-coordinated RMe_3^+, and our results do not indicate contact ion pairing in the AEMs. In contrast, spectra of hydrated CEMs revealed two distinct peaks . This opens the possibility of first-shell coordination interactions. The lower energy peak location does not vary as the counter-ions are exchanged, suggesting that it corresponds to the water-coordinated RSO_3^- group. The higher energy peak does vary as the counter-ions are exchanged, reaching the highest vibrational energy for the Li^+ form CEMs. This vibrational mode gives rise to the high-energy tails of hydrated spectra in Figure 9.6B.

For the Li^+ form CEMs, the second species in the hydrated state corresponds to the lower energy contact ion pair in the dried membrane (Figure 9.6D). For the other counter-ion forms, the second species detected in the hydrated state displayed S–O wavenumbers between those of the two ion pairing modes measured in the dry state. Therefore, only Li^+ contact ion pairing was detected in the hydrated IEMs. The species detected in other cation forms could potentially be solvent-shared ion pairs, where water molecules increase the distance between the paired ions but do not intervene between the two. The qualitative results of this vibrational spectroscopy analysis align strikingly well with the ion pairing trends observed in MD simulations. Li^+ demonstrated a markedly higher tendency to coordinate with RSO_3^- than other cations in the simulated CEMs, but

Na^+ and K^+ had a small population of ions achieving similarly close conformations. Meanwhile, no first-coordination-shell ion pairing in either the simulated or experimental AEMs. Thus, the Raman spectroscopy results bolster our confidence in ion pairing results derived from the simulated IEMs.

We quantified the extent of interactions between the fixed charge groups and nearest-neighbor mobile counter-ions by converting the RDFs from the MD simulations into free energy profiles. These results can also be used to calculate the energy barrier required to remove a counter-ion from its most energetically favorable position and bring it further away from a fixed charge group. This energy of departure, ΔG_{escape}, is significant because it allows us to apply the criterion for ion pairing developed by Bjerrum. According to Bjerrum, ions will become trapped in the vicinity of an oppositely charged ion when the energy of departure exceeds $2k_BT$[357,522]. For our simulation conditions, this translates to an ion pairing criterion of $\Delta G_{escape} > 5\ kJ/mol$. We extracted ΔG_{escape} from the energy profiles in Figure 9.7A and B by calculating the difference between the first local minimum and the first local maximum, with the results shown in Figure 9.7C.

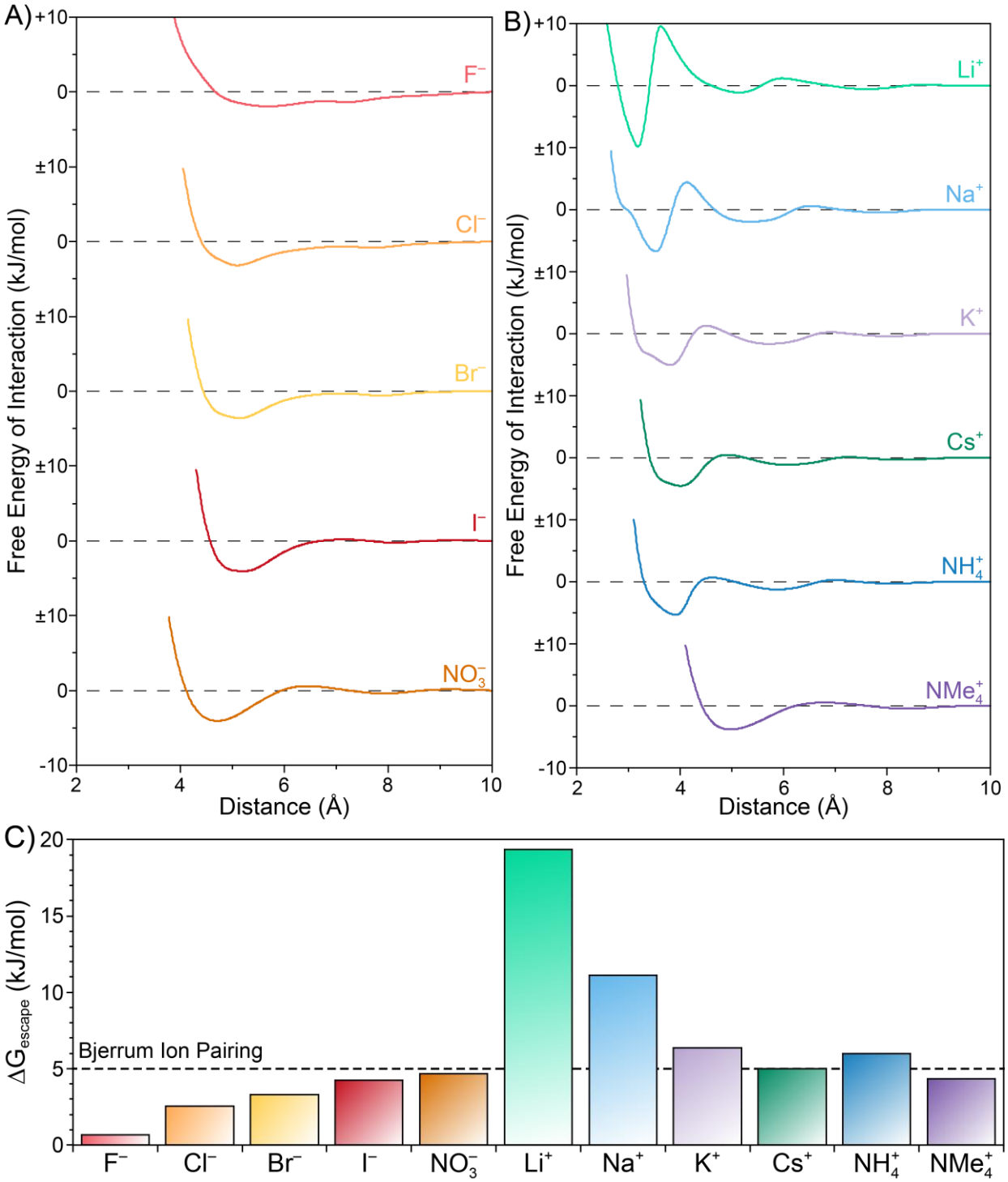


Figure 9.7: Energy of ion/ion interactions from MD simulations. Free energy profiles of interaction between the a) anions and b) cations and the fixed charge groups at 27 ºC as a function of separation distance. c) The energy of departure (ΔG_{escape}) for counter-ions in the primary coordination shell of a fixed charge group. ΔG_{escape} includes favorable interactions which are lost (the well depth of the first energy minimum in panels a and b) and the unfavorable interactions incurred by departure

(the height of the first energy maximum in panels a and b). The dashed line indicates the threshold proposed by Bjerrum for ion pair formation, $2k_BT$, which is ~5 kJ/mol for 27 ºC.

Figure 9.7C immediately shows that some ion interactions surpass Bjerrum's criterion for ion pairing, while others do not. Li^+ and Na^+ clearly require too much energy to escape from RSO_3^-, partially due to the loss of favorable interactions and partially due to a positive energy penalty paid upon departure. K^+, Cs^+, and NH_4^+ meet the Bjerrum criterion and likely form some ion pairs, but these ions do not exceed the 5 kJ/mol threshold to nearly the same extent as Li^+ or Na^+. NMe_4^+ and each anion under study do not meet the Bjerrum criterion for ion pairing. The monatomic anions also never incur an energy penalty to leave (Figure 9.7A); for these ions, ΔG_{escape} stems entirely from a reduction in favorable interactions. Among these non-paired ions, we expect each ion to respond to an applied electric field and contribute to the average ion diffusivity. Meanwhile, for the paired cations, a fraction of these counter-ions should be non-responsive to the electric field and unable to diffuse. The implications of these results regarding the activation energy of ion diffusion are explored in the next section.

9.6 The Source of Diffusion Energy Barriers in IEMs

The understanding of hydration and ion pairing in these IEMs provided by the MD simulations allows us to refine our assessment of SIEs affecting ΔE_a^{m-s}. Ions were only found to show signs of dehydration when trapped in strong ion pairing interactions with the fixed charge groups, which occurs primarily with small, densely charged cations. Conversely, the anions experienced stronger hydrating forces in the IEM than dilute aqueous solution, seemingly because of the collaborative orientation of waters that stabilize both the counter-ions and the fixed charge groups. These findings align with the basis of HSAB, where ion/ion interactions are dominated

not by direct Coulombic forces but by the extent to which ion/ion interactions affect translational freedom of the solvent.

The electrochemical impedance spectroscopy experiments employed to obtain activation energies of diffusion only varied the thermal energy by ±10 % from room temperature, which is a relatively narrow range compared to the calculated ΔG_{escape} values in Figure 9.7C. Without appreciably changing the Bjerrum ion pairing criterion, we hypothesize that the measured ΔE_a^{m-s} values relate to the interactions of only mobile ions, ΔG_{A-g}^{mobile}. To account for this effect, we extracted energies from the first minimum of the energy profiles in Figure 9.7A and B for the anions and NMe_4^+, but we used the second minimum for other cations, assuming that the first minimum corresponds to trapped ions which would not be measurable in transport experiments. This procedure resulted in a trend qualitatively similar to the activation energy trends observed experimentally: F^- was not stabilized much by the fixed charge groups, while I^- interacted strongly. Meanwhile, NMe_4^+ experienced the greatest stabilization energy for the cations, with mobile Na^+ surprisingly interacting more strongly than mobile Li^+ or mobile K^+. We analyzed ΔG_{A-g}^{mobile} in Figure 9.8 using the same data science methods as shown in Figure 9.3. The biplot in Figure 9.8A demonstrates that ΔG_{A-g}^{mobile} correlates most strongly with ΔE_a^{m-s} and explains the most variance of any other variable considered. Figure 9.8B shows a good linear relationship between ΔE_a^{m-s} and ΔG_{A-g}^{mobile} with a reasonably homoskedastic residual profile, suggesting that the major contribution to the barrier for ion diffusion across these IEMs is captured by this extent of interaction between mobile counter-ions and fixed charge groups.

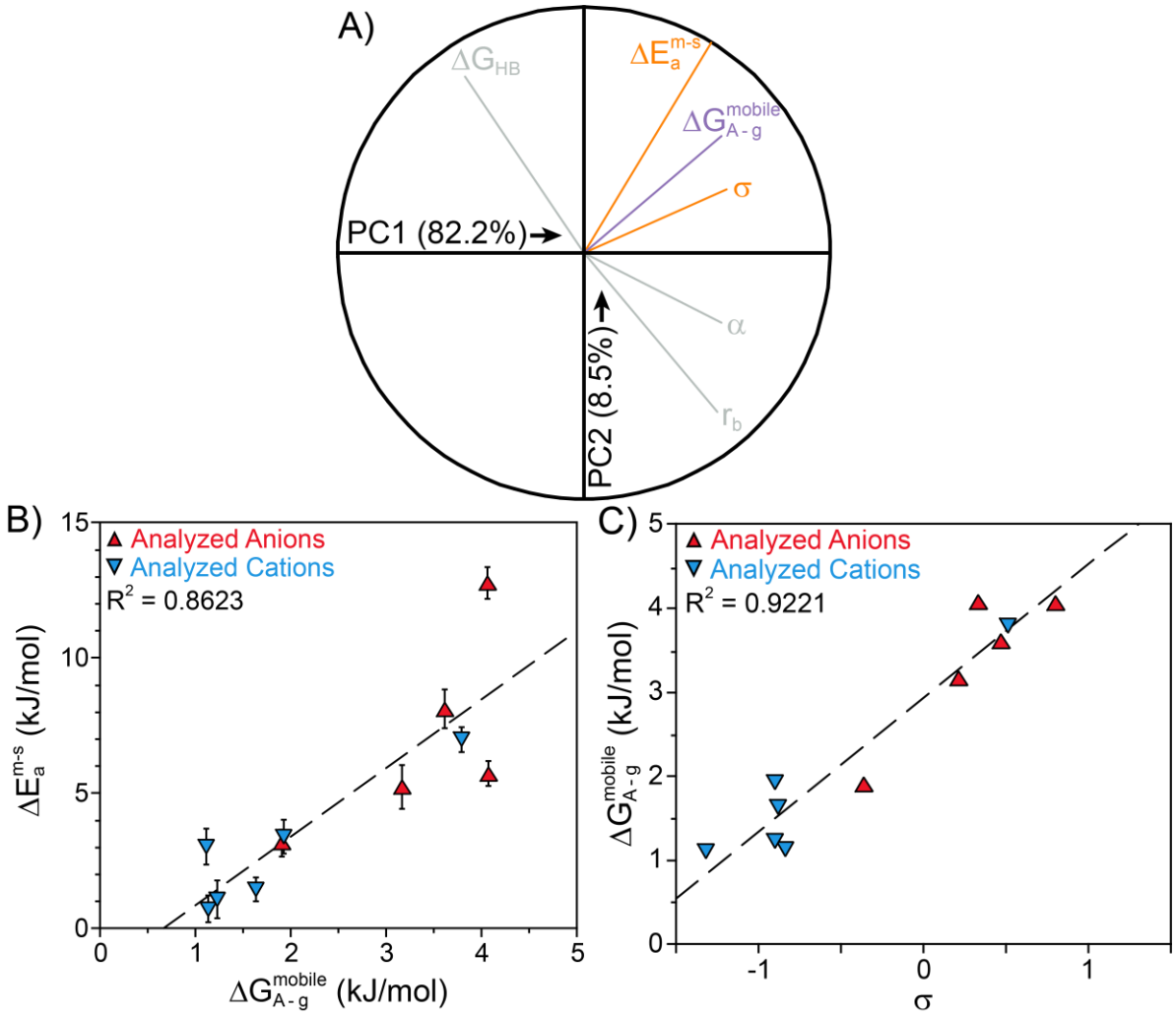


Figure 9.8: Correlation analysis for mobile ions in the IEM. a) Biplot of significant ion properties correlated with ΔE_a^{m-s} and the well depth of fixed charge group interaction for mobile counter-ions, ΔG_{A-g}^{mobile}. b) ΔE_a^{m-s} plotted against ΔG_{A-g}^{mobile} for the ions simulated in this study. c) ΔG_{A-g}^{mobile} plotted against the σ for the ions simulated in this study. Uncertainties were calculated from standard errors of the activation energies using standard propagation of uncertainty methods.

Both the ion softness, σ, and ΔG_{A-g}^{mobile} correlate strongly with ΔE_a^{m-s}. In fact, Figure 9.8A demonstrates that these two parameters explain similar modes of variance within the context of the ion properties correlated with ΔE_a^{m-s}. This is explored further in Figure 9.8C, where these two variables are plotted directly against one another. Although σ does not help to rationalize the onset of strong ion pairs for ions like Li^+, Figure 9.8C demonstrates that variations in energetic hinderance to mobile ion transport can be rationalized almost entirely via differences in σ. As we

mentioned previously, the MD and DSC results indicate that high values of ΔG_{A-g}^{mobile} are primarily a result of compatible hydration tendencies between fixed charge groups and counter-ions, which is exactly the mechanism of interaction described in HSAB. Because the mechanism is identical and the simulated energies are explained extremely well by tabulated values of σ, we conclude that not only does σ correlate with ΔE_a^{m-s}, but the hydration shell interaction mechanism proposed by HSAB is the primary cause of ion-specific energy barriers to transport in these IEMs.

9.7 Conclusions

Installing ion-specific interactions in ion-exchange membranes (IEMs) could enable the separation of ions with similar charge and valence. However, to properly leverage IEMs for this application, foundational understandings of specific ion effects (SIEs) and counter-ion diffusion in IEMs are needed. To develop this understanding, we investigated SIEs in representative highly swollen IEMs by experimentally measuring counter-ion diffusion behavior of an AEM and CEM with 15 different counter-ions. The experimental results were supplemented with atomistic molecular dynamics (MD) simulations using a subset of 11 different counter-ions. The results demonstrate highly ion-specific diffusion behaviors, where ion transport properties of the membrane deviated from aqueous solution transport properties to various extents depending on the counter-ion identity.

We elucidated the source of the observed SIEs by constructing a detailed picture of ion/ion and ion/water interactions in these IEMs. Our analysis, supported by MD simulations and vibrational spectroscopy, revealed that small, densely charged cations interact strongly with the fixed charge groups, resulting in the complete immobilization of a subset of the counter-ions. In contrast, the interactions between the anions and fixed charge groups are comparably weaker. The water coordination behavior observed in the simulated AEMs suggests that anion/fixed charge

group interactions are primarily governed by cooperative solvation, which are insufficiently strong to immobilize the anions. This interpretation is further supported by calorimetric analysis of the states of water in the IEMs, which reveals additional hydration interactions in the studied AEMs, but not in the CEMs.

These findings collectively indicate that solvent-mediated interactions between ions and fixed charge groups are the primary drivers of SIEs in these IEMs. The increased energy barrier of diffusion within the IEM experienced by each ion strongly correlates with the free energies of interaction between fixed charge groups and mobile counter-ions determined from the simulations. These interaction energies also correlate with the ion softness, which is utilized to predict ion/fixed charge group interactions via Pearson's Hard/Soft Acid/Base (HSAB) theory. The HSAB mechanism, characterized by electrostatic interactions driven by ion/water coordination, parallels the cooperative hydration observed in the simulations. By predicting both the mechanism and magnitude of these effects, we identify HSAB theory as the underlying causal mechanism governing SIEs in these highly swollen IEMs.

According to the predictions of HSAB, adjusting the softness of the fixed charge groups emerges as the primary mechanism for influencing SIEs and targeting specific ion interactions for selective separations. If membrane structures can be precisely engineered to fine-tune ion selectivity between like-charged monovalent ions, IEMs with tailored softness could offer a highly effective solution for specific ion separations.

Chapter 10 Conclusions and Recommendations

Ion-exchange membranes (IEMs) frequently limit the energy intensity or energy efficiency of electrochemical technologies. Enhancing membrane design and performance to overcome these restrictions can significantly improve the technoeconomics of many electrochemical processes, thereby reducing the pressures associated with the Water-Energy Nexus. This dissertation has made numerous contributions to the understanding and exploitation of the fundamental principles of ion transport in charged polymer membranes. The key findings are summarized below, alongside recommendations for future research that could expand upon the results of this dissertation.

10.1 Summary of Conclusions

Many lines of investigation within this dissertation have built upon one another. By grounding my approach in large data sets and describing my results with thermodynamic and transport models, I was able to discern the most significant limitations on fast and selective ion transport in IEMs. A series of controlled follow-up studies then validated and deepened the understanding of two primary design strategies identified by my initial modeling efforts.

Chapter 4 established a thorough overview of current IEM structures and performance, bridging interdisciplinary barriers which often inhibit information exchange between different research fields studying IEMs. An experimental survey of commercially available membranes led to a new description of the trade-off between charge selectivity and counter-ion conduction in IEMs. This data set defined the upper bound of fast and selective ion transport and provided

empirical insights into structural features that were correlated with high-performing IEMs. A complementary literature survey of recently developed membranes established a structural trade-off between the charge and water content of IEMs, which appeared to contribute to the observed performance trade-off. I identified membrane structures that achieved unique combinations of charge and water contents, summarizing design strategies and evaluating their potential to overcome the limitations faced by current materials.

In Chapter 5, I built upon the data collected in Chapter 4 to model the upper bound of fast and selective ion transport in IEMs. Leveraging the established Donnan-Manning and Meares-Manning models for ion partitioning and diffusion in charged membranes, I developed an explicit equation describing this upper bound. My modeling efforts elucidated the mechanism underlying the trade-off, which persists through the compensated water content scaling of polymer tortuosity and charge exclusion. This model also identified the two most promising routes to achieve new combinations of counter-ion/co-ion selectivity and counter-ion conductivity for high-performing IEMs. The most reliable approach was to advance the maximum charge density of the polymer (C_A^{max}), which has cubic scaling in the upper bound relationship. There is room to improve C_A^{max}, as current commercial IEMs occupy less than a third of the potential materials space for highly charged polymer membranes. The second strategy involves the diffusivity of counter-ions and resulting diffusion selectivities in IEMs, which remains one of the most significant mysteries in our fundamental understanding of ion transport in IEMs.

Following the actionable recommendations of the newly developed Donnan-Meares-Manning model for the upper bound of ion transport in IEMs, Chapter 6 details the synthesis of ultrahigh charge density (UHCD) IEMs. After considering the various strategies for increasing charge densities in Chapter 4, I developed polymerizable and cross-linkable bis(imidazolium)

monomers with compact molecular structures. These unique IEMs became the most densely charged IEMs I am aware of, reaching charge densities exceeding 5 mol / L[membrane] for the first time. The ion transport properties of these UHCD IEMs redefined the upper bound and were still accurately captured by the model developed in Chapter 5. The successful modeling of UHCD IEM transport properties demonstrates that their ion transport mechanisms are well understood and can be extended to other materials prepared using a similar design strategy.

To better understand the limit of ion-selective transport in UHCD IEMs, Chapter 7 explores the benefits of pushing for more densely charged and more mechanically strained polymer networks. Through the controlled structural characterization of additional imidazolium membranes with yet higher charge densities, I located a soft cap on the advantages of increasing the charge density of polymer networks. At a critical threshold near 8 mol / L[polymer], inter-chain electrostatic forces begin to dominate intra-chain electrostatic forces, causing nonidealities within the polymer structures that significantly restrict ion transport motion compared to IEMs with C_A^{max} < 8 mol / L[polymer].

Complementing the selectivity-focused investigation in Chapter 7, Chapter 8 explores design strategies which might achieve superior ion conduction in highly swollen UHCD IEMs. By exploiting morphological variations caused by polymerization induced phase separation (PIPS), I created water domains that were co-continuously intertwined with the ion-exchange polymer in UHCD IEMs. I employed a percolation model by De Gennes to understand ion conduction in these membranes, alongside a complementary phase additivity model to describe ion partitioning. By fitting the experimental data to these orthogonal models, I provided support for the spinodal decomposition description of water domains in these PIPS membranes and identified a criterion for improved counter-ion conduction beyond what is achievable in homogenous membranes. By

inducing a small extent of phase separation, which allows counter-ions to traverse bulk-water domains without co-ions, it is possible to mitigate some of the tortuosity introduced by the polymer phase. Reducing the tortuosity experienced by counter-ions in this manner increases the effective diffusivity of ions in the IEM.

In parallel with the development and refinement of high charge density IEM design strategies, Chapter 9 presents a fundamental investigation into the governing forces of counter-ion diffusion energetics in IEMs. I examined the energy barriers encountered by counter-ions diffusing across typical IEMs for brackish water desalination, finding strong ion-specific differences between monovalent ions within the same membranes. I was able to correlate these specific ion effects (SIEs) with the ion softness parameter from Pearson's Hard/Soft Acid/Base theory. By supplementing my transport experiments with molecular dynamics simulations, I gained insights into the mechanisms underlying these SIEs. After validating the simulation results with calorimetric and spectroscopic experiments, I concluded that solvent-mediated favorable electrostatic interactions between counter-ions and fixed charge groups contribute to the observed energy barriers for diffusion. This mechanism aligns with Pearson's theory, suggesting that the ion softness parameter measures a causal interaction which dominates experimental energy barriers in the IEM. Based on the Hard/Soft Acid/Base theory, SIEs could be exploited to tune ion diffusion coefficients in IEMs by varying the identity—and consequently, the softness—of fixed charge groups.

10.2 Recommendations for Future Work

10.2.1 Test Additional UHCD IEM Structures

The initial investigations into bis(imidazolium) UHCD IEMs offer valuable insights for membrane design, but the resulting IEM structures are not suitable for many applications. A

significant limitation is the lack of UHCD CEMs in this work. Unlike the diverse functional groups available for synthesizing cationic polymers, sulfonates are nearly the only strongly dissociating fixed charge group employed in CEM production. Networkable, non-terminal anionic fixed charge groups, such as boronic esters, phosphonic esters, or sulfonyl imides, could enable UHCD CEMs similar to the bis(imidazolium) AEMs studied here. These relatively uncommon structures would need to be vetted in terms of their aqueous stability and acid strength before usage. Alternatively, dense sulfonation of cross-liking structures could produce structures which are charged enough to meet the identified soft cap on polymer charge.

Further explorations of UHCD AEMs are also necessary. The unsubstituted imidazolium cations studied in this dissertation are not stable in basic environments, which is a requirement for many technologies in the energy sector. A relatively straightforward way to enhance the base stability of these UHCD structures involves preparation of substituted bis(imidazolium) monomers bearing methyl or phenyl moieties around the imidazolium ring. This modification would remove vulnerable hydrogens and limit the steric accessibility of hydroxide attacks. However, these structures could increase the bulkiness of non-charged portions of the polymer, which would be detrimental to the charge density. Therefore, cations with inherent base stability in compact forms should also be explored.

10.2.2 Validate the In-Device Performance of UHCD IEMs

The bis(imidazolium) UHCD IEMs presented in this dissertation demonstrate improved *ex situ* ion transport performance compared to commercial IEMs. However, it is crucial to assess the *in situ* device performance of systems using UHCD IEMs. Many technologies, such as electrodialysis, require AEMs and CEMs to be used in tandem, making desalination testing contingent upon the preparation of UHCD CEMs. Applications employing a single AEM, like

water electrolysis, use hydroxide counter-ions, necessitating a base-stable UHCD AEM. Furthermore, like most commercially available cross-linked IEMs, the glassy charge polymer constituting UHCD IEMs is too fragile to directly utilize in devices subject to pressure gradients and clamping stresses. Therefore, preparation of composite UHCD IEMs will likely need to precede device performance.

While ion transport is a dominant factor in the energy consumption of electrochemical devices, the other requirements identified in Section 1.2 can become rate-limiting once ion transport properties are improved. After determining limitations in IEM performance, additional functionalization may be necessary in UHCD IEMs. For instance, water transport might be adjusted through the incorporation of additional hydrophilic moieties. Alternatively, dimensional stability could be enhanced by modifying the polymer synthesis conditions. Although these modifications could negatively impact the ion transport properties of UHCD IEM structures, their significant improvement over existing commercial materials provides ample room to balance ion transport with other performance requirements. A carefully conducted technoeconomic assessment of these performance trade-offs will be essential to optimize membrane structures for each individual electrochemical application.

10.2.3 Determine the Mechanism of Donnan Exclusion in UHCD IEMs

Chapter 7 identified the onset of inter-chain electrostatic repulsion in UHCD IEMs but did not fully elucidate the mechanisms governing ion nonidealities. Although charge exclusion is expected to be significantly hindered in these materials due to counter-ion condensation, we hypothesize that an additional phenomenon such as dielectric exclusion bolsters the ion-exclusion performance of these membranes. To comprehensively understand the nature of ion nonidealities

in UHCD IEMs , more detailed studies with advanced characterization techniques will likely be necessary.

10.2.4 Test Predictions of Pearson's HSAB

The ion softness parameter in Pearson's Hard/Soft Acid/Base theory (HSAB) was determined to significantly influence counter-ion diffusion in IEMs. The solvent-mediated interactions described by this theory may hold the key to understanding why certain ions diffuse around membrane obstructions faster than in aqueous solution. The nature of this counter-ion speed-up warrants additional investigation. Specifically, HSAB predicts that interaction extents are determined by the product of cation and anion softness parameters; therefore, the softness of fixed charge groups can be selected to tune counter-ion interactions. Adjusting these interactions could improve counter-ion/co-ion separations and counter-ion/counter-ion separations by enabling diffusion selectivities specifically tailored for specific counter-ions of interest. Comparing the results for the sulfonate-based CEMs and trimethylammonium-based AEMs in Chapter 9 with comparable structures using softer fixed charge groups (e.g., sulfonyl imides, imidazoliums, and other more charge-delocalized ions) will help clarify the implications of HSAB for ion separations in selective membranes.

10.2.5 Intensify the use of Data Science IEM Research

Large data sets were the key to many of the insights in this dissertation. The Donnan-Meares-Manning model could only be validated because of the upper bound plot assembled from numerous different IEMs. Additionally, the untapped potential for highly charged membranes was recognized only by evaluating the charge density of other published IEMs. Without sourcing membranes from various research communities that utilize IEMs, these studies would have

overlooked structures already synthesized and studied in the literature. The unique properties achieved by the UHCD IEMs are only notable due to the exhaustive context provided from these data surveys. By setting this example, I hope that future IEM researcher will increasingly rely on interdisciplinary knowledge already available in the literature, which is accessible once discrete data sources are compiled and compared.

There are numerous opportunities for utilizing large data sets in IEMs research. For instance, machine learning has been particularly useful in compiling results for the caustic stability of IEMs, but this application of machine learning is still in its early stages. Or, characterizing a wide range of energy barriers and diffusion selectivities in IEMs could help identify clearer trends than those observed in this dissertation. Moreover, upper bound plots are typically developed through community efforts; once performance metrics and a standardized method of plotting them have been established, gathering data from multiple labs into selectivity/conductivity trade-off plots will provide a clearer picture of significant developments in novel IEMs. Constructing trade-off plots for salts other than NaCl would also lead to more informed selections of the best IEM for a given application and help validate the Donnan-Meares-Manning upper bound model.

Appendices

Appendix A Mathematical Symbols

Appendix Table A.1: Symbols and variables used throughout the manuscript. For simplicity, this list is abbreviated to only list common symbols used in multiple locations throughout the manuscript.

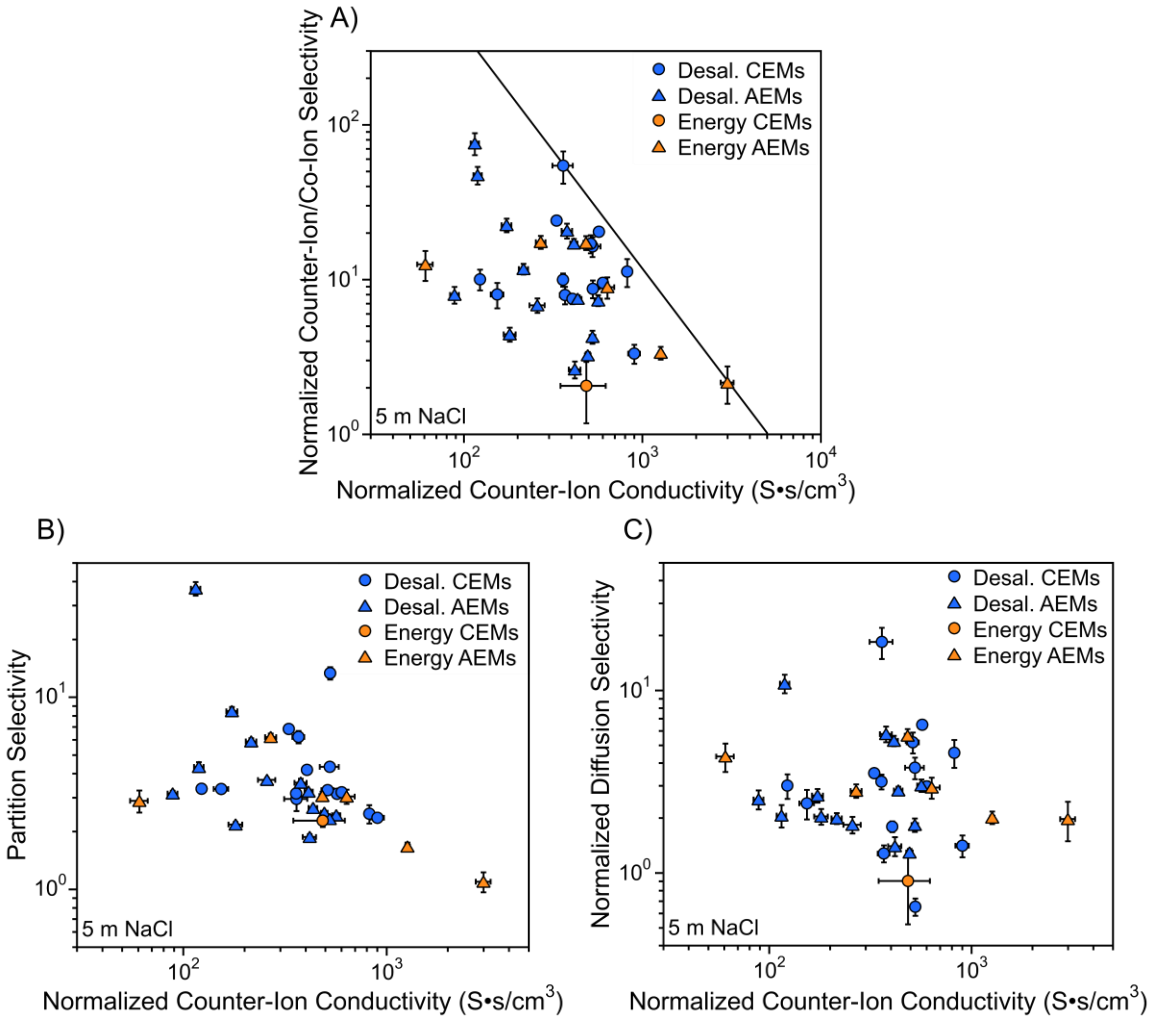
a_i^j	Activity of species *i* in phase *j*
A	Manning's electrostatic friction function
A_x	Cross-sectional area available for transport
B_λ	Upper-bound salt symmetry function
b	Linear spacing between fixed charge groups
$C_i^{m,t}$	Concentration of species i per total membrane volume
$C_i^{m,w}$	Concentration of species i per sorbed membrane water
C_A^{max}	Maximum charge density of the dry polymer membrane
C_i^s	Concentration of species i in the aqueous salt solution
D_i^j	The effective diffusivity of species i fully accounted for in phase *j*
D_0^j	The Arrhenius pre-factor of a species in phase *j*
E'_{SR}	Swelling-reduced storage modulus
E_a^j	Activation energy of diffusion in phase *j*
ΔE_a^{m-s}	Activation energy of diffusion attributable to the membrane
F	Faraday constant
f_c	Fraction of condensed counter-ions

f_u	Fraction of uncondensed counter-ions
f_f	Fraction of freezable water
f_{nf}	Fraction of non-freezable water
IEC	Ion-exchange capacity (meq. g^{-1} dry membrane)
i	The subscripted chemical species for a property
$i = A$	Fixed charge groups, or ions covalently attached to the polymer
$i = c$	Co-ions, or similarly charged ions to the polymer
$i = g$	Counter-ions, or oppositely charged ions to the polymer
$i = g, c$	Counter-ions which have been condensed onto the polymer backbone
$i = g, u$	Counter-ions which remain uncondensed
$i = s$	Salt molecules (counter-ions and co-ions in their stoichiometric ratio)
$i = w$	Water
j	The superscripted phase for a property
$j = b$	The reinforcing backing of the membrane
$j = m$	The ion-exchange membrane phase
$j = ixp$	The swollen ion-exchange polymer of a composite membrane
$j = s$	The external solution phase
$j = t$	The total membrane volume
$j = w$	Sorbed water in the membrane
k_B	The Boltzmann constant
P_s	Salt permeability coefficient of a membrane ($cm^2\ s^{-1}$)
R	Ideal gas constant

$\boldsymbol{T}$	Absolute temperature
$\boldsymbol{t_i^m}$	Transport number of species i in phase j
$\boldsymbol{\bar{V}_w}$	Molar volume of water
$\boldsymbol{WU}$	Water uptake of the membrane
$\boldsymbol{z_i}$	Valence of species i
$\boldsymbol{\alpha_{i1/i2}}$	Membrane selectivity of species $i1$ over species $i2$
$\boldsymbol{(\alpha_{i1/i2})_K}$	Membrane partitioning selectivity of species $i1$ over species $i2$
$\boldsymbol{(\alpha_{i1/i2})_D}$	Membrane diffusion selectivity of species $i1$ over species $i2$
$\boldsymbol{\beta}$	Intercept of the upper bound line
$\boldsymbol{\Delta H_m^j}$	Melting enthalpy of water in phase j
$\boldsymbol{\Gamma}$	The Donnan ideality factor
$\boldsymbol{\gamma_i^m}$	Activity coefficient of species i in phase j
$\boldsymbol{\gamma_{\pm}^s}$	Mean ion activity coefficient in phase j
$\boldsymbol{\varepsilon_0}$	The permittivity of free space
$\boldsymbol{\varepsilon^j}$	Dielectric constant of phase j
$\boldsymbol{\kappa}$	Ionic conductivity
$\boldsymbol{\kappa_i}$	Ionic conductivity of species i
$\boldsymbol{\lambda}$	Membrane hydration number
$\boldsymbol{\lambda}$	Slope of an upper bound line
$\boldsymbol{\lambda_f}$	Freezable membrane hydration number
$\boldsymbol{\lambda_{nf}}$	Non-freezable membrane hydration number
$\boldsymbol{\lambda_B}$	The Bjerrum length

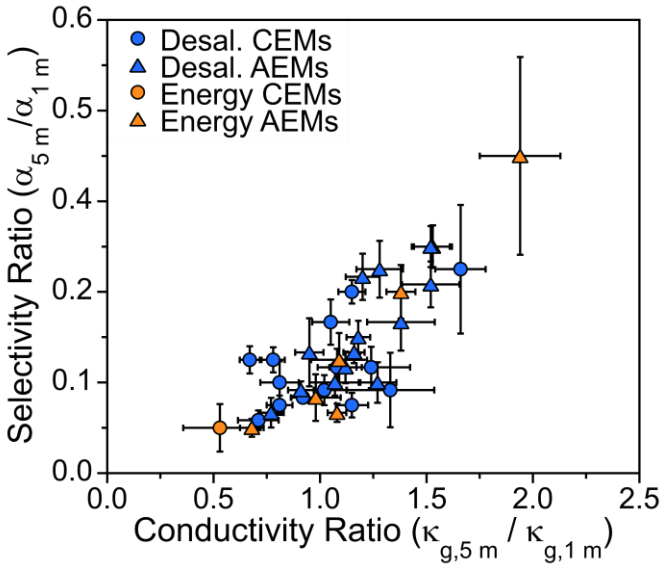
$\boldsymbol{\nu_i}$	Number of molecules of species i per salt molecule
$\boldsymbol{\xi}$	The reduced linear charge density
$\boldsymbol{\xi_{crit}}$	The critical reduced linear charge density
$\boldsymbol{\rho_p}$	Density of polymer (g cm^{-3})
$\boldsymbol{\rho_{pp}}$	Density of the pre-polymer solution (g cm^{-3})
$\boldsymbol{\rho_w}$	Density of water (g cm^{-3})
$\boldsymbol{\tau}$	Tortuosity
$\boldsymbol{\phi_j^{tot}}$	Volume fraction of phase j in the total IEM
$\boldsymbol{\phi_w^j}$	Volume fraction of water in the phase j
$\boldsymbol{\phi_{j,p}^{tot}}$	Critical percolation threshold of phase j in the total IEM
$\boldsymbol{\phi_{w,sat}^{ixp}}$	Maximum water volume accommodated by an ion-exchange polymer
$\boldsymbol{\psi^i}$	Electric potential of phase i (V)

Appendix B Supplemental Content for Chapter 4

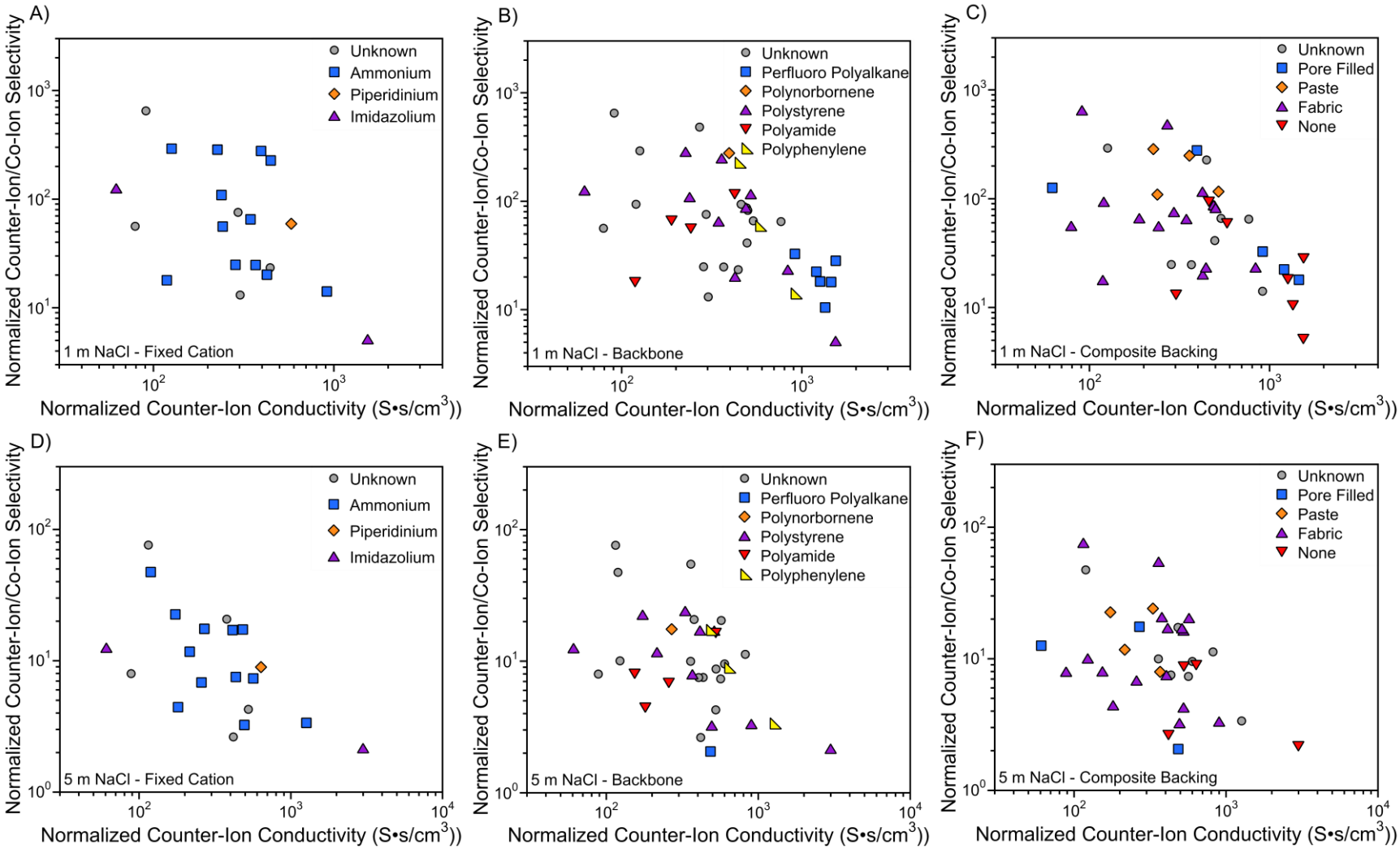


Appendix Figure B.1: Ion transport properties of commercial IEMs contacting 5 m NaCl. A) The normalized charge selectivity ($\bar{\alpha}_{g/c}$) vs. normalized counter-ion conductivity ($\bar{\kappa}_g$) for commercial membranes contacting 5 m NaCl solutions. The solid black line represents an empirically drawn "upper bound," which is of the form $\bar{\alpha}_{g/c} = \beta \bar{\kappa}_g{}^{-\lambda}$. For 5 m NaCl, $\beta = 4.28 \times 10^5$ and $\lambda = 1.52$. B) The partitioning selectivity ($\left(\alpha_{g/c}\right)_K$) plotted against $\bar{\kappa}_g$. C) The normalized diffusion

selectivity ($(\bar{\alpha}_{g/c})_D$) plotted against $\bar{\kappa}_g$.Standard propagation of uncertainty methods were used to calculate uncertainties from measurements on at least 4 independent samples.



Appendix Figure B.2: Comparison of 1 m and 5 m NaCl ion transport. The ratio of counter-ion/co-ion selectivity ($\bar{\alpha}_{g/c}$) at 5 molal NaCl to that at 1 molal NaCl plotted against the ratio of counter-ion conductivity ($\bar{\kappa}_g$) at 5 molal NaCl to that at 1 molal NaCl. Standard propagation of uncertainty methods were used to calculate uncertainties from measurements on at least 4 independent samples.



Appendix Figure B.3: Qualitative structure effects on ion transport. Normalized charge selectivity ($\bar{\alpha}_{g/c}$) vs. normalized counter-ion conductivity ($\bar{\kappa}_g$) classified by various membrane structural characteristics sourced from Table 2.3. A-C) Membrane performance at 1 m NaCl. D-F) Membrane performance at 5 m NaCl. A) and C) AEMs classified by fixed cation. B) and E) Membranes classified by backbone structure. C) and F) Membranes classified by composite backing structure.

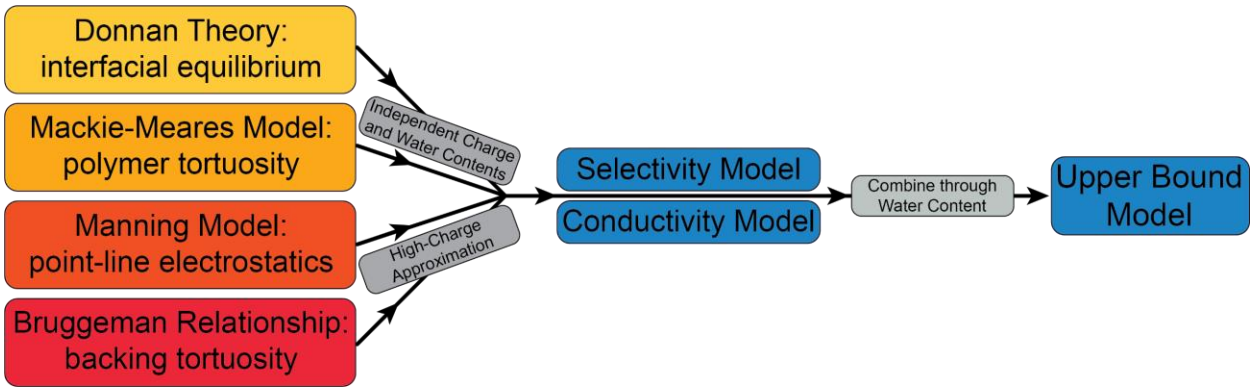
Appendix Table B.1: Condensation in commercial IEMs. Apparent membrane ion activity coefficients and fitted Manning parameters for IEMs equilibrated with both 1 m and 5 m NaCl solutions. Entries of "---" indicate unresolvable data.

Membrane	1 m NaCl		5 m NaCl	
	Apparent $\gamma_{\pm}^{m}$	Fitted ξ	Apparent $\gamma_{\pm}^{m}$	Fitted ξ
AMVN	0.501	1.55	0.906	0.13
CMVN	0.647	0.90	1.033	---
ASE	0.437	2.21	0.859	0.43
CSE	0.593	1.10	0.979	0.06
Nafion 117	0.481	3.52	0.832	1.20
Nafion 212	0.311	---	0.578	---
X37-50	0.336	---	0.705	---
B22-50	0.241	43.45	0.449	---
Type 12 AEM	0.404	3.48	0.824	0.75
Type 12 CEM	0.428	2.78	0.878	0.48
Type 10 AEM	0.469	1.97	0.875	0.47
Type 10 CEM	0.555	1.29	0.955	0.15
Type 2 AEM	0.511	2.04	0.900	0.57
Type 2 CEM	0.507	1.85	1.018	---
FAB-PK	0.473	1.95	2.371	---
FAM-PP	0.490	1.91	0.881	0.45
FAS	0.318	---	0.575	---
FKB-PK	0.691	0.79	0.922	0.33
FKM-PP	0.536	1.54	1.009	---
FKS	0.471	2.30	1.721	---

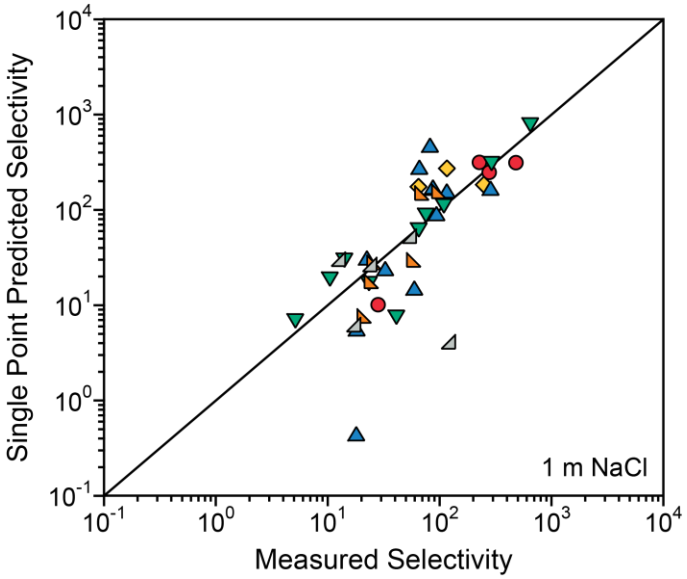
Membrane	1 m NaCl		5 m NaCl	
	Apparent $\gamma_{\pm}^{m}$	Fitted ξ	Apparent $\gamma_{\pm}^{m}$	Fitted ξ
Xergy-Pention	0.357	3.46	0.587	1.82
Xergy-Aquivion	0.350	---	0.589	---
Xergy-Dyneon	0.410	8.15	0.636	---
Xergy-Nafion	0.173	---	0.328	---
AMX	0.387	3.31	0.604	8.36
CMX	0.330	---	0.624	---
AMH-PES	0.453	3.28	0.833	0.88
AMH-PP	0.467	2.59	0.824	0.85
CMH-PES	0.569	1.37	1.046	---
CMH-PP	0.491	2.16	0.918	0.32
AMI-7001	0.468	2.30	0.869	0.53
CMI-7000	0.543	1.52	1.017	---
PCSA	0.293	11.53	0.588	2.84
PCSK	0.427	3.50	0.794	1.12
Aquivion	0.455	3.14	0.885	0.51
AR103P	0.532	1.93	0.936	0.31
AR213T	0.569	1.58	0.980	0.10
CR61P	0.577	1.51	0.949	0.26
CR62T	0.728	0.68	1.109	---
PiperION	0.334	17.98	0.617	5.96

Appendix C Supplemental Content for Chapter 5

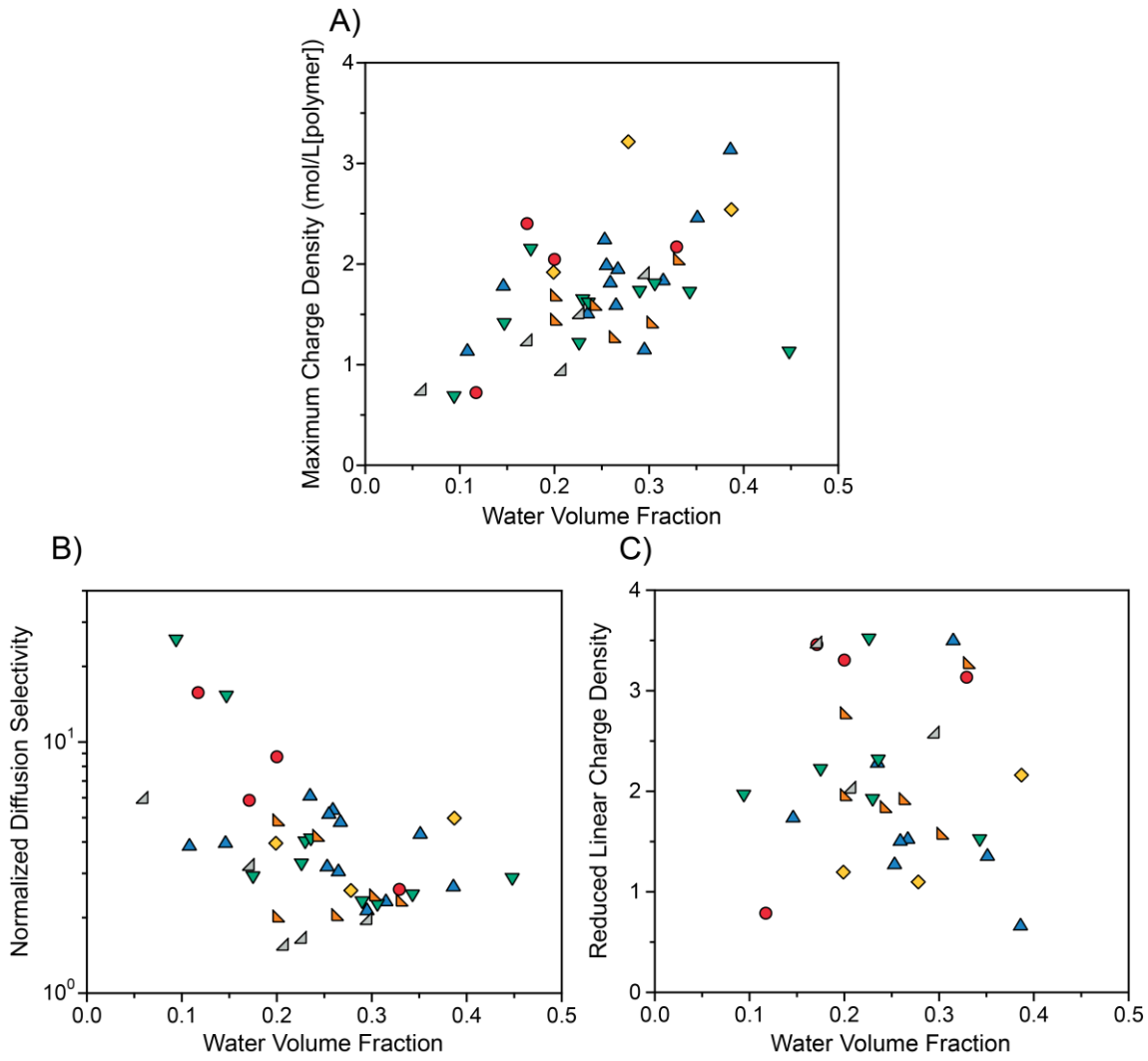
C.1 Supplemental Figures



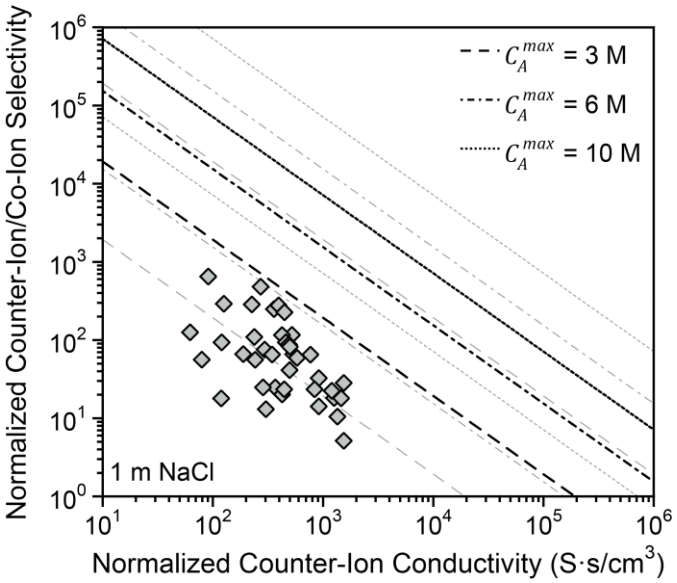
Appendix Figure C.1: The derivation of the Donnan-Meares-Manning model.



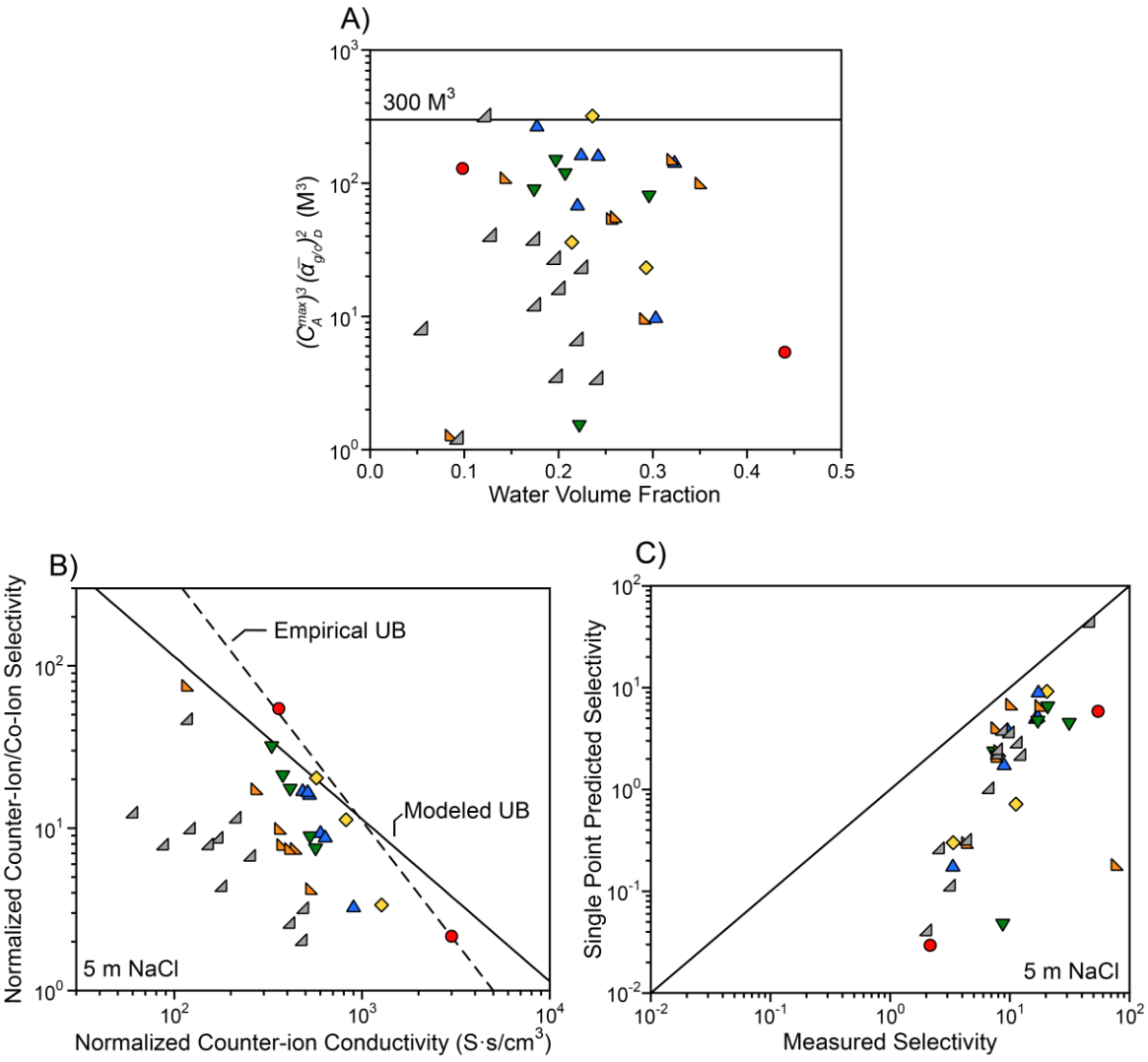
Appendix Figure C.2: Single-point model predictions. The normalized counter-ion/co-ion selectivity, $\bar{\alpha}_{g/c}$, predicted by the model vs. the experimentally determined value for each commercial membrane considered in this study. The predicted value was obtained using the individual inputs to Equation 5.5 for each membrane, including its $C_A^{max,t}$, $\left(\bar{\alpha}_{g/c}\right)_D$, ξ, and $\bar{\kappa}_g$. Membranes for which ξ could not be fit were assigned a value of $\xi = 0.754$ as discussed in Section C.4.1. Data colors and shapes correspond to the distance from the empirical upper bound; each membrane is represented by the same color and shape as in Figure 5.1 in the main body.



Appendix Figure C.3: Upper bound model inputs. The inputs to the intercept function of Equation 5.5 in the main body. A) C_A^{max} plotted against ϕ_w at 1 m NaCl. B) $\left(\bar{\alpha}_{g/c}\right)_D$ plotted against ϕ_w at 1 m NaCl. B) ξ plotted against ϕ_w at 1 m NaCl. Membranes for which ξ could not be fit were excluded from this plot. Data colors and shapes correspond to the distance from the empirical upper bound; each membrane is represented by the same color and shape as in Figure 5.1 in the main body.



Appendix Figure C.4: Additional model predictions future IEMs. Additional predictions for the upper bound of IEMs via Equation 5.5 using various input parameters beyond those outlined in Figure 5.3. Long dashes: $C_A^{max} = 3\ M$; mixed dashes: $C_A^{max} = 6\ M$; short dashes: $C_A^{max} = 10\ M$. The black lines represent the nominal case of $\left(\bar{\alpha}_{g/c}\right)_D^2/\xi = 10$, and the gray lines represent $\left(\bar{\alpha}_{g/c}\right)_D^2/\xi = 1$ or 100.



Appendix Figure C.5: Upper Bound Modeling for membranes contacted by 5 m NaCl. A) The intercept function for the Ideal Donnan/Mackie-Meares model, $(C_A^{max})^3\left(\bar{\alpha}_{g/c}\right)_D^2$, plotted against ϕ_w for 35 commercial membranes. The line indicates the representative intercept function for membranes that are near the upper bound, 300 M^3. B) The normalized counter-ion/co-ion selectivity, $\bar{\alpha}_{g/c}$, plotted against the normalized counter-ion conductivity, $\bar{\kappa}_g$, for 35 commercial membranes. The solid line indicates the predictions of Equation C.23 using an intercept function of 300 M^3. The dashed line represents an empirically drawn upper bound with $\lambda = 1.52$ and $\beta = 4.28 \times 10^5$. C) The normalized counter-ion/co-ion selectivity, $\bar{\alpha}_{g/c}$, predicted by the model vs. the experimentally determined value for each commercial membrane. The predicted values were obtained using the individual inputs to Equation C.23 for each membrane, including its $C_A^{max,t}$, $\left(\bar{\alpha}_{g/c}\right)_D$, and $\bar{\kappa}_g$. Data colors and shapes correspond to the distance from the empirical upper bound; each membrane is represented by the same color and shape in this figure. These colors and shapes were assigned independently from those used in the 1 m NaCl plots.

C.2 The Donnan-Meares-Manning Model for the Upper Bound

Due to the complex interdependence of IEM structure-property relationships, it is virtually impossible to condense the full models introduced in Chapter 3 into a concise equation that describes the trade-off between counter-ion conductivity and selectivity. This task is only made possible by introducing several reasonable assumptions beyond the assumptions of homogeneity and the mean field approximation used in the Donnan-Manning and Meares-Manning models. We first assume that the membrane is much more charged than the surrounding solution, i.e., $C_A^{m,w} \gg C_s^s$. In this regime, charge exclusion is well-maintained, leading to minimal co-ion sorption in the membrane ($C_g^{m,w} \gg C_c^{m,w}$ and $C_g^{m,w} \cong C_A^{m,w}$). This assumption can misrepresent weakly charged membranes, but we expect that membranes at the upper bound are likely to be highly charged, so we execute this assumption without much reservation. In this limit, the co-ion concentration in Equation 3.14 can be simplified via a 2-term Taylor series of the radical term:

$$\frac{C_c^{m,w}}{C_A^{m,w}} = \frac{1}{2} * \left(-1 + \sqrt{1 + \Gamma \left(\frac{2C_s^s}{C_A^{m,w}} \right)^2} \right) \cong \frac{1}{2} \left(-1 + \left(1 + \frac{\Gamma}{2} \left(\frac{2C_s^s}{C_A^{m,w}} \right)^2 \right) \right)$$

$$\frac{C_c^{m,w}}{C_A^{m,w}} \cong \Gamma \left(\frac{C_s^s}{C_A^{m,w}} \right)^2 \qquad \text{C.1}$$

To account for membrane non-idealities, we define Γ using Manning's counter-ion condensation theory. Since the majority of reported IEMs exhibit counter-ion condensation[426,528] ($\xi > 1$), we implement the appropriate form of Equation 3.20 to obtain:

$$\Gamma = \frac{(\gamma_\pm^s)^2}{\gamma_g^m \gamma_c^m} = \frac{(\gamma_\pm^s)^2 (C_A^{m,w} + C_c^{m,w})}{C_A^{m,w}/\xi + C_c^{m,w}} \exp\left(\frac{C_A^{m,w}/\xi}{C_A^{m,w}/\xi + 2C_c^{m,w}} \right) \qquad \text{C.2}$$

We can simplify Equation C.2 by again employing the highly charged IEM approximation. Based on the typically reported values for ξ[426,528] (also see Appendix Table B.1), we specify our claim to be: $C_c^{m,w}/C_A^{m,w} \ll 1/2\xi < 1$.

$$\Gamma = \frac{(\gamma_{\pm}^{s})^2(1 + C_c^{m,w}/C_A^{m,w})}{1/\xi + C_c^{m,w}/C_A^{m,w}} \exp\left(\frac{1/\xi}{1/\xi + 2\,C_c^{m,w}/C_A^{m,w}}\right) \cong \xi(\gamma_{\pm}^{s})^2 \exp(1) \qquad \text{C.3}$$

Combining these equations, we arrive at an analytical equation for the partitioning selectivity:

$$\left(\alpha_{g/c}\right)_K = \frac{C_g^{m,t}}{C_c^{m,t}} \cong \frac{C_A^{m,w}}{C_c^{m,w}} = \frac{1}{\Gamma}\left(\frac{C_A^{m,w}}{C_s^{s}}\right)^2 = \frac{1}{\xi \exp(1)}\left(\frac{C_A^{m,w}}{a_s^{s}}\right)^2 \qquad \text{C.4}$$

In this final step, we have again relied on the highly charged IEM approximation ($C_g^{m,t} \cong C_A^{m,t}$), neglecting the counter-ions that electrically balance the co-ions. The volume scales cancel out in the definition of partitioning selectivity, so the ratio of concentrations per total membrane volume, t, equals the same ratio of concentrations per water volume in the membrane, w. Additionally, the solution activity coefficient and concentration have been combined into a single term for the activity.

Although Equations 3.22 – 3.24 provide a framework to differentiate counter-ion diffusion from co-ion diffusion, we note that counter-ion diffusion remains one of the least-understood aspects of ion transport in IEMs. The presence of an adjustable parameter in these equations reflects the incomplete fundamental understanding of this topic. We explore the use of the condensed counter-ion diffusion framework in Section C.4.3; however, for simplicity, the normalized diffusion selectivity ($\left(\bar{\alpha}_{g/c}\right)_D$) is treated as an adjustable parameter in the derivation that follows. Because Equations 3.21 and 3.22 have been utilized to describe co-ion transport much more reliably than counter-ion transport, we define the counter-ion diffusion coefficient as a function of the co-ion diffusion coefficient.

$$\frac{D_g^m}{D_g^s} = \left(\bar{\alpha}_{g/c}\right)_D \frac{D_c^m}{D_c^s} \qquad \text{C.5}$$

With these assumptions, we combine the partition and normalized diffusion selectivities into an expression for $\bar{\alpha}_{g/c}$ per Equation 5.2:

$$\bar{\alpha}_{g/c} = \frac{\left(\bar{\alpha}_{g/c}\right)_D}{\xi \exp(1)}\left(\frac{C_A^{m,w}}{a_s^s}\right)^2 = \frac{\left(\bar{\alpha}_{g/c}\right)_D}{\xi \exp(1)}\left(\frac{C_A^{max}}{a_s^s}\right)^2 \frac{(1-\phi_w)^2}{\phi_w^2} \quad \text{C.6}$$

In this equation, the second definition implements Equation 4.8 to make all of the scaling with ϕ_w explicit.

A similar process can be used to derive a concise equation for $\bar{\kappa}_g$ in terms of the membrane structural parameters. First, the summation in Equation 3.21 is evaluated using only the second definition for $\xi > 1$. In the limit of $C_c^{m,w}/C_A^{m,w} \ll 1$, the series evaluates to a constant value (with the point (0,0) excluded).

$$A \cong \sum_{m_1=-\infty}^{+\infty} \sum_{m_2=-\infty}^{+\infty} (\pi(m_1^2 + m_2^2) + 1)^{-2} = 0.4033 \quad \text{C.7}$$

Thus, the co-ion diffusivity in Equation 3.22 becomes:

$$\frac{D_c^m}{D_c^s} = \frac{1}{1.16}\left(\frac{\phi_w}{2-\phi_w}\right)^2 \quad \text{C.8}$$

The counter-ion diffusivity is obtained by combining Equations C.5 and C.8. We can then plug these definitions into Equation 5.1:

$$\bar{\kappa}_g = \frac{F^2}{RT} C_g^{m,t} \frac{D_g^m}{D_g^s} \cong \frac{F^2\left(\bar{\alpha}_{g/c}\right)_D}{1.16RT} C_A^{m,t} \left(\frac{\phi_w}{2-\phi_w}\right)^2$$
$$\bar{\kappa}_g \cong \frac{F^2\left(\bar{\alpha}_{g/c}\right)_D}{1.16RT} C_A^{max} \frac{\phi_w^2(1-\phi_w)}{(2-\phi_w)^2} \quad \text{C.9}$$

Here, we again approximate that $C_g^{m,t} \cong C_A^{m,t}$ and use Equation 4.7 to introduce C_A^{max}.

Equations C.6 and C.9 represent the complete model contribution to predicting the upper bound components individually, with the total scaling of C_A^{max} and ϕ_w completely explicit. Comparing these equations, it is apparent that three scaling relationships invoke ϕ_w: the $\phi_w^{\pm 2}$ terms dominate for relatively low ϕ_w, the $(1-\phi_w)$ terms dominate for relatively high ϕ_w, and the $(2-$

ϕ_w) term never contributes a dominant ϕ_w dependance. Because most IEMs on the market and in development have $\phi_w < 0.5$ (Chapter 4), we conclude that the $\phi_w^{\pm 2}$ scaling is the most important water content effect in both equations. Interestingly, the $\phi_w^{\pm 2}$ scaling in Equation C.6 stems from charge dilution, whereas in Equation C.9, it comes from the tortuosity effects. The equal and opposite scaling of the dilution and tortuosity effects with ϕ_w results in the trade-off between counter-ion conductivity and selectivity. Substituting for this $\phi_w^{\pm 2}$ dependence, we combine Equations C.6 and C.9into the upper bound relationship:

$$\bar{\alpha}_{g/c} = \frac{F^2 (C_A^{max})^3 \left(\bar{\alpha}_{g/c}\right)_D^2}{3.14 RT \xi a_s^{s\,2}} \frac{1}{\bar{\kappa}_g} \frac{(1-\phi_w)^3}{(2-\phi_w)^2} \qquad \text{C.10}$$

Or, visualized for the log-log plot typically used to describe this trade-off:

$$\log\left(\bar{\alpha}_{g/c}\right) = \log\left(\frac{F^2 (C_A^{max})^3 \left(\bar{\alpha}_{g/c}\right)_D^2}{12.56 RT \xi a_s^{s\,2}}\right) - \log\left(\bar{\kappa}_g\right) + \log\left(\frac{4(1-\phi_w)^3}{(2-\phi_w)^2}\right) \qquad \text{C.11}$$

In deriving Equation C.11 from the constituent models, the only added assumption so far has been that the high performing membranes of the upper bound are much more densely charged than the surrounding solution. However, this equation still contains a term that depends on ϕ_w in the final form. This term and its coefficient have been separated from the remainder of the equation because they become insignificant as $\phi_w \to 0$. Most commercialized and lab-made membranes have moderate or low ϕ_w (Chapter 4), so it is reasonable to expect that the ϕ_w term should be relatively small for the relevant range of the upper bound. To make the scaling on ϕ_w entirely implicit within this equation, we approximate the limit of small ϕ_w to obtain:

$$\log\left(\bar{\alpha}_{g/c}\right) = \log\left(\frac{F^2 (C_A^{max})^3 \left(\bar{\alpha}_{g/c}\right)_D^2}{12.56 RT \xi a_s^{s\,2}}\right) - \log\left(\bar{\kappa}_g\right) \qquad \text{C.12}$$

We note that the assumption of $\phi_w \to 0$ replaces the previous assumption of $C_A^{m,w} \gg C_s^s$. If $C_A^{max} \neq 0$, letting $\phi_w \to 0$ recovers the highly charged membrane approximation automatically, because charge concentration *per water in the membrane* is the metric that must exceed the concentration of the surrounding salt solution. Making this assumption earlier in the derivation would also take the diffusion coefficients of ions in the membrane to 0, so it is crucial that the primary scaling of ϕ_w has been accounted for (Equation C.10), and that we only take $\phi_w \to 0$ in the secondary-scaling terms which approach finite values at low ϕ_w.

C.3 The Upper Bound Model for Composite Membranes

The equations in Section 3.4 are valid for homogeneous IEMs, but many commercial IEMs have composite structures. The model must be modified to account for the more complicated structures of composite membranes before it can be used to predict the trade-off and upper bound for commercial IEMs. This section relates the overall counter-ion conductivity and selectivity of composite membranes to those of its constituent, homogeneous ion-exchange phase using the porosity, ε_b, and tortuosity, τ_b, of the support material and the equations provided in Section 3.6.

The modified equations for $\bar{\alpha}_{g/c}$ and $\bar{\kappa}_g$, which incorporate the effects of the mechanical support, are given by:

$$\bar{\alpha}_{g/c} = \left(\frac{C_g^{m,p}\varepsilon_b}{C_c^{m,p}\varepsilon_b}\right)\left(\frac{D_g^{m,p}/\tau_b^2}{D_c^{m,p}/\tau_b^2}\frac{D_c^s}{D_g^s}\right) = \left(\frac{C_g^{m,p}}{C_c^{m,p}}\right)\left(\frac{D_g^{m,p}}{D_c^{m,p}}\frac{D_c^s}{D_g^s}\right) \quad \text{C.13}$$

$$\bar{\kappa}_g = \frac{F^2}{RT}C_g^{m,p}\varepsilon_b\frac{D_g^{m,p}/\tau_b^2}{D_g^s} = \frac{F^2}{RT}C_g^{m,t}\frac{D_g^{m,p}}{D_g^s}\frac{\varepsilon_b}{\tau_b^2} \quad \text{C.14}$$

By accounting for the effects of the porosity and tortuosity of the support, these equations define the performance of the total composite membrane based on properties of the constituent ion-exchange polymer. The support porosity and tortuosity affect the counter-ions and co-ions equally,

so the counter-ion/co-ion selectivity remains unchanged in Equation C.13. $\varepsilon_b < 1$ and $\tau_b > 1$, so the counter-ion conductivity of the composite in Equation C.14 is reduced compared to the constituent ion-exchange polymer. Using the process outlined in Section 3.6, we first model the trade-off in the constituent ion-exchange polymer before recasting the equations in terms of the composite IEM. Following the same steps, we arrive at analogues to Equations C.6 and C.9:

$$\bar{\alpha}_{g/c} = \frac{\left(\bar{\alpha}_{g/c}\right)_D}{\xi \exp(1)} \left(\frac{C_A^{max,p}}{a_s^s}\right)^2 \frac{\left(1-\phi_w^p\right)^2}{(\phi_w^p)^2} \tag{C.15}$$

$$\bar{\kappa}_g = \frac{F^2\left(\bar{\alpha}_{g/c}\right)_D}{1.16RT} C_A^{max,p} \frac{(\phi_w^p)^2(1-\phi_w^p)}{\left(2-\phi_w^p\right)^2} \frac{\varepsilon_b}{\tau_b^2} \tag{C.16}$$

These equations have different nomenclature and an additional ε_b/τ_b^2 term but are otherwise identical to the results in Section C.2.

Most commercial IEM structures and supports are kept proprietary, so $C_A^{max,p}$ and ϕ_w^p are usually not available. The final step in the derivation is to recast Equations C.15 and C.16 in terms of the composite membrane properties, which are the experimentally accessible parameters. Using Equations 3.26 and 3.27, we obtain:

$$\bar{\alpha}_{g/c} = \frac{\left(\bar{\alpha}_{g/c}\right)_D}{\xi \exp(1)} \left(\frac{C_A^{max,t}}{\varepsilon_b a_s^s}\right)^2 \frac{\left(1 - \frac{\phi_w^t}{\varepsilon_b}\right)^2}{\left(\frac{\phi_w^t}{\varepsilon_b}\right)^2} \qquad \text{C.17}$$

$$\bar{\alpha}_{g/c} = \frac{\left(\bar{\alpha}_{g/c}\right)_D}{\xi \exp(1)} \left(\frac{C_A^{max,t}}{\varepsilon_b a_s^s}\right)^2 \frac{(\varepsilon_b - \phi_w^t)^2}{(\phi_w^t)^2}$$

$$\bar{\kappa}_g = \frac{F^2\left(\bar{\alpha}_{g/c}\right)_D}{1.16RT} \frac{C_A^{max,t}}{\varepsilon_b} \frac{\left(\frac{\phi_w^t}{\varepsilon_b}\right)^2 \left(1 - \frac{\phi_w^t}{\varepsilon_b}\right)}{\left(2 - \frac{\phi_w^t}{\varepsilon_b}\right)^2} \frac{\varepsilon_b}{\tau_b^2} \qquad \text{C.18}$$

$$\bar{\kappa}_g = \frac{F^2\left(\bar{\alpha}_{g/c}\right)_D}{1.16RT} \frac{C_A^{max,t}}{\varepsilon_b \tau_b^2} \frac{(\phi_w^t)^2(\varepsilon_b - \phi_w^t)}{(2\varepsilon_b - \phi_w^t)^2}$$

Combining Equations C.17 and C.18 results in the upper bound equations for composite IEMs:

$$\bar{\alpha}_{g/c} = \frac{F^2 (C_A^{max,t})^3 \left(\bar{\alpha}_{g/c}\right)_D^2}{3.14RT\xi a_s^{s\,2} \tau_b^2 \varepsilon_b^3} \frac{1}{\bar{\kappa}_g} \frac{(\varepsilon_b - \phi_w^t)^3}{(2\varepsilon_b - \phi_w^t)^2} \qquad \text{C.19}$$

$$\log\left(\bar{\alpha}_{g/c}\right) = \log\left(\frac{F^2 (C_A^{max,t})^3 \left(\bar{\alpha}_{g/c}\right)_D^2}{12.56RT\xi a_s^{s\,2} \tau_b^2\, \varepsilon_b^2}\right) - \log\left(\bar{\kappa}_g\right) + \log\left(\frac{4(\varepsilon_b - \phi_w^t)^3}{\varepsilon_b (2\varepsilon_b - \phi_w^t)^2}\right) \qquad \text{C.20}$$

In Equation C.20, the final term contains all the dependence on ϕ_w^t such that the entire term approaches 0 in the limit of $\phi_w^t \to 0$.

In the final step of letting $\phi_w^t \to 0$, some of the dependence on ε_b disappears; however, ε_b and τ_b remain in the final expression. For the same reasons that $C_A^{max,p}$ and ϕ_w^p are inaccessible for proprietary IEMs, so are ε_b and τ_b. However, there are mathematical relationships that attempt to link the tortuosity of a porous medium to its void fraction[529]. For random porous media in which the obstructions to transport are modeled as random cylinders, the widely used Bruggemen model yields[530]:

$$\tau_b \cong \varepsilon_b^{-1} \text{ or } \tau_b \varepsilon_b = 1 \qquad \text{C.21}$$

Invoking the Bruggeman model removes both variables from the first term of Equation C.20. The Bruggeman model is often used for its simplicity[531]; however, models with broader applicability see more frequent use in applied research[532,533]. Although such relationships could be more useful for modeling a specific membrane backing of known porosity and unknown tortuosity, the Bruggeman model allows the conductivity/selectivity trade-off model to be resolved with extreme generality. Further, we do not believe that the use of the Bruggeman model introduces significant error beyond that introduced by the low water content approximation. It is interesting to note that Equation C.21 does not remove the impact of backing effects on the ion selectivity (Equation C.18), the counter-ion conductivity (Equation C.19), or the trade-off in high water content membranes (the final term of Equation C.21). Only the trade-off for composite IEMs with $\phi_w^t \sim 0$ becomes independent of the backing porosity and tortuosity using this approximation.

This final step results in:

$$\log\left(\bar{\alpha}_{g/c}\right) = \log\left(\frac{F^2 (C_A^{max,t})^3 \left(\bar{\alpha}_{g/c}\right)_D^2}{12.56 RT \xi a_s^{s\,2}}\right) - \log\left(\bar{\kappa}_g\right) \qquad \text{C.22}$$

Analyzing Equations C.12 and C.22, it is apparent that composite and homogeneous membranes can be compared with ease. As long as C_A^{max} is defined per the total membrane volume, all composite backing effects on the upper bound have been accounted for.

C.4 Alternate Forms of the Upper Bound Model

C.4.1 Removing Point-Line Electrostatics (Ideal Donnan Model)

The upper bound model presented in Section C.3 can be simplified by removing the point-line electrostatic effects that are described by Manning's counter-ion condensation framework. This modification, which may be of interest if ξ is not known or attainable for a given membrane,

sacrifices accuracy to obtain simpler model inputs. This "ideal" upper bound model is obtained by using Equation 3.14 with $\Gamma = 1$ (the Ideal Donnan, or ID, model) and Equation 3.15 (the Mackie-Meares model) instead of Equation 3.22. The functional form of this modification is obtained by simply removing ξ, using C_s^s instead of a_s^s, and adjusting the numerical constant. The final result is given by:

$$\log\left(\bar{\alpha}_{g/c}\right) = \log\left(\frac{F^2 (C_A^{max,t})^3 \left(\bar{\alpha}_{g/c}\right)_D^2}{4RTC_s^{s\,2}}\right) - \log\left(\bar{\kappa}_g\right) \qquad \text{C.23}$$

This equation can also be recovered from Equation C.22 by setting $\xi = \left(3.14\left(\gamma_{\pm}^s\right)^2\right)^{-1}$, or 0.754 for 1 m NaCl. Equation C.23 can also be used for homogeneous (i.e., single phase) membranes where $C_A^{max,t} = C_A^{max,p} = C_A^{max}$.

The simplified Ideal Donnan/Mackie-Meares model is also more useful than the Donnan-Manning model for highly concentrated salt solutions. The accuracy of the Donnan-Manning model decreases at high external salt solution concentrations (e.g., greater than 1 m for typical IEMs), so theoretical values of ξ do not usually result in good predictions of ion partitioning. Interestingly, the Ideal Donnan and Modified Manning models often yield better predictions of experimental ion partitioning data at high salt concentrations[426,534]. This result is reasonable because at high external solution salt concentrations the nonidealities in the membrane are less attributable to long-range electrostatics and are instead more linked to water-starvation, ion-pairing, and other effects not captured by Debye-Hückel equations. Concentrated aqueous solutions are qualitatively similar to the interior of an ion-exchange membrane, where water is often in short supply and ions are frequently found in various forms of paired structures. At high salt concentrations, point-line electrostatics are less relevant, and the short-range point-point electrostatics present in solution dominate in the membrane phase.

We demonstrate the ability of Equation C.23 to predict the conductivity/selectivity trade-off for IEMs contacted by highly concentrated brines in Appendix Figure C.5. This figure compares the modeled upper bound to $\bar{\alpha}_{g/c}$ and $\bar{\kappa}_g$ data collected for commercial membranes contacted by 5 m NaCl in Chapter 4. In this case, Equation C.23 can be obtained from Equation C.22 by substituting in $\xi = 0.432$, which uses $\gamma_{\pm}^{s} = 0.8586$ for 5 m NaCl at 22 ºC[383,384].

Appendix Figure C.5A reveals that the highest performing materials do not necessarily have the largest intercept functions, as was the case for IEMs contacted by 1 m NaCl. However, Appendix Figure C.5B demonstrates that Equation C.23 still predicts the location of the upper bound line with reasonable accuracy. This apparent contradiction is rationalized by comparing the accuracy of the model for single membranes in Appendix Figure C.5C. The Ideal Donnan/Mackie-Meares model, in its simplicity, does not accurately capture the behavior of membranes broadly in the way that the Donnan-Meares-Manning model does (c.f. Appendix Figure C.2); however, the model does predict the performance of the highly selective membranes reasonably well. For membranes with lower selectivities, Equation C.23 predicts vastly lower selectivities than the experimentally determined values. The high-selectivity region of the trade-off is modeled reasonably well, and the high-conductivity region of the trade-off appears to be coincidentally near the upper bound model. These membranes, in particular, are likely described poorly by the model due to the breakdown of the highly-charged membrane assumption. For many of the highly-conductive membranes, the 5 m NaCl solution concentration exceeds the fixed charge concentration of the membrane. Perfect agreement between Equation C.23 and the 5 m NaCl data should not be expected given the broad difficulty in modeling ion partitioning in IEMs that sorb excessive amounts of salt[426], but these results are encouraging given the simplicity of the Ideal Donnan/Mackie-Meares models.

C.4.2 Estimating the Reduced Linear Charge Density ξ

For homogeneous IEMs of known structure, Equations 3.16 and 3.18 relate the reduced linear charge density, ξ, to the distance between charge groups, b, and dielectric constants, ε^w and ε^p. Using these equations, the upper bound model can be expressed in terms of b of ξ. Combining Equation 3.16 and 3.18 with Equation C.20 yields:

$$\bar{\alpha}_{g/c} = \frac{4\pi\varepsilon_0 k_B T b F^2 \left(\varepsilon^w \phi_w^t + \varepsilon^p (1-\phi_w^t)\right)(C_A^{max,t})^3 \left(\bar{\alpha}_{g/c}\right)_D^2}{3.14 e^2 R T a_s^{s\,2} \tau_b^2 \varepsilon_b^3} \frac{1}{\bar{\kappa}_g} \frac{(\varepsilon_b - \phi_w^t)^3}{(2\varepsilon_b - \phi_w^t)^2} \qquad \text{C.24}$$

This equation can be simplified by substituting $R/k_B = F/e = N_{AV}$, where N_{AV} is Avogadro's number. Additionally, the T dependence cancels out, and we can approximate that $\pi/3.14 \cong 1$. This final approximation is not exact; truncating fewer digits reveals the ratio to be $\pi/3.1405 \cong 1$. Isolating the water content dependence and performing these simplifications yields:

$$\bar{\alpha}_{g/c} = \frac{\varepsilon_0 \varepsilon^p N_{AV} b (C_A^{max,t})^3 \left(\bar{\alpha}_{g/c}\right)_D^2}{a_s^{s\,2} \tau_b^2 \varepsilon_b^2} \frac{1}{\bar{\kappa}_g} \frac{4\left(\varepsilon^w \phi_w^t + \varepsilon^p (1-\phi_w^t)\right)(\varepsilon_b - \phi_w^t)^3}{\varepsilon_b \varepsilon^p (2\varepsilon_b - \phi_w^t)^2} \qquad \text{C.25}$$

In Equation C.25, the water content has again been grouped into the final portion of the equation, along with constants such that it can be neglected in the limit of $\phi_w^t \to 0$. By invoking this approximation and relying on Equation C.21 for the relationship between tortuosity and porosity, the upper bound equation becomes:

$$\log\left(\bar{\alpha}_{g/c}\right) = \log\left(\frac{\varepsilon_0 \varepsilon^p N_{AV} b \left(C_A^{max,t}\right)^3 \left(\bar{\alpha}_{g/c}\right)_D^2}{a_s^{s\,2}}\right) - \log\left(\bar{\kappa}_g\right) \qquad \text{C.26}$$

Equation C.26 can also be used for homogeneous (i.e., single phase) membranes where $C_A^{max,t} = C_A^{max,p} = C_A^{max}$.

C.4.3 Condensed Counter-Ion Diffusion Model

The various versions of the model presented in the previous sections have treated the normalized diffusion selectivity as the adjustable parameter. In this section, we relax this

assumption and employ the full ion diffusion model described in Section 3.4. Based on the limited data available for IEMs with modeled counter-ion diffusion[426], the ratio $D_{g,c}^{m}/D_{g,u}^{m}$ may be a more universal selection for the fitting parameter than the value α which was previously proposed[428].

The full ion diffusion model provides expressions for both the counter-ion (Equations 3.22 – 3.24) and co-ion (just Equation 3.22) diffusion coefficients in the membrane[426]. Inserting these equations into the definition for the normalized diffusion selectivity yields:

$$\left(\bar{\alpha}_{g/c}\right)_D = \frac{D_g^m}{D_c^m}\frac{D_c^s}{D_g^s} = \left(f_{g,u} + f_{g,c}\frac{D_{g,c}^m}{D_{g,u}^m}\right)\frac{\left(\left(\frac{\phi_w}{2-\phi_w}\right)^2\left(1-\frac{A}{3}\right)\right)}{\left(\left(\frac{\phi_w}{2-\phi_w}\right)^2\left(1-\frac{A}{3}\right)\right)} \qquad \text{C.27}$$

The uncondensed counter-ions do not contribute to any diffusion selectivity because they are predicted to be subject to the same diffusion constraints as the co-ions. These terms cancel out, leaving only the adjustable parameter, $D_{g,c}^{m}/D_{g,u}^{m}$, and the fractions of condensed and uncondensed counter-ions. The fractions of condensed and uncondensed counter-ions are given by Equation 3.19. Combining this equation with Equation C.27 and invoking the highly charged membrane approximation results in:

$$\left(\bar{\alpha}_{g/c}\right)_D = \frac{1}{\xi}\left(1 + (\xi - 1)\frac{D_{g,c}^m}{D_{g,u}^m}\right) \qquad \text{C.28}$$

There is no additional dependence of $\left(\bar{\alpha}_{g/c}\right)_D$ on the water content, so Equation C.28 can be inserted directly into the final upper bound equation to yield:

$$\log\left(\bar{\alpha}_{g/c}\right) = \log\left(\frac{F^2\left(C_A^{max,t}\right)^3\left(1 + (\xi-1)\,D_{g,c}^m/D_{g,u}^m\right)^2}{12.56RT\xi^3 {a_s^s}^2}\right) - \log\left(\bar{\kappa}_g\right) \qquad \text{C.29}$$

C.4.4 Upper Bound Model for Multivalent Ions

For clarity and brevity, multivalent ions were not considered in the primary derivation of the counter-ion conductivity/selectivity upper bound model in Section C.2. However, multivalent ions are present in many practical applications, most commonly as 2-1 salts (such as $MgCl_2$) or 1-2 salts (such as Na_2SO_4). An upper bound model that accounts for the valence of the ions would be useful for such cases and could help to better understand the scaling laws uncovered in this analysis. In this section, we re-introduce the constituent models in their valence-explicit forms to derive a valence-explicit upper bound model.

The counter-ion/co-ion selectivity and counter-ion conductivity depend on the valence of the ions. The full definitions for these parameters from Section 3.1 are given by:

$$\bar{\alpha}_{g/c} = \left(\alpha_{g/c}\right)_K \left(\bar{\alpha}_{g/c}\right)_D = \left(\left|\frac{z_g}{z_c}\right| \frac{C_g^{m,t}}{C_c^{m,t}}\right)\left(\left|\frac{z_g}{z_c}\right| \frac{D_g^m}{D_c^m}\frac{D_c^s}{D_g^s}\right) \tag{C.30}$$

$$\bar{\kappa}_g = \frac{z_g^2 F^2}{RT} C_g^{m,t} \frac{D_g^m}{D_g^s} \tag{C.31}$$

Equation C.30 demonstrates that the normalized selectivity represents the normalized current consumed to transport counter-ions over co-ions. The normalized counter-ion conductivity represents the normalized current consumed to move counter-ions across the membrane. Setting the valences to unity recovers Equations 5.1 and 5.2, where the distinction between current consumption and ion passage is trivial.

To derive the valence-explicit upper bound model, we begin by considering ion partitioning in the membrane. The full form of the Donnan equilibrium condition in Section 3.2 is given by Equations 3.10 or 3.11, the latter of which is reproduced below:

$$\left(\left|\frac{z_A}{z_g}\right| C_A^{m,w} + \left|\frac{z_c}{z_g}\right| C_c^{m,w}\right)^{\nu_g} (C_c^{m,w})^{\nu_c} = \Gamma \nu_g^{\nu_g} \nu_c^{\nu_c} (C_s^s)^{(\nu_g+\nu_c)} \tag{C.32}$$

where ν_i represents the number of species i present in the electroneutral salt. ν_g and ν_c therefore depend on the ratio $|z_g/z_c|$. The full definition of the Donnan ideality ratio must also be utilized: $\Gamma = \left(\gamma_{\pm}^{s}\right)^{(\nu_g+\nu_c)} / \left(\gamma_g^m\right)^{\nu_g} \left(\gamma_c^m\right)^{\nu_c}$. For the case of a 1-1 electrolyte, Equation C.32 reduces into a quadratic equation for $C_c^{m,w}$; however, for an arbitrary electrolyte, this is not the case. To isolate $C_c^{m,w}$, the highly charged membrane approximation must be invoked at this stage, neglecting those counter-ions which electroneutralize co-ions. Doing so yields:

$$C_c^{m,w} = \sqrt[\nu_c]{\Gamma \frac{\nu_g^{\nu_g} \nu_c^{\nu_c} \left(C_s^s\right)^{(\nu_g+\nu_c)}}{\left(\left|\frac{z_A}{z_g}\right| C_A^{m,w}\right)^{\nu_g}}} \qquad \text{C.33}$$

Combining Equation C.33 with Equation C.30 and invoking the highly charged membrane approximation yields an expression for the partitioning selectivity:

$$\begin{gathered} \left(\alpha_{g/c}\right)_K = \left(\left|\frac{z_g}{z_c}\right| \frac{C_g^{m,t}}{C_c^{m,t}}\right) \cong \left(\left|\frac{z_g}{z_c}\right| \left|\frac{z_A}{z_g}\right| \frac{C_A^{m,w}}{C_c^{m,w}}\right) \\ \left(\alpha_{g/c}\right)_K = \left|\frac{z_g}{z_c}\right| \Gamma^{-\frac{1}{\nu_c}} \nu_g^{-\frac{\nu_g}{\nu_c}} \nu_c^{-1} \left(\left|\frac{z_A}{z_g}\right| \frac{C_A^{m,w}}{C_s^s}\right)^{\left(1+\frac{\nu_g}{\nu_c}\right)} \end{gathered} \qquad \text{C.34}$$

To resolve Γ, Manning's equations must also be parameterized for the ion valence[426]. This task requires the introduction of the critical parameter for the onset of counter-ion condensation, $\xi_{crit} = 1/|z_g z_A|$. The equations are rescaled to consider the ratio of ξ/ξ_{crit}, where the ξ_{crit} term reduces to unity for monovalent counter-ions and fixed charge groups (See Section 3.4). Using these equations and the highly charged membrane approximation, we derive an expression for Γ:

$$\Gamma = \left(\frac{\xi}{\xi_{crit}}\right)^{\nu_g} \exp\left[\frac{\nu_g}{2} + \frac{\nu_c}{2}\left(\frac{z_c}{z_g}\right)^2\right] \left(\gamma_{\pm}^{s}\right)^{(\nu_g+\nu_c)} \qquad \text{C.35}$$

Plugging Γ into Equation C.34 results in:

$$\left(\alpha_{g/c}\right)_K = \left|\frac{z_g}{z_c}\right| \left(\left|\frac{z_A}{z_g}\right| \frac{C_A^{m,w}}{a_s^s}\right)^{\left(1+\frac{\nu_g}{\nu_c}\right)} \left(\frac{\xi}{\xi_{crit}}\right)^{-\frac{\nu_g}{\nu_c}} \exp\left[-\frac{1}{2}\frac{\nu_g}{\nu_c}\left(1+\frac{\nu_g}{\nu_c}\right)\right] \nu_g^{-\frac{\nu_g}{\nu_c}} \nu_c^{-1} \qquad \text{C.36}$$

where we have combined the solution activity coefficients with the solution concentration and made use of the relationship $\frac{\nu_g}{\nu_c} = -\frac{z_c}{z_g}$. To condense the notation, we introduce a change of variable: $\lambda = \left(1+\frac{\nu_g}{\nu_c}\right)/2$. As before, the diffusion selectivity is treated as an adjustable parameter, so the normalized selectivity is given by:

$$\bar{\alpha}_{g/c} = \left(\left|\frac{z_A}{z_g}\right| \frac{C_A^{m,w}}{\nu_g a_s^s}\right)^{2\lambda} \left(\frac{\xi}{\xi_{crit}}\right)^{1-2\lambda} \exp[\lambda - 2\lambda^2] \left(\bar{\alpha}_{g/c}\right)_D \qquad \text{C.37}$$

The charge and water content dependences are made explicit via Equation 4.8:

$$\bar{\alpha}_{g/c} = \left(\left|\frac{z_A}{z_g}\right| \frac{C_A^{max}}{\nu_g a_s^s}\right)^{2\lambda} \left(\frac{\xi}{\xi_{crit}}\right)^{1-2\lambda} \exp[\lambda - 2\lambda^2] \left(\bar{\alpha}_{g/c}\right)_D \left(\frac{1-\phi_w}{\phi_w}\right)^{2\lambda} \qquad \text{C.38}$$

The treatment of $\bar{\kappa}_g$ changes less when making the valence explicit. The obstruction portion of the model has no hidden valence scaling. The electrostatic friction components, however, must be rewritten. Within the highly charged membrane approximation, the valence-explicit forms of these equations (provided in Section 3.4) are necessary. However, the summation result of Equation C.7 is still valid, so the equation for the co-ion diffusion coefficients becomes:

$$\frac{D_c^m}{D_c^s} = \left(\frac{\phi_w}{2-\phi_w}\right)^2 \left(1 - \frac{1}{7.44}\left(\frac{z_c}{z_g}\right)^2\right) \qquad \text{C.39}$$

Using the co-ion diffusivity and $\left(\bar{\alpha}_{g/c}\right)_D$ to approximate the counter-ion diffusion contribution to $\bar{\kappa}_g$ and invoking the highly charged membrane approximation yields:

$$\bar{\kappa}_g = \frac{|z_g z_c| F^2}{RT} \left|\frac{z_A}{z_g}\right| C_A^{m,t} \left(\bar{\alpha}_{g/c}\right)_D \left(1 - \frac{1}{7.44}\left(\frac{z_c}{z_g}\right)^2\right) \left(\frac{\phi_w}{2-\phi_w}\right)^2 \qquad \text{C.40}$$

And substituting for C_A^{max}:

$$\bar{\kappa}_g = \frac{z_c z_A F^2}{RT} C_A^{max} \left(\bar{\alpha}_{g/c}\right)_D \left(1 - \frac{1}{7.44}\left(\frac{z_c}{z_g}\right)^2\right) \frac{\phi_w^2 (1-\phi_w)}{(2-\phi_w)^2} \qquad \text{C.41}$$

To combine Equations C.38 and C.41, the dominant ϕ_w scaling for low water content membranes will still provide the most appropriate substitution. However, the exponents are no longer equal-and-opposite. To enable this substitution, we introduce λ into Equation C.41. We also rearrange the equation to group factors of $-z_c/z_g$ into ν_g/ν_c and then λ. The result is:

$$\bar{\kappa}_g^{\lambda} = \left(\frac{z_c z_A F^2}{RT}\right)^{\lambda} (C_A^{max})^{\lambda} \left(\bar{\alpha}_{g/c}\right)_D^{\lambda} \left(1 - \frac{(2\lambda-1)^2}{7.44}\right)^{\lambda} \frac{\phi_w^{2\lambda} (1-\phi_w)^{\lambda}}{(2-\phi_w)^{2\lambda}} \qquad \text{C.42}$$

This equation recovers the equal-and-opposite water content scaling and allows a direct substitution for $\phi_w^{2\lambda}$ into the expression for the normalized selectivity. Grouping terms without simplifying, this upper bound equation becomes:

$$\bar{\alpha}_{g/c} = \left(\left(\frac{z_A}{z_g}\right)^2 \frac{z_c z_A F^2}{RT\left(\nu_g a_s^s\right)^2}\right)^{\lambda} \left(1 - \frac{(2\lambda-1)^2}{7.44}\right)^{\lambda} \exp[\lambda - 2\lambda^2] * \\ (C_A^{max})^{3\lambda} \left(\frac{\xi}{\xi_{crit}}\right)^{1-2\lambda} \left(\bar{\alpha}_{g/c}\right)_D^{\lambda+1} \left(\bar{\kappa}_g\right)^{-\lambda} \frac{(1-\phi_w)^{3\lambda}}{(2-\phi_w)^{2\lambda}} \qquad \text{C.43}$$

It is natural to group z_A with the membrane charge content, and because z_c and z_A have the same sign by definition, we only need the absolute value for each of these valences even when separated (z_A^3/z_c is always positive). We then group the numerical functions of λ into the single term because it has no scaling on any other parameters. For compactness, we isolate this function of λ as B_λ.

$$\bar{\alpha}_{g/c} = \left(\frac{\mathrm{B}_\lambda F^2}{|z_g| RT\left(\nu_g a_s^s\right)^2}\right)^{\lambda} (|z_A| C_A^{max})^{3\lambda} \left(\frac{\xi}{\xi_{crit}}\right)^{1-2\lambda} * \\ \left(\bar{\alpha}_{g/c}\right)_D^{\lambda+1} \left(\bar{\kappa}_g\right)^{-\lambda} \left(\frac{4(1-\phi_w)^3}{(2-\phi_w)^2}\right)^{\lambda} \qquad \text{C.44}$$

$$\mathrm{B}_\lambda = \frac{2\lambda - 1}{4}\left(1 - \frac{(2\lambda-1)^2}{7.44}\right)\exp[1-2\lambda]$$

$$\mathrm{B}_\lambda = \frac{1}{4}\left|\frac{z_c}{z_g}\right|\left(1 - \frac{1}{7.44}\left(\frac{z_c}{z_g}\right)^2\right)\exp\left(\frac{z_c}{z_g}\right) \quad \text{C.45}$$

Introducing $\lambda = 1$ in Equation C.45 yields $1/12.56$, which recovers the numerical constant in Equation C.12 for 1:1 electrolytes.

To adapt Equation C.45 to composite membranes, the same process as in Section C.3 can be followed. Equations C.38 and C.41 do not differ in their concentration and diffusion coefficient scaling, so the added factor of ε_b/τ_b^2 in $\bar{\kappa}_g$ remains unchanged. In the new substitution, this ratio is therefore raised to the power of λ. The final step is to recast the membrane properties to be those of the total composite membrane, yielding:

$$\bar{\alpha}_{g/c} = \left(\frac{\mathrm{B}_\lambda F^2}{|z_g| RT\left(\nu_g a_s^s\right)^2}\right)^\lambda \left(\frac{|z_A| C_A^{max,t}}{\varepsilon_b}\right)^{3\lambda} \left(\frac{\xi}{\xi_{crit}}\right)^{1-2\lambda} * \left(\bar{\alpha}_{g/c}\right)_D^{\lambda+1} \left(\bar{\kappa}_g\right)^{-\lambda} \left(\frac{4(\varepsilon_b - \phi_w^t)^3}{\varepsilon_b(2\varepsilon_b - \phi_w^t)^2}\right)^\lambda \left(\frac{\varepsilon_b}{\tau_b^2}\right)^\lambda \quad \text{C.46}$$

Collecting terms and employing Equation C.21 to eliminate τ_b results in:

$$\bar{\alpha}_{g/c} = \left(\frac{\mathrm{B}_\lambda F^2}{|z_g| RT\left(\nu_g a_s^s\right)^2}\right)^\lambda \left(|z_A| C_A^{max,t}\right)^{3\lambda} \left(\frac{\xi}{\xi_{crit}}\right)^{1-2\lambda} * \left(\bar{\alpha}_{g/c}\right)_D^{\lambda+1} \left(\bar{\kappa}_g\right)^{-\lambda} (\varepsilon_b)^{3\lambda-3\lambda} \left(\frac{4(\varepsilon_b - \phi_w^t)^3}{\varepsilon_b(2\varepsilon_b - \phi_w^t)^2}\right)^\lambda \quad \text{C.47}$$

where the ε_b dependance is constrained to the ϕ_w term, having been reduced to an exponent of $3\lambda - 3\lambda = 0$ in the rest of the equation by the Bruggeman relationship. At this point, we invoke the approximation $\phi_w \to 0$ and log-scale the equation to achieve the valence-explicit equation for the trade-off:

$$\log\left(\bar{\alpha}_{g/c}\right) = \lambda\log\left(\frac{\mathrm{B}_\lambda F^2}{\left|z_g\right| RT\left(\nu_g a_s^s\right)^2}\right) + \log\left(\frac{\left(\left|z_A\right| C_A^{max,t}\right)^{3\lambda}\left(\bar{\alpha}_{g/c}\right)_D^{\lambda+1}}{\left(\frac{\xi}{\xi_{crit}}\right)^{2\lambda-1}}\right) - \lambda\log\left(\bar{\kappa}_g\right) \quad \text{C.48}$$

This upper bound equation has a slope of $-\lambda = -\left(1 + \nu_g/\nu_c\right)/2$ and an intercept that scales with the membrane parameters of C_A^{max}, $\left(\bar{\alpha}_{g/c}\right)_D$, and ξ/ξ_{crit} at different λ exponents. Equation C.48 reveals several interesting results. 2-2 salts are predicted to behave nearly identically to 1-1 salts because they have the same λ value. For electrolytes with more counter-ions than co-ions ($\lambda > 1$), the slope of the upper bound line is steeper, and the intercept depends more strongly on membrane properties than for electrolytes with more co-ions than counter-ions ($\lambda < 1$). Equation C.48 and its implications must be rigorously tested with a robust experimental data set, but that is beyond the scope of this work.

Appendix D Supplemental Content for Chapter 6

D.1 Modifications to the Upper Bound Model

The interdependence between membrane structural properties and transport properties is difficult to deconvolute. To reach a more intuitive understanding of the structure-property relationships, Chapter 5 developed a model to describe the trade-off between the charge selectivity and counterion conductivity ($\bar{\alpha}_{g/c}$ and $\bar{\kappa}_g$) using constituent models introduced in Chapter 3. However, in the development of UHCD IEMs, we have needed to modify this model. The updated Donnan-Meares-Manning model for IEMs contacting 1-1 single electrolyte solutions:

$$\log\left(\bar{\alpha}_{g/c}\right) = \log\left(\frac{F^2 (C_A^{max})^3 \left(\bar{\alpha}_{g/c}\right)_D^n}{12.56RT\xi (a_s^s)^2}\right) - \log\left(\bar{\kappa}_g\right) \quad \text{D.1}$$

Here, C_A^{max} is the maximum charge density of the IEM (mol / L[polymer]), ξ is the reduced linear charge density of the polymer, a_s^s is the salt activity in the external solution, F is Faraday's constant, R is the ideal gas constant, and T is the absolute temperature. $\left(\bar{\alpha}_{g/c}\right)_D^n$ is the diffusion selectivity between counter-ions and co-ions, and the specified exponent n is the modification to the model.

In the original derivation of this model, we assumed that co-ion diffusion coefficients are well described by the Meares-Manning model. In general, counter-ion diffusion coefficients are underpredicted by the Meares-Manning model without consideration of additional effects, such as the diffusivity of condensed counter-ions[426,428]. To rectify this situation, $\left(\bar{\alpha}_{g/c}\right)_D$ was left as a physically grounded, measurable adjustable parameter. Because co-ions were assumed to follow

the Mackie-Meares model while counter-ions diffused faster than predicted, the exponent of $\left(\bar{\alpha}_{g/c}\right)_D$ was $n = 2$. This assumption has been reasonable for all previously reported IEMs analyzed with this framework [426,428], and the success of the model at describing commercial IEMs (c.f. Chapter 5) suggests that this assumption is reasonable for many more IEMs. However, if diffusion selectivity is instead achieved by the suppression of co-ion diffusion, then $n = 1$. This case is more accurate for the imidazolium IEMs discussed in this study (Figure 6.3D).

Additionally, we sought a description of the counter-ion conductivity for membranes contacting DI water. Chapter 5 derived Equation 5.3 for κ_g when IEMs contact salt solutions, which incorporates electrostatic forces and assumes that co-ions are accurately described by the Meares-Manning model. As discussed in the preceding paragraph, this is surprisingly not true for the UHCD IEMs studied in this work. Instead, we derive a simplified model to predict the conductivity of DI water-equilibrated IEMs:

$$\kappa = \frac{F^2}{RT} C_A^{max} D_g^s \frac{\phi_w^2(1-\phi_w)}{(2-\phi_w)^2} \qquad \text{D.2}$$

Here, ϕ_w is the water volume fraction of the IEM and D_g^s represents the diffusivity of counter-ions in dilute aqueous solution. This equation is only valid for IEMs in a monovalent counter-ion form. Like the Donnan-Meares-Manning model for the upper bound, this equation utilizes the Nernst-Einstein assumption and the Mackie-Meares model to describe ion diffusion in polymer membranes. The definition of C_A^{max} in Equation 4.7 is utilized to make all scaling on ϕ_w explicit, but no other steps are required in this derivation. Equation D.2 is therefore extremely straightforward compared to Equation 5.3; however, it should provide a reasonable estimate of the conductivity for IEMs contacting DI water.

D.2 Membrane Preparation

Membranes were prepared according to the recipes in Appendix Table D.1. Because the monomers are similar in structure, the saturation point of each pre-polymer solution did not change across the membrane series; each membrane recipe was prepared at the saturation point. The density of the saturated solution caried slightly across the series of IEMs, creating a less dense polymer network upon gelation for the less cross-linked IEMs.

Appendix Table D.1: Membrane Synthesis Recipes: The compositions and properties of aqueous pre-polymer solutions used in this work. The typical scale of a reaction was a total of 20 g solution. Uncertainties represent the standard deviation of measurements performed on at least five independent samples.

Membrane	Dry Monomer (wt% solution)	HCPK (wt% of monomer)	Pre-polymer Solution Density (g/mL)	Pre-polymer Solution Charge Density (mol[Br-] / L[solution])
100XL	74	0.2	1.333 ± 0.027	4.881 ± 0.100
50XL	74	0.2	1.309 ± 0.022	4.795 ± 0.081
25XL	74	0.2	1.290 ± 0.019	4.723 ± 0.068
20XL	74	0.2	1.299 ± 0.025	4.759 ± 0.093
15XL	74	0.2	1.288 ± 0.025	4.716 ± 0.092
10XL	74	0.2	1.288 ± 0.019	4.716 ± 0.068
5XL	74	0.2	1.286 ± 0.022	4.709 ± 0.078

Appendix Table D.2 presents the gravimetric IEM equilibrium properties of these UHCD IEMs. The average gel fraction (GF) values for all membranes were close to 100 %, indicating nearly complete incorporation of the monomer into the polymer network. However, the realized ion-exchange capacity (IEC) values for the co-polymers were ~91 % of the theoretical value, and 96 % for the 100XL homopolymer, indicating that the charge contents are lower than expected. The fractional realized IEC is not correlated with the co-polymer ratio, suggesting that it is not due

to residual bromo groups on the cross-linker. During IEC measurements, Br^- ions were not detected in the desorption solution via ion chromatography alongside the targeted Cl^- ions, indicating that the diminished values were not due to incomplete conversions between counter-ions. Increasing the number of desorption steps also did not result in additional Cl^-. We attribute the persistent discrepancies to a combination of incomplete drying or carbonate contamination.

Appendix Table D.3 present the volumetric IEM equilibrium properties for these UHCD IEMs. Despite the similar chemical structure, there is a trend in the maximum charge density, C_A^{max}. Appendix Table D.2 demonstrated that the theoretical and realized IECs are nominally the same for this series of membranes, but as the cross-linking density decreases, the dry polymer density also decreases. Consequently C_A^{max} decreases slightly with decreasing cross-linking content. However, due to the small changes in density, the series of UHCD membranes can be considered to have similar charge contents within a reasonable margin of error. Analyzed in aggregate, the membranes have $\rho_p = 1.272 \pm 0.002\ g/cm^3$ and $C_A^{max} = 7.40 \pm 0.04\ mol/L[dry\ polymer]$.

Appendix Table D.2: Gravimetric Membrane Properties: The gel fraction (GF), ion-exchange capacity (IEC), water uptake (WU), and dry polymer density (ρ_p) of each VI membrane. The ion-exchange capacity also displays the percent of the theoretical value predicted by the monomer structure in parentheses, assuming complete monomer functionalization. Uncertainties represent the standard deviation of measurements performed on at least five independent samples.

Membrane	GF (%)	IEC (Cl-) (meq / g[polymer])	WU (g[water] / g[polymer])	ρ_p (g/cm3)
100XL	98.3 ± 1.5	6.083 ± 0.149 (96%)	0.562 ± 0.004	1.309 ± 0.004
50XL	101.0 ± 0.2	5.782 ± 0.046 (91%)	0.705 ± 0.004	1.282 ± 0.005
25XL	100.0 ± 0.6	5.821 ± 0.058 (92%)	0.926 ± 0.004	1.274 ± 0.003
20XL	100.8 ± 0.1	5.799 ± 0.080 (92%)	1.121 ± 0.003	1.266 ± 0.003
15XL	100.7 ± 0.3	5.712 ± 0.053 (90%)	1.396 ± 0.003	1.270 ± 0.009
10XL	100.6 ± 0.2	5.758 ± 0.095 (91%)	1.873 ± 0.022	1.255 ± 0.004
5XL	101.4 ± 0.5	5.749 ± 0.079 (91%)	3.163 ± 0.003	1.251 ± 0.004

Appendix Table D.3: Volumetric Membrane Properties. The water volume fraction (ϕ_w), fixed charge density ($C_A^{m,t}$), fixed charge concentration ($C_A^{m,w}$), maximum charge density (C_A^{max}), and hydration number (λ) of each VI membrane. Uncertainties represent the standard deviation of measurements performed on at least five independent samples.

Membrane	ϕ_w (L[water] / L[membrane])	$C_A^{m,t}$ (mol / L[membrane])	$C_A^{m,w}$(mol / L[sorbed water])	C_A^{max}(mol / L[dry polymer])	λ (mol[sorbed water] / mol[fixed charge])
100XL	0.432 ± 0.012	4.67 ± 0.15	10.82 ± 0.25	7.96 ± 0.03	5.14 ± 0.12
50XL	0.469 ± 0.005	3.83 ± 0.05	8.20 ± 0.07	7.41 ± 0.09	6.78 ± 0.06
25XL	0.551 ± 0.007	3.46 ± 0.06	6.29 ± 0.07	7.41 ± 0.08	8.83 ± 0.10
20XL	0.593 ± 0.011	3.06 ± 0.11	5.17 ± 0.09	7.35 ± 0.11	10.74 ± 0.18
15XL	0.652 ± 0.007	2.66 ± 0.05	4.09 ± 0.04	7.25 ± 0.07	13.58 ± 0.15
10XL	0.679 ± 0.012	2.08 ± 0.08	3.07 ± 0.08	7.22 ± 0.11	18.07 ± 0.47
5XL	0.810 ± 0.015	1.47 ± 0.05	1.82 ± 0.03	7.19 ± 0.12	30.58 ± 0.44

D.3 Polymer Properties of UHCD IEMs

The TGA results indicate that the polymerization kinetics are inhibited in the most heavily cross-linked membranes. The onset of degradation occurs at approximately 280 ºC for all membranes (Appendix Figure D.2), which agrees with reported values for chloride-mediated imidazolium degradation[535]. Notably, the imidazolium degradation slopes are steeper for the less cross-linked membranes than for the more cross-linked membranes. C_2VI units connect to the long-chain polymer backbone only once, but C_4VI_2 units connect at two locations, so the inter-imidazolium alkane would not volatilize until both surrounding imidazoliums are degraded. This rationale should manifest as faster weight loss for less cross-linked membranes once imidazolium degradation begins, which is consistent with the TGA results. The remaining mass after the imidazolium degradation is completed is attributed to the long-chain polyethylene backbone, which begins to degrade at ~400 ºC. There is also a notable difference in degradation slope during polyethylene degradation. We attribute the steeper slope in the highly cross-linked membranes to a greater representation of relatively short polyethylene chains. The less restricted polymerization of the less cross-linked membranes produces a greater fraction of longer, thermally stable polyethylene chains. This conclusion is supported by the FTIR spectra of the dry membranes (Appendix Figure D.1), where unreacted ethylene vibrations are detected (3000-3200 cm^{-1}), consistent with those in the monomer spectra.

The swelling of the UHCD IEMs, especially at high cross-linking contents, creates a highly strained polymer network. This is evident in the X-ray scattering data (Appendix Figure D.3). Other than the broad amorphous peak at scattering vectors greater than 1 $Å^{-1}$ [478,536,537], a single broad peak is observed. This peak corresponds to a Bragg length of 10 Å in every membrane when dried, but increases to a different extent for each membrane in the swollen state. This peak may correspond to the cross-linking C_4VI_2 units, in which imidazoliums are separated by ~8.6 Å and

backbones are separated by ~12.9 Å in the dry state. Peaks at comparable scattering vectors have been assigned to polymer chain correlation lengths in similar imidazolium-based systems[478,538]. The shift in these peaks to larger length scales upon hydration suggests that the chains are uncoiled and highly strained in the hydrated state. The resistance to swelling is attributed to coiling of polymer chains[539], so for the 100XL membrane to exhibit essentially no elongation upon swelling, the swelling resistance must be essentially maximized. That is, the cross-link chain coiling in the 100XL membrane is effective enough to essentially maintain their preferred orientation. Swelling cannot be repressed any further through rubber elasticity.

The DMA results support the interpretation of highly strained networks. Each hydrated membrane exhibits a constant storage modulus (E') between 1 and 0.01 Hz (Appendix Figure D.4A-G). No glass transition was detected for any membrane, as is supported by the dry polymer DSC (Appendix Figure D.5), revealing that each membrane remains in the glassy state with minimal chain mobility. E' and the swelling-reduced storage modulus, E'_{SR}, both increase with the log of the cross-linking fraction (Appendix Figure D.4H), demonstrating that the cross-links control the mechanical properties of the membranes. The constant increase in E'_{SR} suggests that cross-links maintain relatively high efficiency even as they begin to constitute every repeat unit. Therefore, improving cross-linking efficiency would not be an effective way to further reduce membrane swelling.

A single loss tangent peak is present in the low-frequency region of the scan of 100XL, which is not accompanied by any change in E'. This signal may be partially observed at even lower frequencies for the less cross-linked membranes. Because of the lower incorporation of ethylene into the polymer backbone for highly cross-linked membranes, we attribute this signal to the β-

transition for side-chain mobility[540,541]. The partially-incorporated cross-links function as side-chains which should exhibit some motion at high temperatures/times.

From each method of probing the polymer network, the UHCD membranes are apparently a highly strained, efficiently cross-linked system which exerts its full force to restrict swelling. Analysis of the water within the membranes provides additional support to the notion that further increases in membrane charge content would be difficult to produce. Swelling of charged polymer membranes is promoted partly by the requirement of ions to fill their hydration shell. Appendix Figure D.6 and Appendix Figure D.7 demonstrate that freezable water is scarce in the highly cross-linked membranes (raw data are presented in Appendix Table D.4). That is, there is not much membrane hydration beyond that required by the ions. The polymerization of these systems occurs in a saturated solution of monomer, meaning that each membrane starts with minimal excess water beyond that required to dissolve the ions. The most cross-linked membranes take on little additional water when equilibrated in aqueous solutions, containing only enough waters to hydrate the ions. Removing the waters for ion hydration would be difficult and require significantly greater pressure exerted by the cross-linked network. Therefore, for the system of imidazolium/chloride, hydrophobic structures would likely be required to reduce the membrane swelling below a hydration number (λ) of ~5. Such a structure would reduce the maximum charge density, C_A^{max}, of the membrane, further decreasing the fixed charge density.

Appendix Table D.4: Melting enthalpy of water in UHDC IEMs. The enthalpies of melting, normalized to the mass of water in each membrane, of hydrated UHCD membranes equilibrated with DI water and 1 m NaCl. Uncertainties represent the standard deviation of measurements performed on at least five independent samples.

Membrane	DI Water		1 m NaCl	
	Melting Enthalpy (J/g[water])	Fraction Freezable Water	Melting Enthalpy (J/g[water])	Fraction Freezable Water
100XL	36.8 ± 4.3	0.110 ± 0.013	26.8 ± 3.3	0.080 ± 0.010
50XL	107.3 ± 4.3	0.322 ± 0.013	94.2 ± 6.3	0.283 ± 0.019
25XL	143.0 ± 3.3	0.429 ± 0.010	141.4 ± 5.8	0.425 ± 0.017
20XL	168.8 ± 2.8	0.507 ± 0.008	155.9 ± 5.5	0.468 ± 0.017
15XL	191.5 ± 7.8	0.575 ± 0.023	170.7 ± 4.6	0.513 ± 0.014
10XL	234.2 ± 4.8	0.703 ± 0.014	188.5 ± 4.4	0.566 ± 0.013
5XL	272.1 ± 2.9	0.817 ± 0.009	226.9 ± 6.3	0.682 ± 0.019

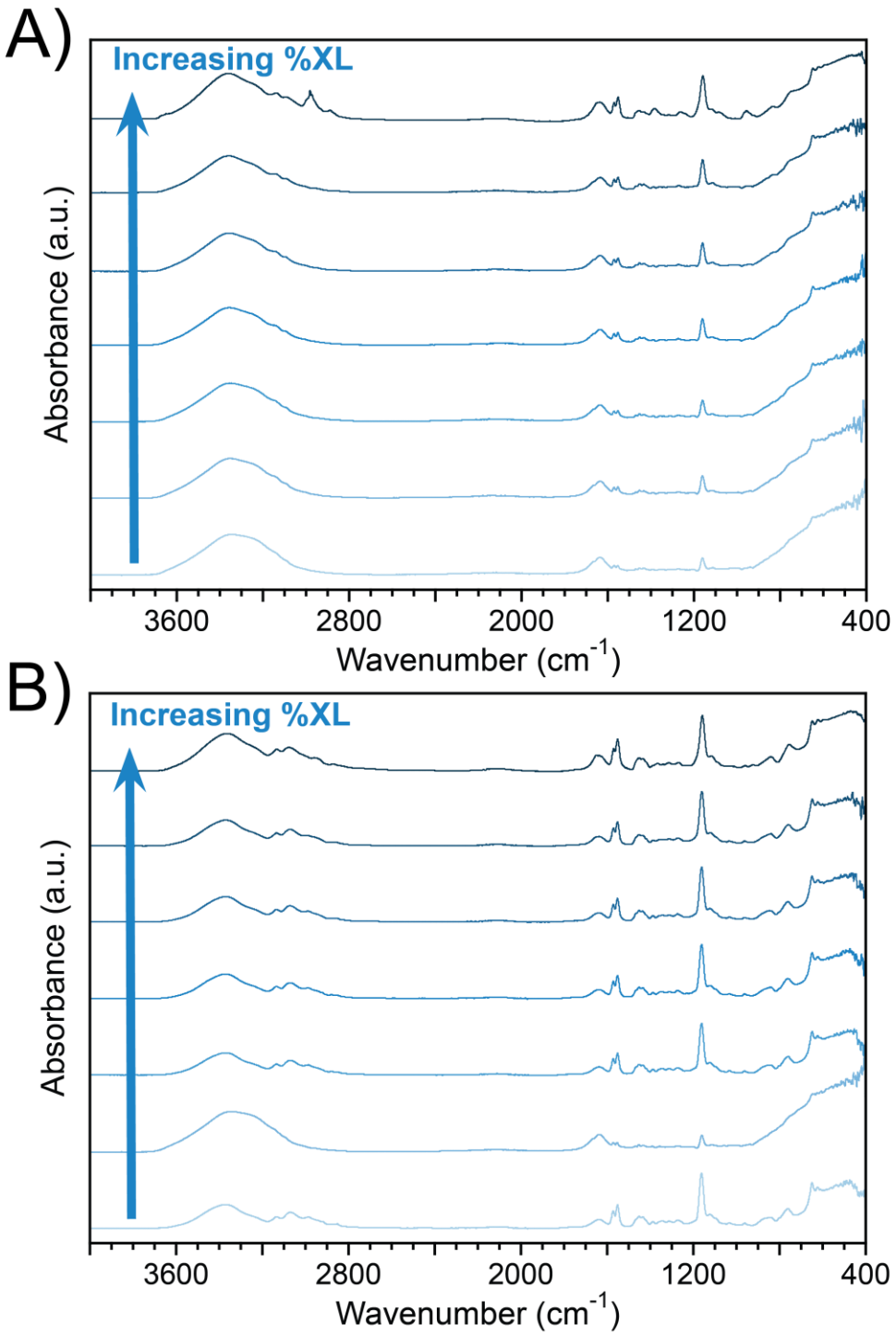
D.4 Transport Properties of UHCD IEMs

The UHCD membranes conform to predictions made by transport models surprisingly well. The partitioning selectivity is strongly correlated with $C_A^{m,w}$ (Figure 6.3C), as predicted by the Donnan model (Section 3.2). The counter-ion diffusion coefficients are predicted by the Mackie-Meares model both for membranes contacting DI water and those contacting 1 m NaCl (Figure 6.4B). However, the co-ion diffusion coefficients are lower than those predicted by the Mackie-Meares model (Figure 6.3D). Thus, the UHCD membranes attain normalized diffusion selectivities greater than 1 by suppressed co-ion diffusion, which contrasts the behavior observed for relatively highly swollen and lower charge content IEMs[426,428]. In these other systems, co-ion diffusion coefficients are predicted reasonably well by the Mackie-Meares model, and diffusion selectivities greater than 1 are due to fast counter-ion diffusion. We rationalized the different

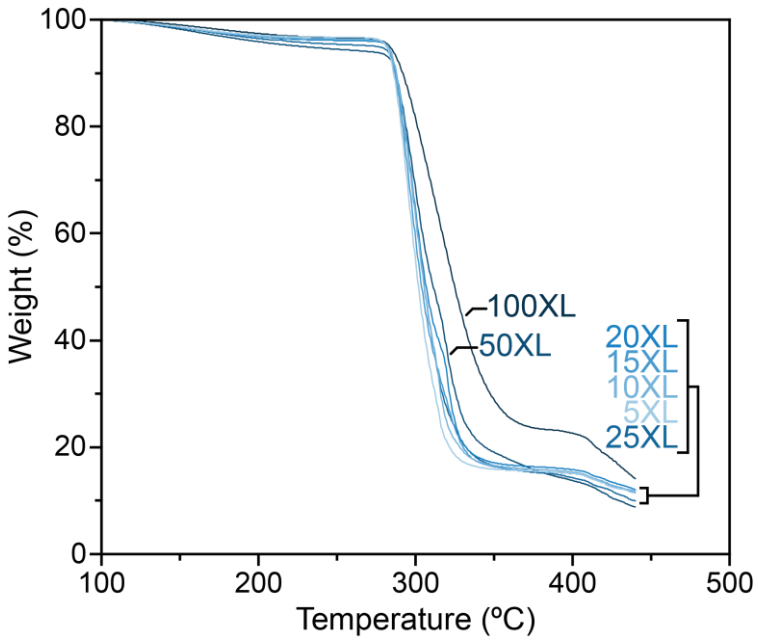
diffusion selectivity mechanism in the UHCD membranes via the freezable water content (Figure 6.3F). Each facet of the exceptional performance of these UHCD membranes can therefore be connected to the unique combinations of charge and water contents achieved by the membrane design strategy.

The counter-ion conductivity/selectivity trade-off of the UHCD membranes cannot be modeled via Equation D.1 due to the inherent assumptions contained within this equation. Notably, secondary water content scaling that is expected to affect only the highest water content IEMs is neglected in this equation (Section C.2). Compared to typical commercial IEMs, the UHCD IEMs have abnormally high water contents, requiring the inclusion of secondary water content scaling in the model. The full implementation of the trade-off model is a system of equations described by the models introduced in 3.4, with complex interconnections that prevent an explicit form. The full model is compared with the linearized model in Figure 5.2. It can be seen that for highly selective membranes, the linearized model aligns with each comparable iteration of the fully parameterized model. However, for highly conductive membranes (like the UHCD IEMs), important trends can be lost as a result of the linearization process. To describe the UHCD membranes with high water contents (reaching $\phi_w = 0.75$ when contacting 1 m NaCl), this implicit version of the model is used in Figure 6.3A.

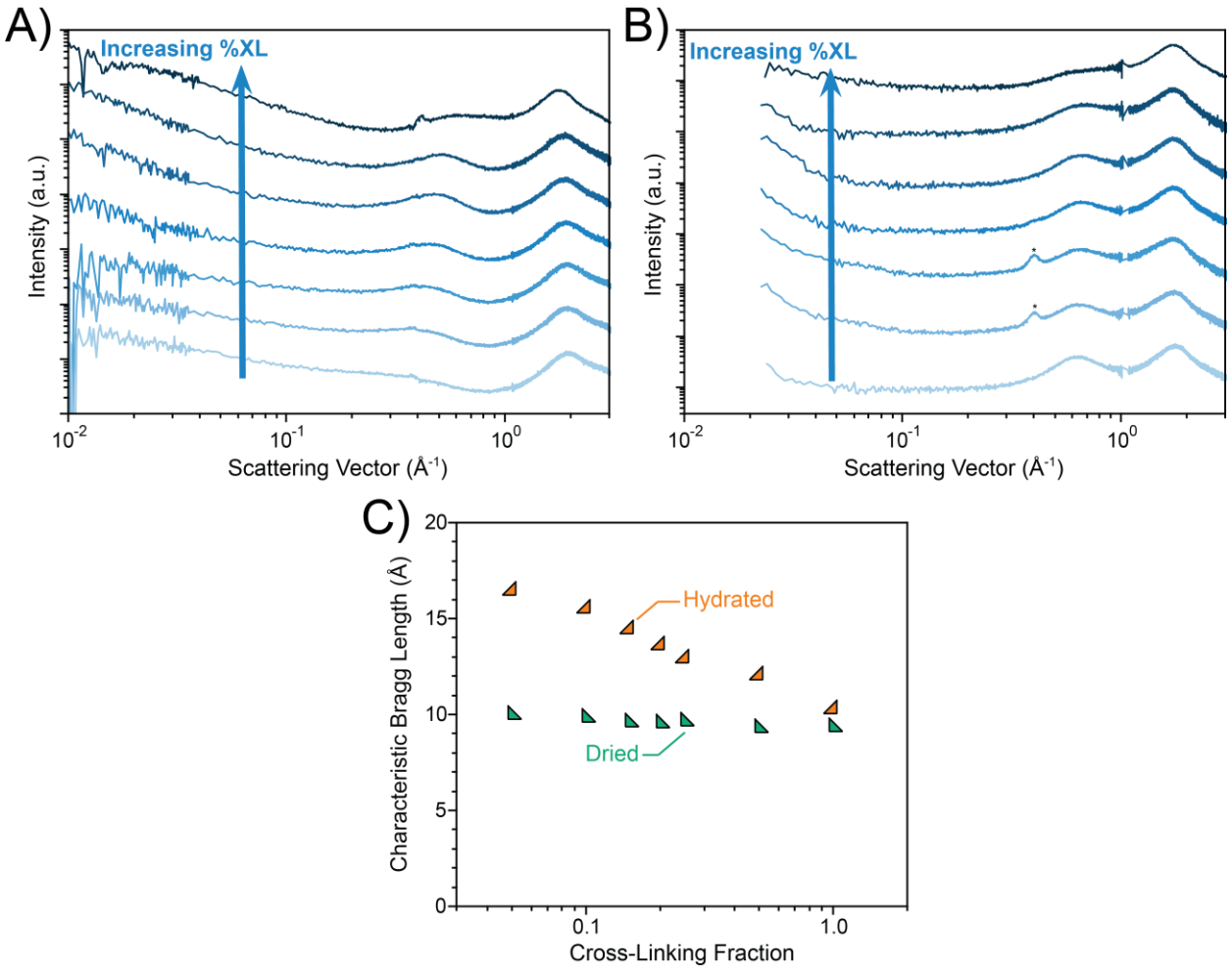
D.5 Supplementary Figures



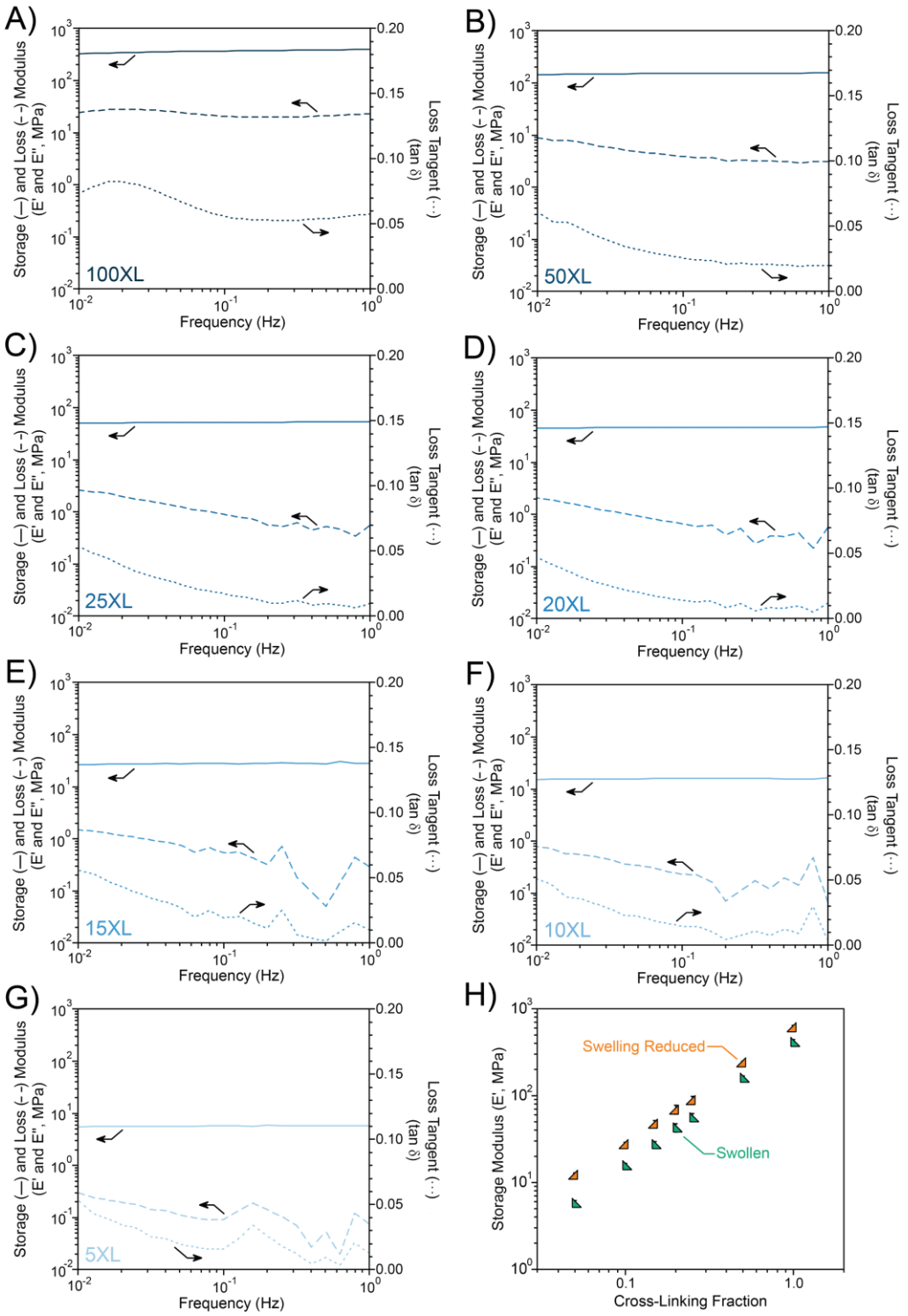
Appendix Figure D.1: Membrane FTIR. Representative ATR-FTIR spectra of the UHCD membranes A) fully hydrated and B) equilibrated with ambient air at 20 ± 10 % humidity.



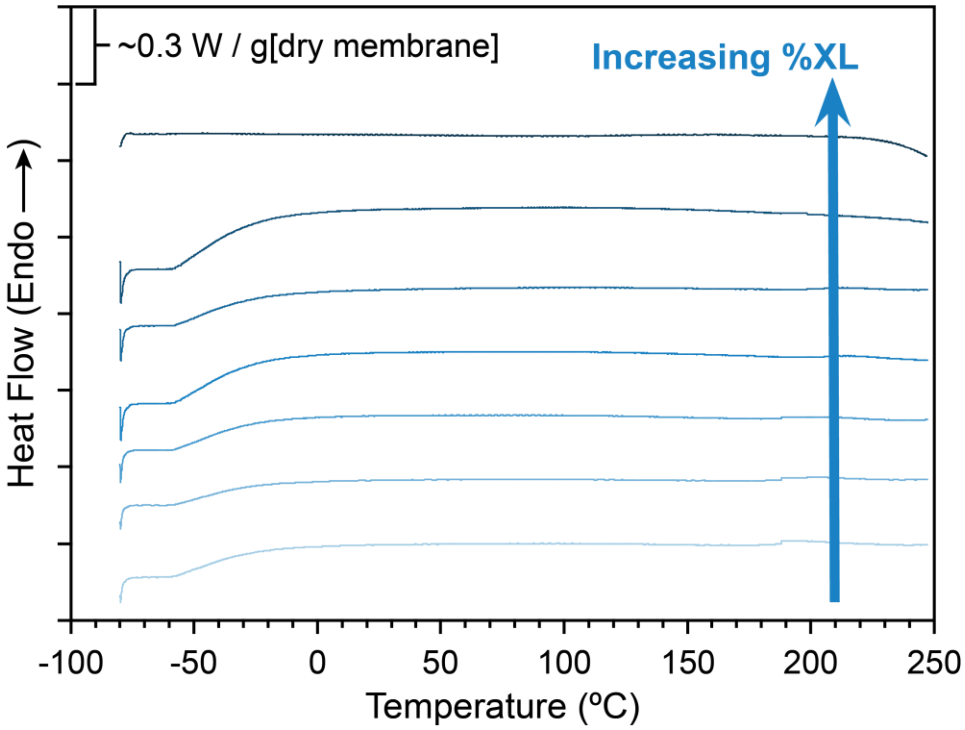
Appendix Figure D.2: TGA for UHCD IEMs. Representative TGA scans of the UHCD membranes. The mass is normalized to that of the dry polymer after annealing at 100 ºC to remove trace water. For each replicate of each membrane, the onset of degradation occurred at approximately 280 ºC.



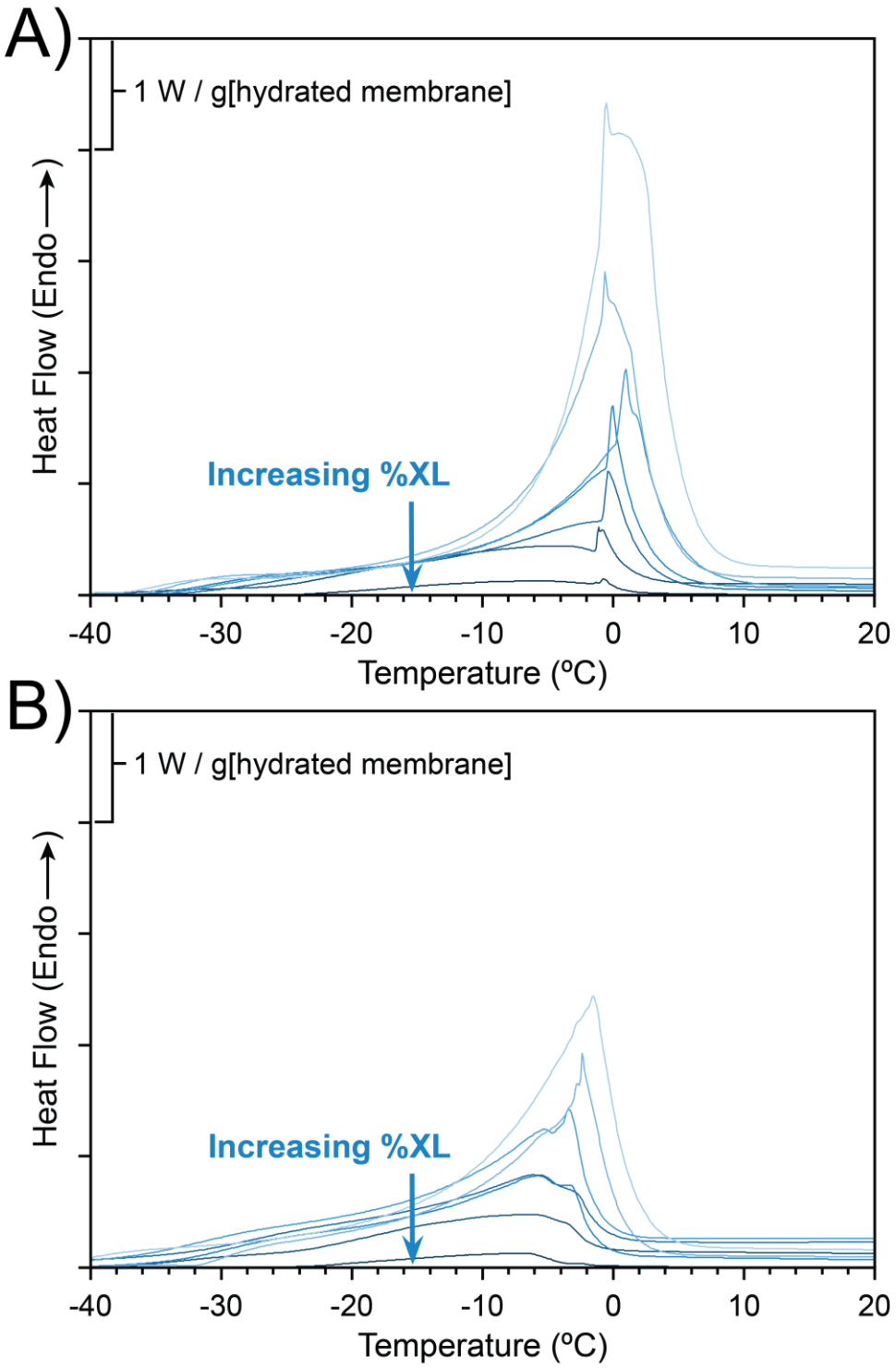
Appendix Figure D.3: SAXS for UHCD IEMs. X-ray scattering results for both A) hydrated and B) dried UHCD membranes. Peaks due to the Kapton tape securing the samples are marked with "*". C) The characteristic Bragg length plotted against the cross-linker content for hydrated and dried membranes extracted from the SAXS data.



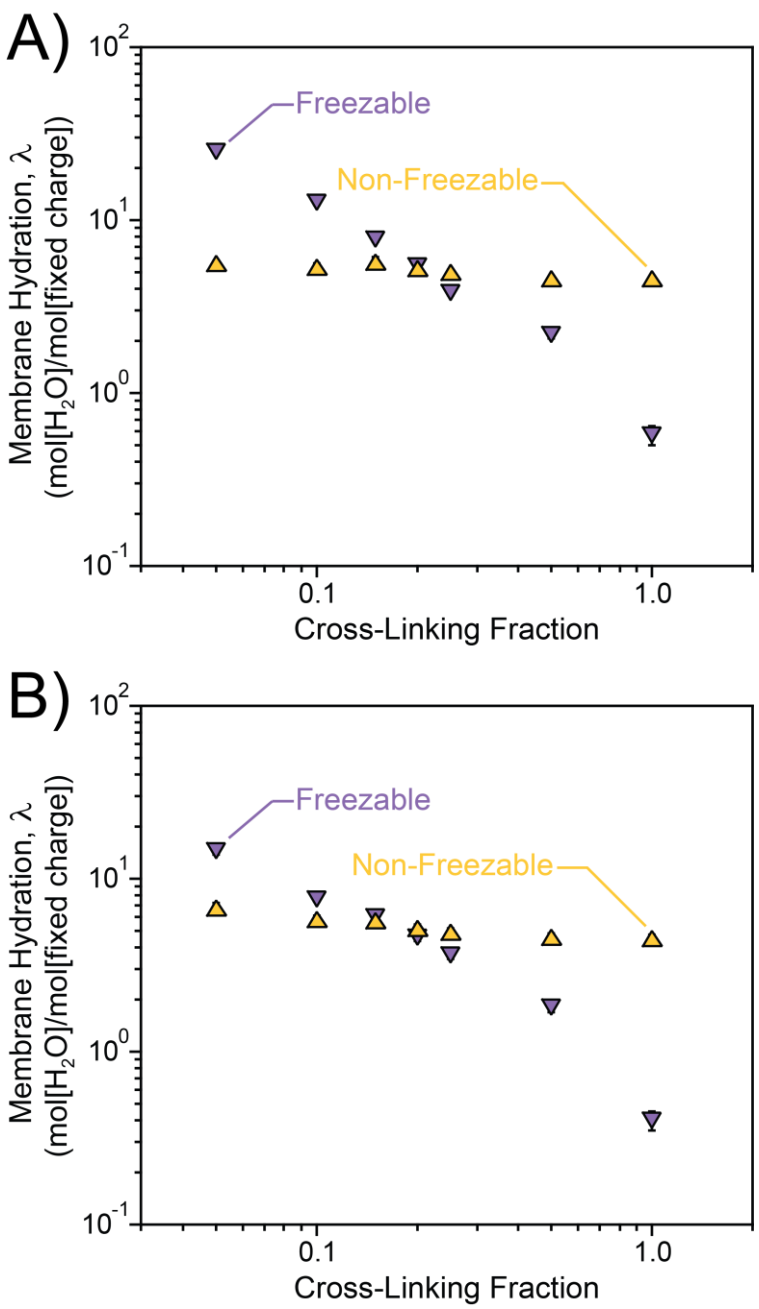
Appendix Figure D.4: DMA results for UHCD IEMs. Representative DMA frequency sweeps for hydrated UHCD membranes at 30 ºC and 0.03 % strain, including the storage modulus (solid line), loss modulus (large dashed line), and loss tangent (small dashed line). A) 100XL. B) 50XL. C) 25XL. D) 20XL. E) 15XL. F) 10XL. G) 5XL. H) The storage modulus and swelling-reduced storage modulus as a function of the cross-linker content of each membrane. Uncertainties represent the standard deviation of measurements on at least 3 separate samples.



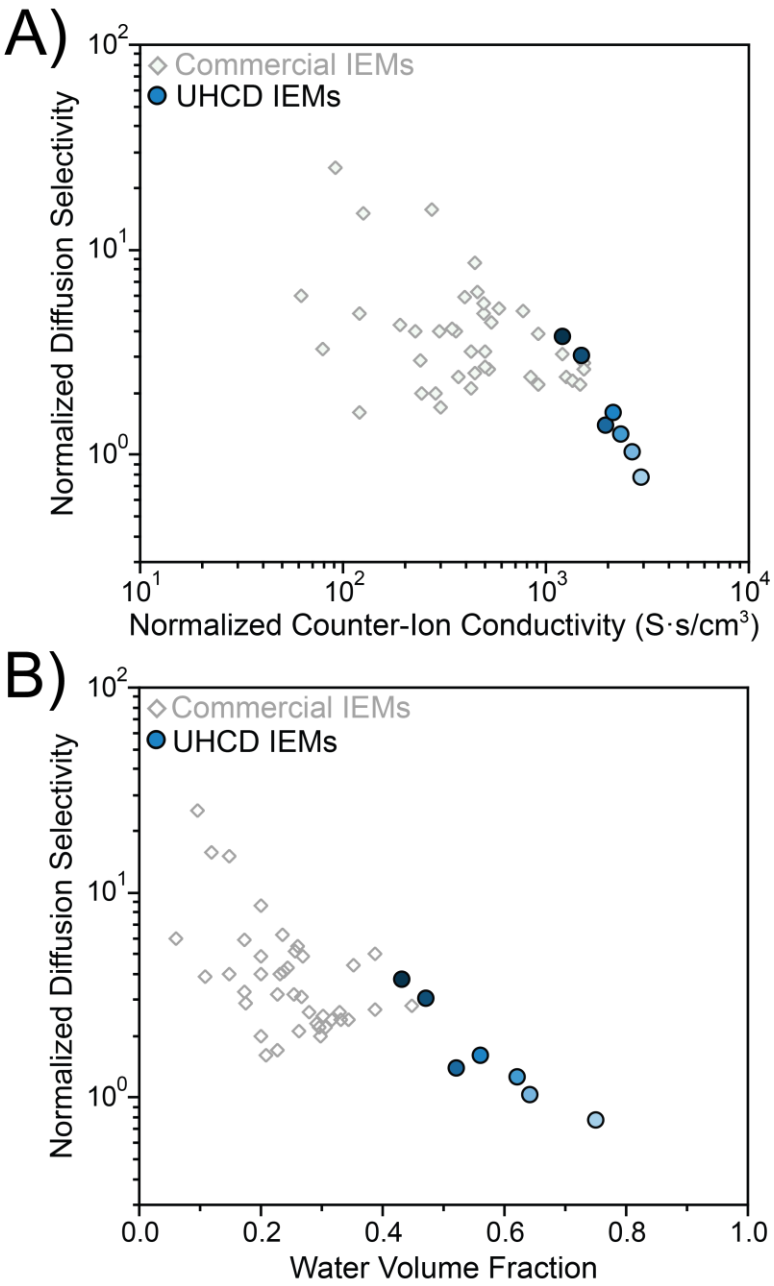
Appendix Figure D.5: Dry membrane DSC for UHCD IEMs. Representative DSC thermograms of the dry UHCD membranes. Each line represents the second heating cycle of a sample at a rate of 5 ºC/min. The heat flow was corrected to the estimated dry mass of samples, but the signal magnitude is only approximate.



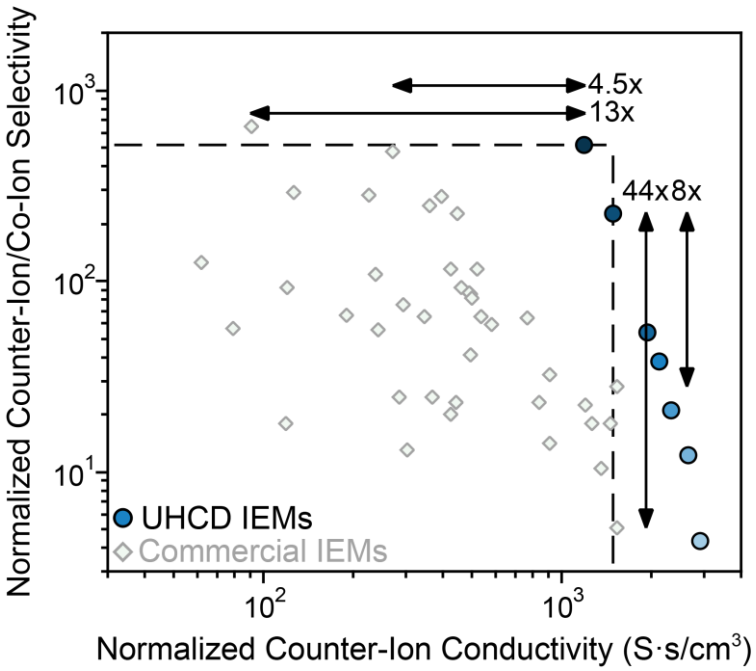
Appendix Figure D.6: Water melting thermograms of UHCD IEMs. Representative DSC thermograms of the UHCD membranes in the hydrated state. Membranes were equilibrated with A) DI water and B) 1 m NaCl.



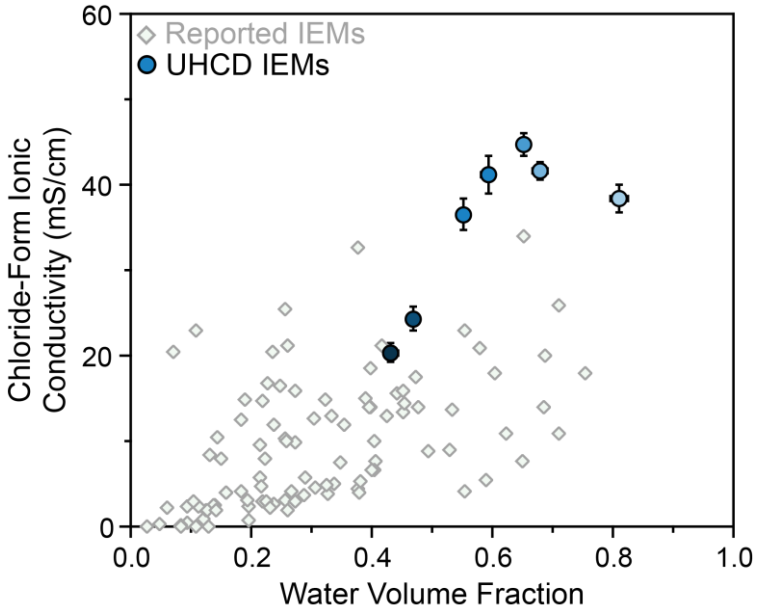
Appendix Figure D.7: Freezable and non-freezable hydration numbers of UHCD IEMs. The freezable and non-freezable hydration numbers, λ_f and λ_{nf}, in UHCD membranes as a function of the cross-linker content. Membranes were equilibrated with A) DI water and B) 1 m NaCl. Uncertainties represent the standard deviation of measurements on at least 5 separate samples.



Appendix Figure D.8: Diffusion selectivity of UHCD IEMs. A) The normalized diffusion selectivity plotted against the normalized counter-ion conductivity for the reference data (Chapter 4) and the UHCD membranes. B) The normalized diffusion selectivity plotted against the water volume fraction for the reference data (Chapter 4) and the UHCD membranes.



Appendix Figure D.9: Performance improvements of UHCD IEMs. The normalized counter-ion/co-ion selectivity plotted against the normalized counter-ion conductivity for the reference data (Chapter 4) and the UHCD membranes. The annotations demonstrate the improvements to selectivity offered by the UHCD membranes against the state-of-the-art commercial IEMs without sacrificing any performance. UHCD membranes have higher conductivities at top-tier selectivities and have higher selectivities at top-tier conductivities.



Appendix Figure D.10: Chloride conductivity comparison. The ionic conductivity plotted against the water volume fraction of reported chloride-form membranes (Chapter 4) and the chloride-form UHCD membranes equilibrated with DI water.

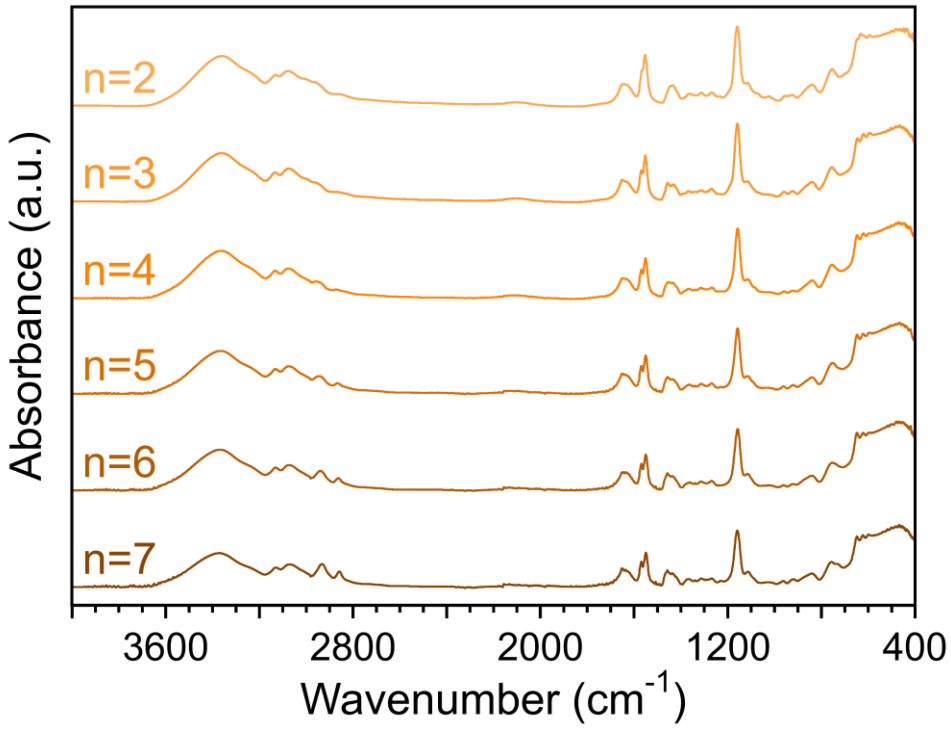


Appendix Figure D.11: Unmarked UHCD IEM photo. Unmarked photograph of free-standing films of each UHCD membrane.

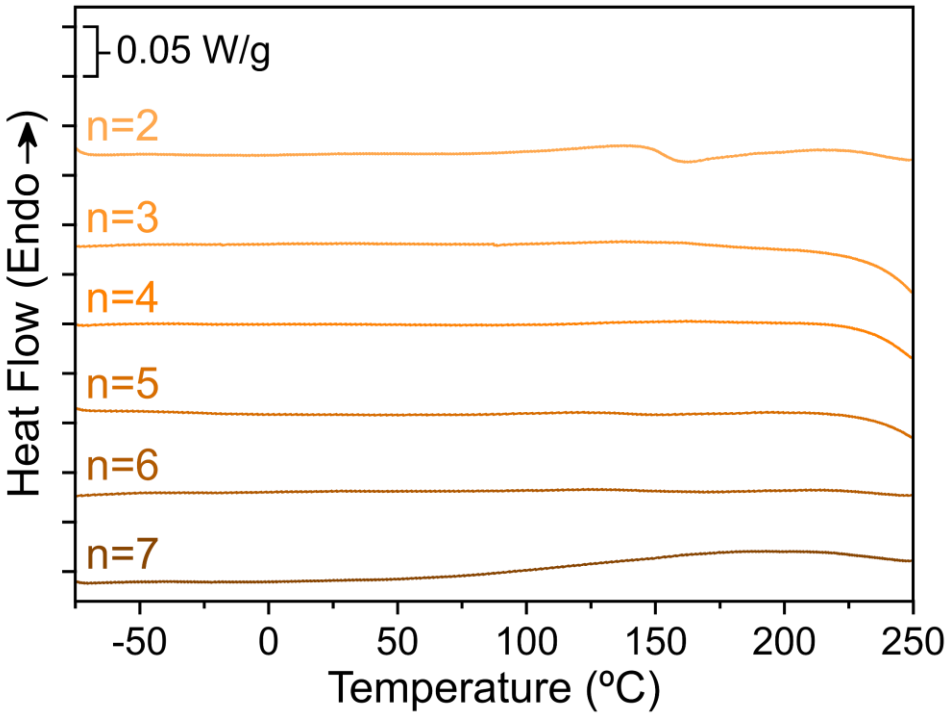
Appendix E Supplemental Content for Chapter 7

Appendix Table E.1: Additional C_nVI_2 membrane properties. The water uptake, ion-exchange capacity, and dry polymer density for each of the membranes studied in Chapter 7. The fraction of theoretical IEC is included in parentheses to verify the structure of the IEMs. Reported uncertainties represent the standard deviation of at least five independent measurements.

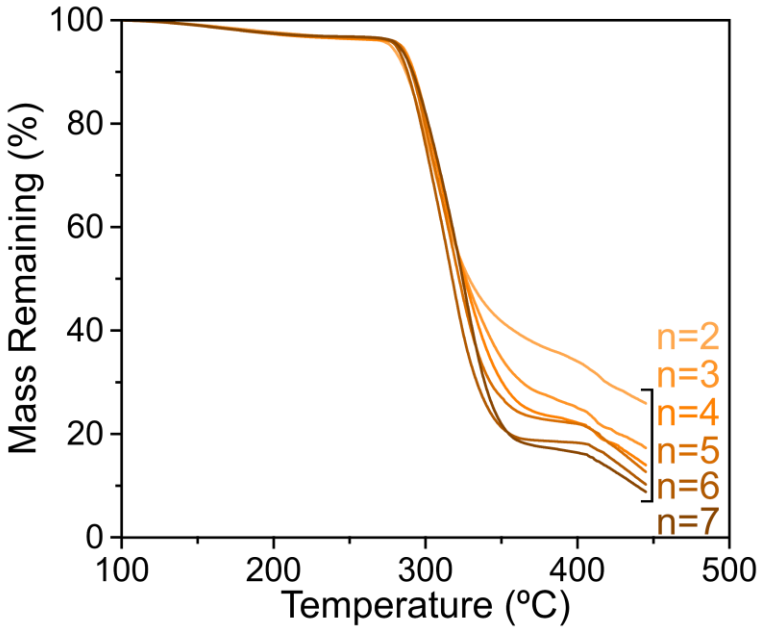
Membrane	IEC (Cl–) (meq / g[polymer])	WU (g[water] / g[polymer])	ρ_p (g/cm3)
C_2VI_2	6.655 ± 0.278 (96%)	0.919 ± 0.034	1.372 ± 0.003
C_3VI_2	6.437 ± 0.215 (97%)	0.525 ± 0.010	1.336 ± 0.003
C_4VI_2	6.083 ± 0.149 (96%)	0.562 ± 0.004	1.309 ± 0.004
C_5VI_2	5.507 ± 0.055 (91%)	0.534 ± 0.007	1.284 ± 0.002
C_6VI_2	5.558 ± 0.096 (95%)	0.570 ± 0.004	1.263 ± 0.002
C_7VI_2	5.319 ± 0.136 (95%)	0.561 ± 0.028	1.246 ± 0.003



Appendix Figure E.1: Vibrational spectroscopy of C_nVI_2 IEMs. Representative ATR-FTIR spectra of C_nVI_2 IEMs equilibrated with ambient air at 20 ± 10 % relative humidity. Unreacted vinyl peaks are detected at ~1650 cm^{-1}.

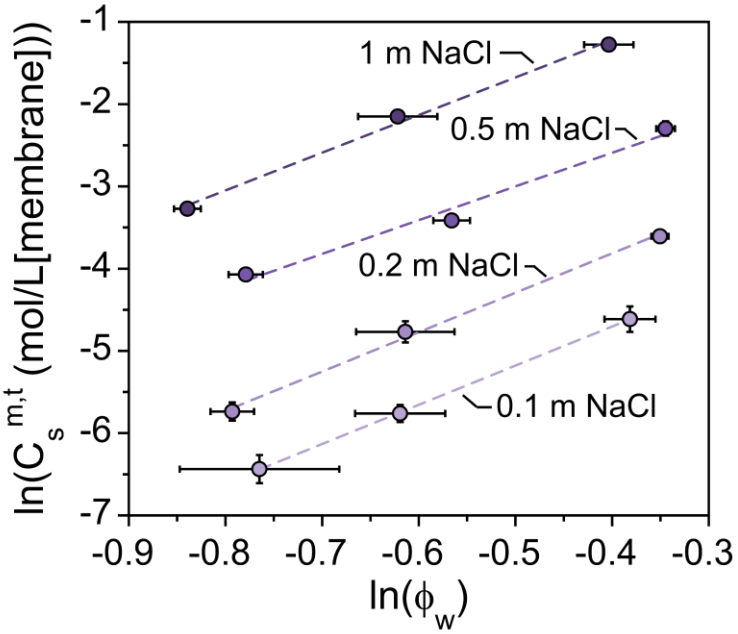


Appendix Figure E.2: Polymer chain mobility in C_nVI_2 IEMs. Representative DSC thermograms of the dry C_nVI_2 IEMs. Each line represents the second heating cycle of a sample at a rate of 5 ºC/min.



Appendix Figure E.3: Thermal degradation of C_nVI_2 IEMs. Representative TGA scans of C_nVI_2 membranes. The mass is referenced to that of the dry polymer after annealing at 100 ºC to drive off trace water. For each replicate of each C_nVI_2 membrane, the onset of degradation occurred at approximately 280 ºC.

Appendix F Supplemental Content for Chapter 8



Appendix Figure F.1: Empirical partitioning equation for homogeneous C_4VI_2 IEMs. The interpolation relationships for co-ion concentrations as a function of homogeneous membrane water content. The regressions were performed on log-log coordinates before transforming back to linear coordinates for use in the modeling relationships. The membranes included are 100X-26W, 25X-26W, and 10X-26W.

Appendix Table F.1: Additional C_4VI_2 thermal membrane properties. The water uptake, ion-exchange capacity, dry polymer density, and visual appearance for each of the membranes studied in Chapter 8. The fraction of theoretical IEC is included in parentheses to verify the structure of the IEMs.

Membrane	IEC (Cl^-) (meq / g[polymer])	WU (g[water] / g[polymer])	ρ_p (g/cm^3)	Appearance
100X-26W	6.099 ± 0.054 (96%)	0.551 ± 0.009	1.333 ± 0.019	Yellow/Clear
100X-33W	5.785 ± 0.127 (91%)	0.731 ± 0.006	1.314 ± 0.005	Yellow/Clear
100X-40W	5.939 ± 0.086 (94%)	0.898 ± 0.008	1.339 ± 0.004	Blue/Clear
100X-50W	5.897 ± 0.050 (93%)	1.291 ± 0.012	1.317 ± 0.026	Blue/Opaque
100X-63W	6.033 ± 0.097 (95%)	2.082 ± 0.018	1.313 ± 0.002	White/Opaque
100X-65W	6.082 ± 0.136 (96%)	2.347 ± 0.009	1.316 ± 0.005	White/Opaque
100X-70W	6.404 ± 0.328 (101%)	2.991 ± 0.017	1.315 ± 0.006	White/Opaque
100X-75W	6.163 ± 0.076 (97%)	3.829 ± 0.038	1.362 ± 0.089	White/Opaque
75X-26W	6.501 ± 0.290 (102%)	0.604 ± 0.013	1.298 ± 0.003	Yellow/Clear
75X-40W	6.172 ± 0.041 (97%)	0.954 ± 0.008	1.298 ± 0.005	Blue/Clear
75X-65W	5.723 ± 0.086 (90%)	2.383 ± 0.022	1.322 ± 0.016	White/Opaque
75X-73W	5.752 ± 0.135 (91%)	3.814 ± 0.030	1.318 ± 0.012	White/Opaque
50X-26W	6.161 ± 0.188 (97%)	0.679 ± 0.043	1.270 ± 0.005	Yellow/Clear
50X-40W	6.215 ± 0.050 (98%)	1.023 ± 0.013	1.292 ± 0.010	Blue/Clear
50X-61W	5.955 ± 0.218 (94%)	2.200 ± 0.013	1.295 ± 0.003	White/Opaque
50X-69W	5.844 ± 0.203 (92%)	3.268 ± 0.084	1.295 ± 0.013	White/Opaque
25X-26W	6.283 ± 0.274 (99%)	0.999 ± 0.012	1.271 ± 0.006	Yellow/Clear
25X-40W	6.120 ± 0.068 (96%)	1.449 ± 0.026	1.259 ± 0.010	Yellow/Clear
25X-58W	5.873 ± 0.205 (93%)	2.338 ± 0.026	1.284 ± 0.015	White/Opaque
25X-69W	5.657 ± 0.070 (89%)	4.566 ± 0.046	1.294 ± 0.018	White/Clear
20X-26W	5.803 ± 0.041 (91%)	1.153 ± 0.004	1.265 ± 0.002	Yellow/Clear
15X-26W	5.718 ± 0.198 (90%)	1.457 ± 0.010	1.284 ± 0.014	Yellow/Clear
10X-26W	5.670 ± 0.056 (89%)	1.961 ± 0.011	1.260 ± 0.006	Yellow/Clear
5X-26W	5.766 ± 0.106 (91%)	3.444 ± 0.021	1.259 ± 0.012	Yellow/Clear

Appendix G Supplemental Content for Chapter 9

G.1 Correcting Diffusivities for Obstruction Effects

The diffusivities accessible via macroscopic conductivity measurements are only effective diffusivities within the total IEM phase[542,543]. The ion-exchange polymer occupies a significant fraction of the membrane, forcing ions to take a tortuous pathway across the IEM. Ions travel further and experience less driving force as a direct result of this tortuosity, so the actual speed of diffusion exhibited by the ions is much greater than the experimentally accessible effective diffusion coefficient[542,543]. Even at temperatures in which all interaction-based limitations to diffusion may be ignored, obstruction effects will continue to create a tortuous route for diffusion. Therefore, the tortuosity of the IEM contributes to the Arrhenius pre-factor, D_0^m.

The tortuosity of an IEM depends on the fraction of volume available for diffusion. This dependence can be approximated via the Mackie-Meares model[544], introduced in Section 3.3.

$$\left(\frac{D_i^m}{D_i^s}\right)_{obs} = \frac{1}{\tau^2} = \left(\frac{\phi_w}{2-\phi_w}\right)^2 \qquad \text{G.1}$$

Here, $(D_i^m/D_i^s)_{obs}$ represents the reduction in effective diffusivity for species i due to obstruction effects in a polymer membrane, τ represents the tortuosity, and ϕ_w is the water volume fraction of the polymer membrane. Approximating that the Mackie-Meares model is exactly accurate, it can be used to correct for obstruction effects in IEMs. The product $D_i^m\tau^2$ represents a corrected ion diffusivity which only deviates from aqueous solution diffusion behavior through interactions which alter the free energy of diffusion (or deviations of obstruction effects from the Mackie-

Meares model). SIEs should fall into this category, so correcting D_i^m using the Mackie-Meares model will be helpful in our analysis.

Arrhenius plots of corrected ion diffusion coefficients are shown in Appendix Figure G.7. Compared to the uncorrected data in Appendix Figure G.3, two primary changes are evident: First, for the AEMs, F^- is no longer the fastest ion. Except for I^-, the relative order of anion membrane diffusivities reverts to that of aqueous solution diffusivities shown in Appendix Figure G.4A. Thus, obstruction effects are at least partially responsible for the anomalous AEM behavior. Second, for the CEMs, NMe_4^+ exhibits the greatest change. NMe_4^+ has both hydrated and Stokes radii less than that of Li^+ (Table 2.5), so it is reasonable to expect NMe_4^+ to be faster than Li^+, which we see in the corrected Appendix Figure G.7B but not Appendix Figure G.3B.

The Arrhenius activation energies and pre-factor changes resulting from the Mackie-Meares diffusivity correction are demonstrated in Appendix Figure G.8 and Appendix Figure G.9. As expected, D_0^m increases significantly, now representing the diffusion speed of the ions within the water domains of the IEMs. Whereas uncorrected membrane pre-factors did not always exceed D_0^s, corrected pre-factors are always greater, indicating faster unhindered diffusion within the IEM. This translates directly to the positive y-intercept of Figure 9.2B which is discussed in the main text. Meanwhile, E_a^m remains essentially unchanged after the Mackie-Meares correction. Because the water swelling does not vary with temperature for these materials (Appendix Figure G.2), the temperature-dependence of D_i^m should not change after the tortuosity correction, resulting in indistinguishable values of E_a^m.

Because $E_a^m \neq E_a^s$ and $D_0^m \neq D_0^s$, each ion should exhibit a temperature at which the solution and membrane diffusivities of an ion are equal ($D_i^m = D_i^s$). One way to visualize this cross-over for a membrane is through a parity line on the solution-normalized linear free energy

plot (Appendix Figure G.11). The slope of the parity lines varies with temperature, but each intercepts the plot at (0,0), representing solution-like behavior. Data points shown above the line for a given temperature represent conditions with faster membrane diffusion, while data points shown below the line for a temperature represent conditions with slower membrane diffusion. Appendix Figure G.11 demonstrates that the compensation of ΔE_a^{m-s} and D_0^m/D_0^s lead to bulk-like diffusion at room temperature for many of the ions studied. Based on the uncertainty of our measurements, F^-, K^+, Cs^+, and NH_4^+ experience a diffusional speed-up by more than one standard deviation at 21 ºC, while only Mg^{2+} and Ca^{2+} experience a diffusional slow-down by more than one standard deviation at 21 ºC. At higher temperatures, more ions exhibit diffusional speed-ups.

G.2 Validation of Simulated Membrane Structures

G.2.1 Pre-Polymer Solutions

To ensure that pre-polymer simulations were resolved adequately and were comparable to experimental pre-polymer solutions, system variables (temperature, pressure, density, and total energy) were monitored during equilibration. Appendix Figure G.12 depicts these system variables over time for the AEM and CEM pre-polymer solution simulations and Appendix Table G.6 contains the final characteristics of the simulated pre-polymer solutions.

The temperature and total energy remained constant and well-controlled within the limits of the MD simulation parameters. The pressures exhibited higher variance, as is expected from liquid solvents. For nearly incompressible liquids such as water, small changes in domain volume can result in significant pressure fluctuations. For both the AEM and CEM pre-polymer solutions, the simulated densities matched the experimentally determined densities within the uncertainties of the experimental measurements.

G.2.2 Polymerization

To ensure that simulation dynamics were adequately resolved during polymerization, we monitored again system level variables as a function of time (Appendix Figure G.13), which indicated that the reactions did not disrupt the accuracy of the simulation. We also monitored the extent of reaction as a function of time (Appendix Figure G.13). Initially chain growth proceeded rapidly, but as the polymerization approached completion, the rate of reaction slowed. the polymerization was deemed complete once the rate of reaction reached less than 10 chain growth steps per simulated ns. Using this criterion, AEM polymerization lasted 15 ns and CEM polymerization lasted 12 ns.

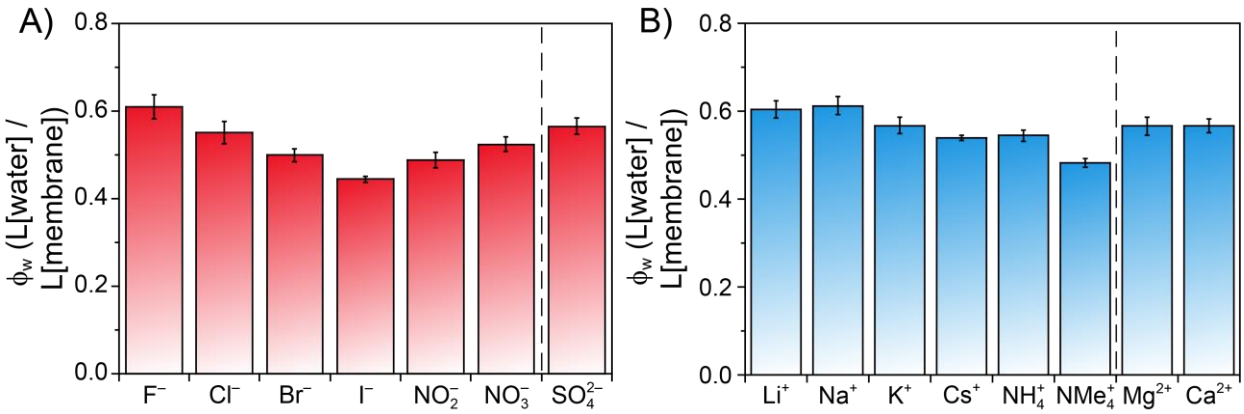
G.2.3 Equilibration

Appendix Table G.7 lists characteristics of the simulated IEMs after polymerization. Both simulations contained unreacted GDMA molecules and charged monomers which needed to be removed from the simulation. Removing non-networked monomers allowed for calculation of the IECs, which were slightly higher than the experimentally determined values. The IEC differences must be attributable to the co-monomer polymerization., since the IEC relates to the molecular composition of the polymer backbone. Because these differences were small, we do not believe the simulated co-polymerization was problematic.

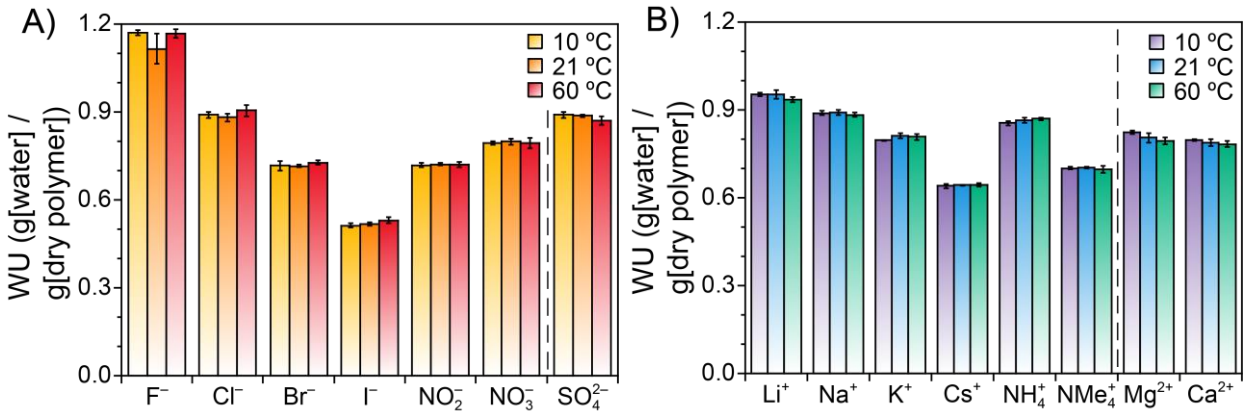
Water was then added to the Cl^- and K^+ form IEM simulations to match the experimental water uptakes of 0.833 and 0.813 g[water] / g[dry polymer]. After equilibration, the total hydrated densities of the simulations were recorded for comparison with experimental values (Appendix Table G.8 and Appendix Table G.9). The CEM in the K^+ form exhibited an equilibrated hydrated density that was the same as the experimentally determined value, within the uncertainty of the experimental data. Meanwhile, the AEM simulation in the Cl^- form possessed a lower density than the experimental result. Although the IEC discrepancy carries over between counter-ion forms, the

hydrated density changes as the simulations are re-equilibrated with the various counter-ion forms. Therefore, we consider the hydrated density of all 11 counter-ion forms (Appendix Table G.8 and Appendix Table G.9) to compare the molecular arrangement of the simulated IEMs with experimental values. The hydrated density of the simulated AEMs and CEMs fell within the uncertainty of the experimental data for a majority of the anions and cations analyzed, respectively. The CEM densities were higher than experimentally measured for Cs^+ and NH_4^+, but within error for Li^+, Na^+, K^+, and NMe_4^+ simulations. Meanwhile, the AEM densities were lower than experimentally measured for Cl^- and I^-, but within error for F^-, Br^-, and NO_3^- simulations. Overall, these results support that the simulations provide a good *in silico* representation of the polymer membranes which were characterized experimentally.

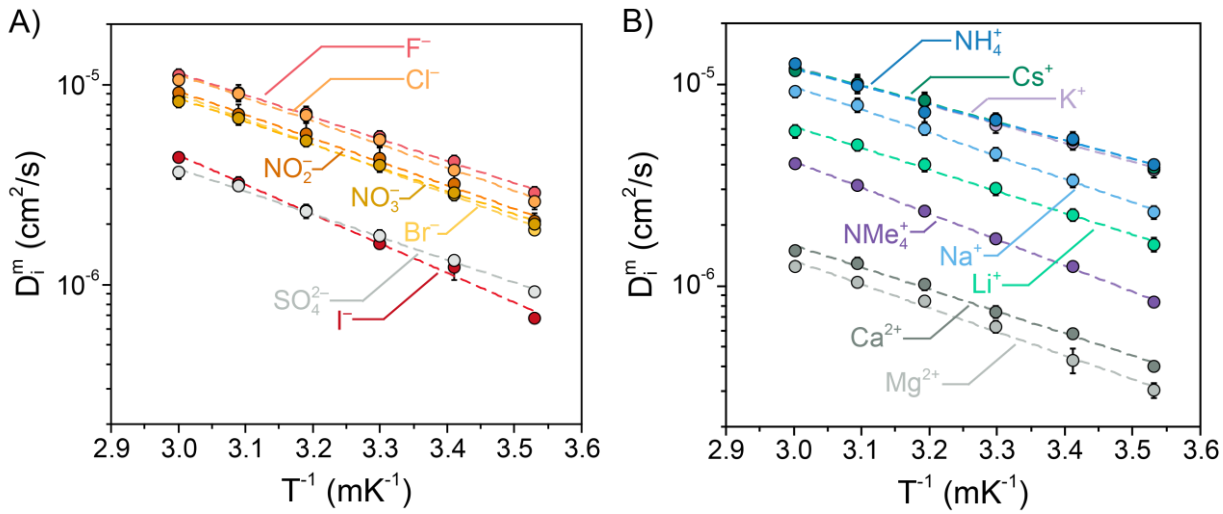
G.3 Supplementary Figures



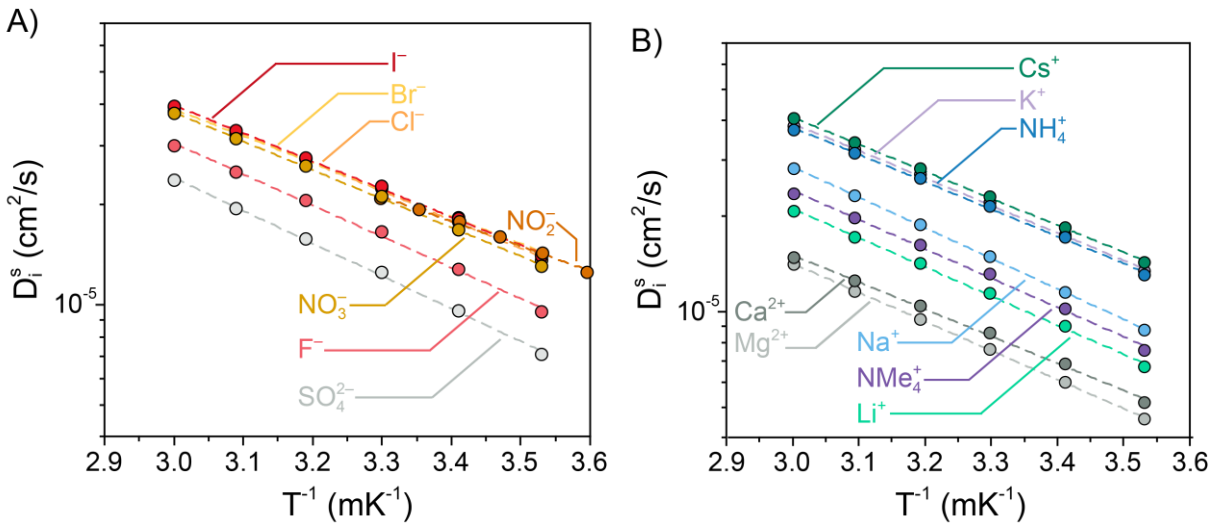
Appendix Figure G.1: Water volume fractions. The water volume fraction (ϕ_w) of A) AEMs and B) CEMs in each counter-ion form under study room temperature (21 ± 1 ºC). Error bars represent the standard deviation of at least five independent samples.



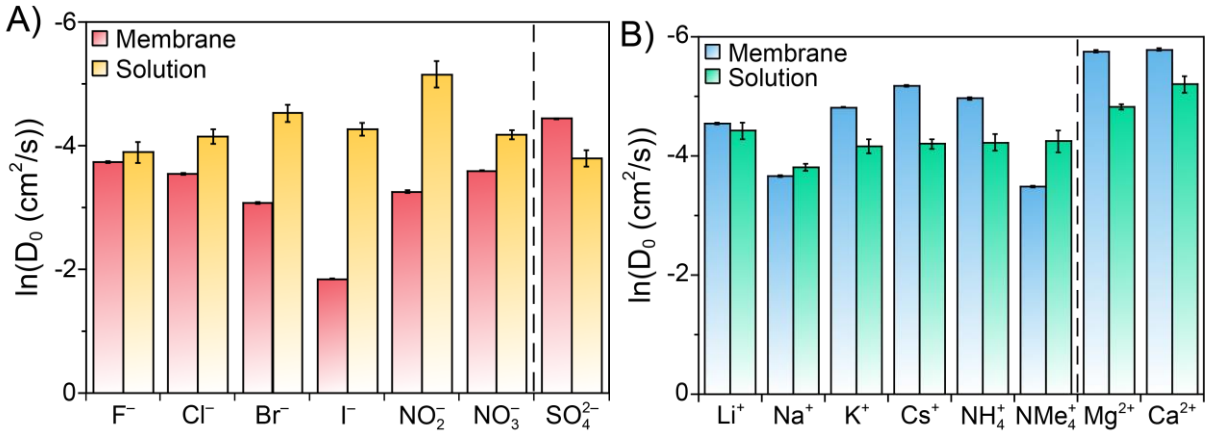
Appendix Figure G.2: Water uptake at various temperatures. The water uptake (WU) of A) AEMs and B) CEMs in each counter-ion form under study collected at 10 ºC, room temperature (21 ± 1 ºC), and 60 ºC. Error bars represent the standard deviation of at least five independent samples.



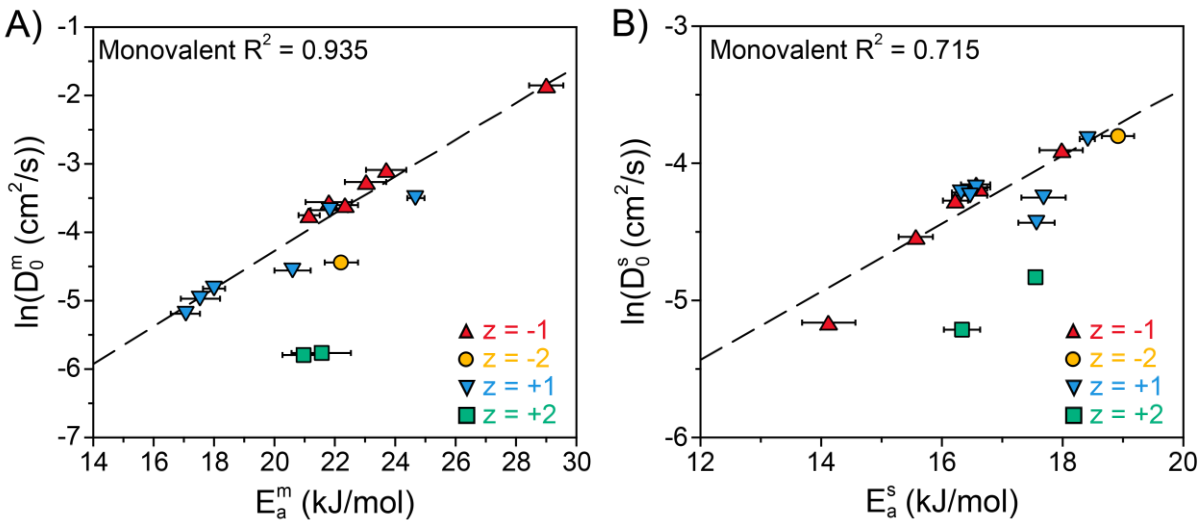
Appendix Figure G.3: Arrhenius plots of membrane ion diffusivities. The logarithm of ion diffusivities (D_i^m) plotted against the inverse temperature (T^{-1}) for A) anions and B) cations in the IEMs. Error bars represent the standard deviation of the data, calculated using standard error propagation methods.



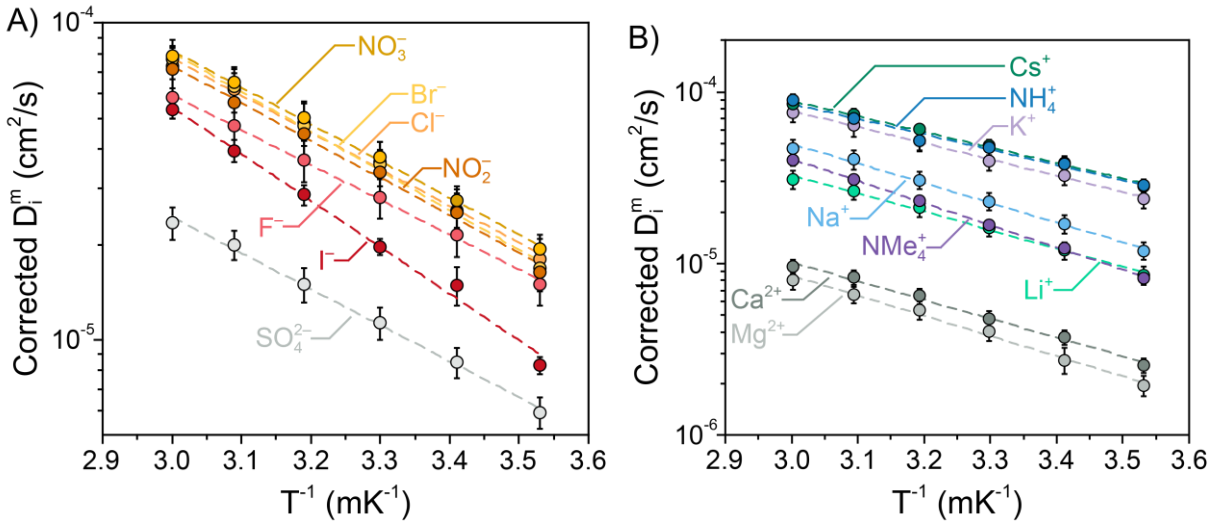
Appendix Figure G.4: Arrhenius plots of aqueous solution ion diffusivities. The logarithm of ion diffusivities (D_i^m) plotted against the inverse temperature (T^{-1}) for A) anions and B) cations in infinitely dilute aqueous solution.



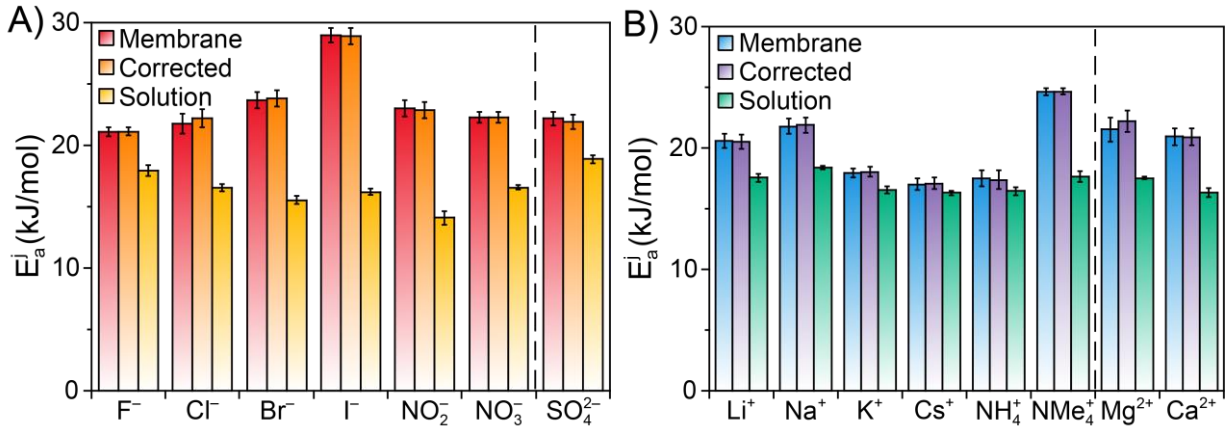
Appendix Figure G.5: Arrhenius pre-factors for ion diffusion. Arrhenius pre-factors (D_0) for A) anions and B) cations using diffusivities in the membrane and in aqueous solution. Uncertainties for the membrane data represent the standard error of the mean Arrhenius fit performed on four independently measured ionic conductivity data sets. Uncertainties for the aqueous solution data represent the standard error of the mean Arrhenius fit on the sampled data from the cubic fit of literature data. The solution pre-factor for NO_2^- is calculated over a narrower temperature range than the other ions, as discussed in Section 2.6.2.



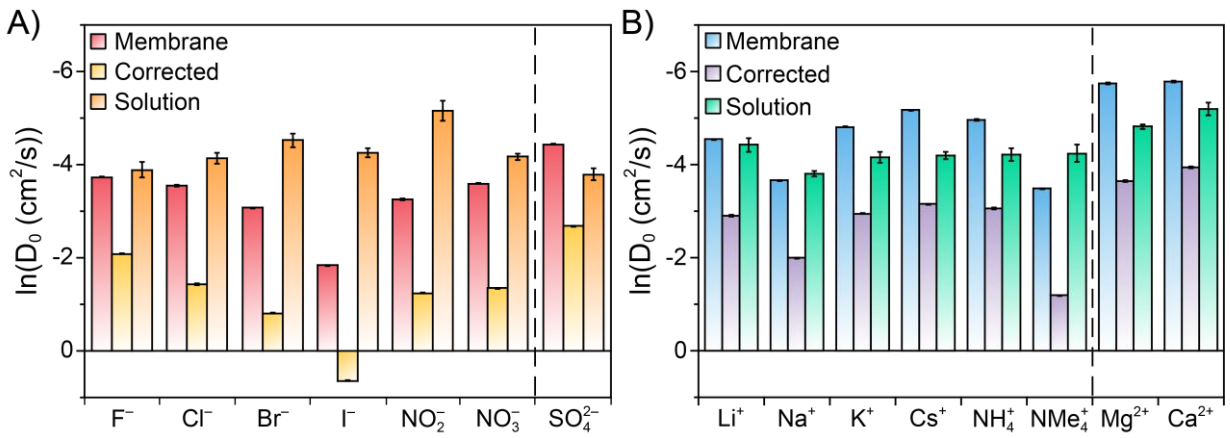
Appendix Figure G.6: Linear free energy relationships. Linear free energy plots for A) membrane diffusivities and B) aqueous solution diffusivities. The dashed lines represent linear fits of the monovalent ions. Divalent ion data are shown but not included in the linear regression. Uncertainties for the membrane data represent the standard error of the mean Arrhenius fit performed on four independently measured ionic conductivity data sets. Uncertainties for the aqueous solution data represent the standard error of the mean Arrhenius fit on the sampled data from the cubic fit of literature data.



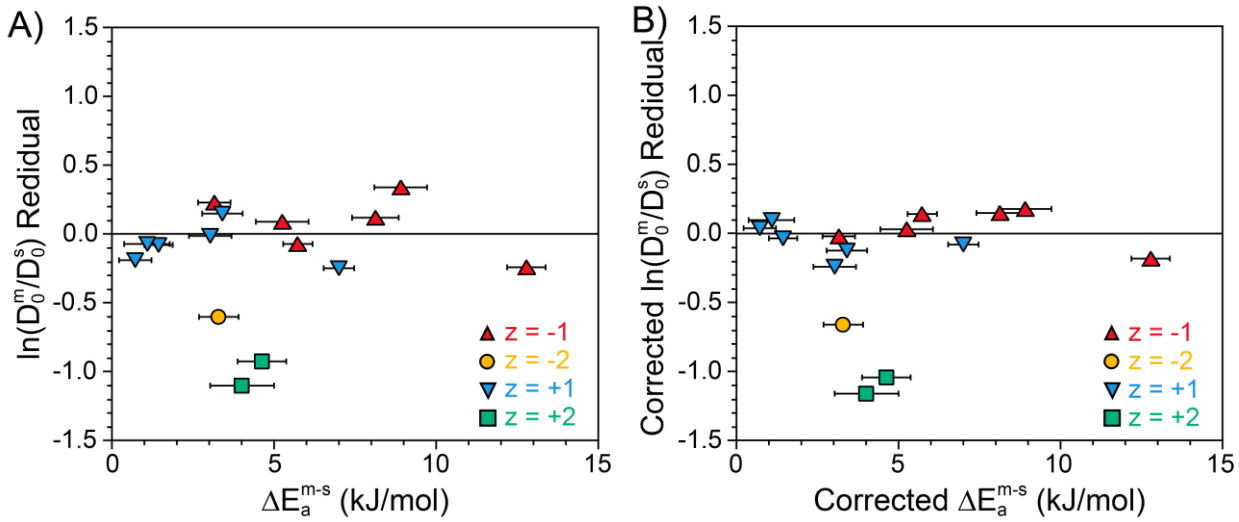
Appendix Figure G.7: Arrhenius plots of corrected ion diffusivities. The logarithm of corrected membrane ion diffusivities (D_i^m) plotted against the inverse temperature (T^{-1}) for A) anions and B) cations. Error bars represent the standard deviation of the data, calculated using standard error propagation methods.



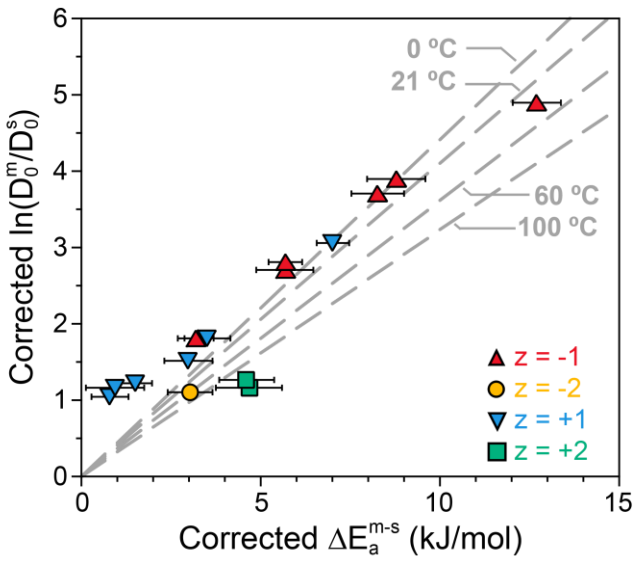
Appendix Figure G.8: Arrhenius activation energies of ion diffusion. Arrhenius activation energies (E_a^j) for A) anions and B) cations using diffusivities in the membrane, in the membrane but corrected using the Mackie-Meares model, and in aqueous solution. Uncertainties for the membrane and corrected data represent the standard error of the mean Arrhenius fit performed on four independently measured ionic conductivity data sets. Uncertainties for the aqueous solution data represent the standard error of the mean Arrhenius fit on the sampled data from the cubic fit of literature data. The solution activation energy for NO_2^- is calculated over a narrower temperature range than the other ions, as discussed in Section 2.6.2.



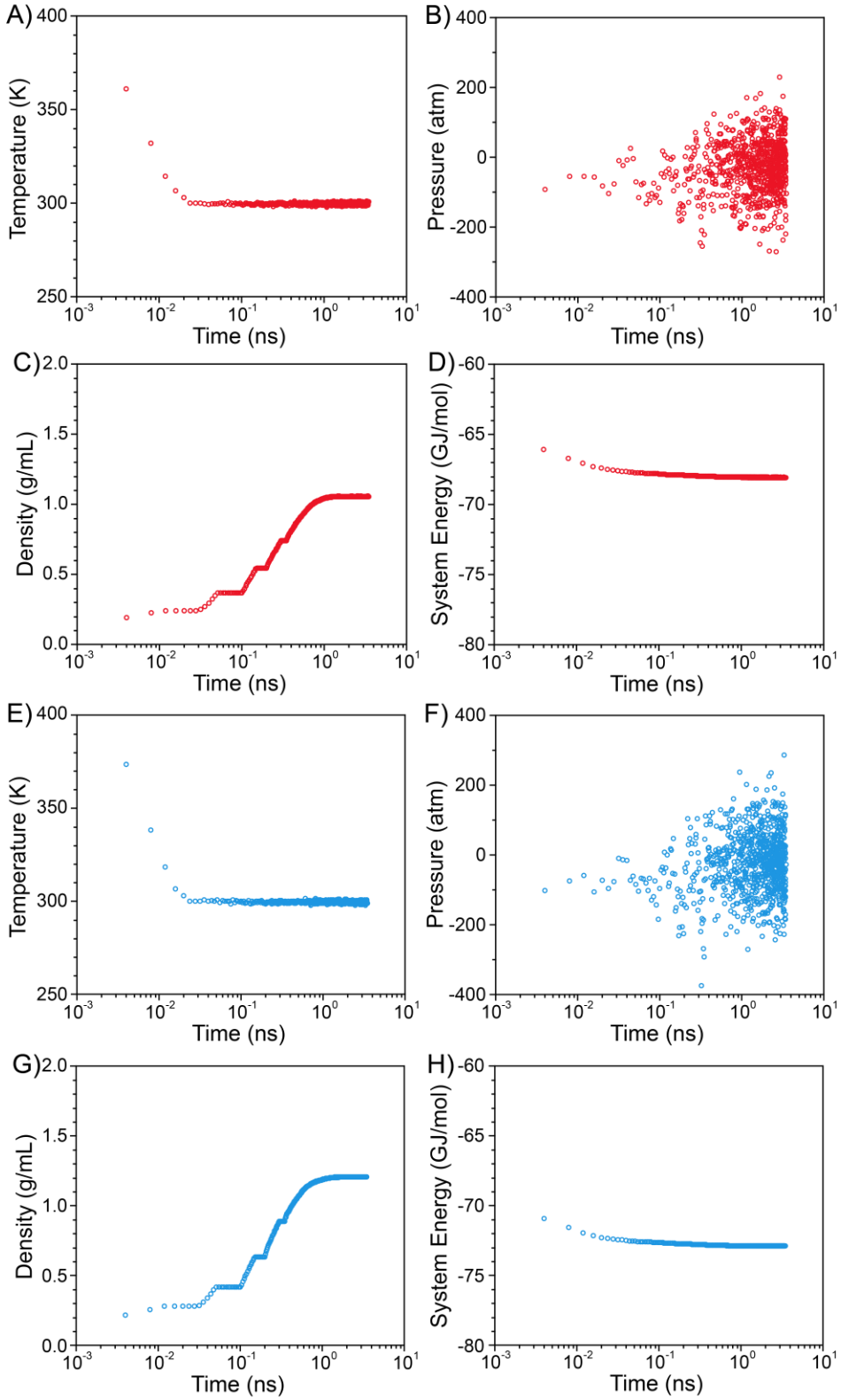
Appendix Figure G.9: Arrhenius pre-factors for ion diffusion. Arrhenius pre-factors (D_0) for A) anions and B) cations using diffusivities in the membrane, in the membrane but corrected using the Mackie-Meares model, and in aqueous solution. Uncertainties for the membrane and corrected data represent the standard error of the mean Arrhenius fit performed on four independently measured ionic conductivity data sets. Uncertainties for the aqueous solution data represent the standard error of the mean Arrhenius fit on the sampled data from the cubic fit of literature data. The solution pre-factor for NO_2^- is calculated over a narrower temperature range than the other ions, as discussed in Section 2.6.2.



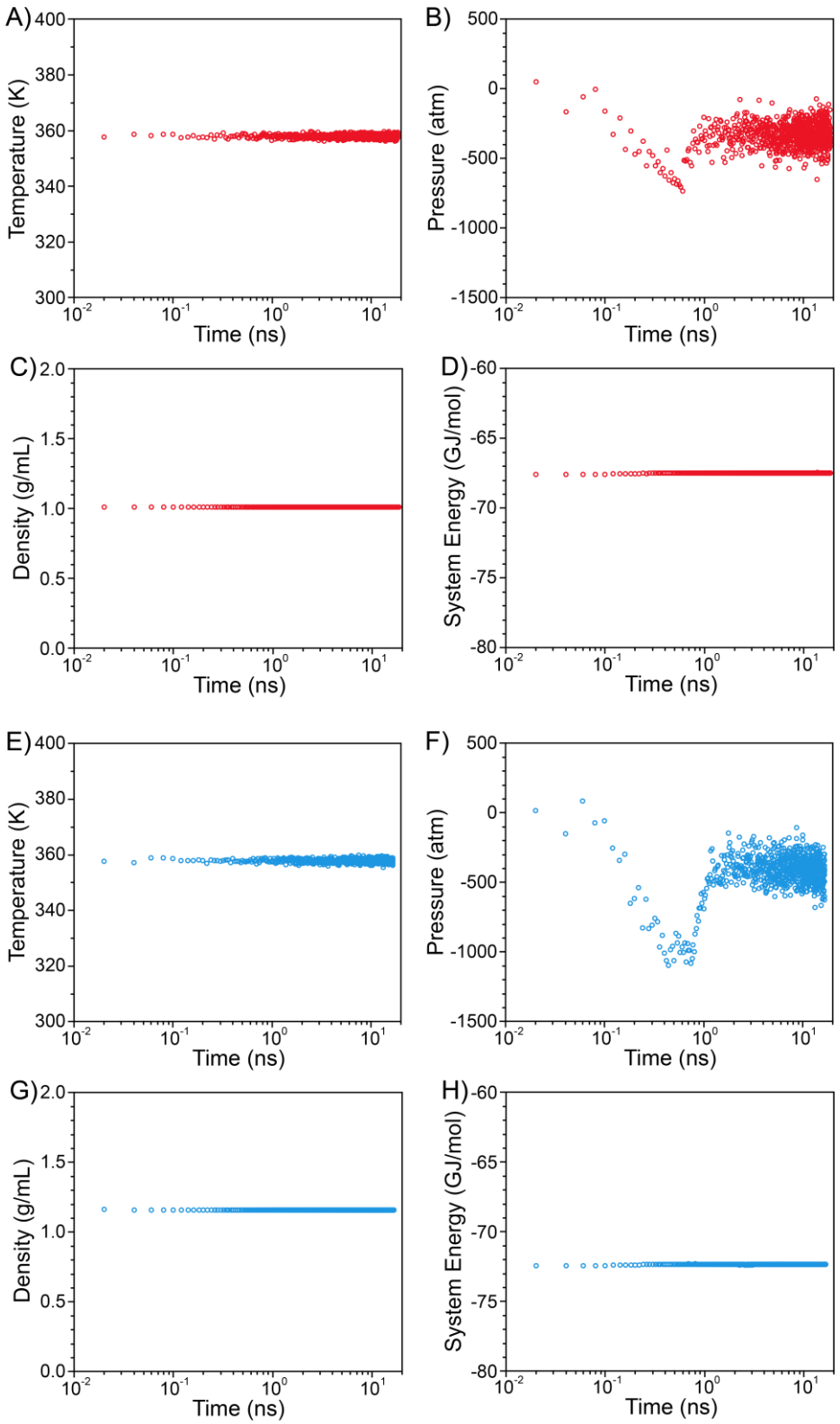
Appendix Figure G.10: Linear free energy residuals. Residual plots for the linear free energy relationships in Figure 3 in the main text. Regressions were performed only using the monovalent data, but the divalent data are shown for completeness. A) Activation energies and pre-factors for membrane diffusion referenced against the same values in aqueous solution. B) Activation energies and pre-factors for diffusivities corrected using the Mackie-Meares model referenced against the same value in aqueous solution. Uncertainties were calculated from standard errors of the activation energies and pre-factors using standard error propagation methods.



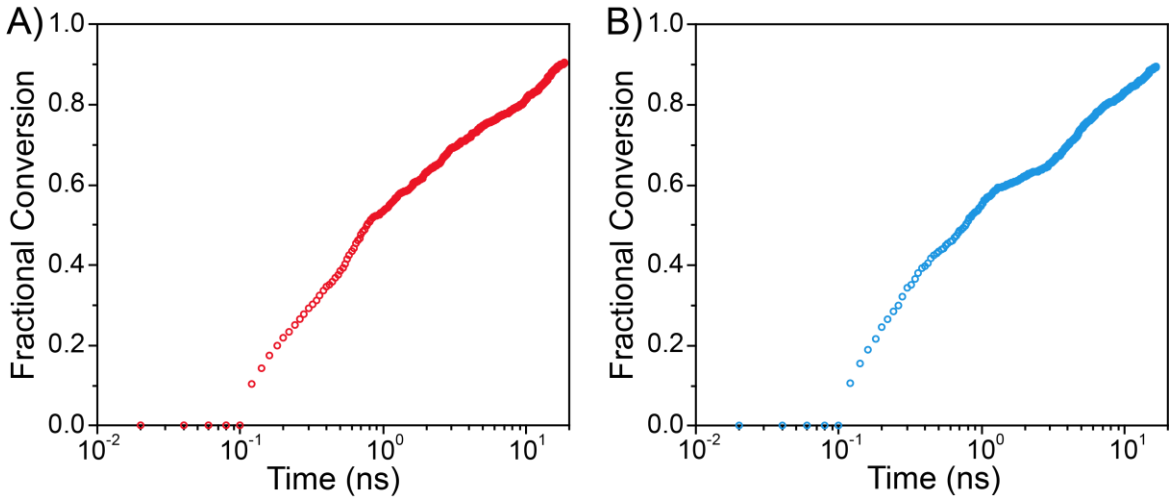
Appendix Figure G.11: Diffusivity parity lines. The linear free energy plot of the Mackie-Meares corrected diffusivities with added parity lines for 0, 10, 60, and 100 ºC. The parity lines compare the tortuosity-corrected diffusivity in the membrane and in aqueous solution. Data points above each line represent faster diffusion in the membrane at that temperature. Data points below each line represent slower diffusion in the membrane at that temperature. Uncertainties were calculated from standard errors of the activation energies and pre-factors using standard error propagation methods.



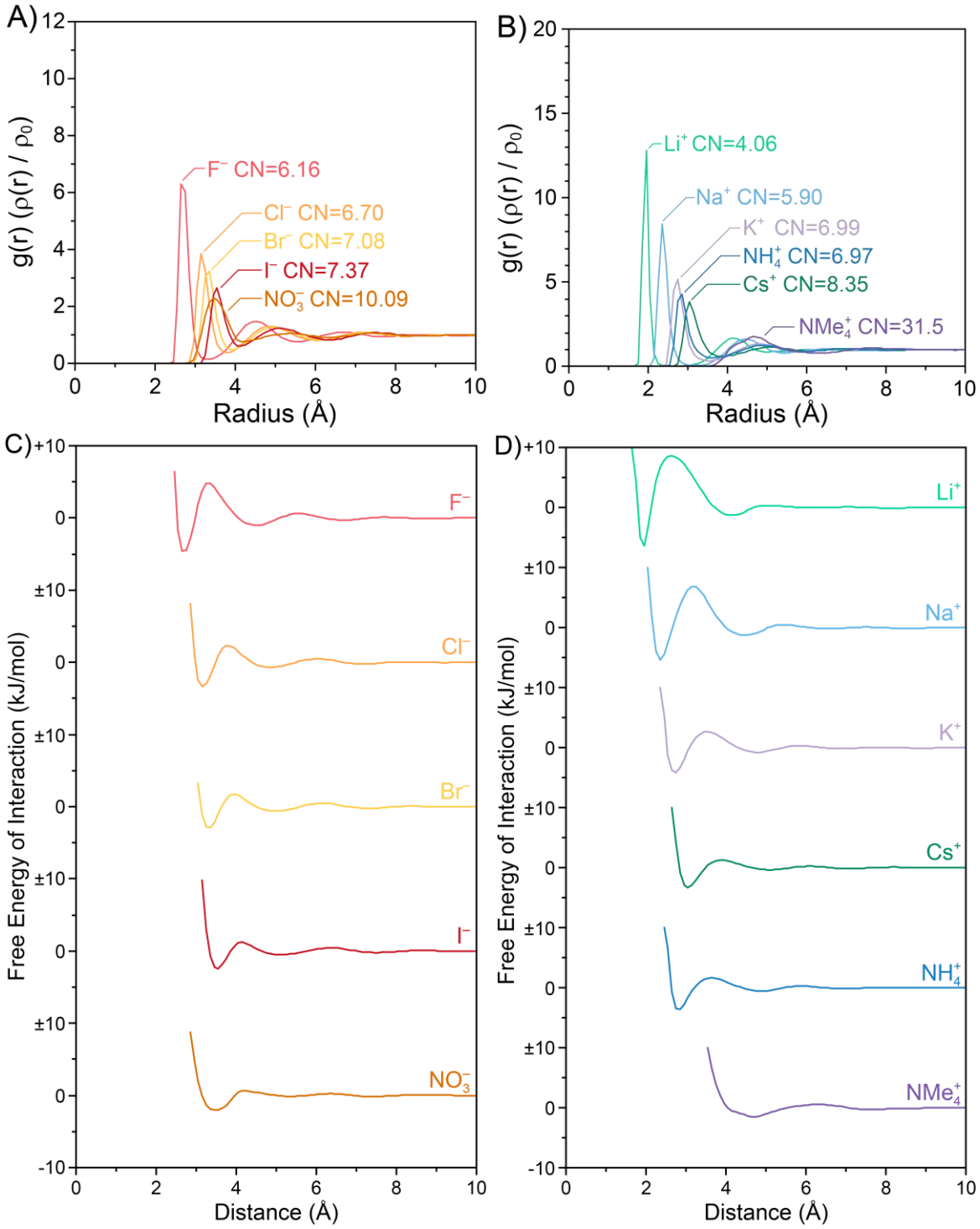
Appendix Figure G.12: Pre-polymer simulation equilibration. The AEM (A-H) and CEM (E-H) system-level variables during equilibration of the pre-polymer solution. Monitored variables include the temperature (A and E), pressure (B and F), density (C and G), and total energy (D and H).



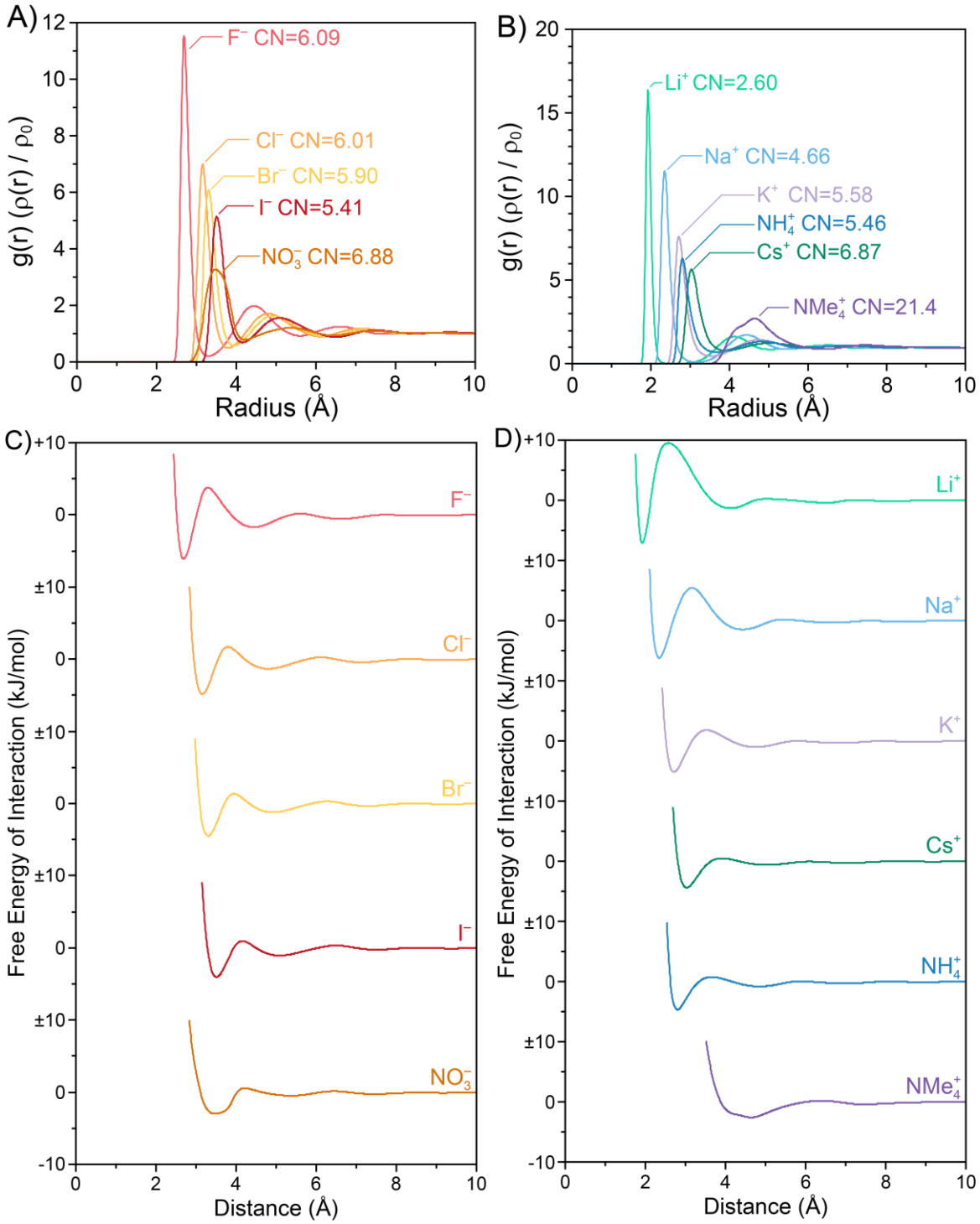
Appendix Figure G.13: System-level variables during polymerization. The AEM (A-D) and CEM (E-H) system-level variables during the polymerization reaction. Monitored variables include the temperature (A and E), pressure (B and F), density (C and G), and total energy (D and H).



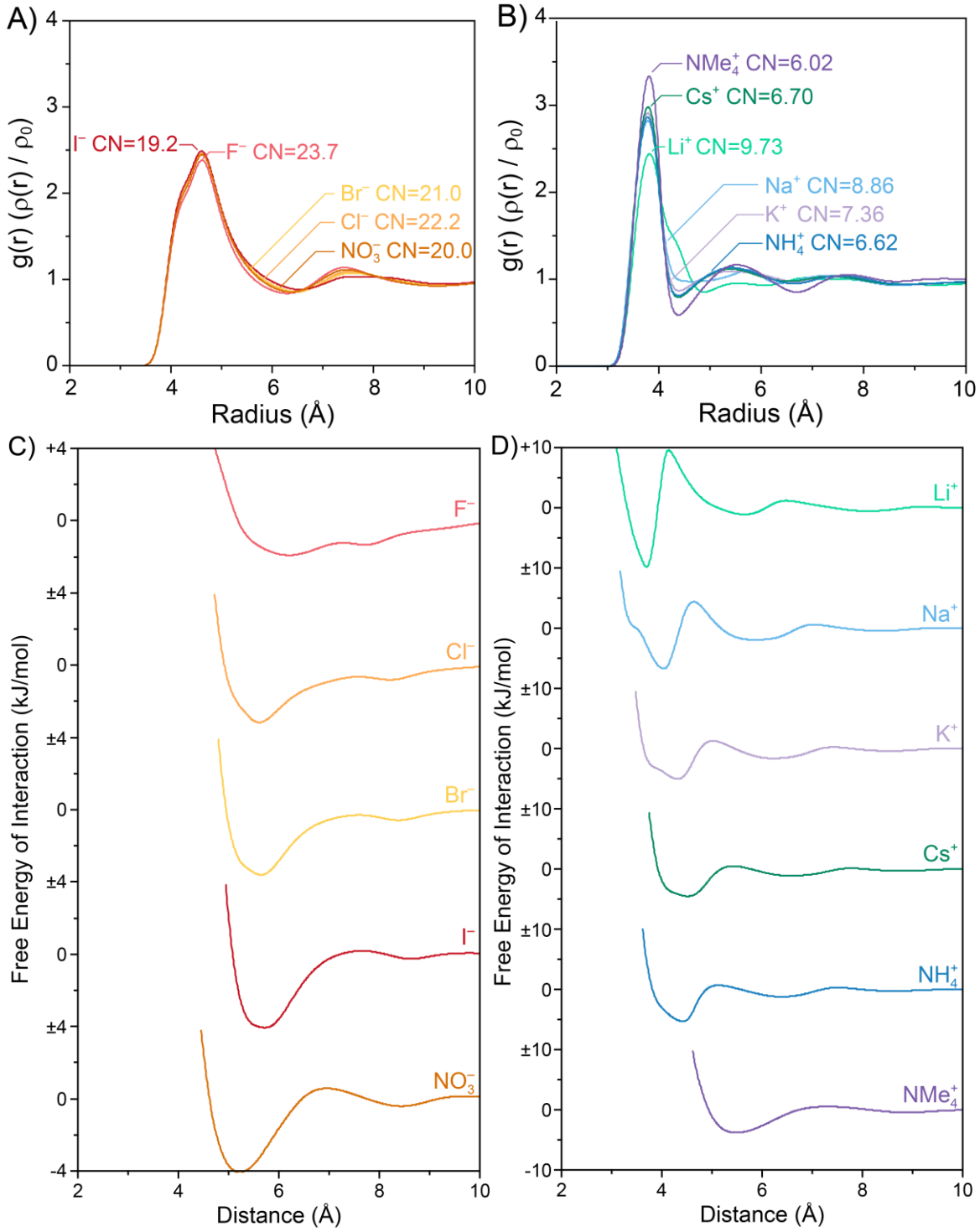
Appendix Figure G.14: Chain growth progression. The extent of reaction for methacrylate chain growth steps during polymerization. Progress is shown for A) the AEM and B) the CEM simulation.



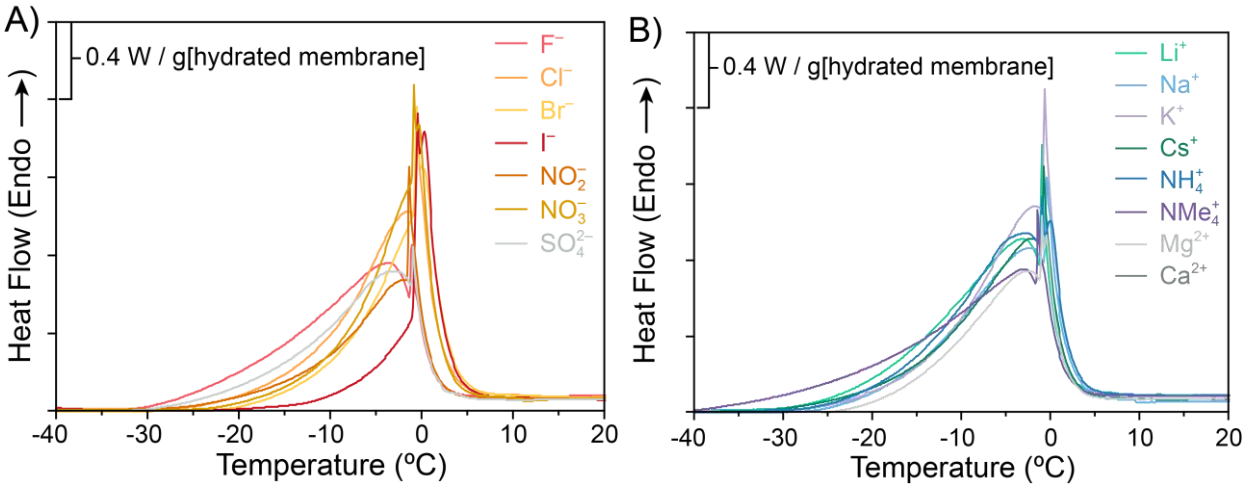
Appendix Figure G.15: Counter-ion/water interactions at infinite dilution. Radial distribution functions (A and A) and free energy profiles (C and D) for the pair formed by the central atom of the counter-ion and the oxygen atom of TIP4P water molecules. Anions are in panels A and C, cations in B and D. The first-shell coordination is listed with the RDFs.



Appendix Figure G.16: Counter-ion /water interactions in IEMs. Radial distribution functions (A and B) and free energy profiles (C and D) for the pair formed by the central atom of the counter-ion and the oxygen atom of TIP4P water molecules. AEMs are in panels A and C, CEMs in B and D. The first-shell coordination is listed with the RDFs.



Appendix Figure G.17: Fixed charge group/water interactions in the IEMs. Radial distribution functions (A and B) and free energy profiles (C and D) for the pair formed by the central atom of the counter-ion and the oxygen atom of TIP4P water molecules. AEMs are in panels A and C, CEMs in B and D. The first-shell coordination is listed with the RDFs.



Appendix Figure G.18: Differential scanning calorimetry thermograms. DSC traces of the water melting behavior for A) AEMs and B) CEMs.

G.4 Supplementary Tables

Appendix Table G.1: Membrane Recipes. Reagents used to prepare a typical batch of pre-polymer solution for the AEM and CEM.

IEM	Charged Monomer	Cross-Linker	Solvent	Initiator
AEM	9.38 g Monomer Solution (7.04 g MOETMA-Cl-)	5.64 g GDMA	9.38 g Monomer Solution (2.35 g Water) 5.71 g Additional Water 1.04 g 1-propanol	150 mg V-50
CEM	10.00 g SPM-K+	6.53 g GDMA	10.00 g Water	165 mg V-50

Appendix Table G.2: Gravimetric membrane structural properties. The ion-exchange capacity (IEC), water uptake (WU), and dry polymer density (ρ_p) for each counter-ion form of IEM. The fraction of theoretical IEC is included in parentheses to demonstrate the agreement between the counter-ion forms. Reported uncertainties represent the standard deviation of at least five independent measurements.

Counter-Ion Form	IEC (meq / g[polymer])	WU (g[water] / g[polymer])	ρ_p (g/cm^3)
F^-	2.546 ± 0.055 (90.8 ± 1.9 %)	1.117 ± 0.051	1.232 ± 0.006
Cl^-	2.460 ± 0.064 (91.8 ± 2.4 %)	0.883 ± 0.013	1.243 ± 0.002
Br^-	2.173 ± 0.056 (90.7 ± 2.3 %)	0.717 ± 0.004	1.356 ± 0.004
I^-	1.972 ± 0.049 (91.6 ± 2.3 %)	0.519 ± 0.005	1.453 ± 0.006
NO_2^-	2.286 ± 0.030 (87.7 ± 1.2 %)	0.800 ± 0.011	1.263 ± 0.005
NO_3^-	2.230 ± 0.014 (89.1 ± 0.5 %)	0.723 ± 0.005	1.288 ± 0.010
SO_4^{2-}	2.230 ± 0.035 (86.0 ± 1.4 %)	0.888 ± 0.004	1.309 ± 0.011
Li^+	2.371 ± 0.113 (90.0 ± 4.3 %)	0.954 ± 0.014	1.399 ± 0.013
Na^+	2.327 ± 0.080 (92.0 ± 3.1 %)	0.892 ± 0.008	1.417 ± 0.008
K^+	2.230 ± 0.132 (91.8 ± 5.4 %)	0.813 ± 0.009	1.442 ± 0.008
Cs^+	1.834 ± 0.028 (92.7 ± 1.4 %)	0.644 ± 0.001	1.701 ± 0.006
NH_4^+	2.852 ± 0.095 (111.4 ± 3.7 %)	0.866 ± 0.008	1.350 ± 0.009
NMe_4^+	2.342 ± 0.066 (104.6 ± 3.0 %)	0.703 ± 0.003	1.257 ± 0.005
Mg^{2+}	2.537 ± 0.036 (97.6 ± 1.4 %)	0.806 ± 0.016	1.427 ± 0.005
Ca^{2+}	2.357 ± 0.089 (82.5 ± 3.5 %)	0.790 ± 0.011	1.428 ± 0.007

Appendix Table G.3: Volumetric membrane structural properties. The water volume fraction (ϕ_w), fixed charge density ($C_A^{m,t}$), fixed charge concentration ($C_A^{m,w}$), maximum charge density (C_A^{max}), and membrane hydration number (λ) for each counter-ion form of IEM. Reported uncertainties represent the standard deviation of at least five independent measurements.

Counter-Ion Form	ϕ_w (L [water] / L [membrane])	$C_A^{m,t}$ (mol / L [membrane])	$C_A^{m,w}$ (mol / L [water])	C_A^{max} (mol / L [dry polymer])	λ (mol [water] / mol [charge])
F^-	0.611 ± 0.027	1.392 ± 0.093	2.279 ± 0.115	3.137 ± 0.069	24.4 ± 1.2
Cl^-	0.552 ± 0.026	1.537 ± 0.086	2.785 ± 0.083	3.057 ± 0.079	19.9 ± 0.6
Br^-	0.500 ± 0.015	1.514 ± 0.061	3.029 ± 0.079	2.947 ± 0.076	18.3 ± 0.5
I^-	0.445 ± 0.007	1.688 ± 0.052	3.796 ± 0.100	2.865 ± 0.072	14.6 ± 0.4
NO_2^-	0.525 ± 0.017	1.498 ± 0.055	2.856 ± 0.055	2.887 ± 0.040	19.4 ± 0.4
NO_3^-	0.489 ± 0.018	1.508 ± 0.058	3.083 ± 0.028	2.873 ± 0.028	18.0 ± 0.2
SO_4^{2-}	0.566 ± 0.019	1.419 ± 0.054	2.509 ± 0.041	2.919 ± 0.052	22.1 ± 0.4
Li^+	0.605 ± 0.020	1.504 ± 0.091	2.486 ± 0.124	3.318 ± 0.162	22.3 ± 1.1
Na^+	0.613 ± 0.021	1.599 ± 0.080	2.608 ± 0.093	3.297 ± 0.114	21.3 ± 0.8
K^+	0.568 ± 0.019	1.558 ± 0.107	2.742 ± 0.165	3.217 ± 0.191	20.3 ± 1.2
Cs^+	0.540 ± 0.006	1.537 ± 0.030	2.849 ± 0.044	3.121 ± 0.049	19.5 ± 0.3
NH_4^+	0.545 ± 0.012	1.796 ± 0.073	3.294 ± 0.114	3.849 ± 0.131	16.9 ± 0.6
NMe_4^+	0.483 ± 0.009	1.607 ± 0.054	3.329 ± 0.095	2.943 ± 0.084	16.7 ± 0.5
Mg^{2+}	0.567 ± 0.021	1.785 ± 0.078	3.146 ± 0.076	3.620 ± 0.054	17.7 ± 0.4
Ca^{2+}	0.567 ± 0.016	1.691 ± 0.083	2.984 ± 0.119	3.366 ± 0.128	18.6 ± 0.7

Appendix Table G.4: Validation of equivalent circuits at high temperatures. In-plane ionic conductivities (κ) measured at elevated temperature using the modified Randles equivalent circuit fitting technique and the varied length technique. The varied length method was relied upon at lower temperatures until values were in agreement, then all lower temperatures were collected automatically using the equivalent circuit technique.

Counter-Ion Form	Temperature (ºC)	κ (mS/cm) Equivalent Circuit	κ (mS/cm) Varied Length
F^-	60	53.12 ± 2.94	52.56 ± 0.71
Cl^-	60	55.88 ± 4.67	54.71 ± 0.50
Br^-	60	44.16 ± 2.05	43.54 ± 0.44
I^-	60	25.76 ± 2.34	24.70 ± 0.84
NO_2^-	60	45.72 ± 6.85	43.65 ± 4.79
NO_3^-	60	42.04 ± 1.31	41.95 ± 1.54
SO_4^{2-}	60	37.47 ± 1.05	34.73 ± 1.94
Li^+	60	30.35 ± 0.87	29.61 ± 1.49
Na^+	60	46.53 ± 2.06	46.47 ± 0.89
K^+	60	54.49 ± 5.83	62.57 ± 1.17
Cs^+	60	64.77 ± 4.41	60.54 ± 2.60
	60	---†	76.16 ± 2.57
NH_4^+	50	---†	61.18 ± 2.67
	40	55.43 ± 0.40	53.10 ± 0.69
NMe_4^+	60	21.92 ± 0.85	21.27 ± 1.47
Mg^{2+}	60	14.81 ± 0.83	15.04 ± 0.27
Ca^{2+}	60	16.97 ± 0.19	17.04 ± 0.45

†Equivalent circuit fitting did not converge.

Appendix Table G.5: Accepted ionic conductivities. The ionic conductivity of each counter-ion form IEM as a function of temperature. Uncertainties represent the standard deviation of four independent measurements.

Counter-Ion Form	10 ºC	20 ºC	30 ºC	40 ºC	50 ºC	60 ºC
F^-	15.96 ± 0.34	21.97 ± 0.52	28.06 ± 1.04	35.636 ± 1.74	44.106 ± 2.62	52.56 ± 0.71
Cl^-	15.87 ± 1.10	21.87 ± 1.97	29.96 ± 1.96	38.62 ± 2.21	47.84 ± 2.73	54.71 ± 0.50
Br^-	11.21 ± 0.41	16.35 ± 0.85	22.39 ± 1.11	28.55 ± 0.89	36.90 ± 1.08	43.54 ± 0.44
I^-	4.55 ± 0.15	7.84 ± 1.02	10.07 ± 0.25	14.18 ± 0.69	18.97 ± 1.16	24.70 ± 0.84
NO_2^-	12.31 ± 1.11	18.28 ± 2.08	23.67 ± 3.36	30.31 ± 3.92	36.98 ± 4.14	45.72 ± 6.85
NO_3^-	12.06 ± 0.24	16.61 ± 0.26	22.07 ± 0.60	28.44 ± 1.22	35.55 ± 1.69	41.95 ± 1.54
SO_4^{2-}	10.33 ± 0.44	14.35 ± 0.64	18.49 ± 1.05	23.65 ± 1.58	30.62 ± 0.61	34.73 ± 1.94
Li^+	9.60 ± 0.42	12.92 ± 0.45	16.90 ± 0.51	21.41 ± 0.76	26.04 ± 0.65	29.61 ± 1.49
Na^+	13.79 ± 0.45	19.13 ± 0.74	25.03 ± 0.93	32.24 ± 0.84	41.23 ± 2.23	46.47 ± 0.89
K^+	23.21 ± 1.01	30.60 ± 1.41	36.12 ± 1.71	45.89 ± 3.47	54.37 ± 4.58	62.57 ± 1.17
Cs^+	23.50 ± 1.64	30.99 ± 2.35	37.95 ± 2.70	45.64 ± 3.05	53.78 ± 4.11	60.54 ± 2.60
NH_4^+	28.36 ± 1.25	36.76 ± 2.54	44.20 ± 2.43	53.10 ± 0.69	61.18 ± 2.67	76.16 ± 2.57
NMe_4^+	5.32 ± 0.10	7.66 ± 0.17	10.13 ± 0.20	13.51 ± 0.43	17.54 ± 0.46	21.92 ± 0.85
Mg^{2+}	4.31 ± 0.32	5.87 ± 0.79	8.34 ± 0.45	10.76 ± 0.37	12.82 ± 0.17	15.04 ± 0.27
Ca^{2+}	5.38 ± 0.11	7.53 ± 0.25	9.33 ± 0.44	12.29 ± 0.42	15.28 ± 0.53	17.04 ± 0.45

Appendix Table G.6: Polymerization simulation conditions. The size and constituent molecules of the pre-polymer solution domains used to prepare the AEM and CEM *in silico*. The density of the simulated and experimental pre-polymer solutions are provided for comparison.

Parameter	AEM	CEM
Number of GDMA	2,100	2,100
Number initiated	47	52
Number of MOETMA	2,900	---
Number initiated	33	---
Number of SPM	---	2,900
Number initiated	---	36
Number of waters	38,500	40,000
Number of atoms	328,500	299,700
Domain side length (Å)	143.1	138.4
Simulated ρ_{pp} (g/cm^3)	1.057	1.208
Experimental ρ_{pp} (g/cm^3)	1.069 ± 0.031	1.193 ± 0.053

Appendix Table G.7: Network incorporation properties. Post-polymerization properties of the simulated AEM and CEM are reported including the total number of unreacted methacrylate groups, the number of unreacted methacrylate groups corresponding to charged monomers (MOETMA and SPM), and the number of unreacted methacrylate groups corresponding to GDMA cross-linkers. The gel fraction (GF) and as-synthesized IEC (the Cl^- form for the AEM and the K^+ form for the CEM) are compared with the corresponding experimental values.

Properties	AEM	CEM
Number of unreacted methacrylate groups	265	199
Number of unreacted charged monomers	209	163
Number of unreacted GDMA methacrylate groups	56	36
Simulated GF (%)	96.0	95.9
Experimental GF (%)	96.0 ± 1.5	96.1 ± 1.2
Simulated IEC (meq / g[dry polymer])	2.59	2.39
Experimental IEC (meq / g[dry polymer])	2.460 ± 0.064	2.230 ± 0.132

Appendix Table G.8: AEM conversion and hydration properties. Experimentally determined water uptakes and hydrated densities are reproduced alongside the number of water molecules which were added to the AEM simulations to match the experimental water uptake. Hydrated densities (ρ_m) collected after the simulation equilibrated with the new ions and waters are compared to the corresponding experimental values.

Properties	F^-	Cl^-	Br^-	I^-	NO_3^-
Experimental WU (g[water] / g[dry polymer])	1.117 ± 0.051	0.883 ± 0.013	0.717 ± 0.004	0.519 ± 0.005	0.723 ± 0.005
Water Molecules Added Post-Polymerization	26109	12691	7944	-1149	6353
Simulated ρ_m (g/cm^3)	1.129	1.121	1.179	1.249	1.172
Experimental ρ_m (g/cm^3)	1.155 ± 0.032	1.205 ± 0.035	1.194 ± 0.038	1.298 ± 0.025	1.163 ± 0.040

Appendix Table G.9: CEM conversion and hydration properties. Experimentally determined water uptakes and hydrated densities are reproduced alongside the number of water molecules which were added to the CEM simulations to match the experimental water uptake. Hydrated densities (ρ_m) collected after the simulation equilibrated with the new ions and waters are compared to the corresponding experimental values.

Properties	Li^+	Na^+	K^+	Cs^+	NH_4^+	NMe_4^+
Experimental WU (g[water] / g[dry polymer])	0.954 ± 0.014	0.892 ± 0.008	0.813 ± 0.009	0.644 ± 0.001	0.866 ± 0.008	0.703 ± 0.003
Water Molecules Added Post-Polymerization	15997	14535	11696	10135	11871	8448
Simulated ρ_m (g/cm^3)	1.201	1.241	1.257	1.396	1.207	1.161
Experimental ρ_m (g/cm^3)	1.208 ± 0.011	1.226 ± 0.047	1.238 ± 0.042	1.375 ± 0.017	1.173 ± 0.027	1.167 ± 0.021

Appendix Table G.10: Water coordination of ions in dilute aqueous solution. Ion-water coordination numbers for ions at infinite dilution (CN_{g-w}^{ID}) in our simulations are compared with accepted literature values compiled by Marcus[363]. Literature values for thermodynamic hydration numbers of each ion at infinite dilution (HN_{g-w}^{ID}) are also included.

Ion	CN_{g-w}^{ID} (Our Simulation)	CN_{g-w}^{ID} (Literature Simulations)	CN_{g-w}^{ID} (Literature Scattering)	HN_{g-w}^{ID} (Literature Thermodynamics)
F^-	6.2	4.6	4.0 – 6.0	4.2
Cl^-	6.7	5.6	5.3 – 8.0	2.0
Br^-	7.1	---	4.2 – 6.5	1.3
I^-	7.4	8.0	4.2 – 9.6	0.9
NO_2^-	---	---	---	2.3
NO_3^-	10.1	12.8	3.0 – 4.3	1.6
SO_4^{2-}	---	11.3	7.6 – 9.6	6.4
Li^+	4.1	11.3	4.0 – 6.0	4.2
Na^+	5.9	---	4.0 – 8.0	3.3
K^+	7.0	4.2	6.0 – 8.0	2.3
Cs^+	8.3	5.4	6.0 – 8.0	1.7
NH_4^+	7.0	---	4.0 – 8.0	1.9
NMe_4^+	31.5	---	---	2.1
Mg^{2+}	---	6.0	6.0	6.0
Ca^{2+}	---	7.0	6.0 – 7.0	7.0

Appendix Table G.11: States of water in the IEM. The enthalpy of water melting (ΔH_m) measured for each counter-ion form IEM alongside the calculated fraction of freezable water (f_f), freezable hydration number (λ_f), and non-freezable hydration number (λ_{nf}). Uncertainties represent the standard deviation calculated using standard error propagation techniques from experimental data averaged over at least 5 samples.

Ion	ΔH_m^m (J / g[water])	f_f	λ_f	λ_{nf}
F^-	119.2 ± 2.8	0.358 ± 0.008	8.72 ± 0.49	15.65 ± 0.82
Cl^-	138.1 ± 5.3	0.415 ± 0.016	8.27 ± 0.40	11.68 ± 0.47
Br^-	140.8 ± 5.7	0.423 ± 0.017	7.76 ± 0.37	10.58 ± 0.42
I^-	104.2 ± 3.5	0.313 ± 0.010	4.58 ± 0.19	10.06 ± 0.31
NO_2^-	160.7 ± 4.1	0.483 ± 0.006	9.39 ± 0.21	10.06 ± 0.22
NO_3^-	149.2 ± 2.0	0.448 ± 0.006	8.07 ± 0.13	9.95 ± 0.14
SO_4^{2-}	119.7 ± 3.0	0.359 ± 0.009	7.96 ± 0.42	14.18 ± 0.31
Li^+	145.9 ± 2.8	0.438 ± 0.008	9.79 ± 0.52	12.56 ± 0.65
Na^+	146.8 ± 1.6	0.441 ± 0.005	9.39 ± 0.35	11.91 ± 0.43
K^+	168.1 ± 3.7	0.505 ± 0.011	10.23 ± 0.65	10.03 ± 0.64
Cs^+	167.2 ± 1.6	0.502 ± 0.005	9.79 ± 0.18	9.71 ± 0.18
NH_4^+	167.9 ± 4.1	0.504 ± 0.012	8.50 ± 0.36	8.36 ± 0.36
NMe_4^+	165.8 ± 3.4	0.498 ± 0.010	8.31 ± 0.29	8.38 ± 0.29
Mg^{2+}	122.6 ± 2.0	0.368 ± 0.006	6.50 ± 0.19	11.16 ± 0.29
Ca^{2+}	130.8 ± 3.1	0.393 ± 0.009	7.31 ± 0.34	11.31 ± 0.48

Bibliography

(1) IPCC. Climate Change 2023: Synthesis Report. Contribution of Working Groups I, II, and III to the Sixth Assessment Report of the Intergovernmental Panel on Climate Change, First.; Lee, H., Romero, J., Series Eds.; Intergovernmental Panel on Climate Change (IPCC), 2023. https://doi.org/10.59327/IPCC/AR6-9789291691647.

(2) WHO; UNICEF. Progress on Household Drinking Water, Sanitation and Hygiene; 2021.

(3) Muhammad Yaqub; Lee, W. Zero-Liquid Discharge (ZLD) Technology for Resource Recovery from Wastewater: A Review. Science of The Total Environment **2019**, 681, 551–563. https://doi.org/10.1016/j.scitotenv.2019.05.062.

(4) Tong, T.; Elimelech, M. The Global Rise of Zero Liquid Discharge for Wastewater Management: Drivers, Technologies, and Future Directions. Environmental Science and Technology **2016**, 50 (13), 6846–6855. https://doi.org/10.1021/acs.est.6b01000.

(5) National Academies of Sciences, Engineering, and Medicine. New Directions for Chemical Engineering; National Academies Press: Washington, D.C., 2022. https://doi.org/10.17226/26342.

(6) IEA. World Energy Outlook 2023; IEA: Paris, 2023. https://www.iea.org/reports/world-energy-outlook-2023.

(7) Metzger, E.; Owens, B.; Reig, P.; Hua Wen, W.; Young, R. Water-Energy Nexus: Business Risks and Rewards. World Resources Institute **2016**.

(8) Sedlak, D.; Mauter, M.; Macknick, J.; Stokes-Draut, J.; Fiske, P.; Agarwal, D.; Borch, T.; Breckenridge, R.; Cath, T.; Chellam, S.; Childress, A.; Dionysiou, D.; Giammar, D.; Hoek, E.; Jiang, S.; Katz, L.; Kim, J.; Kostecki, R.; McCutcheon, J.; Polsky, Y.; Stoll, Z.; Xu, P. National Alliance for Water Innovation (NAWI) Master Technology Roadmap; DOE/GO-102021-5617; 2021. https://doi.org/10.2172/1818076.

(9) Copeland, C.; Carter, N. T. Energy-Water Nexus: The Water Sector's Energy Use. **2017**.

(10) Landsman, M. R.; Sujanani, R.; Brodfuehrer, S. H.; Cooper, C. M.; Darr, A. G.; Davis, R. J.; Kim, K.; Kum, S.; Nalley, L. K.; Nomaan, S. M.; Oden, C. P.; Paspureddi, A.; Reimund, K. K.; Rowles, L. S.; Yeo, S.; Lawler, D. F.; Freeman, B. D.; Katz, L. E. Water Treatment: Are Membranes the Panacea? Annual Review of Chemical and Biomolecular Engineering **2020**, 11, 559–585. https://doi.org/10.1146/annurev-chembioeng-111919-091940.

(11) Ran, J.; Wu, L.; He, Y.; Yang, Z.; Wang, Y.; Jiang, C.; Ge, L.; Bakangura, E.; Xu, T. Ion Exchange Membranes: New Developments and Applications. Journal of Membrane Science **2017**, 522, 267–291. https://doi.org/10.1016/j.memsci.2016.09.033.

(12) Eckard, R. Ion Exchange Materials: Water Applications and Beyond; MST072A; BCC Publishing, 2019.

(13) Jiang, S.; Sun, H.; Wang, H.; Ladewig, B. P.; Yao, Z. A Comprehensive Review on the Synthesis and Applications of Ion Exchange Membranes. Chemosphere **2021**, 282, 130817. https://doi.org/10.1016/j.chemosphere.2021.130817.

(14) Li, K.; Fan, Q.; Chuai, H.; Liu, H.; Zhang, S.; Ma, X. Revisiting Chlor-Alkali Electrolyzers: From Materials to Devices. Trans. Tianjin Univ. **2021**, 27 (3), 202–216. https://doi.org/10.1007/s12209-021-00285-9.
(15) Abbasi, R.; Setzler, B. P.; Lin, S.; Wang, J.; Zhao, Y.; Xu, H.; Pivovar, B.; Tian, B.; Chen, X.; Wu, G.; Yan, Y. A Roadmap to Low-Cost Hydrogen with Hydroxide Exchange Membrane Electrolyzers. Advanced Materials **2019**, 31 (31), 1805876. https://doi.org/10.1002/adma.201805876.
(16) Helfferich, F. Ion Exchange; Dover Science Books: New York, 1995.
(17) Strathmann, H. Ion-Exchange Membrane Separation Processes, First.; Elsevier: Amsterdam, 2004.
(18) Tanaka, Y. Ion Exchange Membranes: Fundamentals and Applications, 2nd edition.; Elsevier: Amsterdam, 2015.
(19) Tricker, A. W.; Lee, J. K.; Shin, J. R.; Danilovic, N.; Weber, A. Z.; Peng, X. Design and Operating Principles for High-Performing Anion Exchange Membrane Water Electrolyzers. Journal of Power Sources **2023**, 567, 232967. https://doi.org/10.1016/j.jpowsour.2023.232967.
(20) Gurreri, L.; Tamburini, A.; Cipollina, A.; Micale, G. Electrodialysis Applications in Wastewater Treatment for Environmental Protection and Resources Recovery: A Systematic Review on Progress and Perspectives. Membranes **2020**, 10 (7), 1–93. https://doi.org/10.3390/membranes10070146.
(21) Strathmann, H. Electrodialysis, a Mature Technology with a Multitude of New Applications. Desalination **2010**, 264 (3), 268–288. https://doi.org/10.1016/j.desal.2010.04.069.
(22) Resnick, P. R. A Short History of Nafion. Actual. Chim. **2006**, 301–302, 144–147.
(23) Xiong, P.; Zhang, L.; Chen, Y.; Peng, S.; Yu, G. A Chemistry and Microstructure Perspective on Ion-Conducting Membranes for Redox Flow Batteries. Angewandte Chemie International Edition **2021**, 60 (47), 24770–24798. https://doi.org/10.1002/anie.202105619.
(24) Yang, Y.; Peltier, C. R.; Zeng, R.; Schimmenti, R.; Li, Q.; Huang, X.; Yan, Z.; Potsi, G.; Selhorst, R.; Lu, X.; Xu, W.; Tader, M.; Soudackov, A. V.; Zhang, H.; Krumov, M.; Murray, E.; Xu, P.; Hitt, J.; Xu, L.; Ko, H.-Y.; Ernst, B. G.; Bundschu, C.; Luo, A.; Markovich, D.; Hu, M.; He, C.; Wang, H.; Fang, J.; DiStasio, R. A.; Kourkoutis, L. F.; Singer, A.; Noonan, K. J. T.; Xiao, L.; Zhuang, L.; Pivovar, B. S.; Zelenay, P.; Herrero, E.; Feliu, J. M.; Suntivich, J.; Giannelis, E. P.; Hammes-Schiffer, S.; Arias, T.; Mavrikakis, M.; Mallouk, T. E.; Brock, J. D.; Muller, D. A.; DiSalvo, F. J.; Coates, G. W.; Abruña, H. D. Electrocatalysis in Alkaline Media and Alkaline Membrane-Based Energy Technologies. Chem. Rev. **2022**, 122 (6), 6117–6321. https://doi.org/10.1021/acs.chemrev.1c00331.
(25) Henkensmeier, D.; Najibah, M.; Harms, C.; Žitka, J.; Hnát, J.; Bouzek, K. Overview: State-of-the Art Commercial Membranes for Anion Exchange Membrane Water Electrolysis. Journal of Electrochemical Energy Conversion and Storage **2021**, 18 (2), 024001. https://doi.org/10.1115/1.4047963.
(26) Patel, S. K.; Lee, B.; Westerhoff, P.; Elimelech, M. The Potential of Electrodialysis as a Cost-Effective Alternative to Reverse Osmosis for Brackish Water Desalination. Water Research **2024**, 250, 121009. https://doi.org/10.1016/j.watres.2023.121009.
(27) Nayar, K. G.; Fernandes, J.; McGovern, R. K.; Dominguez, K. P.; McCance, A.; Al-Anzi, B. S.; Lienhard, J. H. Cost and Energy Requirements of Hybrid RO and ED Brine

Concentration Systems for Salt Production. Desalination **2019**, 456, 97–120. https://doi.org/10.1016/j.desal.2018.11.018.
(28) Zhang, X.; Yao, Y.; Horseman, T.; Wang, R.; Yin, Y.; Zhang, S.; Tong, T.; Lin, S. Electrodialytic Crystallization to Enable Zero Liquid Discharge. Nat Water **2023**, 1 (6), 547–554. https://doi.org/10.1038/s44221-023-00095-4.
(29) Foo, Z. H.; Thomas, J. B.; Heath, S. M.; Garcia, J. A.; Lienhard, J. H. Sustainable Lithium Recovery from Hypersaline Salt-Lakes by Selective Electrodialysis: Transport and Thermodynamics. Environ. Sci. Technol. **2023**, 57 (39), 14747–14759. https://doi.org/10.1021/acs.est.3c04472.
(30) Ranade, A.; Singh, K.; Tamburini, A.; Micale, G.; Vermaas, D. A. Feasibility of Producing Electricity, Hydrogen, and Chlorine via Reverse Electrodialysis. Environ. Sci. Technol. **2022**, 56 (22), 16062–16072. https://doi.org/10.1021/acs.est.2c03407.
(31) Jiao, Y.; Song, L.; Zhao, C.; An, Y.; Lu, W.; He, B.; Yang, C. Membrane-Based Indirect Power Generation Technologies for Harvesting Salinity Gradient Energy - A Review. Desalination **2022**, 525 (December 2021). https://doi.org/10.1016/j.desal.2021.115485.
(32) Yassin, K.; Rasin, I. G.; Brandon, S.; Dekel, D. R. How Can We Design Anion-Exchange Membranes to Achieve Longer Fuel Cell Lifetime? Journal of Membrane Science **2024**, 690, 122164. https://doi.org/10.1016/j.memsci.2023.122164.
(33) Murata, A.; Hori, Y. Product Selectivity Affected by Cationic Species in Electrochemical Reduction of CO2 and CO at a Cu Electrode. Bulletin of the Chemical Society of Japan **1991**, 64, 123–127. https://doi.org/10.1246/bcsj.64.123.
(34) Ringe, S.; Clark, E. L.; Resasco, J.; Walton, A.; Seger, B.; Bell, A. T.; Chan, K. Understanding Cation Effects in Electrochemical CO_2 Reduction. Energy Environ. Sci. **2019**, 12 (10), 3001–3014. https://doi.org/10.1039/C9EE01341E.
(35) Resasco, J.; Chen, L. D.; Clark, E.; Tsai, C.; Hahn, C.; Jaramillo, T. F.; Chan, K.; Bell, A. T. Promoter Effects of Alkali Metal Cations on the Electrochemical Reduction of Carbon Dioxide. J. Am. Chem. Soc. **2017**, 139 (32), 11277–11287. https://doi.org/10.1021/jacs.7b06765.
(36) El-Nagar, G. A.; Haun, F.; Gupta, S.; Stojkovikj, S.; Mayer, M. T. Unintended Cation Crossover Influences CO2 Reduction Selectivity in Cu-Based Zero-Gap Electrolysers. Nat Commun **2023**, 14 (1), 2062. https://doi.org/10.1038/s41467-023-37520-x.
(37) Garg, S.; Giron Rodriguez, C. A.; Rufford, T. E.; Varcoe, J. R.; Seger, B. How Membrane Characteristics Influence the Performance of CO_2 and CO Electrolysis. Energy Environ. Sci. **2022**, 15 (11), 4440–4469. https://doi.org/10.1039/D2EE01818G.
(38) Mardle, P.; Gangrade, A.; Saatkamp, T.; Jiang, Z.; Cassegrain, S.; Zhao, N.; Shi, Z.; Holdcroft, S. Performance and Stability of Aemion and Aemion+ Membranes in Zero-Gap CO2 Electrolyzers with Mild Anolyte Solutions. ChemSusChem **2023**, 16 (14), e202202376. https://doi.org/10.1002/cssc.202202376.
(39) Noack, K.; Schulz, P. S.; Paape, N.; Kiefer, J.; Wasserscheid, P.; Leipertz, A. The Role of the C2 Position in Interionic Interactions of Imidazolium Based Ionic Liquids: A Vibrational and NMR Spectroscopic Study. Phys. Chem. Chem. Phys. **2010**, 12 (42), 14153–14161. https://doi.org/10.1039/C0CP00486C.
(40) Demirci, S.; Kinali-Demirci, S.; Vanveller, B. Surface-Grafted Polymeric Ionic Liquids with Tunable Morphology via In/Ex Situ Cross-Linking Methods. **2020**. https://doi.org/10.1021/acsmacrolett.0c00632.

(41) Yuan, J.; Antonietti, M. Poly(Ionic Liquid) Latexes Prepared by Dispersion Polymerization of Ionic Liquid Monomers. Macromolecules **2011**, 44 (4), 744–750. https://doi.org/10.1021/ma102858b.
(42) Salamone, J. C.; Israel, S. C.; Taylor, P.; Snider, B. Synthesis and Homopolymerization Studies of Vinylimidazolium Salts. Polymer **1973**, 14 (12), 639–644. https://doi.org/10.1016/0032-3861(73)90039-6.
(43) Pan, J.; Tao, Y.; Zhao, L.; Yu, X.; Zhao, X.; Wu, T.; Liu, L. Green Preparation of Quaternized Vinylimidazole-Based Anion Exchange Membrane by Photopolymerization. Separation and Purification Technology **2021**, 276, 119220. https://doi.org/10.1016/j.seppur.2021.119220.
(44) Suo, X.; Cui, X.; Yang, L.; Xu, N.; Huang, Y.; He, Y.; Dai, S.; Xing, H. Synthesis of Ionic Ultramicroporous Polymers for Selective Separation of Acetylene from Ethylene. Advanced Materials **2020**, 32 (29), 1907601. https://doi.org/10.1002/adma.201907601.
(45) Chen, L.; Fu, J.; Lu, Q.; Shi, L.; Li, M.; Dong, L.; Xu, Y.; Jia, R. Cross-Linked Polymeric Ionic Liquids Ion Gel Electrolytes by in Situ Radical Polymerization. **2019**. https://doi.org/10.1016/j.cej.2019.122245.
(46) Le, X. T. Contribution to the Study of Properties of Selemion AMV Anion Exchange Membranes in Acidic Media. Electrochimica Acta **2013**, 108, 232–240. https://doi.org/10.1016/j.electacta.2013.07.011.
(47) Mizutani, Y. Structure of Ion Exchange Membranes. Journal of Membrane Science **1990**, 49 (2), 121–144. https://doi.org/10.1016/S0376-7388(00)80784-X.
(48) Giffin, G. A.; Lavina, S.; Pace, G.; Di Noto, V. Interplay between the Structure and Relaxations in Selemion AMV Hydroxide Conducting Membranes for AEMFC Applications. J. Phys. Chem. C **2012**, 116 (45), 23965–23973. https://doi.org/10.1021/jp3094879.
(49) Selemion Ion-Exchange Membranes Catalog. https://www.agec.co.jp/file.jsp?id=107824 (accessed 2023-02-23).
(50) Mareev, S. A.; Butylskii, D. Yu.; Pismenskaya, N. D.; Larchet, C.; Dammak, L.; Nikonenko, V. V. Geometric Heterogeneity of Homogeneous Ion-Exchange Neosepta Membranes. Journal of Membrane Science **2018**, 563, 768–776. https://doi.org/10.1016/j.memsci.2018.06.018.
(51) Sarapulova, V.; Shkorkina, I.; Mareev, S.; Pismenskaya, N.; Kononenko, N.; Larchet, C.; Dammak, L.; Nikonenko, V. Transport Characteristics of Fujifilm Ion-Exchange Membranes as Compared to Homogeneous Membranes AMX and CMX and to Heterogeneous Membranes MK-40 and MA-41. Membranes **2019**, 9 (7), 84. https://doi.org/10.3390/membranes9070084.
(52) Mizutani, Y.; Yamane, R.; Ihara, H.; Motomura, H. Studies of Ion Exchange Membranes. XVI. The Preparation of Ion Exchange Membranes by the "Paste Method." BCSJ **1963**, 36 (4), 361–366. https://doi.org/10.1246/bcsj.36.361.
(53) Kusoglu, A.; Weber, A. Z. New Insights into Perfluorinated Sulfonic-Acid Ionomers. Chemical Reviews **2017**, 117 (3), 987–1104. https://doi.org/10.1021/acs.chemrev.6b00159.
(54) Nafion Sulfonic Membranes. https://archive.fo/2AujM.
(55) Anion Exchange Membranes and Ionomers | Dioxide Materials. https://archive.fo/Bz0mh (accessed 2023-02-23).
(56) Sustainion X37 Anion Membrane Grade RT Product and Safety Data Sheet, Provided by Manufacturer with Purchase, 2022.
(57) Lindquist, G. A.; Oener, S. Z.; Krivina, R.; Motz, A. R.; Keane, A.; Capuano, C.; Ayers, K. E.; Boettcher, S. W. Performance and Durability of Pure-Water-Fed Anion Exchange

Membrane Electrolyzers Using Baseline Materials and Operation. ACS Appl. Mater. Interfaces **2021**, 13 (44), 51917–51924. https://doi.org/10.1021/acsami.1c06053.
(58) Kaczur, J. J.; Yang, H.; Liu, Z.; Sajjad, S. D.; Masel, R. I. Carbon Dioxide and Water Electrolysis Using New Alkaline Stable Anion Membranes. Frontiers in Chemistry **2018**, 6.
(59) Sustainion PTFE Reinforced B22-50 Anion Membrane Grade-T Product and Safety Data Sheet, Provided by Manufacturer with Purchase, 2022.
(60) Ion Exchange Membranes | Fujifilm [United States]. https://archive.fo/uajo2 (accessed 2023-02-23).
(61) Huang, G.; Mandal, M.; Peng, X.; Yang-Neyerlin, A. C.; Pivovar, B. S.; Mustain, W. E.; Kohl, P. A. Composite Poly(Norbornene) Anion Conducting Membranes for Achieving Durability, Water Management and High Power (3.4 W/Cm ^{2}) in Hydrogen/Oxygen Alkaline Fuel Cells. J. Electrochem. Soc. **2019**, 166 (10), F637–F644. https://doi.org/10.1149/2.1301910jes.
(62) Xergy™ Membranes. https://web.archive.org/web/20230222175908/https://www.fuelcellstore.com/fuel-cell-components/membranes/membrane-brands/xergy-ion-exchange-membranes (accessed 2023-02-22).
(63) Xion AEM-Pention(72 Series, 15% Crosslinking) – Ionix. https://web.archive.org/web/20210925041009/https://ionix.xergyincstore.com/shop/ion-exchange-membranes/xion-aem-pention/xion-aem-pention72-series-15-crosslinking/ (accessed 2023-02-22).
(64) Xion PEM-Aquivion(830 EW series) – Ionix. https://web.archive.org/web/20210925042610/https://ionix.xergyincstore.com/shop/ion-exchange-membranes/xion-pem-aquivion/xion-pem-aquivion830-ew-series/ (accessed 2023-02-22).
(65) Xion PEM-Dyneon(800 EW Series) – Ionix. https://web.archive.org/web/20220122114742/https://ionix.xergyincstore.com/shop/ion-exchange-membranes/xion-pem-dyneon/xion-pem-dyneon800-ew-series/ (accessed 2023-02-22).
(66) Xion PEM-Nafion(1100 EW series) – Ionix. https://web.archive.org/web/20220118112457/https://ionix.xergyincstore.com/shop/ion-exchange-membranes/xion-pem-pfsa/xion-pem-pfsa1100-ew-series/ (accessed 2023-02-22).
(67) Lee, W.-H.; Park, E. J.; Han, J.; Shin, D. W.; Kim, Y. S.; Bae, C. Poly(Terphenylene) Anion Exchange Membranes: The Effect of Backbone Structure on Morphology and Membrane Property. ACS Macro Lett. **2017**, 6 (5), 566–570. https://doi.org/10.1021/acsmacrolett.7b00148.
(68) Orion AMX Technical Data Sheet, Provided by Manufacturer with Purchase, 2022.
(69) Orion CMX Technical Data Sheet, Provided by Manufacturer with Purchase, 2022.
(70) Meek, K. M.; Antunes, C. M.; Strasser, D.; Owczarczyk, Z. R.; Neyerlin, A.; Pivovar, B. S. High-Throughput Anion Exchange Membrane Characterization at NREL. ECS Trans. **2019**, 92 (8), 723–731. https://doi.org/10.1149/09208.0723ecst.
(71) Najibah, M.; Tsoy, E.; Khalid, H.; Chen, Y.; Li, Q.; Bae, C.; Hnát, J.; Plevová, M.; Bouzek, K.; Jang, J. H.; Park, H. S.; Henkensmeier, D. PBI Nanofiber Mat-Reinforced Anion Exchange Membranes with Covalently Linked Interfaces for Use in Water Electrolysers. Journal of Membrane Science **2021**, 640, 119832. https://doi.org/10.1016/j.memsci.2021.119832.

(72) Ralex Membrane AMHPES, 2023. https://www.mega.cz/files/datasheet/MEGA-RALEX-AMH-PES-en.pdf (accessed 2023-02-23).
(73) Ralex Membrane AMHPP, 2023. https://www.mega.cz/files/datasheet/MEGA-RALEX-AMH-PP-en.pdf (accessed 2023-02-23).
(74) Ralex Membrane CMHPES, 2023. https://www.mega.cz/files/datasheet/MEGA-RALEX-CMH-PES-en.pdf (accessed 2023-02-23).
(75) Akberova, E. M.; Vasil'eva, V. I.; Zabolotsky, V. I.; Novak, L. A Study of Ralex Membrane Morphology by SEM. Membranes **2019**, 9 (12), 169. https://doi.org/10.3390/membranes9120169.
(76) Ralex Membrane CMHPP, 2023. https://www.mega.cz/files/datasheet/MEGA-RALEX-CMH-PP-en.pdf (accessed 2023-02-23).
(77) AXM-100 (AMI-7001) Anion Exchange Membranes | Technical Specifications - Membranes International Inc. https://web.archive.org/web/20221209204304/https://ionexchangemembranes.com/ami-7001-anion-exchange-membranes-technical-specifications/ (accessed 2023-02-22).
(78) CXM-200 (CMI-7000) Cation Exchange Membranes | Technical Specifications - Membranes International Inc. https://web.archive.org/web/20221030232413/https://ionexchangemembranes.com/cmi-7000-cation-exchange-membranes-technical-specifications/ (accessed 2023-02-22).
(79) Geise, G. M.; Cassady, H. J.; Paul, D. R.; Logan, B. E.; Hickner, M. A. Specific Ion Effects on Membrane Potential and the Permselectivity of Ion Exchange Membranes. Phys. Chem. Chem. Phys. **2014**, 16 (39), 21673–21681. https://doi.org/10.1039/C4CP03076A.
(80) Yuzer, B.; Selcuk, H.; Chehade, G.; Demir, M. E.; Dincer, I. Evaluation of Hydrogen Production via Electrolysis with Ion Exchange Membranes. Energy **2020**, 190, 116420. https://doi.org/10.1016/j.energy.2019.116420.
(81) Aquivion® E98-15S. https://archive.fo/qYU32 (accessed 2023-02-22).
(82) Kamcev, J.; Paul, D. R.; Freeman, B. D. Ion Activity Coefficients in Ion Exchange Polymers: Applicability of Manning's Counterion Condensation Theory. Macromolecules **2015**, 48 (21), 8011–8024. https://doi.org/10.1021/acs.macromol.5b01654.
(83) Ionics Ion Exchange Membranes, 2022. https://www.watertechnologies.com/products/ionics-ion-exchange-membranes (accessed 2023-02-22).
(84) Wang, J.; Zhao, Y.; Setzler, B. P.; Rojas-Carbonell, S.; Ben Yehuda, C.; Amel, A.; Page, M.; Wang, L.; Hu, K.; Shi, L.; Gottesfeld, S.; Xu, B.; Yan, Y. Poly(Aryl Piperidinium) Membranes and Ionomers for Hydroxide Exchange Membrane Fuel Cells. Nat Energy **2019**, 4 (5), 392–398. https://doi.org/10.1038/s41560-019-0372-8.
(85) Yan, Y.; Xu, B.; Wang, J.; Zhao, Y. Poly(Aryl Piperidinium) Polymers for Use as Hydroxide Exchange Membranes and Ionomers. US 10290890, May 14, 2019. https://image-ppubs.uspto.gov/dirsearch-public/print/downloadPdf/10290890 (accessed 2023-02-22).
(86) Kamcev, J.; Paul, D. R.; Freeman, B. D. Effect of Fixed Charge Group Concentration on Equilibrium Ion Sorption in Ion Exchange Membranes. Journal of Materials Chemistry A **2017**, 5 (9), 4638–4650. https://doi.org/10.1039/c6ta07954g.
(87) Kamcev, J.; Doherty, C. M.; Lopez, K. P.; Hill, A. J.; Paul, D. R.; Freeman, B. D. Effect of Fixed Charge Group Concentration on Salt Permeability and Diffusion Coefficients in Ion Exchange Membranes. Journal of Membrane Science **2018**, 566 (June), 307–316. https://doi.org/10.1016/j.memsci.2018.08.053.

(88) Díaz, J. C.; Kitto, D.; Kamcev, J. Accurately Measuring the Ionic Conductivity of Membranes via the Direct Contact Method. Journal of Membrane Science **2023**, 669, 121304. https://doi.org/10.1016/j.memsci.2022.121304.
(89) Díaz, J. C.; Kamcev, J. Ionic Conductivity of Ion-Exchange Membranes: Measurement Techniques and Salt Concentration Dependence. Journal of Membrane Science **2021**, 618, 118718. https://doi.org/10.1016/j.memsci.2020.118718.
(90) Kamcev, J.; Paul, D. R.; Manning, G. S.; Freeman, B. D. Ion Diffusion Coefficients in Ion Exchange Membranes: Significance of Counterion Condensation. Macromolecules **2018**, 51 (15), 5519–5529. https://doi.org/10.1021/acs.macromol.8b00645.
(91) Kamcev, J. Reformulating the Permselectivity-conductivity Tradeoff Relation in Ion-exchange Membranes. Journal of Polymer Science **2021**, 59 (21), 2510–2520. https://doi.org/10.1002/pol.20210304.
(92) Kamcev, J.; Paul, D. R.; Manning, G. S.; Freeman, B. D. Accounting for Frame of Reference and Thermodynamic Non-Idealities When Calculating Salt Diffusion Coefficients in Ion Exchange Membranes. Journal of Membrane Science **2017**, 537 (March), 396–406. https://doi.org/10.1016/j.memsci.2017.05.034.
(93) Marioni, N.; Zhang, Z.; Zofchak, E. S.; Sachar, H. S.; Kadulkar, S.; Freeman, B. D.; Ganesan, V. Impact of Ion–Ion Correlated Motion on Salt Transport in Solvated Ion Exchange Membranes. ACS Macro Lett. **2022**, 11 (11), 1258–1264. https://doi.org/10.1021/acsmacrolett.2c00361.
(94) Crank, J.; Park, G. S. Diffusion in Polymers, 1st ed.; Academic Press Inc.: New York, 1968.
(95) Lakshminarayanaiah, N. Transport Phenomena in Membranes, 1st ed.; Academic Press, Inc.: New York, 1969. https://doi.org/10.1021/ja01467a065.
(96) Brauner, N.; Shacham, M. Statistical Analysis of Linear and Nonlinear Correlation of the Arrhenius Equation Constants. Chemical Engineering and Processing: Process Intensification **1997**, 36 (3), 243–249. https://doi.org/10.1016/S0255-2701(96)04186-4.
(97) Zwolinski, B. J.; Eyring, H.; Reese, C. E. Diffusion and Membrane Permeability. J. Phys. Chem. **1949**, 53 (9), 1426–1453. https://doi.org/10.1021/j150474a012.
(98) York, D. Least-Squares Fitting of a Straight Line. Can. J. Phys. **1966**, 44 (5), 1079–1086. https://doi.org/10.1139/p66-090.
(99) Kamcev, J.; Paul, D. R.; Freeman, B. D. Effect of Fixed Charge Group Concentration on Equilibrium Ion Sorption in Ion Exchange Membranes. Journal of Materials Chemistry A **2017**, 5 (9), 4638–4650. https://doi.org/10.1039/C6TA07954G.
(100) Tran, T.; Lin, C.; Chaurasia, S.; Lin, H. Elucidating the Relationship between States of Water and Ion Transport Properties in Hydrated Polymers. Journal of Membrane Science **2019**, 574 (December 2018), 299–308. https://doi.org/10.1016/j.memsci.2018.12.059.
(101) Higuchi, A.; Ijima, T. DSC Investigation of the States of Water in Poly(Vinyl Alcohol) Membranes. Polymer **1985**, 26, 1207–1211.
(102) Hodge, R. M.; Edward, G. H.; Simon, G. P. Water Absorption and States of Water in Semicrystalline Poly(Vinyl Alcohol) Films. Polymer **1996**, 37 (8), 1371–1376. https://doi.org/10.1016/0032-3861(96)81134-7.
(103) Hiemenz, P. C.; Lodge, T. P. Polymer Chemistry, 2nd ed.; CRC Press: Boca Raton, 2007. https://doi.org/10.1201/9781420018271.
(104) Flory, P. J. Principles of Polymer Chemistry, 1st ed.; George Banta Publishing Company: Ithaca, 1954.

(105) Bray, J. C.; Merrill, E. W. Poly(Vinyl Alcohol) Hydrogels. Formation by Electron Beam Irradiation of Aqueous Solutions and Subsequent Crystallization. Journal of Applied Polymer Science **1973**, 17 (12), 3779–3794. https://doi.org/10.1002/app.1973.070171219.
(106) Hopkins, J. B.; Gillian, R. E.; Skou, S. BioXTAS RAW: Improvements to a Free Open-Source Program for Small-Angle X-Ray Scattering Data Reduction and Analysis. Journal of Applied Crystallography **2017**, 50, 1545–1553.
(107) Boerner, T. J.; Deems, S.; Furlani, T. R.; Knuth, S. L.; Towns, J. ACCESS: Advancing Innovation: NSF's Advanced Cyberinfrastructure Coordination Ecosystem: Services & Support. In Practice and Experience in Advanced Research Computing; ACM: Portland OR USA, 2023; pp 173–176. https://doi.org/10.1145/3569951.3597559.
(108) Thompson, A. P.; Aktulga, H. M.; Berger, R.; Bolintineanu, D. S.; Brown, W. M.; Crozier, P. S.; In 'T Veld, P. J.; Kohlmeyer, A.; Moore, S. G.; Nguyen, T. D.; Shan, R.; Stevens, M. J.; Tranchida, J.; Trott, C.; Plimpton, S. J. LAMMPS - a Flexible Simulation Tool for Particle-Based Materials Modeling at the Atomic, Meso, and Continuum Scales. Computer Physics Communications **2022**, 271, 108171. https://doi.org/10.1016/j.cpc.2021.108171.
(109) Abascal, J. L. F.; Vega, C. A General Purpose Model for the Condensed Phases of Water: TIP4P/2005. The Journal of Chemical Physics **2005**, 123 (23), 234505. https://doi.org/10.1063/1.2121687.
(110) Kadaoluwa Pathirannahalage, S. P.; Meftahi, N.; Elbourne, A.; Weiss, A. C. G.; McConville, C. F.; Padua, A.; Winkler, D. A.; Costa Gomes, M.; Greaves, T. L.; Le, T. C.; Besford, Q. A.; Christofferson, A. J. Systematic Comparison of the Structural and Dynamic Properties of Commonly Used Water Models for Molecular Dynamics Simulations. J. Chem. Inf. Model. **2021**, 61 (9), 4521–4536. https://doi.org/10.1021/acs.jcim.1c00794.
(111) Joung, I. S.; Cheatham, T. E. Determination of Alkali and Halide Monovalent Ion Parameters for Use in Explicitly Solvated Biomolecular Simulations. J. Phys. Chem. B **2008**, 112 (30), 9020–9041. https://doi.org/10.1021/jp8001614.
(112) Döpke, M. F.; Moultos, O. A.; Hartkamp, R. On the Transferability of Ion Parameters to the TIP4P/2005 Water Model Using Molecular Dynamics Simulations. The Journal of Chemical Physics **2020**, 152 (2), 024501. https://doi.org/10.1063/1.5124448.
(113) Jorgensen, W. L.; Maxwell, D. S.; Tirado-Rives, J. Development and Testing of the OPLS All-Atom Force Field on Conformational Energetics and Properties of Organic Liquids. J. Am. Chem. Soc. **1996**, 118 (45), 11225–11236. https://doi.org/10.1021/ja9621760.
(114) Dodda, L. S.; Cabeza de Vaca, I.; Tirado-Rives, J.; Jorgensen, W. L. LigParGen Web Server: An Automatic OPLS-AA Parameter Generator for Organic Ligands. Nucleic Acids Research **2017**, 45 (W1), W331–W336. https://doi.org/10.1093/nar/gkx312.
(115) Shinoda, W.; Shiga, M.; Mikami, M. Rapid Estimation of Elastic Constants by Molecular Dynamics Simulation under Constant Stress. Phys. Rev. B **2004**, 69 (13), 134103. https://doi.org/10.1103/PhysRevB.69.134103.
(116) Gissinger, J. R.; Jensen, B. D.; Wise, K. E. Modeling Chemical Reactions in Classical Molecular Dynamics Simulations. Polymer **2017**, 128, 211–217. https://doi.org/10.1016/j.polymer.2017.09.038.
(117) Gissinger, J. R.; Jensen, B. D.; Wise, K. E. REACTER: A Heuristic Method for Reactive Molecular Dynamics. Macromolecules **2020**, 53 (22), 9953–9961. https://doi.org/10.1021/acs.macromol.0c02012.

(118) Torrie, G. M.; Valleau, J. P. Nonphysical Sampling Distributions in Monte Carlo Free-Energy Estimation: Umbrella Sampling. Journal of Computational Physics **1977**, 23 (2), 187–199. https://doi.org/10.1016/0021-9991(77)90121-8.
(119) Kumar, S.; Rosenberg, J. M.; Bouzida, D.; Swendsen, R. H.; Kollman, P. A. THE Weighted Histogram Analysis Method for Free-energy Calculations on Biomolecules. I. The Method. J Comput Chem **1992**, 13 (8), 1011–1021. https://doi.org/10.1002/jcc.540130812.
(120) Assumma, L.; Iojoiu, C.; Albayrak Ari, G.; Cointeaux, L.; Sanchez, J.-Y. Polyethersulfone Containing Sulfonimide Groups as Proton Exchange Membrane Fuel Cells. International Journal of Hydrogen Energy **2014**, 39 (6), 2740–2750. https://doi.org/10.1016/j.ijhydene.2013.07.090.
(121) Avci, A. H.; Rijnaarts, T.; Fontananova, E.; Di Profio, G.; Vankelecom, I. F. V.; De Vos, W. M.; Curcio, E. Sulfonated Polyethersulfone Based Cation Exchange Membranes for Reverse Electrodialysis under High Salinity Gradients. Journal of Membrane Science **2020**, 595, 117585. https://doi.org/10.1016/j.memsci.2019.117585.
(122) Ayaz, S.; Yao, Z.-Y.; Chen, Y.-J.; Yu, H.-Y. Preparation of Poly(Arylene Ether Ketone) Based Anion Exchange Membrane with Pendant Pyrimidinium and Pyridazinium Cation Derivatives for Alkaline Fuel Cell. Journal of Membrane Science **2022**, 659, 120778. https://doi.org/10.1016/j.memsci.2022.120778.
(123) Bakangura, E.; Cheng, C.; Wu, L.; He, Y.; Ge, X.; Ran, J.; Emmanuel, K.; Xu, T. Highly Charged Hierarchically Structured Porous Anion Exchange Membranes with Excellent Performance. Journal of Membrane Science **2016**, 515, 154–162. https://doi.org/10.1016/j.memsci.2016.05.059.
(124) Buggy, N. C.; Du, Y.; Kuo, M.-C.; Ahrens, K. A.; Wilkinson, J. S.; Seifert, S.; Coughlin, E. B.; Herring, A. M. A Polyethylene-Based Triblock Copolymer Anion Exchange Membrane with High Conductivity and Practical Mechanical Properties. ACS Appl. Polym. Mater. **2020**, 2 (3), 1294–1303. https://doi.org/10.1021/acsapm.9b01182.
(125) Cai, W.; Fan, K.; Li, J.; Ma, L.; Xu, G.; Xu, S.; Ma, L.; Cheng, H. A Bi-Functional Polymeric Nano-Sieve Nafion Composite Membrane: Improved Performance for Direct Methanol Fuel Cell Applications. International Journal of Hydrogen Energy **2016**, 41 (38), 17102–17111. https://doi.org/10.1016/j.ijhydene.2016.07.128.
(126) Cao, D.; Nie, F.; Liu, M.; Sun, X.; Wang, B.; Wang, F.; Li, N.; Wang, B.; Ma, Z.; Pan, L.; Li, Y. Crosslinked Anion Exchange Membranes Prepared from Highly Reactive Polyethylene and Polypropylene Intermediates. Journal of Membrane Science **2022**, 661, 120921. https://doi.org/10.1016/j.memsci.2022.120921.
(127) Carter, B. M.; Keller, L.; Wessling, M.; Miller, D. J. Preparation and Characterization of Crosslinked Poly(Vinylimidazolium) Anion Exchange Membranes for Artificial Photosynthesis. J. Mater. Chem. A **2019**, 7 (41), 23818–23829. https://doi.org/10.1039/C9TA00498J.
(128) Chen, N.; Park, J. H.; Hu, C.; Wang, H. H.; Kim, H. M.; Kang, N. Y.; Lee, Y. M. Di-Piperidinium-Crosslinked Poly(Fluorenyl-Co-Terphenyl Piperidinium)s for High-Performance Alkaline Exchange Membrane Fuel Cells. J. Mater. Chem. A **2022**, 10 (7), 3678–3687. https://doi.org/10.1039/D1TA10178A.
(129) Chen, N.; Zhu, H.; Chu, Y.; Li, R.; Liu, Y.; Wang, F. Cobaltocenium-Containing Polybenzimidazole Polymers for Alkaline Anion Exchange Membrane Applications. Polym. Chem. **2017**, 8 (8), 1381–1392. https://doi.org/10.1039/C6PY01936F.

(130) Chen, R.; Xu, F.; Fu, K.; Zhou, J.; Shi, Q.; Xue, C.; Lyu, Y.; Guo, B.; Li, G. Enhanced Proton Conductivity and Dimensional Stability of Proton Exchange Membrane Based on Sulfonated Poly(Arylene Ether Sulfone) and Graphene Oxide. Materials Research Bulletin **2018**, 103, 142–149. https://doi.org/10.1016/j.materresbull.2018.02.036.
(131) Chen, W.; Mandal, M.; Huang, G.; Wu, X.; He, G.; Kohl, P. A. Highly Conducting Anion-Exchange Membranes Based on Cross-Linked Poly(Norbornene): Ring Opening Metathesis Polymerization. ACS Appl. Energy Mater. **2019**, 2 (4), 2458–2468. https://doi.org/10.1021/acsaem.8b02052.
(132) Chen, X.; Jiang, Y.; Yang, S.; Pan, J.; Yan, R.; Bruggen, B. V. D.; Sotto, A.; Gao, C.; Shen, J. Internal Cross-Linked Anion Exchange Membranes with Improved Dimensional Stability for Electrodialysis. Journal of Membrane Science **2017**, 542, 280–288. https://doi.org/10.1016/j.memsci.2017.08.026.
(133) Chu, X.; Liu, J.; Miao, S.; Liu, L.; Huang, Y.; Tang, E.; Liu, S.; Xing, X.; Li, N. Crucial Role of Side-Chain Functionality in Anion Exchange Membranes: Properties and Alkaline Fuel Cell Performance. Journal of Membrane Science **2021**, 625, 119172. https://doi.org/10.1016/j.memsci.2021.119172.
(134) Chu, X.; Liu, L.; Huang, Y.; Guiver, M. D.; Li, N. Practical Implementation of Bis-Six-Membered N-Cyclic Quaternary Ammonium Cations in Advanced Anion Exchange Membranes for Fuel Cells: Synthesis and Durability. Journal of Membrane Science **2019**, 578, 239–250. https://doi.org/10.1016/j.memsci.2019.02.051.
(135) Cseri, L.; Baugh, J.; Alabi, A.; AlHajaj, A.; Zou, L.; Dryfe, R. A. W.; Budd, P. M.; Szekely, G. Graphene Oxide–Polybenzimidazolium Nanocomposite Anion Exchange Membranes for Electrodialysis. J. Mater. Chem. A **2018**, 6 (48), 24728–24739. https://doi.org/10.1039/C8TA09160A.
(136) Dai, H.; Guan, R.; Li, C.; Liu, J. Development and Characterization of Sulfonated Poly(Ether Sulfone) for Proton Exchange Membrane Materials. Solid State Ionics **2007**, 178 (5–6), 339–345. https://doi.org/10.1016/j.ssi.2006.09.013.
(137) Dang, H.-S.; Jannasch, P. A Comparative Study of Anion-Exchange Membranes Tethered with Different Hetero-Cycloaliphatic Quaternary Ammonium Hydroxides. J. Mater. Chem. A **2017**, 5 (41), 21965–21978. https://doi.org/10.1039/C7TA06029G.
(138) Dang, H.-S.; Jannasch, P. High-Performing Hydroxide Exchange Membranes with Flexible Tetra-Piperidinium Side Chains Linked by Alkyl Spacers. ACS Appl. Energy Mater. **2018**, 1 (5), 2222–2231. https://doi.org/10.1021/acsaem.8b00294.
(139) Dischinger, S. M.; Gupta, S.; Carter, B. M.; Miller, D. J. Transport of Neutral and Charged Solutes in Imidazolium-Functionalized Poly(Phenylene Oxide) Membranes for Artificial Photosynthesis. Ind. Eng. Chem. Res. **2020**, 59 (12), 5257–5266. https://doi.org/10.1021/acs.iecr.9b05628.
(140) Divya, K.; Sri Abirami Saraswathi, M. S.; Nagendran, A.; Rana, D. Sulfonated Chitosan and HKUST -1 Metal Organic Frameworks Based Hybrid Membranes for Direct Methanol Fuel Cell Applications. J of Applied Polymer Sci **2022**, 139 (36), e52829. https://doi.org/10.1002/app.52829.
(141) Du, S.; Huang, S.; Xie, N.; Zhang, T.; Xu, Y.; Ning, X.; Chen, P.; Chen, X.; An, Z. New Block Poly(Ether Sulfone) Based Anion Exchange Membranes with Rigid Side-Chains and High-Density Quaternary Ammonium Groups for Fuel Cell Application. Polym. Chem. **2022**, 13 (30), 4395–4405. https://doi.org/10.1039/D2PY00588C.

(142) Du, X.; Wang, Z.; Liu, W.; Xu, J.; Chen, Z.; Wang, C. Imidazolium-Functionalized Poly (Arylene Ether Ketone) Cross-Linked Anion Exchange Membranes. Journal of Membrane Science **2018**, 566, 205–212. https://doi.org/10.1016/j.memsci.2018.09.020.
(143) Duan, X.; Wang, C.; Wang, T.; Xie, X.; Zhou, X.; Ye, Y. Comb-Shaped Anion Exchange Membrane to Enhance Phosphoric Acid Purification by Electro-Electrodialysis. Journal of Membrane Science **2019**, 573, 64–72. https://doi.org/10.1016/j.memsci.2018.11.062.
(144) Ertem, S. P.; Caire, B. R.; Tsai, T.; Zeng, D.; Vandiver, M. A.; Kusoglu, A.; Seifert, S.; Hayward, R. C.; Weber, A. Z.; Herring, A. M.; Coughlin, E. B.; Liberatore, M. W. Ion Transport Properties of Mechanically Stable Symmetric ABCBA Pentablock Copolymers with Quaternary Ammonium Functionalized Midblock. J Polym Sci B Polym Phys **2017**, 55 (7), 612–622. https://doi.org/10.1002/polb.24310.
(145) Fan, J.; Willdorf-Cohen, S.; Schibli, E. M.; Paula, Z.; Li, W.; Skalski, T. J. G.; Sergeenko, A. T.; Hohenadel, A.; Frisken, B. J.; Magliocca, E.; Mustain, W. E.; Diesendruck, C. E.; Dekel, D. R.; Holdcroft, S. Poly(Bis-Arylimidazoliums) Possessing High Hydroxide Ion Exchange Capacity and High Alkaline Stability. Nat Commun **2019**, 10 (1), 2306. https://doi.org/10.1038/s41467-019-10292-z.
(146) Fan, J.; Wright, A. G.; Britton, B.; Weissbach, T.; Skalski, T. J. G.; Ward, J.; Peckham, T. J.; Holdcroft, S. Cationic Polyelectrolytes, Stable in 10 M KOH_{aq} at 100 °C. ACS Macro Lett. **2017**, 6 (10), 1089–1093. https://doi.org/10.1021/acsmacrolett.7b00679.
(147) Ge, L.; Mondal, A. N.; Liu, X.; Wu, B.; Yu, D.; Li, Q.; Miao, J.; Ge, Q.; Xu, T. Advanced Charged Porous Membranes with Ultrahigh Selectivity and Permeability for Acid Recovery. Journal of Membrane Science **2017**, 536, 11–18. https://doi.org/10.1016/j.memsci.2017.04.055.
(148) Ge, Q.; Liang, X.; Ding, L.; Hou, J.; Miao, J.; Wu, B.; Yang, Z.; Xu, T. Guiding the Self-Assembly of Hyperbranched Anion Exchange Membranes Utilized in Alkaline Fuel Cells. Journal of Membrane Science **2019**, 573, 595–601. https://doi.org/10.1016/j.memsci.2018.12.049.
(149) Ge, Q.; Liu, Y.; Yang, Z.; Wu, B.; Hu, M.; Liu, X.; Hou, J.; Xu, T. Hyper-Branched Anion Exchange Membranes with High Conductivity and Chemical Stability. Chem. Commun. **2016**, 52 (66), 10141–10143. https://doi.org/10.1039/C6CC04930C.
(150) Ghorai, A.; Sahoo, A.; Baitalik, S.; Banerjee, S. Multifunctional Sulfonated Polytriazoles: Proton-Exchange Membrane Properties, Molecular Logic Gates, and Modeling of Stimuli-Responsive Behaviors. ACS Appl. Polym. Mater. **2022**, 4 (8), 5583–5595. https://doi.org/10.1021/acsapm.2c00629.
(151) Goel, P.; E., B.; Mandal, P.; Shahi, V. K.; Bandyopadhyay, A.; Chattopadhyay, S. Di-Quaternized Graphene Oxide Based Multi-Cationic Cross-Linked Monovalent Selective Anion Exchange Membrane for Electrodialysis. Separation and Purification Technology **2021**, 276, 119361. https://doi.org/10.1016/j.seppur.2021.119361.
(152) Gu, F.; Dong, H.; Li, Y.; Si, Z.; Yan, F. Highly Stable N3-Substituted Imidazolium-Based Alkaline Anion Exchange Membranes: Experimental Studies and Theoretical Calculations. Macromolecules **2014**, 47 (1), 208–216. https://doi.org/10.1021/ma402334t.
(153) Güler, E.; Elizen, R.; Vermaas, D. A.; Saakes, M.; Nijmeijer, K. Performance-Determining Membrane Properties in Reverse Electrodialysis. Journal of Membrane Science **2013**, 446, 266–276. https://doi.org/10.1016/j.memsci.2013.06.045.
(154) Guo, D.; Zhuo, Y. Z.; Lai, A. N.; Zhang, Q. G.; Zhu, A. M.; Liu, Q. L. Interpenetrating Anion Exchange Membranes Using Poly(1-Vinylimidazole) as Bifunctional Crosslinker for

Fuel Cells. Journal of Membrane Science **2016**, 518, 295–304. https://doi.org/10.1016/j.memsci.2016.07.006.
(155) Hao, J.; Gao, X.; Jiang, Y.; Zhang, H.; Luo, J.; Shao, Z.; Yi, B. Crosslinked High-Performance Anion Exchange Membranes Based on Poly(Styrene-b-(Ethylene-Co-Butylene)-b-Styrene). Journal of Membrane Science **2018**, 551, 66–75. https://doi.org/10.1016/j.memsci.2018.01.033.
(156) Hao, L.; Liao, J.; Liu, Y.; Ruan, H.; Sotto, A.; Der Bruggen, B. V.; Shen, J. Highly Conductive Anion Exchange Membranes with Low Water Uptake and Performance Evaluation in Electrodialysis. Separation and Purification Technology **2019**, 211, 481–490. https://doi.org/10.1016/j.seppur.2018.09.042.
(157) Hao, L.; Wang, C.; Chen, Q.; Yu, X.; Liao, J.; Shen, J.; Gao, C. A Facile Approach to Fabricate Composite Anion Exchange Membranes with Enhanced Ionic Conductivity and Dimensional Stability for Electrodialysis. Separation and Purification Technology **2019**, 227, 115725. https://doi.org/10.1016/j.seppur.2019.115725.
(158) Haragirimana, A.; Ingabire, P. B.; Liu, Y.; Li, N.; Hu, Z.; Chen, S. An Effective Strategy to Enhance the Performance of the Proton Exchange Membranes Based on Sulfonated Poly(Ether Ether Ketone)s. International Journal of Hydrogen Energy **2020**, 45 (16), 10017–10029. https://doi.org/10.1016/j.ijhydene.2020.01.180.
(159) He, R.; Wen, P.; Zhang, H.-N.; Guan, S.; Xie, G.; Li, L.-Z.; Lee, M.-H.; Li, X.-D. In-Situ Photocrosslinked Hydroxide Conductive Membranes Based on Photosensitive Poly(Arylene Ether Sulfone) Block Copolymers for Anion Exchange Membrane Fuel Cells. Journal of Membrane Science **2018**, 556, 73–84. https://doi.org/10.1016/j.memsci.2018.03.088.
(160) He, S.; Liu, L.; Wang, X.; Zhang, S.; Guiver, M. D.; Li, N. Azide-Assisted Self-Crosslinking of Highly Ion Conductive Anion Exchange Membranes. Journal of Membrane Science **2016**, 509, 48–56. https://doi.org/10.1016/j.memsci.2016.02.045.
(161) He, X.; Cheng, C.; Huang, S.; Zhang, F.; Duan, Y.; Zhu, C.; Guo, Y.; Wang, K.; Chen, D. Alkaline Anion Exchange Membranes with Imidazolium-Terminated Flexible Side-Chain Cross-Linked Topological Structure Based on ROMP-Type Norbornene Copolymers. Polymer **2020**, 195, 122412. https://doi.org/10.1016/j.polymer.2020.122412.
(162) He, Y.; Wu, L.; Pan, J.; Zhu, Y.; Ge, X.; Yang, Z.; Ran, J.; Xu, T. A Mechanically Robust Anion Exchange Membrane with High Hydroxide Conductivity. Journal of Membrane Science **2016**, 504, 47–54. https://doi.org/10.1016/j.memsci.2016.01.008.
(163) Hofmann, M. A.; Ambler, C. M.; Maher, A. E.; Chalkova, E.; Zhou, X. Y.; Lvov, S. N.; Allcock, H. R. Synthesis of Polyphosphazenes with Sulfonimide Side Groups. Macromolecules **2002**, 35 (17), 6490–6493. https://doi.org/10.1021/ma020330z.
(164) Hong, J. G.; Chen, Y. Nanocomposite Reverse Electrodialysis (RED) Ion-Exchange Membranes for Salinity Gradient Power Generation. Journal of Membrane Science **2014**, 460, 139–147. https://doi.org/10.1016/j.memsci.2014.02.027.
(165) Hong, J. G.; Park, T.-W.; Dhadake, Y. Property Evaluation of Custom-Made Ion Exchange Membranes for Electrochemical Performance in Reverse Electrodialysis Application. Journal of Electroanalytical Chemistry **2019**, 850, 113437. https://doi.org/10.1016/j.jelechem.2019.113437.
(166) Hossain, Md. M.; Hou, J.; Wu, L.; Ge, Q.; Liang, X.; Mondal, A. N.; Xu, T. Anion Exchange Membranes with Clusters of Alkyl Ammonium Group for Mitigating Water Swelling but Not Ionic Conductivity. Journal of Membrane Science **2018**, 550, 101–109. https://doi.org/10.1016/j.memsci.2017.12.062.

(167) Hossain, Md. M.; Wu, L.; Liang, X.; Yang, Z.; Hou, J.; Xu, T. Anion Exchange Membrane Crosslinked in the Easiest Way Stands out for Fuel Cells. Journal of Power Sources **2018**, 390, 234–241. https://doi.org/10.1016/j.jpowsour.2018.04.064.
(168) Hou, J.; Liu, Y.; Ge, Q.; Yang, Z.; Wu, L.; Xu, T. Recyclable Cross-Linked Anion Exchange Membrane for Alkaline Fuel Cell Application. Journal of Power Sources **2018**, 375, 404–411. https://doi.org/10.1016/j.jpowsour.2017.06.073.
(169) Hu, B.; Miao, L.; Bai, Y.; Lü, C. Facile Construction of Crosslinked Anion Exchange Membranes Based on Fluorenyl-Containing Polysulfone via Click Chemistry. Polym. Chem. **2017**, 8 (30), 4403–4413. https://doi.org/10.1039/C7PY00789B.
(170) Hu, C.; Zhang, Q.; Lin, C.; Lin, Z.; Li, L.; Soyekwo, F.; Zhu, A.; Liu, Q. Multi-Cation Crosslinked Anion Exchange Membranes from Microporous Tröger's Base Copolymers. J. Mater. Chem. A **2018**, 6 (27), 13302–13311. https://doi.org/10.1039/C8TA02153H.
(171) Hu, C.; Zhang, Q.; Wu, H.; Deng, X.; Yang, Q.; Liu, P.; Hong, Y.; Zhu, A.; Liu, Q. Dual Hydrophobic Modifications toward Anion Exchange Membranes with Both High Ion Conductivity and Excellent Dimensional Stability. Journal of Membrane Science **2020**, 595, 117521. https://doi.org/10.1016/j.memsci.2019.117521.
(172) Hu, E. N.; Lin, C. X.; Liu, F. H.; Yang, Q.; Li, L.; Zhang, Q. G.; Zhu, A. M.; Liu, Q. L. Cross-Linked Poly(Vinylbenzyl Chloride) Anion Exchange Membranes with Long Flexible Multihead for Fuel Cells. ACS Appl. Energy Mater. **2018**, 1 (7), 3479–3487. https://doi.org/10.1021/acsaem.8b00698.
(173) Ion-Ebrasu, D.; Pollet, B. G.; Spinu-Zaulet, A.; Soare, A.; Carcadea, E.; Varlam, M.; Caprarescu, S. Graphene Modified Fluorinated Cation-Exchange Membranes for Proton Exchange Membrane Water Electrolysis. International Journal of Hydrogen Energy **2019**, 44 (21), 10190–10196. https://doi.org/10.1016/j.ijhydene.2019.02.148.
(174) Irfan, M.; Ge, L.; Wang, Y.; Yang, Z.; Xu, T. Hydrophobic Side Chains Impart Anion Exchange Membranes with High Monovalent–Divalent Anion Selectivity in Electrodialysis. ACS Sustainable Chem. Eng. **2019**, 7 (4), 4429–4442. https://doi.org/10.1021/acssuschemeng.8b06426.
(175) Jeon, J. Y.; Park, S.; Han, J.; Maurya, S.; Mohanty, A. D.; Tian, D.; Saikia, N.; Hickner, M. A.; Ryu, C. Y.; Tuckerman, M. E.; Paddison, S. J.; Kim, Y. S.; Bae, C. Synthesis of Aromatic Anion Exchange Membranes by Friedel–Crafts Bromoalkylation and Cross-Linking of Polystyrene Block Copolymers. Macromolecules **2019**, 52 (5), 2139–2147. https://doi.org/10.1021/acs.macromol.8b02355.
(176) Jiang, S.; Ladewig, B. P. High Ion-Exchange Capacity Semihomogeneous Cation Exchange Membranes Prepared via a Novel Polymerization and Sulfonation Approach in Porous Polypropylene. ACS Appl. Mater. Interfaces **2017**, 9 (44), 38612–38620. https://doi.org/10.1021/acsami.7b13076.
(177) Jiang, T.; Wang, C.; Wang, T.; Wang, X.; Wang, X.; Li, X.; Ding, Y.; Wei, H. Imidazolium Structural Isomer Pyrazolium: A Better Alkali-Stable Anion Conductor for Anion Exchange Membranes. Journal of Membrane Science **2022**, 660, 120843. https://doi.org/10.1016/j.memsci.2022.120843.
(178) Jiang, Y.; Liao, J.; Yang, S.; Li, J.; Xu, Y.; Ruan, H.; Sotto, A.; Van Der Bruggen, B.; Shen, J. Stable Cycloaliphatic Quaternary Ammonium-Tethered Anion Exchange Membranes for Electrodialysis. Reactive and Functional Polymers **2018**, 130, 61–69. https://doi.org/10.1016/j.reactfunctpolym.2018.05.014.

(179) Jiang, Y.; Wang, C.; Pan, J.; Sotto, A.; Shen, J. Constructing an Internally Cross-Linked Structure for Polysulfone to Improve Dimensional Stability and Alkaline Stability of High Performance Anion Exchange Membranes. International Journal of Hydrogen Energy **2019**, 44 (16), 8279–8289. https://doi.org/10.1016/j.ijhydene.2019.02.098.
(180) Jin, K.; Yue, B.; Yan, L.; Qiao, R.; Zhao, H.; Zhang, J. Synthesis and Characterization of Poly(5'-Hexyloxy-1',4-Biphenyl)-b-Poly(2',4'-Bispropoxysulfonate-1',4-Biphenyl) with High Ion Exchange Capacity for Proton Exchange Membrane Fuel Cell Applications. Chemistry – An Asian Journal **2022**, 17 (9), e202200109. https://doi.org/10.1002/asia.202200109.
(181) Kang, M.-S.; Kim, J. H.; Won, J.; Moon, S.-H.; Kang, Y. S. Highly Charged Proton Exchange Membranes Prepared by Using Water Soluble Polymer Blends for Fuel Cells. Journal of Membrane Science **2005**, 247 (1–2), 127–135. https://doi.org/10.1016/j.memsci.2004.09.017.
(182) Khan, M. I.; Mondal, A. N.; Tong, B.; Jiang, C.; Emmanuel, K.; Yang, Z.; Wu, L.; Xu, T. Development of BPPO-Based Anion Exchange Membranes for Electrodialysis Desalination Applications. Desalination **2016**, 391, 61–68. https://doi.org/10.1016/j.desal.2015.11.024.
(183) Khan, M. I.; Zheng, C.; Mondal, A. N.; Hossain, Md. M.; Wu, B.; Emmanuel, K.; Wu, L.; Xu, T. Preparation of Anion Exchange Membranes from BPPO and Dimethylethanolamine for Electrodialysis. Desalination **2017**, 402, 10–18. https://doi.org/10.1016/j.desal.2016.09.019.
(184) Kikhavani, T.; Ashrafizadeh, S. N.; Van Der Bruggen, B. Nitrate Selectivity and Transport Properties of a Novel Anion Exchange Membrane in Electrodialysis. Electrochimica Acta **2014**, 144, 341–351. https://doi.org/10.1016/j.electacta.2014.08.012.
(185) Kim, H.-K.; Lee, M.-S.; Lee, S.-Y.; Choi, Y.-W.; Jeong, N.-J.; Kim, C.-S. High Power Density of Reverse Electrodialysis with Pore-Filling Ion Exchange Membranes and a High-Open-Area Spacer. J. Mater. Chem. A **2015**, 3 (31), 16302–16306. https://doi.org/10.1039/C5TA03571F.
(186) Kim, Y.; Wang, Y.; France-Lanord, A.; Wang, Y.; Wu, Y.-C. M.; Lin, S.; Li, Y.; Grossman, J. C.; Swager, T. M. Ionic Highways from Covalent Assembly in Highly Conducting and Stable Anion Exchange Membrane Fuel Cells. J. Am. Chem. Soc. **2019**, 141 (45), 18152–18159. https://doi.org/10.1021/jacs.9b08749.
(187) Lai, A. N.; Guo, D.; Lin, C. X.; Zhang, Q. G.; Zhu, A. M.; Ye, M. L.; Liu, Q. L. Enhanced Performance of Anion Exchange Membranes via Crosslinking of Ion Cluster Regions for Fuel Cells. Journal of Power Sources **2016**, 327, 56–66. https://doi.org/10.1016/j.jpowsour.2016.07.043.
(188) Lee, S.; Abdi, Z. G.; Chen, J.; Chen, K. Optimal Method for Preparing Sulfonated Polyaryletherketones with High Ion Exchange Capacity by Acid-catalyzed Crosslinking for Proton Exchange Membrane Fuel Cells. Journal of Polymer Science **2021**, 59 (8), 706–720. https://doi.org/10.1002/pol.20200872.
(189) Lee, W.-H.; Mohanty, A. D.; Bae, C. Fluorene-Based Hydroxide Ion Conducting Polymers for Chemically Stable Anion Exchange Membrane Fuel Cells. ACS Macro Lett. **2015**, 4 (4), 453–457. https://doi.org/10.1021/acsmacrolett.5b00145.
(190) Lee, W.-H.; Park, E. J.; Han, J.; Shin, D. W.; Kim, Y. S.; Bae, C. Poly(Terphenylene) Anion Exchange Membranes: The Effect of Backbone Structure on Morphology and Membrane Property. ACS Macro Lett. **2017**, 6 (5), 566–570. https://doi.org/10.1021/acsmacrolett.7b00148.

(191) Li, C.; Wang, G.; Yu, D.; Sheng, F.; Shehzad, M. A.; He, T.; Xu, T.; Ren, X.; Cao, M.; Wu, B.; Ge, L. Cross-Linked Anion Exchange Membranes with Hydrophobic Side-Chains for Anion Separation. Journal of Membrane Science **2019**, 581, 150–157. https://doi.org/10.1016/j.memsci.2019.03.059.
(192) Li, C.; Liu, X.; Zhang, Y.; Dong, J.; Wang, J.; Yang, Z.; Cheng, H. Fabrication of Sulfonated Poly (Ether Ether Ketone)/Sulfonated Fully Aromatic Polyamide Composite Membranes for Direct Methanol Fuel Cells (DMFCs). Energy Tech **2019**, 7 (1), 71–79. https://doi.org/10.1002/ente.201700754.
(193) Li, C.; Zhang, Y.; Liu, X.; Dong, J.; Wang, J.; Yang, Z.; Cheng, H. Cross-Linked Fully Aromatic Sulfonated Polyamide as a Highly Efficiency Polymeric Filler in SPEEK Membrane for High Methanol Concentration Direct Methanol Fuel Cells. J Mater Sci **2018**, 53 (7), 5501–5510. https://doi.org/10.1007/s10853-017-1945-1.
(194) Li, J.; Cai, W.; Zhang, Y.; Cheng, H. Rigid–Flexible Hybrid Proton-Exchange Membranes with Improved Water-Retention Properties and High Stability for Fuel Cells. Energy Tech **2014**, 2 (8), 685–691. https://doi.org/10.1002/ente.201402011.
(195) Li, J.; Cai, W.; Zhang, Y.; Chen, Z.; Xu, G.; Cheng, H. Novel Polyamide Proton Exchange Membranes with Bi-Functional Sulfonimide Bridges for Fuel Cell Applications. Electrochimica Acta **2015**, 151, 168–176. https://doi.org/10.1016/j.electacta.2014.11.047.
(196) Li, J.; Cai, W.; Zhang, Y.; Xu, G.; Cheng, H. 3D-Branched Rigid–Flexible Hybrid Sulfonated Polyamide for Proton Exchange Membranes (PEMs) in Fuel Cell Applications. Energy Tech **2015**, 3 (2), 155–161. https://doi.org/10.1002/ente.201402130.
(197) Li, L.; Deng, B.; Ji, Y.; Yu, Y.; Xie, L.; Li, J.; Lu, X. A Novel Approach to Prepare Proton Exchange Membranes from Fluoropolymer Powder by Pre-Irradiation Induced Graft Polymerization. Journal of Membrane Science **2010**, 346 (1), 113–120. https://doi.org/10.1016/j.memsci.2009.09.027.
(198) Li, L.; Yang, Q.; Gao, X. L.; Wu, H. Y.; Zhang, Q. G.; Zhu, A. M.; Liu, Q. L. Facile Construction of Crosslinked All-Carbon-Backbone Anion-Exchange Membranes with Robust Durability. J. Mater. Chem. A **2018**, 6 (48), 24831–24840. https://doi.org/10.1039/C8TA09466G.
(199) Li, L.; Wang, J.; Ma, L.; Bai, L.; Zhang, A.; Qaisrani, N. A.; Yan, X.; Zhang, F.; He, G. Dual-Side-Chain-Grafted Poly(Phenylene Oxide) Anion Exchange Membranes for Fuel-Cell and Electrodialysis Applications. ACS Sustainable Chem. Eng. **2021**, 9 (25), 8611–8622. https://doi.org/10.1021/acssuschemeng.1c02189.
(200) Li, N.; Wang, L.; Hickner, M. Cross-Linked Comb-Shaped Anion Exchange Membranes with High Base Stability. Chem. Commun. **2014**, 50 (31), 4092. https://doi.org/10.1039/c3cc49027k.
(201) Li, P.; Li, K.; Chen, J.; Zhang, N.; Tang, S. Novel Anion Exchange Membrane with Poly Ionic Liquid-Confined Hypercrosslinked Polymer for Enhanced Anion Conduction and Stability. International Journal of Hydrogen Energy **2021**, 46 (41), 21590–21599. https://doi.org/10.1016/j.ijhydene.2021.03.223.
(202) Li, Y.; Liu, Y.; Savage, A. M.; Beyer, F. L.; Seifert, S.; Herring, A. M.; Knauss, D. M. Polyethylene-Based Block Copolymers for Anion Exchange Membranes. Macromolecules **2015**, 48 (18), 6523–6533. https://doi.org/10.1021/acs.macromol.5b01457.
(203) Liao, J.; Ruan, H.; Gao, X.; Chen, Q.; Shen, J. Exploring the Acid Enrichment Application of Piperidinium-Functionalized Cross-Linked Poly(2,6-Dimethyl-1,4-Phenylene Oxide)

Anion Exchange Membranes in Electrodialysis. Journal of Membrane Science **2021**, 621, 118999. https://doi.org/10.1016/j.memsci.2020.118999.
(204) Lin, B.; Chu, F.; Ren, Y.; Jia, B.; Yuan, N.; Shang, H.; Feng, T.; Zhu, Y.; Ding, J. Alkaline Stable C2-Substituted Imidazolium-Based Cross-Linked Anion Exchange Membranes for Alkaline Fuel Cell Applications. Journal of Power Sources **2014**, 266, 186–192. https://doi.org/10.1016/j.jpowsour.2014.05.003.
(205) Lin, B.; Dong, H.; Li, Y.; Si, Z.; Gu, F.; Yan, F. Alkaline Stable C2-Substituted Imidazolium-Based Anion-Exchange Membranes. Chem. Mater. **2013**, 25 (9), 1858–1867. https://doi.org/10.1021/cm400468u.
(206) Lin, B.; Xu, F.; Su, Y.; Han, J.; Zhu, Z.; Chu, F.; Ren, Y.; Zhu, L.; Ding, J. Ether-Free Polybenzimidazole Bearing Pendant Imidazolium Groups for Alkaline Anion Exchange Membrane Fuel Cells Application. ACS Appl. Energy Mater. **2020**, 3 (1), 1089–1098. https://doi.org/10.1021/acsaem.9b02123.
(207) Lin, C. X.; Zhuo, Y. Z.; Hu, E. N.; Zhang, Q. G.; Zhu, A. M.; Liu, Q. L. Crosslinked Side-Chain-Type Anion Exchange Membranes with Enhanced Conductivity and Dimensional Stability. Journal of Membrane Science **2017**, 539, 24–33. https://doi.org/10.1016/j.memsci.2017.05.063.
(208) Liu, B.; Li, T.; Li, Q.; Zhu, S.; Duan, Y.; Li, J.; Zhang, H.; Zhao, C. Enhanced Diffusion Dialysis Performance of Cross-Linked Poly(Aryl Piperidine) Anion Exchange Membranes by Thiol-Ene Click Chemistry for Acid Recovery. Journal of Membrane Science **2022**, 660, 120816. https://doi.org/10.1016/j.memsci.2022.120816.
(209) Liu, J.; Long, J.; Huang, W.; Xu, W.; Qi, X.; Li, J.; Zhang, Y. Enhanced Proton Selectivity and Stability of Branched Sulfonated Polyimide Membrane by Hydrogen Bonds Construction Strategy for Vanadium Flow Battery. Journal of Membrane Science **2023**, 665, 121111. https://doi.org/10.1016/j.memsci.2022.121111.
(210) Liu, Q.; Wang, Z.; Yu, A.; Li, J.; Shen, H.; Wang, H.; Yang, K.; Zhang, H. A Novel Anion Exchange Membrane Based on Poly (2,6-Dimethyl-1,4-Phenylene Oxide) with Excellent Alkaline Stability for AEMFC. International Journal of Hydrogen Energy **2021**, 46 (47), 24328–24338. https://doi.org/10.1016/j.ijhydene.2021.05.004.
(211) Lu, W.; Shao, Z.-G.; Zhang, G.; Li, J.; Zhao, Y.; Yi, B. Preparation of Anion Exchange Membranes by an Efficient Chloromethylation Method and Homogeneous Quaternization/Crosslinking Strategy. Solid State Ionics **2013**, 245–246, 8–18. https://doi.org/10.1016/j.ssi.2013.05.005.
(212) Lu, W.; Shao, Z.-G.; Zhang, G.; Zhao, Y.; Yi, B. Crosslinked Poly(Vinylbenzyl Chloride) with a Macromolecular Crosslinker for Anion Exchange Membrane Fuel Cells. Journal of Power Sources **2014**, 248, 905–914. https://doi.org/10.1016/j.jpowsour.2013.08.141.
(213) Mandal, M.; Huang, G.; Hassan, N. U.; Peng, X.; Gu, T.; Brooks-Starks, A. H.; Bahar, B.; Mustain, W. E.; Kohl, P. A. The Importance of Water Transport in High Conductivity and High-Power Alkaline Fuel Cells. J. Electrochem. Soc. **2020**, 167 (5), 054501. https://doi.org/10.1149/2.0022005JES.
(214) Mandal, M.; Huang, G.; Kohl, P. A. Anionic Multiblock Copolymer Membrane Based on Vinyl Addition Polymerization of Norbornenes: Applications in Anion-Exchange Membrane Fuel Cells. Journal of Membrane Science **2019**, 570–571, 394–402. https://doi.org/10.1016/j.memsci.2018.10.041.

(215) Mandal, M.; Huang, G.; Kohl, P. A. Highly Conductive Anion-Exchange Membranes Based on Cross-Linked Poly(Norbornene): Vinyl Addition Polymerization. ACS Appl. Energy Mater. **2019**, 2 (4), 2447–2457. https://doi.org/10.1021/acsaem.8b02051.
(216) Maurya, S.; Noh, S.; Matanovic, I.; Park, E. J.; Narvaez Villarrubia, C.; Martinez, U.; Han, J.; Bae, C.; Kim, Y. S. Rational Design of Polyaromatic Ionomers for Alkaline Membrane Fuel Cells with >1 W Cm $^{-2}$ Power Density. Energy Environ. Sci. **2018**, 11 (11), 3283–3291. https://doi.org/10.1039/C8EE02192A.
(217) Mayadevi, T. S.; Sung, S.; Varghese, L.; Kim, T.-H. Poly(Meta/Para-Terphenylene-Methyl Piperidinium)-Based Anion Exchange Membranes: The Effect of Backbone Structure in AEMFC Application. Membranes **2020**, 10 (11), 329. https://doi.org/10.3390/membranes10110329.
(218) Miao, Y.; Jia, Y.; Guo, R.; Wang, M. Heterogeneous Anion-Exchange Membrane: Influences of Charged Binders with Crosslinking Structure on Electrodialytic Performance. Journal of Membrane Science **2018**, 557, 67–75. https://doi.org/10.1016/j.memsci.2018.04.030.
(219) Miyanishi, S.; Yamaguchi, T. Highly Conductive Mechanically Robust High M_w Polyfluorene Anion Exchange Membrane for Alkaline Fuel Cell and Water Electrolysis Application. Polym. Chem. **2020**, 11 (23), 3812–3820. https://doi.org/10.1039/D0PY00334D.
(220) Mohanty, A. D.; Ryu, C. Y.; Kim, Y. S.; Bae, C. Stable Elastomeric Anion Exchange Membranes Based on Quaternary Ammonium-Tethered Polystyrene- b -Poly(Ethylene- Co -Butylene)- b -Polystyrene Triblock Copolymers. Macromolecules **2015**, 48 (19), 7085–7095. https://doi.org/10.1021/acs.macromol.5b01382.
(221) Müller, F.; Andretta, R.; De Oliveira Meneguzzi, L.; Arthur Ferreira, C. Development of Quaternarized Poly(Vinyl Alcohol) Anion-exchange Membranes for Applications in Electrodialysis. J of Applied Polymer Sci **2017**, 134 (31), 44946. https://doi.org/10.1002/app.44946.
(222) Müller, F.; Ferreira, C. A.; Franco, L.; Puiggalí, J.; Alemán, C.; Armelin, E. New Sulfonated Polystyrene and Styrene–Ethylene/Butylene–Styrene Block Copolymers for Applications in Electrodialysis. J. Phys. Chem. B **2012**, 116 (38), 11767–11779. https://doi.org/10.1021/jp3068415.
(223) Naik, N. S.; Padaki, M.; Déon, S.; Murthy, D. H. K. Novel Poly (Ionic Liquid)-Based Anion Exchange Membranes for Efficient and Rapid Acid Recovery from Industrial Waste. Chemical Engineering Journal **2020**, 401, 126148. https://doi.org/10.1016/j.cej.2020.126148.
(224) Nakano, T.; Nagaoka, S.; Kawakami, H. Preparation of Novel Sulfonated Block Copolyimides for Proton Conductivity Membranes. Polym. Adv. Technol. **2005**, 16 (10), 753–757. https://doi.org/10.1002/pat.650.
(225) Noonan, K. J. T.; Hugar, K. M.; Kostalik, H. A.; Lobkovsky, E. B.; Abruña, H. D.; Coates, G. W. Phosphonium-Functionalized Polyethylene: A New Class of Base-Stable Alkaline Anion Exchange Membranes. J. Am. Chem. Soc. **2012**, 134 (44), 18161–18164. https://doi.org/10.1021/ja307466s.
(226) Olsson, J. S.; Pham, T. H.; Jannasch, P. Poly(Arylene Piperidinium) Hydroxide Ion Exchange Membranes: Synthesis, Alkaline Stability, and Conductivity. Advanced Functional Materials **2018**, 28 (2), 1702758. https://doi.org/10.1002/adfm.201702758.
(227) Olsson, J. S.; Pham, T. H.; Jannasch, P. Functionalizing Polystyrene with N -Alicyclic Piperidine-Based Cations via Friedel–Crafts Alkylation for Highly Alkali-Stable Anion-

Exchange Membranes. Macromolecules **2020**, 53 (12), 4722–4732. https://doi.org/10.1021/acs.macromol.0c00201.
(228) Ono, H.; Kimura, T.; Takano, A.; Asazawa, K.; Miyake, J.; Inukai, J.; Miyatake, K. Robust Anion Conductive Polymers Containing Perfluoroalkylene and Pendant Ammonium Groups for High Performance Fuel Cells. J. Mater. Chem. A **2017**, 5 (47), 24804–24812. https://doi.org/10.1039/C7TA09409D.
(229) Pagels, M. K.; Adhikari, S.; Walgama, R. C.; Singh, A.; Han, J.; Shin, D.; Bae, C. One-Pot Synthesis of Proton Exchange Membranes from Anion Exchange Membrane Precursors. ACS Macro Lett. **2020**, 9 (10), 1489–1493. https://doi.org/10.1021/acsmacrolett.0c00550.
(230) Pal, S.; Mondal, R.; Guha, S.; Chatterjee, U.; Jewrajka, S. K. Homogeneous Phase Crosslinked Poly(Acrylonitrile-Co-2-Acrylamido-2-Methyl-1-Propanesulfonic Acid) Conetwork Cation Exchange Membranes Showing High Electrochemical Properties and Electrodialysis Performance. Polymer **2019**, 180, 121680. https://doi.org/10.1016/j.polymer.2019.121680.
(231) Pan, J.; Tao, Y.; Zhao, L.; Yu, X.; Zhao, X.; Wu, T.; Liu, L. Green Preparation of Quaternized Vinylimidazole-Based Anion Exchange Membrane by Photopolymerization. Separation and Purification Technology **2021**, 276, 119220. https://doi.org/10.1016/j.seppur.2021.119220.
(232) Pan, Q.; Hossain, Md. M.; Yang, Z.; Wang, Y.; Wu, L.; Xu, T. One-Pot Solvent-Free Synthesis of Cross-Linked Anion Exchange Membranes for Electrodialysis. Journal of Membrane Science **2016**, 515, 115–124. https://doi.org/10.1016/j.memsci.2016.05.050.
(233) Peng, G.; Zhu, C.; Liao, J.; Gao, X.; Hao, L.; Sotto, A.; Shen, J. A Two-Step Strategy for the Preparation of Anion-Exchange Membranes Based on Poly(Vinylidenefluoride-Co-Hexafluoropropylene) for Electrodialysis Desalination. Polymer **2021**, 218, 123508. https://doi.org/10.1016/j.polymer.2021.123508.
(234) Pham, T. H.; Olsson, J. S.; Jannasch, P. Poly(Arylene Alkylene)s with Pendant N -Spirocyclic Quaternary Ammonium Cations for Anion Exchange Membranes. J. Mater. Chem. A **2018**, 6 (34), 16537–16547. https://doi.org/10.1039/C8TA04699A.
(235) Pham, T. H.; Olsson, J. S.; Jannasch, P. Effects of the N-Alicyclic Cation and Backbone Structures on the Performance of Poly(Terphenyl)-Based Hydroxide Exchange Membranes. J. Mater. Chem. A **2019**, 7 (26), 15895–15906. https://doi.org/10.1039/C9TA05531B.
(236) Price, S. C.; Ren, X.; Savage, A. M.; Beyer, F. L. Synthesis and Characterization of Anion-Exchange Membranes Based on Hydrogenated Poly(Norbornene). Polym. Chem. **2017**, 8 (37), 5708–5717. https://doi.org/10.1039/C7PY01084B.
(237) Qaisrani, N. A.; Ma, Y.; Ma, L.; Liu, J.; Gao, L.; Li, L.; Gong, S.; Yan, X.; Zhang, F.; He, G. Facile and Green Fabrication of Polybenzoxazine-Based Composite Anion-Exchange Membranes with a Self-Cross-Linked Structure. Ionics **2018**, 24 (10), 3053–3063. https://doi.org/10.1007/s11581-017-2433-y.
(238) Rahman, Md. K.; Aiba, G.; Susan, Md. A. B. H.; Sasaya, Y.; Ota, K.; Watanabe, M. Synthesis, Characterization, and Copolymerization of a Series of Novel Acid Monomers Based on Sulfonimides for Proton Conducting Membranes. Macromolecules **2004**, 37 (15), 5572–5577. https://doi.org/10.1021/ma0498058.
(239) Rajput, A.; Sharma, J.; Raj, S. K.; Kulshrestha, V. Dehydrofluorinated Poly(Vinylidene Fluoride-Co-Hexafluoropropylene) Based Crosslinked Cation Exchange Membrane for Brackish Water Desalination via Electrodialysis. Colloids and Surfaces A: Physicochemical and Engineering Aspects **2021**, 630, 127576. https://doi.org/10.1016/j.colsurfa.2021.127576.

(240) Ran, J.; Wu, L.; Ge, Q.; Chen, Y.; Xu, T. High Performance Anion Exchange Membranes Obtained through Graft Architecture and Rational Cross-Linking. Journal of Membrane Science **2014**, 470, 229–236. https://doi.org/10.1016/j.memsci.2014.07.036.
(241) Reig, M.; Farrokhzad, H.; Van Der Bruggen, B.; Gibert, O.; Cortina, J. L. Synthesis of a Monovalent Selective Cation Exchange Membrane to Concentrate Reverse Osmosis Brines by Electrodialysis. Desalination **2015**, 375, 1–9. https://doi.org/10.1016/j.desal.2015.07.023.
(242) Sata, T.; Teshima, K.; Yamaguchi, T. Permselectivity between Two Anions in Anion Exchange Membranes Crosslinked with Various Diamines in Electrodialysis. J. Polym. Sci. A Polym. Chem. **1996**, 34 (8), 1475–1482. https://doi.org/10.1002/(SICI)1099-0518(199606)34:8<1475::AID-POLA11>3.0.CO;2-5.
(243) Sharma, P.; Agrawal, S.; Rathore, M. S.; Shahi, V. K. Cross-Linked Anion-Exchange Membrane with Side-Chain Grafted Multi-Cationic Spacer for Electrodialysis: Imparting Dual Anti-Fouling and Anti-Bacterial Characteristics. Journal of Membrane Science **2022**, 660, 120871. https://doi.org/10.1016/j.memsci.2022.120871.
(244) Si, Z.; Qiu, L.; Dong, H.; Gu, F.; Li, Y.; Yan, F. Effects of Substituents and Substitution Positions on Alkaline Stability of Imidazolium Cations and Their Corresponding Anion-Exchange Membranes. ACS Appl. Mater. Interfaces **2014**, 6 (6), 4346–4355. https://doi.org/10.1021/am500022c.
(245) Su, X.; Wang, J.; Xu, S.; Zhang, D.; He, R. Construction of Macromolecule Cross-Linked Anion Exchange Membranes Containing Free Radical Inhibitor Groups for Superior Chemical Stability. Journal of Membrane Science **2022**, 660, 120844. https://doi.org/10.1016/j.memsci.2022.120844.
(246) Tekinalp, Ö.; Zimmermann, P.; Burheim, O. S.; Deng, L. Designing Monovalent Selective Anion Exchange Membranes for the Simultaneous Separation of Chloride and Fluoride from Sulfate in an Equimolar Ternary Mixture. Journal of Membrane Science **2023**, 666, 121148. https://doi.org/10.1016/j.memsci.2022.121148.
(247) Tinh, V. D. C.; Thuc, V. D.; Jeon, Y.; Gu, G.-Y.; Kim, D. Highly Durable Poly(Arylene Piperidinium) Composite Membranes Modified with Polyhedral Oligomeric Silsesquioxane for Fuel Cell and Water Electrolysis Application. Journal of Membrane Science **2022**, 660, 120903. https://doi.org/10.1016/j.memsci.2022.120903.
(248) Treichel, M.; Tyler Womble, C.; Selhorst, R.; Gaitor, J.; Pathiranage, T. M. S. K.; Kowalewski, T.; Noonan, K. J. T. Exploring the Effects of Bulky Cations Tethered to Semicrystalline Polymers: The Case of Tetraaminophosphoniums with Ring-Opened Polynorbornenes. Macromolecules **2020**, 53 (19), 8509–8518. https://doi.org/10.1021/acs.macromol.0c00422.
(249) Wang, C.; He, Z.; Xie, X.; Mai, X.; Li, Y.; Li, T.; Zhao, M.; Yan, C.; Liu, H.; Wujcik, E. K.; Guo, Z. Controllable Cross-Linking Anion Exchange Membranes with Excellent Mechanical and Thermal Properties. Macro Materials & Eng **2018**, 303 (3), 1700462. https://doi.org/10.1002/mame.201700462.
(250) Wang, C.; Mo, B.; He, Z.; Shao, Q.; Pan, D.; Wujick, E.; Guo, J.; Xie, X.; Xie, X.; Guo, Z. Crosslinked Norbornene Copolymer Anion Exchange Membrane for Fuel Cells. Journal of Membrane Science **2018**, 556, 118–125. https://doi.org/10.1016/j.memsci.2018.03.080.
(251) Wang, C.; Lin, B.; Qiao, G.; Wang, L.; Zhu, L.; Chu, F.; Feng, T.; Yuan, N.; Ding, J. Polybenzimidazole/Ionic Liquid Functionalized Graphene Oxide Nanocomposite Membrane for Alkaline Anion Exchange Membrane Fuel Cells. Materials Letters **2016**, 173, 219–222. https://doi.org/10.1016/j.matlet.2016.03.057.

(252) Wang, G.; Yao, Y.; Xiao, G.; Yan, D. Novel Sulfonated Polybenzothiazoles with Outstanding Dimensional Stability for Proton Exchange Membranes. Journal of Membrane Science **2013**, 425–426, 200–207. https://doi.org/10.1016/j.memsci.2012.08.056.
(253) Wang, J.; Wei, H.; Yang, S.; Fang, H.; Xu, P.; Ding, Y. Constructing Pendent Imidazolium-Based Poly(Phenylene Oxide)s for Anion Exchange Membranes Using a Click Reaction. RSC Adv. **2015**, 5 (113), 93415–93422. https://doi.org/10.1039/C5RA17748K.
(254) Wang, J.; Wang, J.; Zhang, S. Synthesis and Characterization of Cross-Linked Poly(Arylene Ether Ketone) Containing Pendant Quaternary Ammonium Groups for Anion-Exchange Membranes. Journal of Membrane Science **2012**, 415–416, 205–212. https://doi.org/10.1016/j.memsci.2012.04.054.
(255) Wang, J.; Liu, M.; Feng, Z.; Liu, J.; Liao, S.; Li, X.; Yu, Y. Highly Conductive Anion Exchange Membrane with a Stable Double-Sided Anti-Fouling Structure for Electrodialysis Desalination of Protein Systems. Desalination **2023**, 545, 116167. https://doi.org/10.1016/j.desal.2022.116167.
(256) Wang, J.; Gu, S.; Xiong, R.; Zhang, B.; Xu, B.; Yan, Y. Structure–Property Relationships in Hydroxide-Exchange Membranes with Cation Strings and High Ion-Exchange Capacity. ChemSusChem **2015**, 8 (24), 4229–4234. https://doi.org/10.1002/cssc.201501035.
(257) Wang, J.; Zhao, Y.; Setzler, B. P.; Rojas-Carbonell, S.; Ben Yehuda, C.; Amel, A.; Page, M.; Wang, L.; Hu, K.; Shi, L.; Gottesfeld, S.; Xu, B.; Yan, Y. Poly(Aryl Piperidinium) Membranes and Ionomers for Hydroxide Exchange Membrane Fuel Cells. Nat Energy **2019**, 4 (5), 392–398. https://doi.org/10.1038/s41560-019-0372-8.
(258) Wang, L.; Brink, J. J.; Varcoe, J. R. The First Anion-Exchange Membrane Fuel Cell to Exceed 1 W Cm^{-2} at 70 °C with a Non-Pt-Group (O_2) Cathode. Chem. Commun. **2017**, 53 (86), 11771–11773. https://doi.org/10.1039/C7CC06392J.
(259) Wang, L.; Magliocca, E.; Cunningham, E. L.; Mustain, W. E.; Poynton, S. D.; Escudero-Cid, R.; Nasef, M. M.; Ponce-González, J.; Bance-Souahli, R.; Slade, R. C. T.; Whelligan, D. K.; Varcoe, J. R. An Optimised Synthesis of High Performance Radiation-Grafted Anion-Exchange Membranes. Green Chem. **2017**, 19 (3), 831–843. https://doi.org/10.1039/C6GC02526A.
(260) Wang, L.; Peng, X.; Mustain, W. E.; Varcoe, J. R. Radiation-Grafted Anion-Exchange Membranes: The Switch from Low- to High-Density Polyethylene Leads to Remarkably Enhanced Fuel Cell Performance. Energy Environ. Sci. **2019**, 12 (5), 1575–1579. https://doi.org/10.1039/C9EE00331B.
(261) Wang, Q.; Huang, L.; Zheng, J.; Zhang, Q.; Qin, G.; Li, S.; Zhang, S. Design, Synthesis and Characterization of Anion Exchange Membranes Containing Guanidinium Salts with Ultrahigh Dimensional Stability. Journal of Membrane Science **2022**, 643, 120008. https://doi.org/10.1016/j.memsci.2021.120008.
(262) Wang, W.; Wang, S.; Li, W.; Xie, X.; Lv, Y. Synthesis and Characterization of a Fluorinated Cross-Linked Anion Exchange Membrane. International Journal of Hydrogen Energy **2013**, 38 (25), 11045–11052. https://doi.org/10.1016/j.ijhydene.2013.03.166.
(263) Wang, X.; Sheng, W.; Shen, Y.; Liu, L.; Dai, S.; Li, N. N-Cyclic Quaternary Ammonium-Functionalized Anion Exchange Membrane with Improved Alkaline Stability Enabled by Aryl-Ether Free Polymer Backbones for Alkaline Fuel Cells. Journal of Membrane Science **2019**, 587, 117135. https://doi.org/10.1016/j.memsci.2019.05.059.

(264) Wang, X.; Lammertink, R. G. H. Dimensionally Stable Multication-Crosslinked Poly(Arylene Piperidinium) Membranes for Water Electrolysis. J. Mater. Chem. A **2022**, 10 (15), 8401–8412. https://doi.org/10.1039/D1TA10820D.
(265) Wang, Z.; Zhou, S. F.; Zhuo, Y. Z.; Lai, A. N.; Lu, Y. Z.; Wu, X. B. Adamantane-Based Block Poly(Arylene Ether Sulfone)s as Anion Exchange Membranes. Polymer **2022**, 255, 125155. https://doi.org/10.1016/j.polymer.2022.125155.
(266) Weissbach, T.; Wright, A. G.; Peckham, T. J.; Sadeghi Alavijeh, A.; Pan, V.; Kjeang, E.; Holdcroft, S. Simultaneous, Synergistic Control of Ion Exchange Capacity and Cross-Linking of Sterically-Protected Poly(Benzimidazolium)s. Chem. Mater. **2016**, 28 (21), 8060–8070. https://doi.org/10.1021/acs.chemmater.6b03902.
(267) Wright, A. G.; Holdcroft, S. Hydroxide-Stable Ionenes. ACS Macro Lett. **2014**, 3 (5), 444–447. https://doi.org/10.1021/mz500168d.
(268) Xiao, Y.; Xu, J.; Hu, L.; Wang, H.; Gao, L.; Peng, S.; Di, M.; Sun, X.; Liu, J.; Yan, X.; Chen, L.; He, G. Advanced Anion-Selective Membranes with Pendant Quaternary Ammonium for Neutral Aqueous Supporting Redox Flow Battery. Journal of Membrane Science **2022**, 659, 120748. https://doi.org/10.1016/j.memsci.2022.120748.
(269) Xie, H.; Pan, J.; Wei, B.; Feng, J.; Liao, S.; Li, X.; Yu, Y. Anti-Fouling Anion Exchange Membrane for Electrodialysis Fabricated by in-Situ Interpenetration of the Ionomer to Gradient Cross-Linked Network of Ca-Na Alginate. Desalination **2021**, 505, 115005. https://doi.org/10.1016/j.desal.2021.115005.
(270) Xu, F.; Chen, Y.; Li, J.; Han, Y.; Lin, B.; Ding, J. Robust Poly(Alkyl–Fluorene Isatin) Proton Exchange Membranes Grafted with Pendant Sulfonate Groups for Proton Exchange Membrane Fuel Cells. Journal of Membrane Science **2022**, 664, 121045. https://doi.org/10.1016/j.memsci.2022.121045.
(271) Xue, J.; Liu, L.; Liao, J.; Shen, Y.; Li, N. UV-Crosslinking of Polystyrene Anion Exchange Membranes by Azidated Macromolecular Crosslinker for Alkaline Fuel Cells. Journal of Membrane Science **2017**, 535, 322–330. https://doi.org/10.1016/j.memsci.2017.04.049.
(272) Xue, J.; Liu, X.; Zhang, J.; Yin, Y.; Guiver, M. D. Poly(Phenylene Oxide)s Incorporating N-Spirocyclic Quaternary Ammonium Cation/Cation Strings for Anion Exchange Membranes. Journal of Membrane Science **2020**, 595, 117507. https://doi.org/10.1016/j.memsci.2019.117507.
(273) Yadav, V.; Rathod, N. H.; Kulshrestha, V. Series-Connected Tetracation Partially Cross-Linked Anion Exchange Membranes: Insight towards Consequences of Alkyl Spacer Length. ACS Appl. Polym. Mater. **2021**, 3 (7), 3307–3320. https://doi.org/10.1021/acsapm.1c00171.
(274) Yadav, V.; Rathod, N. H.; Sharma, J.; Kulshrestha, V. Long Side-Chain Type Partially Cross-Linked Poly(Vinylidene Fluoride-Co-Hexafluoropropylene) Anion Exchange Membranes for Desalination via Electrodialysis. Journal of Membrane Science **2021**, 622, 119034. https://doi.org/10.1016/j.memsci.2020.119034.
(275) Yang, C.; Liu, L.; Han, X.; Huang, Z.; Dong, J.; Li, N. Highly Anion Conductive, Alkyl-Chain-Grafted Copolymers as Anion Exchange Membranes for Operable Alkaline H_2/O_2 Fuel Cells. J. Mater. Chem. A **2017**, 5 (21), 10301–10310. https://doi.org/10.1039/C7TA00481H.
(276) Yang, C.; Liu, L.; Huang, Y.; Dong, J.; Li, N. Anion-Conductive Poly(2,6-Dimethyl-1,4-Phenylene Oxide) Grafted with Tailored Polystyrene Chains for Alkaline Fuel Cells. Journal of Membrane Science **2019**, 573, 247–256. https://doi.org/10.1016/j.memsci.2018.12.013.

(277) Yang, C.; Wang, S.; Ma, W.; Jiang, L.; Sun, G. Comparison of Alkaline Stability of Quaternary Ammonium- and 1,2-Methylimidazolium-Based Alkaline Anion Exchange Membranes. Journal of Membrane Science **2015**, 487, 12–18. https://doi.org/10.1016/j.memsci.2015.03.067.
(278) Yang, C.; Wang, S.; Ma, W.; Zhao, S.; Xu, Z.; Sun, G. Highly Stable Poly(Ethylene Glycol)-Grafted Alkaline Anion Exchange Membranes. J. Mater. Chem. A **2016**, 4 (10), 3886–3892. https://doi.org/10.1039/C6TA00200E.
(279) Yang, K.; Chu, X.; Zhang, X.; Li, X.; Zheng, J.; Li, S.; Li, N.; Sherazi, T. A.; Zhang, S. The Effect of Polymer Backbones and Cation Functional Groups on Properties of Anion Exchange Membranes for Fuel Cells. Journal of Membrane Science **2020**, 603, 118025. https://doi.org/10.1016/j.memsci.2020.118025.
(280) Yang, Q.; Li, L.; Gao, X. L.; Wu, H. Y.; Liu, F. H.; Zhang, Q. G.; Zhu, A. M.; Zhao, C. H.; Liu, Q. L. Crown Ether Bridged Anion Exchange Membranes with Robust Alkaline Durability. Journal of Membrane Science **2019**, 578, 230–238. https://doi.org/10.1016/j.memsci.2019.02.038.
(281) Yang, Y.; Shi, Z.; Holdcroft, S. Synthesis of Sulfonated Polysulfone- b Lock -PVDF Copolymers: Enhancement of Proton Conductivity in Low Ion Exchange Capacity Membranes. Macromolecules **2004**, 37 (5), 1678–1681. https://doi.org/10.1021/ma035659e.
(282) You, W.; Ganley, J. M.; Ernst, B. G.; Peltier, C. R.; Ko, H.-Y.; DiStasio, R. A.; Knowles, R. R.; Coates, G. W. Expeditious Synthesis of Aromatic-Free Piperidinium-Functionalized Polyethylene as Alkaline Anion Exchange Membranes. Chem. Sci. **2021**, 12 (11), 3898–3910. https://doi.org/10.1039/D0SC05789D.
(283) You, W.; Hugar, K. M.; Coates, G. W. Synthesis of Alkaline Anion Exchange Membranes with Chemically Stable Imidazolium Cations: Unexpected Cross-Linked Macrocycles from Ring-Fused ROMP Monomers. Macromolecules **2018**, 51 (8), 3212–3218. https://doi.org/10.1021/acs.macromol.8b00209.
(284) You, W.; Padgett, E.; MacMillan, S. N.; Muller, D. A.; Coates, G. W. Highly Conductive and Chemically Stable Alkaline Anion Exchange Membranes via ROMP of Trans -Cyclooctene Derivatives. Proc. Natl. Acad. Sci. U.S.A. **2019**, 116 (20), 9729–9734. https://doi.org/10.1073/pnas.1900988116.
(285) Yu, S.; Zhu, J.; Liao, J.; Ruan, H.; Sotto, A.; Shen, J. Homogeneous Trimethylamine-Quaternized Polysulfone-Based Anion Exchange Membranes with Crosslinked Structure for Electrodialysis Desalination. Separation and Purification Technology **2021**, 257, 117874. https://doi.org/10.1016/j.seppur.2020.117874.
(286) Zeng, L.; He, Q.; Liao, Y.; Kuang, S.; Wang, J.; Ding, W.; Liao, Q.; Wei, Z. Anion Exchange Membrane Based on Interpenetrating Polymer Network with Ultrahigh Ion Conductivity and Excellent Stability for Alkaline Fuel Cell. Research **2020**, 2020, 2020/4794706. https://doi.org/10.34133/2020/4794706.
(287) Zhang, A.; Li, L.; Ma, L.; Ren, Y.; Bai, L.; He, G.; Zhang, F. Soft Template Promoted Microphase Separation in Anion Exchange Membrane of Electrodialysis. Journal of Membrane Science **2022**, 658, 120758. https://doi.org/10.1016/j.memsci.2022.120758.
(288) Zhang, M.; Liu, J.; Wang, Y.; An, L.; Guiver, M. D.; Li, N. Highly Stable Anion Exchange Membranes Based on Quaternized Polypropylene. J. Mater. Chem. A **2015**, 3 (23), 12284–12296. https://doi.org/10.1039/C5TA01420D.
(289) Zhang, M.; Shan, C.; Liu, L.; Liao, J.; Chen, Q.; Zhu, M.; Wang, Y.; An, L.; Li, N. Facilitating Anion Transport in Polyolefin-Based Anion Exchange Membranes via Bulky Side

Chains. ACS Appl. Mater. Interfaces **2016**, 8 (35), 23321–23330. https://doi.org/10.1021/acsami.6b06426.
(290) Zhang, P.; Shen, B.; Pu, H. Robust, Dimensional Stable, and Self-Healable Anion Exchange Membranes via Quadruple Hydrogen Bonds. Polymer **2022**, 245, 124698. https://doi.org/10.1016/j.polymer.2022.124698.
(291) Zhang, S.; Liu, H.; Tan, Y.; Lu, C.; Mao, S.; Kang, L.; Liao, H. Novel Trisulfonated Poly(Phthalazinone Ether Phosphine Oxide)s with High Dimensional Stability for Proton Exchange Membrane. Energy Fuels **2020**, 34 (4), 4999–5005. https://doi.org/10.1021/acs.energyfuels.0c00085.
(292) Zhang, S.; Zhu, X.; Jin, C.; Hu, H. Pyridinium-Functionalized Crosslinked Anion Exchange Membrane Based on Multication Side Chain Tethered Elastomeric Triblock Poly(Styrene-b-(Ethylene-Co-Butylene)-b-Styrene). Reactive and Functional Polymers **2019**, 138, 62–69. https://doi.org/10.1016/j.reactfunctpolym.2019.02.012.
(293) Zhang, X.; Guo, J.; Chu, X.; Fang, C.; Huang, Y.; Liu, L.; Li, N. Mechanically Flexible Bulky Imidazolium-Based Anion Exchange Membranes by Grafting PEG Pendants for Alkaline Fuel Cells. Journal of Membrane Science **2022**, 659, 120820. https://doi.org/10.1016/j.memsci.2022.120820.
(294) Zhang, Y.; Li, C.; Liu, X.; Yang, Z.; Dong, J.; Liu, Y.; Cai, W.; Cheng, H. Fabrication of a Polymer Electrolyte Membrane with Uneven Side Chains for Enhancing Proton Conductivity. RSC Adv. **2016**, 6 (83), 79593–79601. https://doi.org/10.1039/C6RA17477A.
(295) Zhang, Y.; Li, C.; Yang, Z.; Liu, X.; Dong, J.; Liu, Y.; Cai, W.; Cheng, H. A Robust Pendant-Type Cross-Linked Anion Exchange Membrane (AEM) with High Hydroxide Conductivity at a Moderate IEC Value. J Mater Sci **2017**, 52 (7), 3946–3958. https://doi.org/10.1007/s10853-016-0656-3.
(296) Zhang, Y.; Wang, H.; Liu, B.; Shi, J.; Zhang, J.; Shi, H. An Ultra-High Ion Selective Hybrid Proton Exchange Membrane Incorporated with Zwitterion-Decorated Graphene Oxide for Vanadium Redox Flow Batteries. J. Mater. Chem. A **2019**, 7 (20), 12669–12680. https://doi.org/10.1039/C9TA01891C.
(297) Zhao, C.; Lin, H.; Shao, K.; Li, X.; Ni, H.; Wang, Z.; Na, H. Block Sulfonated Poly(Ether Ether Ketone)s (SPEEK) Ionomers with High Ion-Exchange Capacities for Proton Exchange Membranes. Journal of Power Sources **2006**, 162 (2), 1003–1009. https://doi.org/10.1016/j.jpowsour.2006.07.055.
(298) Zhao, J.; Chen, Q.; Wang, J. Novel Ecofriendly Cation Exchange Membranes for Low-Cost Electrodialysis of Brackish Water: Desalination and Antiscaling Performance. Journal of Membrane Science **2022**, 661, 120908. https://doi.org/10.1016/j.memsci.2022.120908.
(299) Zhao, J.; Ren, L.; Chen, Q.; Li, P.; Wang, J. Fabrication of Cation Exchange Membrane with Excellent Stabilities for Electrodialysis: A Study of Effective Sulfonation Degree in Ion Transport Mechanism. Journal of Membrane Science **2020**, 615, 118539. https://doi.org/10.1016/j.memsci.2020.118539.
(300) Zhao, Q.; Wei, Y.; Ni, C.; Wang, L.; Liu, B.; Liu, J.; Zhang, M.; Men, Y.; Sun, Z.; Xie, H.; Hu, W.; Lu, Y. Effect of Aminated Nanocrystal Cellulose on Proton Conductivity and Dimensional Stability of Proton Exchange Membranes. Applied Surface Science **2019**, 466, 691–702. https://doi.org/10.1016/j.apsusc.2018.10.063.
(301) Zhao, Y.; Feng, L.; Gao, J.; Zhao, Y.; Wang, S.; Ramani, V.; Zhang, Z.; Xie, X. Study on Tunable Crosslinking Anion Exchange Membranes Fabrication and Degradation Mechanism.

International Journal of Hydrogen Energy **2016**, 41 (36), 16264–16274. https://doi.org/10.1016/j.ijhydene.2016.05.251.

(302) Zhao, Y.; Yoshimura, K.; Mahmoud, A. M. A.; Yu, H.-C.; Okushima, S.; Hiroki, A.; Kishiyama, Y.; Shishitani, H.; Yamaguchi, S.; Tanaka, H.; Noda, Y.; Koizumi, S.; Radulescu, A.; Maekawa, Y. A Long Side Chain Imidazolium-Based Graft-Type Anion-Exchange Membrane: Novel Electrolyte and Alkaline-Durable Properties and Structural Elucidation Using SANS Contrast Variation. Soft Matter **2020**, 16 (35), 8128–8143. https://doi.org/10.1039/D0SM00947D.

(303) Zhong, S.; Cui, X.; Cai, H.; Fu, T.; Zhao, C.; Na, H. Crosslinked Sulfonated Poly(Ether Ether Ketone) Proton Exchange Membranes for Direct Methanol Fuel Cell Applications. Journal of Power Sources **2007**, 164 (1), 65–72. https://doi.org/10.1016/j.jpowsour.2006.10.077.

(304) Zhou, M.; Chen, X.; Pan, J.; Yang, S.; Han, B.; Xue, L.; Shen, J.; Gao, C.; Der Bruggen, B. V. A Novel UV-Crosslinked Sulphonated Polysulfone Cation Exchange Membrane with Improved Dimensional Stability for Electrodialysis. Desalination **2017**, 415, 29–39. https://doi.org/10.1016/j.desal.2017.03.037.

(305) Zhou, S.; Hai, S. D.; Kim, D. Cross-linked Poly(Arylene Ether Ketone) Proton Exchange Membranes with High Ion Exchange Capacity for Fuel Cells. Fuel Cells **2012**, 12 (4), 589–598. https://doi.org/10.1002/fuce.201100147.

(306) Zhu, H.; Sun, Z.; Cao, H.; Wang, B.; Zhao, J.; Pan, J.; Xu, G.; Jin, Z.; Yan, F. Highly Conductive and Dimensionally Stable Anion Exchange Membranes Based on Poly(Dimethoxybenzene- Co -Methyl 4-Formylbenzoate) Ionomers. Macromolecules **2021**, 54 (12), 5557–5566. https://doi.org/10.1021/acs.macromol.1c00704.

(307) Zhu, H.; Li, Y.; Chen, N.; Lu, C.; Long, C.; Li, Z.; Liu, Q. Controllable Physical-Crosslinking Poly(Arylene 6-Azaspiro[5.5] Undecanium) for Long-Lifetime Anion Exchange Membrane Applications. Journal of Membrane Science **2019**, 590, 117307. https://doi.org/10.1016/j.memsci.2019.117307.

(308) Zhu, J.; Liao, J.; Jin, W.; Luo, B.; Shen, P.; Sotto, A.; Shen, J.; Gao, C. Effect of Functionality of Cross-Linker on Sulphonated Polysulfone Cation Exchange Membranes for Electrodialysis. Reactive and Functional Polymers **2019**, 138, 104–113. https://doi.org/10.1016/j.reactfunctpolym.2019.02.006.

(309) Zhu, L.; Pan, J.; Christensen, C. M.; Lin, B.; Hickner, M. A. Functionalization of Poly(2,6-Dimethyl-1,4-Phenylene Oxide)s with Hindered Fluorene Side Chains for Anion Exchange Membranes. Macromolecules **2016**, 49 (9), 3300–3309. https://doi.org/10.1021/acs.macromol.6b00578.

(310) Zhu, L.; Pan, J.; Wang, Y.; Han, J.; Zhuang, L.; Hickner, M. A. Multication Side Chain Anion Exchange Membranes. Macromolecules **2016**, 49 (3), 815–824. https://doi.org/10.1021/acs.macromol.5b02671.

(311) Zhu, L.; Peng, X.; Shang, S.; Kwasny, M. T.; Zimudzi, T. J.; Yu, X.; Saikia, N.; Pan, J.; Liu, Z.; Tew, G. N.; Mustain, W. E.; Yandrasits, M.; Hickner, M. A. High Performance Anion Exchange Membrane Fuel Cells Enabled by Fluoropoly(Olefin) Membranes. Adv Funct Materials **2019**, 29 (26), 1902059. https://doi.org/10.1002/adfm.201902059.

(312) Zhu, L.; Yu, X.; Peng, X.; Zimudzi, T. J.; Saikia, N.; Kwasny, M. T.; Song, S.; Kushner, D. I.; Fu, Z.; Tew, G. N.; Mustain, W. E.; Yandrasits, M. A.; Hickner, M. A. Poly(Olefin)-Based Anion Exchange Membranes Prepared Using Ziegler–Natta Polymerization. Macromolecules **2019**, 52 (11), 4030–4041. https://doi.org/10.1021/acs.macromol.8b02756.

(313) Zhu, L.; Zimudzi, T. J.; Li, N.; Pan, J.; Lin, B.; Hickner, M. A. Crosslinking of Comb-Shaped Polymer Anion Exchange Membranes via Thiol–Ene Click Chemistry. Polym. Chem. **2016**, 7 (14), 2464–2475. https://doi.org/10.1039/C5PY01911G.
(314) Zhu, M.; Zhang, X.; Wang, Y.; Wu, Y.; Wang, H.; Zhang, M.; Chen, Q.; Shen, Z.; Li, N. Novel Anion Exchange Membranes Based on Quaternized Diblock Copolystyrene Containing a Fluorinated Hydrophobic Block. Journal of Membrane Science **2018**, 554, 264–273. https://doi.org/10.1016/j.memsci.2018.01.055.
(315) Zhu, T.; Xu, S.; Rahman, A.; Dogdibegovic, E.; Yang, P.; Pageni, P.; Kabir, M. P.; Zhou, X.; Tang, C. Cationic Metallo-Polyelectrolytes for Robust Alkaline Anion-Exchange Membranes. Angew Chem Int Ed **2018**, 57 (9), 2388–2392. https://doi.org/10.1002/anie.201712387.
(316) Zhuo, Y. Z.; Nan Lai, A.; Zhang, Q. G.; Zhu, A. M.; Ye, M. L.; Liu, Q. L. Highly Ionic-Conductive Crosslinked Cardo Poly(Arylene Ether Sulfone)s as Anion Exchange Membranes for Alkaline Fuel Cells. Journal of Membrane Science **2015**, 491, 138–148. https://doi.org/10.1016/j.memsci.2015.05.023.
(317) Jang, E.-S.; Kamcev, J.; Kobayashi, K.; Yan, N.; Sujanani, R.; Talley, S. J.; Moore, R. B.; Paul, D. R.; Freeman, B. D. Effect of Water Content on Sodium Chloride Sorption in Cross-Linked Cation Exchange Membranes. Macromolecules **2019**, 52 (6), 2569–2579. https://doi.org/10.1021/acs.macromol.8b02550.
(318) Chang, K.; Luo, H.; Bannon, S. M.; Lin, S. Y.; Agata, W. A. S.; Geise, G. M. Methoxy Groups Increase Water and Decrease Salt Permeability Properties of Sulfonated Polysulfone Desalination Membranes. Journal of Membrane Science **2021**, 630 (December 2020), 119298. https://doi.org/10.1016/j.memsci.2021.119298.
(319) Yan, N.; Sujanani, R.; Kamcev, J.; Galizia, M.; Jang, E.-S.; Paul, D. R.; Freeman, B. D. Influence of Fixed Charge Concentration and Water Uptake on Ion Sorption in AMPS/PEGDA Membranes. Journal of Membrane Science **2022**, 644, 120171. https://doi.org/10.1016/j.memsci.2021.120171.
(320) Yan, N.; Sujanani, R.; Kamcev, J.; Jang, E.-S.; Kobayashi, K.; Paul, D. R.; Freeman, B. D. Salt and Ion Transport in a Series of Crosslinked AMPS/PEGDA Hydrogel Membranes. Journal of Membrane Science **2022**, 653, 120549. https://doi.org/10.1016/j.memsci.2022.120549.
(321) McCleskey, R. B. Electrical Conductivity of Electrolytes Found In Natural Waters from (5 to 90) °C. J. Chem. Eng. Data **2011**, 56 (2), 317–327. https://doi.org/10.1021/je101012n.
(322) Ribeiro, A. C. F.; Barros, M. C. F.; Teles, A. S. N.; Valente, A. J. M.; Lobo, V. M. M.; Sobral, A. J. F. N.; Esteso, M. A. Diffusion Coefficients and Electrical Conductivities for Calcium Chloride Aqueous Solutions at 298.15K and 310.15K. Electrochim. Acta **2008**, 54 (2), 192–196. https://doi.org/10.1016/j.electacta.2008.08.011.
(323) Broadwater, T. L.; Evans, D. F. The Conductance of Divalent Ions in H2O at 10 and 25°C and in D2O. J. Solut. Chem. **1974**, 3 (10), 757–769. https://doi.org/10.1007/BF00955708.
(324) Dunsmore, H. S.; Jalota, S. K.; Paterson, R. Irreversible Thermodynamic Parameters for Isothermal Vectorial Transport Processes in Aqueous Caesium Chloride Solutions. J. Chem. Soc. A **1969**, 1061–1065. https://doi.org/10.1039/J19690001061.
(325) Swain, C. G.; Evans, D. F. Conductance of Ions in Light and Heavy Water at 25°. J. Am. Chem. Soc. **1966**, 88 (3), 383–390. https://doi.org/10.1021/ja00955a001.
(326) Miller, D. G. Application of Irreversible Thermodynamics to Electrolyte Solutions. I. Determination of Ionic Transport Coefficients Lij for Isothermal Vector Transport Processes

in Binary Electrolyte Systems. J. Phys. Chem. **1966**, 70 (8), 2639–2659. https://doi.org/10.1021/j100880a033.
(327) Campbell, A. N.; Bock, E. The Limiting Equivalent Conductances of Ammonium Chloride, Ammonium Bromide, and Ammonium Nitrate at 35.00° C. Can. J. Chem. **1958**, 36 (2), 330–338. https://doi.org/10.1139/v58-047.
(328) Foster, N. G.; Amis, E. S. The Equivalent Conductance of Electrolytes in Mixed Solvents. I. Potassium Chloride in the Water-Methanol System. Z. Phys. Chem. **1955**, 3 (5–6), 365–381. https://doi.org/10.1524/zpch.1955.3.5_6.365.
(329) Daggett, H. M.; Bair, E. J.; Kraus, C. A. Properties of Electrolytic Solutions. XLVII. Conductance of Some Quaternary Ammonium and Other Salts in Water at Low Concentration. J. Am. Chem. Soc. **1951**, 73 (2), 799–803. https://doi.org/10.1021/ja01146a090.
(330) McDowell, M. J.; Kraus, C. A. Properties of Electrolytic Solutions. XLIX. Conductance of Some Salts in Water at 25°. J. Am. Chem. Soc. **1951**, 73 (5), 2170–2173. https://doi.org/10.1021/ja01149a074.
(331) Jenkins, I. L.; Monk, C. B. The Conductances of Sodium, Potassium and Lanthanum Sulfates at 25°. J. Am. Chem. Soc. **1950**, 72 (6), 2695–2698. https://doi.org/10.1021/ja01162a096.
(332) Owen, B. B.; Zeldes, H. The Conductance of Potassium Chloride, Potassium Bromide and Potassium Iodide in Aqueous Solutions from 5 to 55°. J. Chem. Phys. **1950**, 18 (8), 1083–1085. https://doi.org/10.1063/1.1747865.
(333) Benson, G. C.; Gordon, A. R. The Conductance of Aqueous Solutions of Calcium Chloride at Temperatures from 15° to 45°C. J. Chem. Phys. **1945**, 13 (11), 470–472. https://doi.org/10.1063/1.1723980.
(334) Benson, G. C.; Gordon, A. R. A Reinvestigation of the Conductance of Aqueous Solutions of Potassium Chloride, Sodium Chloride, and Potassium Bromide at Temperatures from 15° to 45°C. J. Chem. Phys. **1945**, 13 (11), 473–474. https://doi.org/10.1063/1.1723981.
(335) Gunning, H. E.; Gordon, A. R. The Conductance of Aqueous Solutions of Potassium Bromide at Temperatures from 15° to 45°C, and the Limiting Mobility of Bromide Ion. J. Chem. Phys. **1943**, 11 (1), 18–20. https://doi.org/10.1063/1.1723775.
(336) Gunning, H. E.; Gordon, A. R. The Conductance and Ionic Mobilities for Aqueous Solutions of Potassium and Sodium Chloride at Temperatures from 15° to 45°C. J. Chem. Phys. **1942**, 10 (2), 126–131. https://doi.org/10.1063/1.1723667.
(337) Li, N. C. C.; Brüll, W. Conductivity Studies. IV. The Limiting Ionic Mobilities of Several Univalent Ions at Temperatures between 15 and 45°. J. Am. Chem. Soc. **1942**, 64 (7), 1635–1637. https://doi.org/10.1021/ja01259a045.
(338) Li, N. C. C.; Fang, H. Conductivity Studies. III. The Limiting Equivalent Conductances of Potassium Chloride in Water at Temperatures between 15 and 40°. J. Am. Chem. Soc. **1942**, 64 (7), 1544–1547. https://doi.org/10.1021/ja01259a016.
(339) Lange, J. Zur Leitfähigkeit starker Elektrolyte. Z. Phys. Chem. **1941**, 188A (1), 284–315. https://doi.org/10.1515/zpch-1941-18827.
(340) Sen-Gupta, N. C.; Mitra, S. K. Variation of the Absolute Rates of Migration and Transport Number of Electrolytic Ions with Dilution. J. Indian Chem. Soc. **1937**, 14, 645–652. https://doi.org/10.5281/zenodo.6640897.
(341) Jantsch, G.; Grubitsch, H.; Lischka, E. Über die elektrolytischen Leitfähigkeiten wässeriger Lösungen der Halogenide der seltenen Erden. Z. Elektrochem. Angew. Phys. Chem. **1937**, 43 (5), 293–296. https://doi.org/10.1002/bbpc.19370430509.

(342) Shedlovsky, T.; Brown, A. S. The Electrolytic Conductivity of Alkaline Earth Chlorides in Water at 25°. J. Am. Chem. Soc. **1934**, 56 (5), 1066–1071. https://doi.org/10.1021/ja01320a018.
(343) Clews, C. J. B. The Electrical Conductivity of Strong Electrolytes and Its Variation with Temperature. Proc. Phys. Soc. **1934**, 46 (6), 764–771. https://doi.org/10.1088/0959-5309/46/6/304.
(344) Jones, G.; Bickford, C. F. The Conductance of Aqueous Solutions as a Function of the Concentration. I. Potassium Bromide and Lanthanum Chloride. J. Am. Chem. Soc. **1934**, 56 (3), 602–611. https://doi.org/10.1021/ja01318a021.
(345) Scatchard, G.; Prentiss, S. S. The Freezing Points of Aqueous Solutions. IV. Potassium, Sodium and Lithium Chlorides and Bromides. J. Am. Chem. Soc. **1933**, 55 (11), 4355–4362. https://doi.org/10.1021/ja01338a003.
(346) Ekwall, P. Die Leitfähigkeit Alkylierter Ammoniumpikrate in Wässeriger Lösung Bei 0°, 25° Und 90°. III. Über Die Hydrolyse Der Untersuchten Salze. Z. Phys. Chem. **1933**, 163A (1), 331–337. https://doi.org/10.1515/zpch-1933-16337.
(347) Klemenc, A.; Hayek, E. Zur Kenntnis der Dissoziationskonstante der salpetrigen Säure. Montash. Chem. **1929**, 53–54 (1), 407–412. https://doi.org/10.1007/BF01521803.
(348) Lattey, R. T. XXIII. The Influence of the Solvent on the Mobility of Electrolytic Ions. Lond. Edinb. Phil. Mag. **1928**, 6 (35), 258–270. https://doi.org/10.1080/14786440808564600.
(349) Ferguson, A.; Vogel, I. XIX. The Calculation of the Equivalent Conductivity of Strong Electrolytes.—Part I. Aqueous Solutions. (Ii.) Application to Data at 0°, 18°, and 25° C. Lond. Edinb. Phil. Mag. **1927**, 4 (20), 233–242. https://doi.org/10.1080/14786440708564327.
(350) Ferguson, A.; Vogel, I. CV. The Calculation of the Equivalent Conductivity of Strong Electrolytes at Infinite Dilution. Part I.— Aqueous Solutions. Lond. Edinb. Phil. Mag. **1925**, 50 (299), 971–985. https://doi.org/10.1080/14786442508628541.
(351) Noyes, A. A.; Falk, K. G. The Properties of Salt Solutions in Relation to the Ionic Theory III. Electrical Conductance. J. Am. Chem. Soc. **1912**, 34 (4), 454–485. https://doi.org/10.1021/ja02205a013.
(352) Jones, H. C. The Electrical Conductivity, Dissociation, and Temperature Coefficients of Conductivity from Zero to Sixty-Five Degrees of Aqueous Solutions of a Number of Salts and Organic Acids; 170; Carnegie Institution of Washington: Washington, D.C., 1912. https://archive.org/details/carnegieinstitut170carn/mode/2up.
(353) Noyes, A. A.; Melcher, A. C.; Cooper, H. C.; Eastman, G. W. The Conductivity and Ionization of Salts, Acids, and Bases in Aqueous Solutions at High Temperatures. Z. Phys. Chem. **1910**, 70U (1), 335–377. https://doi.org/10.1515/zpch-1910-7027.
(354) Johnston, J. The Change of the Equivalent Conductance of Ions with the Temperature. J. Am. Chem. Soc. **1909**, 31 (9), 1010–1020. https://doi.org/10.1021/ja01939a003.
(355) Noyes, A. A.; Melcher, A. C.; Cooper, H. C.; Eastman, G. W.; Kato, Y. The Conductivity and Ionization of Salts, Acids, and Bases in Aqueous Solutions at High Temperatures. J. Am. Chem. Soc. **1908**, 30 (3), 335–353. https://doi.org/10.1021/ja01945a003.
(356) Lattey, R. T. LXXV. On the Dilution Law for Strong Electrolytes. Lond. Edinb. Phil. Mag. **1927**, 4 (23), 831–836. https://doi.org/10.1080/14786441008564386.
(357) Bockris, J. O.; Reddy, A. K. N. Modern Electrochemistry 1: Ionics, 1st ed.; Kluwer Academic Publishers: New York, 1998. https://doi.org/10.1108/sr.1999.08719baf.011.
(358) Robinson, R. A.; Stokes, R. H. Electrolyte Solutions, 2nd, rev ed.; Dover Publications, Inc.: Mineola, 1965.

(359) Harned, H. S.; Owen, B. B. The Physical Chemistry of Electrolytic Solutions 3rd Ed., Chapter 4. In The Physical Chemistry of Electrolytic Solutions 3rd Ed.; Reinhold Pub. Corp.: New York, 1958; pp 233–234.
(360) Allgood, R. W.; Le Roy, D. J.; Gordon, A. R. The Variation of the Transference Numbers of Potassium Chloride in Aqueous Solution with Temperature. The Journal of Chemical Physics **2004**, 8 (5), 418–422. https://doi.org/10.1063/1.1750676.
(361) Ribeiro, A. C. F.; Valente, A. J. M.; Sobral, A. J. F. N.; Lobo, V. M. M.; Burrows, H. D.; Esteso, M. A. Diffusion Coefficients of Aluminium Chloride in Aqueous Solutions at 298.15, 303.15 and 315.15K. Electrochim. Acta **2007**, 52 (23), 6450–6455. https://doi.org/10.1016/j.electacta.2007.04.041.
(362) Marcus, Y. Ion Properties, 1st ed.; CRC Press: Boca Raton, 1997.
(363) Marcus, Y. Ions in Solution and Their Solvation; John Wiley & Sons, Inc: Hoboken, NJ, 2015. https://doi.org/10.1002/9781118892336.
(364) Gregory, K. P.; Elliott, G. R.; Robertson, H.; Kumar, A.; Wanless, E. J.; Webber, G. B.; Craig, V. S. J.; Andersson, G. G.; Page, A. J. Understanding Specific Ion Effects and the Hofmeister Series. Phys. Chem. Chem. Phys. **2022**, 24 (21), 12682–12718. https://doi.org/10.1039/D2CP00847E.
(365) Marcus, Y. ViscosityB-Coefficients, Structural Entropies and Heat Capacities, and the Effects of Ions on the Structure of Water. J Solution Chem **1994**, 23 (7), 831–848. https://doi.org/10.1007/BF00972677.
(366) Nightingale, E. R. Phenomenological Theory of Ion Solvation. Effective Radii of Hydrated Ions. J. Phys. Chem. **1959**, 63 (9), 1381–1387. https://doi.org/10.1021/j150579a011.
(367) Glikberg, S.; Marcus, Y. Relation of the Gibbs Free Energy of Transfer of Ions from Water to Polar Solvents to the Properties of the Solvents and the Ions. J Solution Chem **1983**, 12 (4), 255–270. https://doi.org/10.1007/BF00646200.
(368) Gregory, K. P.; Wanless, E. J.; Webber, G. B.; Craig, V. S. J.; Page, A. J. The Electrostatic Origins of Specific Ion Effects: Quantifying the Hofmeister Series for Anions. Chem. Sci. **2021**, 12 (45), 15007–15015. https://doi.org/10.1039/D1SC03568A.
(369) Malinowski, E. R. Factor Analysis in Chemistry, 3rd ed.; Wiley, 2002.
(370) Daly, F. P.; Brown, C. W.; Kester, D. R. Sodium and Magnesium Sulfate Ion Pairing. Evidence from Raman Spectroscopy. J. Phys. Chem. **1972**, 76 (24), 3664–3668. https://doi.org/10.1021/j100668a027.
(371) Buchner, R.; Chen, T.; Hefter, G. Complexity in "Simple" Electrolyte Solutions: Ion Pairing in MgSO4(Aq). J. Phys. Chem. B **2004**, 108 (7), 2365–2375. https://doi.org/10.1021/jp034870p.
(372) Hefter, G. When Spectroscopy Fails: The Measurement of Ion Pairing. Pure Appl. Chem. **2006**, 78 (8), 1571–1586. https://doi.org/10.1351/pac200678081571.
(373) Alcorn, C. D.; Cox, J. S.; Applegarth, L. M. S. G. A.; Tremaine, P. R. Investigation of Uranyl Sulfate Complexation under Hydrothermal Conditions by Quantitative Raman Spectroscopy and Density Functional Theory. J. Phys. Chem. B **2019**, 123 (34), 7385–7409. https://doi.org/10.1021/acs.jpcb.9b01544.
(374) Silva, N. J.; Tunega, D.; Korzeniewski, C.; Lischka, H.; Aquino, A. J. A. Microhydration of Polymer Electrolyte Membranes: A Comparison of Hydrogen-Bonding Networks and Spectral Properties of Nafion and Bis[(Perfluoroalkyl)Sulfonyl] Imide. The Journal of Physical Chemistry B **2019**, 123 (46), 9899–9911. https://doi.org/10.1021/acs.jpcb.9b07815.

(375) Kujawski, W.; Nguyen, Q. T.; Neel, J. Infrared Investigations of Sulfonated Ionomer Membranes. I. Water–Alcohol Compositions and Counterions Effects. Journal of Applied Polymer Science **1992**, 44 (6), 951–958. https://doi.org/10.1002/app.1992.070440603.
(376) Byun, C. K.; Sharif, I.; DesMarteau, D. D.; Creager, S. E.; Korzeniewski, C. Infrared Spectroscopy of Bis[(Perfluoroalkyl)Sulfonyl] Imide Ionomer Membrane Materials. The Journal of Physical Chemistry B **2009**, 113 (18), 6299–6304. https://doi.org/10.1021/jp900164x.
(377) Socrates, G. Infrared and Raman Characteristic Group Frequencies: Tables and Charts, 3rd ed.; John Wiley & Sons, Inc: Chinester, 2001.
(378) NIST. Tetramethylammonium Chloride. https://webbook.nist.gov/cgi/inchi/InChI%3D1S/C4H12N.ClH/c1-5(2%2C3)4%3B/h1-4H3%3B1H/q%2B1%3B/p-1 (accessed 2024-08-05).
(379) Sujanani, R.; Reimund, K. K.; Gleason, K. L.; Freeman, B. D. Hydraulic Permeation-Induced Water Concentration Gradients in Ion Exchange Membranes. Journal of Membrane Science **2024**, 122858. https://doi.org/10.1016/j.memsci.2024.122858.
(380) Wijmans, J. G.; Baker, R. W. The Solution-Diffusion Model: A Review. Journal of Membrane Science **1995**, 107 (1–2), 1–21. https://doi.org/10.1016/0376-7388(95)00102-I.
(381) Espinoza, C.; Kitto, D.; Kamcev, J. Ion Transport Properties of Commercial Ion-Exchange Membranes Contacted by Highly Concentrated Salt Solutions. ACS Applied Polymer Materials **2023**. https://doi.org/10.1021/acsapm.3c02102.
(382) Mackie, J. S.; Meares, P. The Sorption of Electrolytes by a Cation-Exchange Resin Membrane. Proceedings of the Royal Society A **1955**, 232 (1191), 485–498. https://doi.org/10.1098/rspa.1955.0233.
(383) Pitzer, K. S. A Thermodynamic Model for Aqueous Solutions of Liquid-Like Density. In Annual Meeting of the Geological Society of America; 1987.
(384) Simoes, M. C.; Hughes, K. J.; Ingham, D. B.; Ma, L.; Pourkashanian, M. Temperature Dependence of the Parameters in the Pitzer Equations. J. Chem. Eng. Data **2017**, 62 (7), 2000–2013. https://doi.org/10.1021/acs.jced.7b00022.
(385) Kitto, D.; Kamcev, J. Manning Condensation in Ion Exchange Membranes: A Review on Ion Partitioning and Diffusion Models. Journal of Polymer Science **2022**, 60 (21), 2929–2973. https://doi.org/10.1002/pol.20210810.
(386) Kamcev, J.; Galizia, M.; Benedetti, F. M.; Jang, E.-S.; Paul, D. R.; Freeman, B. D.; Manning, G. S. Partitioning of Mobile Ions between Ion Exchange Polymers and Aqueous Salt Solutions: Importance of Counter-Ion Condensation. Physical Chemistry Chemical Physics **2016**, 18 (8), 6021–6031. https://doi.org/10.1039/C5CP06747B.
(387) Crank, J.; Park, G. S. Diffusion in Polymers, 1st ed.; Academic Press Inc.: New York, 1968.
(388) Masaro, L.; Zhu, X. X. Physical Models of Diffusion for Polymer Solutions, Gels and Solids. Progress in Polymer Science **1999**, 24 (5), 731–775. https://doi.org/10.1016/S0079-6700(99)00016-7.
(389) Mackie, J. S.; Meares, P. The Diffusion of Electrolytes in a Cation-Exchange Resin Membrane. Proceedings of the Royal Society of London, Series A **1955**, 232 (1191), 498–509. https://doi.org/10.1098/rspa.1955.0234.
(390) Yan, N.; Sujanani, R.; Kamcev, J.; Jang, E.-S.; Kobayashi, K.; Paul, D. R.; Freeman, B. D. Salt and Ion Transport in a Series of Crosslinked AMPS/PEGDA Hydrogel Membranes.

Journal of Membrane Science **2022**, 653, 120549. https://doi.org/10.1016/j.memsci.2022.120549.
(391) Manning, G. S. Limiting Laws and Counterion Condensation in Polyelectrolyte Solutions I. Colligative Properties. The Journal of Chemical Physics **1969**, 51 (3), 924–933. https://doi.org/10.1063/1.1672157.
(392) Kamcev, J.; Paul, D. R.; Freeman, B. D. Ion Activity Coefficients in Ion Exchange Polymers: Applicability of Manning's Counterion Condensation Theory. Macromolecules **2015**, 48 (21), 8011–8024. https://doi.org/10.1021/acs.macromol.5b01654.
(393) Chang, K.; Geise, G. M. Dielectric Permittivity Properties of Hydrated Polymers: Measurement and Connection to Ion Transport Properties. Industrial & Engineering Chemistry Research **2020**, 59 (12), 5205–5217. https://doi.org/10.1021/acs.iecr.9b03950.
(394) Manning, G. S. Counterion Binding in Polyelectrolyte Theory. Accounts of Chemical Research **1979**, 12 (12), 443–449. https://doi.org/10.1021/ar50144a004.
(395) Manning, G. S. Limiting Laws and Counterion Condensation in Polyelectrolyte Solutions II. Self-Diffusion of the Small Ions. The Journal of Chemical Physics **1969**, 51 (3), 934–938. https://doi.org/10.1063/1.1672158.
(396) Manning, G. S. Nonconvective Ionic Flow in Fixed-Charge Systems. The Journal of Chemical Physics **1967**, 46 (6), 2324. https://doi.org/10.1063/1.1841040.
(397) Kamcev, J.; Paul, D. R.; Manning, G. S.; Freeman, B. D. Predicting Salt Permeability Coefficients in Highly Swollen, Highly Charged Ion Exchange Membranes. ACS Applied Materials & Interfaces **2017**, 9 (4), 4044–4056. https://doi.org/10.1021/acsami.6b14902.
(398) Manning, G. S. On the Apparent Saturation of the Dipole Induced in a Rodlike Polyion at High Electric Fields. The Journal of Physical Chemistry B **2009**, 113, 2231–2233. https://doi.org/10.1021/jp8108896.
(399) Manning, G. S. A Condensed Counterion Theory for Polarization of Polyelectrolyte Solutions in High Fields. The Journal of Chemical Physics **1993**, 99 (1), 477–486. https://doi.org/10.1063/1.465772.
(400) Manning, G. S. A Counterion Condensation Theory for the Relaxation, Rise, and Frequency Dependence of the Parallel Polarization of Rodlike Polyelectrolytes. The European Physical Journal E **2011**, 34, 39. https://doi.org/10.1140/epje/i2011-11039-2.
(401) Robeson, L. M. Polymer Blends in Membrane Transport Processes. Ind. Eng. Chem. Res. **2010**, 49 (23), 11859–11865. https://doi.org/10.1021/ie100153q.
(402) Kolařík, J. Simultaneous Prediction of the Modulus, Tensile Strength and Gas Permeability of Binary Polymer Blends. European Polymer Journal **1998**, 34 (5–6), 585–590. https://doi.org/10.1016/S0014-3057(97)00176-6.
(403) Kolařík, J. A Model for the Yield Strength of Binary Blends of Thermoplastics. Polymer **1994**, 35 (17), 3631–3637. https://doi.org/10.1016/0032-3861(94)90539-8.
(404) De Gennes, P. G. On a Relation between Percolation Theory and the Elasticity of Gels. J. Phyique Lett. **1976**, 37 (1), 1–2. https://doi.org/10.1051/jphyslet:019760037010100.
(405) Last, B. J.; Thouless, D. J. Percolation Theory and Electrical Conductivity. Phys. Rev. Lett. **1971**, 27 (25), 1719–1721. https://doi.org/10.1103/PhysRevLett.27.1719.
(406) Utracki, L. A. On the Viscosity-Concentration Dependence of Immiscible Polymer Blends. Journal of Rheology **1991**, 35, 1615–1637. https://doi.org/10.1122/1.550248.
(407) Chapoy, L. L. The Applicability of a Percolation Model to Photoconductivity in Guest–Host Thermotropic Nematic Liquid Crystal Systems. The Journal of Chemical Physics **1986**, 84 (3), 1530–1532. https://doi.org/10.1063/1.450498.

(408) Galizia, M.; Bendetti, F. M.; Paul, D. R.; Freeman, B. D. Monovalent and Divalent Ion Sorption in a Cation Exchange Membrane Based on Cross-Linked Poly (p-Styrene Sulfonate-Co-Divinylbenzene). Journal of Membrane Science **2017**, 535, 132–142. https://doi.org/10.1016/j.memsci.2017.04.007.
(409) Sata, T. Ion Exchange Membranes; Royal Society of Chemistry: Cambridge, 2004.
(410) Luo, T.; Abdu, S.; Wessling, M. Selectivity of Ion Exchange Membranes: A Review. Journal of Membrane Science **2018**, 555, 429–454. https://doi.org/10.1016/j.memsci.2018.03.051.
(411) Shi, L.; Rossi, R.; Son, M.; Hall, D. M.; Hickner, M. A.; Gorski, C. A.; Logan, B. E. Using Reverse Osmosis Membranes to Control Ion Transport during Water Electrolysis. Energy Environ. Sci. **2020**, 13 (9), 3138–3148. https://doi.org/10.1039/D0EE02173C.
(412) Cseri, L.; Baugh, J.; Alabi, A.; AlHajaj, A.; Zou, L.; Dryfe, R. A. W.; Budd, P. M.; Szekely, G. Graphene Oxide–Polybenzimidazolium Nanocomposite Anion Exchange Membranes for Electrodialysis. J. Mater. Chem. A **2018**, 6 (48), 24728–24739. https://doi.org/10.1039/C8TA09160A.
(413) Cho, D. H.; Lee, K. H.; Kim, Y. M.; Park, S. H.; Lee, W. H.; Lee, S. M.; Lee, Y. M. Effect of Cationic Groups in Poly(Arylene Ether Sulfone) Membranes on Reverse Electrodialysis Performance. Chem. Commun. **2017**, 53 (15), 2323–2326. https://doi.org/10.1039/C6CC08440K.
(414) Lee, K. H.; Cho, D. H.; Kim, Y. M.; Moon, S. J.; Kim, J. F.; Lee, Y. M. Isomeric Influences of Naphthalene Based Sulfonated Poly(Arylene Ether Sulfone) Membranes for Energy Generation Using Reverse Electrodialysis and Polymer Electrolyte Membrane Fuel Cell. Journal of Membrane Science **2017**, 535, 35–44. https://doi.org/10.1016/j.memsci.2017.04.020.
(415) Fan, H.; Huang, Y.; Yip, N. Y. Advancing the Conductivity-Permselectivity Tradeoff of Electrodialysis Ion-Exchange Membranes with Sulfonated CNT Nanocomposites. Journal of Membrane Science **2020**, 610, 118259. https://doi.org/10.1016/j.memsci.2020.118259.
(416) Geise, G. M.; Hickner, M. A.; Logan, B. E. Ionic Resistance and Permselectivity Tradeoffs in Anion Exchange Membranes. ACS Applied Materials & Interfaces **2013**, 5 (20), 10294–10301. https://doi.org/10.1021/am403207w.
(417) Robeson, L. M. Correlation of Separation Factor versus Permeability for Polymeric Membranes. Journal of Membrane Science **1991**, 62 (2), 165–185. https://doi.org/10.1016/0376-7388(91)80060-J.
(418) Park, H. B.; Kamcev, J.; Robeson, L. M.; Elimelech, M.; Freeman, B. D. Maximizing the Right Stuff: The Trade-off between Membrane Permeability and Selectivity. Science **2017**, 356 (6343), 1138–1148. https://doi.org/10.1126/science.aab0530.
(419) Kamcev, J. Reformulating the Permselectivity-conductivity Tradeoff Relation in Ion-exchange Membranes. Journal of Polymer Science **2021**, 59 (21), 2510–2520. https://doi.org/10.1002/pol.20210304.
(420) Kingsbury, R. S.; Zhu, S.; Flotron, S.; Coronell, O. Microstructure Determines Water and Salt Permeation in Commercial Ion-Exchange Membranes. ACS Appl. Mater. Interfaces **2018**, 10 (46), 39745–39756. https://doi.org/10.1021/acsami.8b14494.
(421) Kitto, D.; Kamcev, J. The Need for Ion-Exchange Membranes with High Charge Densities. Journal of Membrane Science **2023**, 677, 121608. https://doi.org/10.1016/j.memsci.2023.121608.

(422) Espinoza, C.; Kitto, D.; Kamcev, J. Ion Transport Properties of Commercial Ion-Exchange Membranes Contacted by Highly Concentrated Salt Solutions. ACS Applied Polymer Materials **2023**, 5 (12), 10324–10333. https://doi.org/10.1021/acsapm.3c02102.
(423) Kusoglu, A.; Weber, A. Z. New Insights into Perfluorinated Sulfonic-Acid Ionomers. Chemical Reviews **2017**, 117 (3), 987–1104. https://doi.org/10.1021/acs.chemrev.6b00159.
(424) Kamcev, J.; Paul, D. R.; Freeman, B. D. Equilibrium Ion Partitioning between Aqueous Salt Solutions and Inhomogeneous Ion Exchange Membranes. Desalination **2018**, 446, 31–41. https://doi.org/10.1016/j.desal.2018.08.018.
(425) GLUECKAUF, E.; WATTS, R. E. Non-Uniformity of Cross-Linking in Ion-Exchange Polymers. Nature **1961**, 191 (4791), 904–905. https://doi.org/10.1038/191904a0.
(426) Kitto, D.; Kamcev, J. Manning Condensation in Ion Exchange Membranes: A Review on Ion Partitioning and Diffusion Models. Journal of Polymer Science **2022**, 60 (21), 2929–2973. https://doi.org/10.1002/pol.20210810.
(427) Geise, G. M.; Paul, D. R.; Freeman, B. D. Fundamental Water and Salt Transport Properties of Polymeric Materials. Progress in Polymer Science **2014**, 39 (1), 1–42. https://doi.org/10.1016/j.progpolymsci.2013.07.001.
(428) Kamcev, J.; Paul, D. R.; Manning, G. S.; Freeman, B. D. Ion Diffusion Coefficients in Ion Exchange Membranes: Significance of Counterion Condensation. Macromolecules **2018**, 51 (15), 5519–5529. https://doi.org/10.1021/acs.macromol.8b00645.
(429) Aryal, D.; Ganesan, V. Reversal of Salt Concentration Dependencies of Salt and Water Diffusivities in Polymer Electrolyte Membranes. ACS Macro Letters **2018**, 7 (6), 739–744. https://doi.org/10.1021/acsmacrolett.8b00333.
(430) Liu, H.; She, Q. Influence of Membrane Structure-Dependent Water Transport on Conductivity-Permselectivity Trade-off and Salt/Water Selectivity in Electrodialysis: Implications for Osmotic Electrodialysis Using Porous Ion Exchange Membranes. Journal of Membrane Science **2022**, 650, 120398. https://doi.org/10.1016/j.memsci.2022.120398.
(431) Huang, T.; Zhang, J.; Pei, Y.; Liu, X.; Xue, J.; Jiang, H.; Qiu, X.; Yin, Y.; Wu, H.; Jiang, Z.; Guiver, M. D. Mechanically Robust Microporous Anion Exchange Membranes with Efficient Anion Conduction for Fuel Cells. Chemical Engineering Journal **2021**, 418, 129311. https://doi.org/10.1016/j.cej.2021.129311.
(432) Huang, T.; Qiu, X.; Zhang, J.; Li, X.; Pei, Y.; Jiang, H.; Yue, R.; Yin, Y.; Jiang, Z.; Zhang, X.; Guiver, M. D. Hydrogen Crossover through Microporous Anion Exchange Membranes for Fuel Cells. Journal of Power Sources **2022**, 527, 231143. https://doi.org/10.1016/j.jpowsour.2022.231143.
(433) Yan, N.; Sujanani, R.; Kamcev, J.; Galizia, M.; Jang, E.-S.; Paul, D. R.; Freeman, B. D. Influence of Fixed Charge Concentration and Water Uptake on Ion Sorption in AMPS/PEGDA Membranes. Journal of Membrane Science **2022**, 644, 120171. https://doi.org/10.1016/j.memsci.2021.120171.
(434) Russell, S. T.; Pereira, R.; Vardner, J. T.; Jones, G. N.; Dimarco, C.; West, A. C.; Kumar, S. K. Hydration Effects on the Permselectivity-Conductivity Trade-Off in Polymer Electrolytes. Macromolecules **2020**, 53 (3), 1014–1023. https://doi.org/10.1021/acs.macromol.9b02291.
(435) Yang, Y.; Peltier, C. R.; Zeng, R.; Schimmenti, R.; Li, Q.; Huang, X.; Yan, Z.; Potsi, G.; Selhorst, R.; Lu, X.; Xu, W.; Tader, M.; Soudackov, A. V.; Zhang, H.; Krumov, M.; Murray, E.; Xu, P.; Hitt, J.; Xu, L.; Ko, H.-Y.; Ernst, B. G.; Bundschu, C.; Luo, A.; Markovich, D.; Hu, M.; He, C.; Wang, H.; Fang, J.; DiStasio, R. A.; Kourkoutis, L. F.; Singer, A.; Noonan,

K. J. T.; Xiao, L.; Zhuang, L.; Pivovar, B. S.; Zelenay, P.; Herrero, E.; Feliu, J. M.; Suntivich, J.; Giannelis, E. P.; Hammes-Schiffer, S.; Arias, T.; Mavrikakis, M.; Mallouk, T. E.; Brock, J. D.; Muller, D. A.; DiSalvo, F. J.; Coates, G. W.; Abruña, H. D. Electrocatalysis in Alkaline Media and Alkaline Membrane-Based Energy Technologies. Chem. Rev. **2022**, 122 (6), 6117–6321. https://doi.org/10.1021/acs.chemrev.1c00331.

(436) Keller, J. U.; Rave, H.; Staudt, R. Measurement of Gas Absorption in a Swelling Polymeric Material by a Combined Gravimetric-Dynamic Method. Macromolecular Chemistry and Physics **1999**, 200 (10), 2269–2275. https://doi.org/10.1002/(SICI)1521-3935(19991001)200:10<2269::AID-MACP2269>3.0.CO;2-7.

(437) Kim, Y. S. Polymer Electrolytes with High Ionic Concentration for Fuel Cells and Electrolyzers. ACS Appl. Polym. Mater. **2021**, 3 (3), 1250–1270. https://doi.org/10.1021/acsapm.0c01405.

(438) Carter, B. M.; Keller, L.; Wessling, M.; Miller, D. J. Preparation and Characterization of Crosslinked Poly(Vinylimidazolium) Anion Exchange Membranes for Artificial Photosynthesis. J. Mater. Chem. A **2019**, 7 (41), 23818–23829. https://doi.org/10.1039/C9TA00498J.

(439) Ge, Q.; Liang, X.; Ding, L.; Hou, J.; Miao, J.; Wu, B.; Yang, Z.; Xu, T. Guiding the Self-Assembly of Hyperbranched Anion Exchange Membranes Utilized in Alkaline Fuel Cells. Journal of Membrane Science **2019**, 573, 595–601. https://doi.org/10.1016/j.memsci.2018.12.049.

(440) Zhu, M.; Zhang, X.; Wang, Y.; Wu, Y.; Wang, H.; Zhang, M.; Chen, Q.; Shen, Z.; Li, N. Novel Anion Exchange Membranes Based on Quaternized Diblock Copolystyrene Containing a Fluorinated Hydrophobic Block. Journal of Membrane Science **2018**, 554, 264–273. https://doi.org/10.1016/j.memsci.2018.01.055.

(441) Jin, K.; Yue, B.; Yan, L.; Qiao, R.; Zhao, H.; Zhang, J. Synthesis and Characterization of Poly(5'-Hexyloxy-1',4-Biphenyl)-b-Poly(2',4'-Bispropoxysulfonate-1',4-Biphenyl) with High Ion Exchange Capacity for Proton Exchange Membrane Fuel Cell Applications. Chemistry – An Asian Journal **2022**, 17 (9), e202200109. https://doi.org/10.1002/asia.202200109.

(442) Ramos-Garcés, M. V.; Li, K.; Lei, Q.; Bhattacharya, D.; Kole, S.; Zhang, Q.; Strzalka, J.; Angelopoulou, P. P.; Sakellariou, G.; Kumar, R.; Arges, C. G. Understanding the Ionic Activity and Conductivity Value Differences between Random Copolymer Electrolytes and Block Copolymer Electrolytes of the Same Chemistry. RSC Advances **2021**, 11 (25), 15078–15084. https://doi.org/10.1039/D1RA02519H.

(443) Mandal, M.; Huang, G.; Hassan, N. U.; Mustain, W. E.; Kohl, P. A. Poly(Norbornene) Anion Conductive Membranes: Homopolymer, Block Copolymer and Random Copolymer Properties and Performance. J. Mater. Chem. A **2020**, 8 (34), 17568–17578. https://doi.org/10.1039/D0TA04756B.

(444) Kingsbury, R. S.; Bruning, K.; Zhu, S.; Flotron, S.; Miller, C. T.; Coronell, O. Influence of Water Uptake, Charge, Manning Parameter, and Contact Angle on Water and Salt Transport in Commercial Ion Exchange Membranes. Ind. Eng. Chem. Res. **2019**, 58 (40), 18663–18674. https://doi.org/10.1021/acs.iecr.9b04113.

(445) Ghorai, A.; Sahoo, A.; Baitalik, S.; Banerjee, S. Multifunctional Sulfonated Polytriazoles: Proton-Exchange Membrane Properties, Molecular Logic Gates, and Modeling of Stimuli-Responsive Behaviors. ACS Appl. Polym. Mater. **2022**, 4 (8), 5583–5595. https://doi.org/10.1021/acsapm.2c00629.

(446) Du, X.; Wang, Z.; Liu, W.; Xu, J.; Chen, Z.; Wang, C. Imidazolium-Functionalized Poly (Arylene Ether Ketone) Cross-Linked Anion Exchange Membranes. Journal of Membrane Science **2018**, 566, 205–212. https://doi.org/10.1016/j.memsci.2018.09.020.
(447) Kreuer, K.-D.; Münchinger, A. Fast and Selective Ionic Transport: From Ion-Conducting Channels to Ion Exchange Membranes for Flow Batteries. Annual Review of Materials Research **2021**, 51 (1), 21–46. https://doi.org/10.1146/annurev-matsci-080619-010139.
(448) Manning, G. S. Limiting Laws and Counterion Condensation in Polyelectrolyte Solutions I. Colligative Properties. The Journal of Chemical Physics **1969**, 51 (3), 924–933. https://doi.org/10.1063/1.1672157.
(449) Lei, Q.; Li, K.; Bhattacharya, D.; Xiao, J.; Kole, S.; Zhang, Q.; Strzalka, J.; Lawrence, J.; Kumar, R.; Arges, C. G. Counterion Condensation or Lack of Solvation? Understanding the Activity of Ions in Thin Film Block Copolymer Electrolytes. Journal of Materials Chemistry A **2020**, 8 (31), 15962–15975. https://doi.org/10.1039/D0TA04266H.
(450) Wohlfarth, A.; Smiatek, J.; Kreuer, K.-D.; Takamuku, S.; Jannasch, P.; Maier, J. Proton Dissociation of Sulfonated Polysulfones: Influence of Molecular Structure and Conformation. Macromolecules **2015**, 48 (4), 1134–1143. https://doi.org/10.1021/ma502550f.
(451) Park, H. B.; Kamcev, J.; Robeson, L. M.; Elimelech, M.; Freeman, B. D. Maximizing the Right Stuff: The Trade-off between Membrane Permeability and Selectivity. Science **2017**, 356 (6343), 1138–1148. https://doi.org/10.1126/science.aab0530.
(452) Freeman, B. D. Basis of Permeability/Selectivity Tradeoff Relations in Polymeric Gas Separation Membranes. Macromolecules **1999**, 32 (2), 375–380. https://doi.org/10.1021/ma9814548.
(453) Fan, H.; Huang, Y.; Yip, N. Y. Advancing the Conductivity-Permselectivity Tradeoff of Electrodialysis Ion-Exchange Membranes with Sulfonated CNT Nanocomposites. Journal of Membrane Science **2020**, 610 (March). https://doi.org/10.1016/j.memsci.2020.118259.
(454) Cho, D. H.; Lee, K. H.; Kim, Y. M.; Park, S. H.; Lee, W. H.; Lee, S. M.; Lee, Y. M. Effect of Cationic Groups in Poly(Arylene Ether Sulfone) Membranes on Reverse Electrodialysis Performance. Chem. Commun. **2017**, 53 (15), 2323–2326. https://doi.org/10.1039/C6CC08440K.
(455) Fan, H.; Yip, N. Y. Elucidating Conductivity-Permselectivity Tradeoffs in Electrodialysis and Reverse Electrodialysis by Structure-Property Analysis of Ion-Exchange Membranes. Journal of Membrane Science **2019**, 573, 668–681. https://doi.org/10.1016/j.memsci.2018.11.045.
(456) Cseri, L.; Baugh, J.; Alabi, A.; AlHajaj, A.; Zou, L.; Dryfe, R. A. W.; Budd, P. M.; Szekely, G. Graphene Oxide–Polybenzimidazolium Nanocomposite Anion Exchange Membranes for Electrodialysis. J. Mater. Chem. A **2018**, 6 (48), 24728–24739. https://doi.org/10.1039/C8TA09160A.
(457) Russell, S. T.; Pereira, R.; Vardner, J. T.; Jones, G. N.; Dimarco, C.; West, A. C.; Kumar, S. K. Hydration Effects on the Permselectivity-Conductivity Trade-Off in Polymer Electrolytes. Macromolecules **2020**, 53 (3), 1014–1023. https://doi.org/10.1021/acs.macromol.9b02291.
(458) Huang, Y.; Fan, H.; Yip, N. Y. Influence of Electrolyte on Concentration-Induced Conductivity-Permselectivity Tradeoff of Ion-Exchange Membranes. Journal of Membrane Science **2023**, 668, 121184. https://doi.org/10.1016/j.memsci.2022.121184.
(459) Lee, K. H.; Cho, D. H.; Kim, Y. M.; Moon, S. J.; Kim, J. F.; Lee, Y. M. Isomeric Influences of Naphthalene Based Sulfonated Poly(Arylene Ether Sulfone) Membranes for Energy

Generation Using Reverse Electrodialysis and Polymer Electrolyte Membrane Fuel Cell. Journal of Membrane Science **2017**, 535, 35–44. https://doi.org/10.1016/j.memsci.2017.04.020.
(460) Stenina, I.; Golubenko, D.; Nikonenko, V.; Yaroslavtsev, A. Selectivity of Transport Processes in Ion-Exchange Membranes: Relationship with the Structure and Methods for Its Improvement. IJMS **2020**, 21 (15), 5517. https://doi.org/10.3390/ijms21155517.
(461) Zhang, H.; Geise, G. M. Modeling the Water Permeability and Water/Salt Selectivity Tradeoff in Polymer Membranes. Journal of Membrane Science **2016**, 520, 790–800. https://doi.org/10.1016/j.memsci.2016.08.035.
(462) Jiang, S.; Ladewig, B. P. High Ion-Exchange Capacity Semihomogeneous Cation Exchange Membranes Prepared via a Novel Polymerization and Sulfonation Approach in Porous Polypropylene. ACS Appl. Mater. Interfaces **2017**, 9 (44), 38612–38620. https://doi.org/10.1021/acsami.7b13076.
(463) Kim, Y. S. Polymer Electrolytes with High Ionic Concentration for Fuel Cells and Electrolyzers. ACS Appl. Polym. Mater. **2021**, 3 (3), 1250–1270. https://doi.org/10.1021/acsapm.0c01405.
(464) McCutcheon, J. R.; Mauter, M. S. Fixing the Desalination Membrane Pipeline. Science **2023**, 380 (6642), 242–244. https://doi.org/10.1126/science.ade5313.
(465) Tanaka, Y. Ion Exchange Membranes: Fundamentals and Applications, 2nd edition.; Elsevier: Amsterdam, 2015.
(466) Hanwell, M. D.; Curtis, D. E.; Lonie, D. C.; Vandermeersh, T.; Zurek, E.; Hutchinson, G. R. Avogadro: An Advanced Semantic Chemical Editor, Visualization, and Analysis Platform. Journal of Cheminformatics **2012**, 4, 17.
(467) Marcus, Y. Ions in Solution and Their Solvation; John Wiley & Sons, Inc: Hoboken, NJ, 2015. https://doi.org/10.1002/9781118892336.
(468) Yang, Y.; Li, P.; Zheng, X.; Sun, W.; Dou, S. X.; Ma, T.; Pan, H. Anion-Exchange Membrane Water Electrolyzers and Fuel Cells. Chem. Soc. Rev. **2022**, 51 (23), 9620–9693. https://doi.org/10.1039/D2CS00038E.
(469) Hassan, N. U.; Zheng, Y.; Kohl, P. A.; Mustain, W. E. KOH vs Deionized Water Operation in Anion Exchange Membrane Electrolyzers. J. Electrochem. Soc. **2022**, 169 (4), 044526. https://doi.org/10.1149/1945-7111/ac5f1d.
(470) Shah, K. M.; Billinge, I. H.; Chen, X.; Fan, H.; Huang, Y.; Winton, R. K.; Yip, N. Y. Drivers, Challenges, and Emerging Technologies for Desalination of High-Salinity Brines: A Critical Review. Desalination **2022**, 538, 115827. https://doi.org/10.1016/j.desal.2022.115827.
(471) Freger, V. Dielectric Exclusion, an Éminence Grise. Advances in Colloid and Interface Science **2023**, 319, 102972. https://doi.org/10.1016/j.cis.2023.102972.
(472) Bannon, S. M.; Geise, G. M. Influence of Donnan and Dielectric Exclusion on Ion Sorption in Sulfonated Polysulfones. Journal of Membrane Science **2024**, 122396. https://doi.org/10.1016/j.memsci.2023.122396.
(473) Ji, Y.; Luo, H.; Geise, G. M. Specific Co-Ion Sorption and Diffusion Properties Influence Membrane Permselectivity. Journal of Membrane Science **2018**, 563, 492–504. https://doi.org/10.1016/j.memsci.2018.06.010.
(474) Boyce, M. C.; Arruda, E. M. Swelling and Mechanical Stretching of Elastomeric Materials. Mathematics and Mechanics of Solids **2001**, 6 (6), 641–659. https://doi.org/10.1177/108128650100600605.

(475) Treolar, L. R. G. The Physics of Rubber Elasticity 3rd Ed. **1975**.
(476) Zhong, M.; Wang, R.; Kawamoto, K.; Olsen, B. D.; Johnson, J. A. Quantifying the Impact of Molecular Defects on Polymer Network Elasticity. Science **2016**, 353 (6305), 1264–1268. https://doi.org/10.1126/science.aag0184.
(477) Fan, J.; Willdorf-Cohen, S.; Schibli, E. M.; Paula, Z.; Li, W.; Skalski, T. J. G.; Sergeenko, A. T.; Hohenadel, A.; Frisken, B. J.; Magliocca, E.; Mustain, W. E.; Diesendruck, C. E.; Dekel, D. R.; Holdcroft, S. Poly(Bis-Arylimidazoliums) Possessing High Hydroxide Ion Exchange Capacity and High Alkaline Stability. Nat Commun **2019**, 10 (1), 2306. https://doi.org/10.1038/s41467-019-10292-z.
(478) Salas-de la Cruz, D.; Green, M. D.; Ye, Y.; Elabd, Y. A.; Long, T. E.; Winey, K. I. Correlating Backbone-to-Backbone Distance to Ionic Conductivity in Amorphous Polymerized Ionic Liquids. Journal of Polymer Science Part B: Polymer Physics **2012**, 50 (5), 338–346. https://doi.org/10.1002/polb.23019.
(479) Okay, O. Macroporous Copolymer Networks. Prog. Polym. Sci. **2000**, 25 (6), 711–779. https://doi.org/10.1016/S0079-6700(00)00015-0.
(480) DuChanois, R. M.; Porter, C. J.; Violet, C.; Verduzco, R.; Elimelech, M. Membrane Materials for Selective Ion Separations at the Water–Energy Nexus. Advanced Materials **2021**, 33 (38), 1–18. https://doi.org/10.1002/adma.202101312.
(481) Luo, T.; Abdu, S.; Wessling, M. Selectivity of Ion Exchange Membranes: A Review. Journal of Membrane Science **2018**, 555, 429–454. https://doi.org/10.1016/j.memsci.2018.03.051.
(482) DuChanois, R. M.; Cooper, N. J.; Lee, B.; Patel, S. K.; Mazurowski, L.; Graedel, T. E.; Elimelech, M. Prospects of Metal Recovery from Wastewater and Brine. Nat Water **2023**, 1 (1), 37–46. https://doi.org/10.1038/s44221-022-00006-z.
(483) Foo, Z. H.; Thomas, J. B.; Heath, S. M.; Garcia, J. A.; Lienhard, J. H. Sustainable Lithium Recovery from Hypersaline Salt-Lakes by Selective Electrodialysis: Transport and Thermodynamics. Environ. Sci. Technol. **2023**, 57 (39), 14747–14759. https://doi.org/10.1021/acs.est.3c04472.
(484) Zhang, J.; Cheng, Z.; Qin, X.; Gao, X.; Wang, M.; Xiang, X. Recent Advances in Lithium Extraction from Salt Lake Brine Using Coupled and Tandem Technologies. Desalination **2023**, 547, 116225. https://doi.org/10.1016/j.desal.2022.116225.
(485) Razmjou, A.; Asadnia, M.; Hosseini, E.; Habibnejad Korayem, A.; Chen, V. Design Principles of Ion Selective Nanostructured Membranes for the Extraction of Lithium Ions. Nat Commun **2019**, 10 (1), 5793. https://doi.org/10.1038/s41467-019-13648-7.
(486) Zhang, Y.; Wang, L.; Sun, W.; Hu, Y.; Tang, H. Membrane Technologies for Li+/Mg2+ Separation from Salt-Lake Brines and Seawater: A Comprehensive Review. Journal of Industrial and Engineering Chemistry **2020**, 81, 7–23. https://doi.org/10.1016/j.jiec.2019.09.002.
(487) Vautier, C.; Kolbe, T.; Babey, T.; Marçais, J.; Abbot, B. W.; Laverman, A. M.; Thomas, Z.; Aquilina, L.; Pinay, G.; de Dreuzy, J.-R. What Do We Need to Predict Groundwater Nitrate Recovery Trajectories? Science of the Total Environment **2021**, 788, 147661. https://doi.org/10.1016/j.scitotenv.2021.147661.
(488) Mohapatra, M.; Anand, S.; Mishra, B. K.; Giles, D. E.; Singh, P. Review of Fluoride Removal from Drinking Water. Journal of Environmental Management **2009**, 91 (1), 67–77. https://doi.org/10.1016/j.jenvman.2009.08.015.

(489) IAEA. New Developments and Improvements in Processing of "Problematic" Radioactive Waste; IAEA-TECDOC-1579; International Atomic Energy Agency: Vienna, 2007.
(490) IAEA. Remediation of Large Contaminated Areas Off-Site the Fukushima Dai-Ichi NPP; Japan, 2011. https://www.iaea.org/sites/default/files/reportonfukushima2011.pdf (accessed 2024-05-27).
(491) Sholl, D. S.; Lively, R. P. Seven Chemical Separations to Change the World. Nature **2016**, 532 (7600), 435–437. https://doi.org/10.1038/532435a.
(492) Fan, H.; Huang, Y.; Yip, N. Y. Advancing Ion-Exchange Membranes to Ion-Selective Membranes: Principles, Status, and Opportunities. Front. Environ. Sci. Eng. **2022**, 17 (2), 25. https://doi.org/10.1007/s11783-023-1625-0.
(493) Jiang, S.; Sun, H.; Wang, H.; Ladewig, B. P.; Yao, Z. A Comprehensive Review on the Synthesis and Applications of Ion Exchange Membranes. Chemosphere **2021**, 282 (March), 130817. https://doi.org/10.1016/j.chemosphere.2021.130817.
(494) Rodríguez-Vázquez, N.; Fuertes, A.; Amorín, M.; Granja, J. R. Chapter 14: Bioinspired Artificial Sodium and Potassium Ion Channels. In The Alkali Metal Ions: Their Role for Life; Springer International Publishing: Switzerland, 2016; Vol. 16, pp 485–556.
(495) McCutcheon, J. R.; Mauter, M. S. Fixing the Desalination Membrane Pipeline. Science **2023**, 380 (6642), 242–244. https://doi.org/10.1126/science.ade5313.
(496) Raggam, S.; Mohammad, M.; Choo, Y.; Naidu, G.; Zargar, M.; Shon, H. K.; Razmjou, A. Advances in Metal Organic Framework (MOF) – Based Membranes and Adsorbents for Lithium-Ion Extraction. Separation and Purification Technology **2023**, 307, 122628. https://doi.org/10.1016/j.seppur.2022.122628.
(497) Rahighi, R.; Hosseini-Hosseinabad, S. M.; Zeraati, A. S.; Suwaileh, W.; Norouzi, A.; Panahi, M.; Gholipour, S.; Karaman, C.; Akhavan, O.; Khollari, M. A. R.; Vinu, A.; Rashidi, A.; Abdala, A.; Karimi-Maleh, H.; Orooji, Y. Two-Dimensional Materials in Enhancement of Membrane-Based Lithium Recovery from Metallic-Ions-Rich Wastewaters: A Review. Desalination **2022**, 543, 116096. https://doi.org/10.1016/j.desal.2022.116096.
(498) Collins, K. D. The Behavior of Ions in Water Is Controlled by Their Water Affinity. Quart. Rev. Biophys. **2019**, 52, e11. https://doi.org/10.1017/S0033583519000106.
(499) Moghaddam, S. Z.; Thormann, E. The Hofmeister Series: Specific Ion Effects in Aqueous Polymer Solutions. Journal of Colloid and Interface Science **2019**, 555, 615–635. https://doi.org/10.1016/j.jcis.2019.07.067.
(500) Hofmeister, F. Zur Lehre von Der Wirkung Der Salze. Arch. Exp. Path. Pharm. **1888**, 24, 247–260. https://doi.org/10.1007/BF01918191.
(501) Collins, K. D. Charge Density-Dependent Strength of Hydration and Biological Structure. Biophysical Journal **1997**, 72 (1), 65–76. https://doi.org/10.1016/S0006-3495(97)78647-8.
(502) Tansel, B. Significance of Thermodynamic and Physical Characteristics on Permeation of Ions during Membrane Separation: Hydrated Radius, Hydration Free Energy and Viscous Effects. Separation and Purification Technology **2012**, 86, 119–126. https://doi.org/10.1016/j.seppur.2011.10.033.
(503) Collins, K. D. Ion Hydration: Implications for Cellular Function, Polyelectrolytes, and Protein Crystallization. Biophysical Chemistry **2006**, 119 (3), 271–281. https://doi.org/10.1016/j.bpc.2005.08.010.
(504) Pearson, R. G. Hard and Soft Acids and Bases. J. Am. Chem. Soc. **1963**, 85 (22), 3533–3539. https://doi.org/10.1021/ja00905a001.

(505) Cassady, H. J.; Cimino, E. C.; Kumar, M.; Hickner, M. A. Specific Ion Effects on the Permselectivity of Sulfonated Poly(Ether Sulfone) Cation Exchange Membranes. Journal of Membrane Science **2016**, 508, 146–152. https://doi.org/10.1016/j.memsci.2016.02.048.
(506) Geise, G. M.; Cassady, H. J.; Paul, D. R.; Logan, B. E.; Hickner, M. A. Specific Ion Effects on Membrane Potential and the Permselectivity of Ion Exchange Membranes. Phys. Chem. Chem. Phys. **2014**, 16 (39), 21673–21681. https://doi.org/10.1039/C4CP03076A.
(507) Ji, Y.; Luo, H.; Geise, G. M. Effects of Fixed Charge Group Physicochemistry on Anion Exchange Membrane Permselectivity and Ion Transport. Phys. Chem. Chem. Phys. **2020**, 22 (14), 7283–7293. https://doi.org/10.1039/D0CP00018C.
(508) Sata, T.; Yamaguchi, T.; Matsusaki, K. Effect of Hydrophobicity of Ion Exchange Groups of Anion Exchange Membranes on Permselectivity between Two Anions. J. Phys. Chem. **1995**, 99 (34), 12875–12882. https://doi.org/10.1021/j100034a028.
(509) Díaz, J. C.; Park, J.; Shapiro, A.; Patel, H.; Santiago-Pagán, L.; Kitto, D.; Kamcev, J. Understanding Monovalent Cation Diffusion in Negatively Charged Membranes and the Role of Membrane Water Content. Macromolecules **2024**, 57 (5), 2468–2481. https://doi.org/10.1021/acs.macromol.3c02655.
(510) Epsztein, R.; Shaulsky, E.; Qin, M.; Elimelech, M. Activation Behavior for Ion Permeation in Ion-Exchange Membranes: Role of Ion Dehydration in Selective Transport. Journal of Membrane Science **2019**, 580, 316–326. https://doi.org/10.1016/j.memsci.2019.02.009.
(511) Ritt, C. L.; Liu, M.; Pham, T. A.; Epsztein, R.; Kulik, H. J.; Elimelech, M. Machine Learning Reveals Key Ion Selectivity Mechanisms in Polymeric Membranes with Subnanometer Pores. Sci. Adv. **2022**, 8 (2), eabl5771. https://doi.org/10.1126/sciadv.abl5771.
(512) Diederichsen, K. M.; Buss, H. G.; McCloskey, B. D. The Compensation Effect in the Vogel-Tammann-Fulcher (VTF) Equation for Polymer-Based Electrolytes. Macromolecules **2017**, 50 (10), 3831–3840. https://doi.org/10.1021/acs.macromol.7b00423.
(513) Prabhakar, R. S.; Raharjo, R.; Toy, L. G.; Lin, H.; Freeman, B. D. Self-Consistent Model of Concentration and Temperature Dependence of Permeability in Rubbery Polymers. Industrial & Engineering Chemistry Research **2005**, 44 (5), 1547–1556. https://doi.org/10.1021/ie0492909.
(514) Shefer, I.; Lopez, K.; Straub, A. P.; Epsztein, R. Applying Transition-State Theory to Explore Transport and Selectivity in Salt-Rejecting Membranes: A Critical Review. Environ. Sci. Technol. **2022**, 56 (12), 7467–7483. https://doi.org/10.1021/acs.est.2c00912.
(515) Shefer, I.; Peer-Haim, O.; Epsztein, R. Limited Ion-Ion Selectivity of Salt-Rejecting Membranes Due to Enthalpy-Entropy Compensation. Desalination **2022**, 541, 116041. https://doi.org/10.1016/j.desal.2022.116041.
(516) Ahrland, S. Scales of Softness for Acceptors and Donors. Chemical Physics Letters **1968**, 2 (5), 303–306. https://doi.org/10.1016/0009-2614(68)80081-8.
(517) Ahrland, S. Thermodynamics of Complex Formation between Hard and Soft Acceptors and Donors. In Structure and Bonding; Structure and Bonding; Springer Berlin Heidelberg: Berlin, Heidelberg, 1968; Vol. 5, pp 118–149. https://doi.org/10.1007/BFb0118849.
(518) Ahrland, S.; Chatt, J.; Davies, N. R. The Relative Affinities of Ligand Atoms for Acceptor Molecules and Ions. Q. Rev., Chem. Soc. **1958**, 12 (3), 265. https://doi.org/10.1039/qr9581200265.
(519) Pearson, R. G. Acids and Bases: Hard Acids Prefer to Associate with Hard Bases, and Soft Acids Prefer to Associate with Soft Bases. Science **1966**, 151 (3707), 172–177. https://doi.org/10.1126/science.151.3707.172.

(520) Marcus, Y. The Softness Parameters of Ions. Prediction of the Occurrence of Miscibility Gaps in Molten Salt Mixtures. Israel Journal of Chemistry **1972**, 10 (3), 659–683. https://doi.org/10.1002/ijch.197200065.
(521) Marcus, Y. On Enthalpies of Hydration, Ionization Potentials, and the Softness of Ions. Thermochimica Acta **1986**, 104, 389–394. https://doi.org/10.1016/0040-6031(86)85213-3.
(522) Robinson, R. A.; Stokes, R. H. Electrolyte Solutions, 2nd, rev ed.; Dover Publications, Inc.: Mineola, 1965.
(523) Tran, T.; Lin, C.; Chaurasia, S.; Lin, H. Elucidating the Relationship between States of Water and Ion Transport Properties in Hydrated Polymers. Journal of Membrane Science **2019**, 574 (December 2018), 299–308. https://doi.org/10.1016/j.memsci.2018.12.059.
(524) Vondrasek, B.; Wen, C.; Cheng, S.; Riffle, J. S.; Lesko, J. J. On the Nature of Freezing/Melting Water in Ionic Polysulfones. Macromolecules **2021**, 54 (13), 6477–6488. https://doi.org/10.1021/acs.macromol.1c00591.
(525) Espinoza, C.; Díaz, J.; Kitto, D.; Kim, H.; Kamcev, J. Bound Water Enhances the Ion Selectivity of Highly Charged Polymer Membranes. ACS Appl. Mater. Interfaces **2024**, under review.
(526) Higuchi, A.; Ijima, T. DSC Investigation of the States of Water in Poly(Vinyl Alcohol) Membranes. Polymer **1985**, 26, 1207–1211.
(527) Hodge, R. M.; Edward, G. H.; Simon, G. P. Water Absorption and States of Water in Semicrystalline Poly(Vinyl Alcohol) Films. Polymer **1996**, 37 (8), 1371–1376. https://doi.org/10.1016/0032-3861(96)81134-7.
(528) Kingsbury, R. S.; Zhu, S.; Flotron, S.; Coronell, O. Microstructure Determines Water and Salt Permeation in Commercial Ion-Exchange Membranes. ACS Appl. Mater. Interfaces **2018**, 10 (46), 39745–39756. https://doi.org/10.1021/acsami.8b14494.
(529) Holzer, L.; Marmet, P.; Fingerle, M.; Wiegmann, A.; Neumann, M.; Schmidt, V. Tortuosity-Porosity Relationships: Review of Empirical Data from Literature. In Tortuosity and Microstructure Effects in Porous Media: Classical Theories, Empirical Data and Modern Methods; Holzer, L., Marmet, P., Fingerle, M., Wiegmann, A., Neumann, M., Schmidt, V., Eds.; Springer Series in Materials Science; Springer International Publishing: Cham, 2023; pp 51–89. https://doi.org/10.1007/978-3-031-30477-4_3.
(530) Tjaden, B.; Cooper, S. J.; Brett, D. J.; Kramer, D.; Shearing, P. R. On the Origin and Application of the Bruggeman Correlation for Analysing Transport Phenomena in Electrochemical Systems. Current Opinion in Chemical Engineering **2016**, 12, 44–51. https://doi.org/10.1016/j.coche.2016.02.006.
(531) Welty, J.; Wicks, C.; Wilson, R.; Rorrer, G. Fundamentals of Momentum, Heat and Mass Transfer, 5th Edition, 5th ed.; John Wiley & Sons, Inc, 2008.
(532) Holzer, L.; Marmet, P.; Fingerle, M.; Wiegmann, A.; Neumann, M.; Schmidt, V. Tortuosity-Porosity Relationships: Review of Empirical Data from Literature. In Tortuosity and Microstructure Effects in Porous Media: Classical Theories, Empirical Data and Modern Methods; Holzer, L., Marmet, P., Fingerle, M., Wiegmann, A., Neumann, M., Schmidt, V., Eds.; Springer Series in Materials Science; Springer International Publishing: Cham, 2023; pp 51–89. https://doi.org/10.1007/978-3-031-30477-4_3.
(533) Da Silva, M. T. Q. S.; Do Rocio Cardoso, M.; Veronese, C. M. P.; Mazer, W. Tortuosity: A Brief Review. Materials Today: Proceedings **2022**, 58, 1344–1349. https://doi.org/10.1016/j.matpr.2022.02.228.

(534) Galizia, M.; Manning, G. S.; Paul, D. R.; Freeman, B. D. Ion Partitioning between Brines and Ion Exchange Polymers. Polymer **2019**, 165, 91–100. https://doi.org/10.1016/j.polymer.2019.01.026.
(535) Thomas, E.; Vijayalakshmi, K. P.; George, B. K. Kinetic Stability of Imidazolium Cations and Ionic Liquids: A Frontier Molecular Orbital Approach. Journal of Molecular Liquids **2019**, 276, 721–727. https://doi.org/10.1016/j.molliq.2018.12.034.
(536) Chen, H.; Choi, J.-H.; Salas-de La Cruz, D.; Winey, K. I.; Elabd, Y. A. Polymerized Ionic Liquids: The Effect of Random Copolymer Composition on Ion Conduction. Macromolecules **2009**, 42 (13), 4809–4816. https://doi.org/10.1021/ma900713e.
(537) Xiong, Y.-B.; Wang, H.; Wang, Y.-J.; Wang, R.-M. Novel Imidazolium-Based Poly(Ionic Liquid)s: Preparation, Characterization, and Absorption of CO2. Polymers for Advanced Technologies **2012**, 23 (5), 835–840. https://doi.org/10.1002/pat.1973.
(538) Schibli, E. M.; Wright, A. G.; Holdcroft, S.; Frisken, B. J. Morphology of Anion-Conducting Ionenes Investigated by X-Ray Scattering and Simulation. J. Phys. Chem. B **2018**, 122 (5), 1730–1737. https://doi.org/10.1021/acs.jpcb.7b10177.
(539) Flory, P. J. Principles of Polymer Chemistry, 1st ed.; George Banta Publishing Company: Ithaca, 1954.
(540) Menard, K. Dynamic Mechanical Analysis: A Practical Introduction; CRC Press, 1999. https://doi.org/10.1201/9781420049183.
(541) McCrum, N. G.; Read, B. E.; Williams, G. Anelastic and Dielectric Effects in Polymeric Solids, 2nd ed.; Dover Publications, Inc.: New York, 1991.
(542) Crank, J.; Park, G. S. Diffusion in Polymers, 1st ed.; Academic Press Inc.: New York, 1968.
(543) Masaro, L.; Zhu, X. X. Physical Models of Diffusion for Polymer Solutions, Gels, and Solids. Progress in Polymer Science **1999**, 24 (5), 731–775.
(544) Mackie, J. S.; Meares, P. The Diffusion of Electrolytes in a Cation-Exchange Resin Membrane. Proceedings of the Royal Society of London, Series A **1955**, 232 (1191), 498–509. https://doi.org/10.1098/rspa.1955.0234.